Versatility

by MicroVention

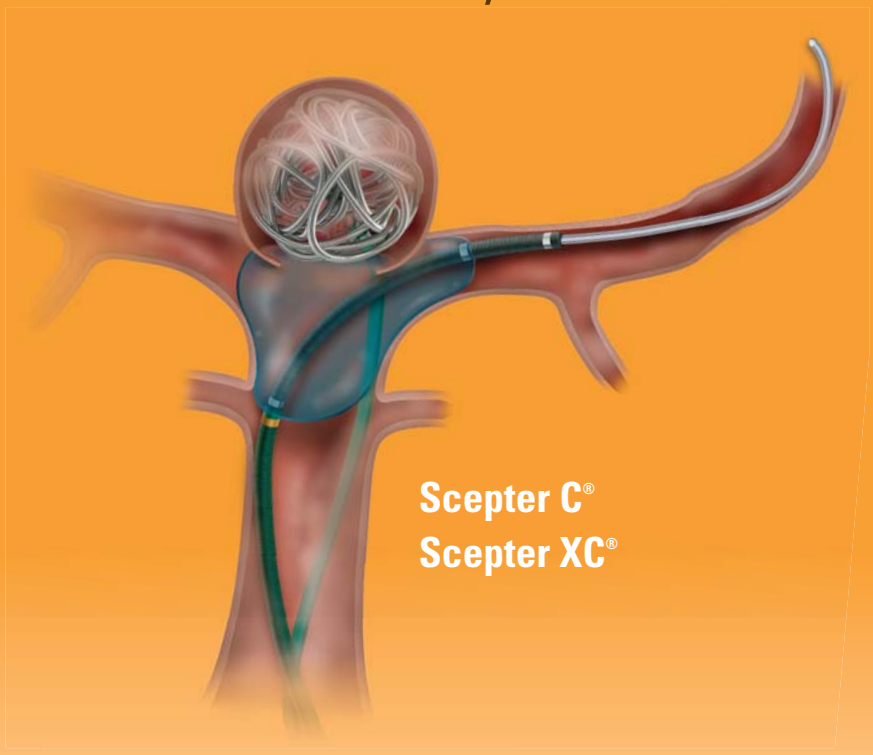

Scepter C®
Scepter XC®

Scepter
Occlusion Balloon Catheter

REDEFINING DELIVERABILITY, VERSATILITY AND CONTROL

MicroVention has developed two occlusion balloon catheters. **Scepter C®** compliant balloon is designed for reliable vessel occlusion yet conforms to vessel anatomy. **Scepter XC®** x-tra compliant balloon conforms to extremely complex anatomies where neck coverage is more challenging.

• *Used with* Headway Microcatheter

For more information or a product demonstration, contact your local MicroVention representative:

MicroVention® TERUMO

MicroVention, Inc.
Worldwide Headquarters PH +1.714.247.8000
1311 Valencia Avenue
Tustin, CA 92780 USA
MicroVention UK Limited PH +44 (0) 191 258 6777
MicroVention Europe, S.A.R.L. PH +33 (1) 39 21 77 46
MicroVention Deutschland GmbH PH +49 211 210 798-0

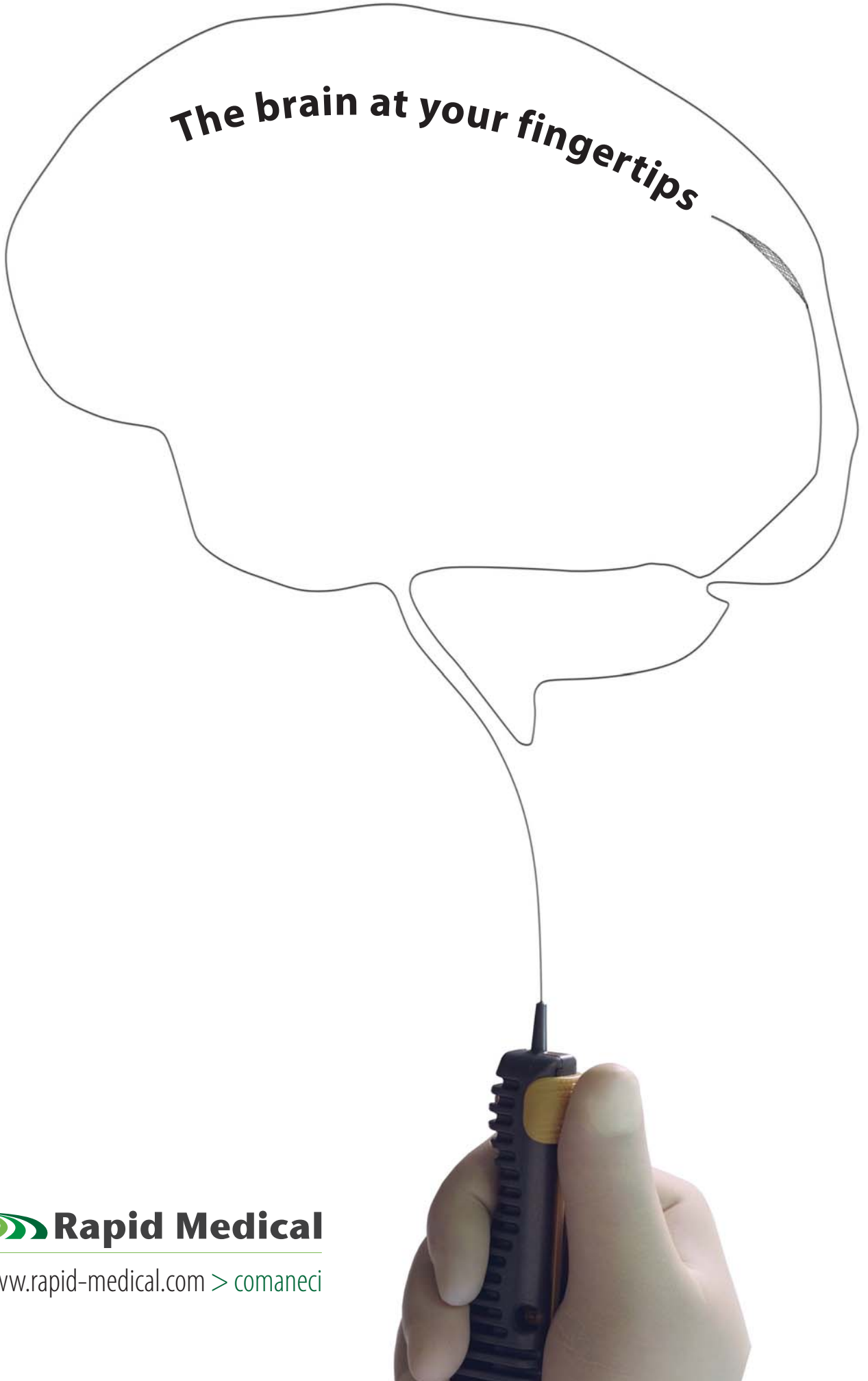

Rapid Medical

www.rapid-medical.com > comaneci

COILING OPTIMIZED

NOW AVAILABLE

BARRICADE COMPLEX FINISHING COIL

- Extremely soft profile of The Barricade Finishing coil now in a complex shape
- Excellent microcatheter stability for confident coil placement
- Available in a size range of 1mm-5mm

BARRICADE™ COIL SYSTEM

MADE IN AMERICA

The Barricade Coil System is intended for the endovascular embolization of intracranial aneurysms and other neurovascular abnormalities such as arteriovenous malformations and arteriovenous fistulae. The System is also intended for vascular occlusion of blood vessels within the neurovascular system to permanently obstruct blood flow to an aneurysm or other vascular malformation and for arterial and venous embolizations in the peripheral vasculature. Refer to the instructions for use for complete product information.

18 TECHNOLOGY DRIVE #169, IRVINE CA 92618
p: 949.788.1443 | f: 949.788.1444

WWW.BLOCKADEMEDICAL.COM

MKTG-031 Rev. A

BLOCKADE MEDICAL

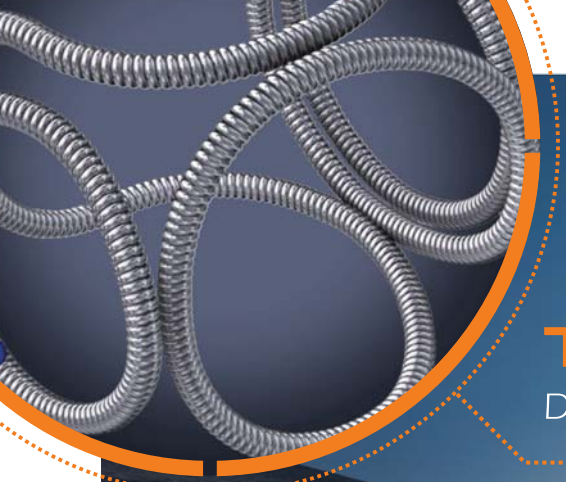

Target®
DETACHABLE COILS

Smooth and Stable

Whether you are framing, filling or finishing, Target Detachable Coils deliver consistently smooth deployment and exceptional microcatheter stability. Focused on design, Target Coils feature a host of advantages to ensure the high-powered performance you demand.

For more information, please visit www.strykerneurovascular.com/Target or contact your local Stryker Neurovascular sales representative.

stryker® Neurovascular

Stroke: *Our Only Focus. Our Ongoing Promise.*

AJNR

CALL FOR AJNR EDITORIAL FELLOWSHIP CANDIDATES

ASNR and AJNR are pleased once again to join efforts with other imaging-related journals that have training programs on editorial aspects of publishing for trainees or junior staff (3–5 years after training), including Radiology (Olmsted fellowship), AJR (Figley and Rogers fellowships), JACR (Bruce J. Hillman fellowship), and Radiologia.

2016 Candidate Information and Requirements

GOALS

- Increase interest in "editorial" and publication-related activities in younger individuals.
- Increase understanding and participation in the AJNR review process.
- Incorporate into AJNR's Editorial Board younger individuals who have previous experience in the review and publication process.
- Fill a specific need in neuroradiology not offered by other similar fellowships.
- Increase the relationship between "new" generation of neuroradiologists and more established individuals.
- Increase visibility of AJNR among younger neuroradiologists.

ACTIVITIES OF THE FELLOWSHIP

- Serve as Editorial Fellow for one year. This individual will be listed on the masthead as such.
- Review at least one manuscript per month for 12 months. Evaluate all review articles submitted to AJNR.
- Access to our electronic manuscript review system will be granted so that the candidate can learn how these systems work.
- Be involved in the final decision of selected manuscripts together with the Editor-in-Chief.
- Participate in all monthly Senior Editor telephone conference calls.
- Participate in all meetings of the Editors and Publications Committee during the annual meetings of ASNR and RSNA as per candidate's availability. The Foundation of the ASNR will provide $2000 funding for this activity.
- Evaluate progress and adjust program to specific needs in annual meeting or telephone conference with the Editor-in-Chief.
- Write at least one editorial for AJNR.
- Embark on an editorial scientific or bibliometric project that will lead to the submission of an article to AJNR or another appropriate journal as determined by the Editor-in-Chief. This project will be presented by the Editorial Fellow at the ASNR annual meeting.
- Serve as liaison between AJNR and ASNR's Young Professionals Network and the 3 YPs appointed to AJNR as special consultants. Participate in meetings and telephone calls with this group. Design one electronic survey/year polling the group regarding readership attitudes and wishes.
- Recruit trainees as reviewers as determined by the Editor-in-Chief.
- Participate in Web improvement projects.
- Invite Guest Editors for AJNR's News Digest to cover a variety of timely topics.

QUALIFICATIONS

- Be a fellow in neuroradiology from North America, including Canada (this may be extended to include other countries).
- Be a junior faculty neuroradiology member (< 3 years) in either an academic or private environment.
- Be an "in-training" or member of ASNR in any other category.

APPLICATION

- Include a short letter of intent with statement of goals and desired research project. CV must be included.
- Include a letter of recommendation from the Division Chief or fellowship program director. A statement of protected time to perform the functions outlined is desirable.
- Applications will be evaluated by AJNR's Senior Editors and the Chair of the Publications Committee prior to the ASNR meeting. The name of the selected individual will be announced at the meeting.
- Applications should be received by March 4, 2016 and sent to Ms. Karen Halm, AJNR Managing Editor, electronically at khalm@asnr.org.

AJNR

AMERICAN JOURNAL OF NEURORADIOLOGY

Publication Preview at www.ajnr.org features articles released in advance of print. Visit www.ajnrblog.org to comment on AJNR content and chat with colleagues and AJNR's News Digest at http://ajnrdigest.org to read the stories behind the latest research in neuroimaging.

DECEMBER 2015 • VOLUME 36 • NUMBER 12 • WWW.AJNR.ORG

AJNR (Am J Neuroradiol ISSN 0195–6108) is a journal published monthly, owned and published by the American Society of Neuroradiology (ASNR), 800 Enterprise Drive, Suite 205, Oak Brook, IL 60523. Annual dues for the ASNR include $170.00 for journal subscription. The journal is printed by Cadmus Journal Services, 5457 Twin Knolls Road, Suite 200, Columbia, MD 21045; Periodicals postage paid at Oak Brook, IL and additional mailing offices. Printed in the U.S.A. POSTMASTER: Please send address changes to American Journal of Neuroradiology, P.O. Box 3000, Denville, NJ 07834, U.S.A. Subscription rates: nonmember $380 ($450 foreign) print and online, $305 online only; institutions $440 ($510 foreign) print and basic online, $875 ($940 foreign) print and extended online, $365 online only (basic), extended online $790; single copies are $35 each ($40 foreign). Indexed by PubMed/Medline, BIOSIS Previews, Current Contents (Clinical Medicine and Life Sciences), EMBASE, Google Scholar, HighWire Press, Q-Sensei, RefSeek, Science Citation Index, and SCI Expanded.

ASNR 2016
Washington, DC

ASFNR • ASHNR • ASPNR • ASSR • SNIS

THE FOUNDATION OF THE ASNR

THE FOUNDATION OF THE ASNR SYMPOSIUM 2016: EMERGENCY NEURORADIOLOGY
MAY 21-22

ASNR 54TH ANNUAL MEETING
MAY 23-26

Howard A. Rowley, MD, ASNR 2016 Program Chair/President-Elect
Programming developed in cooperation with …

American Society of Functional Neuroradiology (ASFNR)
Christopher G. Filippi, MD

American Society of Head and Neck Radiology (ASHNR)
Lindell R. Gentry, MD

American Society of Pediatric Neuroradiology (ASPNR)
Erin Simon Schwartz, MD

American Society of Spine Radiology (ASSR)
Gregory J. Lawler, MD

Society of NeuroInterventional Surgery (SNIS)
Charles J. Prestigiacomo, MD

American Society of Neuroradiology (ASNR) Committee Programming:
Health Policy Committee
Robert M. Barr, MD, FACR

Computer Science and Informatics (CSI) Committee
John L. Go, MD, FACR

Research Scientists Committee
Dikoma C. Shungu, PhD

ABSTRACT DEADLINE:
Friday, December 11, 2015
Please visit www.asnr.org/2016
for more information

ASNR 54TH ANNUAL MEETING
c/o American Society of Neuroradiology
800 Enterprise Drive, Suite 205
Oak Brook, Illinois 60523-4216
Phone: 630-574-0220
Fax: 630 574-0661
www.asnr.org/2016

SCAN NOW
TO VISIT
OUR WEBSITE

SAVE THE DATE... MAY 21-26, 2016
WASHINGTON MARRIOTT WARDMAN PARK • WASHINGTON, DC


European Congress of Radiology
ECR
2016
Vienna
March 2–6
Register Now!
myESR.org

Multidisciplinary Patient Centered Approach:
Synergy of Imaging and Procedures in the Accurate Diagnosis and Treatment of Spinal Disorders

Vendor Sponsored Hands-On Spine Procedures Workshops!

Diagnostic and Interventional Sessions on:

- Spinal Stenosis and Degeneration
- Clinical Skills for the Interventional Spine Radiologist
- Pediatric Spine Imaging
- Advanced Interventional Spine Procedures
- The Valued Spine Imaging Report and Imaging Protocols
- The Operative Spine: Pre-op / Post-op Evaluation and Imaging
- Advanced Imaging Techniques

WORLD-RENOWNED SPEAKERS IN SPINE IMAGING AND PROCEDURES:

Michael T. Modic, MD - Cleveland Clinic Foundation
Jeffrey S. Ross, MD - Mayo Clinic
Wade H.M. Wong, DO - UCSD
Kieran P.J. Murphy, MD, FRCPC - Toronto General Hospital
Erin Simon Schwartz, MD - Children's Hospital of Philadelphia
Jeffrey A. Stone, MD, FACR - Mayo Clinic
Joshua A. Hirsch, MD, FACR, FSIR - Massachusetts General Hospital
Huy M. Do, MD - Stanford University Medical Center
Adam E. Flanders, MD - Thomas Jefferson University Hospital
Johan W. Van Goethem, MD, PhD - University Hospital Antwerp
Majda M. Thurner, MD - Medical University of Vienna
Meng Law, MD, MBBS, FRACR - Keck Medical Center of USC

ATTENTION ALL NON MEMBERS:
Become a member and get an immediate registration discount.
See online registration page for details!

AMERICAN SOCIETY OF SPINE RADIOLOGY
2016 ANNUAL SYMPOSIUM

FEBRUARY 18-21, 2016 - PRESIDENTS' WEEK

HYATT REGENCY COCONUT POINT RESORT AND SPA • BONITA SPRINGS, FLORIDA

20.5 AMA PRA CATEGORY 1 CREDIT(S)™

Specific Sessions of the meeting program will be submitted to the ABR for SAM qualification.

REGISTER NOW!

Visit the ASSR website for registration/hotel links and more information:

www.theASSR.org

Abstract submission deadline is December 21, 2015

Diseases Speak, TOMOgraphically

- 65th Annual Meeting of CTSR
- SCCT Taiwan Forum 2016

March 19-20, 2016, Kaohsiung, Taiwan

Hosted by Chinese Taipei Society of Radiology (CTSR)
The Neuroradiological Society of Taiwan (NRST)
Kaohsiung Veterans General Hospital / E-Da Hospital
SCCT Taiwan IRC

Secretariat 2F, No. 63, Sec. III, Chong-Qing N. Road, Taipei, 10362, Taiwan
Tel: +886-2-25865331~32 Fax: +886-2-25865330
EMail: office@rsroc.org.tw
WebSite: https://www.rsroc.org.tw

CTSR
Chinese Taipei Society of Radiology

wfnrs The World Federation of Neuroradiological Societies
NRST Neuroradiological Society of Taiwan

www.snr2018.org

SNR
XXI Symposium Neuroradiologicum
The World Congress of Neuroradiology
March 19-24, 2018 Taipei Taiwan

One World One Family

Symposium President
Professor Wan-Yuo GUO, M.D., Ph.D.

Symposium Vice-Presidents
Professor Yukunori KOROGI, M.D., Ph.D. (Japan)
Professor Sang-Joon KIM, M.D., Ph.D. (Korea)
Professor Sandy CY CHEN, M.D. (Taiwan)
Professor Ho-Fai WONG, M.D. (Taiwan)

Target® Detachable Coil

See package insert for complete indications, contraindications, warnings and instructions for use.

INTENDED USE / INDICATIONS FOR USE
Target Detachable Coils are intended to endovascularly obstruct or occlude blood flow in vascular abnormalities of the neurovascular and peripheral vessels.

Target Detachable Coils are indicated for endovascular embolization of:
- Intracranial aneurysms
- Other neurovascular abnormalities such as arteriovenous malformations and arteriovenous fistulae
- Arterial and venous embolizations in the peripheral vasculature

CONTRAINDICATIONS
None known.

POTENTIAL ADVERSE EVENTS
Potential complications include, but are not limited to: allergic reaction, aneurysm perforation and rupture, arrhythmia, death, edema, embolus, headache, hemorrhage, infection, ischemia, neurological/intracranial sequelae, post-embolization syndrome (fever, increased white blood cell count, discomfort), TIA/stroke, vasospasm, vessel occlusion or closure, vessel perforation, dissection, trauma or damage, vessel rupture, vessel thrombosis. Other procedural complications including but not limited to: anesthetic and contrast media risks, hypotension, hypertension, access site complications.

WARNINGS
- Contents supplied STERILE using an ethylene oxide (EO) process. Do not use if sterile barrier is damaged. If damage is found, call your Stryker Neurovascular representative.
- For single use only. Do not reuse, reprocess or resterilize. Reuse, reprocessing or resterilization may compromise the structural integrity of the device and/or lead to device failure which, in turn, may result in patient injury, illness or death. Reuse, reprocessing or resterilization may also create a risk of contamination of the device and/or cause patient infection or cross-infection, including, but not limited to, the transmission of infectious disease(s) from one patient to another. Contamination of the device may lead to injury, illness or death of the patient.
- After use, dispose of product and packaging in accordance with hospital, administrative and/or local government policy.
- **This device should only be used by physicians who have received appropriate training in interventional neuroradiology or interventional radiology and preclinical training on the use of this device as established by Stryker Neurovascular.**
- Patients with hypersensitivity to 316LVM stainless steel may suffer an allergic reaction to this implant.
- MR temperature testing was not conducted in peripheral vasculature, arteriovenous malformations or fistulae models.
- The safety and performance characteristics of the Target Detachable Coil System (Target Detachable Coils, InZone Detachment Systems, delivery systems and accessories) have not been demonstrated with other manufacturer's devices (whether coils, coil delivery devices, coil detachment systems, catheters, guidewires, and/or other accessories). Due to the potential incompatibility of non Stryker Neurovascular devices with the Target Detachable Coil System, the use of other manufacturer's device(s) with the Target Detachable Coil System is not recommended.
- To reduce risk of coil migration, the diameter of the first and second coil should never be less than the width of the ostium.
- In order to achieve optimal performance of the Target Detachable Coil System and to reduce the risk of thromboembolic complications, it is critical that a continuous infusion of appropriate flush solution be maintained between a) the femoral sheath and guiding catheter, b) the 2-tip microcatheter and guiding catheters, and c) the 2-tip microcatheter and Stryker Neurovascular guidewire and delivery wire. Continuous flush also reduces the potential for thrombus formation on, and crystallization of infusate around, the detachment zone of the Target Detachable Coil.
- Do not use the product after the "Use By" date specified on the package.
- Reuse of the flush port/dispenser coil or use with any coil other than the original coil may result in contamination of, or damage to, the coil.
- Utilization of damaged coils may affect coil delivery to, and stability inside, the vessel or aneurysm, possibly resulting in coil migration and/or stretching.
- The fluoro-saver marker is designed for use with a Rotating Hemostatic Valve (RHV). If used without an RHV, the distal end of the coil may be beyond the alignment marker when the fluoro-saver marker reaches the microcatheter hub.
- If the fluoro-saver marker is not visible, do not advance the coil without fluoroscopy.
- Do not rotate delivery wire during or after delivery of the coil. Rotating the Target Detachable Coil delivery wire may result in a stretched coil or premature detachment of the coil from the delivery wire, which could result in coil migration.
- Verify there is no coil loop protrusion into the parent vessel after coil placement and prior to coil detachment. Coil loop protrusion after coil placement may result in thromboembolic events if the coil is detached.
- Verify there is no movement of the coil after coil placement and prior to coil detachment. Movement of the coil after coil placement may indicate that the coil could migrate once it is detached.
- Failure to properly close the RHV compression fitting over the delivery wire before attaching the InZone® Detachment System could result in coil movement, aneurysm rupture or vessel perforation.
- Verify repeatedly that the distal shaft of the catheter is not under stress before detaching the Target Detachable Coil. Axial compression or tension forces could be stored in the 2-tip microcatheter causing the tip to move during coil delivery. Microcatheter tip movement could cause the aneurysm or vessel to rupture.
- Advancing the delivery wire beyond the microcatheter tip once the coil has been detached involves risk of aneurysm or vessel perforation.
- The long term effect of this product on extravascular tissues has not been established so care should be taken to retain this device in the intravascular space.

Damaged delivery wires may cause detachment failures, vessel injury or unpredictable distal tip response during coil deployment. If a delivery wire is damaged at any point during the procedure, do not attempt to straighten or otherwise repair it. Do not proceed with deployment or detachment. Remove the entire coil and replace with undamaged product.

- After use, dispose of product and packaging in accordance with hospital, administrative and/or local government policy.

CAUTIONS / PRECAUTIONS
- Federal Law (USA) restricts this device to sale by or on the order of a physician.
- Besides the number of InZone Detachment System units needed to complete the case, there must be an extra InZone Detachment System unit as back up.
- Removing the delivery wire without grasping the introducer sheath and delivery wire together may result in the detachable coil sliding out of the introducer sheath.
- Failure to remove the introducer sheath after inserting the delivery wire into the RHV of the microcatheter will interrupt normal infusion of flush solution and allow back flow of blood into the microcatheter.
- Some low level overhead light near or adjacent to the patient is required to visualize the fluoro-saver marker; monitor light alone will not allow sufficient visualization of the fluoro-saver marker.
- Advance and retract the Target Detachable Coil carefully and smoothly without excessive force. If unusual friction is noticed, slowly withdraw the Target Detachable Coil and examine for damage. If damage is present, remove and use a new Target Detachable Coil. If friction or resistance is still noted, carefully remove the Target Detachable Coil and microcatheter and examine the microcatheter for damage.
- If it is necessary to reposition the Target Detachable Coil, verify under fluoroscopy that the coil moves with a one-to-one motion. If the coil does not move with a one-to-one motion or movement is difficult, the coil may have stretched and could possibly migrate or break. Gently remove both the coil and microcatheter and replace with new devices.
- Increased detachment times may occur when:
  - Other embolic agents are present.
  - Delivery wire and microcatheter markers are not properly aligned.
  - Thrombus is present on the coil detachment zone.
- Do not use detachment systems other than the InZone Detachment System.
- Increased detachment times may occur when delivery wire and microcatheter markers are not properly aligned.
- Do not use detachment systems other than the InZone Detachment System.

Stryker Neurovascular
47900 Bayside Parkway
Fremont, CA 94538-6515

stryker.com/neurovascular

Date of Release: FEB/2014

EX_EN_US

Trevo® XP ProVue Retrievers

See package insert for complete indications, complications, warnings, and instructions for use.

INDICATIONS FOR USE
The Trevo Retriever is intended to restore blood flow in the neurovasculature by removing thrombus in patients experiencing ischemic stroke within 8 hours of symptom onset. Patients who are ineligible for intravenous tissue plasminogen activator (IV t-PA) or who fail IV t-PA therapy are candidates for treatment.

COMPLICATIONS
Procedures requiring percutaneous catheter introduction should not be attempted by physicians unfamiliar with possible complications which may occur during or after the procedure. Possible complications include, but are not limited to, the following: air embolism; hematoma or hemorrhage at puncture site; infection; distal embolization; pain/headache; vessel spasm, thrombosis, dissection, or perforation; emboli; acute occlusion; ischemia; intracranial hemorrhage; false aneurysm formation; neurological deficits including stroke; and death.

COMPATIBILITY
3x20 mm retrievers are compatible with Trevo® Pro 14 Microcatheters (REF 90231) and Trevo® Pro 18 Microcatheters (REF 90238). 4x20 mm retrievers are compatible with Trevo® Pro 18 Microcatheters (REF 90238). Compatibility of the Retriever with other microcatheters has not been established. Performance of the Retriever device may be impacted if a different microcatheter is used. The Merci® Balloon Guide Catheters are recommended for use during thrombus removal procedures. Retrievers are compatible with the Abbott Vascular DOC® Guide Wire Extension (REF 22260).

WARNINGS
- Contents supplied STERILE, using an ethylene oxide (EO) process. Nonpyrogenic.
- To reduce risk of vessel damage, adhere to the following recommendations:
  - Take care to appropriately size Retriever to vessel diameter at intended site of deployment.
  - Do not perform more than six (6) retrieval attempts in same vessel using Retriever devices.
  - Maintain Retriever position in vessel when removing or exchanging Microcatheter.
- To reduce risk of kinking/fracture, adhere to the following recommendations:
  - Immediately after unsheathing Retriever, position Microcatheter tip marker just proximal to shaped section. Maintain Microcatheter tip marker just proximal to shaped section of Retriever during manipulation and withdrawal.
  - Do not rotate or torque Retriever.
  - Use caution when passing Retriever through stented arteries.
- Do not resterilize and reuse. Structural integrity and/or function may be impaired by reuse or cleaning.
- The Retriever is a delicate instrument and should be handled carefully. Before use and when possible during procedure, inspect device carefully for damage. Do not use a device that shows signs of damage. Damage may prevent device from functioning and may cause complications.
- Do not advance or withdraw Retriever against resistance or significant vasospasm. Moving or torquing device against resistance or significant vasospasm may result in damage to vessel or device. Assess cause of resistance using fluoroscopy and if needed resheath the device to withdraw.
- If Retriever is difficult to withdraw from the vessel, do not torque Retriever. Advance Microcatheter distally, gently pull Retriever back into Microcatheter, and remove Retriever and Microcatheter as a unit. If undue resistance is met when withdrawing the Retriever into the Microcatheter, consider extending the Retriever using the Abbott Vascular DOC guidewire extension (REF 22260) so that the Microcatheter can be exchanged for a larger diameter catheter such as a DAC® catheter. Gently withdraw the Retriever into the larger diameter catheter.
- Administer anti-coagulation and anti-platelet medications per standard institutional guidelines.

PRECAUTIONS
- Prescription only – device restricted to use by or on order of a physician.
- Store in cool, dry, dark place.
- Do not use open or damaged packages.
- Use by "Use By" date.
- Exposure to temperatures above 54°C (130°F) may damage device and accessories. Do not autoclave.
- Do not expose Retriever to solvents.
- Use Retriever in conjunction with fluoroscopic visualization and proper anti-coagulation agents.
- To prevent thrombus formation and contrast media crystal formation, maintain a constant infusion of appropriate flush solution between guide catheter and Microcatheter and between Microcatheter and Retriever or guidewire.
- Do not attach a torque device to the shaped proximal end of DOC® Compatible Retriever. Damage may occur, preventing ability to attach DOC® Guide Wire Extension.

Concentric Medical
301 East Evelyn
Mountain View, CA 94041

EC REP

EMERGO Europe
Molenstraat 15
2513 BH, The Hague
The Netherlands

CE 0459

Stryker Neurovascular
47900 Bayside Parkway
Fremont, CA 94538-6515

stryker.com/neurovascular
stryker.com/emea/neurovascular

Date of Release: JUN/2014

EX_EN_GL

Advanced

by MicroVention

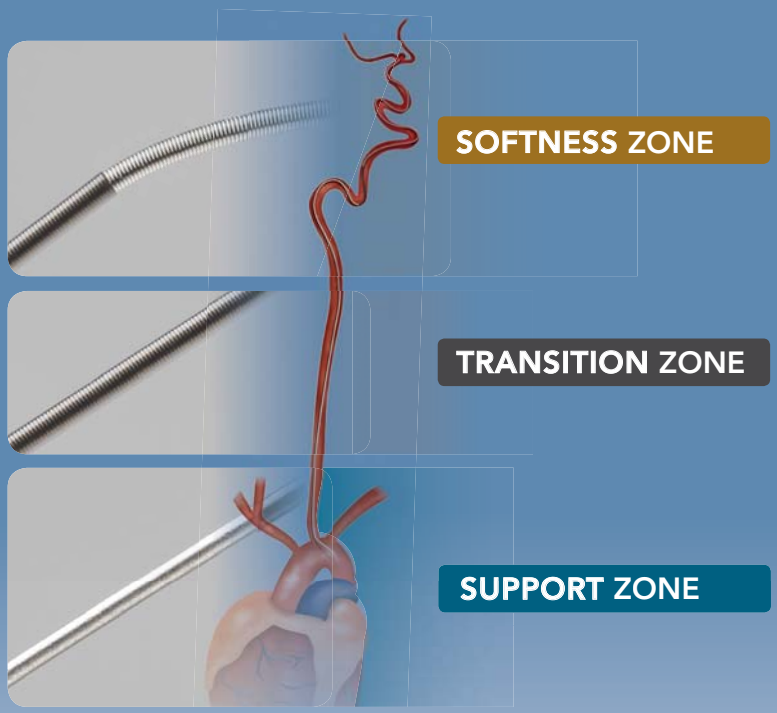

V-Trak® Advanced Coil System

ENHANCED CONTROL TO MAXIMIZE COIL PERFORMANCE

The **V-Trak® Advanced Coil System**, the next generation to power the performance of our most technically advanced line of coils. Offering the optimal combination of support and flexibility.

microvention.com

CE 0297

66%

of Patients in MR CLEAN Were Treated with a Trevo® Stent Retriever

stryker® Neurovascular

Trevo®

PROVUE RETRIEVER

MR CLEAN[1]

First clinical evidence for intra-arterial treatment with stent retrievers

- **Largest** of the randomized AIS trials[2], with over 500 patients enrolled
- The Trevo Retriever was the **#1** device used in the **MR CLEAN** Trial

[1] O.A. Berkhemer et al. A Randomized Trial for Intra-arterial Treatment for Acute Ischemic Stroke. *N Eng J Med* December 2014.
[2] MR CLEAN is the largest AIS Trial in which stent retrievers were used.
http://www.mrclean-trial.org/

Stroke: *Our Only Focus. Our Ongoing Promise.*

stryker®

From cervical to sacral **we've got you covered.**

Introducing the first PMMA indicated for treating pathological fractures of the sacrum.

Stryker set the bar in 2008 with the release of VertaPlex® HV, addressing specific viscosity and working time preferences for treating vertebral compression fractures. Now in 2015, VertaPlex® HV became the first PMMA to receive 510(k) clearance for the fixation of pathological fractures of the sacral vertebral body or ala using sacral vertebroplasty or sacroplasty.

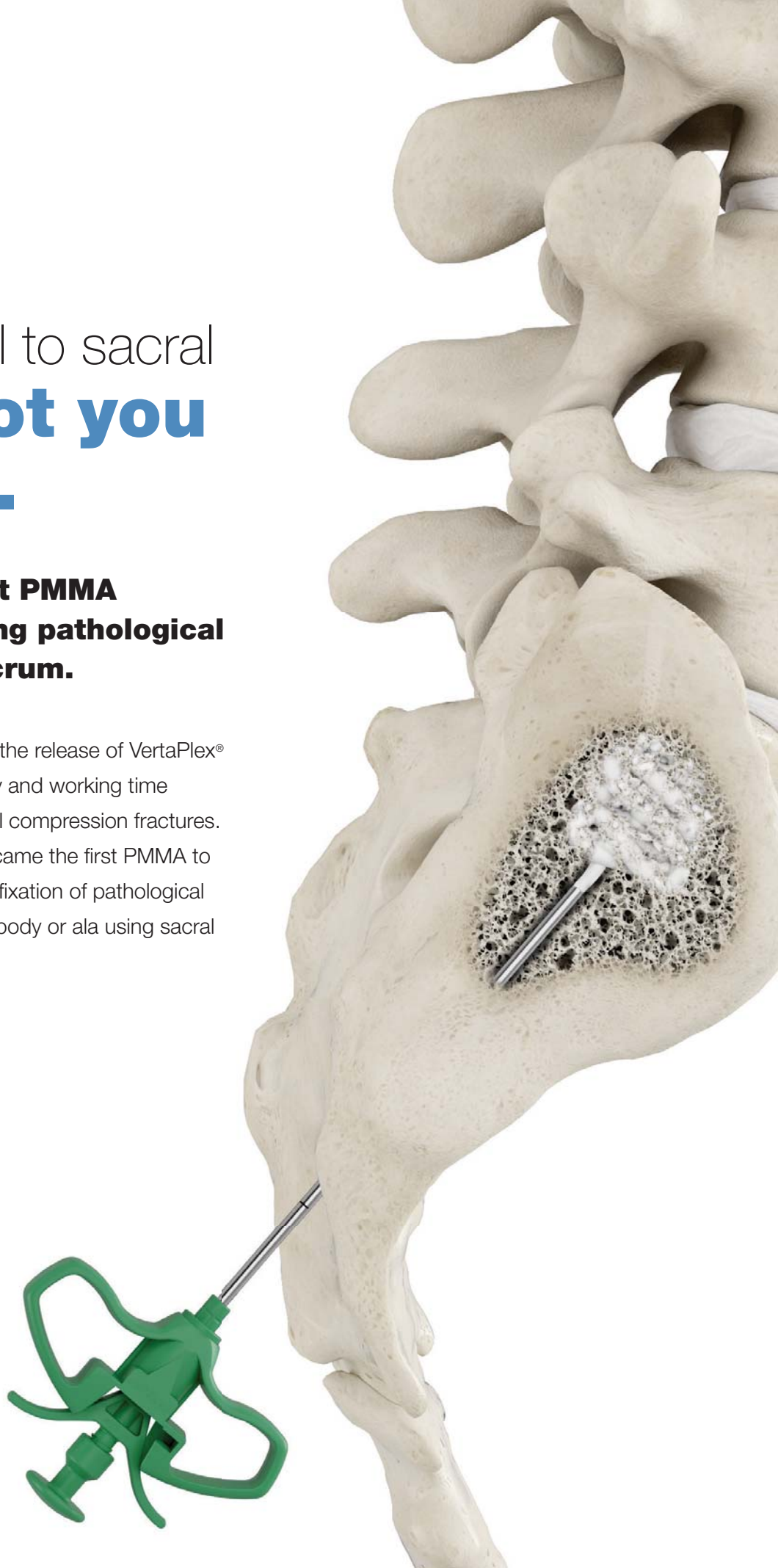

strykerIVS.com

1000-000-008 Rev None

AJNR
AMERICAN JOURNAL OF NEURORADIOLOGY

DECEMBER 2015
VOLUME 36
NUMBER 12
WWW.AJNR.ORG

THE JOURNAL OF DIAGNOSTIC AND INTERVENTIONAL NEURORADIOLOGY

Bone-subtracted spinal CT angiography

Natalizumab-associated progressive multifocal leukoencephalopathy and susceptibility changes

PET, SPECT, and arterial spin-labeling defining tumor recurrence from necrosis

Official Journal ASNR • ASFNR • ASHNR • ASPNR • ASSR

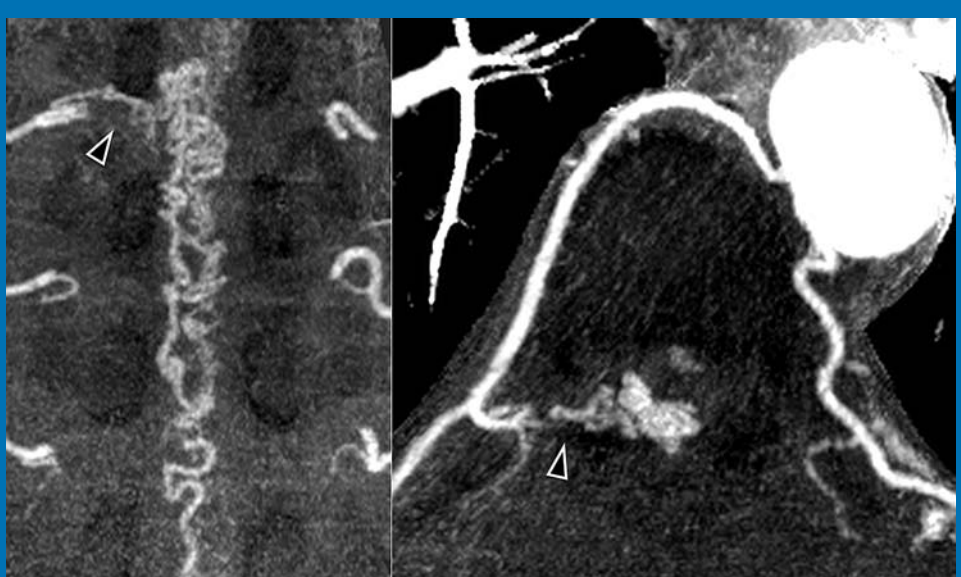

AJNR

AMERICAN JOURNAL OF NEURORADIOLOGY

DECEMBER 2015
VOLUME 36
NUMBER 12
WWW.AJNR.ORG

Publication Preview at www.ajnr.org features articles released in advance of print. Visit www.ajnrblog.org to comment on AJNR content and chat with colleagues and AJNR's News Digest at http://ajnrdigest.org to read the stories behind the latest research in neuroimaging.

ONLINE FEATURES

LETTER

BOOK REVIEWS *R.M. Quencer, Section Editor*

Please visit www.ajnrblog.org to read and comment on Book Reviews.

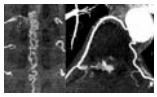

Nonrigid registration subtracted CT angiography demonstrates the right-sided location of the dural fistula while allowing visualization of the adjacent bone as darker structures.

Title: *The Forgotten*

While radiologists typically focus on medical imaging, this single photograph provides a powerful glimpse into a past, and primitive, part of the larger field of medicine. The Georgia Lunatic Asylum (later renamed Central State Hospital) opened in 1842 in the southern town of Milledgeville. This vast facility of 200 buildings over 2000 acres, became the world's largest psychiatric asylum and housed 13,000 patients at its peak occupancy. Patient care approaches consisted of lobotomies, straightjackets, insulin shock, and early forms of electroshock therapy. Today, many of the buildings of Central State Hospital are empty yet preserved with haunting reminders of the poor facility conditions endured by those who lived there. Within the property is Cedar Lane Cemetery, where numbered grave markers coat the hillside to acknowledge the 25,000 inmates who died there. More of the Dr. Meltzer's work can be seen at: http://carolynmeltzer.com/.

Carolyn Meltzer, MD, Atlanta, Georgia

Emergent Neurovascular Imaging: A Necessity for the Work-Up of Minor Stroke and TIA

S.B. Coutts and M. Goyal

Most ischemic strokes are judged "minor" and nondisabling.[1] Symptoms being too mild or minor is the most common reason for withholding thrombolysis.[2] However, this seemingly mild presentation is misleading because the prognosis is not benign, with up to one-third of patients having died or being disabled at follow-up.[2]

Natural History and Imaging Findings

We can identify a subset of patients with minor stroke who are at the highest risk of poor outcome by using noninvasive CT angiography. Patients with minor stroke with documented intracranial arterial occlusion are at particularly high risk of early neurologic deterioration and disability.[3-5] This is true whether the occlusion is proximal or distal[6] or whether the initial deficits have completely resolved.[7] Even in the absence of neurologic deterioration, these patients are at higher risk of disability than those with minor stroke without intracranial occlusion. This presumably is from a mechanism such as silent infarct growth.[8] These patients represent at least 10% of those with minor stroke,[4] and this number is likely higher with better imaging techniques, such as multiphase CTA (mCTA)[9] and perfusion, helping to identify more distal occlusions.

Why Image Minor Stroke?

Why bother identifying patients with minor stroke with intracranial occlusion? We believe that understanding disease pathophysiology is the first step in the treatment of these patients. Stroke is a plumbing disorder, so better identification of the problem and its exact location would result in better diagnosis and treatment. Few stroke physicians, particularly in the era of endovascular treatment[10,11] of stroke, would disagree that early vascular imaging with CTA is crucial for the early management of patients with moderate-to-severe stroke. We believe that the same is true for patients with minor cerebrovascular events (TIA and minor stroke).

What Imaging Technique to Use

In most institutions, imaging of minor stroke is best completed by using CT, CTA and mCTA, or CT perfusion. In some parts of the world, MR imaging is easily performed, but vascular imaging is still required. DWI is useful in confirming that the patient actually has ischemia, but for many patients, the absence of a DWI lesion will not change the management plan.[12] The management plan is driven by finding an intracranial occlusion or an intracranial or extracranial stenotic lesion, thus making urgent vascular imaging a key part of the initial work-up.

Triage and Management Decisions

At our institution, for several years, all patients with suspected stroke symptoms undergo a plain head CT, CTA, and mCTA. Clinical trials are being performed in patients with intracranial occlusion.[13] Ideally, patients would be randomized in such a trial. In the absence of an available trial, a decision can be made on an individual patient basis as to whether to perform thrombolysis or to use dual antiplatelet therapy, for example.[14] Further stroke etiology is an important driver of outcome because it strongly influences the early risk of recurrence with as much as 50% of early recurrences being due to large-artery disease.[15] In addition, recognizing of the magnitude of the problem, better understanding its natural history, and understanding the underlying pathophysiology will trigger new solutions for improving outcomes. Thus, it makes sense to image both the intracranial and extracranial circulation simultaneously in the emergency department. This allows urgent treatment decisions to be made quickly and a treatment plan to be implemented.

We have safely used findings from urgent CTA to triage patients who need to be seen that evening versus those than can be seen in the clinic the next day. Patients with high-risk vascular lesions are seen that night and admitted to the hospital, and those whose symptoms have resolved and have normal CTA findings are usually sent home. From an overall expense perspective, we believe that urgent CTA does not add additional cost because these patients require neurovascular imaging anyway (even if performed in a nonemergent fashion). Additionally, by standardizing the protocol for acute stroke work-up across major and minor stroke, we have been able to improve efficiency at all levels, including image acquisition, postprocessing, and interpretation.

In the near future, all patients with minor stroke and TIA should have emergent neurovascular imaging. This is a necessary step toward improving outcomes in these patients.

Disclosures: Mayank Goyal—*RELATED*: *Other*: GE Healthcare, *Comments*: licensing agreement for Systems of Stroke Diagnosis (patent pending); *UNRELATED*: *Consultancy*: Covidien, *Comments*: for teaching engagements; for design and conduct of the Solitaire With the Intention For Thrombectomy as PRIMary Endovascular Treatment trial; *Grants/Grants Pending*: Covidien,* *Comments*: part funding of the Endovascular Treatment for Small Core and Anterior Circulation Proximal Occlusion with Emphasis on Minimizing CT to Recanalization Times trial. *Money paid to the institution.

REFERENCES

1. Reeves M, Khoury J, Alwell K, et al. **Distribution of National Institutes of Health Stroke Scale in the Cincinnati/Northern Kentucky Stroke Study.** *Stroke* 2013;44:3211–13 CrossRef Medline
2. Smith EE, Fonarow GC, Reeves MJ, et al. **Outcomes in mild or rapidly improving stroke not treated with intravenous recombinant tissue-type plasminogen activator: findings from Get With The Guidelines-Stroke.** *Stroke* 2011;42:3110–15 CrossRef Medline
3. Smith EE, Abdullah AR, Petkovska I, et al. **Poor outcomes in patients who do not receive intravenous tissue plasminogen activator because of mild or improving ischemic stroke.** *Stroke* 2005;36:2497–99 CrossRef Medline
4. Coutts SB, Modi J, Patel SK, et al; Calgary Stroke Program. **CT/CT angiography and MRI findings predict recurrent stroke after transient ischemic attack and minor stroke: results of the prospective CATCH study.** *Stroke* 2012;43:1013–17 CrossRef Medline

http://dx.doi.org/10.3174/ajnr.A4553

5. Coutts SB, Modi J, Patel SK, et al. **What causes disability after transient ischemic attack and minor stroke? Results from the CT and MRI in the Triage of TIA and Minor Cerebrovascular Events to Identify High Risk Patients (CATCH) Study.** *Stroke* 2012;43:3018–22 CrossRef Medline
6. Dubuc V, Singh D, Modi J, et al. **TIA and minor stroke patients with intracranial occlusions in both proximal and distal vessels are most at risk for symptom progression.** *Cerebrovasc Dis* 2014;38:389–90 CrossRef Medline
7. Poisson SN, Nguyen-Huynh MN, Johnston SC, et al. **Intracranial large vessel occlusion as a predictor of decline in functional status after transient ischemic attack.** *Stroke* 2011;42:44–47 CrossRef Medline
8. Asdaghi N, Hill MD, Coulter JI, et al. **Perfusion MR predicts outcome in high-risk transient ischemic attack/minor stroke: a derivation-validation study.** *Stroke* 2013;44:2486–92 CrossRef Medline
9. Menon BK, d'Esterre CD, Qazi E, et al. **Multiphase CT angiography: a new tool for the imaging triage of patients with acute ischemic stroke.** *Neuroradiology* 2015;275:510–20 CrossRef Medline
10. Goyal M, Demchuk AM, Menon BK, et al; ESCAPE Trial Investigators. **Randomized assessment of rapid endovascular treatment of ischemic stroke.** *N Engl J Med* 2015;372:1019–30 CrossRef Medline
11. Berkhemer OA, Fransen PS, Beumer D, et al. **A randomized trial of intraarterial treatment for acute ischemic stroke.** *N Engl J Med* 2015;372:11–20 CrossRef Medline
12. Coutts SB, Cucchiara B. **Stroke risk after TIA: DWI is only part of the answer.** *Neurology* 2013;80:1914–15 CrossRef Medline
13. ClinicalTrials.gov. A Randomized Controlled Trial of TNK-tPA Versus Standard of Care for Minor Ischemic Stroke With Proven Occlusion (TEMPO-2). https://clinicaltrials.gov/ct2/show/NCT02398656?term=TEMPO-2&rank=1. Accessed July 15, 2015
14. Wang Y, Wang Y, Zhao X, et al; CHANCE Investigators. **Clopidogrel with aspirin in acute minor stroke or transient ischemic attack.** *N Engl J Med* 2013;369:11–19 CrossRef Medline
15. Lovett JK, Coull AJ, Rothwell PM. **Early risk of recurrence by subtype of ischemic stroke in population-based incidence studies.** *Neurology* 2004;62:569–73 CrossRef Medline

Recognizing Autoimmune-Mediated Encephalitis in the Differential Diagnosis of Limbic Disorders

A.J. da Rocha, R.H. Nunes, A.C.M. Maia Jr, and L.L.F. do Amaral

ABSTRACT

SUMMARY: Limbic encephalitis is far more common than previously thought. It is not always associated with cancer, and it is potentially treatable. Autoantibodies against various neuronal cell antigens may arise independently or in association with cancer and cause autoimmune damage to the limbic system. Neuroimaging plays a key role in the management of patients with suspected limbic encephalitis by supporting diagnosis and excluding differential possibilities. This article describes the main types of autoimmune limbic encephalitis and its mimic disorders, and emphasizes their major imaging features.

ABBREVIATIONS: AME = autoimmune-mediated encephalopathy; AMPAR = α-amino-3-hydroxy-5-methyl-4-isoxazolepropionic acid; CASPR2, contactin-associated protein-like 2; GAD65 = 65-kD isoform of glutamic acid decarboxylase; GABA = gamma-aminobutyric acid; HSE = herpes virus encephalitis; LE = limbic encephalitis; LGI1 = leucine-rich glioma inactivated 1; PLE = paraneoplastic limbic encephalitis; TL = temporal lobe; VGKC = voltage-gated potassium channel

Limbic encephalitis (LE) was initially described in 3 patients with malignancies (and in the absence of a better explanation) as a subacute encephalitis of later adult life that mainly affected the limbic areas.[1] More than half a century later, most forms of LE have been recognized as a potentially treatable nonparaneoplastic autoimmune encephalopathy with a broad spectrum of recognizable symptoms that include psychiatric or behavioral features, seizures, hallucinations, and cognitive abnormalities.[2,3]

Current knowledge has improved our recognition of the neurologic presentation and outcomes of patients with LE. Early diagnosis is always desirable because a satisfactory response to immunotherapy can be achieved.[3] On electroencephalography or MR imaging, most patients with LE present inflammatory features in the CSF associated with temporal lobe (TL) abnormalities and detectable antineuronal antibodies.[3,4] However, LE is not the first diagnosis in clinical practice because clinical and paraclinical markers are often unavailable. In addition, symptoms can precede the diagnosis of cancer, and T2/FLAIR hyperintensity in the medial aspect of the TL may mimic several other disorders.[4-12]

From the Division of Neuroradiology (A.J.d.R., R.H.N., A.C.M.M., L.L.F.d.A.), Santa Casa de São Paulo School of Medical Sciences, São Paulo, Brazil; Division of Neuroradiology (A.J.d.R., R.H.N., A.C.M.M.), Fleury Medicina e Saúde, São Paulo, Brazil; Research Fellow, University of North Carolina (R.H.N.), Chapel Hill, North Carolina; and Division of Neuroradiology (L.L.F.d.A.), Med Imagem, Hospital da Beneficência Portuguesa de São Paulo, São Paulo, Brazil.

Please address correspondence to Antonio Jose da Rocha, MD, PhD, Santa Casa de Misericórdia de São Paulo – Serviço de Diagnóstico por Imagem, Rua Dr Cesário Motta Junior 112, Vila Buarque, São Paulo – SP, Brazil 01221-020; e-mail: renatohn@hotmail.com

http://dx.doi.org/10.3174/ajnr.A4408

MR imaging plays a key role in the management of patients with suspected LE and is used as part of the LE diagnostic criteria to rule out differential diagnoses. Certain imaging and clinical peculiarities may narrow the list of possible diagnoses; however, a complete list of differential diagnoses remains beyond the scope of this article. Our current aim was to describe the most commonly reported MR features of LE and its mimic disorders.

Autoimmune Encephalopathies

Both paraneoplastic LE (PLE) and nonparaneoplastic LE present a similar clinical picture that includes CSF and MR imaging abnormalities. It is estimated that 60% to 70% of cases are PLE; however, a neurologic disorder can precede neoplasia by months or even years.[2,3]

Autoimmune-mediated encephalopathy (AME) can be distinguished by its association with autoantibodies[3,13] and by certain recognizable features on MR imaging, which (besides LE) include cerebellar degeneration, striatal encephalitis, brain stem encephalitis, and leukoencephalopathy.[14-16] A comprehensive search for an underlying malignancy is always considered when AME is suspected.[3] The position of the causal antigens is correlated with the disease mechanism and with concurrent cancer.[2,3,13] In general, antibodies against intracellular antigens are associated with cytotoxic T-cell mechanisms; in these cases, neuronal damage seems to be irreversible, associations are found with underlying malignancies and poor prognosis, and structural abnormalities are not restricted to the limbic structures.[10] Conversely, in restricted LE, neuronal cell-surface antigens are targeted, an associated malignancy is unusual, and its expected response to immunotherapy is superior.[3]

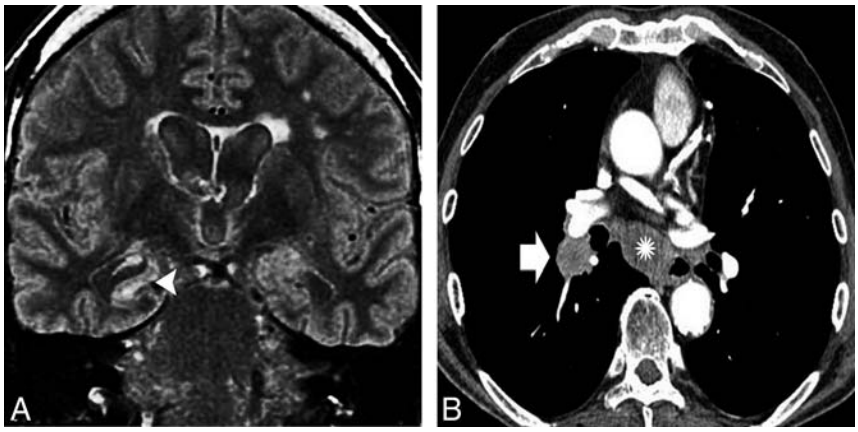

FIG 1. A 62-year-old man with subacute cognitive impairment and seizures. *A*, An enlarged and hyperintense right hippocampus in a coronal FLAIR image (*arrowhead*). Additional right amygdala involvement was observed, but no abnormal enhancement was documented after intravenous gadolinium administration (not shown). *B*, Body CT after contrast administration shows a right hilar mass (*arrow*) with an enlarged lower paratracheal lymph node (*asterisk*). Endobronchial biopsy specimen revealed an small cell lung carcinoma, and the diagnosis was consistent with PLE.

Paraneoplastic LE

The classic mechanism reported in PLE is a systemic neoplasia that expresses coincident antigens within the CNS, which results in the production of antibodies that target neoplastic tissue (onconeural antigens) as well as intracellular antigens.[2,13,14] The correct diagnosis of PLE is relevant because earlier recognition often allows the discovery and treatment of the underlying malignancy. Cancer control is a crucial step in the management of PLE, which is usually followed by the remission of the paraneoplastic syndrome.[17]

PLE Associated with Autoantibodies against Intracellular Antigens

Hu Antibodies. The Hu antineuronal nuclear antibody is a type IIa antineuronal nuclear antibody type I, which can appear in any part of the nervous system. Approximately 75% of the patients have small cell lung carcinoma and often develop symptoms related to inflammation across widespread areas of the CNS or the peripheral nervous system.[18] MR imaging reveals variable abnormalities according to clinical features, including T2/FLAIR hyperintensity in the mesial TL (Fig 1), cerebellar edema or atrophy, and brain stem abnormalities.[4] Rarely, patients have epilepsia partialis continua, which results from restricted lesions in nonlimbic cortical areas.[19] First-line immunotherapies often fail, and the prognosis of this condition is usually poor despite immunotherapy.[20]

Ma2 Antibodies. Patients with Ma2 antineuronal nuclear antibody–related encephalitis often have accompanying symptoms of diencephalic inflammation (sleep disturbances, dysthermia, and endocrine abnormalities) and upper brain stem inflammation (eye movement abnormalities and hypokinetic syndrome). Approximately 75% of patients have abnormal MRI, usually with classic LE findings.[21] The remaining patients have signal abnormalities that are either isolated or associated with the hypothalamus and thalamus or with the brain stem.[22] Nodular parenchymal enhancement in the affected regions has been reported, which may mimic a brain tumor or an infection.[21,22] This AME occurs mostly in association with testicular germinal cell tumors in younger male individuals; but, in older individuals, there may be an underlying non–small cell lung carcinoma or breast cancer.[23] Improvement with immunotherapy is more likely than in other forms of LE that involve antibodies against intracellular antigens.[22]

CV2/Collapsing Response Mediator Protein-5 Antibodies. Bilateral striatal encephalitis with T2/FLAIR hyperintensity is a typical finding, which causes choreiform movement disorders and is highly suggestive of CV2/collapsing response mediator protein-5 antineuronal nuclear antibody–related encephalitis associated with underlying small cell lung carcinoma or malignant thymoma, among others disorders.[24,25] However, patients may also present with a range of imaging patterns that rarely include LE and typically do not include striatal restriction on DWI, which may help to distinguish this AME from prion diseases.[25]

PLE Associated with Autoantibodies against Extracellular Antigens

N-Methyl-D-Aspartate Receptor Antibodies. A specific immunoglobulin G antibody against the GluN1 subunit of the anti–*N*-methyl-D-aspartate receptor results in a highly characteristic and recognizable LE that is far more common than previously believed[26] and mostly affects young women and children.[27] Two major well-characterized stages are noticeable.[28] A viral-like prodrome followed by severe psychiatric features characterizes the earliest involvement of the cortical regions. In addition, patients may develop amnesia and seizures.[29] After a few days to a few weeks, subcortical areas are affected and a movement disorder appears (often dyskinesia of the mouth and face) followed by a decreased level of consciousness and dysautonomia, which requires intensive care support. A lymphocytic pleocytosis is observed in the CSF, and, less commonly, increased protein and/or oligoclonal bands are present.[27]

The most common MR imaging abnormality is unilateral or bilateral LE[30,31]; however, approximately 66% of patients have an unremarkable MR imaging. Cerebellitis, striatal abnormalities, and brain stem encephalitis have also been described.[30,31] Gadolinium enhancement is uncommon, and imaging follow-up could reveal complete recovery or focal atrophy (Fig 2).[27,30,31]

The concurrence of tumors is reportedly age dependent. Whereas approximately 45% of adult woman had ovarian teratoma, only 9% of younger girls had this type of tumor. Identification and removal of the tumor were crucial because patients without tumor removal recovered less frequently and had an increased risk of relapse.[27] In patients older than 45 years, the outcome was reportedly favorable, whereas 23% of patients had underlying carcinomas instead of teratomas.[32] Despite this ominous

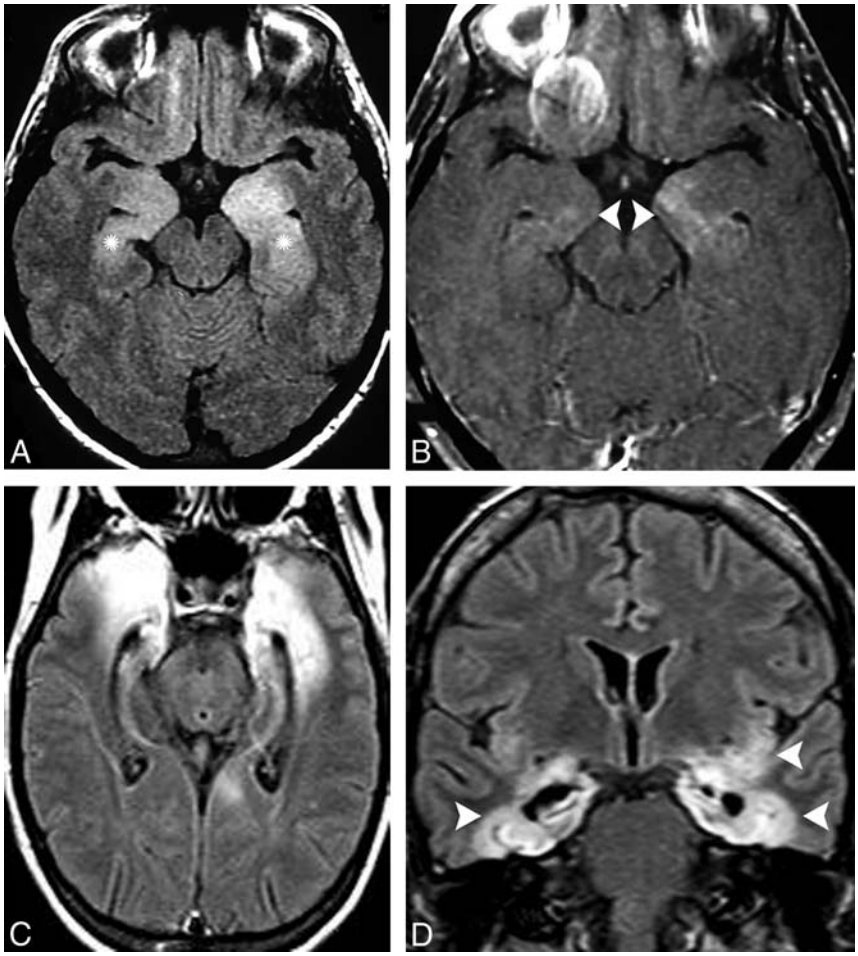

FIG 2. A previously healthy 44-year-old woman presented with subacute psychiatric disturbance with no fever or seizures. *A*, Bilateral and asymmetric hyperintensity was observed on an axial FLAIR image in the enlarged amygdalae and hippocampi (*asterisks*), predominantly on the left side. *B*, A faint ill-defined enhancement of the left hippocampus was documented on an axial T1 postcontrast image (*arrowheads*). Autoimmune encephalitis was considered, and the presence of anti–*N*-methyl-D-aspartate receptor autoantibodies was confirmed. *C* and *D*, Imaging follow-up revealed signal abnormalities and atrophy on FLAIR that involved the hippocampus, amygdala, parahippocampal gyrus, and left insula (*arrowheads*), compatible with severe sequelae.

clinical presentation, approximately 50% of patients respond to first-line immunotherapies, often with full remission, whereas patients who do not respond to treatment or who experience relapse should be reassessed for the presence of an underlying contralateral or recurrent teratoma.[33]

Gamma-Aminobutyric Acid Receptor Antibodies. Anti–gamma-aminobutyric acid (GABA) B-receptor antibody-related encephalitis usually presents as LE. Most patients have early and frequent seizures associated with unilateral or bilateral T2/FLAIR hyperintensity in the mesial TL that are potentially reversible after treatment.[34]

As is most commonly reported in older patients, approximately 50% of patients with GABA B-receptor AMEs have underlying small cell lung carcinoma or lung neuroendocrine tumors.[35] This AME usually precedes a cancer diagnosis but represents the second most common cause of LE related to small cell lung carcinoma.[36]

An AME associated with anti–GABA A-receptor antibodies was recently described in children and adults who developed a rapidly progressive encephalopathy with refractory seizures, status epilepticus, and/or epilepsia partialis continua that was preceded by or associated with behavioral changes.[37] Unlike patients with other LEs in whom MR imaging is either normal or shows predominant involvement of the limbic system, these patients have multifocal and extensive T2/FLAIR brain abnormalities. In addition, they respond well to immunotherapy and rarely have an underlying tumor. When a tumor is present, it is usually a thymoma. Patients are often misdiagnosed with the 65-kD isoform of glutamic acid decarboxylase (GAD65) antibody-associated encephalitis or Hashimoto encephalitis due to the frequent co-occurrence of GAD65 and antithyroid antibodies.[16,37]

Other PLEs with Autoantibodies against Extracellular Antigens. In anti–α-amino-3-hydroxy-5-methyl-4-isoxazolepropionic acid receptor (AMPAR) encephalitis, patients develop antibodies against the GluR1 and GluR2 subunits of the AMPAR, and present with symptoms and MR imaging features of unilateral or bilateral LE that rarely involve extrahippocampal limbic structures. In some cases, the manifestations are purely psychiatric. Most of these patients are women who are harboring a tumor in the lung, breast, or thymus.[38]

Hodgkin lymphoma is the third most common cause of LE after small cell lung carcinoma and testicular germ cell tumors.[4] This association has been called Ophelia syndrome, and it is characterized by generalized or partial complex seizures in 50% of the patients. It is also more commonly associated with short-term memory loss or amnesia, psychiatric changes, and even frank psychosis with visual or auditory hallucinations or paranoid ideation.[17,39]

Intriguingly, AME is not typically associated with non-Hodgkin lymphoma.[17] Although Hodgkin lymphoma rarely infiltrates the CNS, the onset of an LE in this setting should be attributable to either a concurrent infection or an AME (Fig 3). Successful treatment of the tumor results in complete neurologic recovery, probably due to an association with an antibody against the metabotropic glutamate receptor 5, which is highly expressed in the hippocampus and presumably promotes reversible neuronal dysfunction rather than neuronal death.[17,40]

Nonparaneoplastic LE

It is assumed that nonparaneoplastic LE is more common than classic PLE and affects a wider age range of patients, though predominantly young patients. Nonparaneoplastic LE is a re-

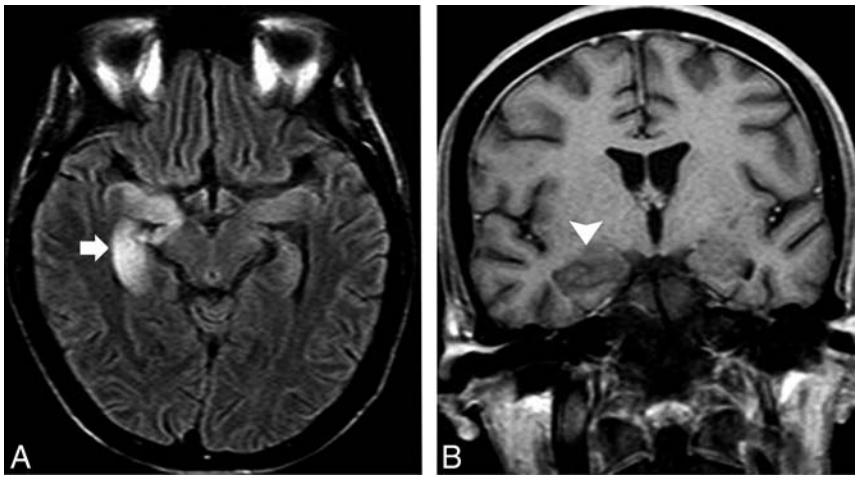

FIG 3. A 22-year-old man with Hodgkin lymphoma presented with acute onset of short-term memory loss and mental confusion. *A*, An evident hyperintensity and subtle enlargement of the right hippocampus and amygdala were noticed on an axial FLAIR image (*arrow*). *B*, No parenchymal enhancement was observed (*arrowhead*). In addition to the fact that CNS involvement is not expected in Hodgkin lymphoma, a lack of enhancement is not the expected imaging pattern. After the patient did not respond to antiviral treatment, PLE was considered. The findings fulfilled the criteria for Ophelia syndrome, which consists in an interval of <4 years between the onset of neuropsychiatric disturbance and the diagnosis of the Hodgkin lymphoma, exclusion of other cancer-related complications, and evidence of hippocampal abnormalities on MR imaging.

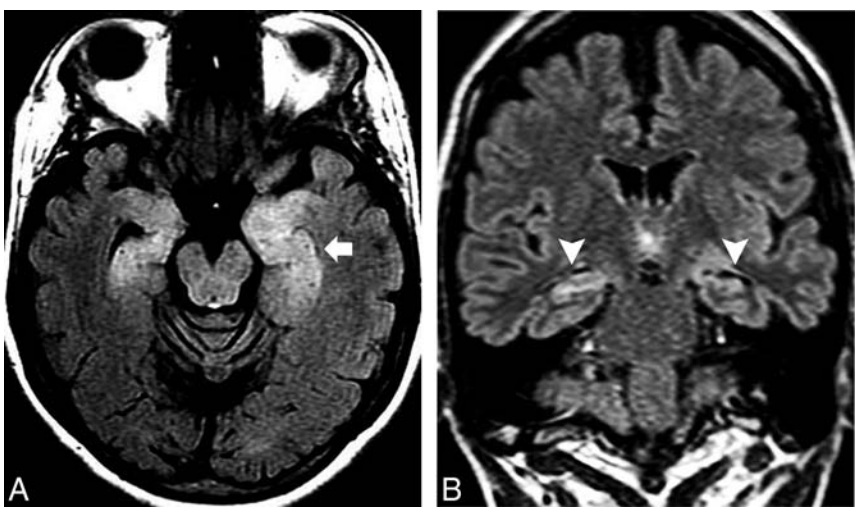

FIG 4. A 38-year-old woman presented with personality and behavioral changes associated with progressive drug-resistant epilepsy. Memory testing revealed an anterograde episodic memory disorder, and electroencephalography showed TL epileptiform discharges. *A*, A selective hyperintensity in the hippocampi that extended to the amygdalae bilaterally was noticed on an axial FLAIR image, predominantly on the left side *(arrow)*. *B*, Imaging follow-up revealed bilateral hippocampal sclerosis, which is shown in a coronal FLAIR image (*arrowheads*). Whole-body PET/CT and pelvic sonography were unremarkable (not shown). Autoimmune encephalitis was suggested, and a high titer of GAD65 antibodies was confirmed.

sult of antibodies against neuronal cell surface or synaptic receptors.[2]

Nonparaneoplastic LE Associated with Autoantibodies against Intracellular Antigens

GAD65 Antibodies. Some patients with nonparaneoplastic LE have antibodies against the intracellular antigen GAD65. However, unlike other intracellular antibodies, anti-GAD65 is not typically related to underlying malignancies. Patients typically present with stiff man syndrome or cerebellar ataxia, but they also may present with severe TL epilepsy, with less pronounced cognitive-behavioral features and a poorer response to first-line epilepsy drugs.[41]

MR imaging frequently shows signal abnormalities and swelling predominantly in the amygdala and hippocampus, which may resolve or progress to mesial temporal sclerosis on follow-up imaging (Fig 4).[41]

Nonparaneoplastic LE Associated with Autoantibodies against Extracellular Antigens

Voltage-Gated Potassium Channel-Complex Antibodies. Anti–leucine-rich glioma inactivated 1 (LGI1) and anti–contactin-associated protein-like 2 (CASPR2) antibodies have been described as voltage-gated potassium channel (VGKC) antibodies and the most common cause of nonparaneoplastic LE.[16] Results of recent studies highlight the relevance of discriminating both LGI1 and CASPR2 from VGKC-complex antibodies. Although LGI1 and contactin-associated protein-like 2 antibodies are specifically associated with limited subsets of syndromes, VGKC-complex antibodies lack specificity and may be found in nonautoimmune diseases, including Creutzfeldt-Jakob disease.[42,43]

LGI1 antibodies occur most often in young male patients (2:1) who develop a classic LE with peculiar features, such as hyponatremia (60%), rapid eye movement–sleep behavior disorders, and normal CSF. In a few patients, a characteristic clinical manifestation described as faciobrachial dystonic or tonic seizures is observed. Fewer than 10% of patients with LGI1 antibodies have an underlying neoplasm, which is usually a thymoma.[16,44]

Approximately 78.6% of patients present with typical LE MR imaging findings (Fig 5). Restricted DWI is observed in approximately 50% of these patients, whereas up to 25% have associated mild, ill-defined contrast enhancement and extrahippocampal involvement, including striatal encephalitis.[11,45]

Antibodies against the VGKC-complex have been identified in a subgroup of patients with epilepsy that appears on imaging as mesial temporal sclerosis, which indicates that some patients with epilepsy who are poorly responsive to conventional antiepileptic drugs may have an immune-mediated etiology.[11,46] Recognition and appropriate treatment with immunotherapy are recom-

mended to prevent structural damage due to severe encephalitis as well as cognitive dysfunction.[16,47]

LGI1 antibodies are almost exclusively expressed in the CNS. They often result in LE or epilepsy but primarily result in nonparaneoplastic LE (Fig 5). Conversely, CASPR2 antibodies expressed in the peripheral nervous system are involved in Morvan disease or peripheral nerve hyperexcitability–neuromyotonia spectrum disorders and are typically associated with thymomas. Myasthenia gravis and LE can also be found in some patients.[48]

Limbic Disorders That Mimic AME

Abnormal MR signal intensity that involves the TL has a broad differential diagnosis that includes a range of unrelated disorders that are rarely reported, for example, Whipple disease,[49] 4-aminopyridine toxicity,[50] and hypoglycemia.[51] Neuroradiologists must recognize these disorders and their imaging features more often.

Infectious LE

Herpes Virus Encephalitis. Herpes virus encephalitis (HSE) causes at least 20% of acute LE cases.[52] Although human herpes virus 6 is associated with posttransplantation acute LE,[10] the most common agent is herpes virus type 1, which has high mortality and morbidity rates.[52]

The clinical and imaging findings of LE caused by either AME or HSE may overlap. Although almost 50% of patients with AME present with or develop fever during their disease course and have prodromal symptoms with abnormal CSF, these findings favor HSE. The absence of psychiatric symptoms and the sudden and rapid progression also support the early administration of antiviral therapy based on a presumed diagnosis of HSE.[10] In addition, even though both HSE and LE involve the TL, basal ganglia involvement on MR imaging favors nonherpetic etiologies.[12]

It has been demonstrated that some types of viral encephalitis can trigger autoimmune LE,[53,54] particularly anti-*N*-methyl-D-aspartate receptor encephalitis.[55] This phenomenon occurs when prolonged or atypical neurologic symptoms recur after successful control of the viral infection. Some patients with negative viral results develop a syndrome described as relapsing post-HSE or choreoathetosis post-HSE. A few weeks after recovery from HSE, children present with abnormal movement and adults

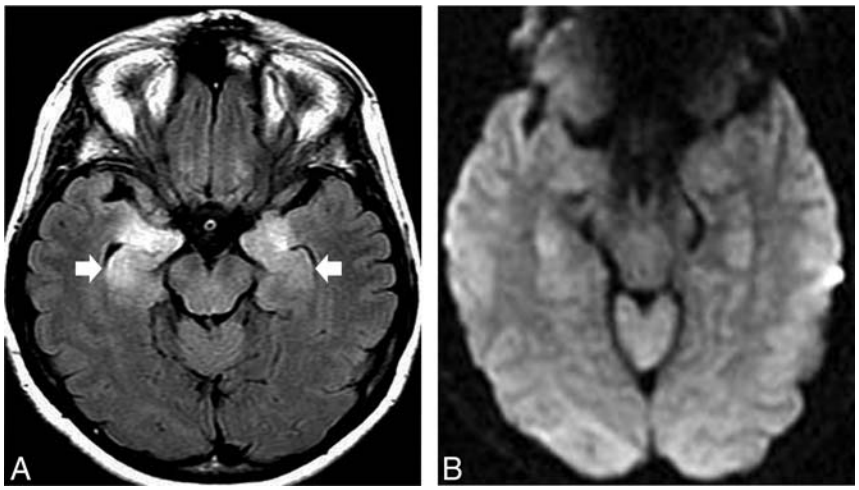

FIG 5. A healthy 46-year-old woman presented with an acute onset of psychiatric disturbance and hyponatremia. *A*, Bilateral hyperintensity and mild enlargement were noticed on an axial FLAIR image in both hippocampi and amygdalae. *B*, No abnormal restricted diffusion was observed on DWI. The final diagnosis was anti-VGKC encephalitis. Restricted diffusion may occur in approximately 50% of patients at this phase and is usually restricted to the limbic system. The presence of faciobrachial dystonic or tonic seizures, hyponatremia, and unremarkable CSF in the setting of LE should raise concern that anti-LGI1 encephalitis is present.

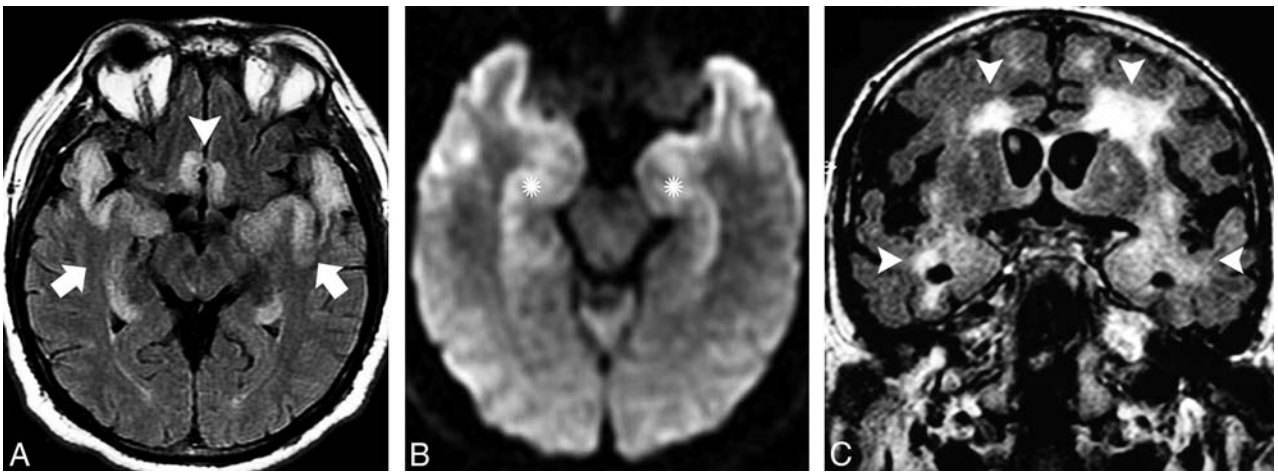

FIG 6. A 47-year-old man with HSE. *A*, Bilateral symmetric cortical swelling and hyperintensity on axial FLAIR were observed in the anteromedial TLs (*arrows*) and also affected the insular cortex and rectus gyri (*arrowhead*). *B*, Restricted diffusion was documented in the same areas on DWI (*asterisks*). Bilateral and usually asymmetric involvement of the limbic system sparing the basal ganglia in the setting of acute LE should raise concerns for HSE. The presence of hemorrhagic foci and gyriform enhancement are also of diagnostic value in more-advanced disease. *C*, A similar pattern with bilateral asymmetrical involvement of the anteromedial TLs (*arrows*) on coronal FLAIR was observed in addition to the extensive white matter changes (*arrowheads*) in a 59-year-old man with progressive dementia who was later diagnosed with neurosyphilis.

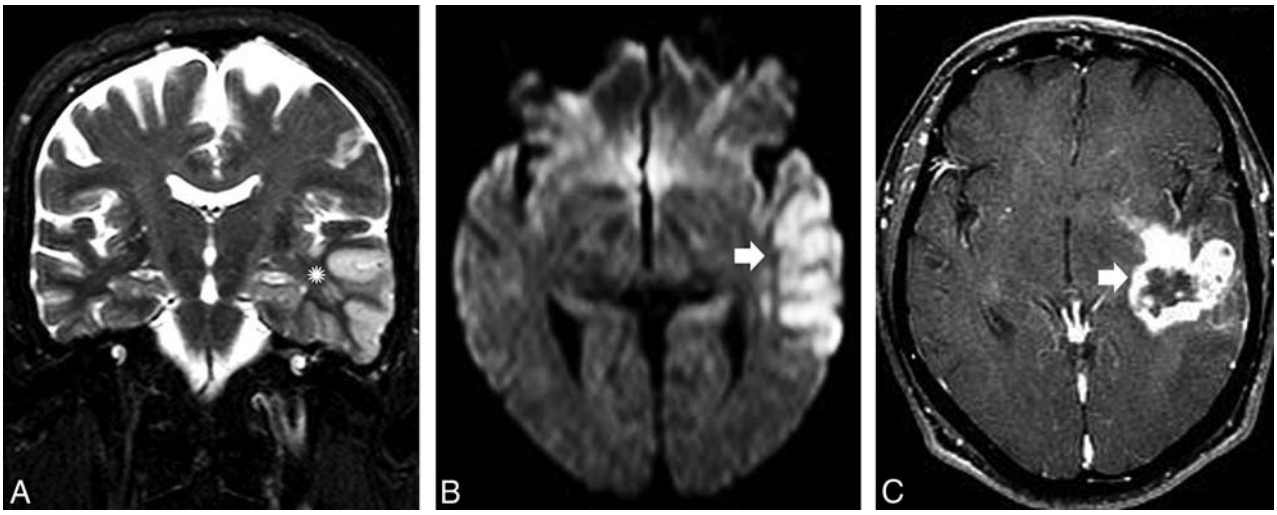

FIG 7. A previously healthy 67-year-old man presented with a transient isolated episode of partial complex seizures and dysphasia. *A*, A cortical abnormality that involved the lateral aspect of the left TL (*asterisk*) and a subtle hyperintensity on coronal T2 were noticed in the ipsilateral hippocampus. *B*, Restricted diffusion on DWI was visible in the same areas (*arrowhead*), and a diagnosis of postictal edema was considered. *C*, After 2 months and a worsening of the clinical manifestations, a necrotic mass in the left TL (*arrow*) was observed on a T1 postcontrast image. A diagnosis of glioblastoma was confirmed after surgery. High-grade gliomas can manifest early as ill-defined lesions that usually have restricted diffusion and involve the cortex with a lack of a mass effect. Follow-up imaging and advanced imaging techniques are crucial for making the diagnosis.

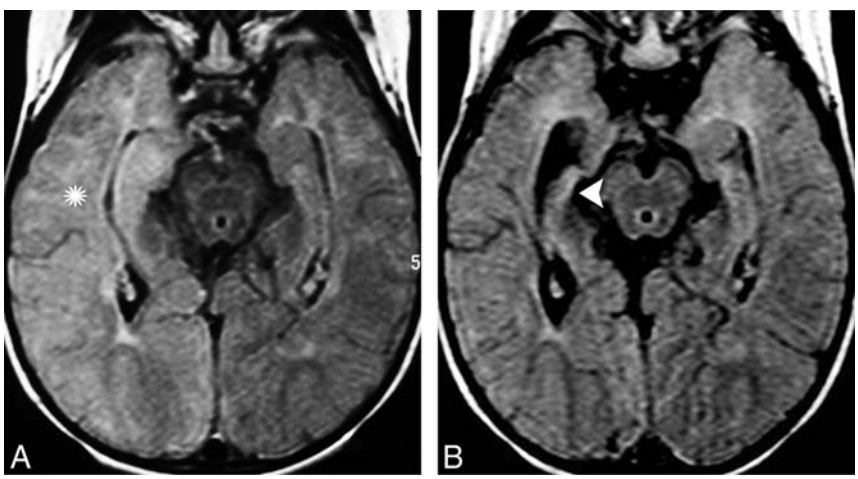

FIG 8. A 15-month-old child presented with a prolonged generalized tonic-clonic seizure episode. *A*, Extensive hyperintensity on an axial FLAIR image that involves the cortex and the white matter of the right TL (*asterisk*) indicated postictal edema. *B*, Comparative FLAIR imaging results on follow-up after 6 months are consistent with right mesial temporal sclerosis (*arrowhead*) in this patient who developed chronic epilepsy.

present with behavioral changes that are not associated with additional brain lesions on MR imaging or response to antiviral therapy.

Neurosyphilis. The incidence of neurosyphilis, caused by a spirochete (*Treponema pallidum*), has once again begun to increase in the era of acquired immunodeficiency syndrome.[56] MR imaging shows a variety of usually nonspecific findings, including selective involvement of the TL that mimics HSE and LE.[10,56] In older subjects with a long latency period of infection or in patients who are immunocompromised, T2/FLAIR hyperintensities in the mesial TL areas that may or may not be associated with either atrophic or gadolinium-enhanced areas increase the likelihood that neurosyphilis is present rather than other etiologies (Fig 6).

Neoplastic Limbic Disorders

Diffuse gliomas and gliomatosis cerebri may mimic the imaging features of LE. The hallmark feature on MR imaging is an infiltrative pattern with poorly demarcated boundaries that is usually not restricted to the limbic system.[8,14,57] Gliomatosis cerebri, as well as low-grade diffuse gliomas, may progress slowly, with seizures or even focal deficits. Moreover, high-grade tumors might present with atypical imaging features that rarely mimic LE but then progress invariably to a recognizable MR imaging pattern of necrotic lesions (Fig 7). In this setting, MR-perfusion and MR-spectroscopy techniques are useful to detect brain tumors and enable surgical planning.[58]

Vascular Limbic Disorders

Differentiation between primary vasculitis and LE may represent a real challenge under certain conditions of subacute presentation. Abnormal vessels on angiography and cytotoxic edema on DWI that usually extends throughout the compromised vascular territory and is not restricted to the limits of the limbic system are helpful to confirm imaging suspicions.[9] Transient global amnesia also affects the hippocampal formation, but its clinical and imaging presentation is rather typical.[59]

Seizure-Related Limbic Disorders

Hippocampal sclerosis associated with TL abnormalities is the multifactorial hallmark of mesial temporal sclerosis. This condition could be a consequence of prolonged unilateral febrile seizures or status epilepticus, which occurs mainly in children when

the hippocampus is more vulnerable to convulsion-induced excitotoxic damage and involves the sectors of the hippocampus rich in kainate or *N*-methyl-D-aspartate receptors and, therefore, that lack protection against calcium overload.[60]

Prolonged seizures or status epilepticus may appear as TL abnormalities on MR imaging, including cortical hyperintensities on DWI that mimic LE and are attributable to hippocampal postictal edema.[9,61] Imaging follow-up with typical clinical and electroencephalographic features may aid diagnosis. This condition is potentially reversible or can result in atrophy with mesial temporal sclerosis (Fig 8).[62]

Hippocampal sclerosis may also be related to a rare neurodegenerative condition called pure hippocampal sclerosis dementia. Despite its similarity to mesial temporal sclerosis on imaging, dementia is always observed in the absence of epilepsy and usually occurs in the elderly.[63]

Febrile infection–related epilepsy syndrome, or acute encephalitis with refractory repetitive partial seizures, is considered a severe epileptic encephalopathy with multifocal refractory status epilepticus, which occurs mostly in young children but also in adult patients.[64] The initial phase is characterized by a simple febrile infection, followed by an acute phase with recurrent focal seizures that evolve rapidly into refractory status epilepticus, generally without fever and additional neurologic features. The diagnosis is made after an exhaustive negative search for an active CNS infection and autoimmune or metabolic disorders. Early MR imaging may be normal in approximately half of the cases; however, T2 abnormalities are detected in some patients, predominantly in the temporal regions but also in the insula and basal ganglia, which mimics LE.[64,65] In the chronic phase, MR imaging shows mesial temporal sclerosis in half of the patients, and bilateral hypometabolism of orbitofrontal and temporoparietal regions is often demonstrated on PET.[64] The etiology and mechanisms that underlie it are still unknown, and, even though an autoimmune mechanism could be considered and autoantibodies have previously been described in epilepsy, up to now there is no evidence to support that autoantibodies are the etiology of febrile infection-related epilepsy syndrome.[64,66]

Other Autoimmune Disorders

Autoimmune systemic disorders are associated with LE.[2] Sjögren syndrome, lupus erythematosus, Beçhet disease, primary angiitis of the CNS, and antiphospholipid syndrome can occasionally cause clinical and/or radiologic abnormalities in the limbic system that are not antibody mediated but that are accompanied by histopathologic evidence of cellular inflammation.[3]

Hashimoto encephalopathy or steroid-responsive encephalopathy associated with autoimmune thyroiditis[67] manifests as a diffuse progressive AME characterized by dementia, psychiatric disturbances, and seizures; there also is a vasculitic type characterized by multiple strokelike episodes, seizures, and fluctuating consciousness.[68] This disorder is more common in women and is associated with autoimmune antithyroid antibodies. There is increasing evidence that these antibodies are not pathogenic but rather are markers of autoimmunity for other associated but currently unclassified antineuronal antibodies.[69] MR imaging may mimic patterns of LE (Fig 9),[70] but leukoencephalopathy with bilateral patchy or confluent supratentorial subcortical and periventricular white matter T2/FLAIR hyperintensities is the most common abnormality and is usually reversible after corticotherapy.[67]

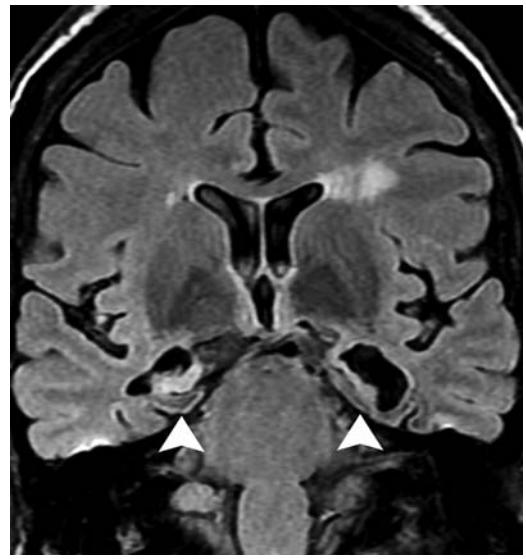

FIG 9. A 45-year-old woman presented with strokelike episodes associated with fluctuating and progressive cognitive impairment. Severe atrophy and bilateral hyperintensity in the hippocampi (*arrowheads*) along with mild cortical atrophy and scattered white matter changes were observed on a coronal FLAIR image. Although the patient had euthyroid status, she presented with high titers of serum antithyroperoxidase (490 U/mL; reference value, <60 U/mL). After excluding other causes, the diagnosis of steroid-responsive encephalopathy associated with autoimmune thyroiditis was considered.

A rare cause of LE is relapsing polychondritis, in which clinicoradiologic involvement of the limbic system might be more common than was previously thought.[71,72] This condition is a disorder of unknown etiology that manifests as episodic and progressive inflammation of the cartilaginous structures of the body, as is suggested by the detection of autoantibodies against type II collagen restricted to the cartilage in the sera of 30%–50% of affected patients.[73] MR imaging findings are coincident with LE; however, peculiar cartilage involvement may help identify this entity.

Recommended Diagnostic Approach to Limbic Disorders

An algorithm that describes an approach to the diagnosis of limbic disorders by using clinical and neuroimaging features is presented in Fig 10.

CONCLUSIONS

LE and the mimic disorders presented in this review have always existed. However, they have just begun to be clearly distinguished over the past decade. Their association with autoantibodies influences their prognosis and results in recognizable imaging patterns that vary according to the position of the causal antigens (intra- or extracellular) and the concurrence of cancer. Mimic disorders may represent a complication of an underlying malignancy or may occur independently. MR imaging is the best technique for

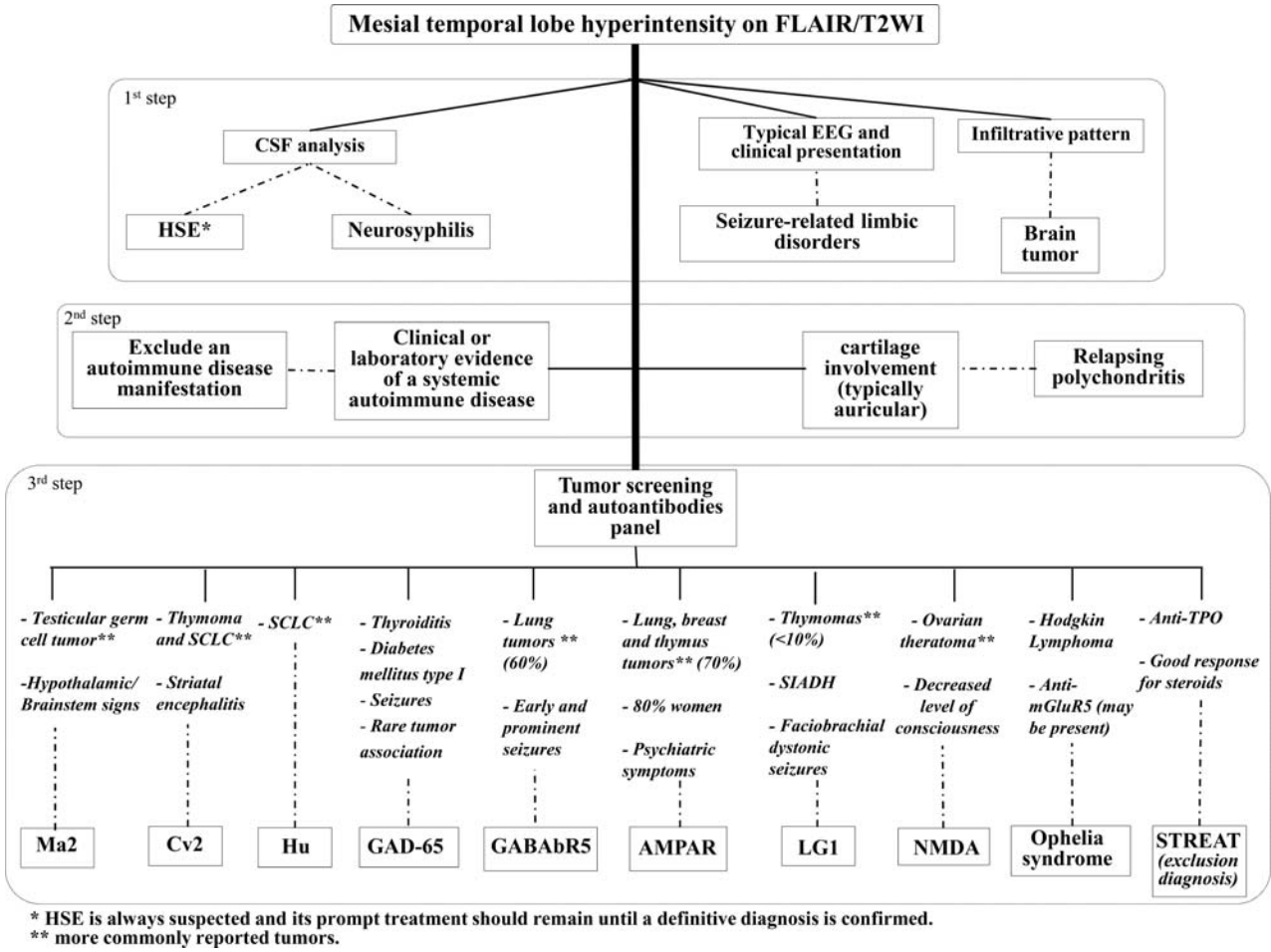

FIG 10. Proposed approach to the diagnosis of LE and its mimic disorders. SCLC indicates small cell lung carcinoma; SIADA, syndrome of inappropriate antidiuretic hormone; TPO, thyroperoxidase; NMDA, *N*-methyl-D-aspartate; STREAT, steroid-responsive encephalopathy associated with autoimmune thyroiditis; AMPAR, α-amino-3-hydroxy-5-methyl-4-isoxazolepropionic acid receptor.

recognizing limbic disorders and is useful for differentiating among them and for improving their investigation.

REFERENCES

1. Brierley JB, Corsellis JA, Hierons R, et al. **Subacute encephalitis of later adult life mainly affecting the limbic areas.** *Brain* 1960;83:357–68 CrossRef
2. Vernino S, Geschwind M, Boeve B. **Autoimmune encephalopathies.** *Neurologist* 2007;13:140–47 CrossRef Medline
3. Tüzun E, Dalmau J. **Limbic encephalitis and variants: classification, diagnosis and treatment.** *Neurologist* 2007;13:261–71 CrossRef Medline
4. Gultekin SH, Rosenfeld MR, Voltz R, et al. **Paraneoplastic limbic encephalitis: neurological symptoms, immunological findings and tumour association in 50 patients.** *Brain* 2000;123(pt 7):1481–94 CrossRef Medline
5. Vieira Santos A, Matias S, Saraiva P, et al. **Differential diagnosis of mesiotemporal lesions: case report of neurosyphilis.** *Neuroradiology* 2005;47:664–67 CrossRef Medline
6. Kararizou E, Markou I, Zalonis I, et al. **Paraneoplastic limbic encephalitis presenting as acute viral encephalitis.** *J Neurooncol* 2005;75:229–32 CrossRef Medline
7. Tyler KL. **Emerging viral infections of the central nervous system: part 1.** *Arch Neurol* 2009;66:939–48 CrossRef Medline
8. Nagata R, Ikeda K, Nakamura Y, et al. **A case of gliomatosis cerebri mimicking limbic encephalitis: malignant transformation to glioblastoma.** *Int Med* 2010;49:1307–10 CrossRef Medline
9. Förster A, Griebe M, Gass A, et al. **Diffusion-weighted imaging for the differential diagnosis of disorders affecting the hippocampus.** *Cerebrovasc Dis* 2012;33:104–15 CrossRef Medline
10. Armangue T, Leypoldt F, Dalmau J. **Autoimmune encephalitis as differential diagnosis of infectious encephalitis.** *Curr Opin Neurol* 2014;27:361–68 CrossRef Medline
11. Kotsenas AL, Watson RE, Pittock SJ, et al. **MRI findings in autoimmune voltage-gated potassium channel complex encephalitis with seizures: one potential etiology for mesial temporal sclerosis.** *AJNR Am J Neuroradiol* 2014;35:84–89 CrossRef Medline
12. Oyanguren B, Sánchez V, González FJ, et al. **Limbic encephalitis: a clinical-radiological comparison between herpetic and autoimmune etiologies.** *Eur J Neurol* 2013;20:1566–70 CrossRef Medline
13. Dalmau J, Bataller L. **Clinical and immunological diversity of limbic encephalitis: a model for paraneoplastic neurologic disorders.** *Hematol Oncol Clin North Am* 2006;20:1319–35 CrossRef Medline
14. Demaerel P, Van Dessel W, Van Paesschen W, et al. **Autoimmune-mediated encephalitis.** *Neuroradiology* 2011;53:837–51 CrossRef Medline
15. Darnell RB, Posner JB. **Paraneoplastic syndromes involving the nervous system.** *N Engl J Med* 2003;349:1543–54 CrossRef Medline
16. Dalmau J, Rosenfeld MR. **Autoimmune encephalitis update.** *Neuro Oncol* 2014;16:771–78 CrossRef Medline
17. Graus F, Ariño H, Dalmau J. **Paraneoplastic neurological syndromes in Hodgkin and non-Hodgkin lymphomas.** *Blood* 2014;123:3230–38 CrossRef Medline
18. Graus F, Keime-Guibert F, Reñe R, et al. **Anti-Hu-associated para-**

neoplastic encephalomyelitis: analysis of 200 patients. *Brain* 2001; 124(pt 6):1138–48 CrossRef Medline
19. Shavit YB, Graus F, Probst A, et al. **Epilepsia partialis continua: a new manifestation of anti-Hu-associated paraneoplastic encephalomyelitis.** *Ann Neurol* 1999;45:255–58 CrossRef Medline
20. Keime-Guibert F, Graus F, Fleury A, et al. **Treatment of paraneoplastic neurological syndromes with antineuronal antibodies (Anti-Hu, anti-Yo) with a combination of immunoglobulins, cyclophosphamide, and methylprednisolone.** *J Neurol Neurosurg Psychiatry* 2000;68:479–82 CrossRef Medline
21. Rosenfeld MR, Eichen JG, Wade DF, et al. **Molecular and clinical diversity in paraneoplastic immunity to Ma proteins.** *Ann Neurol* 2001;50:339–48 CrossRef Medline
22. Dalmau J, Graus F, Villarejo A, et al. **Clinical analysis of anti-Ma2-associated encephalitis.** *Brain* 2004;127(pt 8):1831–44 CrossRef Medline
23. Dalmau J, Gultekin SH, Voltz R, et al. **Ma1, a novel neuron- and testis-specific protein, is recognized by the serum of patients with paraneoplastic neurological disorders.** *Brain* 1999;122(pt 1):27–39 CrossRef Medline
24. Honnorat J, Cartalat-Carel S, Ricard D, et al. **Onco-neural antibodies and tumour type determine survival and neurological symptoms in paraneoplastic neurological syndromes with Hu or CV2/CRMP5 antibodies.** *J Neurol Neurosurg Psychiatry* 2009;80:412–16 CrossRef Medline
25. Vernino S, Tuite P, Adler CH, et al. **Paraneoplastic chorea associated with CRMP-5 neuronal antibody and lung carcinoma.** *Ann Neurol* 2002;51:625–30 CrossRef Medline
26. Gable MS, Sheriff H, Dalmau J, et al. **The frequency of autoimmune N-methyl-D-aspartate receptor encephalitis surpasses that of individual viral etiologies in young individuals enrolled in the California Encephalitis Project.** *Clin Infect Dis* 2012;54:899–904 CrossRef Medline
27. Titulaer MJ, McCracken L, Gabilondo I, et al. **Treatment and prognostic factors for long-term outcome in patients with anti-NMDA receptor encephalitis: an observational cohort study.** *Lancet Neurol* 2013;12:157–65 CrossRef Medline
28. Irani SR, Bera K, Waters P, et al. **N-methyl-D-aspartate antibody encephalitis: temporal progression of clinical and paraclinical observations in a predominantly non-paraneoplastic disorder of both sexes.** *Brain* 2010;133(pt 6):1655–67 CrossRef Medline
29. Kayser MS, Titulaer MJ, Gresa-Arribas N, et al. **Frequency and characteristics of isolated psychiatric episodes in anti–N-methyl-d-aspartate receptor encephalitis.** *JAMA Neurol* 2013;70:1133–39 CrossRef Medline
30. Dalmau J, Gleichman AJ, Hughes EG, et al. **Anti-NMDA-receptor encephalitis: case series and analysis of the effects of antibodies.** *Lancet Neurol* 2008;7:1091–98 CrossRef Medline
31. Dalmau J, Tüzün E, Wu HY, et al. **Paraneoplastic anti-N-methyl-D-aspartate receptor encephalitis associated with ovarian teratoma.** *Ann Neurol* 2007;61:25–36 CrossRef Medline
32. Titulaer MJ, McCracken L, Gabilondo I, et al. **Late-onset anti-NMDA receptor encephalitis.** *Neurology* 2013;81:1058–63 CrossRef Medline
33. Johnson N, Henry C, Fessler AJ, et al. **Anti-NMDA receptor encephalitis causing prolonged nonconvulsive status epilepticus.** *Neurology* 2010;75:1480–82 CrossRef Medline
34. Lancaster E, Lai M, Peng X, et al. **Antibodies to the GABA(B) receptor in limbic encephalitis with seizures: case series and characterisation of the antigen.** *Lancet Neurol* 2010;9:67–76 CrossRef Medline
35. Höftberger R, Titulaer MJ, Sabater L, et al. **Encephalitis and GABAB receptor antibodies: novel findings in a new case series of 20 patients.** *Neurology* 2013;81:1500–06 CrossRef Medline
36. Boronat A, Sabater L, Saiz A, et al. **GABA(B) receptor antibodies in limbic encephalitis and anti-GAD-associated neurologic disorders.** *Neurology* 2011;76:795–800 CrossRef Medline
37. Petit-Pedrol M, Armangue T, Peng X, et al. **Encephalitis with refractory seizures, status epilepticus, and antibodies to the GABAA receptor: a case series, characterisation of the antigen, and analysis of the effects of antibodies.** *Lancet Neurol* 2014;13:276–86 CrossRef Medline
38. Graus F, Boronat A, Xifró X, et al. T**he expanding clinical profile of anti-AMPA receptor encephalitis.** *Neurology* 2010;74:857–59 CrossRef Medline
39. Carr I. **The Ophelia syndrome: memory loss in Hodgkin's disease.** *Lancet* 1982;1:844–45 Medline
40. Mat A, Adler H, Merwick A, et al. **Ophelia syndrome with metabotropic glutamate receptor 5 antibodies in CSF.** *Neurology* 2013;80: 1349–50 CrossRef Medline
41. Malter MP, Helmstaedter C, Urbach H, et al. **Antibodies to glutamic acid decarboxylase define a form of limbic encephalitis.** *Ann Neurol* 2010;67:470–78 CrossRef Medline
42. Grau-Rivera O, Sánchez-Valle R, Saiz A, et al. **Determination of neuronal antibodies in suspected and definite Creutzfeldt-Jakob disease.** *JAMA Neurol* 2014;71:74–78 CrossRef Medline
43. Paterson RW, Zandi MS, Armstrong R, et al. **Clinical relevance of positive voltage-gated potassium channel (VGKC)-complex antibodies: experience from a tertiary referral centre.** *J Neurol Neurosurg Psychiatry* 2014;85:625–30 CrossRef Medline
44. Irani SR, Michell AW, Lang B, et al. **Faciobrachial dystonic seizures precede Lgi1 antibody limbic encephalitis.** *Ann Neurol* 2011;69:892–900 CrossRef Medline
45. Hiraga A, Kuwabara S, Hayakawa S, et al. **Voltage-gated potassium channel antibody-associated encephalitis with basal ganglia lesions.** *Neurology* 2006;66:1780–81 CrossRef Medline
46. Majoie HJ, de Baets M, Renier W, et al. **Antibodies to voltage-gated potassium and calcium channels in epilepsy.** *Epilepsy Res* 2006;71: 135–41 CrossRef Medline
47. Vincent A, Buckley C, Schott JM, et al. **Potassium channel antibody-associated encephalopathy: a potentially immunotherapy-responsive form of limbic encephalitis.** *Brain* 2004;127(pt 3):701–12 CrossRef Medline
48. Lancaster E, Huijbers MG, Bar V, et al. **Investigations of caspr2, an autoantigen of encephalitis and neuromyotonia.** *Ann Neurol* 2011; 69:303–11 CrossRef Medline
49. Blanc F, Ben Abdelghani K, Schramm F, et al. **Whipple limbic encephalitis.** *Arch Neurol* 2011;68:1471–73 CrossRef Medline
50. Badruddin A, Menon RS, Reder AT. **4-Aminopyridine toxicity mimics autoimmune-mediated limbic encephalitis.** *Neurology* 2009;72: 1100–01 CrossRef Medline
51. Boeve BF, Bell DG, Noseworthy JH. **Bilateral temporal lobe MRI changes in uncomplicated hypoglycemic coma.** *Can J Neurol Sci* 1995;22:56–8 Medline
52. Baringer JR. **Herpes simplex infections of the nervous system.** *Neurol Clin* 2008;26:657–74, viii CrossRef Medline
53. Armangue T, Leypoldt F, Málaga I, et al. **Herpes simplex virus encephalitis is a trigger of brain autoimmunity.** *Ann Neurol* 2014;75: 317–23 CrossRef Medline
54. Schäbitz WR, Rogalewski A, Hagemeister C, et al. **VZV brainstem encephalitis triggers NMDA receptor immunoreaction.** *Neurology* 2014;83:2309–11 CrossRef Medline
55. Höftberger R, Armangue T, Leypoldt F, et al. **Clinical neuropathology practice guide 4–2013: post-herpes simplex encephalitis: N-methyl-Daspartate receptor antibodies are part of the problem.** *Clin Neuropathol* 2013;32:251–54 CrossRef Medline
56. Karsan N, Barker R, O'Dwyer JP. **Clinical reasoning: the "great imitator."** *Neurology* 2014;83:e188–96 CrossRef Medline
57. Vates GE, Chang S, Lamborn KR, et al. **Gliomatosis cerebri: a review of 22 cases.** *Neurosurgery* 2003;53:261–71, discussion 271 CrossRef Medline
58. Maia AC Jr, Malheiros SM, da Rocha AJ, et al. **Stereotactic biopsy guidance in adults with supratentorial nonenhancing gliomas: role of perfusion-weighted magnetic resonance imaging.** *J Neurosurg* 2004;101:970–76 CrossRef Medline
59. Sedlaczek O, Hirsch JG, Grips E, et al. **Detection of delayed focal MR changes in the lateral hippocampus in transient global amnesia.** *Neurology* 2004;62:2165–70 CrossRef Medline

60. Cendes F. **Febrile seizures and mesial temporal sclerosis.** *Curr Opin Neurol* 2004;17:161–64 CrossRef Medline
61. Kim JA, Chung JI, Yoon PH, et al. **Transient MR signal changes in patients with generalized tonicoclonic seizure or status epilepticus: periictal diffusion-weighted imaging.** *AJNR Am J Neuroradiol* 2001; 22:1149–60 Medline
62. Cox JE, Mathews VP, Santos CC, et al. **Seizure-induced transient hippocampal abnormalities on MR: correlation with positron emission tomography and electroencephalography.** *AJNR Am J Neuroradiol* 1995;16:1736–38 Medline
63. Hatanpaa KJ, Blass DM, Pletnikova O, et al. **Most cases of dementia with hippocampal sclerosis may represent frontotemporal dementia.** *Neurology* 2004;63:538–42 CrossRef Medline
64. Caraballo RH, Reyes G, Avaria MF, et al. **Febrile infection-related epilepsy syndrome: a study of 12 patients.** *Seizure* 2013;22:553–59 CrossRef Medline
65. van Baalen A, Häusler M, Boor R, et al. **Febrile infection-related epilepsy syndrome (FIRES): a nonencephalitic encephalopathy in childhood.** *Epilepsia* 2010;51:1323–28 CrossRef Medline
66. Venkatesan A, Benavides DR. **Autoimmune encephalitis and its relation to infection.** *Curr Neurol Neurosci Rep* 2015;15:3 CrossRef
67. Castillo P, Woodruff B, Caselli R, et al. **Steroid-responsive encephalopathy associated with autoimmune thyroiditis.** *Arch Neurol* 2006; 63:197–202 CrossRef Medline
68. Hollowell JG, Staehling NW, Flanders WD, et al. **Serum TSH, T(4), and thyroid antibodies in the United States population (1988 to 1994): National Health and Nutrition Examination Survey (NHANES III).** *J Clin Endocrinol Metab* 2002;87:489–99 CrossRef Medline
69. Ferracci F, Carnevale A. **The neurological disorder associated with thyroid autoimmunity.** *J Neurol* 2006;253:975–84 CrossRef Medline
70. Song YM, Seo DW, Chang GY. **MR findings in Hashimoto encephalopathy.** *AJNR Am J Neuroradiol* 2004;25:807–08 Medline
71. Fujiki F, Tsuboi Y, Hashimoto K, et al. **Non-herpetic limbic encephalitis associated with relapsing polychondritis.** *J Neurol Neurosurg Psychiatry* 2004;75:1646–47 CrossRef Medline
72. Kumar N, Leep Hunderfund AN, Kutzbach BR, et al. **A limbic encephalitis MR imaging in a patient with Behcet disease and relapsing polychondritis.** *AJNR Am J Neuroradiol* 2009;30:E96 CrossRef Medline
73. Foidart JM, Abe S, Martin GR, et al. **Antibodies to type II collagen in relapsing polychondritis.** *N Engl J Med* 1978;299:1203–07 CrossRef Medline

Multimodal Diagnostic Imaging for Hyperacute Stroke

K.D. Vo, A.J. Yoo, A. Gupta, Y. Qiao, A.S. Vagal, J.A. Hirsch, D.M. Yousem, and C. Lum

ABSTRACT

SUMMARY: In April 2015, the American Roentgen Ray Society and the American Society of Neuroradiology cosponsored a unique program designed to evaluate the state of the art in the imaging work-up of acute stroke. This topic has grown in importance because of the recent randomized controlled trials demonstrating the clear efficacy of endovascular stroke treatment. The authors, who were participants in that symposium, will highlight the points of emphasis in this article.

ABBREVIATIONS: NINDS = National Institute of Neurological Disorders and Stroke; ECASS = European Cooperative Acute Stroke Study; MR CLEAN = Multicenter Randomized Clinical Trial of Endovascular Treatment for Acute Ischemic Stroke in the Netherlands; ESCAPE = Endovascular Treatment for Small Core and Anterior Circulation Proximal Occlusion with Emphasis on Minimizing CT to Recanalization Times; EVT = endovascular treatment; EXTEND-IA = Extending the Time for Thrombolysis in Emergency Neurological Deficits–Intra-Arterial; MR RESCUE = Mechanical Retrieval and Recanalization of Stroke Clots Using Embolectomy; SWIFT-PRIME = Solitaire With the Intention for Thrombectomy as Primary Endovascular Treatment

For >2 decades, intravenous tissue plasminogen activator was the only proved therapy for acute ischemic stroke, despite having limited efficacy for large-vessel occlusions and a restrictive timeframe for administration.[1,2] The recent publication of randomized controlled trials demonstrating a high degree of efficacy for endovascular treatment (EVT) in strokes caused by large-vessel occlusions heralds a new era of acute stroke therapy. The Multicenter Randomized Clinical Trial of Endovascular Treatment for Acute Ischemic Stroke in the Netherlands (MR CLEAN),[3] Endovascular Treatment for Small Core and Anterior Circulation Proximal Occlusion with Emphasis on Minimizing CT to Recanalization Times (ESCAPE),[4] Extending the Time for Thrombolysis in Emergency Neurological Deficits–Intra-Arterial (EXTEND-IA),[5] and Solitaire With the Intention for Thrombectomy as Primary Endovascular Treatment (SWIFT-PRIME)[6] trials demonstrated that patients with acute ischemic stroke with a proximal large-vessel occlusion of the anterior circulation have significantly improved functional outcomes when EVT is initiated within 6 hours after stroke onset. EVT was used in combination with standard-of-care IV-tPA, resulting in an absolute risk reduction of stroke disability by 14%–31% (the number of patients needed to treat for one patient to have good outcome ranged from 3 to 6).

So why did these trials work when other endovascular trials, including the Interventional Management of Stroke-III,[7] the Mechanical Retrieval and Recanalization of Stroke Clots Using Embolectomy (MR RESCUE),[8] and the Local Versus Systemic Thrombolysis for Acute Ischemic Stroke[9] trials, had failed? A major contributor to the success of these endovascular trials was superior mechanical thrombectomy devices resulting in safer, faster, and higher rates of reperfusion. Another contributor to the success of these trials seems to have been the use of rapid and accurate imaging screens to select patients with the greatest potential to benefit from the EVT.[10,11]

As treatment for stroke has advanced, the demands for imaging to help select appropriate patients for various treatments have increased. Initially, imaging was used primarily to rule out hemorrhage and stroke mimics. With the more advanced therapeutic options that are currently available, imaging is now used to determine the following: 1) the location of thrombus, 2) the volume of the infarct core, 3) tissue viability, and 4) the degree of collateral circulation. In this portion of the review, we will debate the merits of multimodal CT versus multimodal MR imaging as a tool to identify candidates for intervention, address safety and quality

From the Mallinckrodt Institute of Radiology (K.D.V.), Washington University School of Medicine, St. Louis, Missouri; Division of Neurointervention (A.J.Y.), Texas Stroke Institute, Plano, Texas; Department of Radiology and Feil Family Brain and Mind Research Institute (A.G.), Weill Cornell Medical College, New York, New York; Department of Radiology (Y.Q.), Johns Hopkins School of Medicine, Baltimore, Maryland; Department of Radiology (A.S.V.), University of Cincinnati Medical Center, Cincinnati, Ohio; NeuroInterventional Radiology (J.A.H.), Massachusetts General Hospital, Boston, Massachusetts; Department of Radiology (D.M.Y.), Johns Hopkins Medical Institution, Baltimore, Maryland; and Interventional Neuroradiology (C.L.), Ottawa Hospital Research Institute, University of Ottawa, Ottawa, Ontaria, Canada.

Please address correspondence to Katie D. Vo, MD, Mallinckrodt Institute of Radiology, Washington University School of Medicine, 510 South Kingshighway Blvd, Campus Box 8131, St. Louis, MO 63110-1076; e-mail: vok@wustl.edu

Indicates open access to non-subscribers at www.ajnr.org

Indicates article with supplemental on-line photo.

http://dx.doi.org/10.3174/ajnr.A4530

Efficacious acute stroke randomized controlled trials

Trial	Time Window (hr)	Treatment	Screening Imaging Modality
NINDS[1]	0–3	IV-tPA	NCCT
ECASS III[2]	3–4.5	IV-tPA	NCCT
TNK[25]	0–6	IV tenecteplase	NCCT+CTA+CTP
MR CLEAN[3]	0–6	IA thrombectomy	NCCT+CTA/MRA/DSA
ESCAPE[4]	0–12	IA thrombectomy	NCCT+multiphase CTA
EXTEND-IA[5]	0–6	IA thrombectomy	NCCT+CTA+CTP
SWIFT-PRIME[6]	0–6	IA thrombectomy	NCCT+CTA/MRA±CTP/MRP

Note:—NINDS indicates National Institute of Neurological Disorders and Stroke; ECASS, European Cooperative Acute Stroke Study; TNK, tenecteplase; MR CLEAN, Multicenter Randomized Clinical Trial of Endovascular Treatment for Acute Ischemic Stroke in the Netherlands; IA, intra-arterial; MRP, MR perfusion.

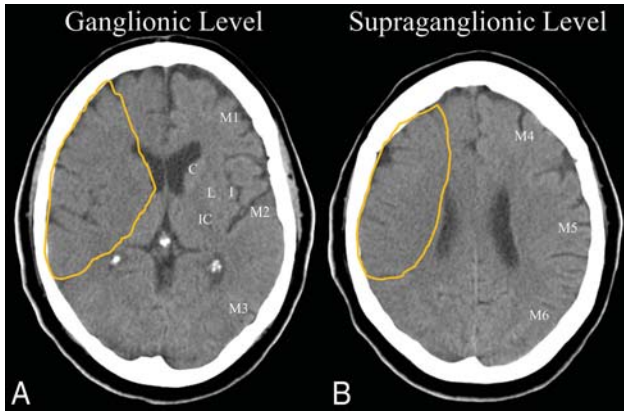

FIGURE. ASPECTS[21] scoring on an NCCT of a 52-year-old woman 2.5 hours after the onset of a left hemiparesis. Ten defined regions of the MCA distribution are identified on a normal left cerebral hemisphere at ganglionic (*A*) and supraganglionic (*B*) levels: the caudate nucleus (C), the lentiform nucleus (L), the internal capsule (IC), the insular cortex (I), and M1, M2, M3, M4, M5, and M6. The outlined areas in the right hemisphere show hypoattenuation in 8 regions given an ASPECTS score of 2.

issues in stroke imaging, and highlight key aspects of vessel wall imaging.

Multimodal CT as an Effective Screening Tool for Acute Stroke Treatment

A review of each of the positive randomized controlled trials for acute ischemic stroke treatment revealed that CT was the imaging technique of choice to select patients for treatment (Table). Only a few randomized controlled trials, Echo planar Imaging Thrombolytic Evaluation trial,[12] Study of Desmoteplase In Acute Ischemic Stroke phase II,[13] and MR RESCUE,[8] used MR imaging as a screening tool (some also permitted CTP); but none of these trials demonstrated efficacy. Multimodal CT, including NCCT, CTP, and CTA, is capable of addressing all the acute imaging needs required for screening thrombectomy candidates: ruling out hemorrhage and identifying large-vessel occlusion, detecting infarct core and penumbra, and assessing collateral flow. Most important, in most settings, accessibility to CT is fast and efficient.

Rule Out Hemorrhage. NCCT is widely accepted as the criterion standard for imaging intracerebral hemorrhage and can reliably identify acute hemorrhage with high sensitivity. Despite the heightened sensitivity of SWI to microbleeds, several studies suggest that neither the presence nor the number of cerebral microbleeds is associated with a significantly increased risk of hemorrhagic transformation in tPA-treated or untreated patients.[14-16] One study showed a higher risk of symptomatic hemorrhage after intravenous thrombolysis in patients with >5 microbleeds but no association with less favorable outcome.[17] More studies to assess the safety and effectiveness of thrombolysis in patients with microbleeds are needed.

Detection of Large-Vessel Occlusion. Vascular imaging was required in all 4 of the positive endovascular trials. CTA was the imaging technique of choice in the 4 randomized controlled trials for thrombectomy.[18] CTA can be performed immediately following NCCT. It is fast, less prone to motion, and widely available in the community. It is safe and can be performed without first screening for renal function (discussed below). The only contraindication to CTA is a severe contrast allergy, in which case MRA can be performed but will potentially delay time-sensitive therapies by 18–30 minutes.[19,20]

Detection of Core and Penumbra. Patients with a large infarct core are unlikely to benefit from endovascular therapy. One surrogate measure for the extent of the core is the semiquantitative Alberta Stroke Program Early CT Score (Figure), which quantifies early ischemic changes in the middle cerebral artery territory on NCCT.[21] This 10-point scoring system systematically rates early signs of ischemia in defined brain regions; a score of 10 indicates a scan with normal findings, and 1 point is subtracted for each abnormal brain region. A score of <4 is considered significant, indicating a large infarct core, and is associated with increased risk of hemorrhagic transformation and poor outcomes after thrombolysis.[22] Because of these associations, patients with an ASPECTS of <6 were excluded from enrollment in 3 of the 4 positive thrombectomy trials.[4-6]

The ischemic penumbra, defined as brain tissue that will die if untreated but survive if reperfused, can be assessed with either MR perfusion or CTP. There are strong advocates for using CTP to select patients for endovascular therapy, though a growing number think that CTP is inappropriate in an individual patient, arguing that the error bars associated with the noisy postprocessing algorithms are large.[23,24] CTP was used in 3 positive randomized controlled trials of endovascular therapy (ESCAPE,[4] EXTEND-IA,[5] and SWIFT-PRIME[6]) and a trial using IV tenecteplase[25] (genetically modified tissue plasminogen activator), to identify the penumbra before inclusion in the trials. These outcomes do not establish the necessity of CTP for identifying patients who will benefit from reperfusion therapy because numerous trials that did not use perfusion imaging still demonstrated efficacy.

Detection of Collateral Flow. Multiphase CTA is a new technique that allows a quick visual assessment of collateral flow in the affected territory.[26] The technique requires 3 scans after a contrast bolus to capture the arterial, midvenous, and late venous phases. The degree of enhancement of pial arteries distal to the occlusion positively correlates with the degree of collaterals (On-line Figure). In the setting of a proximal large-vessel occlusion, the presence of good collateral vessels is more likely to be associated with a smaller core and more salvageable brain tissue and has been shown to be a strong predictor of good outcomes. Patients with

poor collaterals were excluded from the ESCAPE and SWIFT PRIME trials, to help refine patient selection. The challenge of using collateral-based selection is the following: the nonstandardized approach to collateral grading and the dependence of the technique on noninvasive evaluation.[27]

CT has the advantage of having a rapid and efficient workflow (see discussion below). "Time is brain" is an important concept that stems from meta-analyses of IV-tPA trials demonstrating that the number of patients needed to be treated for 1 good outcome increases from 5 to 9 to 15 patients with every 90-minute delay in treatment.[28] A similar inverse relationship is seen between outcome and time to reperfusion for endovascular interventions.[29] The total scan time for a multimodal CT is approximately 5 minutes, while rapid MR imaging protocols can be reduced to 10–15 minutes. Although the difference in actual imaging time between CT and MR imaging is small, a number of additional hurdles can add significantly to MR imaging times: the availability of a scanner, screening for MR imaging safety, transporting patients to the scanner often outside the emergency department, transferring patients in and out of the scanner with MR imaging–compatible equipment, positioning the patient, and so forth. These delays of 18–30 minutes may seem small, but when considering an emergency department arrival to groin puncture times of 95 minutes, the delays are significant.[19,20] In addition to delays, MR imaging is contraindicated in up to 20% of patients with acute stroke due to patient-related factors such as cardiac pacemakers and medical instability.[30]

In summary, MR imaging may be equivalent or superior to CT in its ability to address all imaging goals for acute ischemic stroke. However, obstacles for its use in the acute setting of stroke may limit its utility, though these obstacles may be overcome with workflow optimization. CT is faster and, some argue, able to satisfy the various imaging requirements for current time-sensitive therapeutics in a wider population. Most important, it is the most consistently used imaging technique in the trials of acute ischemic stroke treatments that were shown to be efficacious.

Multimodal MR Imaging as an Effective Screening Tool for Acute Stroke Treatment

All of the recent positive trials used CT for imaging selection. As such, no class I clinical evidence supports patient evaluation by using MR imaging. However, this lack of evidence does not signify the superiority of CT, just its greater feasibility in current clinical practice. Strong evidence supports the use of MR imaging to improve the safety profile and cost-effectiveness of intra-arterial treatment, which relies primarily on the greater accuracy of DWI to depict acute brain infarction. Using a streamlined protocol, MR imaging can provide all the necessary information for treatment decision-making and can be performed without a significant time delay.[31]

Rule Out Hemorrhage. Gradient recalled-echo T2*-weighted imaging and SWI are highly sensitive to blood-breakdown products. In acute stroke, gradient recalled-echo T2*WI has been shown to be as accurate as NCCT for the detection of acute intracranial hemorrhage and is superior to CT in the detection of chronic hemorrhage.[32] Within 6 hours of stroke onset (ie, treatment window for reperfusion), 1 study found a 96% concordance between CT and MR imaging for acute intracranial hemorrhage,[32] while another study reported a 100% accuracy of MR imaging for detecting intracerebral hemorrhage by using experienced readers and NCCT as the reference standard.[33] On the basis of these results, MR imaging is an excellent technique for distinguishing ischemic and hemorrhagic stroke for consideration of reperfusion therapy and is supported by recent American Heart Association guidelines (class I, level of evidence A).[34]

Documenting Proximal Artery Occlusion. Occlusive thrombus in the proximal intracranial arteries is the target of intra-arterial therapy. Therefore, noninvasive vessel imaging is critical for the rational delivery of this treatment (American Heart Association class I, level of evidence A).[34] Moreover, it provides important pretreatment data for the neurointerventionalist, who can choose the appropriate access tools in the case of arterial tortuosity or when treatment is required for steno-occlusive disease at the carotid bifurcation.

Although CTA provides the best noninvasive evaluation of the intracranial vessels,[35] MRA appears sufficient for decision-making regarding intra-arterial therapy. 3D TOF MRA has been shown to have 84%–87% sensitivity and 85%–98% specificity for identifying proximal artery occlusion.[18,36] Contrast-enhanced MRA offers faster acquisition times, wider coverage, and less flow-related signal loss but has lower spatial resolution and venous contamination.[37] Both CTA and MRA are recommended for noninvasive vessel imaging during acute stroke evaluation by American Heart Association guidelines (class I, level of evidence A).[34]

Identifying Large Infarcts for Treatment Exclusion. It is biologically intuitive that patients with large infarcts will do poorly irrespective of treatment. Although thresholds that define what is too large for treatment vary depending on the clinical setting (eg, age, outcomes of interest), it is generally accepted that infarct volumes of >70–100 mL are highly predictive of poor outcome.[38,39] This volume approximates one-third of the MCA territory, but quantification (eg, by using the ABC/2 ellipsoid approximation) improves the precision over the traditional method of gross visual estimation. Moreover, such infarcts appear to be at higher risk for treatment-related complications, namely reperfusion hemorrhage.[38,40] For these reasons, it is important to have an accurate and reliable method for determining infarct volume in the treatment window.

Currently, DWI is the best clinically available technique to depict hyperacute infarction (American Heart Association class I, level of evidence A).[41,42] It has a reported 91%–100% sensitivity and 86%–100% specificity for infarct detection within the first 6 hours, as well as excellent interrater reliability.[43,44] Moreover, given the superior tissue contrast, it allows volumetric quantification. Despite early reports of diffusion lesion reversal, subsequent studies have shown that true reversal is rare and not clinically significant.[45] Even with near-complete (>90%) reperfusion, the rate of significant diffusion lesion volume reversal was <5%.[46] In comparison, all the CT-based techniques have major limitations. Like CTP, CTA source imaging is limited by technique, and hypoattenuated lesion volume has been shown to vary depending on when the brain is imaged during contrast transit.[47] The most reliable CT sign of early infarction is tissue hypoattenuation on

NCCT, which reflects a net increase in tissue water. This sign demonstrates limited sensitivity (~70%) but is highly specific (100%) for infarction.[48]

Two recent studies have shown the superiority of DWI over NCCT for evaluating patients who undergo EVT. The first was a post hoc analysis of patients receiving EVT in the Diffusion Weighted Imaging Evaluation for Understanding Stroke Evolution Study 2 who had pretreatment MR imaging and NCCT. The investigators found that ASPECTS graded on DWI had superior interrater agreement (intraclass correlation coefficient, 0.87 versus 0.58) and predicted 90-day good outcome better (C statistic, 0.71 versus 0.55; $P = .03$) than NCCT ASPECTS.[49] The second study was a single-center cohort analysis in which 2 separate imaging-selection approaches were compared.[50] In the first cohort, patients with proximal artery occlusions were evaluated for intra-arterial therapy by using NCCT and CTA, and in a subsequent cohort, DWI was performed in addition to NCCT and CTA. Most important, in both cohorts, the investigators analyzed outcomes in patients who were both treated and excluded from treatment and found that the cohort in which DWI was performed had better 30-day good outcomes (mRS 0–2: 23.6% versus 9.1%), lower mortality (25% versus 48.5%), and lower symptomatic hemorrhage rates (3.9% versus 10.2%), despite fewer patients being treated endovascularly (51.7% versus 96.6%). This finding suggests that MR imaging is appropriately excluding patients who are being harmed by intra-arterial therapy, namely those with large infarcts, and it equates to more cost-effective treatment delivery. Taken together, these studies support the promise of improved patient selection by using MR imaging.

Quality and Safety in Stroke Imaging

Imaging in the Stroke Workflow. As we integrate the evidence from the newer trials into our stroke workflow, time is critical. The national quality-improvement initiative of the American Heart Association and American Stroke Association to improve care in acute stroke, termed "Target: Stroke," highlights best practice strategies to reduce treatment times.[51] Urging rapid acquisition and interpretation of brain imaging, the authors recommend that 80% of patients with acute stroke evaluated for revascularization should have NCCT or MR imaging within 25 minutes, and 80% of patients should have interpretations within 45 minutes of arrival.[52]

Given the overwhelmingly positive results of the randomized controlled trials, there will be a shift toward increased use of advanced imaging in acute stroke. However, the randomized controlled trials also emphasized faster door-to-reperfusion times. In fact, the stroke workflow needs to run in a parallel fashion rather than being a linear process.[53,54] IV-tPA could be administered in the imaging suite as soon as the NCCT excludes hemorrhage, while CTA/CTP imaging is simultaneously being performed.[55] The stroke imaging protocols need to be modeled after trauma, necessitating the same level of urgency, targeting all points of delay: stroke-alert notification to radiologists, point-of-care testing, forgo blood work to verify creatinine levels, separation of reads of NCCT from multimodal imaging (CTA/CTP), rapid automated postprocessing of perfusion when performed, and convergence of teams to CT/MR imaging, where management decisions are made.[55]

MR imaging protocols usually have longer acquisition times and limited availability compared with CT, taking up to 15–20 minutes.[56] A faster 6-minute multimodal MR imaging protocol for acute stroke by using a combination of echo-planar and parallel acquisition has recently been published.[31] Centers that routinely use MR imaging–based paradigms for stroke need to design efficient process flows, including the availability of MR imaging in the emergency department, rapid safety screening (from charts, patients, family, and examination for scars), point-of-care creatinine level evaluation to minimize the risk for gadolinium-induced nephrogenic systemic fibrosis, and efficient stroke protocols.

In addition, one must optimize data collection to drive system improvement,[57] including time intervals and clinical outcomes, into a database, trial, or registry such as Get With The Guidelines Stroke Patient Management Tool (http://www.heart.org/HEARTORG/HealthcareResearch/GetWithTheGuidelines/GetWithTheGuidelines-Stroke/Get-With-The-Guidelines-Stroke-Patient-Management-Tool_UCM_308035_Article.jsp). Standardized and comprehensive data collection can be a powerful tool in providing feedback and bench marking to national averages and eventually changing outcomes.

Radiation Safety. It has been well-publicized in the media that >200 patients undergoing CTP in 1 center were exposed to >8 times the normal radiation dose, resulting in bandlike alopecia. One reason cited was an unrecognized alteration in the scanning protocols that did not diminish image quality and thus went undetected.[58]

Dose-length product is routinely used to estimate dose per patient. This can be converted to millisieverts as a measurement of "effective dose." The typical millisievert exposure for a total stroke imaging NCCT, CTA, and CTP is approximately 9–10 mSv. If one puts that into perspective, a head CT with and without contrast is estimated to have an effective dose of 4 mSv, equivalent to approximately 16 months' background radiation.[59] Some centers without CTP are using multiphase CTA, which incurs an incremental 1 mSv of exposure.[26]

Dose is dependent on tube current (milliampere-second), kilovolt peak, pitch, and collimation. The most frequent method used to limit dose is to reduce the milliampere-second; however, this reduction increases image noise. Image noise may be partially compensated by postprocessing techniques such as iterative reconstruction without incurring a dose penalty. Iterative reconstruction leads to a qualitative smoothing of image edges. Reducing kilovolt peak is a well-accepted strategy as long as it is not met with an automatic increase in milliampere-second to compensate for image quality. Currently, 80 kilovolt peak is the standard for CTP, with some newer research exploring the dose benefits of 70 kilovolt peak.[60] Another method of potentially reducing exposure is increasing the sampling interval for CTP examinations without significantly impacting image quality.[61] Therefore, awareness of the dose parameters affecting imaging quality is imperative. Add to the CT dosage the new recommendations for fluoroscopically guided EVT, and radiation exposure in a young patient with stroke may become a safety consideration.

Contrast Safety. The overall risk of contrast-induced nephropathy is approximately 2%–5% for patients with a glomerular filtration rate of 15–40 and higher for patients with a glomerular filtration rate of <15.[62] Multiple studies have demonstrated that administration of a contrast-enhanced protocol involving CTA/CTP and DSA in select patients does not appear to increase the incidence of contrast-induced nephropathy.[63,64] The risk of contrast-induced nephropathy is overestimated, and a significant proportion of transient creatinine elevation is due to expected fluctuation and underlying disease.[65] Hence the concern regarding the need to verify renal function before administering iodinated contrast in the acute stroke setting is overstated. Nephrogenic systemic fibrosis has been virtually eliminated by restricting gadolinium usage to patients with glomerular filtration rates of >30.[66]

Endovascular Treatment Center Availability. Historically, it has been difficult to estimate the number of patients treated with EVT.[67,68] Increasing demands for EVT will be accompanied by a commensurate change in the workload for existing regional and comprehensive stroke centers. Currently, it is estimated that adequate staffing is available to roughly 95% of the US population.[69] However, the recent trials have set lofty targets for revascularization times. In ESCAPE, the median time from stroke onset to CT imaging was 134 minutes and an imaging to groin puncture was 51 minutes, resulting in an onset-to-reperfusion time of just >4 hours (241 minutes). In SWIFT PRIME, the median time from arrival in the emergency department to groin puncture was 90 minutes, and from qualifying image to groin puncture, it was 57 minutes. Achieving these targets will be challenging in regions where geography limits accessibility to centers with neurointerventional expertise.

The Future of Hyperacute Stroke Imaging: Emphasis on Large Vessels?

With the recent excitement over the success of EVT, there will no doubt be increasing demands on acute multimodal diagnostic imaging to further guide therapeutic decision-making to enhance efficacy. In particular, large vessels may need further characterization to assess the benefits and risks tailored to specific acute therapies or for subsequent management decisions. Many studies have focused on direct cranial intravascular thrombus imaging by using NCCT or MR imaging to predict recanalization efficacy with EVT. Because a large thrombus burden is associated with lower rates of recanalization with EVT,[70] reconstructed thin-section NCCT (0.625–1.25 mm) has been used to improve the sensitivity of clot detection and the accuracy of clot quantification in the middle cerebral artery.[71,72] In addition, unlike pharmacologic fibrinolysis, recanalization rates by using mechanical thrombectomy are influenced more by the morphology of the target thrombus than its volume. One study showed that the recanalization rate is 3 times more common with a straight unbranched thrombus than with a branched tortuous thrombus as measured on gradient recalled-echo T2*WI by using the Merci device (Concentric Medical, Mountain View, California) for thrombectomy.[73] This outcome is primarily due to the mechanical force dispersion with a different shape of the clot during the retrieval. Thus, imaging characteristics of the thrombus may help in choosing the best EVT for successful recanalization.

Although past vascular imaging effort was largely focused on extracranial vessel imaging, some of the same principles may apply to large proximal intracranial vessels. This research will have greater application for intracranial atherosclerotic disease and its treatment than for embolic occlusions, which account for most conditions of patients undergoing thrombectomy.

MR vessel wall imaging is a powerful tool for extracranial (eg, carotid) plaque characterization, enabling the determination of stroke risk from carotid plaque rupture.[74] Recently, this technique has been implemented in several population-based studies to determine the plaque component prevalence and the associated risk that leads to stroke.[75] Both the Atherosclerosis Risk in Communities study[76] and the Multi-Ethnic Study of Atherosclerosis[77] have shown that the extent of carotid plaque and lipid core presence measured on MR imaging is associated with blood cholesterol levels. However, very few epidemiologic MR imaging studies have reached adequate numbers of outcomes (stroke events) since the initial MR imaging study. The Multi-Ethnic Study of Atherosclerosis carotid MR imaging study first reported associations of carotid plaque features with future events.[78] It showed that the remodeling index and lipid core presence measured on MR imaging added a risk for a new event beyond traditional risk factors in individuals without a history of cardiovascular disease. Future population-based studies to explore the predictive value of other high-risk plaque elements (eg, intraplaque hemorrhage or fibrous cap thinning/rupture) could provide insight in identifying asymptomatic individuals at risk for events. This insight will allow us to define a subgroup of asymptomatic patients who may benefit from therapeutic strategies that can target such vulnerable features.

Compared with extracranial atherosclerosis, intracranial atherosclerosis has been much less commonly studied in epidemiologic research due to the lack of an appropriate diagnostic tool to depict the intracranial vessel wall. Recent developments in 3D vessel wall MR imaging enable screening of major intracranial atherosclerosis[79,80] and provides reliable wall measurements in a population-based study (Atherosclerosis Risk in Communities–Neurocognitive study[81]). The prevalence of intracranial atherosclerosis in the Atherosclerosis Risk in Communities population (mean age, 77.1 years) was 34.4% and higher in African Americans compared with whites.[81] Future prospective epidemiologic studies that examine intracranial plaque burden in relation to risk factors and vascular markers (contemporaneous and change from earlier baseline measures) would contribute to a more comprehensive understanding of stroke risk.

Vessel wall imaging techniques have emerged to complement luminal stenosis assessments by providing a more detailed evaluation of intracranial vasculopathies. For example, recent studies suggest that multisequence, high-resolution MR wall imaging may differentiate atherosclerosis from other causes of vessel narrowing, such vasculitis,[82] and might aid in determining the etiology after acute ischemic stroke, given that culprit atherosclerotic lesions may preferentially demonstrate wall enhancement.[83] Larger, prospective studies with vessel wall imaging techniques are warranted to examine whether such methods could play a

more routine role in stroke prevention and diagnosis in patients with large-vessel atherosclerotic disease.

CONCLUSIONS

As we enter this new era of acute stroke therapeutics, our reliance on rapid diagnostic imaging to help guide therapy will continue to increase. The goal of imaging is to enhance the therapeutic index of available treatment options by selecting patients who have the greatest potential to benefit. Vital to the efficacy of any acute stroke treatment is time; therefore, diagnostic tests must be fast, reliable, and operationally efficient. Current treatment algorithms favor multimodal CT imaging even though MR imaging may be superior in individual diagnostic tasks. MR imaging shows promise in providing signatures for penumbra and core and may one day provide information beyond anatomic large-vessel occlusion to help guide advanced endovascular approaches as our therapeutic and diagnostic technology evolves.

Disclosures: Albert J. Yoo—*UNRELATED*: *Consultancy*: Neuravi*; *Grants/Grants Pending*: Penumbra,* Neuravi,* *Comments*: core imaging lab. Ajay Gupta—*UNRELATED*: *Grants/Grants Pending*: Foundation of the American Society of Neuroradiology Scholar Award,* National Institutes of Health/National Center for Advancing Translational Sciences Grant No. UL1TR00457,* *Comments*: grants supporting research related to imaging of stroke and cerebrovascular disease. Ye Qiao—*UNRELATED: Grants/Grants Pending:* NIH K99HL106232 and R00HL106232. *Comments:* MRI imaging of intracranial atherosclerosis. Achala S. Vagal—*UNRELATED*: *Grants/Grants Pending*: Clinical and Translational Science Awards 8 UL1 TR000077–05 KL2 research award,* Genentech (research grant).* Joshua A. Hirsch—*UNRELATED*: *Consultancy*: Medtronic, CareFusion, *Comments*: Medtronic, interventional spine, ongoing; CareFusion, single episode in time; taught a spine-related course; *Stock/Stock Options*: Intratech, InNeuroCo, *Comments*: Intratech, development-stage stroke company; InNeuroCo, development-stage catheter company. David M. Yousem—*UNRELATED*: *Expert Testimony*: Medicolegal consultations; *Payment for Lectures (including service on Speakers Bureaus)*: American College of Radiology Education Center*; *Royalties*: Elsevier; *Payment for Development of Educational Presentations*: CMEInfo.com for Hopkins Continuing Medical Education courses.* *Money paid to the institution.

REFERENCES

1. National Institute of Neurological Disorders and Stroke rt-PA Stroke Study Group. **Tissue plasminogen activator for acute ischemic stroke.** *N Engl J Med* 1995;333:1581–87 CrossRef Medline
2. Hacke W, Kaste M, Bluhmki E, et al; ECASS Investigators. **Thrombolysis with alteplase 3 to 4.5 hours after acute ischemic stroke.** *N Engl J Med* 2008;359:1317–29 CrossRef Medline
3. Berkhemer OA, Fransen PS, Beumer D, et al; MR CLEAN Investigators. **A randomized trial of intraarterial treatment for acute ischemic stroke.** *N Engl J Med* 2015;372:11–20 CrossRef Medline
4. Goyal M, Demchuk AM, Menon BK, et al; ESCAPE Trial Investigators. **Randomized assessment of rapid endovascular treatment of ischemic stroke.** *N Engl J Med* 2015;372:1019–30 CrossRef Medline
5. Campbell BC, Mitchell PJ, Kleinig TJ, et al; EXTEND-IA Investigators. **Endovascular therapy for ischemic stroke with perfusion-imaging selection.** *N Engl J Med* 2015;372:1009–18 CrossRef Medline
6. Saver JL, Goyal M, Bonafe A, et al; SWIFT PRIME Investigators. **Stent-retriever thrombectomy after intravenous t-PA vs. t-PA alone in stroke.** *N Engl J Med* 2015;372:2285–95 CrossRef Medline
7. Broderick JP, Palesch YY, Demchuk AM, et al; Interventional Management of Stroke (IMS) III Investigators. **Endovascular therapy after intravenous t-PA versus t-PA alone for stroke.** *N Engl J Med* 2013;368:893–903 CrossRef Medline
8. Kidwell CS, Jahan R, Gornbein J, et al; MR RESCUE Investigators. **A trial of imaging selection and endovascular treatment for ischemic stroke.** *N Engl J Med* 2013;368:914–23 CrossRef Medline
9. Ciccone A, Valvassori L, Nichelatti M, et al; SYNTHESIS Expansion Investigators. **Endovascular treatment for acute ischemic stroke.** *N Engl J Med* 2013;368:904–13 CrossRef Medline
10. Albuquerque FC, Fiorella D, Hirsch JA, et al. **The tribulations of stroke trials.** *J Neurointerv Surg* 2013;5:181–83 CrossRef Medline
11. Fiorella D, Hirsch JA, Mocco J. **In search of the optimized stroke trial design.** *J Neurointerv Surg* 2014;6:249–51 CrossRef Medline
12. Davis SM, Donnan GA, Parsons MW, et al; EPITHET investigators. **Effects of alteplase beyond 3 h after stroke in the Echoplanar Imaging Thrombolytic Evaluation Trial (EPITHET): a placebo-controlled randomised trial.** *Lancet Neurol* 2008;7:299–309 CrossRef Medline
13. Hacke W, Furlan AJ, Al-Rawi Y, et al. **Intravenous desmoteplase in patients with acute ischaemic stroke selected by MRI perfusion-diffusion weighted imaging or perfusion CT (DIAS-2): a prospective, randomised, double-blind, placebo-controlled study.** *Lancet Neurol* 2009;8:141–50 CrossRef Medline
14. Fiehler J, Albers GW, Boulanger JM, et al; MR STROKE Group. **Bleeding risk analysis in stroke imaging before thrombolysis (BRASIL): pooled analysis of T2*-weighted magnetic resonance imaging data from 570 patients.** *Stroke* 2007;38:2738–44 CrossRef Medline
15. Lee SH, Kang BS, Kim N, et al. **Does microbleed predict haemorrhagic transformation after acute atherothrombotic or cardioembolic stroke?** *J Neurol Neurosurg Psychiatry* 2008;79:913–16 CrossRef Medline
16. Kakuda W, Thijs VN, Lansberg MG, et al; DEFUSE Investigators. **Clinical importance of microbleeds in patients receiving IV thrombolysis.** *Neurology* 2005;65:1175–78 CrossRef Medline
17. Dannenberg S, Scheitz JF, Rozanski M, et al. **Number of cerebral microbleeds and risk of intracerebral hemorrhage after intravenous thrombolysis.** *Stroke* 2014;45:2900–05 CrossRef Medline
18. Bash S, Villablanca JP, Jahan R, et al. **Intracranial vascular stenosis and occlusive disease: evaluation with CT angiography, MR angiography, and digital subtraction angiography.** *AJNR Am J Neuroradiol* 2005;26:1012–21 Medline
19. Menon BK, Almekhlafi MA, Pereira VM, et al; STAR Study Investigators. **Optimal workflow and process-based performance measures for endovascular therapy in acute ischemic stroke: analysis of the Solitaire FR thrombectomy for acute revascularization study.** *Stroke* 2014;45:2024–29 CrossRef Medline
20. Sheth KN, Terry JB, Nogueira RG, et al. **Advanced modality imaging evaluation in acute ischemic stroke may lead to delayed endovascular reperfusion therapy without improvement in clinical outcomes.** *J Neurointerv Surg* 2013;5(suppl 1):i62–65 CrossRef Medline
21. Pexman JH, Barber PA, Hill MD, et al. **Use of the Alberta Stroke Program Early CT Score (ASPECTS) for assessing CT scans in patients with acute stroke.** *AJNR Am J Neuroradiol* 2001;22:1534–42 Medline
22. Yoo AJ, Zaidat OO, Chaudhry ZA, et al; Penumbra Pivotal and Penumbra Imaging Collaborative Study (PICS) Investigators. **Impact of pretreatment noncontrast CT Alberta Stroke Program Early CT Score on clinical outcome after intra-arterial stroke therapy.** *Stroke* 2014;45:746–51 CrossRef Medline
23. González RG. **Low signal, high noise and large uncertainty make CT perfusion unsuitable for acute ischemic stroke patient selection for endovascular therapy.** *J Neurointerv Surg* 2012;4:242–45 CrossRef Medline
24. González RG, Copen WA, Schaefer PW, et al. **The Massachusetts General Hospital acute stroke imaging algorithm: an experience and evidence based approach.** *J Neurointerv Surg* 2013;5(suppl 1): i7–12 CrossRef Medline
25. Parsons M, Spratt N, Bivard A, et al. **A randomized trial of tenecteplase versus alteplase for acute ischemic stroke.** *N Engl J Med* 2012; 366:1099–107 CrossRef Medline
26. Menon BK, d'Esterre CD, Qazi EM, et al. **Multiphase CT angiography: a new tool for the imaging triage of patients with acute ischemic stroke.** *Radiology* 2015;275:510–20 CrossRef Medline
27. McVerry F, Liebeskind DS, Muir KW. **Systematic review of methods**

for assessing leptomeningeal collateral flow. *AJNR Am J Neuroradiol* 2012;33:576–82 CrossRef Medline
28. Lees KR, Bluhmki E, von Kummer R, et al. **Time to treatment with intravenous alteplase and outcome in stroke: an updated pooled analysis of ECASS, ATLANTIS, NINDS, and EPITHET trials.** *Lancet* 2010;375:1695–703 CrossRef Medline
29. Khatri P, Yeatts SD, Mazighi M, et al. **Time to angiographic reperfusion and clinical outcome after acute ischaemic stroke: an analysis of data from the Interventional Management of Stroke (IMS III) phase 3 trial.** *Lancet Neurol* 2014;13:567–74 CrossRef Medline
30. Singer OC, Sitzer M, du Mesnil de Rochemont R, et al. **Practical limitations of acute stroke MRI due to patient-related problems.** *Neurology* 2004;62:1848–49 CrossRef Medline
31. Nael K, Khan R, Choudhary G, et al. **Six-minute magnetic resonance imaging protocol for evaluation of acute ischemic stroke: pushing the boundaries.** *Stroke* 2014;45:1985–91 CrossRef Medline
32. Kidwell CS, Chalela JA, Saver JL, et al. **Comparison of MRI and CT for detection of acute intracerebral hemorrhage.** *JAMA* 2004;292:1823–30 CrossRef Medline
33. Fiebach JB, Schellinger PD, Gass A, et al. **Stroke magnetic resonance imaging is accurate in hyperacute intracerebral hemorrhage: a multicenter study on the validity of stroke imaging.** *Stroke* 2004;35:502–06 CrossRef Medline
34. Jauch EC, Saver JL, Adams HP Jr, et al; American Heart Association Stroke Council, Council on Cardiovascular Nursing, Council on Peripheral Vascular Disease, Council on Clinical Cardiology. **Guidelines for the early management of patients with acute ischemic stroke: a guideline for healthcare professionals from the American Heart Association/American Stroke Association.** *Stroke* 2013;44:870–947 CrossRef Medline
35. Lev MH, Farkas J, Rodriguez VR, et al. **CT angiography in the rapid triage of patients with hyperacute stroke to intraarterial thrombolysis: accuracy in the detection of large vessel thrombus.** *J Comput Assist Tomogr* 2001;25:520–28 CrossRef Medline
36. Tomanek AI, Coutts SB, Demchuk AM, et al. **MR angiography compared to conventional selective angiography in acute stroke.** *Can J Neurol Sci* 2006;33:58–62 CrossRef Medline
37. Alfke K, Jensen U, Pool C, et al. **Contrast-enhanced magnetic resonance angiography in stroke diagnostics: additional information compared with time-of-flight magnetic resonance angiography?** *Clin Neuroradiol* 2011;21:5–10 CrossRef Medline
38. Olivot JM, Mosimann PJ, Labreuche J, et al. **Impact of diffusion-weighted imaging lesion volume on the success of endovascular reperfusion therapy.** *Stroke* 2013;44:2205–11 CrossRef Medline
39. Yoo AJ, Chaudhry ZA, Nogueira RG, et al. **Infarct volume is a pivotal biomarker after intra-arterial stroke therapy.** *Stroke* 2012;43:1323–30 CrossRef Medline
40. Lansberg MG, Thijs VN, Bammer R, et al; DEFUSE Investigators. **Risk factors of symptomatic intracerebral hemorrhage after tPA therapy for acute stroke.** *Stroke* 2007;38:2275–78 CrossRef Medline
41. Schellinger PD, Bryan RN, Caplan LR, et al; Therapeutics and Technology Assessment Subcommittee of the American Academy of Neurology. **Evidence-based guideline: the role of diffusion and perfusion MRI for the diagnosis of acute ischemic stroke—report of the Therapeutics and Technology Assessment Subcommittee of the American Academy of Neurology.** *Neurology* 2010;75:177–85 CrossRef Medline
42. Latchaw RE, Alberts MJ, Lev MH, et al; American Heart Association Council on Cardiovascular Radiology and Intervention, Stroke Council, and the Interdisciplinary Council on Peripheral Vascular Disease. **Recommendations for imaging of acute ischemic stroke: a scientific statement from the American Heart Association.** *Stroke* 2009;40:3646–78 CrossRef Medline
43. Fiebach JB, Schellinger PD, Jansen O, et al. **CT and diffusion-weighted MR imaging in randomized order: diffusion-weighted imaging results in higher accuracy and lower interrater variability in the diagnosis of hyperacute ischemic stroke.** *Stroke* 2002;33:2206–10 CrossRef Medline
44. González RG, Schaefer PW, Buonanno FS, et al. **Diffusion-weighted MR imaging: diagnostic accuracy in patients imaged within 6 hours of stroke symptom onset.** *Radiology* 1999;210:155–62 CrossRef Medline
45. Campbell BC, Purushotham A, Christensen S, et al; EPITHET–DEFUSE Investigators. **The infarct core is well represented by the acute diffusion lesion: sustained reversal is infrequent.** *J Cereb Blood Flow Metab* 2012;32:50–56 CrossRef Medline
46. Wheeler HM, Mlynash M, Inoue M, et al; DEFUSE 2 Investigators. **Early diffusion-weighted imaging and perfusion-weighted imaging lesion volumes forecast final infarct size in DEFUSE 2.** *Stroke* 2013;44:681–85 CrossRef Medline
47. Pulli B, Schaefer PW, Hakimelahi R, et al. **Acute ischemic stroke: infarct core estimation on CT angiography source images depends on CT angiography protocol.** *Radiology* 2012;262:593–604 CrossRef Medline
48. Lev MH, Farkas J, Gemmete JJ, et al. **Acute stroke: improved nonenhanced CT detection–benefits of soft-copy interpretation by using variable window width and center level settings.** *Radiology* 1999;213:150–55 CrossRef Medline
49. McTaggart RA, Jovin TG, Lansberg MG, et al; DEFUSE 2 Investigators. **Alberta stroke program early computed tomographic scoring performance in a series of patients undergoing computed tomography and MRI: reader agreement, modality agreement, and outcome prediction.** *Stroke* 2015;46:407–12 CrossRef Medline
50. Wisco D, Uchino K, Saqqur M, et al. **Addition of hyperacute MRI aids in patient selection, decreasing the use of endovascular stroke therapy.** *Stroke* 2014;45:467–72 CrossRef Medline
51. Fonarow GC, Smith EE, Saver JL, et al. **Improving door-to-needle times in acute ischemic stroke: the design and rationale for the American Heart Association/American Stroke Association's Target: Stroke initiative.** *Stroke* 2011;42:2983–89 CrossRef Medline
52. Leifer D, Bravata DM, Connors JJ 3rd, et al; American Heart Association Special Writing Group of the Stroke Council, Atherosclerotic Peripheral Vascular Disease Working Group, Council on Cardiovascular Surgery and Anesthesia, Council on Cardiovascular Nursing. **Metrics for measuring quality of care in comprehensive stroke centers: detailed follow-up to Brain Attack Coalition comprehensive stroke center recommendations—a statement for healthcare professionals from the American Heart Association/American Stroke Association.** *Stroke* 2011;42:849–77 CrossRef Medline
53. Mehta BP, Leslie-Mazwi TM, Chandra RV, et al. **Reducing door-to-puncture times for intra-arterial stroke therapy: a pilot quality improvement project.** *J Am Heart Assoc* 2014;3:e000963 CrossRef Medline
54. Gomez MA 2nd, Hirsch JA, Stingley P, et al. **Applying the lean management philosophy to neurointerventional radiology.** *J Neurointerv Surg* 2010;2:83–86 CrossRef Medline
55. Goyal M, Menon BK, Hill MD, et al. **Consistently achieving computed tomography to endovascular recanalization <90 minutes: solutions and innovations.** *Stroke* 2014;45:e252–56 CrossRef Medline
56. Schellinger PD, Jansen O, Fiebach JB, et al. **A standardized MRI stroke protocol: comparison with CT in hyperacute intracerebral hemorrhage.** *Stroke* 1999;30:765–68 CrossRef Medline
57. Ford AL, Williams JA, Spencer M, et al. **Reducing door-to-needle times using Toyota's lean manufacturing principles and value stream analysis.** *Stroke* 2012;43:3395–98 CrossRef Medline
58. Wintermark M, Lev MH. **FDA investigates the safety of brain perfusion CT.** *AJNR Am J Neuroradiol* 2010;31:2–3 CrossRef Medline
59. Radiation dose in X-ray and CT exams. http:www.radiologyinfo.org/en/info.cfm?pg=safety-x-ray. Accessed September 6, 2015
60. Corcuera-Solano I, McLellan AM, Doshi AH, et al. **Whole-brain adaptive 70-kVp perfusion imaging with variable and extended sampling improves quality and consistency while reducing dose.** *AJNR Am J Neuroradiol* 2014;35:2045–51 CrossRef Medline
61. Shankar JJ, Lum C, Sharma M. **Whole-brain perfusion imaging with 320-MDCT scanner: reducing radiation dose by increasing sam-**

pling interval. *AJR Am J Roentgenol* 2010;195:1183–86 CrossRef Medline
62. Davenport MS, Khalatbari S, Dillman JR, et al. **Contrast material-induced nephrotoxicity and intravenous low-osmolality iodinated contrast material.** *Radiology* 2013;267:94–105 CrossRef Medline
63. Krol AL, Dzialowski I, Roy J, et al. **Incidence of radiocontrast nephropathy in patients undergoing acute stroke computed tomography angiography.** *Stroke* 2007;38:2364–66 CrossRef Medline
64. Hopyan JJ, Gladstone DJ, Mallia G, et al. **Renal safety of CT angiography and perfusion imaging in the emergency evaluation of acute stroke.** *AJNR Am J Neuroradiol* 2008;29:1826–30 CrossRef Medline
65. Bruce RJ, Djamali A, Shinki K, et al. **Background fluctuation of kidney function versus contrast-induced nephrotoxicity.** *AJR Am J Roentgenol* 2009;192:711–18 CrossRef Medline
66. Wang Y, Alkasab TK, Narin O, et al. **Incidence of nephrogenic systemic fibrosis after adoption of restrictive gadolinium-based contrast agent guidelines.** *Radiology* 2011;260:105–11 CrossRef Medline
67. Fiorella D, Hirsch JA, Woo HH, et al. **Should neurointerventional fellowship training be suspended indefinitely?** *J Neurointerv Surg* 2012;4:315–18 CrossRef Medline
68. Hirsch JA, Yoo AJ, Nogueira RG, et al. **Case volumes of intra-arterial and intravenous treatment of ischemic stroke in the USA.** *J Neurointerv Surg* 2009;1:27–31 CrossRef Medline
69. Zaidat OO, Lazzaro M, McGinley E, et al. **Demand-supply of neurointerventionalists for endovascular ischemic stroke therapy.** *Neurology* 2012;79:S35–41 CrossRef Medline
70. Barreto AD, Albright KC, Hallevi H, et al. **Thrombus burden is associated with clinical outcome after intra-arterial therapy for acute ischemic stroke.** *Stroke* 2008;39:3231–35 CrossRef Medline
71. Riedel CH, Jensen U, Rohr A, et al. **Assessment of thrombus in acute middle cerebral artery occlusion using thin-slice nonenhanced computed tomography reconstructions.** *Stroke* 2010;41:1659–64 CrossRef Medline
72. Riedel CH, Zoubie J, Ulmer S, et al. **Thin-slice reconstructions of nonenhanced CT images allow for detection of thrombus in acute stroke.** *Stroke* 2012;43:2319–23 CrossRef Medline
73. Zhu L, Liebeskind DS, Jahan R, et al. **Thrombus branching and vessel curvature are important determinants of middle cerebral artery trunk recanalization with Merci thrombectomy devices.** *Stroke* 2012;43:787–92 CrossRef Medline
74. Gupta A, Baradaran H, Schweitzer AD, et al. **Carotid plaque MRI and stroke risk: a systematic review and meta-analysis.** *Stroke* 2013;44:3071–77 CrossRef Medline
75. Wasserman BA, Astor BC, Sharrett AR, et al. **MRI measurements of carotid plaque in the Atherosclerosis Risk in Communities (ARIC) study: methods, reliability and descriptive statistics.** *J Magn Reson Imaging* 2010;31:406–15 CrossRef Medline
76. Virani SS, Catellier DJ, Pompeii LA, et al. **Relation of cholesterol and lipoprotein parameters with carotid artery plaque characteristics: the Atherosclerosis Risk in Communities (ARIC) carotid MRI study.** *Atherosclerosis* 2011;219:596–602 CrossRef Medline
77. Wasserman BA, Sharrett AR, Lai S, et al. **Risk factor associations with the presence of a lipid core in carotid plaque of asymptomatic individuals using high-resolution MRI: the Multi-Ethnic Study of Atherosclerosis (MESA).** *Stroke* 2008;39:329–35 CrossRef Medline
78. Zavodni AE, Wasserman BA, McClelland RL, et al. **Carotid artery plaque morphology and composition in relation to incident cardiovascular events: the Multi-Ethnic Study of Atherosclerosis (MESA).** *Radiology* 2014;271:381–89 CrossRef Medline
79. Qiao Y, Steinman DA, Qin Q, et al. **Intracranial arterial wall imaging using three-dimensional high isotropic resolution black blood MRI at 3.0 Tesla.** *J Magn Reson Imaging* 2011;34:22–30 CrossRef Medline
80. Qiao Y, Zeiler SR, Mirbagheri S, et al. **Intracranial plaque enhancement in patients with cerebrovascular events on high-spatial-resolution MR images.** *Radiology* 2014;271:534–42 CrossRef Medline
81. Qiao Y, Liu L, Zhang Y. **Abstract T P108: MRI measurements of intracranial atherosclerosis in the ARIC neurocognitive study: methods, reliability and descriptive statistics.** In: *International Stroke Conference*, Nashville, Tennessee. February 10–12, 2015
82. Mossa-Basha M, Hwang WD, De Havenon A, et al. **Multicontrast high-resolution vessel wall magnetic resonance imaging and its value in differentiating intracranial vasculopathic processes.** *Stroke* 2015;46:1567–73 CrossRef Medline
83. Vakil P, Vranic J, Hurley MC, et al. **T1 gadolinium enhancement of intracranial atherosclerotic plaques associated with symptomatic ischemic presentations.** *AJNR Am J Neuroradiol* 2013;34:2252–58 CrossRef Medline

MRI Texture Analysis Reveals Bulbar Abnormalities in Friedreich Ataxia

T.A. Santos, C.E.B. Maistro, C.B. Silva, M.S. Oliveira, M.C. França, Jr, and G. Castellano

ABSTRACT

BACKGROUND AND PURPOSE: Texture analysis is an image processing technique that can be used to extract parameters able to describe meaningful features of an image or ROI. Texture analysis based on the gray level co-occurrence matrix gives a second-order statistical description of the image or ROI. In this work, the co-occurrence matrix texture approach was used to extract information from brain MR images of patients with Friedreich ataxia and a control group, to see whether texture parameters were different between these groups. A longitudinal analysis was also performed.

MATERIALS AND METHODS: Twenty patients and 21 healthy controls participated in the study. Both groups had 2 sets of T1-weighted MR images obtained 1 year apart for every subject. ROIs chosen for analysis were the medulla oblongata and pons. Texture parameters were obtained for these ROIs for every subject, for the 2 sets of images. These parameters were compared longitudinally within groups and transversally between groups.

RESULTS: The comparison between patients and the control group showed a significant differences for the medulla oblongata (*t* test, $P < .05$, Bonferroni-corrected) but did not show a statistically significant difference for the pons. Longitudinal comparison of images obtained 1 year apart did not show differences for either patients or for controls, in any of the analyzed structures.

CONCLUSIONS: Gray level co-occurrence matrix–based texture analysis showed statistically significant differences for the medulla oblongata of patients with Friedreich ataxia compared with controls. These results highlight the medulla as an important site of damage in Friedreich ataxia.

ABBREVIATIONS: C1 = the first control acquisition; C2 = the second control acquisition; FA = Friedreich ataxia; GLCM = gray level co-occurrence matrix; P1 = the first patient acquisition; P2 = the second patient acquisition

Digital images have revolutionized medicine because in addition to the readily available visual information provided by their analog counterparts, they can be mathematically manipulated by myriad processing techniques that allow extraction of many other types of information. In particular, the human eye can only distinguish around 60 shades of gray for a given adjustment of the pupil, whereas digital medical images such as those provided by MR imaging or x-ray CT normally use around 4000 gray levels for data encoding. Texture analysis[1] is the name given to a set of image-processing approaches that may be used for an efficient image classification based on a reduced parameter set or to detect subtle alterations in the gray level distribution of an image or ROI. Texture analysis approaches have been widely applied in medicine to differentiate normal and pathologic tissue, such as in epilepsy,[2-4] Machado-Joseph disease,[5] and central nervous system tumors.[6-8] In particular, texture analysis based on the gray level co-occurrence matrix (GLCM) gives a second-order statistical description of the image or ROI.[9,10] In this work, the GLCM approach was used to extract information from brain MR images of patients with Friedreich ataxia (FA) and a control group. We were primarily interested in looking for differences between these groups, but we also investigated whether texture parameters correlated with clinical data in the FA group.

FA is the most common autosomal recessive ataxia, and it is

Received January 30, 2015; accepted after revision May 18.

From the Neurophysics Group (T.A.S., C.E.B.M., M.S.O., G.C.), Gleb Wataghin Physics Institute, and Department of Neurology (C.B.S., M.C.F.), Medical Sciences School, University of Campinas, Brazil; and Brazilian Institute of Neuroscience and Neurotechnology (BRAINN) (São Paulo Research Foundation) (T.A.S., C.E.B.M., C.B.S., M.S.O., M.C.F., G.C.), Campinas, São Paulo, Brazil.

This work was supported by São Paulo Research Foundation (Brazil), grants 2012/24363-2, 2013/01766-7, 2013/07559-3, 2013/16273-6.

Please address correspondence to Gabriela Castellano, PhD, University of Campinas/IFGW, Rua Sergio Buarque de Holanda, 777, Cidade Universitária "Zeferino Vaz," 13083-859-Campinas-São Paulo, Brazil; e-mail: gabriela@ifi.unicamp.br

Indicates open access to non-subscribers at www.ajnr.org

Indicates article with supplemental on-line table.

Evidence-Based Medicine Level 2.

http://dx.doi.org/10.3174/ajnr.A4455

characterized by early onset and slowly progressive gait ataxia, dysmetria, dysarthria, and deep sensory abnormalities.[11] It is caused by homozygous triplet *GAA* expansions in the first intron of the *FXN* gene on chromosome 9q13 in 96% of patients.[12,13] This leads to dramatic underexpression of the encoded protein frataxin, which is essential for proper neuronal mitochondrial functioning.[11] The net results of the mutation are marked and progressive neuronal loss in the dorsal root ganglia, pyramidal tracts, and dentate nuclei of the cerebellum.[14]

Brain MR imaging of patients with FA does not present clearly visible changes. However, some previous studies have already shown alterations by using advanced techniques. Indeed, previous voxel-based morphometry studies showed gray matter and white matter atrophy in portions of the cerebellum and brain stem in FA.[15-18] The spinal cord area was found to be reduced in these patients.[19] Also, patients with FA have WM damage in the brain stem, cerebellum, and cerebellar peduncles.[16,17,20-22] To the best of our knowledge, there is no previous study on GLCM texture analysis of MR imaging in FA. We believe such a study would be important because texture analysis is a powerful tool able to identify subtle abnormalities before true atrophy appears.[2,3] It has proved useful in finding damaged areas in closely related conditions, such as Machado-Joseph disease.[5] In addition, it is highly reproducible and provides quantitative results. Taken together, these characteristics make texture analysis a technique appropriate for longitudinal MR imaging–based studies, which are extremely rare in FA. In this scenario, we recruited a representative cohort of patients who underwent 2 MR imaging scans 1 year apart and performed transversal and longitudinal texture analyses. We focused the analyses on brain stem structures, the pons and medulla oblongata, because these play a key role in the pathogenesis of the disease.

MATERIALS AND METHODS

Twenty patients with FA (mean age, 27.6 ± 9.6 years; 14 women) and a control group of 21 healthy subjects (mean age, 28.6 ± 5.3 years; 12 women) participated in this study. All patients had molecular confirmation of FA and were followed at the Neurogenetics Clinic at the University of Campinas. Mean ages at diagnosis and disease duration were 15.4 ± 5.2 and 13.1 ± 8.4 years, respectively. We used the Friedreich ataxia rating scale at each visit to quantify disease severity for each patient.[23] The study was approved by the local ethics committee, and all participants signed an informed consent form, before data acquisition.

MR imaging data were acquired in a 3T Achieva scanner (Philips Healthcare, Best, the Netherlands) at the Clinics Hospital of our university. Images used for texture analysis were T1-weighted, acquired with an 8-channel head coil, with an FOV of $240 \times 240 \times 180$ mm^3, voxel size of $1 \times 1 \times 1$ mm^3, TR of 7 ms, and TE of 3.2 ms.

Given an ROI in an image and a pixel distance in a given direction (eg, 2 pixels in the vertical direction), the GLCM approach consists of calculating, for every possible pair of gray levels, how many times they co-occur in the ROI in this direction and distance. From a GLCM, statistical parameters can then be computed, the most usual ones being the following[24]: contrast, homogeneity, correlation, variance, sum average, sum variance, difference variance, uniformity, entropy, sum entropy, and difference entropy. Formulas and descriptions for these parameters can be found in the On-line Table.

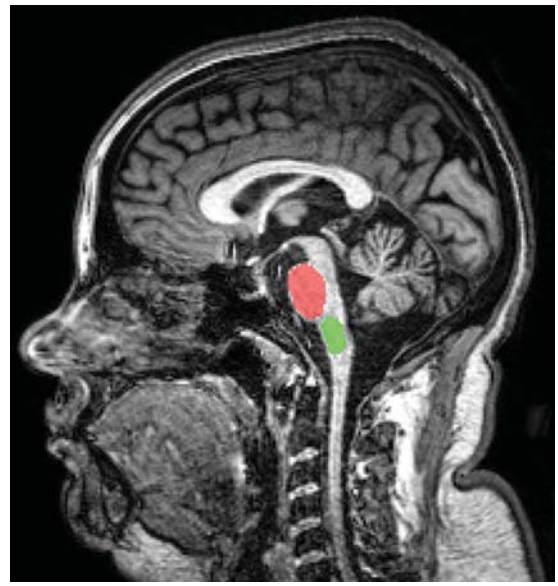

FIG 1. Example of segmented ROIs in the center section of the MR imaging examination for a patient with FA. The region in red indicates the pons, and the region in green indicates the medulla oblongata.

As mentioned, the ROIs investigated in this work were the medulla oblongata and the pons, known to be affected by FA. These structures were manually segmented, by using MaZda software (http://www.eletel.p.lodz.pl/programy/mazda/),[25] in 7 sagittal sections for each subject (consisting of the central section plus 3 anterior and 3 posterior sections). Figure 1 shows an example of these ROIs, segmented in 1 section, for a patient with FA, where the region in red is the pons and the region in green is the medulla oblongata. GLCMs were computed for every section, also by using the MaZda software. This software computes GLCMs for 4 directions (horizontal, vertical, and 2 diagonals) and 5 distances (1–5 pixels), giving 20 GLCMs per section or, in the present case, 140 GLCMs per ROI (280 per subject). Because the aforementioned 11 parameters were computed for every GLCM, the total number of parameters was 1540 per ROI (3080 per subject).

To reduce the number of parameters, we computed 2 averages. First, an average over the 7 ROI sections was calculated for each parameter, weighted by the segmented area in each section; this procedure had the effect of "merging" the information obtained for a given ROI that was previously "sliced." Second, an average over the 4 directions was calculated for each parameter. The idea behind this approach was to make the parameters direction-independent, because even if a given tissue had a preferred structural direction, the position axes of the acquired MR images might be slightly different for different subjects; this difference could affect the results. After these procedures, parameters were reduced to 55 per ROI (110 per subject).

Finally, GLCM texture parameters were compared statistically, by using a t test, Bonferroni corrected, with a significance level of $\alpha = .05$. Each GLCM parameter was analyzed longitudinally within a group, comparing images taken 1 year apart, and transversally between the groups. For the longitudinal compari-

GLCM texture parameters, which were significantly different between patients with FA and controls for at least 1 comparison between groups[a]

GLCM Distance (pixel)	Parameter	Group (Mean)				Comparison (*P* Value, Bonferroni-Corrected, *t* Test)			
		P1	P2	C1	C2	P1 × C1	P1 × C2	P2 × C1	P2 × C2
Medulla oblongata									
1	Correlation	0.27 ± 0.03	0.25 ± 0.05	0.45 ± 0.09	0.41 ± 0.10	.000[b]	.000[b]	.000[b]	.000[b]
1	Variance	11.84 ± 3.36	12.80 ± 4.14	17.71 ± 5.10	15.60 ± 4.83	.008[b]	.188	.413	1.00
1	Sum average	86.25 ± 3.45	86.18 ± 2.62	110.75 ± 5.83	103.48 ± 14.32	.000[b]	.002[b]	.000[b]	.002[b]
1	Sum variance	32.55 ± 9.52	34.61 ± 10.86	50.24 ± 16.52	43.56 ± 14.79	.014[b]	.103	.484	1.00
1	Entropy	1.46 ± 0.15	1.47 ± 0.07	2.00 ± 0.08	1.86 ± 0.23	.000[b]	.000[b]	.000[b]	.000[b]
1	Sum entropy	0.98 ± 0.08	0.99 ± 0.04	1.36 ± 0.06	1.25 ± 0.17	.000[b]	.000[b]	.000[b]	.000[b]
1	Difference entropy	0.71 ± 0.04	0.72 ± 0.04	0.93 ± 0.05	0.86 ± 0.11	.000[b]	.000[b]	.000[b]	.002[b]
1	Homogeneity	0.21 ± 0.05	0.20 ± 0.02	0.27 ± 0.03	0.27 ± 0.04	.004[b]	.165	.000[b]	.000[b]
2	Correlation	0.05 ± 0.05	0.04 ± 0.06	0.18 ± 0.08	0.17 ± 0.10	.000[b]	.001[b]	.000[b]	.002[b]
3	Correlation	0.04 ± 0.05	0.02 ± 0.05	0.13 ± 0.07	0.14 ± 0.08	.002[b]	.004[b]	.000[b]	.000[b]
4	Correlation	−0.01 ± 0.04	−0.03 ± 0.05	0.08 ± 0.07	0.08 ± 0.08	.004[b]	.013[b]	.000[b]	.001[b]
5	Correlation	−0.02 ± 0.03	−0.03 ± 0.05	0.06 ± 0.07	0.05 ± 0.07	.006[b]	.055	.008[b]	.049[b]
Pons									
1	Difference variance	7.27 ± 2.24	7.56 ± 1.89	5.58 ± 1.45	5.38 ± 1.11	.490	.142	.125	.034[b]

[a] Both patient acquisitions were compared with both control acquisitions.
[b] Significant.

son, only 16 (of 20) patients had the corresponding MR imaging acquisitions; therefore, these analyses were made considering this reduced group (16 patients). In addition, GLCM parameters that were found significant were correlated to clinical variables (age, age at onset, disease duration, *GAA1*, *GAA2*, Friedreich Ataxia Rating Scale total score) within the patient group. A *t* test comparing the age of the groups was also performed to ensure that ages were matched.

RESULTS

We will refer to P1 as the group corresponding to the first set of images (20 images) of the patients with FA, P2 as the group corresponding to the second set (16 images, obtained 1 year later) of the patients with FA, and C1 and C2 correspond to the first and second sets of control acquisitions, respectively (21 images each, obtained 1 year apart).

The FA and control groups were not significantly different regarding age (*t* test; $P = .99$ for P1 × C1; $P = .69$ for P1 × C2; $P = .60$ for P2 × C1; $P = .86$ for P2 × C2).

Longitudinal comparison of GLCM texture parameters for images obtained 1 year apart did not show significant alterations for either the control group (C1 × C2, *t* test, $P > .05$ for all parameters) or the FA group (P1 × P2, *t* test, $P > .05$ for all parameters) for the analyzed structures (medulla oblongata and pons).

For the transversal study, because there were no significant age differences between groups, both patient acquisitions were compared with both control acquisitions, to verify the reproducibility of the results. Significant changes between patients with FA and controls were found for many GLCM parameters for the medulla oblongata, for all comparisons (P1 × C1, P1 × C2, P2 × C1, P2 × C2); and only 1 parameter, for 1 comparison (P2 × C2), showed significant differences for the pons. These results are summarized in the Table. In this Table, only parameters that were significant for at least 1 comparison are shown. All remaining parameters were not significant, for any comparison.

There were no significant correlations between significant GLCM parameters and clinical variables.

DISCUSSION

The aim of the present work was to investigate brain stem damage in FA by using texture analysis of T1-weighted images. Indeed, texture analysis based in the GLCM is a technique capable of extracting a set of parameters that characterize the gray level distribution of the analyzed ROIs. In turn, the gray level distribution reflects physical properties of the underlying tissues, in this case related to the local proton attenuation and T1 constant of the tissue, because T1-weighted MR images were used. In addition, because the resolution of the images used was 1 mm^3, the reflected tissue properties are an average of microscopic characteristics (see De Certaines et al[26] for a discussion on the limitations of correlating texture analysis results to histology). Nevertheless, obtained results showed significant alterations for patients with FA compared with controls, mainly for the medulla oblongata. In particular, the results for the medulla were very robust because most of the significant parameters were robust for all the comparisons made between the different sets of images obtained from patients with FA and controls. Conversely, the result found for the pons, in which only 1 parameter was significant (difference variance) for only 1 of the comparisons (P2 × C2), may be regarded as a highly probable spurious finding. Most interesting, there were no alterations found in the longitudinal study. This could be because the time span (1 year) was too small for noticeable changes in such a slowly evolving disorder. In fact, in analyses of a large set of control images, no changes with age were found in texture parameters for the medulla oblongata or pons (unpublished data, T.A.S. and G.C., 2014).

We believe that the texture abnormalities found here reflect bulbar structural changes, but not exactly atrophy of the structure. This hypothesis is supported by a previous texture-based study in patients with a related neurodegenerative disorder, namely amyotrophic lateral sclerosis, that identified prominent

texture abnormalities earlier than true volumetric reduction.[27] Also in line with these findings, some previous volumetric studies in FA failed to identify bulbar atrophy,[17] and others actually found it,[15] but it was restricted to the dorsal part of the structure in such a way that it would be difficult to explain our consistent texture modifications. Therefore, we opted not to include volumetric measurements of the medulla as a covariate in our statistical approach to compare groups.

The GLCM parameters that were significant for the medulla oblongata can be roughly divided into 3 groups, according to "the purpose of the weights in the corresponding equations."[28] These groups can help chart a slightly more intuitive meaning of the findings.

One group is related to descriptive statistical measures of the GLCM[28] and includes the parameters correlation, variance, sum average, and sum variance. In particular, the correlation parameter, which gives a measure of the linear dependency between the gray levels of co-occurring (separated by the given distance) pixels, was consistently significant for the medulla oblongata for all GLCM distances for all comparisons, with the only exception being distance 5 for P1 × C2, though in this case, the *P* value was very close to significance ($P = .055$, Table). It has already been shown that this measure has the same expectation as the autocorrelation coefficient, particularly when the distance between pixels used in the GLCM calculation is small compared with the ROI dimensions,[29] which was the case here for the smallest GLCM distances (1 and 2 pixels) (Appendix). The correlation was smaller for patients compared with controls, for all distances; this difference therefore indicates a decrease in the autocorrelation coefficient for the gray level distribution of the medulla oblongata for the patients with FA. In other words, the gray level distribution of this ROI is less stationary or less periodic for patients than for controls.

The variance parameter measures the dispersion of the gray level distribution; the sum average and sum variance parameters measure, respectively, the mean and the dispersion of the distribution related to the sum of the co-occurring gray levels (On-line Table). From these 3 parameters, only the sum average was significant for all comparisons (Table), with variance and sum variance only significant for the comparison P1 × C1. All these parameters were smaller for patients with FA compared with controls. This finding therefore indicates a smaller mean and perhaps a tendency to a decrease in dispersion of the co-occurring gray level values for the medulla oblongata of patients with FA.

In another group are the entropy measures (entropy, sum entropy, and difference entropy). Entropy is a widely known measure coming from information theory,[30] which can be used to evaluate the amount of orderliness or the information content of a dataset. The greater the entropy, the more random is the underlying distribution (in this case, the distribution of the co-occurring gray levels or the distribution of the sum of the co-occurring gray levels or the distribution of the difference of the co-occurring gray levels). In the present analysis, all these measures were decreased for patients with FA compared with controls. In terms of the gray level distributions (both the original between co-occurring pixels and the sum and difference distributions), the decrease of the entropy measures points to the appearance of some sort of orderliness in the data of patients with FA for the medulla oblongata, which was not there in the control data.

Finally, in the last group, related to contrast measures, which "use weights related to the distance from the GLCM diagonal,"[28] is homogeneity, which, as shown by its name, is related to the homogeneity of the ROI. This parameter was significant for 3 of the comparisons (the only exception being P1 × C2, Table), and it decreased for patients with FA compared with controls.

Together, these results indicate probable changes in the underlying tissue composing the medulla oblongata. Although, to the best of our knowledge, there are no studies correlating in vivo texture measures with histopathology, Zhang et al[31] performed a study in which they found correlation among histopathology and texture parameters obtained from MR imaging of postmortem tissue samples of patients with multiple sclerosis. Possible tissue changes in the medulla oblongata are in line with previous pathologic reports in FA. In fact, medullar atrophy has been described since the original descriptions of Nikolaus Friedreich.[32] This atrophy is mostly due to neuronal loss and shrinkage of gracile and cuneate nuclei, which are related to the dorsal sensory pathways in the spinal cord. In addition, corticospinal tracts are also damaged at this point.[14] The lack of correlation between texture parameters and clinical data was somewhat unexpected but might be related to our segmentation strategy. We opted to use large ROIs that included the whole medulla oblongata, and neurodegeneration in FA is not homogeneous in this region (posterior structures are more severely damaged). Future studies using smaller ROIs within the medulla might prove useful in this setting.

CONCLUSIONS

In the present work, we found statistically significant differences for the medulla oblongata of patients with Friedreich ataxia compared with healthy individuals, by using GLCM-based texture analysis. These results highlight the medulla as an important site of damage in FA.

APPENDIX

ROI dimensions decrease with GLCM distance. In this work, the mean ROI areas used ranged approximately from 110 pixels (for a distance of 5 pixels) to 240 pixels (for a distance of 1 pixel) for the medulla of the patients with FA; from 160 to 300 pixels for the medulla of the controls; from 380 to 570 pixels for the pons of the patients with FA; and from 320 to 500 pixels for the pons of the controls. The area distributions were not significantly different between groups for any of the ROIs.

Disclosures: Thallis A. Santos—*RELATED*: *Grant*: São Paulo Research Foundation (undergraduate student). Márcia S. Oliveira—*UNRELATED*: *Grants/Grants Pending*: São Paulo Research Foundation. Marcondes C. França, Jr—*RELATED*: *Grant*: São Paulo Research Foundation grant 13/01766–7,* *Comments*: The São Paulo Research Foundation is a governmental agency that supports research in Brazil. Gabriela Castellano—*RELATED*: *Other*: São Paulo Research Foundation,* *Comments*: São Paulo Research Foundation has provided financial support for purchasing most of the equipment used in this study, such as computers and, especially, the MRI scanner. *Money paid to the institution.

REFERENCES

1. Hajek M, Dezortova M, Materka A, et al. *Texture Analysis for Magnetic Resonance Imaging*. Prague: Med4Publishing; 2006
2. Bonilha L, Kobayashi E, Castellano G, et al. **Texture analysis of hippocampal sclerosis.** *Epilepsia* 2003;44:1546–50 CrossRef Medline
3. Coelho GR, Kobayashi E, Bonilha L, et al. **Hippocampal texture analysis in patients with familial mesial temporal lobe epilepsy.** *Arq Neuropsiquiatr* 2003;61(suppl 1):83–87 CrossRef Medline
4. de Oliveira MS, Betting LE, Mory SB, et al. **Texture analysis of magnetic resonance images of patients with juvenile myoclonic epilepsy.** *Epilepsy Behav* 2013;27:22–28 CrossRef Medline
5. de Oliveira MS, D'Abreu A, França Jr MC, et al. **MRI-texture analysis of corpus callosum, thalamus, putamen, and caudate in Machado-Joseph disease.** *J Neuroimaging* 2012;22:46–52 CrossRef Medline
6. Mahmound-Ghoneim D, Toussaint G, Constans JM, et al. **Three dimensional texture analysis in MRI: a preliminary evaluation in gliomas.** *Magn Reson Imaging* 2003;21:983–87 CrossRef Medline
7. Herlidou-Même S, Constans JM, Carsin B, et al. **MRI texture analysis on texture test objects, normal brain and intracranial tumors.** *Magn Reson Imaging* 2003;21:989–93 CrossRef Medline
8. Sasikala M, Kumaravel. **A wavelet-based optimal texture feature set for classification of brain tumours.** *J Med Eng Technol* 2008; 32:198–205 CrossRef Medline
9. Haralick R, Shanmungam K, Dinstein I. **Textural features for image classification.** *IEEE Trans Syst Man Cybern* 1973;3:610–12 CrossRef
10. Haralick R. **Statistical and structural approaches to texture.** *Proc IEEE* 1979;67:786–804 CrossRef
11. Pandolfo M. **Friedreich ataxia.** *Arch Neurol* 2008;65:1296–303 CrossRef Medline
12. Fogel BL, Perlman S. **Clinical features and molecular genetics of autosomal recessive cerebellar ataxias.** *Lancet Neurol* 2007;6:245–57 CrossRef Medline
13. Campuzano V, Montermini L, Moltò MD, et al. **Friedreich's ataxia: autosomal recessive disease caused by an intronic GAA triplet repeat expansion.** *Science* 1996;271:1423–27 CrossRef Medline
14. Koeppen AH, Mazurkiewicz JE. **Friedreich ataxia: neuropathology revised.** *J Neuropathol Exp Neurol* 2013;72:78–90 CrossRef Medline
15. Della Nave R, Ginestroni A, Giannelli M, et al. **Brain structural damage in Friedreich's ataxia.** *J Neurol Neurosurg Psychiatry* 2008;79:82–85 CrossRef Medline
16. Della Nave R, Ginestroni A, Diciotti S, et al. **Axial diffusivity is increased in the degenerating superior cerebellar peduncles of Friedreich's ataxia.** *Neuroradiology* 2011;53:367–72 CrossRef Medline
17. França MC Jr, D'Abreu A, Yassuda CL, et al. **A combined voxel-based morphometry and 1H-MRS study in patients with Friedreich's ataxia.** *J Neurol* 2009;256:1114–20 CrossRef Medline
18. Silva CB, Yasuda CL, D'Abreu A, et al. **Neuroanatomical correlates of depression in Friedreich's ataxia: a voxel-based morphometry study.** *Cerebellum* 2013;12:429–36 CrossRef Medline
19. Chevis CF, da Silva CB, D'Abreu A, et al. **Spinal cord atrophy correlates with disability in Friedreich's ataxia.** *Cerebellum* 2013;12:43–47 CrossRef Medline
20. Rizzo G, Tonon C, Valentino ML, et al. **Brain diffusion-weighted imaging in Friedreich's ataxia.** *Mov Disord* 2011;26:705–12 CrossRef Medline
21. Pagani E, Ginestroni A, Della Nave R, et al. **Assessment of brain white matter bundle atrophy in patients with Friedreich ataxia.** *Radiology* 2010;255:882–87 CrossRef Medline
22. Akhlaghi H, Corben L, Georgiou-Karistianis N, et al. **Superior cerebellar peduncle atrophy in Friedreich's ataxia correlates with disease symptoms.** *Cerebellum* 2011;10:81–87 CrossRef Medline
23. Subramony SH, May W, Lynch D, et al; Cooperative Ataxia Group. **Measuring Friedreich ataxia: interrater reliability of a neurologic rating scale.** *Neurology* 2005;64:1261–62 CrossRef Medline
24. Materka A, Strzelecki M. **Texture analysis methods: a review**. In: *Proceedings of the Annual Meeting of COST B11: Technical University of Lodz, Poland,* Brussels, Belgium. June 25–28, 1988
25. Materka A. *MaZda User's Manual.* Version 3.30. Lodz University of Technology; Institute of Electronics: 1998–2000. http://www.eletel.p.lodz.pl/programy/mazda/download/mazda_manual.pdf. Accessed August 13, 2015.
26. De Certaines JD, Larcher T, Duda D, et al. **Application of texture analysis to muscle MRI: 1-what kind of information should be expected from texture analysis?** *EPJ Nonlinear Biomedical Physics* 2015;3:3 CrossRef
27. de Albuquerque M, Anjos LG, Maia Tavares de Andrade H, et al. **MRI texture analysis reveals deep gray nuclei damage in amyotrophic lateral sclerosis.** *J Neuroimaging* 2015 May 25. [Epub ahead of print]
28. The GLCM Tutorial Home Page. *http://www.fp.ucalgary.ca/mhallbey/tutorial.htm*. Accessed March 29, 2015
29. van der Sanden JJ, Hoekman DH. **Review of relationships between grey-tone co-occurrence, semivariance, and autocorrelation based image texture analysis approaches.** *Canadian Journal of Remote Sensing* 2005;31:207–13 CrossRef
30. Shannon CE. **A mathematical theory of communication.** *The Bell System Technical Journal* 1948;27:379–423 CrossRef
31. Zhang Y, Moore GR, Laule C, et al. **Pathological correlates of magnetic resonance imaging texture heterogeneity in multiple sclerosis.** *Ann Neurol* 2013;74:91–99 CrossRef Medline
32. Friedreich N. **Ueber Ataxie mit besonderer Berücksichtigung der hereditären Formen: Nachtrag.** *Virchows Arch Pathol Anat Physiol Klin Med* 1877;70: 140–52

Longitudinal Study of Gray Matter Changes in Parkinson Disease

X. Jia, P. Liang, Y. Li, L. Shi, D. Wang, and K. Li

ABSTRACT

BACKGROUND AND PURPOSE: The pathology of Parkinson disease leads to morphological brain volume changes. So far, the progressive gray matter volume change across time specific to patients with Parkinson disease compared controls remains unclear. Our aim was to investigate the pattern of gray matter changes in patients with Parkinson disease and to explore the progressive gray matter volume change specific to patients with Parkinson disease with disease progression by using voxel-based morphometry analysis.

MATERIALS AND METHODS: Longitudinal cognitive assessment and structural MR imaging of 89 patients with Parkinson disease (62 men) and 55 healthy controls (33 men) were from the Parkinson's Progression Markers Initiative data base, including the initial baseline and 12-month follow-up data. Two-way analysis of covariance was performed with covariates of age, sex, years of education, imaging data from multiple centers, and total intracranial volume by using Diffeomorphic Anatomical Registration Through Exponentiated Lie Algebra tool from SPM8 software.

RESULTS: Gray matter volume changes for patients with Parkinson disease were detected with decreased gray matter volume in the frontotemporoparietal areas and the bilateral caudate, with increased gray matter volume in the bilateral limbic/paralimbic areas, medial globus pallidus/putamen, and the right occipital cortex compared with healthy controls. Progressive gray matter volume decrease in the bilateral caudate was found for both patients with Parkinson disease and healthy controls, and this caudate volume was positively associated with cognitive ability for both groups. The progressive gray matter volume increase specific to the patients with Parkinson disease was identified close to the left ventral lateral nucleus of thalamus, and a positive relationship was found between the thalamic volume and the tremor scores in a subgroup with tremor-dominant patients with Parkinson disease.

CONCLUSIONS: The observed progressive changes in gray matter volume in Parkinson disease may provide new insights into the neurodegenerative process. The current findings suggest that the caudate volume loss may contribute to cognitive decline in patients with Parkinson disease and the progressive thalamus enlargement may have relevance to tremor severity in Parkinson disease.

ABBREVIATIONS: BA = Brodmann area; Control1 = control baseline; Control2 = control follow-up; DARTEL = Diffeomorphic Anatomical Registration Through Exponentiated Lie Algebra Toolbox; GMV = gray matter volume; MDS-UPDRS III = Movement Disorder Society–Unified Parkinson's Disease Rating Scale III; MNI = Montreal Neurological Institute; MoCA = Montreal Cognitive Assessment; PD = Parkinson disease; PD1 = PD baseline; PD2 = PD follow-up; VBM = voxel-based morphometry

Parkinson disease (PD) is a progressive neurodegenerative disorder characterized by the degeneration of dopamine neurons in the substantia nigra, with other neurons in the cortex and subcortical nuclei also affected during the course of the disease. This pathology might lead to morphologic brain changes.

Voxel-based morphometry (VBM) analysis has been used to

Received June 27, 2014; accepted after revision April 20, 2015.

From the Department of Radiology (X.J., P.L., Y.L., K.L.), Xuanwu Hospital, Capital Medical University, Beijing, China; Beijing Key Laboratory of MRI and Brain Informatics (X.J., P.L., Y.L., K.L.), Beijing, China; and Department of Imaging and Interventional Radiology (L.S., D.W.), The Chinese University of Hong Kong, Shatin, New Territories, Hong Kong SAR, China.

The Parkinson's Progression Markers Initiative is funded by the Michael J. Fox Foundation for Parkinson's Research and funding partners, including Abbott, Avid, Biogen Idec, Bristol-Myers Squibb, Covance, Elan, GE Healthcare, Genentech, GlaxoSmithKline, Lilly, Merck, Meso Scale Discovery, Pfizer, Roche, and Union chimique belge (details of the Parkinson's Progression Markers Initiative funding partners is found at http://www.ppmi-info.org/about-ppmi/who-we-are/study-sponsors/). This work was supported by a grant from the National Natural Science Foundation of China (61105118, 31400958, 61473196), the Beijing Nova Program (No. Z121111000250000, Z131107000413120), the Key Projects in the National Science and Technology Pillar Program during the Twelfth Five-Year Plan Period (2012BAI10B04), and the Open Research Fund of the State Key Laboratory of Cognitive Neuroscience and Learning (CNLZD1302).

Please address correspondence to Kuncheng Li, MD, Xuanwu Hospital, Capital Medical University, 45 Chang Chun St, Xi Cheng District, Beijing 100053, China; e-mail: cjr.likuncheng@vip.163.com

Indicates open access to non-subscribers at www.ajnr.org

Indicates article with supplemental on-line photos.

http://dx.doi.org/10.3174/ajnr.A4447

assess the cortical gray matter changes in patients with PD. Some cross-sectional studies were performed to compare the differences between patients with PD and healthy controls. However, these PD-VBM studies have not yet drawn any congruent conclusions. Some studies have shown distributed brain atrophy in cortical and subcortical regions, including the frontal lobe, temporal lobe, parietal lobe, occipital lobe, and the limbic/paralimbic areas.[1-8] On the other hand, 1 study reported an increase of GM in the thalamus in patients with PD with unilateral resting tremor compared with controls.[9] A recent study has observed not only brain volume loss in the occipital region but also volume increase in the limbic/paralimbic system.[10] In addition, some studies have failed to find any GM change.[11-14] In fact, few of these previous findings were wholly consistent with each other. These inconsistencies may result from the patient heterogeneity, such as the age, disease duration, disease severity, and variable covariates used in VBM analysis, which may confound the effect of results in between-group differences. Therefore, this issue of brain volume change in PD groups required further examination.

To our knowledge, few studies have focused on the progression of regional volume changes in PD by using VBM. One longitudinal study showed a progressive gray matter volume (GMV) decrease in patients with PD with and without dementia with disease progression during a mean follow-up period of 25 months.[15] In that study, a progressive GMV decrease in the limbic/paralimbic and temporo-occipital regions was observed in patients with PD, while in patients with dementia, the loss mainly involved the neocortical regions. However, in that study, no healthy matched controls were included. So far, the progressive GMV change across time specific to patients with PD compared with controls remains unclear.

Thus, the main goals of the present study were to examine the GMV change in the PD group compared with healthy controls and to explore the progressive GMV change specific to patients with PD compared with controls with disease progression.

MATERIALS AND METHODS

Data Acquisition Centers

In the present study, the data were selected from the following 7 MR imaging centers: Emory University, Atlanta, Georgia; Johns Hopkins University, Baltimore, Maryland; Northwestern University, Chicago, Illinois; Baylor College of Medicine, Houston, Texas; Universitat Tubingen, DZNE und Hertie-Institut fur Klinische Hirnforschung, Tubingen, Germany; Paracelsus-Elena Clinic Kassel/University of Marburg, Kassel, Germany; and Cleveland Clinic Foundation, Cleveland, Ohio.

Subjects

Data used in this article were from the Parkinson's Progression Markers Initiative data base (http://www.ppmi-info.org/data). This is the first large-scale, comprehensive, observational, international, multicenter study to identify PD progression biomarkers to improve the understanding of the disease etiology and the effectiveness of disease-modifying therapeutic trials.[16] Inclusion criteria of patients with PD for multiple centers were the following: 1) at least 2 of the following: resting tremor, bradykinesia, and rigidity (must have either resting tremor or bradykinesia) or either asymmetric resting tremor or asymmetric bradykinesia; 2) Hoehn and Yahr stage 1 or 2 at baseline; 3) dopamine transporter SPECT scan showing a dopamine transporter deficit; 4) not expected to require PD medication within at least 6 months from baseline; and 5) 30 years of age or older. Exclusion criteria for patients with PD were the following: 1) currently taking levodopa, dopamine agonists, monoamine oxidase inhibitors–B, amantadine, or other PD medications or taking them within 60 days of baseline; and 2) use of investigational drugs or devices within 60 days before baseline.

Inclusion criterion for healthy controls was 30 years of age or older. Exclusions were the following: 1) current or active clinically significant neurologic disorder; 2) first-degree relative with idiopathic PD; 3) Montreal Cognitive Assessment (MoCA) score of $\leq$26; and 4) use of investigational drugs or devices within 60 days before baseline.

In the present study, all subjects were selected on the basis of the following criteria: 1) Participants did not have depression, with a Geriatric Depression Scale score of $<$5,[17] or dementia, which was determined by the following: A) cognitive function that is impaired in $>$1 cognitive domain, B) decline from premorbid function, and C) significant impact of cognitive impairment on daily function;[16] 2) Subjects were studied 2 times (ie, baseline and 1-year follow-up) by September 12, 2013, and with the same scanning parameters; and 3) all MR imaging data were obtained on a Tim Trio 3T scanner (Siemens, Erlangen, Germany). There were 89 patients with PD (62 men, 62.0 $\pm$ 8.7 years of age) and 55 healthy controls (33 men, 58.4 $\pm$ 11.1 years of age). Table 1 shows the demographic and clinical data of the subjects.

Clinical Assessment

For patients with PD, the disease stage was scored by using the Hoehn and Yahr stage score, and the disease severity, by using the Movement Disorder Society–Unified Parkinson's Disease Rating Scale III (MDS-UPDRS III). In addition, all subjects were administered the University of Pennsylvania Smell Identification Test for assessment of olfactory function and Scales for Outcomes in Parkinson's Disease–Autonomic for assessment of autonomic disorder. To evaluate the neuropsychological state, we administered the following to all the subjects: the Benton Judgment of Line Orientation Score, the Geriatric Depression Scale, the MoCA, the Semantic Fluency total score, the Hopkins Verbal Learning Test, the Modified Schwab and England Activities of Daily Living, and the Symbol Digit Modalities score.

MR Imaging Data Acquisition

MR imaging data acquisition was performed on a Tim Trio 3T scanner (Siemens). High-resolution structural images were collected by using a 3D magnetization-prepared rapid acquisition of gradient echo T1-weighted sequence with the following parameters: sagittal section thickness, 1.0 mm; no gap; TR, 2300 ms; TE, 2.98 ms; flip angle, 9°; FOV, 240 $\times$ 256 mm; matrix size, 240 $\times$ 256; TI, 900 ms; voxel size, 1 $\times$ 1 $\times$1 mm^3. The image plane aligned in the sagittal plane along the hemispheric fissure and axially along the anterior/posterior commissure plane. The 176

Table 1: Clinical results at baseline and follow-up in PD and control samples[a]

	Baseline			Follow-Up		
	PD (n = 89)	Control (n = 55)	P Value[b]	PD (n = 89)	Control (n = 55)	P Value
Age (yr)	62.0 ± 8.7	58.4 ± 11.1	<.05	63.0 ± 8.7	59.4 ± 11.1	<.05
Sex (male/female)	62/27	33/22	.234	62/27	33/22	.234
Education (yr)	15.2 ± 2.9	15.4 ± 2.9	.62	15.2 ± 2.9	15.4 ± 2.9	.62
Total intracranial volume (mL)	1570.2 ± 143.5	1,505.9 ± 142.3	.01	1,560.2 ± 143.1	1,515.3 ± 140.9	.057
Hoehn and Yahr stage	1.6 ± 0.5	–	–	1.8 ± 0.5	–	–
MDS-UPDRS Part III[c]	21.9 ± 9.1	0.55 ± 1.33	<.001	23.0 ± 10.0	0.82 ± 1.44	<.001
Dose of levodopa-equivalent medication (mg/day)[d]	–	–	–	409.8 ± 369.3	–	–
Benton Judgment of Line Orientation score	12.7 ± 2.2	13.3 ± 1.8	.099	12.53 ± 2.2	12.6 ± 2.5	.146
Geriatric Depression Scale	2.7 ± 2.9	1.5 ± 3.0	<.05	2.8 ± 3.0	1.4 ± 2.5	<.05
Montreal Cognitive Assessment[e]	27.5 ± 2.0	28.4 ± 1.2	.001	26.2 ± 2.9	27.6 ± 2.0	0.002
Semantic Fluency total score	48.7 ± 9.8	52.4 ± 11.6	<.05	48.2 ± 10.3	53.7 ± 11.6	<.05
HVLT Delayed Recognition False Alarms	1.5 ± 1.5	1.5 ± 1.9	.958	1.3 ± 1.3	1.3 ± 1.7	.943
HVLT Delayed Recognition hits	11.5 ± 0.8	11.2 ± 1.0	<.05	11.5 ± 0.8	11.0 ± 1.6	<.05
HVLT Immediate Recall	26.4 ± 4.7	24.3 ± 5.4	<.05	27.2 ± 4.4	23.3 ± 6.1	<.001
Modified Schwab and England ADL	94.7 ± 5.4	–	–	91.8 ± 6.8	–	–
Symbol Digit Modalities score	40.9 ± 9.9	48.9 ± 11.20	<.001	39.6 ± 11.2	47.1 ± 10.0	<.001
UPSIT	21.1 ± 9.0	33.2 ± 4.9	<.001	–	–	–
SCOPA-AUT	9.2 ± 6.4	6.9 ± 4.4	<.001	11.9 ± 6.4	7.6 ± 5.8	<.001

Note:—MDS-UPDRS indicates Movement Disorder Society-Unified Parkinson's Disease Rating Scale; HVLT, Hopkins Verbal Learning Test; ADL, Activities of Daily Living; UPSIT, University of Pennsylvania Smell Identification Test; SCOPA-AUT, Scales for Outcomes in Parkinson's Disease–Autonomic; –, no value.

[a] Values are expressed as mean (SD).

[b] P values were derived from the Student t-test comparing the 2 groups except for "Sex," which was derived using the χ^2 test.

[c] MDS-UPDRS III was performed in the off-state at follow-up.

[d] There were 83.15 % of patients with PD who were on dopaminergic therapy at 1-year follow-up.

[e] Significant score decrease in the follow-up both for patients with PD and healthy controls compared with baseline ($P < .05$).

sections covered the entire brain from ear to ear and the bottom of the cerebellum to the vertex.

VBM–Diffeomorphic Anatomical Registration Through Exponentiated Lie Algebra Analysis

Voxel-based morphometry was performed by using SPM8 (http://www.fil.ion.ucl.ac.uk/spm/software/spm8) and the Diffeomorphic Anatomical Registration Through Exponentiated Lie Algebra Toolbox (DARTEL, part of SPM) registration method.[18] The VBM preprocessing included 5 steps: 1) T1-weighted images were segmented by using the standard unified segmentation model in SPM8 to produce gray matter, white matter, and CSF probability maps in the Montreal Neurological Institute (MNI) space; 2) the study-specific GM templates were created from the entire image dataset by using the DARTEL technique; 3) an initial affine registration of the GM templates to the tissue probability maps in MNI space was performed; 4) nonlinear warping of GM images to the GM template in MNI space was performed and then was used in the modulation step to ensure that the relative volumes of GM were preserved following the spatial normalization procedure by the Jacobian determinant of the deformation field to adjust volume changes;[19] and 5) The modulated, normalized GM images (representing GMV; voxel size, 1.5 × 1.5 × 1.5 mm^3) were smoothed with a 6-mm full width at half maximum isotropic Gaussian kernel. The total intracranial volume was represented by the sum of the GM, WM, and CSF volumes. In addition, in the VBM-DARTEL analysis, checking of sample homogeneity was performed in SPM8 on the normalized data for quality control.

Statistical Analysis

Demographic data and neuropsychological measures at baseline were analyzed by SPSS, Version 19 (IBM, Armonk, New York), with the Student t test for continuous variables and the χ^2 test for dichotomous variables.

The present study was organized into 2 [(time: 12-month follow-up versus baseline) × 2 (group: PD versus control)] flexible factorial designs. We thus had 4 conditions: PD baseline (PD1), PD follow-up (PD2), control baseline (Control1), and control follow-up (Control2). Age, sex, years of education, imaging data from multiple centers, and total intracranial volume were entered as regressors into the flexible factorial design to establish the regional GM volume changes.

The main effect of "group" was revealed by the following 2 contrasts: The decreased GM volumes for patients with PD were determined by the contrast of [(Control1 + Control2) > (PD1 + PD2)], and the increased GM volumes for patients with PD were determined by the contrast of [(PD1 + PD2) > (Control1 + Contol2)].

The main effect of "time" was revealed by the following 2 contrasts: The decreased GM volumes for follow-up were determined by the contrast of [(PD1 + Control1) > (PD2 + Control2)], and the increased GM volumes for follow-up were determined by the contrast of [(PD2 + Control2) > (PD1 + Control1)]. In addition, 2 simple main effects of (PD1 > PD2) and (Control1 > Control2) were performed.

The interaction effect of "group" by "time" was revealed by the following 2 contrasts: The increased GM volumes specific to patients with PD with time was determined by the contrast of [(PD2 > PD1) > (Control2 > Control1)], and the decreased GM volumes specific to patients with PD with time were determined by the contrast of [(PD1 > PD2) > (Control1 > Control2)].

The statistical significance threshold was set at $P < .001$ cor-

Table 2: GMV changes for patients with PD compared with controls

Regions	BA	Cluster Size (Voxel)	MNI			*T* Score
			X	Y	Z	
Control > PD						
Rt. superior frontal gyrus	9	262	24	56	40	17.19
Rt. superior frontal gyrus	9		18	60	36	8.52
Rt. middle frontal gyrus	10		24	63	27	7.00
Rt. middle frontal gyrus	9	466	39	42	42	11.48
Rt. middle frontal gyrus	10		39	62	16	10.62
Rt. superior frontal gyrus	9		36	53	31	9.84
Lt. superior frontal gyrus	9	790	−18	59	34	13.37
Lt. superior frontal gyrus	8		−26	44	48	13.05
Lt. superior frontal gyrus	9		−23	53	42	12.68
Lt. inferior temporal gyrus	37	813	−65	−60	−8	10.78
Lt. middle temporal gyrus	21		−65	−62	6	10.15
Lt. inferior temporal gyrus	20		−63	−54	−20	10.10
Rt. superior parietal lobule	7	225	45	−69	48	8.55
Rt. inferior parietal lobule	40		53	−61	48	7.75
Rt. angular gyrus	39		57	−67	36	7.38
Lt. caudate body		459	−9	−1	21	13.90
Lt. caudate body			−6	3	15	13.24
Lt. caudate body			−12	−9	22	11.04
Rt. caudate body		460	8	6	15	11.70
Rt. caudate body			12	−6	22	9.48
Rt. caudate body			15	−15	25	8.52
PD > Control						
Lt. inferior frontal gyrus	47	109	−15	24	−15	10.63
Rt. superior frontal gyrus	11	212	23	51	−23	9.35
Rt. superior frontal gyrus			24	60	−21	8.63
Rt. superior frontal gyrus			32	47	−18	7.56
Rt. anterior cingulate cortex	32	182	17	30	30	11.73
Rt. anterior cingulate cortex			15	21	39	10.82
Rt. anterior cingulate cortex			20	35	21	9.28
Rt. middle occipital gyrus	19	124	42	−90	18	7.89
Lt. globus pallidus internus		390	−9	0	−5	13.84
Lt. hippocampus			−30	−19	−9	9.78
Lt. globus pallidus internus			−14	−6	−8	8.47
Lt. subthalamic nucleus		113	−11	−12	−5	11.80
Rt. globus pallidus internus		451	18	−7	−8	11.59
Rt. globus pallidus internus			12	3	−5	11.26
Rt. putamen			30	−18	−8	10.97

Note:—BA indicates Brodmann area; Rt., right; Lt., left.

rected for multiple comparisons (family-wise error) with a minimum cluster size of 100 contiguous voxels, but with an exception of 50 contiguous voxels for the interaction effect. The coordinates of voxels were transferred from Montreal Neurological Institute space to Talairach space by using M. Brett's transformation (http://imaging.mrc-cbu.cam.ac.uk/imaging/MniTalairach).

ROI Analysis

To examine the GMV change with time in the present study, we defined the ROIs by using 2 methods. On the one hand, those ROIs based on the results in the present study were defined by cluster-based method—that is, clusters that showed significant differences in the contrasts of [(PD1 + Control1) > (PD2 + Control2)] (bilateral caudate body; MNI coordinates: −8, 3, 18; 9, 5, 18) and [(PD2 > PD1) > (Control2 > Control1)] (left thalamus; MNI coordinates: −21, −24, 3) were defined as ROIs by using xjView software (http://www.alivelearn.net/xjview). On the other hand, to compare with the previous longitudinal study,[15] we defined additional ROIs on the basis of a sphere with a radius of 6 mm centered at the anterior cingulate cortex (MNI coordinates: 1, 31 19), posterior cingulate cortex (MNI coordinates: 11, −49, 30), hippocampus (MNI coordinates: −22, −19, −11), and hypothalamus (MNI coordinates: 1, −9, −5) by using WFU_PickAtlas software (http://software.incf.org/software/wfu_pickatlas/download). For each subject at a single time point (baseline and follow-up), the GMV in each ROI was computed by the sum of the volume of each voxel in the ROI. To illustrate the mean change in volume, we computed annualized percentage change by subtracting the baseline volume from the follow-up value, dividing by the baseline volume and multiplying by 100.

Correlation Analysis

The Pearson correlation was performed to evaluate the relationship between the GMV in ROIs and clinical assessments in Table 1, including the Hoehn and Yahr stage, MDA-UPDRS III, Benton Judgment of Line Orientation score, Geriatric Depression Scale, MoCA, Semantic Fluency score, Hopkins Verbal Learning Test, Activities of Daily Living, Symbol Digit Modalities score, University of Pennsylvania Smell Identification Test, and Scales for Outcomes in Parkinson's disease–Autonomic. Two-tailed $P < .01$ was considered statistically significant.

RESULTS

Demographic Characteristics

No significant differences in sex, education level, and total intracranial volume were found between the patients with PD and controls. The MDS-UPDRS III of PD was significantly higher than that of controls ($P < .001$). Neuropsychological tests showed that behavioral deficits in the Geriatric Depression Scale ($P < .05$) and cognitive deficits in the MoCA ($P < .05$), semantic fluency total score ($P < .05$), Hopkins Verbal Learning Test Immediate Recall ($P < .05$) and delayed recall ($P < .05$), Symbol Digit Modalities score ($P < .001$), Smell Identification Test ($P < .001$), and Scales for Outcomes in Parkinson's Disease–Autonomic ($P < .001$) were more severe in the patients with PD than in the control group. In addition, a cognitive decline in the MoCA scores was found both for patients with PD ($P < .05$) and controls ($P < .05$) at follow-up compared with baseline. No significant differences in other cognitive subdomains (Benton Judgment of Line Orientation Score, Hopkins Verbal Learning Test Delayed Recognition False Alarms) were found between the 2 groups (Table 1).

VBM Results

The main effect of "group" revealed cortical and subcortical GM volume changes for patients with PD in contrast to controls. The

decreased GM volume was found in the bilateral superior/middle frontal gyrus (Brodmann area [BA] 9/10), left inferior/middle temporal gyrus (BA 21/20/37), right superior/inferior parietal lobule (BA 7/40) and angular gyrus (BA 39), and the bilateral caudate body, while the increased GM volume was identified in the left inferior frontal gyrus (orbital, BA 47), right middle occipital gyrus (BA 19), right anterior cingulate cortex (anterior cingulate cortex, BA 32), bilateral globus pallidus internus, right putamen, left hippocampus, and left subthalamic nucleus (Table 2 and Fig 1).

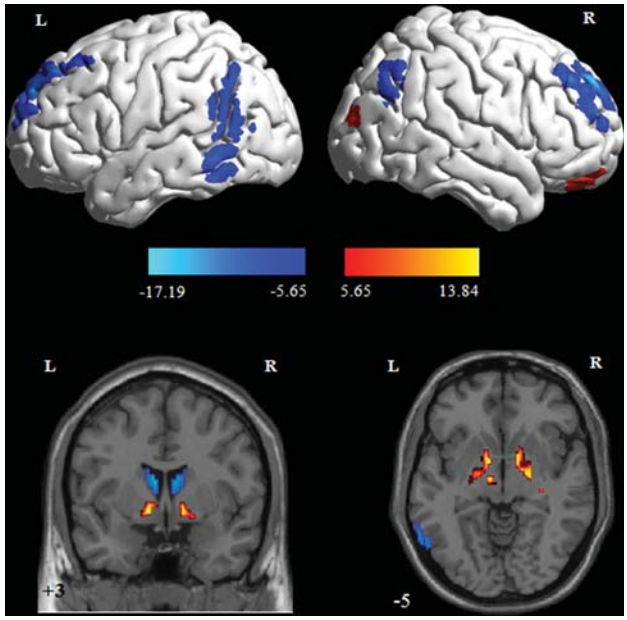

FIG 1. Gray matter volume changes between patients with PD and controls. The warm color indicates increased gray matter volume for patients with PD in contrast to controls, while the cool color indicates decreased gray matter volume for patients with PD in contrast to controls. Color bars indicate *t* scores.

The main effect of "time" revealed decreased GM volume in the bilateral caudate body for follow-up in contrast to baseline (Table 3 and Fig 2). In addition, the 2 simple main effects of time for patients with PD and controls also revealed decreased GM volume change in the bilateral caudate body with time (Table 3). Reduction in the caudate between baseline and 1-year follow-up was 1.96% for healthy controls and 1.1% for patients with PD. To compare with a previous study that observed volume reduction in the limbic/paralimbic regions for patients with PD with disease progression, we extracted the volumes in these regions. The results of paired *t* tests showed that the decreased volumes in these regions did not reach significant differences.

In addition, we identified progressive GMV increase specific to patients with PD in the left thalamus with 160 voxels ($P < .05$ family-wise error corrected) (MNI coordinates: −21, −24, 3) close to the ventral lateral nucleus by an interaction effect of "group" by "time" [(PD2 > PD1) > (Control2 > Control1)] (Fig 3).

Correlation Results

There were significant positive correlations between the caudate volume and the MoCA score for patients with PD and controls ($r = 0.32$, $P = .0039$, and $r = 0.38$, $P = .0047$, respectively; On-line Fig 1). There was no significant relationship between enlarged thalamic volume and MDS-UPDRS III scores. Twenty-three tremor-dominant patients with PD presented initially with tremor with relatively mild bradykinesia and rigidity, and the tremor scores were calculated on the basis of the summation of the rest tremor amplitude of the upper and lower limbs. However, the post hoc 2-tailed 2-sample *t* test analysis showed that a positive relationship was found between the thalamic volume and the rest tremor score of 23 tremor-dominant patients with PD with scores ranging between 2 and 3 (On-line Fig 2).

To clarify the contributions of these measurements with significant differences between groups to the enlarged thalamic volume, we performed additional correlations, controlling these measurements as covariates of no interest. There was no significant correlation.

Table 3: GMV changes with time

Regions	BA	Cluster Size (Voxel)	MNI X	MNI Y	MNI Z	*T* Score
Baseline vs follow-up: [(PD1 + Control1) > (PD2 + Control2)]						
Lt. caudate body		566	−8	3	18	14.55
Lt. caudate body			−6	11	13	14.24
Lt. caudate body			−12	−12	22	12.23
Rt. caudate body		535	9	5	18	14.23
Rt. caudate body			12	−3	22	13.17
Rt. caudate body			14	−13	22	11.31
Follow-up vs baseline: [(PD2 + Control2) > (PD1 + Control1)]						
No significant activation						
PD1 > PD2						
Rt. caudate body		192	8	9	15	8.27
Lt. caudate body		151	−6	12	10	7.92
Control1 > Control2						
Lt. caudate body		570	−8	3	18	16.85
Lt. caudate body			−12	−13	22	15.49
Lt. caudate body			−17	−21	24	7.37
Rt. caudate body		552	12	−3	22	15.21
Rt. caudate body			9	3	18	14.11
Rt. caudate body			14	−15	22	14.09
(PD2 > Control2) > (PD1 > Control1)[a]						
Lt. thalamus		160	−21	−24	3	5.79
(PD1 > Control1) > (PD2 > Control2)[a]						
No significant activation						

[a] $P < .05$ family-wise error correction; cluster size >100.

DISCUSSION

The aim of the present study was to investigate the GMV change in patients with PD and to explore the progressive GMV change specific to patients with PD with disease progression compared with controls. Reduced GMV was identified in the bilateral caudate for both patients with PD and healthy controls with time. It was revealed that patients with PD exhibited increased GMV in

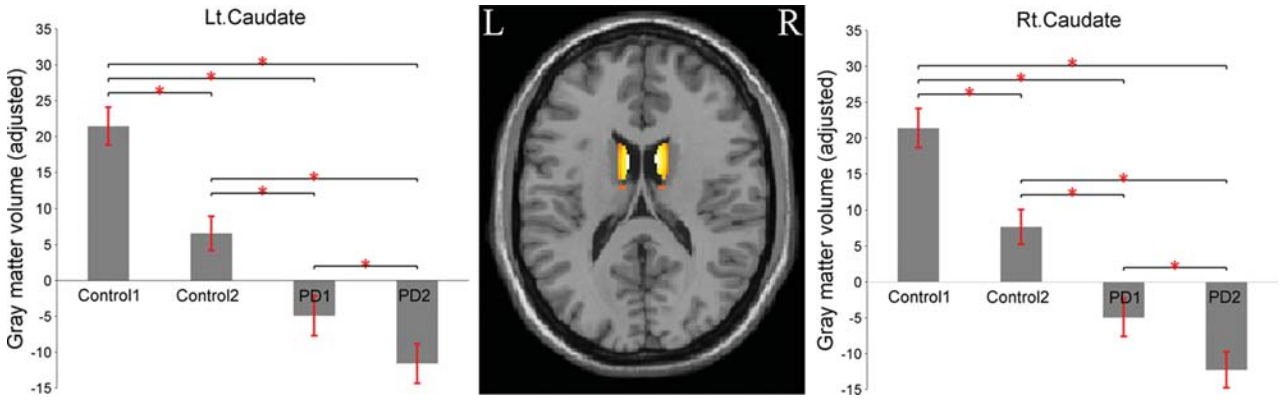

FIG 2. Barplot depicting the mean (and standard error) of the volume in the bilateral caudate between the 2 groups across time (adjusted for age, sex, years of education, imaging data from multiple centers, and total intracranial volume). The asterisk indicates significant differences at $P < .001$.

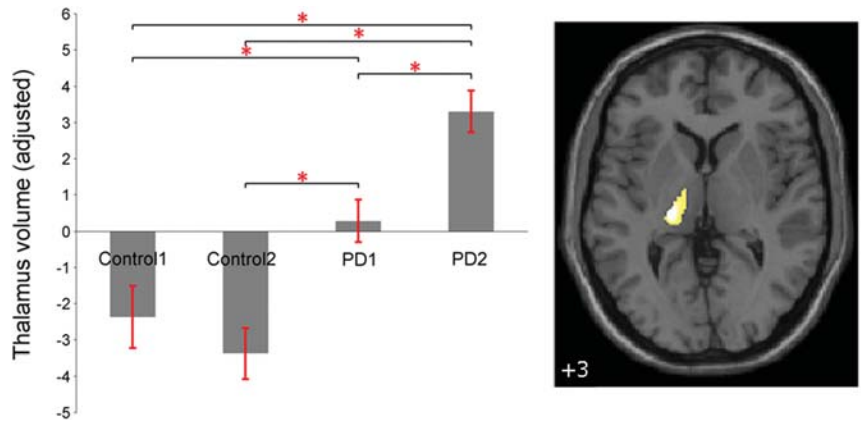

FIG 3. Barplot depicting the mean (and standard error) of the volume in the left thalamus specific to patients with PD across time (adjusted for age, sex, years of education, imaging data from multiple centers, and total intracranial volume). The asterisk indicates significant differences at $P < .001$.

the orbitofrontal gyrus, occipital cortex, limbic/paralimbic areas, and globus pallidus internus/putamen, whereas they had reduced GMV in the frontotemporoparietal network and the bilateral caudate, compared with controls. In addition, the progressive GMV change specific to patients with PD was found in the left thalamus.

Group Differences: GMV Changes for Patients with PD Compared with Controls

Previous studies have reported GMV loss in patients with PD with dementia (for a review, see Pan et al[20]). The present study extended the knowledge by showing that GMV loss can be found even in patients with early-stage PD. These regions included the frontal, temporal, and parietal regions and the subcortical area in the caudate bilaterally. The findings suggest that the observed GMV decreases may represent an early manifestation of underlying Parkinson disease–related pathologic changes.[6,7]

However, the neuropathologic correlates of an increase in GMV are less clear. Consistent with previous studies, the present study observed the increased GMV in the limbic/paralimbic system and globus pallidus internus/putamen in patients with PD compared with controls.[10,21,22] Although the present study provides no evidence regarding the mechanisms leading to increased brain volume in PD, as a chronically progressive neurodegenerative disorder, the effect may be due to a compensatory response to impaired cerebral function in early PD.[10,21-24]

In the present study, the findings of GMV changes (decrease and increase) in patients with PD were not wholly consistent with findings in any of the previous studies. The patient's heterogeneity (eg, age, sex, education, disease severity) may contribute to the inconsistencies in the pattern of findings among the studies. Further studies are required with a large sample size, controlling for the potential confounding effect.

Longitudinal Evaluation: Progressive Caudate Volume Loss in Patients with PD and Controls

In the present study, a significantly progressive decrease in the volume of the bilateral caudate was observed both in the patients with PD and controls. The reduction in the caudate was observed in several cross-sectional studies as part of the normal aging process.[25-27] In the present study, the reduction of caudate volume was 1.96%/year for healthy controls and 1.1%/year for patients with PD. The reduction rates in the present study are similar to the ones reported in a 6-month longitudinal study,[28] but greater than the ones reported in a 5-year longitudinal study.[29] This heterogeneity may partially reflect differences among these populations. Additionally, follow-up intervals may contribute to differences in the reduction rate. In the present study, a reduction in the caudate was observed in patients with PD compared with controls both at baseline and follow-up, and this reduction remained in the comparison of baseline and control follow-up of patients with PD. Furthermore, a significant positive correlation was found between the MoCA score and the caudate volume for both patients with PD and healthy controls. The caudate is linked with the dorsolateral prefrontal cortex and lateral orbitofrontal cortex, and the dysfunction in this region is thought to contribute to the cog-

nitive impairment in PD.[30-33] The results suggest that the loss in caudate volume contributed to the cognitive decline for both groups with time, while the striatal dopaminergic deficiency in patients with PD may worsen the caudate volume loss compared with healthy controls.

A previous longitudinal study observed limbic/paralimbic loss including the hippocampus, hypothalamus, posterior cingulate cortex, and anterior cingulate cortex for patients with PD with disease progression with time.[15] In contrast, we extracted the GMV in these regions, and the results showed that the decreased volumes did not reach a significant difference. The heterogeneity, methodologic differences, and sample size of patients between the 2 studies may have led to the discrepancies. In particular, the patients with PD in the present study had a shorter follow-up period (mean, 12 months) at an earlier disease stage (mean Hoehn and Yahr stage, 1.6 ± 0.5) than the patients in that study (mean follow-up period, 25 months; mean Hoehn and Yahr stage, 2.9 ± 0.8) and a larger sample size (89 patients with PD) than in that study (13 patients with PD without dementia). In addition, no covariate was included in that study, though age, sex, years of education, and total intracranial volume may confound the results.

Longitudinal Evaluation of Patients with PD versus Controls: Progressive Thalamic Volume Increase Specific to the Patients with PD

In the present study, the progressive thalamic volume increase was observed specific to patients with PD compared with controls. On the contrary, the thalamic volume tended to decrease with time in controls. The thalamus occupies a pivotal position within the striatothalamocortical circuits,[30,34,35] in which the thalamus receives input from the basal ganglia.[36] In the present study, the enlarged thalamus close to the ventral lateral nucleus may relate to motor control.[31,36] Consistent with previous studies, the positive correlation between the thalamic volume and the tremor score further suggests that the enlarged thalamic volume (mainly in the ventral lateral) may relate to tremor severity in PD.[9,37]

CONCLUSIONS

The present study investigated the progressive GMV change across time in patients with PD compared with controls. The observed progressive changes in gray matter volume in PD may provide new insights into the neurodegenerative process. The findings suggest that the caudate volume loss may contribute to cognitive decline in patients with PD and the progressive thalamic volume increase may relate to tremor severity in PD. However, the present study has the following 3 limitations: First, considering the highly nonlinear effect in age range,[38] further study should be limited to a restricted sample with less age heterogeneity. Second, the brain volume change in the present study was seen only at 1-year follow-up, and further study should include multiple follow-up time windows to explore the dynamic changes of GM volume. Finally, to clarify whether the presence of tremor was actually driving the larger thalamic volumes, the study should compare thalamic volumes of tremor- and non-tremor-dominant patients with PD.

Disclosures: Xiuqin Jia—*UNRELATED*: *Grants/Grants Pending*: National Natural Science Foundation of China.

REFERENCES

1. Burton EJ, McKeith IG, Burn DJ, et al. **Cerebral atrophy in Parkinson's disease with and without dementia: a comparison with Alzheimer's disease, dementia with Lewy bodies and controls.** *Brain* 2004;127:791–800 CrossRef Medline
2. Beyer MK, Larsen JP, Aarsland D. **Gray matter atrophy in Parkinson disease with dementia and dementia with Lewy bodies.** *Neurology* 2007;69:747–54 CrossRef Medline
3. Kostic VS, Agosta F, Petrović I, et al. **Regional patterns of brain tissue loss associated with depression in Parkinson disease.** *Neurology* 2010;75:857–63 CrossRef Medline
4. Kostic VS, Agosta F, Pievani M, et al. **Pattern of brain tissue loss associated with freezing of gait in Parkinson disease.** *Neurology* 2012;78:409–16 CrossRef Medline
5. Compta Y, Ibarretxe-Bilbao N, Pereira J, et al. **Grey matter volume correlates of cerebrospinal markers of Alzheimer-pathology in Parkinson's disease and related dementia.** *Parkinsonism Relat Disord* 2012;18:941–47 CrossRef Medline
6. Hong J, Lee JE, Sohn YH, et al. **Neurocognitive and atrophic patterns in Parkinson's disease based on subjective memory complaints.** *J Neurol* 2012;259:1706–12 CrossRef Medline
7. Lee EY, Sen S, Eslinger PJ, et al. **Early cortical gray matter loss and cognitive correlates in non-demented Parkinson's patients.** *Parkinsonism Relat Disord* 2013;19:1088–93 CrossRef Medline
8. Lee JE, Cho KH, Ham JH, et al. **Olfactory performance acts as a cognitive reserve in non-demented patients with Parkinson's disease.** *Parkinsonism Relat Disord* 2014;20:186–91 CrossRef Medline
9. Kassubek J, Juengling FD, Hellwig B, et al. **Thalamic gray matter changes in unilateral Parkinsonian resting tremor: a voxel-based morphometric analysis of 3-dimensional magnetic resonance imaging.** *Neurosci Lett* 2002;323:29–32 CrossRef Medline
10. Pagonabarraga J, Soriano-Mas C, Llebaria G, et al. **Neural correlates of minor hallucinations in non-demented patients with Parkinson's disease.** *Parkinsonism Relat Disord* 2014;20:290–96 CrossRef Medline
11. Nagano-Saito A, Washimi Y, Arahata Y, et al. **Cerebral atrophy and its relation to cognitive impairment in Parkinson disease.** *Neurology* 2005;64:224–29 CrossRef Medline
12. Ibarretxe-Bilbao N, Ramirez-Ruiz B, Tolosa E, et al. **Hippocampal head atrophy predominance in Parkinson's disease with hallucinations and with dementia.** *J Neurol* 2008;255:1324–31 CrossRef Medline
13. Tessitore A, Amboni M, Cirillo G, et al. **Regional gray matter atrophy in patients with Parkinson disease and freezing of gait.** *AJNR Am J Neuroradiol* 2012;33:1804–09 CrossRef Medline
14. Ellfolk U, Joutsa J, Rinne JO, et al. **Striatal volume is related to phonemic verbal fluency but not to semantic or alternating verbal fluency in early Parkinson's disease.** *J Neural Transm* 2014;121:33–40 CrossRef Medline
15. Ramirez-Ruiz B, Marti MJ, Tolosa E, et al. **Longitudinal evaluation of cerebral morphological changes in Parkinson's disease with and without dementia.** *J Neurol* 2005;252:1345–52 CrossRef Medline
16. Parkinson Progression Marker Initiative. **The Parkinson Progression Marker Initiative (PPMI).** *Prog Neurobiol* 2011;95:629–35 CrossRef Medline
17. Yesavage JA. **Geriatric Depression Scale.** *Psychopharmacol Bull* 1988; 24:709–11 Medline
18. Ashburner J. **A fast diffeomorphic image registration algorithm.** *Neuroimage* 2007;38:95–113 CrossRef Medline
19. Good CD, Johnsrude IS, Ashburner J, et al. **A voxel-based morphometric study of ageing in 465 normal adult human brains.** *Neuroimage* 2001;14:21–36 CrossRef Medline
20. Pan P, Shi H, Zhong J, et al. **Gray matter atrophy in Parkinson's disease with dementia: evidence from meta-analysis of voxel-based morphometry studies.** *Neurol Sci* 2013;34:613–19 CrossRef Medline

21. Binkofski F, Reetz, Gaser C, et al. **Morphometric fingerprint of asymptomatic Parkin and PINK1 mutation carriers in the basal ganglia.** *Neurology* 2007;69:842–50 CrossRef Medline
22. Krabbe K, Karlsborg M, Hansen A, et al. **Increased intracranial volume in Parkinson's disease.** *J Neurol Sci* 2005;239:45–52 CrossRef Medline
23. Helmich RC, de Lange FP, Bloem BR, et al. **Cerebral compensation during motor imagery in Parkinson's disease.** *Neuropsychologia* 2007;45:2201–15 CrossRef Medline
24. Palop JJ, Chin J, Mucke L. **A network dysfunction perspective on neurodegenerative diseases.** *Nature* 2006;443:768–73 CrossRef Medline
25. Jernigan TL, Archibald SL, Berhow MT, et al. **Cerebral structure on MRI, Part I: localization of age-related changes.** *Biol Psychiatry* 1991;29:55–67 CrossRef Medline
26. Walhovd KB, Fjell AM, Reinvang I, et al. **Effects of age on volumes of cortex, white matter and subcortical structures.** *Neurobiol Aging* 2005;26:1261–70; discussion 1275–78 CrossRef Medline
27. Abedelahi A, Hasanzadeh H, Hadizadeh H, et al. **Morphometric and volumetric study of caudate and putamen nuclei in normal individuals by MRI: effect of normal aging, gender and hemispheric differences.** *Pol J Radiol* 2013;78:7–14 CrossRef Medline
28. Raz N, Schmiedek F, Rodrigue KM, et al. **Differential brain shrinkage over 6 months shows limited association with cognitive practice.** *Brain Cogn* 2013;82:171–80 CrossRef Medline
29. Raz N, Lindenberger U, Rodrigue KM, et al. **Regional brain changes in aging healthy adults: general trends, individual differences and modifiers.** *Cerebral Cortex* 2005;15:1676–89 CrossRef Medline
30. Alexander GE, DeLong MR, Strick PL. **Parallel organization of functionally segregated circuits linking basal ganglia and cortex.** *Ann Rev Neurosci* 1986;9:357–81 CrossRef Medline
31. Poston KL, Eidelberg D. **Functional brain networks and abnormal connectivity in the movement disorders.** *Neuroimage* 2012;62:2261–70 CrossRef Medline
32. Jokinen P, Brück A, Aalto S, et al. **Impaired cognitive performance in Parkinson's disease is related to caudate dopaminergic hypofunction and hippocampal atrophy.** *Parkinsonism Relat Disord* 2009;15:88–93 CrossRef Medline
33. Rinne JO, Portin R, Ruottinen H, et al. **Cognitve impairment and the brain dopaminergic system in Parkinson disease: [F18] fluorodopa positron emission tomographic study.** *Arch Neurol* 2000;57:470–75 CrossRef Medline
34. Albin RL, Young AB, Penney JB. **The functional anatomy of basal ganglia disorders.** *Trends Neurosci* 1989;12:366–75 CrossRef Medline
35. Evarts EV, Kimura M, Wurtz RH, et al. **Behavioral correlates of activity in basal ganglia neurons.** *Trends in Neurosci* 1984;7:447–53 CrossRef
36. DeLong MR, Wichmann T. **Circuits and circuit disorders of the basal ganglia.** *Arch Neurol* 2007;64:20–24 CrossRef Medline
37. Halliday GM. **Thalamic changes in Parkinson's disease.** *Parkinsonism Relat Disord* 2009;15:S152–S155 CrossRef
38. Fjell AM, Westlye LT, Grydeland H, et al; Alzheimer Disease Neuroimaging Initiative. **Critical ages in the life course of the adult brain: nonlinear subcortical aging.** *Neurobiol Aging* 2013;34:2239–47 CrossRef Medline

Differentiation of Parkinsonism-Predominant Multiple System Atrophy from Idiopathic Parkinson Disease Using 3T Susceptibility-Weighted MR Imaging, Focusing on Putaminal Change and Lesion Asymmetry

I. Hwang, C.-H. Sohn, K.M. Kang, B.S. Jeon, H.-J. Kim, S.H. Choi, T.J. Yun, and J.-h. Kim

ABSTRACT

BACKGROUND AND PURPOSE: Asymmetric presentation of clinical feature in parkinsonism is common, but correlatable radiologic feature is not clearly defined. Our aim was to evaluate 3T susceptibility-weighted imaging findings for differentiating parkinsonism-predominant multiple system atrophy from idiopathic Parkinson disease, focusing on putaminal changes and lesion asymmetry.

MATERIALS AND METHODS: This retrospective cohort study included 27 patients with parkinsonism-predominant multiple system atrophy and 50 patients with idiopathic Parkinson disease diagnosed clinically. Twenty-seven age-matched subjects without evidence of movement disorders who underwent SWI were included as the control group. A consensus was reached by 2 radiologists who visually assessed SWI for the presence of putaminal atrophy and marked signal hypointensity on each side of the posterolateral putamen. We also quantitatively measured putaminal width and phase-shift values.

RESULTS: The mean disease duration was 4.7 years for the patients with parkinsonism-predominant multiple system atrophy and 7.8 years for the patients with idiopathic Parkinson disease. In the patients with parkinsonism-predominant multiple system atrophy, putaminal atrophy was frequently observed (14/27, 51.9%) and was most commonly found in the unilateral putamen (13/14). Marked signal hypointensity was observed in 12 patients with parkinsonism-predominant multiple system atrophy (44.4%). No patients with idiopathic Parkinson disease or healthy controls showed putaminal atrophy or marked signal hypointensity. Quantitatively measured putaminal width, phase-shift values, and the ratio of mean phase-shift values for the dominant and nondominant sides were significantly different between the parkinsonism-predominant multiple system atrophy group and the idiopathic Parkinson disease and healthy control groups ($P < .001$).

CONCLUSIONS: 3T SWI can visualize putaminal atrophy and marked signal hypointensity in patients with parkinsonism-predominant multiple system atrophy with high specificity. Furthermore, it clearly demonstrates the dominant side of putaminal changes, which correlate with the contralateral symptomatic side of patients.

ABBREVIATIONS: IPD = idiopathic Parkinson disease; MSA-p = parkinsonism-predominant multiple system atrophy; MSA-c = cerebellar dysfunction type multiple system atrophy; ROC = receiver operating characteristic

Parkinsonism-predominant multiple system atrophy (MSA-p) is one of the Parkinson-plus syndromes that has a clinical manifestation similar to that of idiopathic Parkinson disease (IPD) and is often challenging to diagnose in its early stage. MR imaging plays a role in differentiating MSA-p from IPD and is included as an additional feature for the diagnosis of possible multiple system atrophy.[1] Various conventional and functional MR imaging findings regarding the putamen in MSA-p have been reported.[2-6] However, these findings had limited sensitivity and specificity.[6]

An asymmetric presentation of clinical features is common for IPD in its early stage, while symmetric symptoms are more common in MSA-p than in IPD.[7,8] However, the clinical manifestation of parkinsonism develops asymmetrically in many patients with MSA-p, and it has been reported that approximately 40%–50% of patients with MSA-p present with initial asymmetric symptoms.[8,9] This presentation increases the difficulty of clinically differentiating IPD from MSA-p in the early stage of disease. However, to our knowledge, there are few previous reports that used imaging to examine the asymmetry of putaminal abnormalities in MSA-p.

Susceptibility-weighted imaging (SWI), which was recently

Received December 16, 2014; accepted after revision April 23, 2015.

From the Departments of Radiology (I.H., C.-H.S., K.M.K, S.H.C., T.J.Y., J.-h.K.) and Neurology (B.S.J., H.-J.K.), Seoul National University Hospital, Seoul, Korea; Department of Radiology (C.-H.S.), Seoul National University College of Medicine, Seoul, Korea; and Institute of Radiation Medicine (C.-H.S.), Seoul National University Medical Research Center, Seoul, Korea.

Please address correspondence to Chul-Ho Sohn, MD, Department of Radiology, Seoul National University College of Medicine, 101 Daehak-ro, Jongno-gu, Seoul, 110-744, Korea; e-mail: neurorad63@gmail.com

Indicates article with supplemental on-line table.

http://dx.doi.org/10.3174/ajnr.A4442

introduced and is now widely used in clinical brain imaging, reflects the physical magnetic properties of tissues because susceptibility changes in tissues, such as iron deposition, are very sensitive.[10] In addition to the sensitivity of SWI to paramagnetic material, corrected phase images that are calculated to form final SWI can provide quantitative phase-shift values that reflect tissue iron content.[11] Recently published studies attempted to use SWI to differentiate movement disorders, including MSA-p,[12] and demonstrated different iron-deposition patterns between MSA-p and IPD by measuring phase-shift values by using corrected phase images of SWI sequences.[13] However, most previous studies regarding SWI were performed on 1.5T or weaker main magnetic field MR imaging machines. When main magnetic field is increased to 3T, spins process at a higher frequency, which may result in phase shifts caused by susceptibility changes being more exaggerated on SWI.

Thus, the purpose of the present study was to evaluate the imaging findings of 3T SWI for differentiating MSA-p from IPD, focusing on putaminal changes and lesion asymmetry.

MATERIALS AND METHODS

Study Population

This retrospective cohort study was approved by the institutional review board of our hospital, and the requirement for informed consent was waived. The investigators searched all patients who were referred from the Movement Disorder Center to undergo brain MR imaging, including SWI, for further evaluation of parkinsonism between April 2010 and May 2012 ($n = 207$). Among those patients, we enrolled subjects who had been initially, clinically diagnosed with either MSA-p ($n = 33$) or IPD ($n = 50$). All routine brain MR imaging protocols performed during the study period for the evaluation of movement disorders included SWI, except in 1 patient. Neurologists experienced with movement disorders (H.-J.K. and B.S.J.) made the final clinical diagnosis by reviewing the initial and follow-up clinical data in December 2013. MSA-p was diagnosed according to the "Second Consensus Statement on the Diagnosis of Multiple System Atrophy"[1] and was categorized as probable or possible. IPD was diagnosed on the basis of the UK Parkinson's Disease Society Brain Bank criteria.[14]

Five initial patients with MSA-p were excluded for the following reasons: an old intracerebral hemorrhage involved the basal ganglia ($n = 1$), diagnoses were changed to cerebellar dysfunction type multiple system atrophy (MSA-c) ($n = 3$), and final diagnosis found no movement disorder ($n = 1$). One initial patient with IPD was excluded due to lack of SWI by a technical error. One initial patient with MSA-p had the final diagnosis changed to IPD. Finally, there were 27 patients with MSA-p and 50 patients with IPD. Twenty-seven age-matched subjects who met the following criteria were enrolled as the control group: 1) They underwent brain MR imaging with SWI between September 2012 and November 2012, 2) had no definite focal lesions in the brain parenchyma, and 3) had no clinical evidence of neurodegenerative diseases or movement disorders. The control group subjects were age-matched 1:1 with the subjects with MSA-p. Finally, our study included 27 patients with MSA-p (17 probable and 10 possible), 50 patients with IPD, and 27 healthy control subjects.

MR Imaging Protocol

All subjects underwent brain MR imaging by using a 3T scanner (Magnetom Verio; Siemens, Erlangen, Germany) with a 32-channel head coil. A set of images was acquired by using a 3D fully flow-compensated gradient-echo SWI sequence along the transverse plane parallel to the anterior/posterior commissure lines. The imaging parameters were as follows: TR = 28 ms, TE = 20 ms, flip angle = 15°, section thickness = 2 mm, FOV = 178 × 220 mm, matrix size = 364 × 448, and number of excitations = 1. Therefore, the voxel size was $0.49 \times 0.49 \times 2.0$ mm^3. The magnitude and phase images were processed to create final SWI on the MR imaging console workstation (syngo MR B17; Siemens). The corrected phase images and final processed SWI were used for further analyses.

Image Interpretation

Two radiologists (I.H. and C.-H.S., with 4 and 17 years of experience in neuroradiology, respectively), who reached a consensus, reviewed the processed SWI. The investigators qualitatively evaluated the imaging findings for putaminal atrophy and signal intensity of the posterolateral putamen compared with adjacent structures in the basal ganglia (eg, globus pallidus). In particular, loss of lateral convexity of the posterolateral putaminal border was also indicative of putaminal atrophy.[2] In addition to the SWI findings, cerebellar and brain stem findings were also reviewed with T2-weighted axial images for the following: 1) hot-cross bun sign of the pons, 2) high signal intensity in the middle cerebellar peduncle, and 3) cerebellar atrophy. The putaminal signal intensity was graded by using a relative 4-step scale introduced by Kraft et al,[15] in which the signal of the putamen was rated as higher = 0, equal = 1, hypointense = 2, or markedly hypointense = 3. Other image findings were rated as negative = 0, suspicious = 1, or definitely positive = 2. Laterality was also recorded if a finding of putaminal atrophy was rated as suspicious or definitely positive or the signal intensity was rated as marked hypointensity. During the interpretation, images were presented randomly and investigators were blinded to the patients' diagnoses.

Quantitative Image Analysis

We quantitatively measured the putaminal width and phase-shift values in corrected phase images. Image analyses were also performed by 2 radiologists who performed qualitative image interpretation and reached a consensus. The most representative section demonstrating the largest width and most well-demarcated border of the posterior putamen was selected for further analysis. The images were analyzed by using ImageJ 1.46r software (National Institutes of Health, Bethesda, Maryland) with 400% magnification to more easily determine the boundaries of the basal ganglia structures. Investigators drew 3 straight lines with widths of 3 pixels crossing the midportion, posterior half, and far posterior portion of the putamen in the right-to-left direction, as shown in Fig 1*A*. Using the Plot Profile function in ImageJ, we plotted phase-shift values along the straight line, and putaminal positive phase-shift values were easily recognized (Fig 1*A*). The width and the mean phase-shift value on each side of the putamen were recorded by using the 3 lines. The phase-shift value was recorded in Siemens Phase Units, which range from 0 to 4096

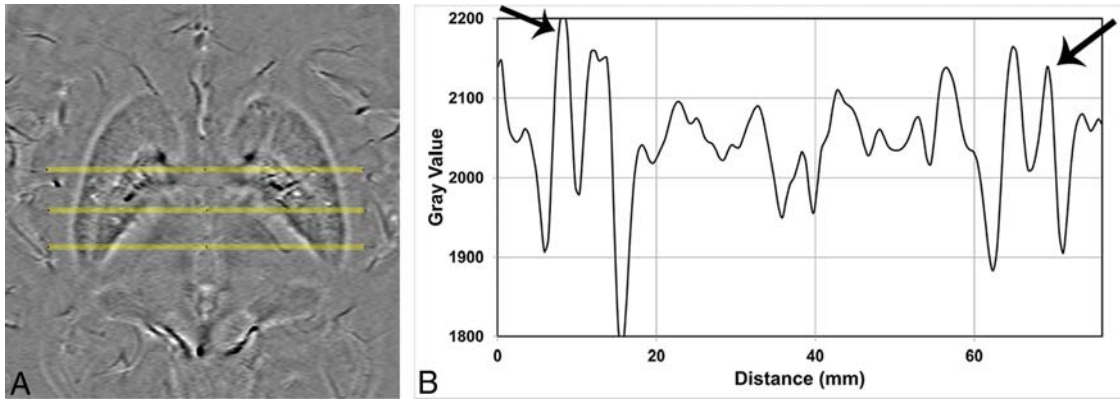

FIG 1. Measurement of putaminal width and mean phase-shift values from corrected phase images by using ImageJ software. *A*, Three lines crossing the mid-, posterior half, and far posterior putamen are drawn to allow measurements. *B*, The corresponding plot profile of the line crossing the far posterior portion of the putamen demonstrates increased phase-shift values in both putamina (*arrows*).

Table 1: Demographic and clinical characteristics of the study groups[a]

	MSA-p	IPD	Healthy Control	*P* Value
No.	27	50	27	
Mean age (yr)	64.8 ± 8.6 (47–77)	66.5 ± 6.7 (54–81)	64.7 ± 8.5 (47–77)	.521[b]
Male/female ratio	13:14	23:27	11:16	.850[c]
Mean disease duration (yr)	4.7 ± 2.9	7.8 ± 5.0	NA	.010[d]
H&Y scale	2.85 ± 0.72	1.95 ± 0.57	NA	<.001[d]
No. of patients with asymmetric presentation	17	10	NA	<.001[c]

Note:—H&Y scale indicates modified Hoehn and Yahr scale; NA, not applicable.
[a] Data are presented as mean ± SD, with ranges in the parentheses.
[b] One-way analysis of variance test.
[c] χ^2 test.
[d] Mann-Whitney *U* test.

corresponding to $-\pi$ to $+\pi$ radian.[16] To normalize the putamen width by brain size, we also measured the largest biparietal diameter of the brain parenchyma on the same image plane. The normalized putaminal width (putaminal width/biparietal diameter × mean of biparietal diameter of all subjects) was calculated and used for the statistical analysis. Dominant-side values (shorter putamen width or higher mean phase-shift value) and the mean of the values of both sides were calculated and used for the statistical analysis. Finally, to evaluate the asymmetry of the measured values, we also calculated the dominant/nondominant side ratios of the measured values. All analyses were performed for each straight line drawn at the mid-, posterior half, and far posterior portion of the putamen; then, the level that showed the most differentiation was selected and further analyzed.

Neurologic Assessment

Experienced neurologists (H.-J.K. and B.S.J.) assessed the final clinical diagnoses of IPD or MSA-p by reviewing the initial and follow-up clinical data. Those neurologists also assessed initial modified Hoehn and Yahr scale scores. In addition, the clinical-onset side of resting tremors or bradykinesia was recorded if the patient presented with asymmetric symptoms at the time of disease onset. If the symptom onset was not asymmetric or information regarding the side of onset was unclear, the more severe symptomatic side was recorded.

Statistical Analyses

All statistical analyses were performed by using MedCalc for Windows, Version 14.10.2 (MedCalc Software, Mariakerke, Belgium). For all statistical analyses, a *P* value < .05 was considered a statistically significant difference. For the qualitative assessment, the prevalence of each finding was calculated. In addition, the sensitivity and specificity for differentiating MSA-P from IPD were also investigated. To assess interrater agreement, we calculated the weighed κ coefficient for 2 major qualitative imaging findings (putaminal atrophy and signal intensity of the posterolateral putamen) on the basis of the initial review data before the 2 reviewers arrived at a consensus. A χ^2 test, Mann-Whitney test, 1-way analysis of variance test, and Kruskal-Wallis test were used to compare the clinicopathologic characteristics and quantitatively measured values for the MSA-p, IPD, and control subjects, as appropriate. A pair-wise comparison was used for the post hoc analysis. Furthermore, a receiver operating characteristic (ROC) curve was drawn for the variables that were significantly different by the Kruskal-Wallis test for differentiating MSA-p from IPD. The area under the ROC curve was calculated to evaluate the diagnostic performance of those variables.

RESULTS

Demographic and Clinical Characteristics

The demographic and clinical characteristics of each group are described in Table 1. The mean disease duration at the time of MR imaging was significantly longer for the IPD group than the MSA-p group.

Qualitative Image Interpretation

Table 2 shows the prevalence of putaminal atrophy and marked signal hypointensity. No subject showed suspicious or definite

Table 2: Prevalence of each image finding by visual interpretation of SWI in each group

Imaging Finding	MSA-p	IPD	Healthy Control
No.	27	50	27
Putaminal atrophy			
Suspicious	3 (11.1%)	0	0
Definite	11 (40.7%)	0	0
Putaminal signal intensity			
Hyperintense	10 (37.0%)	24 (48.0%)	15 (55.6%)
Isointense	3 (11.1%)	22 (44.0%)	10 (37.0%)
Hypointense	2 (7.4%)	4 (8.0%)	2 (7.4%)
Markedly hypointense	12 (44.4%)	0	0
Hot-cross bun sign	2 (7.4%)	0	0
High signal intensity of middle cerebellar peduncle			
Suspicious	3 (11.1%)	0	0
Definite	1 (3.7%)	0	0
Cerebellar atrophy			
Suspicious	11 (40.7%)	10 (20.0%)	0
Definite	3 (11.1%)	0	0

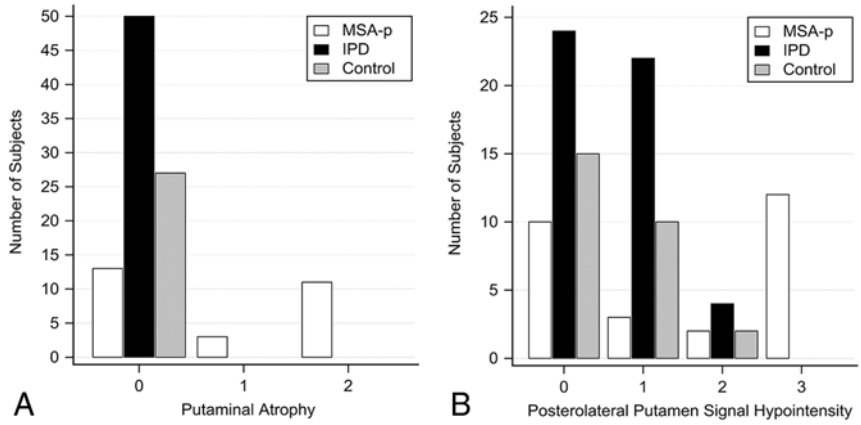

FIG 2. Distribution of putaminal atrophy (*A*) and posterolateral putaminal signal intensity (*B*) in each group. Putaminal atrophy: 0 = negative, 1 = suspicious, 2 = definite; posterolateral putaminal signal intensity: 0 = hyperintense, 1 = isointense, 2 = hypointense, 3 = markedly hypointense.

Table 3: Correlation between the clinically symptomatic side and asymmetry of imaging findings

	Putaminal Atrophy (*n = 14*)			Marked Signal Hypointensity (*n = 12*)		
Clinical Symptom	Symmetric	Right	Left	Symmetric	Right	Left
Symmetric	0	1	2	1	1	0
Right-dominant	1	0	4	2	0	3
Left-dominant	0	5	1	1	3	1

putaminal atrophy or marked signal hypointensity in the IPD or healthy control groups. Therefore, the specificity for each finding was 100%. The sensitivities of putaminal atrophy and marked signal hypointensity were 51.9% (14/27) and 44.4% (12/27), respectively (Fig 2). Most of these findings were unilateral rather than bilateral (Table 3).

Table 3 summarizes the correlation between the clinically symptomatic side and asymmetry in the imaging findings. Among 14 subjects with MSA-p with suspicious or definite putaminal atrophy, 9 subjects presented with a symptomatic side that was contralateral to the atrophy side determined by imaging. The relationship between the clinically symptomatic side and marked signal hypointensity was weaker: Six subjects demonstrated a contralateral correlation between the symptomatic side and the marked hypointense signal side.

Simultaneous putaminal atrophy with marked putaminal signal hypointensity was observed in 11 of 27 patients with MSA-p (40.7%). One patient with MSA-p had bilateral marked signal hypointensity without putaminal atrophy. Otherwise, all patients with MSA-p with marked signal hypointensity showed a loss of lateral convexity. Representative images from the patients with MSA-p and patients with IPD are shown in the Figs 3 and 4.

The weighted κ coefficients for 2 major qualitative imaging findings—putaminal atrophy and signal intensity of the posterolateral putamen—were 0.728 (95% CI, 0.561–0.894) and 0.636 (95% CI, 0.461–0.812), respectively.

Comparison of Measured Putaminal Width and Phase-Shift Values

The On-line Table summarizes the measured values and the dominant/nondominant side ratios of the measured values at

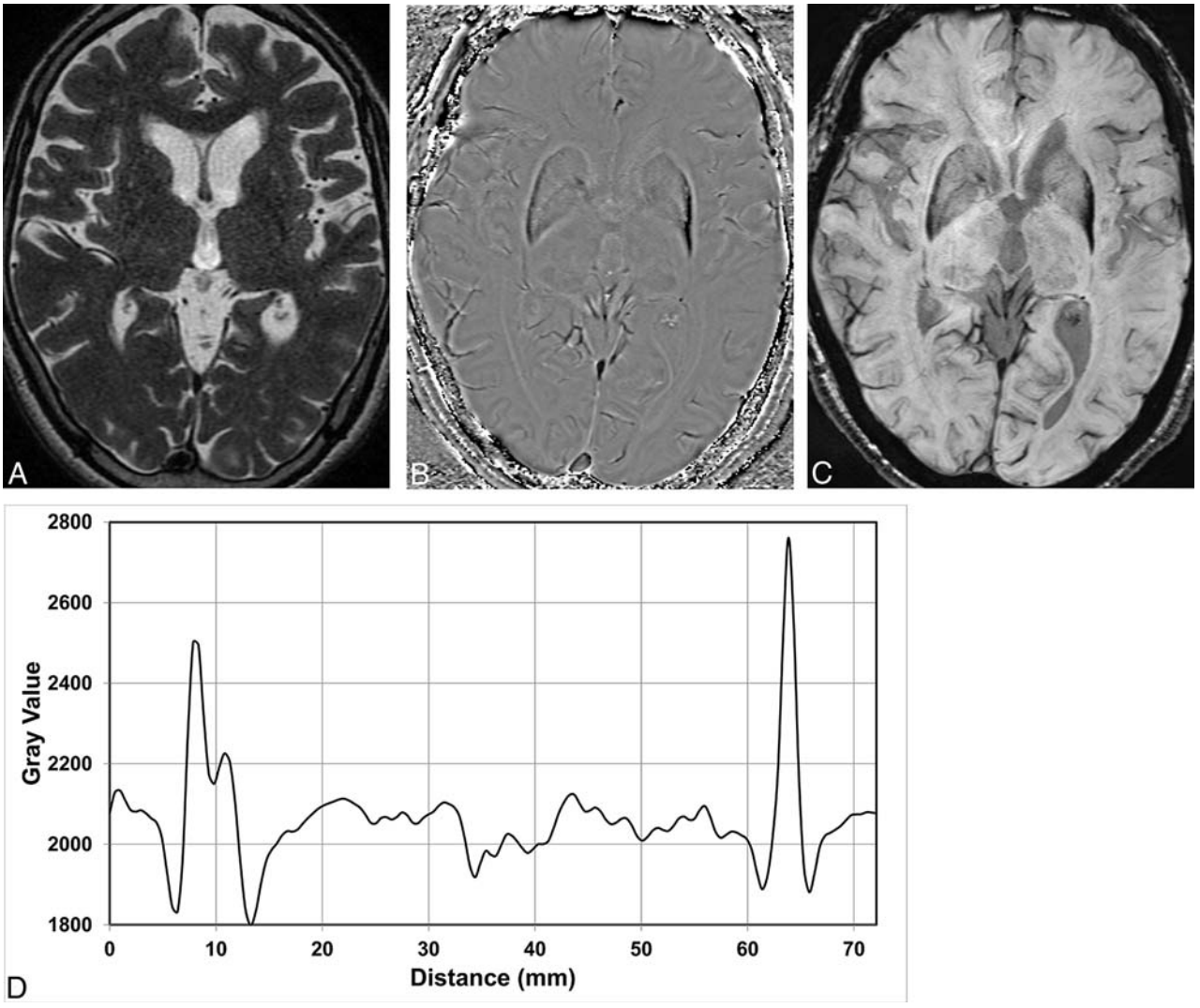

FIG 3. A 71-year-old woman who initially presented with right-leg dragging 3 years ago was clinically diagnosed as having probable MSA-p. *A*, On the T2-weighed axial image, the bilateral posterolateral putamen shows subtle hypointensity. The phase image (*B*) and final SWI (*C*) show a marked phase shift in the left posterolateral putamen with loss of lateral convexity of the posterolateral aspect of the putamen, suggesting atrophic change. *D*, Phase values along the far posterior of both putamina show asymmetric phase-shift values, and mean phase-shift values of the left putamina are measured as 2686.5 Siemens Phase Units.

the midportion, posterior half, and far posterior portion of the putamen. The measured values at the far posterior putamen showed the most significant differences between the MSA-p and IPD and control groups. Table 4 demonstrates the values of the far posterior putamen, and further analyses were based on the values measured at the far posterior putamen. The dominant-side (shorter) putaminal width and the mean of both putaminal widths were smaller in the MSA-p group compared with IPD and healthy control groups. The dominant-side mean phase-shift values and the mean phase-shift values of both putamina were also significantly different in the MSA-p group compared with the IPD and healthy control groups. The MSA-p group showed the highest phase-shift values among all groups. In terms of the dominant/nondominant side ratios, the differences in the putaminal width ratios were marginally insignificant between groups. The dominant/nondominant side ratio of the mean phase-shift values was significantly different between the MSA-p group and the IPD and healthy control groups; this difference suggested that the phase-shift value was significantly more asymmetric in the MSA-p group compared with the IPD and healthy control groups.

ROC Curve Analysis for Values Measured to Differentiate MSA-p from IPD

An ROC curve analysis was performed for the values that were quantitatively measured at the far posterior portion of the putamen to differentiate MSA-p from IPD. The area under the ROC curve was highest for the phase-shift value of both putamina (0.803; 95% CI, 0.697–0.885), followed by the phase-shift value of the dominant side (0.793; 95% CI, 0.685–0.877), the putaminal width of the dominant side (0.761; 95% CI, 0.650–0.851), the mean putaminal width of both sides (0.754; 95% CI, 0.643–0.845), and the dominant-to-nondominant side ratio of the phase-shift value (0.752; 95% CI, 0.640–0.843). Figure 5 demonstrates the ROC curve of the measured values. The optimal cutoff point of the phase-shift value of both putamina was 2121.6 Sie-

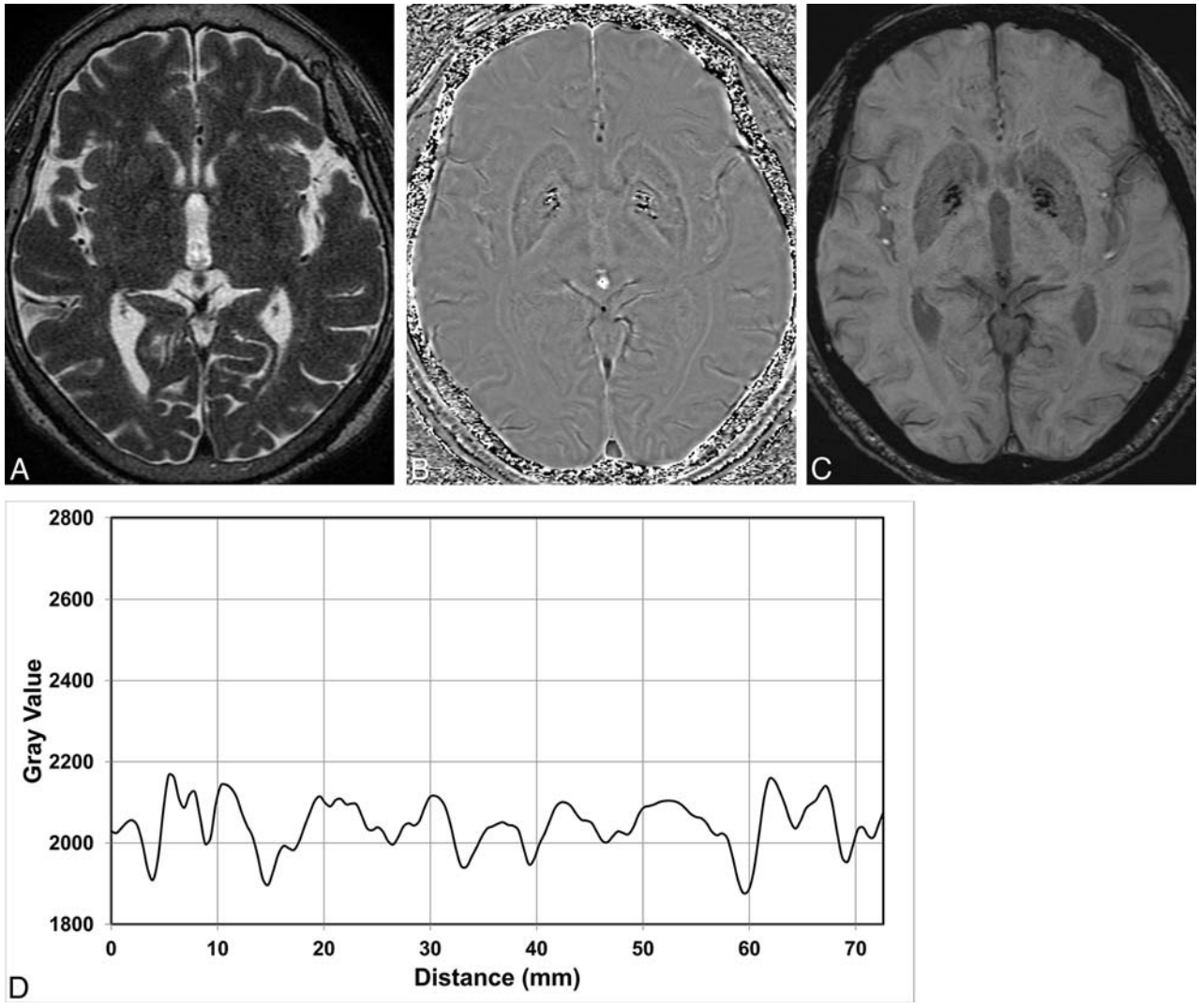

FIG 4. A 69-year-old woman who initially presented with gait disturbance and bradykinesia 8 years ago was clinically diagnosed with IPD. The T2-weighed axial image (*A*), phase image (*B*), and final SWI (*C*) show no substantial signal alteration or atrophy in the bilateral putamina, while excessive iron deposition in the bilateral globus pallidus is observed. *D*, Phase values along the far posterior portion of both putamina show symmetric phase-shift values, and mean phase-shift values of the right and left putamina are measured as 2114.5 and 2111.7 Siemens Phase Units, respectively.

Table 4: Quantitatively measured putaminal width and phase-shift values: the ratios of dominant-to-nondominant-side values in the far posterior portion of putamen[a]

	MSA-p	IPD	Healthy Control	*P* Value
Measured values: dominant side				
Putamen width[b]	3.17 ± 0.65	3.81 ± 0.53	3.87 ± 0.47	<.001
Phase-shift value[b]	2322.2 ± 236.9	2121.5 ± 44.4	2136.7 ± 45.8	<.001
Measured values: mean of both sides				
Putamen width[b]	3.42 ± 0.57	3.98 ± 0.52	4.05 ± 0.45	<.001
Phase-shift value[b]	2258.4 ± 180.1	2108.1 ± 39.8	2122.5 ± 37.6	<.001
Ratio of dominant/nondominant side				
Putamen width (shorter/longer side)	0.866 ± 0.123	0.921 ± 0.070	0.912 ± 0.048	.095
Phase-shift value[b] (higher/lower side)	1.057 ± 0.065	1.013 ± 0.011	1.013 ± 0.011	<.001

[a] Data are presented as means.
[b] MSA-p was significantly different ($P < .05$) from IPD and healthy controls by post hoc analysis.

mens Phase Units, and the diagnostic performance was defined by 77.8% sensitivity and 76.0% specificity.

DISCUSSION

We investigated the 2 imaging findings of the putamen, putaminal atrophy and marked signal hypointensity, as a result of iron deposition on 3T SWI. Our results suggest that these image findings are very specific for patients with MSA-p (100% specificity) and appear asymmetrically in those patients. The sensitivity of previously reported imaging findings for MSA-p ranged from approximately 50% to 85%.[6] Previous studies were most commonly performed by using an MR imaging system with a main magnetic

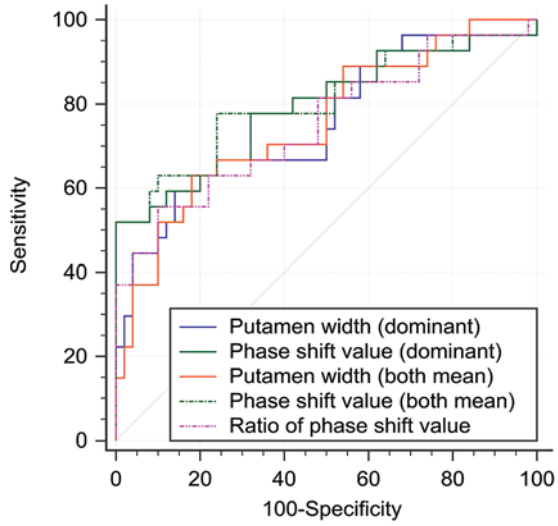

FIG 5. Receiver operating characteristic curves of values measured at the far posterior putamen to distinguish MSA-p from IPD.

field of ≤1.5T and fast spin-echo techniques; this procedure may be the reason for the lower sensitivity of these studies because multiple refocusing radiofrequency pulses during fast spin-echo imaging reduce the paramagnetic effect of T2 hypointensity generated by iron deposition.[3] However, our study was performed on a 3T MR imaging scanner and also revealed only slightly >50% sensitivity for the detection of MSA-p. In contrast, the specificity of our findings was 100%, suggesting that putaminal atrophy and marked signal hypointensity in the posterior putamen could be specific, rather than sensitive, findings for MSA-p. The sensitivity of this study was similar or slightly lower than those previously published for studies that used conventional fast spin-echo-based 3T MR imaging findings.[17,18] The sensitivity of our study was comparable with those of published studies that used T2*-weighted imaging.[19,20] By ROC curve analysis of the quantitative phase-shift values, sensitivity was increased to 77.8%, while specificity was slightly decreased (76.0%). We suggest that quantitative measurement could be used to increase the sensitivity for the detection of MSA-p.

By visual assessment, putaminal atrophy and marked signal hypointensity usually occurred asymmetrically. Quantitative measurement of the phase-shift value of the posterior aspect of the putamen showed significantly higher asymmetry in the MSA-p group compared with the IPD and healthy control groups. These findings suggest that iron deposition in the posterior putamen in patients with MSA-p usually occurs asymmetrically. Furthermore, these imaging findings were frequently detected in the contralateral side of the symptomatic, dominant side. Our results were consistent with a few previous studies that used MR imaging and [^{18}F] fluorodeoxyglucose positron-emission tomography.[21,22] As mentioned earlier, the clinical manifestation of parkinsonism develops asymmetrically in approximately 40%–50% of patients with MSA-p.[8,9] We believe that 3T SWI can visualize asymmetric putaminal changes, including atrophy and iron deposition, in the contralateral, symptomatic side. This finding was not clearly indicated by previous imaging studies, even those that used 3T imaging or 3T SWI.[18,23]

Our quantitative measurement method was not a volumetric method and did not include all putaminal areas or consider the high-iron-deposition area that was proposed to be meaningful by previous publications.[11,13] Haacke et al[11] demonstrated that putative iron deposition in the high-iron-content region increases with age. Our study was focused on imaging findings, and quantitative measurement was performed to support our imaging findings. For routine clinical practice, volume measurements would not be practical because they require meticulous drawing of the volume of interest and are time-consuming. In contrast, our measurement method can be easily performed, is less time-consuming, and might be used for cases that are highly suspicious for MSA-p clinically but do not show asymmetry by visual analysis. When putaminal atrophy was severe, the posterior putamen was difficult to differentiate from the medial and lateral portions of the putamen and globus pallidus. This problem makes volumetric measurement of the posterior putaminal signal and volume separate from the pallidum difficult to achieve. However, our method can be easily used in this situation and could supplement the visual assessment of putaminal atrophy.

For differentiation of parkinsonism with imaging techniques, advanced MR imaging with a machining-learning technique showed excellent discrimination of IPD from atypical parkinsonism by support vector machine analysis by using DTI data.[24] In that study, consecutive symptomatic patients with parkinsonism were referred for imaging to minimize confounding for individual-level classification. Our study also intended to differentiate IPD and MSA-p by using SWI for the patients who were referred for further evaluation of parkinsonism. Although machine learning–based classification showed excellent discrimination, that method could be easily but not directly available for routine clinical practice. Our visual inspection and measurement method of SWI can be directly applicable in routine clinical practice and does not require additional resources. In addition, our study demonstrated frequent asymmetric presentation of known putaminal change in MSA-p, which may not be discovered by support vector machine analysis.

In addition to the intrinsic limits of retrospective studies, a few limitations of this study should be mentioned. First, our study did not directly compare the diagnostic performance of our method with that of known findings on conventional spin-echo MR images and T1- and T2-weighted images. However, the diagnostic performance of our method could be compared with those of previous studies. Second, the longer disease duration in the IPD group may have decreased the proportion of unilateral disease manifestation. In the early disease stage, IPD frequently shows asymmetric symptoms, but in later stages, IPD has a more symmetric presentation. However, it is well-known that IPD shows no substantial putaminal changes by imaging studies, and our results were consistent with those of previous studies.[6] Third, the diagnosis at the time of MR imaging did not discriminate between probable and possible MSA-p. Unfortunately, the data for probable and possible diagnosis for MSA-p were not available in all patients due to retrospective study design. The final diagnosis was made by reviewing the initial and follow-up clinical data in December 2013, while the imaging study had been done before May 2012. The direct comparison of imaging findings between final probable and possible MSA-p groups might lead to misclassifica-

tion bias. Thus, imaging differences between patients with probable and possible MSA-p could not be analyzed.

CONCLUSIONS

3T SWI can visualize putaminal atrophy and marked signal hypointensity in patients with MSA-p with high specificity. Furthermore, it clearly demonstrates the dominant side of putaminal changes, which correlate with the contralateral symptomatic side of patients. We suggest that 3T SWI is a practical method for the evaluation of putaminal atrophy and iron deposition; thus, it could be helpful for differentiating MSA-p from IPD in clinical practice.

Disclosures: Beom S. Jeon—*UNRELATED*: Ipsen, Norvartis; Boehringer Ingelheim; the Korea Health 21 R&D project; Ministry of Health & Welfare, Republic of Korea; the National Research Foundation of Korea; Ministry of Education, Science and Technology; Advanced Biometric Research Center; Korean Science and Engineering Foundation; Seoul National University Hospital; the Mr. Chung Suk-Gyoo and Sinyang Cultural Foundation; and the Song Foundation, *Comments*: research support as Principal Investigator; *Travel/Accommodations/Meeting Expenses Unrelated to Activities Listed*: Korea Research-Based Pharmaceutical Industry Association and Korean Pharmaceutical Manufacturers Association. *Money paid to the institution.

REFERENCES

1. Gilman S, Wenning GK, Low PA, et al. **Second consensus statement on the diagnosis of multiple system atrophy.** *Neurology* 2008;71:670–76 CrossRef Medline
2. Ito S, Shirai W, Hattori T. **Evaluating posterolateral linearization of the putaminal margin with magnetic resonance imaging to diagnose the Parkinson variant of multiple system atrophy.** *Mov Disord* 2007;22:578–81 CrossRef Medline
3. Watanabe H, Ito M, Fukatsu H, et al. **Putaminal magnetic resonance imaging features at various magnetic field strengths in multiple system atrophy.** *Mov Disord* 2010;25:1916–23 CrossRef Medline
4. Tha KK, Terae S, Tsukahara A, et al. **Hyperintense putaminal rim at 1.5 T: prevalence in normal subjects and distinguishing features from multiple system atrophy.** *BMC Neurol* 2012;12:39 CrossRef Medline
5. Tsukamoto K, Matsusue E, Kanasaki Y, et al. **Significance of apparent diffusion coefficient measurement for the differential diagnosis of multiple system atrophy, progressive supranuclear palsy, and Parkinson's disease: evaluation by 3.0-T MR imaging.** *Neuroradiology* 2012;54:947–55 CrossRef Medline
6. Savoiardo M. **Differential diagnosis of Parkinson's disease and atypical parkinsonian disorders by magnetic resonance imaging.** *Neurol Sci* 2003;24(suppl 1):S35–37 CrossRef Medline
7. Hoehn MM, Yahr MD. **Parkinsonism: onset, progression and mortality.** *Neurology* 1967;17:427–42 CrossRef Medline
8. Gómez-Esteban JC, Tijero B, Ciordia R, et al. **Factors influencing the symmetry of Parkinson's disease symptoms.** *Clin Neurol Neurosurg* 2010;112:302–05 CrossRef Medline
9. Wüllner U, Schmitz-Hübsch T, Abele M, et al. **Features of probable multiple system atrophy patients identified among 4770 patients with parkinsonism enrolled in the multicentre registry of the German Competence Network on Parkinson's disease.** *J Neural Transm* 2007;114:1161–65 CrossRef Medline
10. Haacke EM, Xu Y, Cheng YC, et al. **Susceptibility weighted imaging (SWI).** *Magn Reson Med* 2004;52:612–18 CrossRef Medline
11. Haacke EM, Miao Y, Liu M, et al. **Correlation of putative iron content as represented by changes in R2* and phase with age in deep gray matter of healthy adults.** *J Magn Reson Imaging* 2010;32:561–76 CrossRef Medline
12. Gupta D, Saini J, Kesavadas C, et al. **Utility of susceptibility-weighted MRI in differentiating Parkinson's disease and atypical parkinsonism.** *Neuroradiology* 2010;52:1087–94 CrossRef Medline
13. Wang Y, Butros SR, Shuai X, et al. **Different iron-deposition patterns of multiple system atrophy with predominant parkinsonism and idiopathetic Parkinson diseases demonstrated by phase-corrected susceptibility-weighted imaging.** *AJNR Am J Neuroradiol* 2012;33:266–73 CrossRef Medline
14. Hughes AJ, Daniel SE, Kilford L, et al. **Accuracy of clinical diagnosis of idiopathic Parkinson's disease: a clinico-pathological study of 100 cases.** *J Neurol Neurosurg Psychiatry* 1992;55:181–84 CrossRef Medline
15. Kraft E, Trenkwalder C, Auer DP. **T2*-weighted MRI differentiates multiple system atrophy from Parkinson's disease.** *Neurology* 2002;59:1265–67 CrossRef Medline
16. Haacke EM, Ayaz M, Khan A, et al. **Establishing a baseline phase behavior in magnetic resonance imaging to determine normal vs. abnormal iron content in the brain.** *J Magn Reson Imaging* 2007;26:256–64 CrossRef Medline
17. Lee JY, Yun JY, Shin CW, et al. **Putaminal abnormality on 3-T magnetic resonance imaging in early parkinsonism-predominant multiple system atrophy.** *J Neurol* 2010;257:2065–70 CrossRef Medline
18. Feng JY, Huang B, Yang WQ, et al. **The putaminal abnormalities on 3.0T magnetic resonance imaging: can they separate parkinsonism-predominant multiple system atrophy from Parkinson's disease?** *Acta Radiol* 2015;56:322–28 CrossRef Medline
19. Arabia G, Morelli M, Paglionico S, et al. **An magnetic resonance imaging T2*-weighted sequence at short echo time to detect putaminal hypointensity in Parkinsonisms.** *Mov Disord* 2010;25:2728–34 CrossRef Medline
20. von Lewinski F, Werner C, Jörn T, et al. **T2*-weighted MRI in diagnosis of multiple system atrophy: a practical approach for clinicians.** *J Neurol* 2007;254:1184–88 CrossRef Medline
21. Kato T, Kume A, Ito K, et al. **Asymmetrical FDG-PET and MRI findings of striatonigral system in multiple system atrophy with hemiparkinsonism.** *Radiat Med* 1992;10:87–93 Medline
22. Kume A, Shiratori M, Takahashi A, et al. **Hemi-parkinsonism in multiple system atrophy: a PET and MRI study.** *J Neurol Sci* 1992;110:37–45 CrossRef Medline
23. Meijer FJ, van Rumund A, Fasen BA, et al. **Susceptibility-weighted imaging improves the diagnostic accuracy of 3T brain MRI in the work-up of parkinsonism.** *AJNR Am J Neuroradiol* 2015;36:454–60 CrossRef Medline
24. Haller S, Badoud S, Nguyen D, et al. **Individual detection of patients with Parkinson disease using support vector machine analysis of diffusion tensor imaging data: initial results.** *AJNR Am J Neuroradiol* 2012;33:2123–28 CrossRef Medline

The Added Prognostic Value of Preoperative Dynamic Contrast-Enhanced MRI Histogram Analysis in Patients with Glioblastoma: Analysis of Overall and Progression-Free Survival

Y.S. Choi, D.W. Kim, S.-K. Lee, J.H. Chang, S.-G. Kang, E.H. Kim, S.H. Kim, T.H. Rim, and S.S. Ahn

ABSTRACT

BACKGROUND AND PURPOSE: The prognostic value of dynamic contrast-enhanced MR imaging in patients with glioblastoma is controversial. We investigated the added prognostic value of dynamic contrast-enhanced MR imaging to clinical parameters and molecular biomarkers in patients with glioblastoma by using histogram analysis.

MATERIALS AND METHODS: This retrospective study consisted of 61 patients who underwent preoperative dynamic contrast-enhanced MR imaging for glioblastoma. The histogram parameters of dynamic contrast-enhanced MR imaging, including volume transfer constant, extravascular extracellular volume fraction, and plasma volume fraction, were calculated from entire enhancing tumors. Univariate analyses for overall survival and progression-free survival were performed with preoperative clinical and dynamic contrast-enhanced MR imaging parameters and postoperative molecular biomarkers. Multivariate Cox regression was performed to build pre- and postoperative models for overall survival and progression-free survival. The performance of models was assessed by calculating the Harrell concordance index.

RESULTS: In univariate analysis, patients with higher volume transfer constant and extravascular extracellular volume fraction values showed worse overall survival and progression-free survival, whereas plasma volume fraction showed no significant correlation. In multivariate analyses for overall survival, the fifth percentile value of volume transfer constant and kurtosis of extravascular extracellular volume fraction were independently prognostic in the preoperative model, and kurtosis of volume transfer constant and extravascular extracellular volume fraction were independently prognostic in the postoperative model. For progression-free survival, independent prognostic factors were minimum and fifth percentile values of volume transfer constant and kurtosis of extravascular extracellular volume fraction in the preoperative model and kurtosis of extravascular extracellular volume fraction in the postoperative model. The performance of preoperative models for progression-free survival was significantly improved when minimum or fifth percentile values of volume transfer constant and kurtosis of extravascular extracellular volume fraction were added.

CONCLUSIONS: Higher volume transfer constant and extravascular extracellular volume fraction values are associated with worse prognosis, and dynamic contrast-enhanced MR imaging may have added prognostic value in combination with preoperative clinical parameters, especially in predicting progression-free survival.

ABBREVIATIONS: DCE = dynamic contrast-enhanced; EGFR = epidermal growth factor receptor; KPS = Karnofsky performance scale; K^{trans} = volume transfer constant; MGMT = O6-methylguanine-DNA methyltransferase; OS = overall survival; p = percentile; PFS = progression-free survival; v_e = extravascular extracellular volume fraction; v_p = plasma volume fraction

Glioblastoma is the most common primary brain malignancy and its prognosis is dismal.[1] Although the median survival time is approximately 14 months, occasional long-term survival and significant response to therapy have been reported in a subset of patients.[2,3] Many investigations have been conducted to elucidate the prognostic factors of glioblastoma, including clinical factors such as age, Karnofsky performance scale (KPS), and extent of tumor resection.[4,5] Molecular and genetic biomarkers of glioblastoma, including O6-methylguanine-DNA methyltransferase (MGMT) promoter methylation, epidermal growth factor receptor (EGFR), p53, and Ki-67 index, are also emerging prognostic

Received January 20, 2015; accepted after revision April 20.

From the Departments of Radiology and Research Institute of Radiological Science (Y.S.C., S.-K.L., S.S.A.), Neurosurgery (J.H.C., S.-G.K., E.H.K.), Pathology (S.H.K.), and Ophthalmology (T.H.R.), Yonsei University College of Medicine, Seoul, Korea; and Department of Policy Research Affairs (D.W.K.), National Health Insurance Service Ilsan Hospital, Goyang, Gyeonggi-do, Korea.

Please address correspondence to Sung Soo Ahn, MD, PhD, Department of Radiology, College of Medicine, Yonsei University, 50 Yonsei-ro, Seodaemun-gu, Seoul 120–752, Korea; e-mail: SUNGSOO@yuhs.ac

Indicates article with supplemental on-line tables.

http://dx.doi.org/10.3174/ajnr.A4449

factors predicting the biologic behavior of tumors.[6-10] However, profiles of molecular biomarkers can only be obtained by invasive procedures such as biopsy or resection. Thus, MR imaging has been actively applied as a noninvasive tool for prognosis prediction and diagnosis and evaluation of treatment response; conventional imaging findings, such as edema, necrosis, or tumor size, have been known to be related to prognosis.[5,11-14] Advanced MR imaging techniques have also been found to be of increasing utility in predicting prognosis of gliomas. For example, the lower apparent diffusion coefficient of diffusion-weighted imaging and higher relative cerebral blood volume of dynamic susceptibility contrast imaging have been reported to be correlated with worse prognosis in gliomas.[15-18] Nevertheless, conflicting results were reported for the prognostic value of apparent diffusion coefficient.[15,16,19] In addition, relative cerebral blood volume may involve biases of T1 effects and extravascular contrast leakage of tumor vessels and susceptibility artifacts,[20] though T1 effects and extravascular contrast leakage can be limited by several techniques.[20-23]

Using dynamic contrast-enhanced (DCE)–MR imaging, one can evaluate the blood-brain barrier by measuring quantitative permeability parameters such as volume transfer constant (K^{trans}), extravascular extracellular volume fraction (v_e), and plasma volume fraction (v_p), which are quantitative metrics of vascular permeability, extravascular extracellular volume, and plasma volume, respectively. While K^{trans} has been reported to increase with glioma grade, its prognostic value for overall survival (OS) remains controversial[24,25] and its prognostic value for progression-fee survival (PFS) and added value to other previously known prognostic factors have not been investigated.

The purpose of our study was to investigate the association of DCE-MR imaging–derived parameters with OS and PFS in patients with glioblastoma, and their added prognostic value to preoperative clinical parameters and postoperative molecular biomarkers by using histogram analysis.

MATERIALS AND METHODS

This retrospective study was approved by the Severance Hospital of Yonsei University College of Medicine review board, which waived the requirement for informed consent.

Subjects

From October 2010 through April 2014, 98 consecutive patients with newly diagnosed glioblastoma, who underwent preoperative DCE–MR imaging, were reviewed. All patients were treated according to the standard regimen consisting of an operation and postoperative involved-field radiation therapy with temozolomide, as described elsewhere.[26] Inclusion criteria were the following: 1) pure glioblastoma without other cell components mentioned in the pathologic report; 2) available profile of molecular biomarkers reported postoperatively, including MGMT methylation, EGFR, p53, Ki-67 index, and *isocitrate dehydrogenase 1* mutation; and 3) patients who underwent either total, subtotal, or partial resection of tumor. Exclusion criteria were the following: 1) glioblastoma mixed with other cell components, such as an oligodendroglial component, or any specific subtype of glioblastoma such as giant cell glioblastoma or gliosarcoma ($n = 22$); 2) positive or unknown *isocitrate dehydrogenase 1* mutation status ($n = 10$); and 3) patients who did not undergo an operation ($n = 2$) or underwent biopsy only ($n = 3$). We excluded glioblastomas with heterogeneous cellular components and *isocitrate dehydrogenase 1* mutations, to exclude confounding factors that affect prognosis[27,28] and to conduct accurate survival analysis with pure primary glioblastoma only. Therefore, 61 patients were enrolled in this study (male/female ratio = 32:29; 63.0 ± 9.8 years of age).

Image Acquisition

Preoperative MR imaging was performed by using 3T imaging (Achieva; Philips Healthcare, Best, the Netherlands) and an 8-channel sensitivity encoding head coil. The preoperative MR imaging protocol included conventional sequences consisting of T1-weighted imaging (TR, 2000 ms; TE, 10 ms; FOV, 240 mm; section thickness, 5 mm; and matrix, 256 × 256), T2-weighted imaging (TR, 3000 ms; TE, 80 ms; FOV, 240 mm; section thickness, 5 mm; and matrix, 256 × 256), and fluid-attenuated inversion recovery imaging (TR, 10,000 ms; TE, 125 ms; FOV, 240 mm; section thickness, 5 mm; and matrix, 256 × 256). For DCE–MR imaging, 60 dynamic phases of DCE T1-weighted images were acquired with the following parameters: TR, 6.3 ms; TE, 3.1 ms; FOV, 240 mm; matrix, 192 × 192 mm; section thickness, 3 mm; and flip angle, 15°. After acquiring the fifth phase of image volume, gadolinium-based contrast (0.1-mL/kg gadobutrol, Gadavist; Bayer Schering Pharma, Berlin, Germany) was injected at a rate of 3 mL/s. The total acquisition time for DCE–MR imaging was 6 minutes 18 seconds.

DCE–MR Imaging Analysis

DCE–MR imaging data were moved to a personal computer and processed off-line with commercial software (nordicICE; NordicNeuroLab, Bergen, Norway), which is based on the pharmacokinetic model established by Tofts et al.[29] DCE–MR imaging parameter maps of K^{trans}, v_e, and v_p were generated after calibration of motion correction and determination of arterial input function, which was calculated from 5 spots on the M1 segment ipsilateral to the tumor. The baseline T1 value was fixed at 1000 ms in this study.[30-33] The ROI was drawn by 1 neuroradiologist (Y.S.C.) and confirmed by another neuroradiologist (S.S.A.) on the basis of the last phase of DCE–MR images to contain the entire enhancing tumor volume by using a semiautomatic method by thresholding of signal intensity. The histogram parameters consisting of mean, minimum, fifth percentile (p5), and 25th (p25), 50th (p50), 75th (p75), and 95th (p95) percentiles and maximum values, skewness, and kurtosis of K^{trans}, v_e, and $v_{p,}$ were calculated from ROIs overlaid on DCE–MR imaging parameter maps.

Other Prognostic Parameters

We recorded the following clinical parameters: age, sex, and preoperative KPS. The extent of tumor resection was classified as total, subtotal, or partial on the basis of the surgeon's intraoperative impression in conjunction with examination of postoperative images, with "subtotal resection" meaning <100% but ≥75% tumor removal and "partial resection" meaning <75% gross tumor removal. In addition, tumor descriptors on conventional MR images were determined by consensus of 2 neuroradiologists

(Y.S.C. and S.S.A., with 2 and 5 years of experience in brain MR imaging, respectively) and were considered preoperative parameters in subsequent analyses, which consisted of enhancing tumor volume, degree of edema, and the presence of non-contrast-enhancing tumor. Enhancing tumor volume was automatically calculated from ROIs drawn for DCE–MR imaging analysis. Edema was scored by using the maximum distance of edema from the tumor margin as 0 (not apparent), if <1 cm; 1 (mild to moderate), if >1 and <2 cm; and 2 (severe), if >2 cm. Non-contrast-enhancing tumor was defined as intermediate T2 signal intensity (less than the intensity of CSF) that is associated with mass effect and architectural distortion. Non-contrast-enhancing tumor was visually assessed and classified as positive if non-contrast-enhancing tumor volume was >25% of enhancing tumor volume, or negative otherwise.

We also recorded postoperatively obtained profiles of molecular biomarkers, including MGMT methylation, EGFR, p53, and Ki-67 index.

Definition of Survival Time

"Overall survival" was defined as the time from diagnosis to death or last follow-up date when the patient was known to be alive. "Progression-free survival" was defined as the time from diagnosis to tumor progression, recurrence, death, or the last follow-up date in which the patient showed no disease progression. The definition and date of tumor progression were based on the Response Assessment in Neuro-Oncology criteria: in brief, 1) the first follow-up date showing ≥25% increase in an enhancing lesion or an increase in a nonenhancing lesion inside the radiation field, which increased in size at a consecutive MR imaging follow-up or was pathologically proved to be a recurrent tumor; 2) the initial follow-up date with a newly appearing enhancing lesion outside the radiation field; 3) the date showing clinical deterioration secondary to disease; and 4) the date of death for patients who died and did not meet the above criteria. The date of tumor progression on MR imaging was determined by consensus of 2 neuroradiologists (Y.S.C. and S.S.A.).

Statistical Analysis

Univariate analysis by using the Cox proportional hazard analysis was performed for both OS and PFS, with the histogram parameters of DCE–MR imaging (K^{trans}, v_e, and v_p), clinical parameters (age, sex, KPS, extent of resection), tumor descriptors (eg, enhancing tumor volume, edema, non-contrast-enhancing tumor), and postoperative molecular biomarkers (MGMT methylation, EGFR overexpression, p53, and Ki-67 index). Continuous variables, including DCE–MR imaging parameters, and categoric variables of >3 categories were dichotomized by using the K-adaptive partitioning algorithm to identify the most significant cutoff points affecting OS and PFS.[34,35]

Multivariate analysis by using the Cox regression model was performed with significant factors on univariate analysis to build prognostic models predicting OS and PFS. The prognostic models were built in 2 ways each for OS and PFS to investigate the added value of DCE–MR imaging in preoperative and postoperative settings: preoperative models with clinical and DCE–MR imaging parameters and postoperative models with clinical and DCE–MR imaging parameters and molecular biomarkers.

Table 1: Patient characteristics ($n = 61$)

Variables	Mean (SD) or No. (%)
Age (year)[a]	63.0 (9.8)
Sex	
Male	32 (52.5%)
Female	29 (47.5%)
Karnofsky performance scale[a]	72.1 (12.1)
Enhancing tumor volume (cm^3)[a]	23.5 (19.1)
Extent of resection	
Total	28 (45.9%)
Subtotal or partial	33 (54.1%)
Edema	
None	9 (14.8%)
Mild-to-moderate	15 (24.6%)
Severe	37 (60.6%)
Non-contrast-enhancing tumor	
Negative	26 (42.6%)
Positive	35 (57.4%)
MGMT	
Unmethylated	38 (62.3%)
Methylated	23 (37.7%)
EGFR	
0	10 (16.4%)
1+	3 (4.9%)
2+	15 (24.6%)
3+	33 (54.1%)
p53[a]	17.5 (28.0)
Ki-67[a]	23.4 (19.0)

[a] Indicates mean and SD in parentheses.

After multivariate analysis, performance of each prognostic model was evaluated by using the Harrell concordance index (C-index). A C-index value of 0.5 indicates random prediction, and 1.0 indicates perfect prediction. C-indexes were compared between the models, with and without DCE–MR imaging parameters, according to the Newson method.[36,37] To avoid overestimation of the performance of prognostic models, we used the jacknife data resampling technique in calculating C-indexes and their 95% confidence intervals. In addition, multicollinearity was checked by calculating the variable inflation factor of each variable included in the models. A variable inflation factor of >2.5 was considered multicollinearity, influencing the estimated β power. Variable inflation factors of all variables included in prognostic models were <2.0. Statistical analyses were conducted with the Stata software package (Version 12.1; StataCorp, College Station, Texas), and a P value <.05 was considered statistically significant.

RESULTS

Characteristics of the 61 enrolled patients are summarized in Table 1. The locations of the tumors were as follows: frontal ($n = 19$), temporal ($n = 18$), parietal ($n = 15$), occipital lobe ($n = 2$), basal ganglia ($n = 1$), thalamus ($n = 4$), and corpus callosum ($n = 2$). Thirteen patients had tumors encasing or abutting the ipsilateral M1 segment. Among the 61 patients, 29 deaths and 37 tumor progressions occurred. The restricted mean and standard error of overall survival time was 552.6 ± 40.6 days, and the restricted mean and standard error of progression-free survival time was 359.7 ± 31.2 days. The follow-up for those still alive ranged from 24 to 893 days.

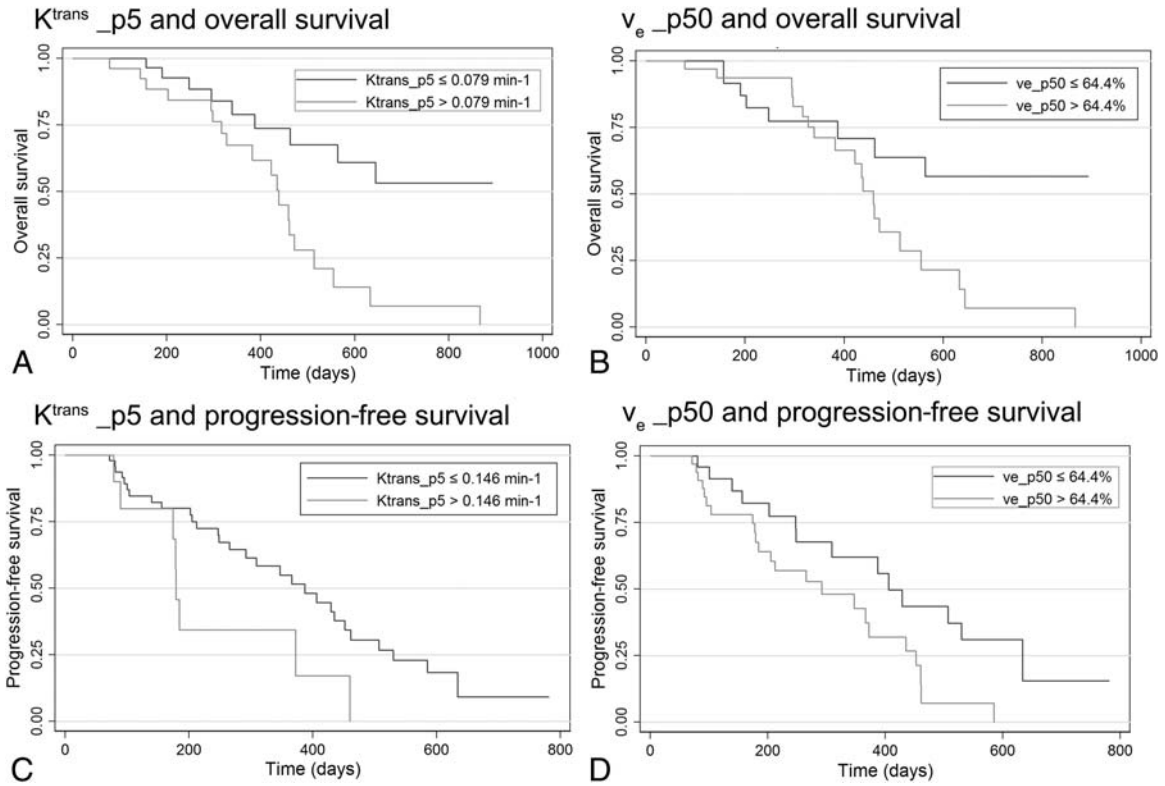

FIG 1. Kaplan-Meier analysis of overall survival according to K^{trans} (*A*) and v_e (*B*), and progression-free survival according to K^{trans} (*C*) and v_e (*D*).

Table 2: Preoperative and postoperative prognostic models for overall survival

	Model 1[a]		Model 2[a]		Model 3[a]		Model 4[b]		Model 5[b]	
Parameters	HR (95% CI)	*P* Value	HR	*P* Value	HR	*P* Value	HR	*P* Value	HR	*P* Value
Enhancing tumor volume	1.38 (0.53–3.60)	.509	2.49 (1.11–5.58)	.027	1.09 (0.43–2.78)	.855	0.80 (0.31–2.05)	.643	0.94 (0.38–2.37)	.904
Age	3.47 (1.42–8.49)	.007	2.49 (1.00–6.19)	.049	1.55 (1.25–8.26)	.015	2.91 (1.20–7.04)	.018	2.66 (1.08–6.58)	.034
KPS	2.86 (1.15–7.15)	.024	2.87 (1.13–7.24)	.026	2.54 (1.02–6.33)	.046	1.09 (0.34–3.47)	.888	1.12 (0.35–3.63)	.845
K^{trans}_p5	2.82 (1.04–7.70)	.043	–		2.93 (1.64–15.74)	.005	–		–	
v_e_kurtosis	–		7.57 (1.49–38.51)	.015	21.90 (3.79–145.91)	.001	–		5.65 (1.13–28.37)	.035
K^{trans}_kurtosis	–		–		–		4.99 (1.05–23.78)	.044	–	
MGMT	–		–		–		7.80 (1.96–31.04)	.004	6.82 (1.77–26.31)	.005
EGFR	–		–		–		4.25 (1.44–12.61)	.009	3.65 (1.21–10.95)	.021

Note:— – indicates not applicable; HR, hazard ratio.

[a] Preoperative models.

[a] Postoperative models.

Univariate Analysis for Overall Survival

Histogram analysis of DCE–MR imaging parameters (On-line Table 1) revealed that high K^{trans} and v_e values showed a trend toward worse OS and that this trend was statistically significant in kurtosis, minimum, p5, p25, and p50 values of K^{trans} (*P* values = .016, .007, .004, .012, and .023, respectively) and kurtosis, mean, p5, p25, p50, p75, and p95 values of v_e (*P* values = .005, .034, .005, .040, .027, .041, and .02, respectively). Histogram parameters of v_p showed no significant correlation with OS. Kaplan-Meier curves of representative prognostic parameters of K^{trans} and v_e are depicted in Fig 1. Among other parameters, older than 68 years of age, KPS of <70, enhancing tumor volume of >30 cm^2, MGMT unmethylation, and EGFR > 2+ were associated with worse OS (On-line Table 2).

Multivariate Analysis for Overall Survival

In multivariate analysis for preoperative prognostic models with clinical and DCE–MR imaging parameters, p5 value of K^{trans} and kurtosis of v_e were independently prognostic for OS in addition to age and KPS, and these 2 parameters remained independently prognostic when entered into multivariate analysis at the same time (Table 2). In multivariate analysis for postoperative prognostic models with molecular biomarkers added, kurtosis of K^{trans} and v_e were independently prognostic for OS, and these 2 parameters became insignificant when both were entered into multivariate analysis at the same time.

Univariate Analysis for Progression-Free Survival

Histogram analysis of DCE–MR imaging parameters (On-line Table 1) revealed that high K^{trans} and v_e values showed a trend toward worse PFS and that this trend was statistically significant in kurtosis, minimum, p5, and p25 values of K^{trans} (*P* value = .033, .008, .029, and .043, respectively) and kurtosis, p5, p50, and p95 values of v_e (*P* value = .004, .046, 0031, and .029, respectively). Histogram parameters of v_p showed no significant corre-

Table 3: Preoperative and postoperative prognostic models for progression-free survival

Parameters	Model 1[a]		Model 2[a]		Model 3[a]		Model 4[a]		Model 5[a]		Model 6[b]	
	HR	*P* Value	HR	*P* Value	HR	*P* Value	HR	*P* Value	HR	*P* Value	HR	*P* Value
Enhancing tumor volume	2.9 (1.4–6.0)	.005	1.9 (0.9–4.0)	.105	2.4 (1.1–5.0)	.023	3.1 (1.5–6.7)	.003	1.8 (0.8–3.9)	.135	1.4 (0.6–3.2)	.423
Age	2.4 (1.2–4.8)	.015	3.1 (1.4–6.6)	.004	2.4 (1.1–4.9)	.020	2.5 (1.2–5.2)	.011	3.4 (1.6–7.6)	.002	2.4 (1.1–4.9)	.020
K^{trans}_min	2.8 (1.4–5.6)	.004	–		–		3.3 (1.6–6.7)	.001	–		–	
K^{trans}_p5	–		2.9 (1.2–7.2)	.020	–		–		4.0 (1.5–10.4)	.004	–	
v_e_kurtosis	–		–		4.4 (1.7–11.3)	.002	5.7 (2.2–15.2)	.000	6.0 (2.2–16.3)	.000	5.3 (2.0–14.0)	.001
MGMT	–		–		–		–		–		3.1 (1.3–7.4)	.012

Note:— – indicates that the model doesn't have the corresponding factor as a covacriate; HR, hazard ratio.

[a] Preoperative models.

[b] Postoperative model.

lation with PFS. Kaplan-Meier curves of representative prognostic parameters of K^{trans} and v_e are depicted in Fig 1. Among other parameters, age older than 68 years, enhancing tumor volume >30 cm^3, and MGMT unmethylation were associated with worse PFS (On-line Table 2).

Multivariate Analysis for Progression-Free Survival

In multivariate analysis for preoperative prognostic models with clinical and DCE–MR imaging parameters, minimum and p5 of K^{trans} and kurtosis of v_e were independently prognostic for PFS in addition to age, and these DCE–MR imaging parameters remained independently prognostic when combined and entered into the multivariate analysis (Table 3). In multivariate analysis for postoperative prognostic models with molecular biomarkers added, only kurtosis of v_e remained independently prognostic for PFS.

Comparison of the Performance of the Prognostic Models

Comparisons of the performance of the prognostic models are summarized in On-line Table 3. The C-indexes ranged from 0.75 to 0.82 in prognostic models for OS, indicating good performance, and were higher in models with DCE–MR imaging parameters than in those without, though it was not statistically significant ($P > .05$). The C-indexes ranged from 0.70 to 0.74 in prognostic models for PFS and were higher in models with DCE–MR imaging parameters than in those without. Performance of the models appeared to be significantly improved when kurtosis of v_e, combined with either minimum or p5 of K^{trans}, was added into the preoperative models for PFS (*P* values were .034 and .046 for models with kurtosis of v_e + minimum of K^{trans}, and kurtosis of v_e + p5 of K^{trans}, respectively).

DISCUSSION

We investigated the prognostic value of DCE–MR imaging in predicting OS and PFS and its added value to preoperative clinical parameters and postoperative molecular biomarkers in patients with glioblastoma. Higher cumulative histogram parameters and higher kurtosis of K^{trans} and v_e had a trend toward worse OS and PFS with statistical significance, which means that tumors having relatively higher frequency and peaks at higher v_e and K^{trans} values were correlated with worse prognosis.

The C-indexes were higher in models with either K^{trans} or v_e or both added than in models without DCE–MR imaging parameters, though the difference in C-indexes was statistically significant only in the preoperative models for PFS. Our results imply that DCE–MR imaging may have added prognostic value in combination with preoperative clinical parameters, especially in predicting PFS. However, we carefully suggest that the added prognostic value of DCE–MR imaging in combination with postoperative molecular biomarkers is uncertain. In our opinion, the small sample size and the small number of deaths and disease progression that occurred in our study cohort are primarily responsible for the lack of significant added value of DCE–MR imaging in the prognostic models. Another possible explanation is that DCE–MR imaging parameters would be less likely to show added prognostic value in combination with molecular biomarkers in postoperative models if correlation between DCE–MR imaging parameters and molecular biomarkers is one of the mechanisms by which DCE–MR imaging parameters exhibit prognostic value. Thus, further investigation with a larger cohort and analysis of biomarkers is necessary.

The K^{trans} value reflects vascular permeability. In theory, tumor aggressiveness increases in tumors with higher K^{trans} value, probably due to increased neoangiogenesis and vascular permeability required for tumor growth,[38] by which the correlation between higher K^{trans} value and worse prognosis is expected, as seen in our results. Nonetheless, the relationship between K^{trans} and the prognosis of glioblastoma has been controversial.[24,25,39] Mills et al[24] reported that higher K^{trans} was correlated with good overall survival in glioblastoma. In contrast, Awasthi et al[40] reported the correlation between higher vascular permeability (K^{trans} and v_e) and higher expression of matrix metalloproteinases, which has been associated with poor survival in glioblastoma. Nguyen et al[25] reported that high K^{trans} and v_p values were associated with poor overall survival of high-grade glioma, while v_p values were not significantly correlated with prognosis in our study. These conflicting results might be due to the enrollment of heterogeneous gliomas of various grades or with the oligodendroglial component, different methods of ROI drawing, and different effects of covariates affecting survival such as age, KPS, extent of tumor resection, edema, or necrosis.

V_e is a quantitative metric of extravascular extracellular space volume on DCE–MR imaging and is considered an index of tumor necrosis.[41] The correlation between higher v_e and worse prognosis indicates that tumors with higher necrotic portions have worse prognoses, reflecting microscopic levels of necrosis undetectable on conventional MR imaging, though we excluded the gross necrotic portion and included only enhancing tumor volume in ROIs. This result agrees with a previous study that reported a positive correlation between v_e value and matrix met-

alloproteinases, an index reflecting cellular proliferation and invasion of tumors.[40]

The v_p value reflects vascular volume fraction on DCE–MR imaging. However, no parameter of v_p showed significant correlation with OS or PFS in our study, whereas previous studies with dynamic susceptibility contrast imaging suggested that increased relative cerebral blood volume is related to tumor grade, aggressiveness, and OS.[42-45] In our opinion, these conflicting results for v_p might be partially attributed to the limited accuracy of v_p in a temporal resolution of >2 seconds. Previous studies recommended a temporal resolution of approximately 2 seconds or faster if plasma flow is to be estimated,[46-48] and our measurement of v_p might be inaccurate because we used a temporal resolution of 6 seconds. Nonetheless, a previous study with DCE–MR imaging reported v_p as a prognostic parameter[25] and suggested that conflicting results may also be related to differences in DCE–MR imaging protocol and methods for calculating arterial input function and ROI selection.

As far as we know, our study is the first investigation of the prognostic value of DCE–MR imaging with the largest and most homogeneous cohort of glioblastomas. Another strong point of our study is the semiautomatic drawing of ROIs with thresholds containing the entire enhancing tumor volume for histogram analysis of DCE parameters, because visually assessing several "hot spots" and not containing the entire enhancing tumor might be subjective and fail to reflect the characteristics of entire tumor. Additionally, we dichotomized the histogram parameters of K^{trans} and v_e with the most significant cutoff values affecting survival, which were identified by the K-adaptive partitioning algorithm. The trade-off of this method is that extreme cutoff values can be selected causing uneven dichotomization. For example, tumors with a kurtosis of v_e of >50.3% occupied only 6.6% of the entire cohort. Similarly, tumors with a kurtosis of K^{trans} of >0.042 minutes^{-1} and kurtosis of v_e of >27.8% occupied 13.1% and 11.5%, respectively. These extreme cutoff values and subsequent uneven dichotomization may be more useful as adjunct prognostic parameters to other prognostic parameters, rather than as a single prognostic parameter alone.

There are several limitations in our study. First is a lack of generalizability and standardization of DCE-MR imaging–derived parameters, which can be affected by postprocessing software, calibration for T1 relaxation, and the protocol of DCE–MR imaging. Hence, any specific cutoff values of K^{trans} or v_e in this study cannot be generally used, and this study suggests only the potential for the added prognostic value of DCE–MR imaging. In addition, the repeatability of DCE–MR imaging parameters has been a major problem, though this can be reduced with improved methodologies for data acquisition and postprocessing.[30,49-51] Also, arterial input function calculation might have been inaccurate, especially in the 13 patients with tumors encasing the ipsilateral M1 segment. Second, the number of deaths and disease progressions that occurred in our study cohort might be too small to show the statistically significant added value of DCE–MR imaging in the prognostic models, except in preoperative models for PFS.

CONCLUSIONS

Higher K^{trans} and v_e values were associated with worse prognosis, and DCE–MR imaging may have added prognostic value to preoperative clinical imaging parameters, especially in predicting progression-free survival.

REFERENCES

1. Van Meir EG, Hadjipanayis CG, Norden AD, et al. **Exciting new advances in neuro-oncology: the avenue to a cure for malignant glioma.** *CA Cancer J Clin* 2010;60:166–93 CrossRef Medline
2. Zikou AK, Alexiou GA, Kosta P, et al. **Diffusion tensor and dynamic susceptibility contrast MRI in glioblastoma.** *Clin Neurol Neurosurg* 2012;114:607–12 CrossRef Medline
3. Liu Y, Shete S, Etzel CJ, et al. **Polymorphisms of LIG4, BTBD2, HMGA2, and RTEL1 genes involved in the double-strand break repair pathway predict glioblastoma survival.** *J Clin Oncol* 2010;28:2467–74 CrossRef Medline
4. Stark AM, Stepper W, Mehdorn HM. **Outcome evaluation in glioblastoma patients using different ranking scores: KPS, GOS, mRS and MRC.** *Eur J Cancer Care (Engl)* 2010;19:39–44 CrossRef Medline
5. Lacroix M, Abi-Said D, Fourney DR, et al. **A multivariate analysis of 416 patients with glioblastoma multiforme: prognosis, extent of resection, and survival.** *J Neurosurg* 2001;95:190–98 CrossRef Medline
6. Mellinghoff IK, Wang MY, Vivanco I, et al. **Molecular determinants of the response of glioblastomas to EGFR kinase inhibitors.** *N Engl J Med* 2005;353:2012–24 CrossRef Medline
7. Hegi ME, Diserens AC, Gorlia T, et al. **MGMT gene silencing and benefit from temozolomide in glioblastoma.** *N Engl J Med* 2005;352:997–1003 CrossRef Medline
8. Simmons ML, Lamborn KR, Takahashi M, et al. **Analysis of complex relationships between age, p53, epidermal growth factor receptor, and survival in glioblastoma patients.** *Cancer Res* 2001;61:1122–28 Medline
9. Shiraishi S, Tada K, Nakamura H, et al. **Influence of p53 mutations on prognosis of patients with glioblastoma.** *Cancer* 2002;95:249–57 CrossRef Medline
10. Shinojima N, Tada K, Shiraishi S, et al. **Prognostic value of epidermal growth factor receptor in patients with glioblastoma multiforme.** *Cancer Res* 2003;63:6962–70 Medline
11. Pope WB, Sayre J, Perlina A, et al. **MR imaging correlates of survival in patients with high-grade gliomas.** *AJNR Am J Neuroradiol* 2005;26:2466–74 Medline
12. Chaichana KL, Kosztowski T, Niranjan A, et al. **Prognostic significance of contrast-enhancing anaplastic astrocytomas in adults.** *J Neurosurg* 2010;113:286–92 CrossRef Medline
13. Tynninen O, Aronen HJ, Ruhala M, et al. **MRI enhancement and microvascular density in gliomas: correlation with tumor cell proliferation.** *Invest Radiol* 1999;34:427 CrossRef Medline
14. Hammoud MA, Sawaya R, Shi W, et al. **Prognostic significance of preoperative MRI scans in glioblastoma multiforme.** *J Neurooncol* 1996;27:65–73 CrossRef Medline
15. Higano S, Yun X, Kumabe T, et al. **Malignant astrocytic tumors: clinical importance of apparent diffusion coefficient in prediction of grade and prognosis.** *Radiology* 2006;241:839–46 CrossRef Medline
16. Oh J, Henry RG, Pirzkall A, et al. **Survival analysis in patients with glioblastoma multiforme: predictive value of choline-to-N-acetylaspartate index, apparent diffusion coefficient, and relative cerebral blood volume.** *J Magn Reson Imaging* 2004;19:546–54 CrossRef Medline
17. Murakami R, Sugahara T, Nakamura H, et al. **Malignant supratentorial astrocytoma treated with postoperative radiation therapy: prognostic value of pretreatment quantitative diffusion-weighted MR imaging.** *Radiology* 2007;243:493–99 CrossRef Medline
18. Law M, Young RJ, Babb JS, et al. **Gliomas: predicting time to progression or survival with cerebral blood volume measurements at**

dynamic susceptibility-weighted contrast-enhanced perfusion MR imaging. *Radiology* 2008;247:490–98 CrossRef Medline
19. Pope WB, Lai A, Mehta R, et al. **Apparent diffusion coefficient histogram analysis stratifies progression-free survival in newly diagnosed bevacizumab-treated glioblastoma.** *AJNR Am J Neuroradiol* 2011;32:882–89 CrossRef Medline
20. Boxerman J, Schmainda K, Weisskoff R. **Relative cerebral blood volume maps corrected for contrast agent extravasation significantly correlate with glioma tumor grade, whereas uncorrected maps do not.** *AJNR Am J Neuroradiol* 2006;27:859–67 Medline
21. Paulson ES, Schmainda KM. **Comparison of dynamic susceptibility-weighted contrast-enhanced MR methods: recommendations for measuring relative cerebral blood volume in brain tumors.** *Radiology* 2008;249:601–13 CrossRef Medline
22. Hu L, Baxter L, Pinnaduwage D, et al. **Optimized preload leakage-correction methods to improve the diagnostic accuracy of dynamic susceptibility-weighted contrast-enhanced perfusion MR imaging in posttreatment gliomas.** *AJNR Am J Neuroradiol* 2010;31:40–48 CrossRef Medline
23. Boxerman J, Prah D, Paulson E, et al. **The role of preload and leakage correction in gadolinium-based cerebral blood volume estimation determined by comparison with MION as a criterion standard.** *AJNR Am J Neuroradiol* 2012;33:1081–87 CrossRef Medline
24. Mills SJ, Patankar TA, Haroon HA, et al. **Do cerebral blood volume and contrast transfer coefficient predict prognosis in human glioma?** *AJNR Am J Neuroradiol* 2006;27:853–58 Medline
25. Nguyen TB, Cron GO, Mercier JF, et al. **Preoperative prognostic value of dynamic contrast-enhanced MRI-derived contrast transfer coefficient and plasma volume in patients with cerebral gliomas.** *AJNR Am J Neuroradiol* 2015;36:63–69 CrossRef Medline
26. Kim YS, Kim SH, Cho J, et al. **MGMT gene promoter methylation as a potent prognostic factor in glioblastoma treated with temozolomide-based chemoradiotherapy: a single-institution study.** *Int J Radiat Oncol Biol Phys* 2012;84:661–67 CrossRef Medline
27. Wang Y, Li S, Chen L, et al. **Glioblastoma with an oligodendroglioma component: distinct clinical behavior, genetic alterations, and outcome.** *Neuro Oncol* 2012;14:518–25 CrossRef Medline
28. Parsons DW, Jones S, Zhang X, et al. **An integrated genomic analysis of human glioblastoma multiforme.** *Science* 2008;321:1807–12 CrossRef Medline
29. Tofts PS, Brix G, Buckley DL, et al. **Estimating kinetic parameters from dynamic contrast-enhanced T (1)-weighted MRI of a diffusable tracer: standardized quantities and symbols.** *J Magn Reson Imaging* 1999;10:223–32 CrossRef Medline
30. Haacke EM, Filleti CL, Gattu R, et al. **New algorithm for quantifying vascular changes in dynamic contrast-enhanced MRI independent of absolute T1 values.** *Magn Reson Med* 2007;58:463–72 CrossRef Medline
31. Yun TJ, Park CK, Kim TM, et al. **Glioblastoma treated with concurrent radiation therapy and temozolomide chemotherapy: differentiation of true progression from pseudoprogression with quantitative dynamic contrast-enhanced MR imaging.** *Radiology* 2015;274:830–40 CrossRef Medline
32. Jung SC, Yeom J, Kim JH, et al. **Glioma: application of histogram analysis of pharmacokinetic parameters from T1-weighted dynamic contrast-enhanced MR imaging to tumor grading.** *AJNR Am J Neuroradiol* 2014;35:1103–10 CrossRef Medline
33. Alcaide-Leon P, Pareto D, Martinez-Saez E, et al. **Pixel-by-pixel comparison of volume transfer constant and estimates of cerebral blood volume from dynamic contrast-enhanced and dynamic susceptibility contrast-enhanced MR imaging in high-grade gliomas.** *AJNR Am J Neuroradiol* 2015;36:871–76 CrossRef Medline
34. Kang HJ, Eo SH, Kim SC, et al. **Increased number of metastatic lymph nodes in adenocarcinoma of the ampulla of Vater as a prognostic factor: a proposal of new nodal classification.** *Surgery* 2014;155:74–84 CrossRef Medline
35. Palumbo A, Avet-Loiseau H, Oliva S, et al. **Revised International Staging System for Multiple Myeloma: A Report From International Myeloma Working Group.** *J Clin Oncol* 2015;33:2863–69 CrossRef Medline
36. Newson RB. **Comparing the predictive powers of survival models using Harrell's C or Somers' D.** *Stata Journal* 2010;10:339–58
37. Dolcetta-Capuzzo A, Villa V, Albarello L, et al. **Gastroenteric neuroendocrine neoplasms classification: comparison of prognostic models.** *Cancer* 2013;119:36–44 CrossRef Medline
38. Venkatasubramanian R, Arenas R, Henson M, et al. **Mechanistic modelling of dynamic MRI data predicts that tumour heterogeneity decreases therapeutic response.** *Br J Cancer* 2010;103:486–97 CrossRef Medline
39. Bonekamp D, Deike K, Wiestler B, et al. **Association of overall survival in patients with newly diagnosed glioblastoma with contrast-enhanced perfusion MRI: Comparison of intraindividually matched T1-and T2*-based bolus techniques.** *J Magn Reson Imaging* 2015;42:87–96 CrossRef Medline
40. Awasthi R, Pandey CM, Sahoo P, et al. **Dynamic contrast-enhanced magnetic resonance imaging-derived kep as a potential biomarker of matrix metalloproteinase 9 expression in patients with glioblastoma multiforme: a pilot study.** *J Comput Assist Tomogr* 2012;36:125–30 CrossRef Medline
41. Carmeliet P, Jain RK. **Angiogenesis in cancer and other diseases.** *Nature* 2000;407:249–57 CrossRef Medline
42. Law M, Oh S, Johnson G, et al. **Perfusion magnetic resonance imaging predicts patient outcome as an adjunct to histopathology: a second reference standard in the surgical and nonsurgical treatment of low-grade gliomas.** *Neurosurgery* 2006;58:1099–107; discussion 1099–107 CrossRef Medline
43. Caseiras GB, Chheang S, Babb J, et al. **Relative cerebral blood volume measurements of low-grade gliomas predict patient outcome in a multi-institution setting.** *Eur J Radiol* 2010;73:215–20 CrossRef Medline
44. Sugahara T, Korogi Y, Kochi M, et al. **Correlation of MR imaging-determined cerebral blood volume maps with histologic and angiographic determination of vascularity of gliomas.** *AJR Am J Roentgenol* 1998;171:1479–86 CrossRef Medline
45. Law M, Yang S, Babb JS, et al. **Comparison of cerebral blood volume and vascular permeability from dynamic susceptibility contrast-enhanced perfusion MR imaging with glioma grade.** *AJNR Am J Neuroradiol* 2004;25:746–55 Medline
46. Ingrisch M, Dietrich O, Attenberger UI, et al. **Quantitative pulmonary perfusion magnetic resonance imaging: influence of temporal resolution and signal-to-noise ratio.** *Invest Radiol* 2010;45:7–14 CrossRef Medline
47. Ingrisch M, Sourbron S. **Tracer-kinetic modeling of dynamic contrast-enhanced MRI and CT: a primer.** *J Pharmacokinet Pharmacodyn* 2013;40:281–300 CrossRef Medline
48. Sourbron S. **Technical aspects of MR perfusion**. *Eur J Radiol* 2010;76:304–13 CrossRef Medline
49. Ahearn T, Staff R, Redpath T, et al. **The effects of renal variation upon measurements of perfusion and leakage volume in breast tumours.** *Phys Med Boil* 2004;49:2041–51 CrossRef Medline
50. Dale BM, Jesberger JA, Lewin JS, et al. **Determining and optimizing the precision of quantitative measurements of perfusion from dynamic contrast enhanced MRI.** *J Magn Reson Imaging* 2003;18:575–84 CrossRef Medline
51. Galbraith SM, Lodge MA, Taylor NJ, et al. **Reproducibility of dynamic contrast-enhanced MRI in human muscle and tumours: comparison of quantitative and semi-quantitative analysis.** *NMR Biomed* 2002;15:132–42 CrossRef Medline

Impact of Software Modeling on the Accuracy of Perfusion MRI in Glioma

L.S. Hu, Z. Kelm, P. Korfiatis, A.C. Dueck, C. Elrod, B.M. Ellingson, T.J. Kaufmann, J.M. Eschbacher, J.P. Karis, K. Smith, P. Nakaji, D. Brinkman, D. Pafundi, L.C. Baxter, and B.J. Erickson

ABSTRACT

BACKGROUND AND PURPOSE: Relative cerebral blood volume, as measured by T2*-weighted dynamic susceptibility-weighted contrast-enhanced MRI, represents the most robust and widely used perfusion MR imaging metric in neuro-oncology. Our aim was to determine whether differences in modeling implementation will impact the correction of leakage effects (from blood-brain barrier disruption) and the accuracy of relative CBV calculations as measured on T2*-weighted dynamic susceptibility-weighted contrast-enhanced MR imaging at 3T field strength.

MATERIALS AND METHODS: This study included 52 patients with glioma undergoing DSC MR imaging. Thirty-six patients underwent both non-preload dose– and preload dose–corrected DSC acquisitions, with 16 patients undergoing preload dose–corrected acquisitions only. For each acquisition, we generated 2 sets of relative CBV metrics by using 2 separate, widely published, FDA-approved commercial software packages: IB Neuro and nordicICE. We calculated 4 relative CBV metrics within tumor volumes: mean relative CBV, mode relative CBV, percentage of voxels with relative CBV $>$ 1.75, and percentage of voxels with relative CBV $>$ 1.0 (fractional tumor burden). We determined Pearson (r) and Spearman (ρ) correlations between non-preload dose– and preload dose–corrected metrics. In a subset of patients with recurrent glioblastoma ($n = 25$), we determined receiver operating characteristic area under the curve for fractional tumor burden accuracy to predict the tissue diagnosis of tumor recurrence versus posttreatment effect. We also determined correlations between rCBV and microvessel area from stereotactic biopsies ($n = 29$) in 12 patients.

RESULTS: With IB Neuro, relative CBV metrics correlated highly between non-preload dose– and preload dose–corrected conditions for fractional tumor burden ($r = 0.96$, $\rho = 0.94$), percentage $>$ 1.75 ($r = 0.93$, $\rho = 0.91$), mean ($r = 0.87$, $\rho = 0.86$), and mode ($r = 0.78$, $\rho = 0.76$). These correlations dropped substantially with nordicICE. With fractional tumor burden, IB Neuro was more accurate than nordicICE in diagnosing tumor versus posttreatment effect (area under the curve = 0.85 versus 0.67) ($P < .01$). The highest relative CBV–microvessel area correlations required preload dose and IB Neuro ($r = 0.64$, $\rho = 0.58$, $P = .001$).

CONCLUSIONS: Different implementations of perfusion MR imaging software modeling can impact the accuracy of leakage correction, relative CBV calculation, and correlations with histologic benchmarks.

ABBREVIATIONS: FTB = fractional tumor burden; GBCA = gadolinium-based contrast agents; IBN = IB Neuro; MVA = microvessel area; NICE = nordicICE; PLD = preload dose; pMRI = perfusion MR imaging; rCBV = relative cerebral blood volume

Perfusion MR imaging (pMRI) has emerged as a powerful diagnostic tool in neuro-oncology. Multiple independent studies have shown how measures of microvessel volume, which are linked closely to histologic identity and malignant potential, can facilitate diagnoses that have historically eluded conventional MR imaging.[1-7] For instance, the metric relative cerebral blood volume (rCBV), as measured by dynamic susceptibility-weighted contrast-enhanced pMRI, can identify high-grade components within nonenhancing glioma,[6,7] distinguish tumor recurrence from posttreatment effects (ie, pseudoprogression, radiation ne-

Received March 4, 2015; accepted after revision April 30.

From the Department of Radiology (L.S.H.) and Biostatistics (A.C.D.), Mayo Clinic, Phoenix/Scottsdale, Arizona; the Department of Radiology (Z.K., P.K., T.J.K., B.J.E.), Mayo Clinic, Rochester, Minnesota; the Keller Center for Imaging Innovation (L.S.H., C.E., J.P.K., L.C.B.) and Departments of Neuropathology (J.M.E.), Neuroradiology (J.P.K.), and Neurosurgery (K.S., P.N.), Barrow Neurological Institute, Phoenix, Arizona; the Department of Radiological Sciences (B.M.E.), David Geffen School of Medicine, University of California, Los Angeles, California; and the Department of Radiation Oncology (D.B., D.P.), Mayo Clinic, Rochester, Minnesota.

This work was supported by the National Institutes of Health, NS 082609-01, CA 01-16045, and the Mayo Clinic Foundation.

Please address correspondence to Leland S. Hu, MD, Department of Radiology, Mayo Clinic, 13400 E Shea Blvd, Scottsdale, Arizona 85259; e-mail: Hu.Leland@Mayo.Edu

Indicates open access to non-subscribers at www.ajnr.org

Indicates article with supplemental on-line tables.

http://dx.doi.org/10.3174/ajnr.A4451

crosis),[8-11] and predict tumoral response and patient survival after targeted therapy.[12-16]

Despite the potential clinical impact of pMRI, broad-scale integration has been slowed by the need to define optimal methodologic conditions to maximize rCBV accuracy. While a number of factors can affect rCBV measurements (eg, image acquisition, motion correction, signal fitting, and mathematic modeling), most methodologic studies have focused on techniques that correct for T1-weighted leakage errors from blood-brain barrier disruption and T2/T2*-weighted residual errors from contrast recirculation within tortuous microvasculature.[17-24] Specifically, DSC relies on the assumptions that gadolinium-based contrast agents (GBCA) transit through tissue as a single bolus and remain within the vascular lumen. Yet, these premises are often violated in the setting of high-grade glioma, increasing the likelihood of rCBV inaccuracies.

On the basis of previous comparison studies, the administration of GBCA preload dose (PLD) and the subsequent use of software modeling (during image postprocessing) offer the most effective methods for rCBV correction.[17-19] PLD, given before DSC acquisition, minimizes T1 leakage effects by presaturating tissue T1 signal and decreasing subsequent GBCA extravascular diffusion.[17-22,25,26] Because of theoretic dose-dependent risks of nephrogenic systemic fibrosis, the GBCA dose is generally minimized, with most studies showing effective T1 leakage-correction with a PLD as low as 0.05–0.1 mmol/kg.[19] Additionally, modeling correction has proved necessary to correct residual T1 errors and T2/T2*-weighted recirculation effects following PLD. While a number of modeling algorithms have been proposed, the method published by Boxerman et al[17] remains the most highly cited and validated algorithm to date, and it is widely considered the standard for DSC-pMRI.

Generally speaking, modeling correction requires implementation of mathematic algorithms through computer software programs developed either in-house by individual academic centers or incorporated within vendor-supplied commercial packages. Vendor-supplied options offer the advantage of wide availability and ease of standardization across multiple institutions, but the methods by which the algorithms are implemented can vary by vendor. While we generally assume negligible differences in how various software programs incorporate mathematic modeling to calculate rCBV, this assumption has not been directly tested, particularly with validation against standard benchmarks such as histology.

In this study, we compared 2 commonly published, commercially available implementations of the Boxerman algorithm,[17] as integrated within the IB Neuro (IBN, Version 1.1; Imaging Biometrics, Elm Grove, Wisconsin) and nordicICE (NICE, Version 2.3.13; NordicNeuroLab, Bergen, Norway) software packages.[8,9,14-18,20,25-28] We present data from a cohort of 52 patients with glioma who underwent DSC-pMRI acquisition at the time of clinical MR imaging. The goals of this study are to determine the equivalency of modeling implementation and rCBV calculation across platforms and to assess whether rCBV variations, if present, will significantly impact correlations with histologic benchmarks. Our overarching goal is to provide information that will help work toward consensus and standardization of pMRI methodology.

MATERIALS AND METHODS

Subjects

We searched our data base (2007–2013) for patients with histopathologically confirmed glioma who had conventional 3T MR imaging with pMRI at 2 different institutions. We included patients in whom the same examination contained 2 separate DSC-pMRI acquisitions (and separate bolus contrast injections) and/or the MR imaging was performed preoperatively for stereotactic resection and/or biopsy within 1 day after imaging. Subjects were pooled from 2 separate institutions: Barrow Neurological Institute at St. Joseph's Hospital and Medical Center and Mayo Clinic, Arizona. All patient data were anonymized for Health Insurance Portability and Accountability Act compliance. The institutional review board approved our study. All patients undergoing pMRI had estimated glomerular filtration rates of >60 mg/min/1.72 m^2.

Perfusion MR Imaging Data Acquisition

Each 3T examination was performed on 1 of 2 MR imaging magnets (Signa HDx; GE Healthcare, Milwaukee, Wisconsin; or Magnetom Skyra; Siemens, Erlangen, Germany). All patients underwent initial preload dose administration that allowed the acquisition of PLD-corrected DSC-pMRI data, which were all acquired via a second GBCA injection (0.05-mmol/kg, gadodiamide or gadobenate dimeglumine) by using previously described methods.[8,19] In all patients, the PLD amount totaled 0.1 mmol/kg, administered via either a single bolus injection or 2 separate (0.05-mmol/kg) bolus injections, depending on the departmental protocol at the time of imaging. In a subset of patients, we acquired non-PLD-corrected DSC-pMRI data during the initial PLD bolus injection, by using either 0.05- or 0.1-mmol/kg GBCA injections, depending on the clinical perfusion MR imaging protocol used at the time of acquisition. We performed a separate subanalysis to determine the impact of different injection doses as shown in On-line Table 1.

All DSC data (gradient-echo echo-planar imaging with TR/TE/flip angle = 1500–2000/20 ms/60°, FOV = 24 × 24 cm, matrix = 128 × 128, 5-mm section, no gap) were acquired during 3 minutes with the bolus injection occurring at the 1-minute mark after the start of the DSC sequence. All GBCA injections were via power injector at 3–5 mL/s, followed by a 20-mL normal saline flush. The final GBCA dose for all patients (irrespective of the method of PLD administration) was 0.15 mmol/kg of body weight.

Perfusion MR Imaging Data Analysis

After transferring all MR imaging data to an off-line workstation and removing baseline points collected during the first 5 seconds, we generated whole-brain rCBV maps by using 2 commonly published commercial software packages: nordicICE (Version 2.3.13) and IB Neuro (Version 1.1), both approved by the US Food and Drug Administration. For NICE, we used all available default options and included leakage correction in all cases. Default options consisted of automatic prebolus baseline selection to define the

prebolus baseline and integration intervals and subsequent noise threshold adjustment to maximize brain tissue used for CBV calculation. We did not use spatial or temporal smoothing for either software package, to help maintain data integrity and limit potential confounding factors. We performed rCBV calculations with γ variate fitting before leakage correction or without γ variate fitting. For IBN, we used all default options including leakage correction: 1) automated detection of brain tissue mask for voxels used in CBV calculation, 2) automated detection of contrast arrival within brain mask voxels to define the prebolus baseline and integration intervals, and 3) leakage correction based on Boxerman et al.[17] For rCBV generated with either NICE or IBN, we coregistered the rCBV maps with stereotactic anatomic images by using registration methods implemented in the Insight Segmentation and Registration Toolkit (www.itk.org) within the IB Suite (Version 1.0.454; Imaging Biometrics), as previously described.[17,18,29,30]

We normalized all rCBV maps to mean CBV from two 3×3 voxel-sized square ROIs within the contralateral frontal and parietal normal-appearing white matter.[8,19] To reduce variability, we used identical normal-appearing white matter ROIs for both software package analyses to generate all rCBV metrics. We calculated multiple previously published rCBV metrics including the following: 1) volume fraction of tumor voxels above the rCBV threshold of 1.75 (percentage >1.75); 2) volume fraction of tumor voxels above the rCBV threshold of 1.0, also known as perfusion MR imaging fractional tumor burden (FTB); 3) histogram mean rCBV; and 4) histogram mode rCBV for all tumor voxels. We chose the thresholds of 1.0 and 1.75 because of previous studies reporting the biologic significance of these values.[6,8,30] On the basis of the rCBV maps generated from NICE and IBN packages, we calculated volume fraction metrics by using the IB Suite and histogram metrics by using custom code written in Matlab (Version R2012a; MathWorks, Natick, Massachusetts). To reduce variability, we also used identical segmented enhancing tumor volumes for both software analyses and all rCBV metrics (as described below).

Conventional MR Imaging Acquisition and Analysis

For each examination, we acquired routine conventional contrast-enhanced MR imaging that included pre- and postcontrast T1-weighted spoiled gradient-echo (inversion recovery prepped) stereotactic (ie, volumetric) MR imaging datasets (TI/TR/TE = 300/6.8/2.8 ms, matrix = 320×224, FOV = 26 cm, section thickness = 2 mm). Tumor volumes were defined as abnormal enhancing tissue by an experienced neuroradiologist (L.S.H.). In nonenhancing glioma, we defined tumor volumes by using T2-weighted stereotactic MR imaging (TR/TE = 4500/82 ms, matrix = 256×256, FOV = 26 cm, section thickness = 2 mm).

Stereotactic Biopsy, Image Coregistration, and Histologic Microvessel Analysis

Our cohort included a subset of patients in whom neurosurgeons collected an average of 2–3 tissue specimens from each tumor by using stereotactic surgical localization, following the smallest possible diameter craniotomies to minimize brain shift. Biopsies were performed without knowledge of rCBV analyses. Similar to those in previous studies, biopsy locations and neuronavigational coordinates were recorded and coregistered with MR imaging to enable localized rCBV measurement (3×3 voxel-sized ROIs) at corresponding biopsy sites.[11,31] Multiple biopsy targets in the same patient were separated by a minimum of 2 cm. The neurosurgeon visually validated stereotactic imaging locations with corresponding intracranial anatomic landmarks, such as vascular structures. Stereotactic biopsy samples were sectioned (10-μm thickness), CD-34 stained, and submitted for quantification of total microvessel area (MVA) by using previously published methods.[31-34] Corresponding sections were also stained with hematoxylin-eosin per standard protocol. For each CD-34-stained slide, we measured total microvessel area as previously described.[31,32,35] Raw data from 7 of these patients were studied previously.[31] The current study differs in the following ways: 1) We used commercial software packages and modeling correction to measure rCBV, 2) we determined test performance differences between packages, and 3) we compared PLD against non-PLD conditions.

Quantification of Histologic Tumor Fraction in Recurrent Glioblastoma Multiforme

Our cohort included a subset of 25 patients with recurrent glioblastoma multiforme, previously treated with the protocol of Stupp et al.[36] We enrolled each of these patients at the time of recurrence, at which time they underwent preoperative MR imaging (including pMRI) for surgical debulking of newly developed or enlarging lesions suspicious for recurrence identified on surveillance contrast-enhanced MR imaging.

Following debulking, we fixed all surgical tissue specimens in 10% formalin, embedded them in paraffin, sectioned them (10 μm), and stained them with hematoxylin-eosin per standard diagnostic protocol at our institution. Two neuropathologists quantified glioblastoma multiforme and/or posttreatment effect elements for all specimens without knowledge of DSC-MR imaging, by simultaneously estimating histologic fractional volume of tumor relative to nonneoplastic treatment-related features, as previously described.[8,30,37,38] Features of tumor recurrence[38] and posttreatment effect[37,39] were quantified and used to determine the histologic tumor fraction from surgical resection material to diagnose either tumor progression (histologic tumor fraction of $\geq$50%) or posttreatment effect (histologic tumor fraction of <50%) on the basis of group median values. Raw data from these 25 patients have been studied previously.[8] Like the prior study, the current study measures FTB but with several important differences in experimental design: 1) We used and compared 2 separate modeling algorithm implementations to calculate FTB, 2) we assessed performance differences between methods by comparing test accuracies (with receiver operating characteristic analysis), and 3) we use a simplified classification system to establish the clinical presence/absence of tumor progression.

Statistical Analysis

A biostatistician performed all analyses. We first determined Pearson and Spearman correlations between non-PLD- and PLD-corrected conditions for all rCBV metrics as calculated by IBN and NICE. Second, we used receiver operating characteristic anal-

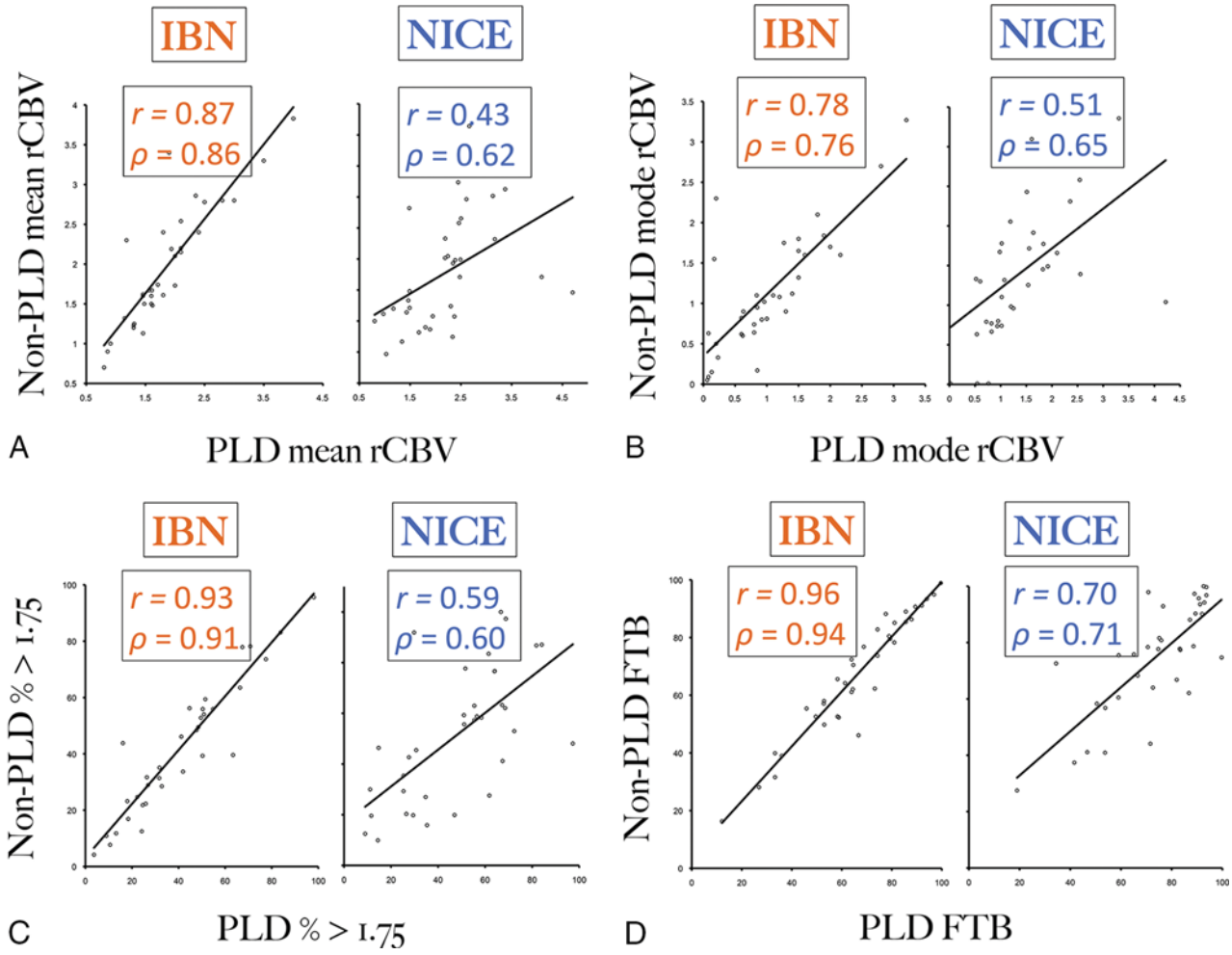

FIG 1. *A–D*, Scatterplots correlating rCBV metrics with and without preload dosing (PLD), as measured by 2 separate modeling algorithms (IBN, NICE without γ variate fitting). PLD- and non-PLD corrected values are shown in the x- and y-axes, respectively. Overall, IBN measurements demonstrate consistently higher Pearson (*r*) and Spearman (*ρ*) correlations for mean rCBV, mode rCBV, fractional tumor burden (FTB), and percentage of voxels > 1.75. The thresholding metrics (FTB, percentage > 1.75) correlate most strongly between PLD- and non-PLD-corrected conditions.

ysis to determine the accuracy of FTB (as measured by IBN and NICE) to diagnose tumor versus posttreatment effect. Finally, we determined Pearson and Spearman correlations between localized rCBV and MVA from corresponding stereotactic biopsies. $P < .05$ was statistically significant.

RESULTS

Subjects and Tumor Types

We enrolled 52 patients (17 women, 35 men; mean age, 53 years), of whom 87% (45/52) had high-grade gliomas with 78% (35/45) presenting at recurrence after standard multimodal therapy. On-line Table 2 summarizes the tumor types for primary and recurrent cases.

Comparing rCBV Measurements in the Presence and Absence of Preload Dose

Comparing rCBV between PLD and non-PLD conditions gives an indication of how well modeling implementation corrects T1 leakage errors. We acquired both PLD- and non-PLD-corrected rCBV values in a subset of patients ($n = 36$) for whom we calculated 4 separate rCBV metrics (mean, mode, percentage >1.75, and FTB) by using both IB Neuro and nordicICE software packages. When we used IBN (Fig 1), rCBV thresholding metrics correlated very highly between non-PLD- and PLD-corrected conditions (FTB: $r = 0.96$, $\rho = 0.94$; percentage > 1.75: $r = 0.93$, $\rho = 0.91$); correlations were also high for mean rCBV ($r = 0.87$, $\rho = 0.86$) and mode rCBV ($r = 0.78$, $\rho = 0.76$). With NICE modeling, these correlations dropped substantially (Fig 1) for thresholding metrics (FTB: $r = 0.70$, $\rho = 0.71$; percentage > 1.75: $r = 0.59$, $\rho = 0.60$), mean rCBV ($r = 0.43$, $\rho = 0.62$), and mode rCBV ($r = 0.51$, $\rho = 0.65$). When we added γ variate fitting, correlations for mean rCBV by using NICE decreased though the other metrics remained largely unchanged (Table 1). On visual inspection of thresholding maps, non-PLD and PLD-corrected voxels showed greater spatial correspondence when using IBN compared with NICE (Fig 2). Table 1 summarizes correlations for all conditions. Of these 36 patients, 10 received PLD via 2 separate half-dose injections. To assess the potential effects of heterogeneity in PLD administration, we performed a subanalysis ($n = 26$) excluding these 10 subjects, which showed correlations consistent with the original analysis (On-line Table 1).

Table 1: Pearson (r) and Spearman (ρ) correlations between rCBV metrics under PLD-corrected and non-PLD-corrected conditions, as measured by IBN and NICE perfusion software algorithms[a]

rCBV Metric	Non-PLD vs PLD (IBN)	*P* Value	Non-PLD vs PLD (NICE) with gvf	*P* Value	Non-PLD vs PLD (NICE) without gvf	*P* Value
Mean	$r = 0.87$	<.001	$r = 0.11$	.54	$r = 0.43$	.01
	$\rho = 0.86$	<.001	$\rho = 0.42$	.02	$\rho = 0.62$	<.001
Mode	$r = 0.78$	<.001	$r = 0.44$	.01	$r = 0.51$	.01
	$\rho = 0.76$	<.001	$\rho = 0.65$	<.001	$\rho = 0.65$	<.001
% < 1.75	$r = 0.93$	<.001	$r = 0.55$	<.001	$r = 0.59$	<.001
	$\rho = 0.91$	<.001	$\rho = 0.61$	<.001	$\rho = 0.60$	<.001
FTB	$r = 0.96$	<.001	$r = 0.79$	<.001	r = 0.70	<.001
	$\rho = 0.94$	<.001	$\rho = 0.72$	<.001	$\rho = 0.71$	<.001

Note:—gvf indicates γ variate fitting.

[a] NICE calculations were performed with and without gvf. IBN modeling shows substantially higher correlation between PLD and non-PLD metrics (compared with NICE), suggesting higher rCBV accuracy in the absence of PLD correction. Statistical significance is *P* value < .05.

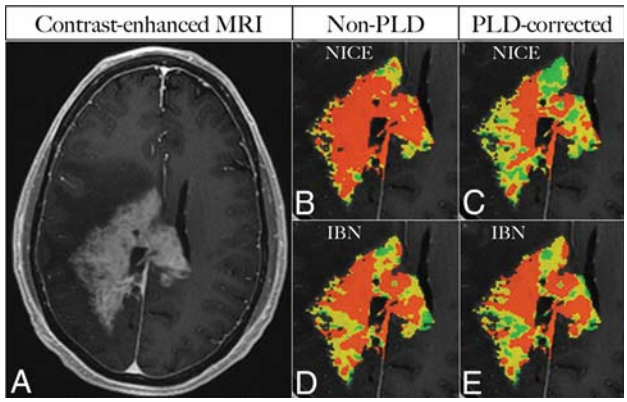

FIG 2. Image of a representative case in a 39-year-old patient with recurrent high-grade ganglioglioma shows an enhancing mass (*A*). Color overlay percentage > 1.75 thresholding maps (*B–E*) depict orange voxels with high rCBV > 1.75, compared with intermediate yellow voxels (rCBV, 1.0–1.75) and low green voxels (rCBV < 1.0). With NICE, both spatial distribution and percentage of orange voxels show high discrepancy between non-PLD- (70%, *B*) and PLD-corrected (35%, *C*) maps. With IBN, the percentage of orange voxels on the non-PLD map (54%, *D*) approximates that on the PLD-corrected map (51%, *E*) with high spatial congruence.

The Type of Modeling Implementation Impacts the Accuracy of rCBV to Diagnose Tumor versus Pseudoprogression/Radiation Necrosis

In a subset of patients with recurrent glioblastoma multiforme ($n = 25$) undergoing surgical debulking for suspected tumor recurrence, we used receiver operating characteristic analysis to determine the accuracy of FTB, as measured by IBN or NICE, to diagnosed tumor versus posttreatment effect (ie, pseudoprogression, radiation necrosis). We used histologic tumor fraction from surgical resection to categorize each subject's diagnosis as either tumor recurrence (histologic tumor fraction of ≥50%) or posttreatment effect (histologic tumor fraction of <50%). We used PLD correction for all cases. The area under the curve for FTB, as measured by IBN (0.85), was significantly higher than that by NICE (0.67; $P < .01$) (Fig 3).

Influence of PLD and Modeling Correction on the Correlation of rCBV with Stereotactic Microvessel Area Quantification

We measured localized rCBV values corresponding to coregistered stereotactic biopsy samples ($n = 29$) in a subset of patients ($n = 12$). We determined Spearman and Pearson correlations between matched rCBV and histologic microvessel area measurements under multiple conditions, which varied by method of modeling correction or the presence/absence of PLD correction (Table 2). Both PLD correction and IBN modeling were needed to maximize rCBV correlations with MVA ($r = 0.64$, $\rho = 0.58$, $P = .001$).

DISCUSSION

Relative CBV represents the most robust and widely used perfusion MR imaging metric in neuro-oncology.[1-31,40-46] Of the techniques that measure rCBV, DSC is the most commonly used method because of wide availability, straightforward postprocessing, and easy-to-use software programs.[40,41] DSC uses the indicator dilution theory based on susceptibility (T2-/T2*-weighted signal drop) from first-pass transit of a single GBCA bolus injection. DSC assumes an intact BBB with no extravascular GBCA leakage or recirculation and thus requires correction methods when these factors occur (discussed below). Dynamic contrast-enhancement MRI and arterial spin-labeling offer alternative approaches to DSC for calculation of rCBV. The theory and limitations of these techniques have been described previously.[23,24,40-42]

Correctly performing DSC requires several technical considerations based on comparison data from prior studies validating optimal conditions for best practice. First, DSC-pMRI generally necessitates both PLD and mathematic modeling to achieve the highest degree of T1 leakage correction and rCBV accuracy.[17-19] Results from our study support this requirement (Table 2). Regarding PLD amount, most groups use a single dose (0.1 mmol/kg) of GBCA,[8,9,14-20,22,25,26,42] particularly at 1.5T, though adequate PLD correction could be achieved with a GBCA dose as low as 0.05 mmol/kg at 3T.[19] Second, gradient-echo T2*-weighted DSC represents the most preferred and widely published method for DSC. While spin-echo T2-weighted DSC offers a higher signal-to-noise ratio and fewer susceptibility artifacts,[45] double or triple GBCA injection doses (0.2–0.3 mmol/kg) are typically needed during the acquisition of spin-echo DSC,[2,7,30] to overcome the lower contrast-to-noise ratio (ie, signal drop in response to the GBCA first-pass bolus). Compared with spin-echo, gradient-echo DSC offers advantages such as the following: 1) superior contrast-to-noise ratio (ie, greater signal drop during GBCA first-pass), which allows lower contrast dosage during DSC acquisition (0.05–0.1 mmol/kg) and improves the quality of rCBV data, minimizing the need for signal denoising; 2) greater sensitivity to microvessels of all sizes (including larger tortuous glomeruloid-type vessels commonly observed in high-grade gliomas); and 3) the ability to use flip angles of <90° to minimize T1 leakage effects.[11,19,31,42,44,45] Finally, in regard to mathematic modeling, the algorithm published by Boxerman et al[17] remains the most highly cited and validated method to date and has been implemented commercially for widespread use.

The study results here underscore the importance of how soft-

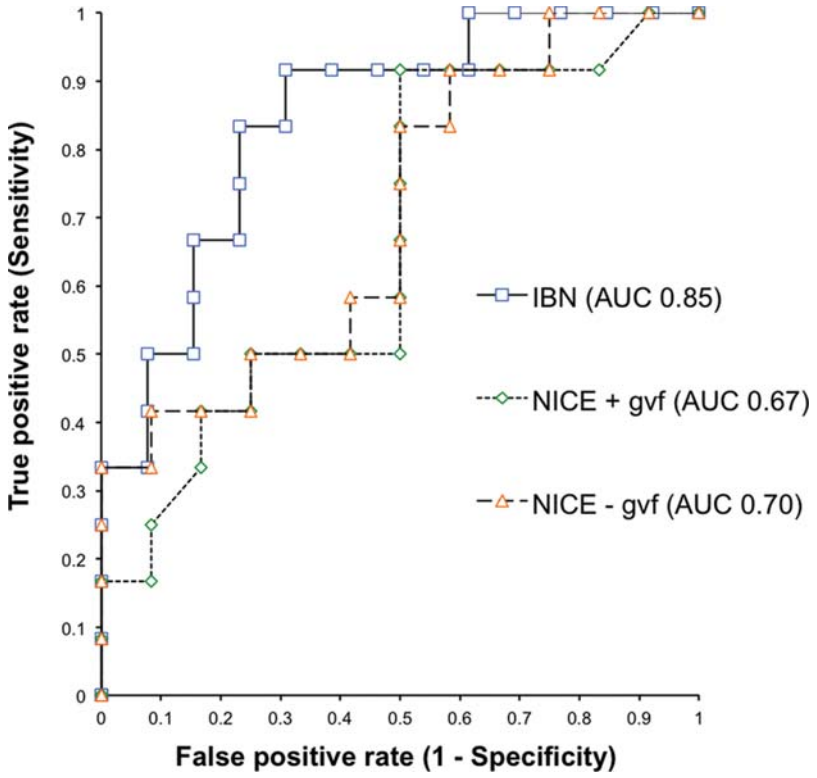

FIG 3. Receiver operating characteristic curves for fractional tumor burden to predict histopathology (tumor versus posttreatment effect) in patients with recurrent glioblastoma multiforme ($n = 25$). FTB by IB Neuro (blue) demonstrates a significantly larger area under the curve (AUC) compared with nordicICE (without γ variate fitting, orange) FTB measurements (0.85 versus 0.70, $P < .01$), suggesting that different modeling algorithms can impact the accuracy in predicting histopathologic diagnosis. Adding γ variate fitting further reduces NICE estimates of FTB (0.67, green).

Table 2: Correlations between rCBV and fractional MVA under different PLD and modeling conditions[a]

Conditions for rCBV Measurement	Pearson Correlation (*r*)	*P* Value	Spearman Correlation (ρ)	*P* Value
Fractional MVA	1.00	–	1.00	–
No PLD (IBN)	0.46	.02	0.33	.12
No PLD (NICE + gvf)	0.51	.01	0.26	.19
No PLD (NICE − gvf)	0.35	.10	0.18	.39
PLD (IBN)	0.64	<.001	0.58	.001
PLD (NICE + gvf)	0.53	<.01	0.28	.15
PLD (NICE − gvf)	0.59	.001	0.40	.04

Note:—+ indicates with; −, without; –, not applicable; gvf, γ variate fitting.

[a] Both PLD correction and IBN software modeling were needed to achieve maximal correlation.

ware programs implement a particular modeling algorithm for rCBV calculation. In this study, we tested 2 widely published FDA-approved commercial packages that offer separate implementations of the Boxerman method,[8,9,14-21,24,26-28] and we evaluated how the modeling implementation by each software program would impact T1 leakage correction and rCBV correlation with histologic measures. We minimized potential confounding factors by using identical segmented tumor volumes and regions in normalized white matter to evaluate each implementation method, and we used default settings and leakage correction for both software packages. For NICE, these included automated selection of the prebolus baseline and subsequent noise thresholding to maximize brain tissue for calculation of CBV. The rCBV metrics on IBN (compared with NICE) demonstrated greater consistency between PLD and non-PLD conditions, most notably with mean rCBV (IBN: $r = 0.87$; NICE: $r = 0.43$) and percentage > 1.75 (IBN: $r = 0.93$; NICE: $r = 0.59$). This suggests that the modeling correction by IBN provides more effective correction of T1 errors, which are most prominent at non-PLD conditions.

While we observed strong correlations between non-PLD and PLD measures (when using IBN), further studies are likely needed to determine the following: 1) whether PLD can or should be omitted, 2) what the optimal conditions would be to allow PLD omission (ie, modeling implementation, 3T field strength), and 3) whether this omission would significantly impact prognostic and diagnostic accuracy. Under PLD conditions, separate experiments confirmed significantly higher FTB accuracy with IBN (area under the curve = 0.84), compared with NICE (area under the curve = 0.67, $p < 0.01$), in diagnosing histopathologically confirmed tumor versus posttreatment effect (ie, pseudoprogression, radiation necrosis). IBN also provided the highest degree of correlation between localized rCBV and tissue microvessel area (Table 2).

In this study, we chose to validate rCBV measurements against histopathology rather than outcomes. Imaging measurements such as rCBV are most directly related to histologic correlates such as microvessel volume and histologic identity (eg, tumor grade, tumor versus posttreatment effect). How these histologic features (and their imaging correlates) predict survival may be confounded by a number of different factors such as age, molecular markers (isocitrate dehydrogenase), methylation status (eg, O6-methylguanine-DNA methyltransferase), extent of resection, salvage therapy at the time of recurrence, and so forth.[6-16,47,48] While clinical outcomes are desirable as end points, they must be correlated with imaging and histologic features together in a controlled trial with a larger patient cohort, which is beyond the scope of this article. Our purpose in this study was simply to determine which method of rCBV measurement (ie, which software package) came closest to informing of underlying tissue features. We think that this context justifies the rationale for validating rCBV against histopathologic benchmarks.

We recognize potential study limitations. First, we limited the scope of the evaluation to 2 specific software packages, though many commercial options exist. We simplified the project to maximize the potential clinical impact because we evaluated the most published and validated modeling algorithm to date (Box-

erman et al[17]) and the 2 most commonly published commercial platforms that implement that algorithm. Future studies may incorporate other vendor packages in a more comprehensive fashion. In fact, the study results here may motivate the development of a framework by which to standardize or evaluate modeling implementation for all vendors. Second, we did not evaluate the factors underlying the differences in modeling implementation because the software code was not made available to us for analysis or modification. Regardless, this comparison study simulates what would be available to end users within the clinical environment and demonstrates that differences between programs can significantly impact rCBV accuracy. Future efforts to develop or use open-source software may help elucidate some of the differences among commercial packages. Third, nonuniformity in PLD administration (single-dose bolus versus 2 separate half-dose injections) may theoretically degrade correlations between non-PLD- and PLD-corrected rCBV. However, strong correlations within the full cohort and subanalysis (On-line Table 1) suggest negligible impact. Fourth, while we used 2 different MR imaging scanners (Signa HDx; Magnetom Skyra), all MR imaging–histologic correlations came from 1 scanner (Signa HDx). Moreover, both scanners used identical field strengths (3T) and DSC parameters (ie, pulse sequence, injection rates, and so forth). These factors, along with strong correlations in a subanalysis (On-line Table 3), suggest a negligible impact on study results. Fifth, the observed strength of rCBV-MVA correlations in this study (at best $r = 0.64$) may be underestimated because Pathak et al[46] have shown that correlations between rCBV and histologic vascular fraction can be further improved when accounting for histologic section thickness as a potential confound. Sixth, there was variability in the TR (1.5 versus 2.0 seconds) of the DSC acquisitions for some patients, depending on the clinical protocol used at the time of imaging. While we do not anticipate this having a significant effect on correlations, we recognize it as a potential limitation. Finally, nonuniformity of the GBCA type (gadodiamide or gadobenate dimeglumine) resulted from protocol changes during the study. Subanalysis (On-line Table 4) based on GBCA type suggested negligible effects.

CONCLUSIONS

Different implementations of perfusion MR imaging software modeling can impact the accuracy of leakage correction, rCBV calculation, and correlations with histologic benchmarks. Future decisions about pMRI standardization should incorporate comparison data that have validated rCBV measurements against clinical benchmarks such as histopathology.

Disclosures: Leland S. Hu, Zachary Kelm, Leslie C. Baxter—*RELATED*: *Grant*: National Institutes of Health.* Timothy J. Kaufmann—*UNRELATED*: *Consultancy*: SpineThera, *Comments*: startup company hoping to create a sustained-release epidural corticosteroid preparation. Peter Nakaji—*UNRELATED*: *Board Membership*: Foundation for International Education for Neurological Surgery, Barrow Neurological Institute co-management*; *Consultancy*: Zeiss, Aesculap, AlloSource; *Grants/Grants Pending*: Barrow Neurological Foundation*; *Payment for Lectures (including service on Speakers Bureaus)*: Zeiss; *Patents (planned, pending or issued)*: AlloSource, GammaTile, Incubeon; *Stock/Stock Options*: Microfabrica. Bradley J. Erickson, P. Korfiatis—*RELATED*: *Grant*: National Cancer Institute (1U01CA160045).* *Money paid to the institution.

REFERENCES

1. Fink JR, Carr RB, Matsusue E, et al. **Comparison of 3 Tesla proton MR spectroscopy, MR perfusion and MR diffusion for distinguishing glioma recurrence from posttreatment effects.** *J Magn Reson Imaging* 2012;35:56–63 CrossRef Medline
2. Lev MH, Ozsunar Y, Henson JW, et al. **Glial tumor grading and outcome prediction using dynamic spin-echo MR susceptibility mapping compared with conventional contrast-enhanced MR: confounding effect of elevated rCBV of oligodendrogliomas [corrected].** *AJNR Am J Neuroradiol* 2004;25:214–21; Erratum in: *AJNR Am J Neuroradiol* 2004;25:B1
3. Knopp EA, Cha S, Johnson G, et al. **Glial neoplasms: dynamic contrast-enhanced T2*-weighted MR imaging.** *Radiology* 1999;211:791–98 CrossRef Medline
4. Cha S, Lupo JM, Chen MH, et al. **Differentiation of glioblastoma multiforme and single brain metastasis by peak height and percentage of signal intensity recovery derived from dynamic susceptibility-weighted contrast-enhanced perfusion MR imaging.** *AJNR Am J Neuroradiol* 2007;28:1078–84 CrossRef Medline
5. Law M, Yang S, Wang H, et al. **Glioma grading: sensitivity, specificity, and predictive values of perfusion MR imaging and proton MR spectroscopic imaging compared with conventional MR imaging.** *AJNR Am J Neuroradiol* 2003;24:1989–98 Medline
6. Law M, Young RJ, Babb JS, et al. **Gliomas: predicting time to progression or survival with cerebral blood volume measurements at dynamic susceptibility-weighted contrast-enhanced perfusion MR imaging.** *Radiology* 2008;247:490–98 CrossRef Medline
7. Maia AC Jr, Malheiros SM, da Rocha AJ, et al. **Stereotactic biopsy guidance in adults with supratentorial nonenhancing gliomas: role of perfusion-weighted magnetic resonance imaging.** *J Neurosurg* 2004;101:970–76 CrossRef Medline
8. Hu LS, Eschbacher JM, Heiserman JE, et al. **Reevaluating the imaging definition of tumor progression: perfusion MRI quantifies recurrent glioblastoma tumor fraction, pseudoprogression, and radiation necrosis to predict survival.** *Neuro Oncol* 2012;14:919–30 CrossRef Medline
9. Gahramanov S, Muldoon LL, Varallyay CG, et al. **Pseudoprogression of glioblastoma after chemo- and radiation therapy: diagnosis by using dynamic susceptibility-weighted contrast-enhanced perfusion MR imaging with ferumoxytol versus gadoteridol and correlation with survival.** *Radiology* 2013;266:842–52 CrossRef Medline
10. Barajas RF Jr, Chang JS, Segal MR, et al. **Differentiation of recurrent glioblastoma multiforme from radiation necrosis after external beam radiation therapy with dynamic susceptibility-weighted contrast-enhanced perfusion MR imaging.** *Radiology* 2009;253:486–96 CrossRef Medline
11. Hu LS, Baxter LC, Smith KA, et al. **Relative cerebral blood volume values to differentiate high-grade glioma recurrence from posttreatment radiation effect: direct correlation between image-guided tissue histopathology and localized dynamic susceptibility-weighted contrast-enhanced perfusion MR imaging measurements.** *AJNR Am J Neuroradiol* 2009;30:552–58 CrossRef Medline
12. Sawlani RN, Raizer J, Horowitz SW, et al. **Glioblastoma: a method for predicting response to antiangiogenic chemotherapy by using MR perfusion imaging—pilot study.** *Radiology* 2010;255:622–28 CrossRef Medline
13. Galbán CJ, Chenevert TL, Meyer CR, et al. **Prospective analysis of parametric response map-derived MRI biomarkers: identification of early and distinct glioma response patterns not predicted by standard radiographic assessment.** *Clin Cancer Res* 2011;17:4751–60 CrossRef Medline
14. LaViolette PS, Cohen AD, Prah MA, et al. **Vascular change measured with independent component analysis of dynamic susceptibility contrast MRI predicts bevacizumab response in high-grade glioma.** *Neuro Oncol* 2013;15:442–50 CrossRef Medline
15. Schmainda KM, Prah M, Connelly J, et al. **Dynamic-susceptibility contrast agent MRI measures of relative cerebral blood volume pre-**

dict response to bevacizumab in recurrent high-grade glioma. *Neuro Oncol* 2014;16:880–88 CrossRef Medline
16. Schmainda KM, Zhang Z, Prah M, et al. **Dynamic susceptibility contrast MRI measures of relative cerebral blood volume as a prognostic marker for overall survival in recurrent glioblastoma: results from the ACRIN 6677/RTOG 0625 multicenter trial.** *Neuro Oncol* 2015;17:1148–56. CrossRef Medline
17. Boxerman JL, Schmainda KM, Weisskoff RM. **Relative cerebral blood volume maps corrected for contrast agent extravasation significantly correlate with glioma tumor grade, whereas uncorrected maps do not.** *AJNR Am J Neuroradiol* 2006;27:859–67 Medline
18. Paulson ES, Schmainda KM. **Comparison of dynamic susceptibility-weighted contrast-enhanced MR methods: recommendations for measuring relative cerebral blood volume in brain tumors.** *Radiology* 2008;249:601–13 CrossRef Medline
19. Hu LS, Baxter LC, Pinnaduwage DS, et al. **Optimized preload leakage-correction methods to improve the diagnostic accuracy of dynamic susceptibility-weighted contrast-enhanced perfusion MR imaging in posttreatment gliomas.** *AJNR Am J Neuroradiol* 2010;31:40–48 CrossRef Medline
20. Emblem KE, Bjornerud A, Mouridsen K, et al. **T(1)- and T(2)(*)-dominant extravasation correction in DSC-MRI, Part II: predicting patient outcome after a single dose of cediranib in recurrent glioblastoma patients.** *J Cereb Blood Flow Metab* 2011;31:2054–64 CrossRef Medline
21. Liu HL, Wu YY, Yang WS, et al. **Is Weisskoff model valid for the correction of contrast agent extravasation with combined T1 and T2* effects in dynamic susceptibility contrast MRI?** *Med Phys* 2011;38:802–09 CrossRef Medline
22. Quarles CC, Gochberg DF, Gore JC, et al. **A theoretical framework to model DSC-MRI data acquired in the presence of contrast agent extravasation.** *Phys Med Biol* 2009;54:5749–66 CrossRef Medline
23. Law M, Young R, Babb J, et al. **Comparing perfusion metrics obtained from a single compartment versus pharmacokinetic modeling methods using dynamic susceptibility contrast-enhanced perfusion MR imaging with glioma grade.** *AJNR Am J Neuroradiol* 2006;27:1975–82 Medline
24. Johnson G, Wetzel SG, Cha S, et al. **Measuring blood volume and vascular transfer constant from dynamic, T(2)*-weighted contrast-enhanced MRI.** *Magn Reson Med* 2004;51:961–68 CrossRef Medline
25. Batchelor TT, Sorensen AG, di Tomaso E, et al. **AZD2171, a pan-VEGF receptor tyrosine kinase inhibitor, normalizes tumor vasculature and alleviates edema in glioblastoma patients.** *Cancer Cell* 2007;11:83–95 CrossRef Medline
26. Sorensen AG, Emblem KE, Polaskova P, et al. **Increased survival of glioblastoma patients who respond to antiangiogenic therapy with elevated blood perfusion.** *Cancer Res* 2012;72:402–07 CrossRef Medline
27. Roder C, Bender B, Ritz R, et al. **Intraoperative visualization of residual tumor: the role of perfusion-weighted imaging in a high-field intraoperative magnetic resonance scanner.** *Neurosurgery* 2013;72(2 suppl operative):ons151–58; discussion ons158 Medline
28. Jain R, Poisson L, Narang J, et al. **Genomic mapping and survival prediction in glioblastoma: molecular subclassification strengthened by hemodynamic imaging biomarkers.** *Radiology* 2013;267:212–20 CrossRef Medline
29. Emblem KE, Scheie D, Due-Tonnessen P, et al. **Histogram analysis of MR imaging-derived cerebral blood volume maps: combined glioma grading and identification of low-grade oligodendroglial subtypes.** *AJNR Am J Neuroradiol* 2008;29:1664–70 CrossRef Medline
30. Gasparetto EL, Pawlak MA, Patel SH, et al. **Posttreatment recurrence of malignant brain neoplasm: accuracy of relative cerebral blood volume fraction in discriminating low from high malignant histologic volume fraction.** *Radiology* 2009;250:887–96 CrossRef Medline
31. Hu LS, Eschbacher JM, Dueck AC, et al. **Correlations between perfusion MR imaging cerebral blood volume, microvessel quantification, and clinical outcome using stereotactic analysis in recurrent high-grade glioma.** *AJNR Am J Neuroradiol* 2012;33:69–76 CrossRef Medline
32. Sharma S, Sharma MC, Sarkar C. **Morphology of angiogenesis in human cancer: a conceptual overview, histoprognostic perspective and significance of neoangiogenesis.** *Histopathology* 2005;46:481–89 CrossRef Medline
33. Leon SP, Folkerth RD, Black PM. **Microvessel density is a prognostic indicator for patients with astroglial brain tumors.** *Cancer* 1996;77:362–72 Medline
34. Folkerth RD. **Histologic measures of angiogenesis in human primary brain tumors.** *Cancer Treat Res* 2004;117:79–95 CrossRef Medline
35. Wesseling P, van der Laak JA, de Leeuw H, et al. **Quantitative immunohistological analysis of the microvasculature in untreated human glioblastoma multiforme: computer-assisted image analysis of whole-tumor sections.** *J Neurosurg* 1994;81:902–09 CrossRef Medline
36. Stupp R, Mason WP, van den Bent MJ, et al; European Organisation for Research and Treatment of Cancer Brain Tumor and Radiotherapy Groups, National Cancer Institute of Canada Clinical Trials Group. **Radiotherapy plus concomitant and adjuvant temozolomide for glioblastoma.** *N Engl J Med* 2005;352:987–96 CrossRef Medline
37. Burger PC, Mahley MS Jr, Dudka L, Vogel FS. **The morphologic effects of radiation administered therapeutically for intracranial gliomas: a postmortem study of 25 cases.** *Cancer* 1979;44:1256–72 Medline
38. Forsyth PA, Kelly PJ, Cascino TL, et al. **Radiation necrosis or glioma recurrence: is computer-assisted stereotactic biopsy useful?** *J Neurosurg* 1995;82:436–44 CrossRef Medline
39. Louis DN. *WHO Classification of Tumors of the Central Nervous System*. 4th ed. Lyon, France: International Agency for Research on Cancer, World Health Organization; 2007
40. Essig M, Shiroishi MS, Nguyen TB, et al. **Perfusion MRI: the five most frequently asked technical questions.** *AJR Am J Roentgenol* 2013;200:24–34 CrossRef Medline
41. Falk A, Fahlström M, Rostrup E, et al. **Discrimination between glioma grades II and III in suspected low-grade gliomas using dynamic contrast-enhanced and dynamic susceptibility contrast perfusion MR imaging: a histogram analysis approach.** *Neuroradiology* 2014;56:1031–38 CrossRef Medline
42. Kassner A, Annesley DJ, Zhu XP, et al. **Abnormalities of the contrast re-circulation phase in cerebral tumors demonstrated using dynamic susceptibility contrast-enhanced imaging: a possible marker of vascular tortuosity.** *J Magn Reson Imaging* 2000;11:103–13 CrossRef Medline
43. Young GS, Setayesh K. **Spin-echo echo-planar perfusion MR imaging in the differential diagnosis of solitary enhancing brain lesions: distinguishing solitary metastases from primary glioma.** *AJNR Am J Neuroradiol* 2009;30:575–77 CrossRef Medline
44. Sugahara T, Korogi Y, Kochi M, et al. **Perfusion-sensitive MR imaging of gliomas: comparison between gradient-echo and spin-echo echo-planar imaging techniques.** *AJNR Am J Neuroradiol* 2001;22:1306–15 Medline
45. Schmainda KM, Rand SD, Joseph AM, et al. **Characterization of a first-pass gradient-echo spin-echo method to predict brain tumor grade and angiogenesis.** *AJNR Am J Neuroradiol* 2004;25:1524–32 Medline
46. Pathak AP, Schmainda KM, Ward BD, et al. **MR-derived cerebral blood volume maps: issues regarding histological validation and assessment of tumor angiogenesis.** *Magn Reson Med* 2001;46:735–47 CrossRef Medline
47. Thuy MN, Kam JK, Lee GC, et al. **A novel literature-based approach to identify genetic and molecular predictors of survival in glioblastoma multiforme: analysis of 14,678 patients using systematic review and meta-analytical tools.** *J Clin Neurosci* 2015;22:785–99 CrossRef Medline
48. Sanai N, Polley MY, McDermott MW, et al. **An extent of resection threshold for newly diagnosed glioblastomas.** *J Neurosurg* 2011;115:3–8 CrossRef Medline

Diagnostic Accuracy of PET, SPECT, and Arterial Spin-Labeling in Differentiating Tumor Recurrence from Necrosis in Cerebral Metastasis after Stereotactic Radiosurgery

G. Lai, A. Mahadevan, D. Hackney, P.C. Warnke, F. Nigim, E. Kasper, E.T. Wong, B.S. Carter, and C.C. Chen

ABSTRACT

BACKGROUND AND PURPOSE: Radiographic assessment of cerebral metastasis after stereotactic radiosurgery remains a major challenge in neuro-oncology. It is often difficult to distinguish tumor progression from radiation necrosis in this setting using conventional MR imaging. The objective of this study was to compare the diagnostic sensitivity and specificity of different functional imaging modalities for detecting tumor recurrence after stereotactic radiosurgery.

MATERIALS AND METHODS: We retrospectively reviewed patients treated between 2007 and 2010 and identified 14 patients with cerebral metastasis who had clinical or radiographic progression following stereotactic radiosurgery and were imaged with arterial spin-labeling, FDG-PET, and thallium SPECT before stereotactic biopsy. Diagnostic accuracy, specificity, sensitivity, positive predictive value, and negative predictive value were calculated for each imaging technique by using the pathologic diagnosis as the criterion standard.

RESULTS: Six patients (42%) had tumor progression, while 8 (58%) developed radiation necrosis. FDG-PET and arterial spin-labeling were equally sensitive in detecting tumor progression (83%). However, the specificity of arterial spin-labeling was superior to that of the other modalities (100%, 75%, and 50%, respectively). A combination of modalities did not augment the sensitivity, specificity, positive predictive value, or negative predictive value of arterial spin-labeling.

CONCLUSIONS: In our series, arterial spin-labeling positivity was closely associated with the pathologic diagnosis of tumor progression after stereotactic radiosurgery. Validation of this finding in a large series is warranted.

ABBREVIATIONS: ASL = arterial spin-labeling; CE = contrast-enhanced; NPV = negative predictive value; PPV = positive predictive value; RN = radiation necrosis; SRS = stereotactic radiosurgery; SUV = standard uptake value; TP = tumor progression

Stereotactic radiosurgery (SRS) has emerged as an important treatment technique for patients with cerebral metastasis. A major challenge in the clinical management of these patients involves determination of tumor response to treatment.[1] Radiographically, SRS can induce reactive changes in the irradiated volume and edema in the surrounding cerebrum. These changes lead to breakdown of the blood-brain barrier, resulting in contrast enhancement on conventional MR imaging.[2-4] This phenomenon, termed "radiation necrosis" (RN), is often difficult to distinguish from tumor progression (TP) by using standard contrast-enhanced MR imaging (CE-MR imaging). Patients with RN are treated with steroids, anticoagulants, hyperbaric oxygen, or antiangiogenic therapy, while patients with TP require either surgical intervention or chemotherapy.[5,6] Thus, the ability to distinguish RN from TP fundamentally drives clinical decision-making and patient care.

Currently, patients with radiographically ambiguous lesions undergo surgical biopsy or resection.[5] While these procedures are generally safe, morbidity ranges from 1% to 9%.[7-9] Most often, the morbidities involve transient neurologic deficits, but rare devastating neurologic consequences and death have also been reported.[7-9] In this context, there is a critical need for noninvasive modalities that would allow reliable discrimination of RN from TP.

Advances in physiologic imaging hold promise as alternate modalities to aid in the discrimination of RN from TP. Rather than relying on contrast extravasation, such imaging is based on the principle of measuring differences in physiologic states between proliferative tumor tissue and normal cerebrum. To the extent that RN and TP exhibit distinct metabolic states, physio-

Received February 21, 2015; accepted after revision May 3.

From the School of Medicine (G.L., B.S.C., C.C.C.), University of California, San Diego, La Jolla, California; Departments of Radiation Oncology (A.M.) and Radiology (D.H.), Division of Neurosurgery (F.N., E.K.), and Department of Neurology (E.T.W.), Beth Israel Deaconess Medical Center, Harvard Medical School, Boston, Massachusetts; and Division of Neurosurgery (P.C.W.), University of Chicago, Chicago, Illinois.

Please address correspondence to Clark C. Chen, MD, PhD, Division of Neurosurgery, University of California, San Diego, 3855 Health Science Dr, No. 0987, La Jolla, CA 92093-0987; e-mail: clarkchen@ucsd.edu

Indicates article with supplemental on-line table.

http://dx.doi.org/10.3174/ajnr.A4475

Table 1: Demographic information, clinical course, location of tumor, radiation dose, time between SRS and follow-up imaging, biopsy results, and imaging results of each patient[a]

Pt	Age (yr)	Clinical Course	Location	SRS Dose	SRS to Imaging	Bx	PET	SPECT	MR ASL
1	69	RCC, s/p SRS and stent, new CE	Left paraventricular	22 Gy × 1	11 Mo	RN	Negative	Positive	Negative
2	63	NSCLC, s/p SRS, new CE	Right frontal	19 Gy × 1	12 Mo	TP	SUV 20	Positive	Positive
3	79	NSCLC, s/p SRS, neurologic deterioration	Right frontal	22 Gy × 1	8 Mo	RN	SUV 4.9	Negative	Negative
4	64	Esophageal cancer, s/p SRS, new CE	Left frontal	21 Gy × 1	4 Mo	TP	Negative	Positive	Positive
5	72	SCLC, 3 lesions s/p WBRT + SRS	Left parietal	22 Gy × 1	7 Mo	TP	SUV 10.3	Positive	Positive
6	46	Breast cancer, s/p SRS, new CE	Right cerebellar	22 Gy × 1	4 Mo	TP	SUV 6.6	Negative	Positive
7	65	Melanoma, s/p SRS, neurologic decline	Right temporal	18 Gy × 1	10 Mo	RN	SUV 7.2	Positive	Negative
8	63	RCC, s/p SRS, new CE	Right thalamus	16 Gy × 1	6 Mo	RN	Negative	Negative	Negative
9	58	Melanoma, s/p IR, enlarged CE	Right frontal	19 Gy × 1	4 Mo	TP	SUV 10.7	Negative	Negative
10	52	NSCLC, s/p SRS, new CE	Right cerebellar	18 Gy × 1	3 Mo	RN	Negative	Positive	Negative
11	59	Melanoma, s/p SRS	Left frontal	22 Gy × 1	3 Mo	TP	SUV 8	Negative	Positive
12	52	Breast cancer, s/p SRS	Right temporal	8 Gy × 3	11 Mo	RN	Negative	Negative	Negative
13	56	RCC, s/p SRS	Left temporal	21 Gy × 1	12 Mo	RN	Negative	Negative	Negative
14	49	Melanoma, s/p SRS	Right frontal	21 Gy × 1	8 Mo	RN	Negative	Negative	Negative

Note:—RCC indicates renal cell carcinoma; Bx, biopsy; s/p, status-pos; IR, ionizing radiation; NSCLC, non-small cell lung cancer; SCLC, small cell lung cancer; WBRT, whole brain radiation therapy.

[a] Patients 1, 6, and 9 are those featured in the illustrative cases. Cells next to patients 1, 3, 7, 8, 10, and 12–14 represent RN on biopsy; other cells represent TN.

logic imaging may better distinguish these phenomena than structural imaging.

The objective of the current study was to compare the diagnostic utility of FDG-PET, thallium SPECT, and arterial spin-labeling (ASL)-MR imaging in the setting of brain metastasis with progression on CE-MR imaging after SRS treatment. We retrospectively identified patients with a definitive pathologic diagnosis who underwent FDG-PET, thallium SPECT, and ASL before stereotactic biopsy. Most important, biopsies were targeted to regions of positive signals in these modalities. Sensitivity, specificity, positive predictive value, and negative predictive values were calculated.

MATERIALS AND METHODS

Patients

This research was approved by the Beth Israel Deaconess Medical Center, Harvard Medical School Institutional Review Board (IRB 2010-P-000134). The cohort of 267 consecutively biopsied patients from 2007 to 2011 was previously described.[10] The inclusion criteria for this study were the following patients: 1) those who underwent stereotactic radiosurgery; 2) had radiographic progression on conventional CE-MR imaging accompanied by clinical deterioration; 3) underwent FDG-PET, thallium SPECT, and ASL-MR imaging before biopsy; and 4) had a definitive tissue diagnosis after biopsy. Patients underwent physiologic imaging studies and biopsy after review of a brain tumor board consisting of 3 neurosurgeons, 2 radiation oncologists, 2 neuro-oncologists, a neuroradiologist, and a neuropathologist. Patient characteristics are summarized in Table 1.

Image Acquisition and Interpretation

All images were reviewed by a board-certified neuroradiologist as a part of standard patient care. Radiologists interpreting functional results were not precluded from comparing any one study with studies acquired previously. MR images were acquired on a Signa HDx 3T scanner (GE Healthcare, Milwaukee, Wisconsin) with standard T2-weighted, FLAIR, and T1 sequences. Contrast-enhanced images were obtained after intravenous administration of Gd-DTPA (Magnevist; Bayer HealthCare Pharmaceuticals, Wayne, New Jersey). FDG-PET images were obtained on a 4-MDCT PET/CT scanner (GE Healthcare). One hour after IV injection of 20 mCi of FDG, noncontrast CT images were obtained for attenuation correction and fusion with emission PET images. A series of overlapping PET images was then obtained. CT images were coregistered and fused with emission PET images.[11] The maximum standard uptake value (SUV) within an ROI drawn around the lesion was calculated. SUV maximum values of >3.0 were defined as a positive signal. SPECT scanning was performed after IV injection of 3 mCi of thallium 201 as previously described.[12]

For ASL, imaging was achieved with pseudocontinuous labeling[13] and an interleaved stack of variable-attenuation, spiral, fast spin-echo sequence. Eight spiral interleaves were performed to achieve an in-plane resolution of 3.7 mm, and forty 4-mm axial sections were acquired. A postlabeling delay of 1.5 seconds and a labeling duration of 1.5 seconds were chosen.[14] Background suppression was performed with selective and nonselective inversion pulses applied at optimized times.[15,16] Three averages of label and control images were performed and then automatically subtracted. An additional reference image with a single saturation applied 2 seconds before imaging was also acquired to enable flow quantification. Quantification of blood flow was performed by using previously published methods.[17]

For ASL, positivity was determined by the neuroradiologist (D.H.) by visual inspection according to routine clinical practice. There have been no clinically used defined thresholds for quantitative measurements of blood flow to differentiate tumor and nontumor tissue, and calculated thresholds by using the same dataset would necessarily bias toward maximum accuracy.

Image-Guided Stereotactic Biopsy

The target location for biopsy was determined by the neurosurgeons (C.C.C., P.C.W., E.K.) and was performed as previously described.[10] The Riechert frame was used in all biopsies. Biopsies were performed by using standard Nashold needles with a 10-mm side-cutting window (Integra LifeSciences, Plainsboro, NJ). To determine biopsy trajectories, we fused CE-MR imaging, PET, SPECT, and ASL by using Inomed software (Stereoplan Plus, Freiburg, Germany). Using these

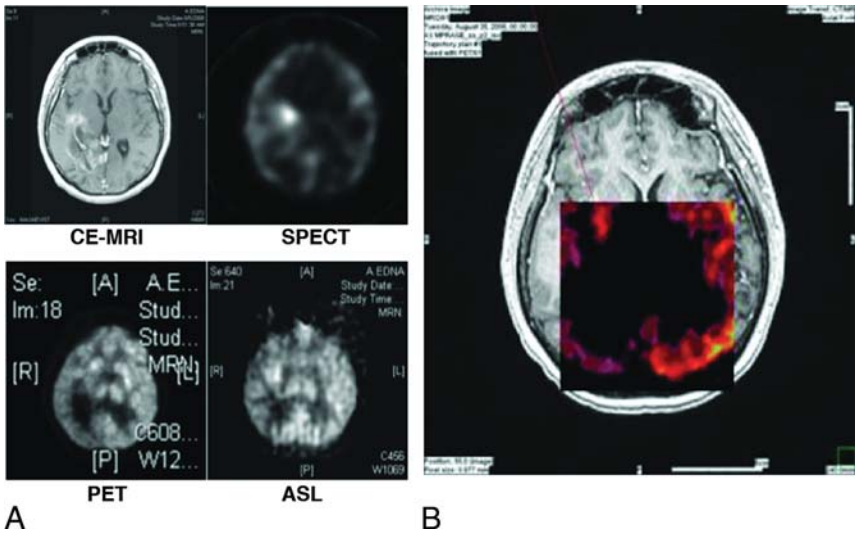

FIG 1. Individual images (*A*) CE MR imaging, thallium SPECT, FDG-PET, and ASL-MR imaging, and fused images (*B*) overlaid on CE-MR imaging. *Red line* represents the biopsy trajectory.

Table 2: Accuracy, sensitivity, specificity, PPV, and NPV for each imaging modality

	CE-MRI	PET	SPECT	MR ASL
Accuracy	46.2%	78.6%	57.1%	92.9%
Sensitivity	–	83.3%	50.0%	83.3%
Specificity	–	75.0%	62.5%	100.0%
PPV	–	71.4%	50.0%	100.0%
NPV	–	85.7%	62.5%	88.9%

Note:— – indicates unable to calculate; CE-MRI were all positive for tumor progression.

Table 3: Accuracy, sensitivity, specificity, PPV, and NPV[a]

	PET or ASL +	PET or SPECT +	SPECT or ASL +	Any One +
Accuracy	85.7%	71.4%	71.4%	71.4%
Sensitivity	100.0%	100.0%	66.7%	100.0%
Specificity	75.0%	50.0%	62.5%	50.0%
PPV	75.0%	60.0%	57.1%	60.0%
NPV	100.0%	100.0%	71.4%	100.0%

[a] Positive = 1 modality positive.

reconstructions, we selected biopsy trajectories to afford sampling of CE-MR imaging, PET, SPECT, and ASL regions positive for tumor progression. To maximize the volume of tumor sampled, we planned a linear trajectory to allow serial sampling through the largest diameter of the tumor based on the imaging technique with the largest signal. In all cases, the region of biopsy was positive in at least 1 of the imaging modalities. While positivity differed among modalities within a single region, in no cases did 2 different modalities define distinct regions as scoring positive. For instance, there were no cases in which 1 region of the tumor scored positive for ASL while another scored positive for PET.

Pathology results were reviewed by a board-certified neuropathologist as a part of standard patient care. In accordance with the standard clinical practice, patients were classified as having tumor progression if the neuropathologist identified any histologic evidence of viable tumor. Patients were classified as having radiation necrosis only when no evidence of viable tumor was found by the neuropathologist. Results were reviewed with the neuropathologist at the tumor conference to confirm that the diagnosis stated in the formal pathology report was accurate.

Statistical Analysis

Sensitivity, specificity, positive predictive value (PPV), and negative predictive value (NPV) were calculated for each imaging technique (CE-MR imaging, FDG-PET, thallium SPECT, and ASL) as they related to the pathology findings. Accuracy for each technique was calculated as (true positives + true negatives)/(all positives + all negatives). Values were also calculated for combinations of 2 or all 3 modalities. More stringent criteria were defined as positive tumor recurrence if all modalities were positive for TP. Less stringent criteria for positivity were defined if at least 1 technique was positive for TP.

RESULTS

Of 267 patients stereotactically biopsied between 2007 and 2011, 14 underwent CE-MR imaging, FDG-PET, thallium SPECT, and ASL before surgical biopsy for definitive tissue diagnosis. The demographics of the study population are shown in Table 1. The patient ages ranged from 46 to 79 years. There were 9 male and 5 female patients. The patients had cerebral metastases from a spectrum of primary sites, including 4 lung cancers, 2 breast cancers, 3 renal cell carcinomas, 4 melanomas, and 1 esophageal cancer. On the basis of the final pathology, 6 patients (42%) had tumor progression, while 8 (58%) developed radiation necrosis. A representative coregistration of the 4 imaging modalities and the definition of the stereotactic target are shown in Fig 1.

Accuracy for tumor recurrence in metastatic cancer was highest by using ASL (87%), followed by FDG-PET (73%) and SPECT (53%), and lowest for CE-MR imaging (50%). Sensitivity was highest for ASL and PET (71%) and lowest for SPECT (43%). ASL had a specificity of 100%, while PET and SPECT were 75% and 63%, respectively. ASL also had the highest PPV (100%) and NPV (89%), whereas SPECT had the lowest (PPV, 50%; NPV, 63%). For FDG-PET, PPV was 71% and NPV was 86%. Results are summarized in Table 2. Although not used in the current analysis, quantitative values for ASL analyses are included in the On-line Table for reference.

For both positive and negative results, ASL and PET measures were in agreement 74% of the time; ASL and SPECT, 64%; and PET and SPECT, 50%. Agreement among all 3 modalities was 43%. When ASL-PET, PET-SPECT, and all 3 were in agreement, the accuracy was 100% in all cases. Accuracy was 93% when ASL and SPECT were in agreement.

A combination of different modalities did not result in higher accuracy than ASL alone when positivity was defined as a positive result in any 1 of a combination of 2 or all 3 modalities (Table 3). Sensitivity and NPV were both 100% when at one of modality (PET, ASL, or SPECT) was positive. However, specificity and PPV were lower than those for ASL alone at 75% and 50% for specificity and 75% and 66.7% for PPV, respectively. SPECT or ASL yielded lower predictive values for all

measures relative to ASL alone. The combination of all 3 modalities also had high sensitivity and NPV (100%) but low specificity and PPV (50% and 60%).

If positivity was defined more stringently as a positive result in both modalities, specificity increased to 100% for all combinations, which did not differ from findings in ASL alone. However, sensitivities were low. When both ASL and PET-positive, sensitivity = 67%; when both ASL and SPECT were positive, sensitivity = 50%; and when both SPECT and PET were positive, sensitivity = 50%; and when all 3 were positive, sensitivity = 33%. PPV was 100% for all combinations, but NPVs were all ≤80%. The accuracy of any of the combinations was never higher than that of ASL alone. See Table 4 for a summary.

Illustrative Cases

Case 1: Radiation Necrosis. A 69-year-old man had a solitary renal cell carcinoma metastasis to the periventricular white matter of the posterior left lateral horn. Progression on CE-MR imaging was noted 13 months following radiosurgery (18 Gy in a single fraction, Fig 2*A*). Physiologic imaging findings were only positive on SPECT. Biopsy revealed radiation necrosis.

Case 2: Tumor Recurrence. A 46-year-old woman had metastatic breast cancer metastasis to the right cerebellum. Progression on CE-MR imaging was noted 9 months following radiosurgery (5 Gy ×5 fractions, Fig 2*B*). Physiologic imaging showed positive signals on ASL and PET (SUV = 6.6). Thallium SPECT findings were negative. Biopsy revealed tumor recurrence.

Case 3: Tumor Recurrence. A 58-year-old man had a solitary melanoma metastasis to the right inferior frontal cortex. Progression on CE-MR imaging was noted 22 months after SRS (18 Gy in a single fraction, Fig 2*C*). Physiologic imaging findings were positive on PET only (SUV = 10.7). Biopsy revealed tumor recurrence.

Table 4: Accuracy, sensitivity, specificity, PPV, and NPV[a]

	PET and ASL +	PET and SPECT +	SPECT and ASL +	All +
Accuracy	85.7%	78.6%	78.6%	71.4%
Sensitivity	66.7%	50.0%	66.7%	100.0%
Specificity	100.0%	100.0%	100.0%	100.0%
PPV	100.0%	100.0%	100.0%	100.0%
NPV	80.0%	72.7%	72.7%	66.7%

[a] Positive = all modalities positive.

DISCUSSION

This study compares the diagnostic utility of FDG-PET, thallium SPECT, and ASL in the post-SRS setting by using pathologic diagnoses secured through targeted biopsies as the criterion standard. We analyzed imaging results in 14 patients with cerebral metastases who underwent SRS and were biopsied after clinical or radiographic progression. Only 46% of patients with enlarging contrast enhancement on MR imaging had tumor progression confirmed by histopathology. This finding highlights the inadequacy of conventional MR imaging in this setting. Of the 3 physiologic imaging modalities studied, ASL exhibited the highest level of sensitivity and specificity in terms of discriminating between RN and TP. Combining imaging modalities did not substantially improve the diagnostic utility of ASL (Table 3).

In clinical practice, FDG-PET and thallium SPECT are often used for detection of intracranial lesions. In prior studies, the sensitivity and specificity of FDG-PET for discriminating TP and RN for primary gliomas ranged from 77% to 81% and 63% to 90%, respectively.[18-20] Sensitivity and specificity for brain metastases were 86% and 80%.[18] These results are largely in line with those observed in this study (sensitivity 83%, specificity 75%). However, thallium SPECT results reported in this study (sensitivity 50%, specificity 63%) were markedly lower than those previously reported (specificity and sensitivity values of 82.7%–91% and 82.8%–90% for primary gliomas and metastases[21,22]). In fact, a recent review reported that SPECT was superior to other imaging modalities for differentiating radiation necrosis and TP in primary gliomas.[23]

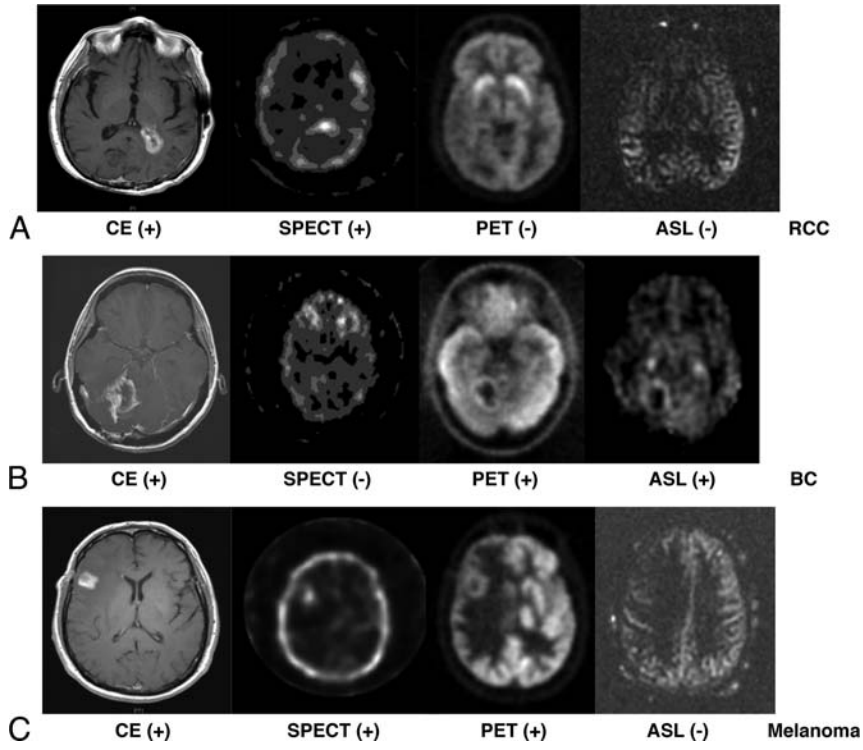

FIG 2. CE-MR imaging, thallium SPECT, FDG-PET, and ASL-MR images from case 1 (*A*) with metastatic renal cell carcinoma to periventricular white matter of the posterior left lateral horn. CE-MR imaging shows new enhancement in the region treated. SPECT was positive while PET and ASL were negative for tumor recurrence. Biopsy of the target region indicated radiation necrosis in case 2 (*B*) with metastatic breast cancer to the right cerebellum. CE-MR imaging shows new enhancement in the region treated. PET (SUV = 6.6) and ASL were positive for tumor recurrence. Biopsy of the target region indicated tumor recurrence in case 3 (*C*) with metastatic melanoma to the right inferior frontal cortex. Only PET was positive for tumor recurrence (SUV = 10.7). Biopsy of the target region indicated tumor recurrence.

However, no studies have directly compared SPECT and ASL in the same patient population, to our knowledge.

Although ASL perfusion is not yet widely used clinically in the setting of neoplasm, perfusion MR imaging such as dynamic susceptibility contrast MR imaging has been of recent interest for the investigation of brain tumors. Like ASL, DSC measures brain perfusion but relies on dynamic measurement of intravenous contrast agents.[23] Because intravenous contrast agents are typically administered in the oncologic population, each additional scan that requires contrast compounds the risk of morbidity. In terms of the diagnostic utility of the 2 MR perfusion modalities, studies directly comparing CBF values in ASL and DSC for tumor,[17,24] ischemic tissue, and normal brain have consistently noted[24] high correlations. For brain metastases, DSC–MR imaging yielded sensitivity and specificity values from 70% to 100% and 95.2% to 100% for differentiation of necrosis and tumor recurrence.[25,26] In differentiating tumor recurrence and radiation necrosis or pseudoprogression of primary gliomas, direct comparison between ASL and DSC–MR imaging showed no statistical significance, with sensitivity and specificity values of 79%–94% and 64%–88%.[20,27] In terms of detection of gliomas and metastases, ASL and DSC–MR imaging also showed similar diagnostic yields.[28,29] However, ASL has the advantages of better signal-to-noise ratio, fewer distortion effects secondary to hemorrhage, and the potential for quantification.[17] More definitive studies comparing the 2 modalities will be needed in the patient population with postradiation metastasis. Furthermore, larger studies using ASL for tumor identification will be necessary to establish generalizable thresholds for interpretation of quantitative ASL values.

Supporting the idea that perfusion imaging would be an ideal technique for differentiation of tumor progression and radiation necrosis is the assumption that tumor has sufficiently more vascularity than fibrous or necrotic tissue. Likewise, FDG-PET positivity depends on glucose uptake. If the metabolism of the tumor does not require glucose uptake, then FDG-PET will be falsely negative. Thallium SPECT positivity is determined by the presence of functional sodium-potassium adenosine triphosphatase. If this transporter is not active in the tumor, thallium SPECT findings will be falsely positive. Reliable detection of tumor postradiation may require different functional modalities, depending on specific characteristics of the tumor. Furthermore, a fundamental question in imaging revolves around the resolution and sensitivity of the imaging technique relative to the strength of signal based on size, attenuation, and intensity of the measure of interest of a tumor.

With regard to the use of image-guided stereotactic biopsy, possible errors of coregistration remain an important consideration. However, our method of registration and biopsy has been shown, by our group and others, to be highly accurate. Nondiagnostic tissue samples occurred at a rate of 4.6%–5%.[10,30]

In the current practice setting, there is a high degree of subjectivity in the management of patients with cerebral metastasis who have radiographic and/or clinical progression after SRS. While our study is limited by the small sample size, it represents a systematic effort to address a clinically important question. Most studies investigating posttreatment imaging use presumptive diagnoses or have only a subset of patients with histology. Another limitation is the heterogeneity of metastatic tumor types represented in this study. Metastases may exhibit varying levels of flow depending on their primary location and individual variability in tumor physiology. For example, melanomas have a short T1, and accumulation of the ASL signal can be attenuated.[31] Furthermore, flow in regions with reduced activity due to radiation or vascular disease may be underestimated by ASL due to delayed arrival of arterial blood. Such underestimation might be addressed by newer ASL techniques that can label for longer and also measure the arterial transit delay.[32,33] However, despite the predicted underestimation of effect size given the heterogeneity of our sample, ASL appeared to provide useful diagnostic information. A larger study comparing perfusion imaging (ASL and DSC) with tissue diagnosis would be of importance to validate the present results and has the potential to fundamentally alter our clinical practice in the surveillance and management of patients with cancer after SRS treatment.

CONCLUSIONS

Our results suggest that ASL offers a noninvasive method in the discrimination of RN from TP in patients with cerebral metastasis who underwent SRS. Results from the present study provide a basis for future prospective studies with larger sample sizes to validate the use of ASL in this setting.

Disclosures: Anand Mahadevan—*UNRELATED*: *Board Membership*: Radiosurgery Society, *Comments*: Nonpaid board member, President; *Royalties*: UptoDate. David Hackney—*UNRELATED*: *Consultancy*: University of California, San Francisco, *Comments*: I am a consultant to the brain tumor group, serving on the External Advisory Board for their brain tumor Specialized Program of Research Excellence and Program Project. Thus, my work is relevant to the broad issue of brain tumor imaging, but it does not influence what I might say about this study. I am paid an honorarium for my participation in the annual Educational Advisory Board meeting in San Francisco Peter C. Warnke—*UNRELATED*: *Consultancy*: Gerson Lehrman Group (consulting firm). Ekkehard Kasper—*UNRELATED*: *Expert Testimony*: McKeen &Associates; Detroit, Michigan, *Comments*: occasional legal expert witness work for this Detroit law firm. Eric T. Wong—*UNRELATED*: *Grants/Grants Pending*: AngioChem,* AstraZeneca,* Cephalon,* Eli Lilly,* Northwest Biotherapeutics,* Novartis,* Novocure,* Pfizer,* Plexxicon.* *Money paid to the institution.

REFERENCES

1. Chernov M, Hayashi M, Izawa M, et al. **Differentiation of the radiation-induced necrosis and tumor recurrence after gamma knife radiosurgery for brain metastases: importance of multi-voxel proton MRS.** *Minim Invasive Neurosurg* 2005;48:228–34 CrossRef Medline
2. Shah R, Vattoth S, Jacob R, et al. **Radiation necrosis in the brain: imaging features and differentiation from tumor recurrence.** *Radiographics* 2012;32:1343–59 CrossRef Medline
3. Stockham AL, Tievsky AL, Koyfman SA, et al. **Conventional MRI does not reliably distinguish radiation necrosis from tumor recurrence after stereotactic radiosurgery.** *J Neurooncol* 2012;109:149–58 CrossRef Medline
4. Dooms GC, Hecht S, Brant-Zawadzki M, et al. **Brain radiation lesions: MR imaging.** *Radiology* 1986;158:149–55 CrossRef Medline
5. Rahmathulla G, Marko NF, Weil RJ. **Cerebral radiation necrosis: a review of the pathobiology, diagnosis and management considerations.** *J Clin Neurosci* 2013;20:485–502 CrossRef Medline
6. Chao ST, Ahluwalia MS, Barnett GH, et al. **Challenges with the diagnosis and treatment of cerebral radiation necrosis.** *Int J Radiat Oncol Biol Phys* 2013;87:449–57 CrossRef Medline
7. Woodworth GF, McGirt MJ, Samdani A, et al. **Frameless image-guided stereotactic brain biopsy procedure: diagnostic yield, surgical morbidity, and comparison with the frame-based technique.** *J Neurosurg* 2006;104:233–37 CrossRef Medline

8. Sawin PD, Hitchon PW, Follett KA, et al. **Computed imaging-assisted stereotactic brain biopsy: a risk analysis of 225 consecutive cases.** *Surg Neurol* 1998;49:640–49 CrossRef Medline
9. McGirt MJ, Woodworth GF, Coon AL, et al. **Independent predictors of morbidity after image-guided stereotactic brain biopsy: a risk assessment of 270 cases.** *J Neurosurg* 2005;102:897–901 CrossRef Medline
10. Waters JD, Gonda DD, Reddy H, et al. **Diagnostic yield of stereotactic needle-biopsies of sub-cubic centimeter intracranial lesions.** *Surg Neurol Int* 2013;4:S176–81 CrossRef Medline
11. Williams G, Kolodny GM. **Method for decreasing uptake of 18F-FDG by hypermetabolic brown adipose tissue on PET.** *AJR Am J Roentgenol* 2008;190:1406–09 CrossRef Medline
12. Hill TC, Holman BL, Lovett R, et al. **Initial experience with SPECT (single-photon computerized tomography) of the brain using N-isopropyl I-123 p-iodoamphetamine: concise communication.** *J Nucl Med* 1982;23:191–95 Medline
13. Dai W, Garcia D, de Bazelaire C, et al. **Continuous flow-driven inversion for arterial spin labeling using pulsed radio frequency and gradient fields.** *Magn Reson Med* 2008;60:1488–97 CrossRef Medline
14. Alsop DC, Detre JA. **Reduced transit-time sensitivity in noninvasive magnetic resonance imaging of human cerebral blood flow.** *J Cereb Blood Flow Metab* 1996;16:1236–49 Medline
15. Ye FQ, Frank JA, Weinberger DR, et al. **Noise reduction in 3D perfusion imaging by attenuating the static signal in arterial spin tagging (ASSIST).** *Magn Reson Med* 2000;44:92–100 CrossRef Medline
16. Maleki N, Dai W, Alsop DC. **Optimization of background suppression for arterial spin labeling perfusion imaging.** *MAGMA* 2012;25:127–33 CrossRef Medline
17. Järnum H, Steffensen EG, Knutsson L, et al. **Perfusion MRI of brain tumours: a comparative study of pseudo-continuous arterial spin labelling and dynamic susceptibility contrast imaging.** *Neuroradiology* 2010;52:307–17 CrossRef Medline
18. Chao ST, Suh JH, Raja S, et al. **The sensitivity and specificity of FDG PET in distinguishing recurrent brain tumor from radionecrosis in patients treated with stereotactic radiosurgery.** *Int J Cancer* 2001;96:191–97 CrossRef Medline
19. Tan H, Chen L, Guan Y, Lin X. **Comparison of MRI, F-18 FDG, and 11C-choline PET/CT for their potentials in differentiating brain tumor recurrence from brain tumor necrosis following radiotherapy.** *Clin Nucl Med* 2011;36:978–81 CrossRef Medline
20. Ozsunar Y, Mullins ME, Kwong K, et al. **Glioma recurrence versus radiation necrosis? A pilot comparison of arterial spin-labeled, dynamic susceptibility contrast enhanced MRI, and FDG-PET imaging.** *Acad Radiol* 2010;17:282–90 CrossRef Medline
21. Serizawa T, Saeki N, Higuchi Y, et al. **Diagnostic value of thallium-201 chloride single-photon emission computerized tomography in differentiating tumor recurrence from radiation injury after gamma knife surgery for metastatic brain tumors.** *J Neurosurg* 2005;102(suppl):266–71 CrossRef Medline
22. Matsunaga S, Shuto T, Takase H, et al. **Semiquantitative analysis using thallium-201 SPECT for differential diagnosis between tumor recurrence and radiation necrosis after gamma knife surgery for malignant brain tumors.** *Int J Radiat Oncol Biol Phys* 2013;85:47–52 CrossRef Medline
23. Shah AH, Snelling B, Bregy A, et al. **Discriminating radiation necrosis from tumor progression in gliomas: a systematic review what is the best imaging modality?** *J Neurooncol* 2013;112:141–52 CrossRef Medline
24. Jiang J, Zhao L, Zhang Y, et al. **Comparative analysis of arterial spin labeling and dynamic susceptibility contrast perfusion imaging for quantitative perfusion measurements of brain tumors.** *Int J Clin Exp Pathol* 2014;7:2790–99 Medline
25. Hoefnagels FW, Lagerwaard FJ, Sanchez E, et al. **Radiological progression of cerebral metastases after radiosurgery: assessment of perfusion MRI for differentiating between necrosis and recurrence.** *J Neurol* 2009;256:878–87 CrossRef Medline
26. Mitsuya K, Nakasu Y, Horiguchi S, et al. **Perfusion weighted magnetic resonance imaging to distinguish the recurrence of metastatic brain tumors from radiation necrosis after stereotactic radiosurgery.** *J Neurooncol* 2010;99:81–88 CrossRef Medline
27. Choi YJ, Kim HS, Jahng GH, et al. **Pseudoprogression in patients with glioblastoma: added value of arterial spin labeling to dynamic susceptibility contrast perfusion MR imaging.** *Acta Radiol* 2013;54:448–54 CrossRef Medline
28. Lehmann P, Monet P, de Marco G, et al. **A comparative study of perfusion measurement in brain tumours at 3 Tesla MR: arterial spin labeling versus dynamic susceptibility contrast-enhanced MRI.** *Eur Neurol* 2010;64:21–26 CrossRef Medline
29. Warmuth C, Gunther M, Zimmer C. **Quantification of blood flow in brain tumors: comparison of arterial spin labeling and dynamic susceptibility-weighted contrast-enhanced MR imaging.** *Radiology* 2003;228:523–32 CrossRef Medline
30. Tilgner J, Herr M, Ostertag C, Volk B. **Validation of intraoperative diagnoses using smear preparations from stereotactic brain biopsies: intraoperative versus final diagnosis—influence of clinical factors.** *Neurosurgery* 2005;56:257–65; discussion 257–65 CrossRef Medline
31. Isiklar I, Leeds NE, Fuller GN, et al. **Intracranial metastatic melanoma: correlation between MR imaging characteristics and melanin content.** *AJR Am J Roentgenol* 1995;165:1503–12 CrossRef Medline
32. Dai W, Shankaranarayanan A, Alsop DC. **Volumetric measurement of perfusion and arterial transit delay using Hadamard encoded continuous arterial spin labeling.** *Magn Reson Med* 2013;69:1014–22 CrossRef Medline
33. Dai W, Robson PM, Shankaranarayanan A, et al. **Reduced resolution transit delay prescan for quantitative continuous arterial spin labeling perfusion imaging.** *Magn Reson Med* 2012;67:1252–65 CrossRef Medline

T1-Weighted Dynamic Contrast-Enhanced MRI as a Noninvasive Biomarker of Epidermal Growth Factor Receptor vIII Status

J. Arevalo-Perez, A.A. Thomas, T. Kaley, J. Lyo, K.K. Peck, A.I. Holodny, I.K. Mellinghoff, W. Shi, Z. Zhang, and R.J. Young

ABSTRACT

BACKGROUND AND PURPOSE: Epidermal growth factor receptor variant III is a common mutation in glioblastoma, found in approximately 25% of tumors. Epidermal growth factor receptor variant III may accelerate angiogenesis in malignant gliomas. We correlated T1-weighted dynamic contrast-enhanced MR imaging perfusion parameters with epidermal growth factor receptor variant III status.

MATERIALS AND METHODS: Eighty-two consecutive patients with glioblastoma and known epidermal growth factor receptor variant III status who had dynamic contrast-enhanced MR imaging before surgery were evaluated. Volumes of interest were drawn around the entire enhancing tumor on contrast T1-weighted images and then were transferred onto coregistered dynamic contrast-enhanced MR imaging perfusion maps. Histogram analysis with normalization was performed to determine the relative mean, 75th percentile, and 90th percentile values for plasma volume and contrast transfer coefficient. A Wilcoxon rank sum test was applied to assess the relationship between baseline perfusion parameters and positive epidermal growth factor receptor variant III status. The receiver operating characteristic method was used to select the cutoffs of the dynamic contrast-enhanced MR imaging perfusion parameters.

RESULTS: Increased relative plasma volume and increased relative contrast transfer coefficient parameters were both significantly associated with positive epidermal growth factor receptor variant III status. For epidermal growth factor receptor variant III–positive tumors, relative plasma volume mean was 9.3 and relative contrast transfer coefficient mean was 6.5; for epidermal growth factor receptor variant III–negative tumors, relative plasma volume mean was 3.6 and relative contrast transfer coefficient mean was 3.7 (relative plasma volume mean, $P < .001$, and relative contrast transfer coefficient mean, $P = .008$). The predictive powers of relative plasma volume histogram metrics outperformed those of the relative contrast transfer coefficient histogram metrics ($P <= .004$).

CONCLUSIONS: Dynamic contrast-enhanced MR imaging shows greater perfusion and leakiness in epidermal growth factor receptor variant III–positive glioblastomas than in epidermal growth factor receptor variant III–negative glioblastomas, consistent with the known effect of epidermal growth factor receptor variant III on angiogenesis. Quantitative evaluation of dynamic contrast-enhanced MR imaging may be useful as a noninvasive tool for correlating epidermal growth factor receptor variant III expression and related tumor neoangiogenesis. This potential may have implications for monitoring response to epidermal growth factor receptor variant III–targeted therapies.

ABBREVIATIONS: DCE = dynamic contrast-enhanced; EGFR = epidermal growth factor receptor; K^{trans} = contrast transfer coefficient; rK^{trans} = relative K^{trans}; ROC = receiver operating characteristic; rVP = relative plasma volume; 75%tile = 75th percentile; 90%tile = 90th percentile; VP = plasma volume

Glioblastoma is the most common and aggressive primary brain tumor. A highly malignant tumor, it is associated with a dismal median survival of only 14 months with standard radiochemotherapy.[1] Glioblastoma is characterized by histologic heterogeneity with areas of active cellular proliferation and mitoses admixed with areas of necrosis. Large-scale genetic sequencing has revealed "driver" mutations in several common pathways that contribute to glioblastoma growth.[2] Among these, overactivation of the epidermal growth factor receptor (EGFR) membrane ty-

Received March 6, 2015; accepted after revision April 30.

From the Departments of Radiology (J.A.-P., J.L., A.I.H., R.J.Y.), Neurology (A.A.T., T.K., I.K.M.), Medical Physics (K.K.P.), and Epidemiology and Biostatistics (W.S., Z.Z.), and the Brain Tumor Center (T.K., J.L., A.I.H., R.J.Y.), Memorial Sloan Kettering Cancer Center, New York, New York.

Drs Julio Arevalo-Perez and Alissa A. Thomas contributed equally to the work as coauthors.

Julio Arevalo-Perez was supported by a grant from the Spanish foundation "Fundación Alfonso Martín Escudero." The research of Weiji Shi and Zhigang Zhang was partly supported by the National Institutes of Health Core Grant P30 CA008748.

Paper previously presented as a scientific poster at: Annual Meeting of the American Society of Neuroradiology and the Foundation of the ASNR Symposium, April 25–30, 2015; Chicago, Illinois.

Please address correspondence to Robert J. Young, MD, Department of Radiology, Memorial Sloan Kettering Cancer Center, 1275 York Ave, NY, New York 10065; e-mail: youngr@mskcc.org

http://dx.doi.org/10.3174/ajnr.A4484

rosine kinase receptor pathway contributes to rapid aberrant cell proliferation and drives tumor growth and development.[3-5] EGFR variant III (EGFRvIII) is the most common EGFR mutation in glioblastoma, occurring in 25%–35% of cases.[6] EGFRvIII is characterized by deletion of exons 2–7 in the extracellular domain, rendering the receptor constitutively active. EGFRvIII status is determined either through exon sequencing or fluorescence in situ hybridization on tumor specimens.

The growing interest in EGFRvIII-specific therapy and other EGFR-targeted treatments for glioblastoma demands a better understanding of the correlation between molecular changes in tumors and neuroimaging features. Prior studies have demonstrated a correlation of T2* dynamic susceptibility contrast MR imaging perfusion with EGFR amplification and EGFRvIII mutations.[5,7] The role of T1-weighted dynamic contrast-enhanced (DCE)–MR imaging in distinguishing molecular subpopulations of glioblastoma, however, has not been well-established, to our knowledge. DCE–MR imaging offers several technical advantages over DSC–MR imaging, including improved characterization of tumor vascularity through quantification of plasma volume (VP) and improved characterization of tumor leakiness through calculation of the contrast transfer coefficient (K^{trans}).[8-10] The purpose of this study was to examine the relationship between T1-weighted DCE–MR imaging perfusion parameters and EGFRvIII status in patients with newly diagnosed glioblastoma. We hypothesized that patients with glioblastomas positive for EGFRvIII would demonstrate increased perfusion and leakiness at DCE–MR imaging compared with patients with EGFRvIII-negative glioblastomas.

MATERIALS AND METHODS

Protocol Approval and Informed Consent

The local institutional review board approved this retrospective study, which was compliant with the Health Insurance Portability and Accountability Act regulations. The requirement to obtain patient informed consent was waived.

Subjects

A hospital data base was queried from March 2011 through March 2014 to identify all patients meeting the following inclusion criteria: 1) pathologically confirmed glioblastoma diagnosis after biopsy or resection, 2) EGFRvIII status obtained from the biopsy or the resection specimen, and 3) baseline DCE–MR imaging perfusion scan with matching postcontrast axial T1-weighted images before surgery. EGFRvIII status was determined by reverse transcriptase polymerase chain reaction amplification of the corresponding exons followed by a single base extension at the site of the mutation. The single base extension product was detected by tandem mass spectrometry on a MassArray Spectrometer (Sequenom, San Diego, California) and reported in a binary manner as either positive or negative.

MR Imaging Protocol

MR imaging sequences were acquired with a 1.5T or 3T MR imaging scanner (Signa Excite, HDx, and Discovery 750; GE Healthcare, Milwaukee, Wisconsin) and a standard 8-channel head coil. Gadopentetate dimeglumine (Magnevist; Bayer HealthCare Pharmaceuticals, Wayne, New Jersey) was power-injected via an intravenous catheter (18–21 ga) at doses standardized by patient body weight (0.2 mL/kg body weight, maximum 20 mL) at 2–3 mL/s. DCE–MR imaging of the brain was acquired as part of a standard clinical protocol with a 3D T1-weighted echo-spoiled gradient-echo sequence (TR, 4–5 ms; TE, 1–2 ms; section thickness, 5 mm; flip angle, 25°; FOV, 24 cm; matrix, 256 × 256; temporal resolution, 5–6 seconds. Ten phases were acquired preinjection followed by another 30 phases during the dynamic injection of intravenous contrast and then a 40-mL saline flush. Matching contrast T1-weighted (TR/TE, 600/8 ms; thickness, 5 mm) spin-echo images were obtained.

Imaging Analysis

DCE perfusion MR imaging raw data and T1-weighted images were transferred to an off-line workstation and processed by using commercially available software (nordicICE; (NordicNeuroLab, Bergen, Norway) by a trained radiologist who was blinded to the EGFRvIII status. Preprocessing steps included noise adjustments and semiautomated selection of the arterial input function. These steps allowed the operator to optimize the signal-to-noise ratio and the arterial input function by selecting an appropriate artery to characterize the input function curve and the concentration-time curve.[11] The arterial input function was calculated individually for every patient. Appropriate curves demonstrating an optimal relationship between the arterial input function and the concentration-time curve were selected. On the basis of the 2-compartment pharmacokinetic model proposed by Tofts et al,[12] the perfusion analysis method was applied to determine pharmacokinetic parameters, and the results were displayed as parametric maps. Volumes of interest were drawn on axial planes on contrast T1-weighted images, excluding intralesional macrovessels, to not contaminate the measurements. VOIs were transferred to coregistered parametric maps to obtain the pharmacokinetic parameters VP and K^{trans}. Parameters were then normalized by using the ratio of tumor to normal white matter by placing ROIs in normal white matter of the contralateral hemisphere in a healthy-appearing area of brain parenchyma. The values were then binned into histograms, and the relative mean VP (rVP_{mean}), 90th percentile VP ($rVP_{90\%tile}$), and 75th percentile ($rVP_{75\%tile}$) ratios were recorded, along with the relative mean K^{trans} ($rK^{trans}{}_{mean}$), 90th percentile K^{trans} ($rK^{trans}{}_{90\%tile}$), and 75th percentile K^{trans} ($rK^{trans}{}_{75\%tile}$) ratios.

Statistical Analysis

Univariate analysis by using the Wilcoxon rank sum test was performed to examine the correlations between the rVP and rK^{trans} histogram parameters and EGFRvIII status. The cutoffs of the DCE–MR imaging perfusion parameters were selected by using the receiver operating characteristic (ROC) method. The areas under the ROC curves of the perfusion parameters were compared by using the Delong test. The statistical analysis was performed with the software SAS, Version 9.2 (SAS Institute, Cary, North Carolina) and R package ROCR and pROC (Version 3.1.2; R statistical computing software; http://www.r-project.org/). The significance level was set to $P = .05$.

RESULTS

Patient Characteristics

Eighty-two consecutive treatment-naïve patients with glioblastoma were included in the study. Twenty-four (29.3%) patients had positive EGFRvIII status, while 58 (70.7%) had negative EGFRvIII status. The median age was 66.7 years (range, 38–87) years; there were 21 women (25.6%) and 61 men (74.4%).

DCE–MR Imaging

As summarized in the Table, increased VP and K^{trans} were associated with positive EGFRvIII status for all histogram metrics. rVP_{mean}, $rVP_{90\%tile}$, and $rVP_{75\%tile}$ were better predictors than $rK^{trans}{}_{mean}$, $rK^{trans}{}_{90\%tile}$, and $rK^{trans}{}_{75\%tile}$, with P values $\leq .004$. A representative case is shown in Fig 1. The areas under the ROC curves for the VP metrics were 0.818–0.833, while those for the K^{trans} metrics were 0.669–0.692. With ROC analysis, a threshold value for $VP_{90\%tile} > 9.50$ yielded a specificity of 89.7% and a sensitivity of 62.5% for predicting positive EGFRvIII status (Fig 2).

Analysis of the relationship between baseline perfusion parameters and EGFRvIII mutation status

Perfusion Parameter[a]	EGFRvIII Status (Median, Range) Negative (n = 58)	Positive (n = 24)	P Value	AUC
rVP_{mean}	3.6 (1.5–18.1)	9.3 (2.9–29.3)	<.001	0.818
$rVP_{90\%tile}$	5.1 (1.6–19.1)	10.7 (4.1–30.2)	<.001	0.833
$rVP_{75\%tile}$	4.2 (1.6–18.4)	9.2 (3.5–28.1)	<.001	0.821
$rK^{trans}{}_{mean}$	3.7 (1.1–20.3)	6.5 (1.7–22.4)	.008	0.688
$rK^{trans}{}_{90\%tile}$	4.8 (1.5–22.6)	7.6 (2.1–31.8)	.02	0.669
$rK^{trans}{}_{75\%tile}$	4.2 (1.4–19.7)	6.8 (1.9–24.7)	.007	0.692

Note:—AUC indicates area under the curve in the ROC analysis.
[a] All values are relative ratios normalized to tumor/contralateral normal tissue.

DISCUSSION

We demonstrated that perfusion and leakiness, as determined by rVP and rK^{trans} histogram parameters, respectively, were greater in EGFRvIII-positive glioblastomas than in EGFRvIII-negative glioblastomas. These results suggest that DCE–MR imaging parameters may be useful imaging biomarkers to follow in patients with EGFRvIII-positive tumors or other tumors with abnormal pretreatment parameters. We postulate that this radiogenomic characterization may be particularly relevant in patients undergoing active targeted, mutation-specific treatment, in which changes in perfusion and leakiness could be used to repetitively and noninvasively evaluate treatment efficacy in lieu of surgery.

Alteration of *EGFR* is among the frequent oncogene muta-

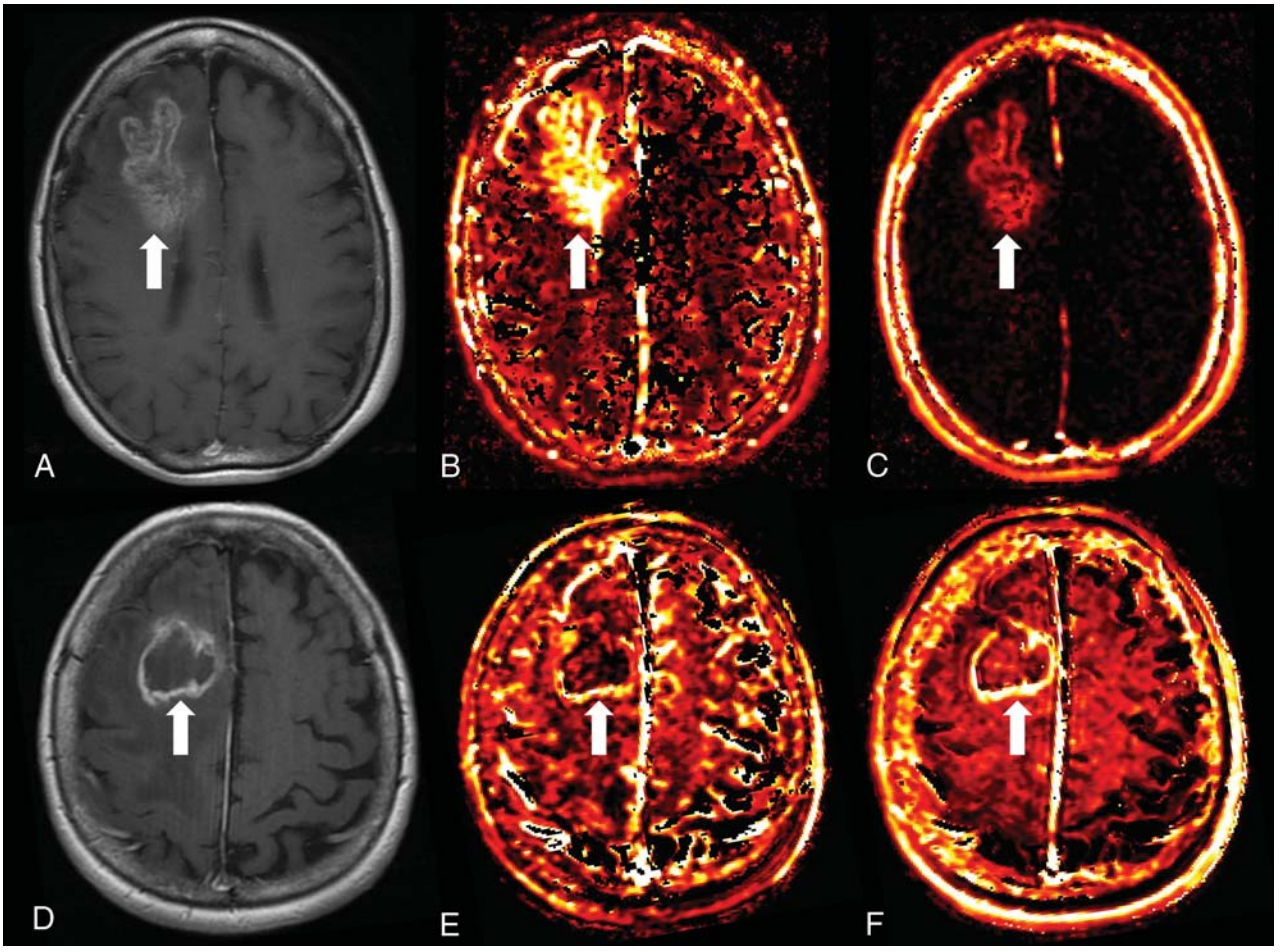

FIG 1. Representative DCE–MR images and parametric maps from a patient with EGFRvIII-positive glioblastoma. Axial contrast T1-weighted (*A*) image demonstrates a large heterogeneously enhancing tumor in the right frontal lobe. Corresponding VP (*B*) and K^{trans} (*C*) maps reveal increased perfusion and increased leakiness, respectively, as indicated by the *arrows*. Matching images in a non-EGFRvIII glioblastoma in the right frontal lobe (*D–F*) show little increase in VP or K^{trans}.

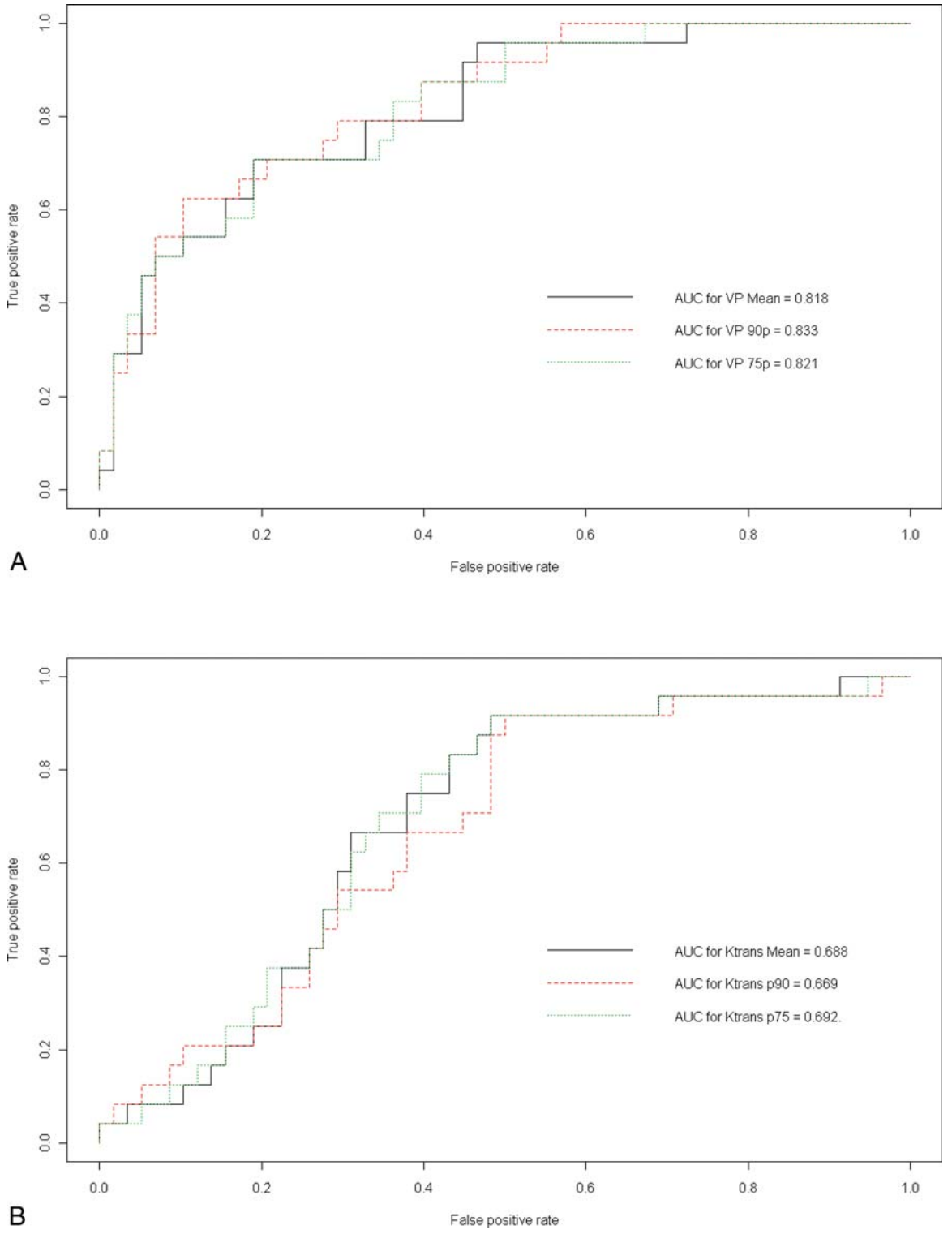

FIG 2. Discrimination power of baseline VP (*A*) and K^{trans} (*B*) perfusion parameters for EGFR status (positive versus negative).

tions in primary glioblastomas.[13-15] In addition to promoting cellular growth and proliferation, EGFRvIII accelerates tumor angiogenesis and induction of proangiogenic factors, including vascular endothelial growth factor, interleukin 18, and angiopoietin-like 4 in the extracellular signal-regulated kinase and *c-Myc* pathways, to confer a more heterogeneous and aggressive phenotype.[16-19] These increases in angiogenic activity in patients with EGFRvIII may manifest at DCE–MR imaging as increased VP, which is a measure of the tumor blood plasma volume per unit volume of tissue, and as increased K^{trans}, the volume transfer constant between the blood plasma and the extravascular extracellular space.

Due to its unique protein sequence and tumor-specific expression, EGFRvIII is an attractive target for drug therapy. Several

small molecular tyrosine kinase inhibitors with affinity for the *EGFR* receptor are available on the market and under development in clinical trials.[20] A glioblastoma vaccine based on a unique EGFRvIII peptide sequence is currently under investigation in a phase III clinical trial.[21] Effective implementation of these novel targeted therapies will require parallel development of targeted imaging technologies such as DCE–MR imaging, also specific for particular mutations.

Perfusion on MR imaging has been shown to correlate with glioma grade, prognosis, and response to treatment.[22-26] Perfusion parameters may be useful as imaging markers of vascular attenuation and angiogenesis in gliomas.[2,27] Increased relative tumor blood volume shown by DSC perfusion MR imaging has been associated with EGFR amplification and EGFRvIII mutation.[5,7] The T2* technique may render DSC–MR imaging inadequate, however, in areas with leakage of contrast through an abnormal blood-brain barrier or in areas with strong susceptibility artifacts due to blood, vessel, bone, and air interfaces such as those near the skull base.[10-28] DCE–MR imaging offers several potential advantages,[8] the most important of which is the more accurate quantification of perfusion and leakiness through greater spatial resolution, steady-state imaging, and advanced compartmental modeling.[8-10] We also advocate the use of histogram analysis after whole-tumor VOI evaluation, which should yield measurements that are more objective and reproducible and less user-dependent than those obtained with the usual ROI-based methods.[7-29]

There are a few potential limitations to the present study. First, this retrospective study included patients with glioblastoma with EGFRvIII status determined by reverse transcriptase polymerase chain reaction. Whole exome sequencing was not available for these patients, so we did not account for other mutations or amplifications in EGFR that may also correlate with changes in DCE–MR imaging. Our observed frequency of mutant EGFRvIII, however, was consistent with the frequency reported in the literature.[5-30] Second, given the retrospective nature of this study, an inherent limitation is the absence of stereotactic localization in cases of biopsy or subtotal resection. Tissue sampling error may confound the assessment of EGFRvIII status (ie, undersampling of less metabolically active areas in heterogeneous tumors may lead to erroneous correlations, eg, false-negatives). Third, the VOIs were manually drawn around the enhancing tumor and then transferred onto the coregistered DCE–MR imaging perfusion maps, which may have introduced bias and variability. For example, subjectivity would be expected in terms of exclusion of vessels within the lesions. To account for this subjectivity, we inspected the VOIs in each case and adjusted them as necessary to match the enhancing tumor. To reduce operator variability, we chose to have all of these steps performed by a single experienced user trained in the use of the DCE–MR imaging software. Other groups have advocated semiautomated segmentation and coregistration; however, the validity and interinstitutional reproducibility of results obtained with their proprietary tools, which were developed in-house, remain unproven.[31] We believe that the expertise of a trained user of commercially available DCE–MR imaging software best matches the expertise available at most institutions and broadens the applicability of our results. A dual-rater or multiple-rater consensus approach could have also been an optimal way to assess uniform ROI placement.

CONCLUSIONS

We found that EGFRvIII-positive glioblastomas demonstrate greater vascular leakiness and perfusion than do EGFRvIII-negative glioblastomas. Quantitative evaluation of DCE–MR imaging may be useful as a noninvasive tool for correlating EGFRvIII expression and related tumor neoangiogenesis. This may have implications for monitoring response to EGFRvIII-targeted therapies.

ACKNOWLEDGMENTS

The authors are grateful for the expert editorial advice provided by Ada Muellner, MS.

Disclosures: Julio Arevalo-Perez—*OTHER RELATIONSHIPS*: Research fellow at the Memorial Sloan Kettering Cancer Center supported by a grant from the Spanish foundation "Fundación Alfonso Martín Escudero." Andrei I. Holodny—*UNRELATED*: *Other*: fMRI Consulting, LLC, *Comments*: a purely educational endeavor. Robert J. Young—*UNRELATED*: *Payment for Development of Educational Presentations*: Novocure; *Travel/Accommodations/Meeting Expenses Unrelated to Activities Listed*: Agios.

REFERENCES

1. Stupp R, Mason WP, van den Bent MJ, et al; European Organisation for Research and Treatment of Cancer Brain Tumor and Radiotherapy Groups, National Cancer Institute of Canada Clinical Trials Group. **Radiotherapy plus concomitant and adjuvant temozolomide for glioblastoma.** *N Engl J Med* 2005;352:987–96 CrossRef Medline
2. Jain R, Poisson L, Narang J, et al. **Correlation of perfusion parameters with genes related to angiogenesis regulation in glioblastoma: a feasibility study.** *AJNR Am J Neuroradiol* 2012;33:1343–48 CrossRef Medline
3. Huang PH, Xu AM, White FM. **Oncogenic EGFR signaling networks in glioma.** *Sci Signal* 2009;2:re6 CrossRef Medline
4. Mellinghoff IK, Wang MY, Vivanco I, et al. **Molecular determinants of the response of glioblastomas to EGFR kinase inhibitors.** *N Engl J Med* 2005;353:2012–24 CrossRef Medline
5. Gupta A, Young RJ, Shah AD, et al. **Pretreatment dynamic susceptibility contrast MRI perfusion in glioblastoma: prediction of EGFR gene amplification.** *Clin Neuroradiol* 2015;25:143–50 CrossRef Medline
6. Kastenhuber ER, Huse JT, Berman SH, et al. **Quantitative assessment of intragenic receptor tyrosine kinase deletions in primary glioblastomas: their prevalence and molecular correlates.** *Acta Neuropathol* 2014;127:747–59 CrossRef Medline
7. Tykocinski ES, Grant RA, Kapoor GS, et al. **Use of magnetic perfusion-weighted imaging to determine epidermal growth factor receptor variant III expression in glioblastoma.** *Neuro Oncol* 2012;14:613–23 CrossRef Medline
8. Essig M, Shiroishi MS, Nguyen TB, et al. **Perfusion MRI: the five most frequently asked technical questions.** *AJR Am J Roentgenol* 2013;200:24–34 CrossRef Medline
9. Cao Y, Sundgren PC, Tsien CI, et al. **Physiologic and metabolic magnetic resonance imaging in gliomas.** *J Clin Oncol* 2006;24:1228–35 CrossRef Medline
10. Shin KE, Ahn KJ, Choi HS, et al. **DCE and DSC MR perfusion imaging in the differentiation of recurrent tumour from treatment-related changes in patients with glioma.** *Clin Radiol* 2014;69:e264–72 CrossRef Medline
11. Jung SC, Yeom JA, Kim JH, et al. **Glioma: application of histogram analysis of pharmacokinetic parameters from T1-weighted**

dynamic contrast-enhanced MR imaging to tumor grading. *AJNR Am J Neuroradiol* 2014;35:1103–10 CrossRef Medline
12. Tofts PS, Brix G, Buckley DL, et al. **Estimating kinetic parameters from dynamic contrast-enhanced T(1)-weighted MRI of a diffusable tracer: standardized quantities and symbols.** *J Magn Reson Imaging* 1999;10:223–32 CrossRef Medline
13. Brennan CW, Verhaak RG, McKenna A, et al. **The somatic genomic landscape of glioblastoma.** *Cell* 2013;155:462–77 CrossRef Medline
14. Cancer Genome Atlas Research Network. **Comprehensive genomic characterization defines human glioblastoma genes and core pathways.** *Nature* 2008;455:1061–68 CrossRef Medline
15. Heimberger AB, Hlatky R, Suki D, et al. **Prognostic effect of epidermal growth factor receptor and EGFRvIII in glioblastoma multiforme patients.** *Clin Cancer Res* 2005;11:1462–66 CrossRef Medline
16. Hirata A, Ogawa S, Kometani T, et al. **ZD1839 (Iressa) induces antiangiogenic effects through inhibition of epidermal growth factor receptor tyrosine kinase.** *Cancer Res* 2002;62:2554–60 Medline
17. Ali MM, Janic B, Babajani-Feremi A, et al. **Changes in vascular permeability and expression of different angiogenic factors following anti-angiogenic treatment in rat glioma.** *PLoS One* 2010;5:e8727 CrossRef Medline
18. Katanasaka Y, Kodera Y, Kitamura Y, et al. **Epidermal growth factor receptor variant type III markedly accelerates angiogenesis and tumor growth via inducing c-myc mediated angiopoietin-like 4 expression in malignant glioma.** *Mol Cancer* 2013;12:31 CrossRef Medline
19. Inda MM, Bonavia R, Mukasa A, et al. **Tumor heterogeneity is an active process maintained by a mutant EGFR-induced cytokine circuit in glioblastoma.** *Genes Dev* 2010;24:1731–45 CrossRef Medline
20. Thomas AA, Brennan CW, DeAngelis LM, et al. **Emerging therapies for glioblastoma.** *JAMA Neurol* 2014;71:1437–44 CrossRef Medline
21. Xu LW, Chow KK, Lim M, et al. **Current vaccine trials in glioblastoma: a review.** *J Immunol Res* 2014;2014:796856 CrossRef Medline
22. Mills SJ, Patankar TA, Haroon HA, et al. **Do cerebral blood volume and contrast transfer coefficient predict prognosis in human glioma?** *AJNR Am J Neuroradiol* 2006;27:853–58 Medline
23. Law M, Oh S, Babb JS, et al. **Low-grade gliomas: dynamic susceptibility-weighted contrast-enhanced perfusion MR imaging–prediction of patient clinical response.** *Radiology* 2006;238:658–67 CrossRef Medline
24. Aronen HJ, Gazit IE, Louis DN, et al. **Cerebral blood volume maps of gliomas: comparison with tumor grade and histologic findings.** *Radiology* 1994;191:41–51 CrossRef Medline
25. Ellika SK, Jain R, Patel SC, et al. **Role of perfusion CT in glioma grading and comparison with conventional MR imaging features.** *AJNR Am J Neuroradiol* 2007;28:1981–87 CrossRef Medline
26. Wetzel SG, Cha S, Johnson G, et al. **Relative cerebral blood volume measurements in intracranial mass lesions: interobserver and intraobserver reproducibility study.** *Radiology* 2002;224:797–803 CrossRef Medline
27. Jain R, Gutierrez J, Narang J, et al. **In vivo correlation of tumor blood volume and permeability with histologic and molecular angiogenic markers in gliomas.** *AJNR Am J Neuroradiol* 2011;32:388–94 CrossRef Medline
28. Fatterpekar GM, Galheigo D, Narayana A, et al. **Treatment-related change versus tumor recurrence in high-grade gliomas: a diagnostic conundrum—use of dynamic susceptibility contrast-enhanced (DSC) perfusion MRI.** *AJR Am J Roentgenol* 2012;198:19–26 CrossRef Medline
29. Young R, Babb J, Law M, et al. **Comparison of region-of-interest analysis with three different histogram analysis methods in the determination of perfusion metrics in patients with brain gliomas.** *J Magn Reson Imaging* 2007;26:1053–63 CrossRef Medline
30. Gan HK, Kaye AH, Luwor RB. **The EGFRvIII variant in glioblastoma multiforme.** *J Clin Neurosci* 2009;16:748–54 CrossRef Medline
31. Jung SC, Choi SH, Yeom JA, et al. **Cerebral blood volume analysis in glioblastomas using dynamic susceptibility contrast-enhanced perfusion MRI: a comparison of manual and semiautomatic segmentation methods.** *PLoS One* 2013;8:e69323 CrossRef Medline

Optimal Diagnostic Indices for Idiopathic Normal Pressure Hydrocephalus Based on the 3D Quantitative Volumetric Analysis for the Cerebral Ventricle and Subarachnoid Space

S. Yamada, M. Ishikawa, and K. Yamamoto

ABSTRACT

BACKGROUND AND PURPOSE: Despite the remarkable progress of 3D graphics technology, the Evans index has been the most popular index for ventricular enlargement. We investigated a novel reliable index for the MR imaging features specified in idiopathic normal pressure hydrocephalus, rather than the Evans index.

MATERIALS AND METHODS: The patients with suspected idiopathic normal pressure hydrocephalus on the basis of the ventriculomegaly and a triad of symptoms underwent the CSF tap test. CSF volumes were extracted from a T2-weighted 3D spin-echo sequence named "sampling perfection with application-optimized contrasts by using different flip angle evolutions (SPACE)" on 3T MR imaging and were quantified semiautomatically. Subarachnoid spaces were divided as follows: upper and lower parts and 4 compartments of frontal convexity, parietal convexity, Sylvian fissure and basal cistern, and posterior fossa. The maximum length of 3 axial directions in the bilateral ventricles and their frontal horns was measured. The "z-Evans Index" was defined as the maximum z-axial length of the frontal horns to the maximum cranial z-axial length. These parameters were evaluated for the predictive accuracy for the tap-positive groups compared with the tap-negative groups and age-adjusted odds ratios at the optimal thresholds.

RESULTS: In this study, 24 patients with tap-positive idiopathic normal pressure hydrocephalus, 25 patients without response to the tap test, and 23 age-matched controls were included. The frontal horns of the bilateral ventricles were expanded, with the most excessive expansion being toward the z-direction. The CSF volume of the parietal convexity had the highest area under the receiver operating characteristic curve (0.768), the z-Evans Index was the second (0.758), and the upper-to-lower subarachnoid space ratio index was the third (0.723), to discriminate the tap-test response.

CONCLUSIONS: The CSF volume of the parietal convexity of $<$38 mL, upper-to-lower subarachnoid space ratio of $<$0.33, and the z-Evans Index of $>$0.42 were newly proposed useful indices for the idiopathic normal pressure hydrocephalus diagnosis, an alternative to the Evans Index.

ABBREVIATIONS: AUC = area under the receiver operating characteristic curve; DESH = disproportionately enlarged subarachnoid space; iNPH = idiopathic normal pressure hydrocephalus; SPACE = sampling perfection with application-optimized contrasts by using different flip angle evolutions

Idiopathic normal pressure hydrocephalus (iNPH) has been diagnosed since the evidence-based guidelines for diagnosis and management of iNPH were announced in Japan, the United States, and Europe.[1-5] Frequently, patients with iNPH have short-stepped gaits at first, followed by cognitive impairment and urinary incontinence. The Study of iNPH on Neurologic Improvement (SINPHONI) showed that narrow sulci at the high convexity and an enlarged Sylvian fissure with ventricular dilation, which was designated as "disproportionately enlarged subarachnoid-space hydrocephalus (DESH)," were important MR imaging features for iNPH diagnosis.[6] The SINPHONI also confirmed that a lumbar CSF tap test was a necessary diagnostic test for probable iNPH and predicted a favorable response to a ventriculoperitoneal shunt surgery.[7]

Despite the remarkable progress of 3D graphics technology, the Evans Index proposed by William Evans in 1942 has been the most popular index of ventricular enlargement,[8] and an Evans Index of $>$0.3 has been adopted as a criterion for ventriculomegaly in the Japanese and international iNPH guidelines.[1-5] However, some studies using volumetric analysis suggested that it was not a sufficient linear index for evaluating ventricular enlargement.[9,10] In recent years, a T2-weighted 3D spin-echo se-

Received March 4, 2015; accepted after revision May 1.

From the Normal Pressure Hydrocephalus Center (S.Y., M.I.) and Department of Neurosurgery and Stroke Center (S.Y., M.I., K.Y.), Rakuwakai Otowa Hospital, Kyoto, Japan.

Please address correspondence to Shigeki Yamada, MD, PhD, Normal Pressure Hydrocephalus Center, Department of Neurosurgery and Stroke Center, Rakuwakai Otowa Hospital, Otowachinji-cho 2, Yamashina-ku, Kyoto 607-8602, Japan; e-mail: shigekiyamada3@gmail.com

Indicates open access to non-subscribers at www.ajnr.org

Indicates article with supplemental on-line table.

http://dx.doi.org/10.3174/ajnr.A4440

quence with sampling perfection with application-optimized contrasts by using different flip angle evolutions (SPACE sequence; Siemens, Erlangen, Germany) has been developed.[11-14] This volumetric sequence enables the decrease of specific absorption rate limits and a scan of the whole brain in a single slab and a true isotropic 3D data record with high resolution (voxel size ≤ 1 mm^3 without interpolation). Taking advantage of the high sensitivity to detect CSF on the T2-weighted 3D-SPACE sequence, a new automated segmentation technique by using a simple threshold algorithm has been developed.[15] The aim of the present study was to investigate the association between several 1D and 3D parameters of the ventricles and subarachnoid space and the response to the CSF tap test in patients with suspected iNPH in a systematic manner.

MATERIALS AND METHODS

Study Population

The study design and protocol were approved by the ethics committee for human research at our hospital. We prospectively collected the patients for 3T MR imaging beginning in November 2013, when the best protocols of imaging acquisition and extraction of ventricular and subarachnoid CSF were determined. Patients 60 years of age or older who had ventriculomegaly and symptoms of short-stepped gait and/or cognitive impairment were referred to our iNPH center as having suspected iNPH by neurologists and neurosurgeons around Kyoto. The comorbidities, including Alzheimer disease and cerebrovascular diseases, were diagnosed by the neurologists before referral to our iNPH center and were confirmed on MR imaging and ^{123}I-N-isopropyl-p-iodoamphetamine-SPECT in our center. Forty-nine consecutive patients with suspected iNPH underwent CSF removal of 30 mL via a lumbar tap (CSF tap test) concurrently with a T2-weighted 3D-SPACE sequence on 3T MR imaging and ^{123}I-N-isopropyl-p-iodoamphetamine-SPECT. According to the Japanese iNPH guidelines,[4] improvements of symptoms were assessed by the iNPH grading scale and the quantitative examination of gait and cognition before and at 1 day and 4 days after the CSF tap test. Gait was assessed with a 3-m Timed Up and Go Test and a 10-m straight walk (time in seconds and number of steps). Cognition was assessed by the Mini-Mental State Examination, the Frontal Assessment Battery, and the Trail-Making Test. Clinical improvement was defined as $\geq$10% improvement of the best changes in any of the quantitative examinations or $\geq$1 point of improvement of the iNPH grading scale. On the basis of the response to the CSF tap test, 49 patients with suspected iNPH were divided into 24 patients with positive response to the tap test and 25 with negative response to the tap test. Additionally, 23 age-matched controls consisting of the healthy volunteers or patients who were 60 years of age or older who did not have ventriculomegaly, the classic triad of iNPH, a massive intracranial lesion, or a fluid collection such as subdural hematoma underwent a T2-weighted 3D-SPACE sequence with informed written consent. Patients diagnosed with secondary normal pressure hydrocephalus or congenital/developmental etiology normal pressure hydrocephalus were excluded from this study. Seventy-two patients (mean age, 76.8 $\pm$ 6.8 years; range, 61–89 years; 46 men, 26 women) were included in this study.

Image Acquisition

All MR imaging examinations were performed with a 64-channel 3T MR imaging system (Magnetom Skyra; Siemens). We preliminarily examined the most adequate TR and TE of the T2-weighted 3D-SPACE sequence for CSF discrimination. The parameters of the T2-weighted 3D-SPACE sequence were set at TR, 2800 ms; TE, 286 ms; section thickness, 0.9 mm with 192 sections in a single slab; FOV, 230 mm; bandwidth, 789 Hz/Px; matrix (pixel size), 192 $\times$ 192; voxel size, 0.6 $\times$ 0.6 $\times$ 0.9 mm. Image acquisition time was 4 minutes 16 seconds.

Segmentation and Quantification of the Ventricular and Subarachnoid Space

The sagittal source images of T2-weighted 3D-SPACE were automatically processed to create 3D volume-rendering reconstruction and MPR images by using an independent 3D volume-analyzer workstation (SYNAPSE 3D; Japanese local name, SYNAPSE VINCENT; Fujifilm Medical Systems, Tokyo, Japan). The intracranial volume was segmented by the use of the combined techniques of the edge-guided nonlinear interpolation and user-steered live-wire segmentation.[16,17] After that, the CSF spaces were automatically segmented from brain parenchyma by using a simple threshold algorithm (Fig 1).[15] The threshold range for the signal intensity of CSF on the T2-weighted 3D-SPACE sequence of 3T MR imaging was extremely stable at 650–700 of the lower limit threshold and no upper limit threshold. The bilateral, third, and fourth ventricles were manually segmented, respectively, and they were subsequently combined as a total ventricle.

Subarachnoid spaces were automatically segmented as the total intracranial CSF space minus a total ventricle. Furthermore, subarachnoid spaces were divided into the upper and lower parts in a horizontal section on the anterior/posterior commissure plane at the level of the junction point of the vein of Galen and the straight sinus. The upper-to-lower subarachnoid space ratio was defined as the upper part to the lower part of the subarachnoid spaces (Fig 2). In addition, the subarachnoid space was divided into 4 parts, frontal convexity, parietal convexity, Sylvian fissure and basal cistern, and posterior fossa, by using the manual segmentation technique, as shown in Fig 3. The parietal convexity was defined as the posterior part from the central sulcus.

The labeling of the segmented volumes was measured by counting the number of voxels automatically. The volume ratios of the ventricles and subarachnoid spaces (%) were calculated as ratios of the ventricle volumes to the intracranial volume. To evaluate the validity of the measured volumes, we segmented and measured the ventricles and subarachnoid spaces in the first 11 consecutive patients by using the SYNAPSE 3D workstation and the open-source 3D Slicer software package (www.slicer.org).[18] The Pearson correlation coefficients among the 2 software packages were 0.838 for a total intracranial CSF space and 0.989 for the total ventricular volumes.

3D Coordinates of the Bilateral Ventricle

Three axes for the spatial coordinates of the head position were used as follows: x is the left/right dimension, y is the posterior/anterior dimension, and z is the ventral/dorsal or inferior/superior dimension. The x and z dimensions were perpendicular, and

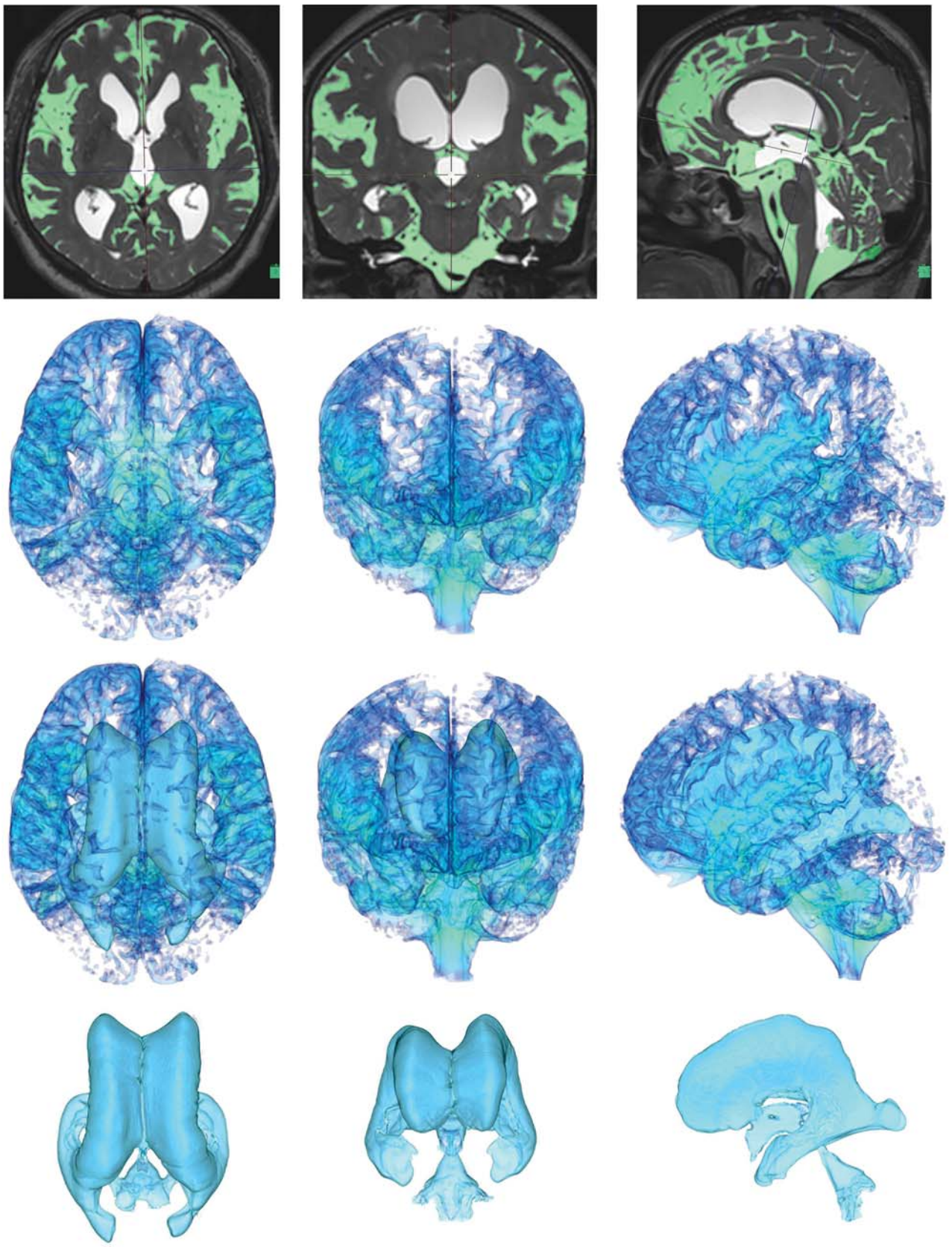

FIG 1. Automatic extraction of CSF space. The figures in the top row show the MIP images on the T2-weighted 3D-SPACE sequence in the representative iNPH case. Light green indicates the subarachnoid space segmented automatically at a threshold intensity of >700 on the SYNAPSE 3D workstation. The other figures show the 3D volume-rendering reconstruction images of the subarachnoid space on the *second line*, total CSF on the *third line*, and ventricles on the *last line*. The *left*, *middle*, and *right* column figures show axial, coronal, and sagittal dimensional views, respectively.

the y dimension was parallel to the anterior/posterior commissure line. The Evans Index was measured as the maximal width of the frontal horns of the bilateral ventricles to the maximal width of the internal diameter of the cranium on the basis of the x dimension.[9,10] The z-Evans Index was defined as the maximum z-axial length of the frontal horn, which was between the roof and bottom of the larger lateral ventricle to the maximum cranial z-axial length at the base of the posterior end of the foramen of Monro (Fig 4). In the same procedure, the y-Evans Index was defined as the maximum y-axial length between the posterior end of the foramen of Monro and the anterior end of the frontal horns to the maximum cranial y-axial length. Additionally, x-, y-, and z-Maximum Indices were measured as the maximum width of the bilateral ventricles to the maximum internal cranium width on each of 3 dimensions, as shown in Fig 4.

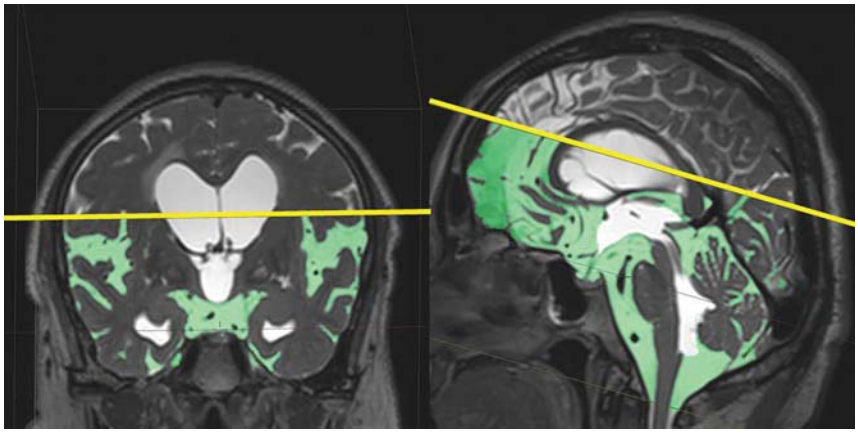

FIG 2. Division of the subarachnoid space into the upper and lower parts. The subarachnoid space was divided into the upper and lower parts in a horizontal section on the anterior/posterior commissure plane at the level of the junction point of the vein of Galen and the straight sinus. The *left* and *right* figures show coronal and sagittal views. The Sylvian fissure is typically included in the lower part of the subarachnoid space. The upper-to-lower subarachnoid space ratio was defined as the upper part to the lower part of the subarachnoid space.

Statistical Analysis

The prevalence ratios of high-convexity tightness, enlarged Sylvian fissure, and comorbidities such as Alzheimer disease or dementia with Lewy bodies, Parkinsonism, cerebrovascular diseases, narrow spinal canal, and disuse muscle atrophy were compared among the 3 groups by the χ^2 test. Mean values and SDs for age and 3D and 1D indices among the tap-positive, tap-negative,

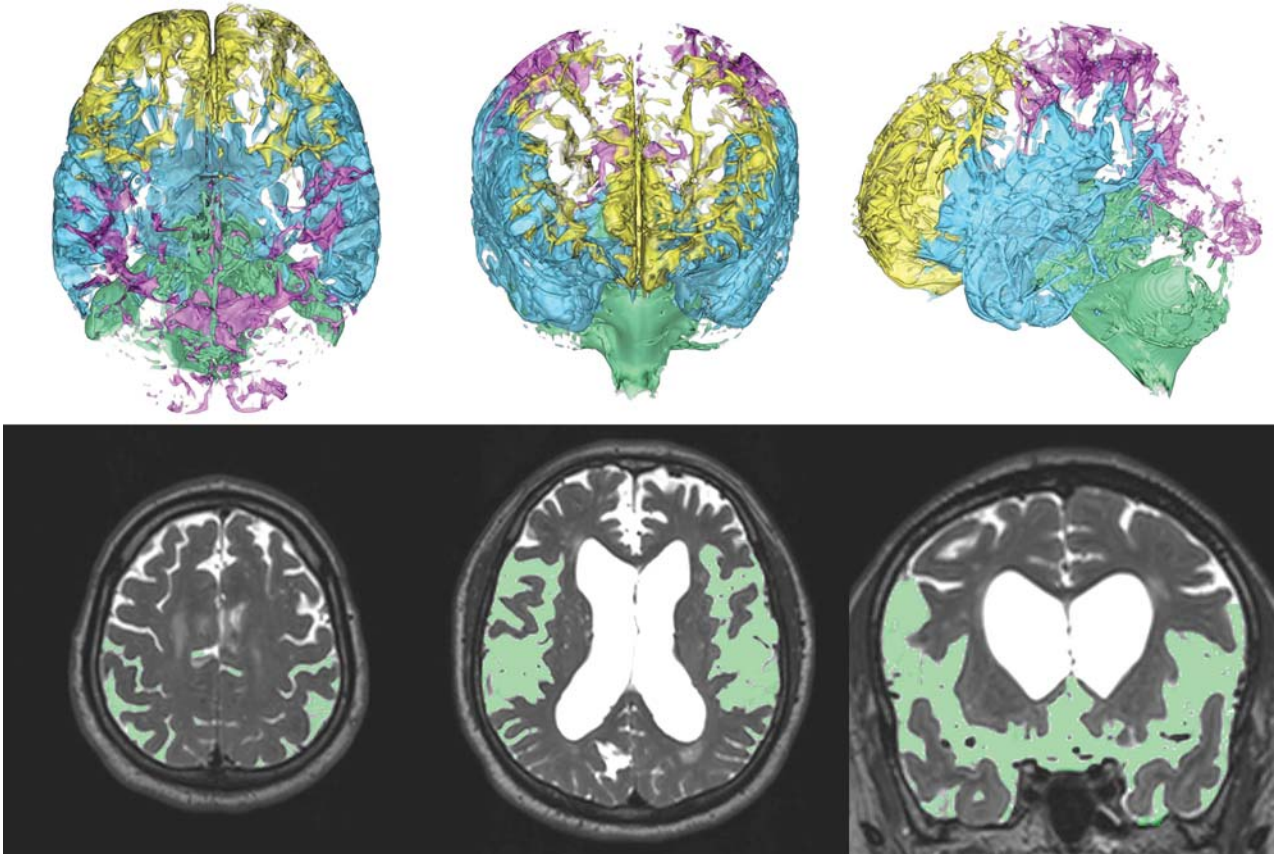

FIG 3. Division of the subarachnoid space into the 4 parts. The subarachnoid space was divided into the following 4 parts: frontal convexity (yellow), parietal convexity (magenta), Sylvian fissure and basal cistern (sky blue), and posterior fossa (light green) in the 3D segmentation. The *left*, *middle*, *right* upper 3D volume-rendering reconstruction images show the axial, coronal, and sagittal dimensional views, respectively. Light green in the *left lower* axial MIP image indicates the segmented region of the parietal convexity of the subarachnoid space, and that in the *middle* and *right* lower MIP images indicates axial and coronal views of the Sylvian fissure and basal cistern.

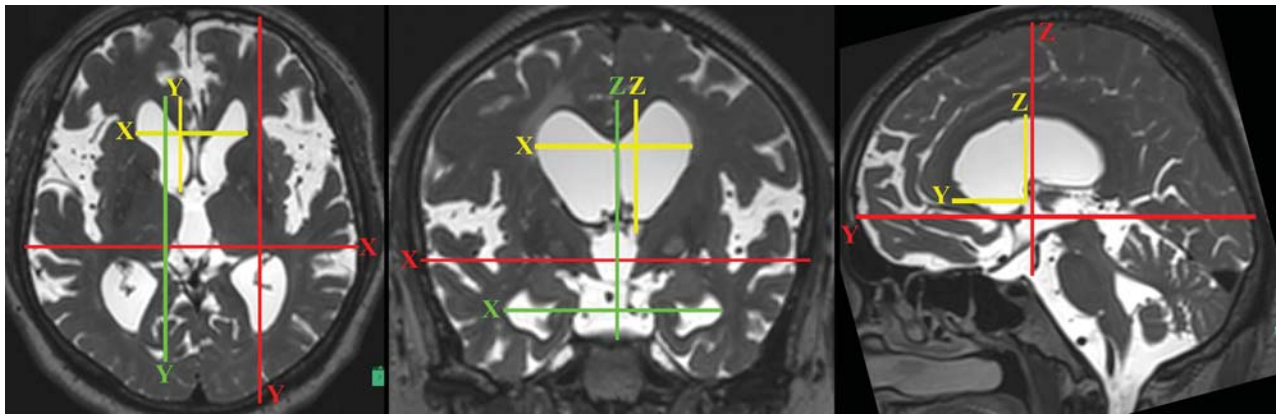

FIG 4. Three-directional linear indicators for evaluating the size of bilateral ventricles. The figures are the 3-directional MPR reconstruction images of the T2-weighted 3D SPACE. On the basis of the anterior/posterior commissure line, x-, y-, and z-axes for spatial coordinates of head position were defined. The *green lines* show the maximum length of 3-axial directions of the bilateral ventricles. The *yellow lines* show the maximum 3-axial length of the frontal horn of the bilateral ventricles. The *red lines* show the maximum intracranial 3-axial width. In addition to the original Evans Index, the y- and z-Evans Indices were defined as the maximum length from the foramen of Monro to the anterior and superior extremities of the frontal horns (*yellow lines*)/the maximum intracranial y- and z-axial length (*red lines*), respectively. The x-, y-, and z-Maximum Indices were defined as the maximum width of the bilateral ventricles (*green lines*)/the maximum intracranial width on the each of the 3 dimensions (*red lines*).

Table 1: Clinical characteristics of the study population

	No. (%) (72 Total)	No. (%) (24 Tap-Positive)	*P* Value[1a]	*P* Value[2b]	No. (%) (25 Tap-Negative)	*P* Value[3c]	No. (%) (23 Controls)
Male sex	46 (64%)	15 (62%)	1.000	.917	17 (68%)	.831	14 (61%)
Evans Index >0.3	42 (58%)	19 (79%)	.005[d]	.252	15 (60%)	.145	8 (35%)
Callosal angle <90°	46 (64%)	21 (88%)	<.001[d]	.962	23 (92%)	<.001[d]	2 (9%)
High-convexity tightness	35 (49%)	19 (79%)	<.001[d]	.154	14 (56%)	.002[d]	2 (9%)
Enlarged Sylvian fissure	33 (46%)	19 (79%)	<.001[d]	.154	14 (56%)	<.001[d]	0
Alzheimer disease	22 (31%)	4 (17%)	.666	.042[d]	12 (48%)	.205	6 (26%)
Parkinsonism	5 (7%)	2 (8%)	.489	1.000	3 (12%)	.263	0
Cerebrovascular diseases	15 (21%)	1 (4%)	.022[d]	.115	6 (24%)	.615	8 (35%)
Narrow spinal canal	7 (10%)	3 (13%)	.248	1.000	4 (16%)	.139	0
Muscle atrophy of lower leg	12 (17%)	5 (21%)	.065	.802	7 (28%)	.019[d]	0
Mean age (± SD) (yr)	76.8 (±6.8)	76.2 (±7.5)	.741	.541	77.3 (±5.4)	.893	76.8 (±7.8)

[a] *P* value[1]: probability value for the χ^2 test between the tap-positive group and controls.
[b] *P* value[2]: probability value for the χ^2 test between the tap-positive and tap-negative groups.
[c] *P* value[3]: probability value for the χ^2 test between tap-negative group and controls.
[d] Significant.

and control groups were calculated and compared in each group by the Mann-Whitney-Wilcoxon test. The volumes and volume ratios of the total ventricles, bilateral ventricles and total subarachnoid space, the 4 segmented parts of the subarachnoid spaces, upper-to-lower subarachnoid space ratio, 3-directional linear 1D indices of the bilateral ventricles, and the callosal angle were calculated as the area under the receiver operating characteristic curves (AUC) to evaluate the optimal thresholds to maximize the sum of sensitivities and specificities for differentiation between the tap-positive and the tap-negative groups. Using the optimal thresholds from AUC analyses, we calculated age-adjusted ORs and 95% CIs for comparing the tap-positive group with the tap-negative group in a multivariate logistic regression model. Additionally, 14 patients with shunt-effective iNPH were evaluated, and their 3D and 1D indices were compared to 25 patients without response to the tap test. The relationships between the 2 indices were compared by using the Pearson correlation coefficient (r). Age was treated as a continuous variable for all statistical analyses. All missing data were treated as deficit data that did not affect other variables. Statistical significance was assumed at $P < .05$. Statistical analysis was performed by using R software (Version 3.0.1; http://www.R-project.org).

RESULTS

Clinical Characteristics

An Evans Index of >0.3, callosal angle of <90°, narrow sulci at the high convexity, and an enlarged Sylvian fissure, which were conventional morphologic indices for iNPH diagnosis, were significantly different between the tap-positive group and the controls, but there was not any statistical significance between the tap-positive and tap-negative groups (Table 1). The tap-negative group had a higher frequency of Alzheimer disease (48%) and cerebrovascular diseases (26%) compared with the tap-positive group.

Parameters Associated with CSF Tap-Test Responses

Table 2 shows the result of the mean values of the 3D and 1D indices. Among the 3D indices, volume ratios of the total ventricle or bilateral ventricles, CSF volume of the total subarachnoid space or parietal convexity, and upper-to-lower subarachnoid space ra-

Table 2: Parameters among the tap-positive, tap-negative, and control groups

	Mean (72 Total)	Mean (24 Tap-Positive)	*P* Value[1a]	*P* Value[2b]	Mean (25 Tap-Negative)	*P* Value[3c]	Mean (23 Controls)
Total ventricle volume (mL)	123	157	<.001[d]	.060	135	<.001[d]	75.4
Total ventricle volume ratio (%)	8.1	10.5	<.001 [d]	.017[d]	8.8	<.001[d]	5
Bilateral ventricle volume (mL)	114	147	<.001[d]	.060	125	<.001[d]	66.9
Bilateral ventricle volume ratio (%)	7.5	9.8	<.001[d]	.013[d]	8.2	<.001[d]	4.4
Total subarachnoid space volume (mL)	270	251	.678	.010[d]	294	.127	264
Total subarachnoid space volume ratio (%)	18.0	16.8	.587	.030[d]	19.3	.223	17.8
CSF volume of frontal convexity (mL)	51.1	41.0	.003[d]	.016[d]	52.1	.218	51.1
CSF volume of parietal convexity (mL)	42.4	28.4	<.001[d]	<.001[d]	44.1	.162	42.4
CSF volume of Sylvian fissure and basal cistern (mL)	119	121	.030[d]	.077	136	<.001[d]	119
CSF volume of posterior fossa (mL)	57.1	59.1	.232	1.000	58.9	.226	57.1
Upper-to-lower subarachnoid space ratio	0.55	0.37	<.001[d]	.008[d]	0.49	<.001[d]	0.79
Evans Index	0.31	0.34	<.001[d]	.028[d]	0.32	.004[d]	0.29
Y-Evans Index	0.22	0.23	.001[d]	.053	0.22	.095	0.21
Z-Evans Index	0.38	0.43	<.001[d]	.002[d]	0.39	<.001[d]	0.31
X-Max Index	0.63	0.65	<.001[d]	.073	0.64	<.001[d]	0.60
Y-Max Index	0.63	0.67	<.001[d]	.048[d]	0.64	.001[d]	0.58
Z-Max Index	0.70	0.74	<.001[d]	.613	0.74	<.001[d]	0.62
Callosal angle (degree)	80.9	66.2	<.001[d]	.117	73.4	<.001[d]	104

Note:—Max indicates maximum.
[a] *P* value[1]: probability value for the Mann-Whitney-Wilcoxon test between the tap-positive group and controls.
[b] *P* value[2]: probability value for the Mann-Whitney-Wilcoxon test between the tap-positive and tap-negative groups.
[c] *P* value[3]: probability value for the Mann-Whitney-Wilcoxon test between the tap-negative group and controls.
[d] Significant.

Table 3: At the maximum AUC, thresholds, sensitivity, specificity, and age-adjusted OR (95% CI) for the tap-positive compared with the tap-negative group

Tap-Positive vs Tap-Negative	AUC	Optimal Threshold	Sensitivity	Specificity	OR (95% CI)	*P* Value[a]
Total ventricle volume (mL)	0.657	155	58.3	80.0	1.49 (1.13–1.96)	.004
Total ventricle volume ratio (%)	0.700	8.6	79.2	56.0	1.49 (1.13–1.96)	.005
Bilateral ventricle volume (mL)	0.657	147	54.2	84	1.52 (1.15–2.07)	.003
Bilateral ventricle volume ratio (%)[b]	0.705	7.9	83.3	56.0	1.40 (1.06–1.84)	.019
Total subarachnoid space volume (mL)[b]	0.714	312	87.5	48.0	0.66 (0.49–0.89)	.006
Total subarachnoid space volume ratio (%)	0.682	17.9	75.0	72.0	0.63 (0.48–0.82)	<.001
CSF volume of frontal convexity (mL)[b]	0.701	45.9	79.2	76.0	0.58 (0.45–0.74)	<.001
CSF volume of parietal convexity (mL)[b]	0.768	37.9	91.7	52.0	0.60 (0.45–0.79)	<.001
CSF volume of Sylvian fissure and basal cistern (mL)	0.648	137	75.0	56.0	0.71 (0.52–0.96)	.028
CSF volume of posterior fossa (mL)	0.500	78.7	16.7	96.0	1.41 (0.89–2.25)	.146
Upper-to-lower subarachnoid space ratio[b]	0.723	0.33	45.8	92.0	0.62 (0.46–0.83)	.002
Evans Index	0.683	0.33	58.3	80.0	1.37 (1.04–1.80)	.026
Y-Evans Index	0.662	0.24	41.7	92.0	1.42 (0.99–2.03)	.057
Z-Evans Index[b]	0.758	0.42	66.7	88.0	1.74 (1.35–2.24)	<.001
X-Max Index	0.640	0.62	70.8	60.0	1.55 (1.12–2.16)	.009
Y-Max Index	0.665	0.69	45.8	92.0	1.69 (1.26–2.27)	<.001
Z-Max Index	0.543	0.74	58.3	60.0	1.13 (0.85–1.52)	.401
Callosal angle (degree)	0.632	77.3	87.5	48.0	1.51 (1.13–2.02)	.005

[a] Probability value for the age-adjusted ORs in a logistic regression model.
[b] Rows in which the AUC > 0.7 and *P* <. 05 are at the optimal threshold.

tio were significantly different between the tap-positive and tap-negative groups. The bilateral ventricular volume ratio seemed to be robust and representative of the ventriculomegaly. The ranges of the 3-directional expanding ratios for the bilateral ventricles were 0.55–0.70 at the x-Maximum Index, 0.49–0.71 at the y-Maximum Index, and 0.36–0.81 at the z-Maximum Index; and those for the frontal horns were 0.22–0.39 at the Evans Index, 0.17–0.26 at the y-Evans Index, and 0.17–0.48 at the z-Evans Index. The bilateral ventricles and their frontal horns were most expanded toward to the z-axial direction in the tap-positive group with iNPH. The Evans Index, z-Evans Index, and y-Maximum Index were statistically significant between the tap-positive and tap-negative groups. For discriminating the tap-test response, the CSF volume of the parietal convexity was the highest index (AUC, 0.768; sensitivity, 91.7%; specificity, 52.0%), the z-Evans Index was the second (AUC, 0.758; sensitivity, 66.7%; specificity, 88.0%), and the upper-to-lower subarachnoid space ratio index was the third (AUC, 0.723; sensitivity, 45.8%; specificity, 92.0%), as shown in Table 3 and Fig 5. These 3 indices remained statistically significant for discriminating the shunt-effective iNPH group from the tap-negative group (On-line Table). There was a significant relationship between the upper-to-lower subarachnoid space ratio and CSF volume of the parietal convexity (r, 0.680; 95% CI, −0.533 to −0.788; $P < .001$). Furthermore, the z-Evans Index was significantly associated with the upper-to-lower subarachnoid space ratio (r, −0.527; 95% CI, −0.676 to −0.336; $P < .001$) or the CSF volume of the parietal convexity (r, −0.238; 95% CI, −0.445 to −0.007; $P = .004$). If the patients with

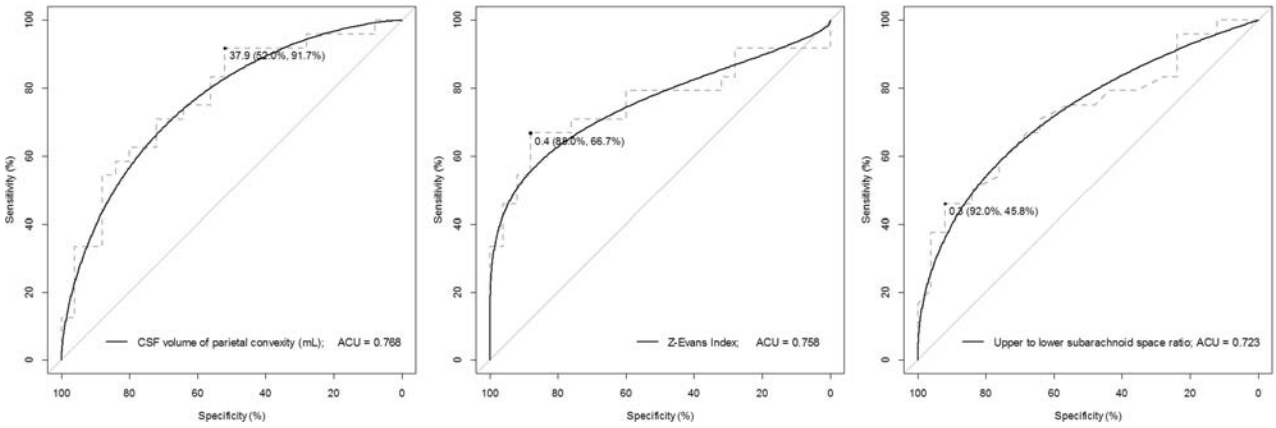

FIG 5. Receiver operating characteristic curves for discriminating tap-positive from the tap-negative group. The ROC graphs show specificity on the x-axis and sensitivity on the y-axis. The *left* graph shows the ROC curve of the parietal convexity of the subarachnoid space, the *middle* one shows that of the z-Evans Index, and the *right* one shows that of the upper-to-lower subarachnoid space ratio. The *black circle points* indicate the optimal cutoff points of the maximum area under the ROC curve.

suspected iNPH had any of the MR imaging findings—that is, the CSF volume of the parietal convexity of <38 mL, upper-to-lower subarachnoid space ratio of <0.33, and/or z-Evans Index of >0.42—they had the possibility of a >1.5-times higher effectiveness of the CSF tap test. No useful combination of parameters obviously increased the AUC compared with the single parameter.

DISCUSSION

Our quantitative volumetric analyses determined that volume expansion of the bilateral ventricles, especially at the frontal horns, was toward the z-axial direction, rather than the x-axial direction, in the patients with iNPH. Therefore, we newly proposed the z-Evans Index, which was a representative index for z-axial directional expansion of the frontal horns of the bilateral ventricles. We found that the z-Evans Index had the most significant relationship with the patients with iNPH responded to the tap test among the parameters of the ventricles. Because DESH or high-convexity tightness has been recognized as a highly sensitive radiologic finding for iNPH diagnosis,[6,19] a coronal MR imaging section has been recommended for this diagnosis.[6,20] A coronal MR imaging section is also suitable for the measurement of the z-Evans Index, the same as the DESH and callosal angle. As quantitative indices representing high-convexity tightness and the enlarged Sylvian fissure, the upper-to-lower subarachnoid space ratio and the CSF volume of the 4 segmented parts of the subarachnoid spaces were newly proposed in this study. These 2 parameters were confirmed to have a significant correlation with each other, and there was a significantly inverse correlation between the upper-to-lower subarachnoid space ratio and the z-Evans Index. These findings support the view that high-convexity tightness in iNPH is caused by outside compression from the z-directional expansion of the bilateral ventricles.

Our study had some limitations. First, the highest AUC for discriminating the tap-test response was 0.768, which was relatively low. Although differentiating the tap-positive iNPH group from the controls was simple by using the z-Evans Index (AUC of 0.91), the same as the Evans Index (AUC of 0.84), or the callosal angle (AUC of 0.93), the Evans Index and callosal angle were not sufficiently able to estimate the tap-test response in this study. These reasons would mainly complicate iNPH diagnosis only by radiologic findings, and we emphasize that the CSF tap test is important for the diagnosis of iNPH, though the CSF tap test has high specificity (73–100%), its sensitivity is low (26–61%) for diagnosing shunt-responsive iNPH.[7,21,22] The other limitation was that the signal-intensity-based CSF segmentation method based on the T2-weighted 3D-SPACE sequence had not yet been used in the field of neuroradiology, compared with the atlas-based automatic segmentation method. However, this simple segmentation method by using high-contrast CSF on a T2-weighted sequence will spread throughout the field of neuroradiology with the progression of high-field MR imaging scanners.

CONCLUSIONS

This study provides novel morphologic evidence that volume expansion of the bilateral ventricle is toward the z-axial direction, rather than the x-axial direction, in patients with iNPH responded to the tap test. In particular, the z-directional expansion of the frontal horn of the bilateral ventricles, named the z-Evans Index, was found to be a useful index for predicting the response to the CSF tap test. Cases of z-directional ventriculomegaly concurrent with decreased CSF volume at the parietal convexity subarachnoid space or a decreased upper-to-lower subarachnoid space ratio are thought to constitute a pivotal morphologic finding for iNPH diagnosis. These novel morphologic findings may contribute to future studies concerning the pathogenesis of iNPH underlying simultaneous enlargement of the ventricles, basal cistern, and Sylvian fissure and narrowing of the sulci at high convexity.

ACKNOWLEDGMENTS

We would like to thank Dr Yasutaka Fushimi, Department of Diagnostic Imaging and Nuclear Medicine, Kyoto University Graduate School of Medicine, for his advice concerning the MR imaging techniques; and also Professor Kazunari Ishii, Department of Radiology and Nuclear Medicine, Hyogo Brain and Heart Center, for the transfer of his original AVSIS 2013 software package by using the SPM8 software program. We would also like to thank the radiology staff of the Rakuwakai Otowa Hospital, par-

ticularly Masatoshi Katayama, Masaru Yamazaki, and Rikiya Kikumoto.

Disclosures: Masatsune Ishikawa—*RELATED*: *Grant*: Health and Labor Sciences Research Grant on Measures for Intractable Disease: studies on the epidemiology, pathophysiology, and treatment of normal pressure hydrocephalus; *UNRELATED*: *Payment for Lectures (including service on Speakers Bureaus)*: lecture fees from Medtronic Japan (plus honoraria) and Codman Japan.

REFERENCES

1. Ishikawa M; Guideline Committee for Idiopathic Normal Pressure Hydrocephalus, Japanese Society of Normal Pressure Hydrocephalus. **Clinical guidelines for idiopathic normal pressure hydrocephalus.** *Neurol Med Chir (Tokyo)* 2004;44:222–23 CrossRef Medline
2. Ishikawa M, Hashimoto M, Kuwana N, et al. **Guidelines for management of idiopathic normal pressure hydrocephalus.** *Neurol Med Chir (Tokyo)* 2008;48(suppl):S1–23 CrossRef Medline
3. Marmarou A, Bergsneider M, Relkin N, et al. **Development of guidelines for idiopathic normal-pressure hydrocephalus: introduction.** *Neurosurgery* 2005;57:S1–3; discussion ii–v Medline
4. Mori E, Ishikawa M, Kato T, et al; Japanese Society of Normal Pressure Hydrocephalus. **Guidelines for management of idiopathic normal pressure hydrocephalus: second edition.** *Neurol Med Chir (Tokyo)* 2012;52:775–809 CrossRef Medline
5. Relkin N, Marmarou A, Klinge P, et al. **Diagnosing idiopathic normal-pressure hydrocephalus.** *Neurosurgery* 2005;57(3 suppl):S4–16; discussion ii–v CrossRef Medline
6. Hashimoto M, Ishikawa M, Mori E, et al; Study of INPH on neurological improvement (SINPHONI). **Diagnosis of idiopathic normal pressure hydrocephalus is supported by MRI-based scheme: a prospective cohort study.** *Cerebrospinal Fluid Res* 2010;7:18 CrossRef Medline
7. Ishikawa M, Hashimoto M, Mori E, et al. **The value of the cerebrospinal fluid tap test for predicting shunt effectiveness in idiopathic normal pressure hydrocephalus.** *Fluids Barriers CNS* 2012;9:1 CrossRef Medline
8. Evans WA. **An encephalographic ratio for estimating ventricular enlargement and cerebral atrophy.** *Arch NeurPsych* 1942;47:931–37 CrossRef
9. Ambarki K, Israelsson H, Wahlin A, et al. **Brain ventricular size in healthy elderly: comparison between Evans index and volume measurement.** *Neurosurgery* 2010;67:94–99; discussion 99 CrossRef Medline
10. Toma AK, Holl E, Kitchen ND, et al. **Evans' index revisited: the need for an alternative in normal pressure hydrocephalus.** *Neurosurgery* 2011;68:939–44 CrossRef Medline
11. Algin O, Turkbey B. **Evaluation of aqueductal stenosis by 3D sampling perfection with application-optimized contrasts using different flip angle evolutions sequence: preliminary results with 3T MR imaging.** *AJNR Am J Neuroradiol* 2012;33:740–46 CrossRef Medline
12. Kartal MG, Algin O. **Evaluation of hydrocephalus and other cerebrospinal fluid disorders with MRI: an update.** *Insights Imaging* 2014;5:531–41 CrossRef Medline
13. Lichy MP, Wietek BM, Mugler JP 3rd, et al. **Magnetic resonance imaging of the body trunk using a single-slab, 3-dimensional, T2-weighted turbo-spin-echo sequence with high sampling efficiency (SPACE) for high spatial resolution imaging: initial clinical experiences.** *Invest Radiol* 2005;40:754–60 CrossRef Medline
14. Mugler JP 3rd. **Optimized three-dimensional fast-spin-echo MRI.** *J Magn Reson Imaging* 2014;39:745–67 CrossRef Medline
15. Gao KC, Nair G, Cortese IC, et al. **Sub-millimeter imaging of brain-free water for rapid volume assessment in atrophic brains.** *Neuroimage* 2014;100:370–78 CrossRef Medline
16. Falcão AX, Udupa JK. **A 3D generalization of user-steered live-wire segmentation.** *Med Image Anal* 2000;4:389–402 CrossRef Medline
17. Zhang L, Wu X. **An edge-guided image interpolation algorithm via directional filtering and data fusion.** *IEEE Trans Image Process* 2006;15:2226–38 CrossRef Medline
18. Fedorov A, Beichel R, Kalpathy-Cramer J, et al. **3D Slicer as an image computing platform for the quantitative imaging network.** *Magn Reson Imaging* 2012;30:1323–41 CrossRef Medline
19. Sasaki M, Honda S, Yuasa T, et al. **Narrow CSF space at high convexity and high midline areas in idiopathic normal pressure hydrocephalus detected by axial and coronal MRI.** *Neuroradiology* 2008;50:117–22 CrossRef Medline
20. Virhammar J, Laurell K, Cesarini KG, et al. **Preoperative prognostic value of MRI findings in 108 patients with idiopathic normal pressure hydrocephalus.** *AJNR Am J Neuroradiol* 2014;35:2311–18 CrossRef Medline
21. Kubo Y, Kazui H, Yoshida T, et al. **Validation of grading scale for evaluating symptoms of idiopathic normal-pressure hydrocephalus.** *Dement Geriatr Cogn Disord* 2008;25:37–45 CrossRef Medline
22. Wikkelsø C, Hellstrom P, Klinge PM, et al; European iNPH Multicentre Study Group. **The European iNPH Multicentre Study on the predictive values of resistance to CSF outflow and the CSF tap test in patients with idiopathic normal pressure hydrocephalus.** *J Neurol Neurosurg Psychiatry* 2013;84:562–68 CrossRef Medline

Juxtacortical Lesions and Cortical Thinning in Multiple Sclerosis

D. Pareto, J. Sastre-Garriga, C. Auger, Y. Vives-Gilabert, J. Delgado, M. Tintoré, X. Montalban, and A. Rovira

ABSTRACT

BACKGROUND AND PURPOSE: The role of juxtacortical lesions in brain volume loss in multiple sclerosis has not been fully clarified. The aim of this study was to explore the role of juxtacortical lesions on cortical atrophy and to investigate whether the presence of juxtacortical lesions is related to local cortical thinning in the early stages of MS.

MATERIALS AND METHODS: A total of 131 patients with clinically isolated syndrome or with relapsing-remitting MS were scanned on a 3T system. Patients with clinically isolated syndrome were classified into 3 groups based on the presence and topography of brain lesions: no lesions ($n = 24$), only non–juxtacortical lesions ($n = 33$), and juxtacortical lesions and non–juxtacortical lesions ($n = 34$). Patients with relapsing-remitting MS were classified into 2 groups: only non–juxtacortical lesions ($n = 10$) and with non–juxtacortical lesions and juxtacortical lesions ($n = 30$). A juxtacortical lesion probability map was generated, and cortical thickness was measured by using FreeSurfer.

RESULTS: Juxtacortical lesion volume in relapsing-remitting MS was double that of patients with clinically isolated syndrome. The insula showed the highest density of juxtacortical lesions, followed by the temporal, parietal, frontal, and occipital lobes. Patients with relapsing-remitting MS with juxtacortical lesions showed significantly thinner cortices overall and in the parietal and temporal lobes compared with those with clinically isolated syndrome with normal brain MR imaging. The volume of subcortical structures (thalamus, pallidum, putamen, and accumbens) was significantly decreased in relapsing-remitting MS with juxtacortical lesions compared with clinically isolated syndrome with normal brain MR imaging. The spatial distribution of juxtacortical lesions was not found to overlap with areas of cortical thinning.

CONCLUSIONS: Cortical thinning and subcortical gray matter volume loss in patients with a clinically isolated syndrome or relapsing-remitting MS was related to the presence of juxtacortical lesions, though the cortical areas with the most marked thinning did not correspond to those with the largest number of juxtacortical lesions.

ABBREVIATIONS: CIS = clinically isolated syndrome; CISj = CIS with juxtacortical lesion; CISn = CIS with normal brain MR imaging; CISnj = CIS without juxtacortical lesion; JL = juxtacortical lesion; JLV = juxtacortical lesion volume; LV = lesion volume; RRj = relapsing-remitting MS with JL; RRMS = relapsing-remitting MS; RRnj = relapsing-remitting MS without JL

Multiple sclerosis is a chronic, persistent inflammatory-demyelinating disease of the central nervous system, characterized pathologically by focal areas of inflammation, demyelination, axonal loss, and gliosis. Brain MR imaging typically shows multifocal lesions, mainly in white matter regions,[1] though focal cortical demyelinated plaques are also a prominent feature, even in the earliest phases of the disease.[2] Unfortunately, conventional MR imaging has limited sensitivity for detecting cortical lesions because of their small size, the poor contrast resolution, and the partial volume effects of the subarachnoid spaces and surrounding cortex.[3,4] Thus, histopathologic studies are the only way to describe, quantify, and classify gray matter lesions according to their position in relation to the gray-white matter surface (leukocortical or juxtacortical; intracortical and subpial).[5,6] Despite the limited sensitivity of MR imaging for detecting cortical lesions in MS, results of several studies showed that cross-sectional cortical lesion volume and its increase over time are associated with progression of disability and cognitive impairment in MS.[7-10]

Received March 10, 2015; accepted after revision May 8.

From Unitat de Ressonància Magnètica (IDI), Servei de Radiologia (D.P., C.A., A.R.), Servei de Neurologia/Neuroimmunologia, Multiple Sclerosis Centre of Catalonia (Cemcat) (J.S.-G., M.T., X.M.), Hospital Universitari Vall d'Hebron, and Port d'Informació Científica (Y.V.-G., J.D.), Universitat Autònoma de Barcelona, Barcelona, Spain.

Please address correspondence to Àlex Rovira, MD, Unitat de Ressonància Magnètica (IDI), Servei de Radiologia, Hospital Universitari Vall d'Hebron, Passeig Vall d'Hebron 119-129, 08035 Barcelona, Spain; e-mail: alex.rovira@idi.gencat.cat

http://dx.doi.org/10.3174/ajnr.A4485

Table 1: Demographic and clinical features of the study sample

	CISn	CISnj	CISj	RRnj	RRj
N (women)	24 (15)	33 (20)	34 (20)	10 (4)	30 (20)
Mean (SD) age, y	36 ± 10	36 ± 7	35 ± 8	34 ± 7	36 ± 7
Mean (SD) EDSS	1.4 ± 0.9	1.4 ± 0.9	1.9 ± 1.1	3.2 ± 2.0	2.5 ± 1.6
Mean (SD) DIS	3–5 mo	3–5 mo	3–5 mo	10.4 ± 8.2 y	10.6 ± 7.1 y
LV mL (SD)	0	0.75 ± 1.17	4.10 ± 6.38	3.12 ± 3.71	9.10 ± 7.86

Note:—EDSS indicates expanded disability scale; DIS, disease duration.

Brain atrophy, which is also frequently detected by MR from the earliest stages of MS, is associated with irreversible neurologic disability, including cognitive impairment.[11-14] Whole-brain atrophy has emerged as a clinically relevant component of disease progression, and results of several studies showed that this parameter correlates better with disability and, in particular, with cognitive impairment than with focal lesions.[15] Although most brain atrophy measurements are based on global or regional (gray and white matter) brain volume assessment, cortical thickness has recently emerged as a new way to assess cortical gray matter atrophy because decreased thickness is related to fatigue, disability in general, and cognitive impairment in particular.[13,16] This measurement seems to be dependent on focal white matter lesion volume,[17] but a potential relationship between the presence and location of demyelinating juxtacortical lesions (JLs) and cortical atrophy has not been elucidated. Therefore, the aim of this study was to explore the role of JLs on cortical atrophy and to investigate whether their presence is related to local cortical thinning in the early stages of MS.

MATERIALS AND METHODS

Patients

A sample of 91 consecutive patients with a clinically isolated syndrome (CIS) and 40 patients with relapsing-remitting MS (RRMS) who were undergoing brain MR imaging at Vall d'Hebron University Hospital for diagnostic purposes or monitoring disease evolution were included in the study. CIS is a clinical description, and many lesions may exist on MR imaging in these patients.[18] Patients with CIS were classified into 3 groups according to the presence of JLs and other typical demyelinating lesions on brain MR examination: no lesions (CISn, $n = 24$), only non-JLs (CISnj, $n = 33$), and with JLs plus non-JLs (CISj, $n = 34$). Patients with RRMS were divided into 2 groups (none of the patients with RRMS had normal MR images): with only non-JLs (RRnj, $n = 10$) and with JLs plus non-JLs (RRj, $n = 30$). None of the patients had only JLs in the absence of other typical MS lesions on MR imaging. The characteristics of the 5 groups are summarized in Table 1. The study was approved by the local ethics committee. Because the study was based on MR imaging data acquired in regular clinical practice, the need for written informed consent from the participants was waived.

MR Image Acquisition

Images were acquired on a 3T whole-body MR scanner (Tim Trio, Siemens; Erlangen, Germany) with a 12-channel phased-array head coil and a whole-body transmit coil. The standard MS protocol included (besides other sequences): 1) fast dual-echo T2-weighted transverse sequence (TR = 3080 milliseconds, $TE_1 = 21$ milliseconds, $TE_2 = 91$ milliseconds, voxel size = 0.78 × 0.78 × 3.0 mm^3); 2) transverse T2-FLAIR sequence (TR = 9000 milliseconds, TE = 87 milliseconds, TI = 2500 milliseconds, voxel size = 0.49 × 0.49 × 3.0 mm^3); and 3) sagittal 3D T1-weighted gradient-echo (MPRAGE) sequence (TR = 2300 milliseconds, TE = 3000 milliseconds, voxel size = 1.0 × 1.0 × 1.2 mm^3). Total scanning time for these sequences was 15 minutes.

Image Analysis

All supratentorial JLs were identified and manually delineated on T2-FLAIR images by using Jim software (http://www.xinapse.com/home.php). JL volume (JLV) was also calculated. To obtain JL probability maps, T2-FLAIR images and the corresponding lesion masks were normalized to the Montreal Neurological Institute template by using Statistical Parametric Mapping software (SPM8; Wellcome Department of Imaging Neuroscience, London, U.K.; http://www.fil.ion.ucl.ac.uk/spm/software/spm8). Once images and masks were spatially normalized, a mean image, which represents the JL probability map, was generated for the CIS and RRMS groups. A ROI for each brain lobe was delineated, based on the Automatic Anatomical Labeling set of ROIs.[19] The final ROI included gray and white matter. The percentage of JLs in each brain lobe relative to the total number of JLs in the whole brain was calculated and normalized to the ROI volume. White matter lesion volume (LV) was estimated for each patient by using the automated Lesion Segmentation Toolbox,[20] which obtains lesion masks and associated total LVs based on the T2-FLAIR and 3D T1-weighted images. Toolbox parameters had been optimized previously for the 2D T2-FLAIR images included in this cohort.[21] Cortical thickness was measured in single time points with MPRAGE images by using the FreeSurfer program suite (version 5.1; http://surfer.nmr.mgh.harvard.edu/).[10] Briefly, white matter points are chosen based on their locations in the Talairach space as well as on their intensity and the local neighborhood intensities. Voxels are then classified as white matter or something other than white matter based on intensity and neighbor constraints. Cutting planes are chosen to separate the hemispheres from each other. An initial surface is then generated for each hemisphere by tiling the outside of the white matter mass for that hemisphere. This initial surface is then refined to follow the intensity gradients between the white and gray matter (this is referred to as the white surface). The white surface is then nudged to follow the intensity gradients between the gray matter and CSF (this is the pial surface). The distance between the white and the pial surface gives us the thickness at each location of cortex.[22,23] Subcortical gray matter volume measurements were also obtained as part of the established pipeline.[22,23] Estimated subcortical gray matter volumes were multiplied by 100 and divided by the corresponding estimated total intracranial volume obtained for each subject. Finally, the FreeSurfer output segmentations were carefully reviewed, particularly checking for accuracy at the sites where JLs occurred. Cortical thickness was estimated in the whole brain, lobes, and regions, and at the vertex level in each patient. The mean cortical thickness value for each lobe was the average of values obtained for various FreeSurfer parcellations as follows—frontal lobe: caudal anterior cingulate, caudal middle frontal, isthmus cingulate, lateral orbitofrontal, medial orbitofrontal, paracentral, pars opercularis, pars orbitalis, pars triangularis, pre-

central, rostral anterior cingulate, superior frontal, and frontal pole; parietal lobe: inferior parietal, pericalcarine, postcentral, posterior cingulate, precuneus, and supramarginal; temporal lobe: banks of superior temporal sulcus, fusiform, entorhinal, inferior temporal, middle temporal, parahippocampal, superior temporal, temporal pole, and transverse temporal; and occipital lobe: cuneus, lateral occipital, and lingual; and insula.

Statistical Analysis

Whole white matter LV and JLV and distribution were compared across groups by means of 1-way ANOVA by using the factor group, followed by pair-wise Bonferroni post hoc comparison to account for multiple comparisons.

Differences in cortical thickness between the groups were assessed at 3 different levels: by using the global values; by using values after the parcellation process; and, at the vertex level, by using the cortical thickness map. First, differences between the left and right hemispheres were tested by 1-way ANOVA by using the factor hemisphere, followed by post hoc Bonferroni comparison. Then, the cortical thickness values obtained were compared across groups by 1-way ANOVA, followed by pair-wise Bonferroni post hoc comparison. As to the vertex level comparison, statistical difference maps (between patients with CISnj and patients with CISj, and RRnj and RRj) were generated based on general linear model analysis by using the FreeSurfer QDEC tool.

In the estimation of subcortical gray matter volumes, the right-left difference was assessed by 1-way ANOVA with the factor hemisphere. Differences in subcortical gray matter volumes were compared across groups by 1-way ANOVA with the factor group, followed by pair-wise Bonferroni post hoc comparison.

Finally, to assess which disease burden–related parameter (presence of JL, JLV, or LV) was more relevant in the cortical thickness measurements, 3 multivariate models were tested by using the presence of JL, JLV, or white matter LV, as independent variables. The 3 models included age and sex as covariates. Significance was set at $P < .05$.

RESULTS

Whole White Matter Lesion Volume

The mean LV in the various patient groups is reported in Table 1. The rank order was CISnj < RRnj < CISj < RRj. The between-group differences in LV were significant ($P < .001$), and statistically significant differences were observed for the following post hoc comparisons ($P < .002$): RRj > RRnj, RRj > CISj, RRj > CISnj, and CISj > CISnj.

Juxtacortical Lesion Volume and Distribution, and Probability Maps

Mean JLV was 1.28 mL (range, 0.03–14.14 mL) in patients with CIS, and 3.41 mL (range, 0.10–22.70 mL) in those with RRMS. The absolute JLV was greater at the frontal lobe, followed by the parietal, temporal, and occipital lobe, and insula in both CIS and RRMS (Table 2). The calculation of JLV relative to the total volume of each lobe in patients with CIS showed that the insula had the highest volume of JLs per volume of lobe, followed by the temporal, parietal, frontal, and occipital lobes. The rank order for RRMS was insula, followed by temporal, frontal, parietal, and occipital (Table 2).

Global and Lobar Cortical Thickness

In general, the lowest cortical thickness was measured in patients with RRj, followed by CISj, RRnj, CISnj, and CISn at both global and lobar levels (Table 3). The percentage difference between CISn and RRj ranged from 0% (insula) to 4%–4.5% (occipital, temporal, and parietal lobes). Regions with the highest attenuation of JL do not correspond to the ones with the largest thickness loss. A visual comparison of the lobar cortical thickness loss (mean of the right and left hemispheres) in RRj compared with

Table 2: Distribution of JLs[a]

Lobe	LPMvol CIS, no. (%)	LPMρ CIS, %	LPMvol RRMS, no. (%)	LPMρ RRMS, %
Frontal	11.6 (39.3)	1.7	27.0 (46)	4.0
Insula	1.3 (4.5)	5.0	1.9 (3.2)	7.0
Parietal	7.7 (26.2)	2.0	14.2 (24.3)	3.7
Temporal	7.7 (26.12)	2.6	13.9 (23.8)	4.7
Occipital	1.1 (3.9)	0.7	1.6 (2.8)	0.9

Note:—LPM indicates lesion probability map; LPMvol, absolute volume in milliliters of JL per lobe (percentage of global JL volume); LPMρ, percentage of JL volume relative to lobe volume.

[a] Total JLV (LPMvol) in milliliters (percentage relative to global amount), and percentage relative to lobe volume in patients with CIS and patients with RRMS.

Table 3: Global and lobar mean cortical thickness (in mm) for the groups studied

Lobe	*P* Value (Factor Group)[a]	CISn	CISnj	CISj	RRnj	RRj	*P* Value (R vs L)[b]
Global_R	.064	2.50 (0.13)[c]	2.47 (0.09)	2.44 (0.16)	2.47 (0.09)	2.40 (0.13)	.806
Global_L	.074	2.50 (0.13)	2.48 (0.19)	2.45 (0.16)	2.49 (0.09)	2.41 (0.13)	
Frontal_R	.389	2.55 (0.16)	2.53 (0.16)	2.51 (0.16)	2.55 (0.11)	2.49 (0.11)	.006
Frontal_L	.424	2.52 (0.17)	2.47 (0.11)	2.46 (0.15)	2.50 (0.13)	2.46 (0.12)	
Insula_R	.944	3.01 (0.16)	3.04 (0.14)	3.02 (0.25)	2.99 (0.15)	3.03 (0.13)	.711
Insula_L	.881	3.05 (0.19)	3.05 (0.14)	3.01 (0.24)	3.03 (0.16)	3.02 (0.15)	
Parietal_R	.056	2.22 (0.11)[c]	2.17 (0.07)	2.15 (0.17)	2.19 (0.08)	2.12 (0.13)	.414
Parietal_L	.025	2.22 (0.11)[c]	2.20 (0.09)	2.17 (0.17)	2.21 (0.09)	2.12 (0.14)	
Temporal_R	.119	2.93 (0.14)	2.90 (0.17)	2.87 (0.21)	2.91 (0.21)	2.80 (0.21)	.002
Temporal_L	.084	3.01 (0.14)	2.97 (0.16)	2.94 (0.20)	2.96 (0.16)	2.88 (0.19)	
Occipital_R	.014	2.29 (0.14)	2.30 (0.11)[c]	2.24 (0.17)	2.29 (0.12)	2.19 (0.14)	.224
Occipital_L	.047	2.30 (0.13)	2.31 (0.09)[c]	2.28 (0.13)	2.29 (0.11)	2.22 (0.15)	

Note:—R indicates right hemisphere; L, left hemisphere. Numbers in parentheses are the SD.

[a] *P* value of the 1-way ANOVA test with group as a factor.

[b] *P* value of the hemisphere effect (R vs L hemispheres values).

[c] $P < .05$ compared with RRj.

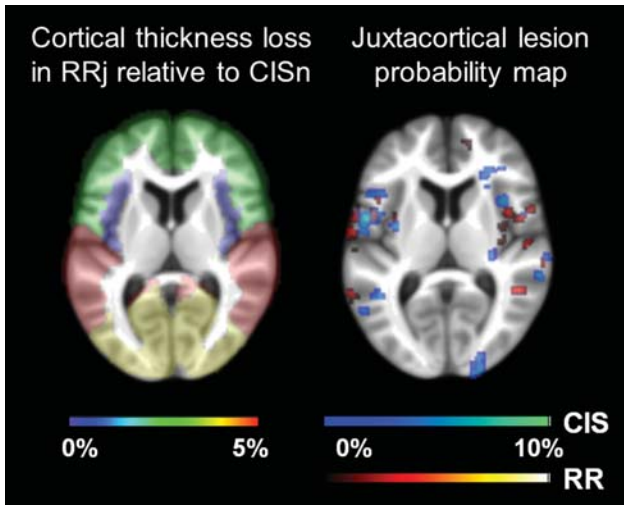

FIG 1. Percentage cortical thickness loss in RRj relative to CISn for the different brain lobes (frontal, insula, parietal, temporal, and occipital). Values were color-coded and ranged from 0%–5%. Juxtacortical lesion probability map (right) for patients with CIS (cold scale) and patients with RRMS (warm scale), scaled to the maximum value (10%). Results were overlaid on the mean filled structural image of the whole cohort studied.

CISnj and the JL probability map (of patients with CIS and patients with RRMS) can be seen in Fig 1.

On multivariate analysis of global values, the presence of JLs was significant (P, adjusted R^2) in the right (.004, 0.166) and left (.005, 0.165) hemispheres, JLV was significant in the right hemisphere (.033, 0.303), and LV was significant in the left hemisphere (.039, 0.646). Lobar analysis showed that insular cortical thickness was not related with the presence of JLs, JLV, or LV, in either hemisphere. The (P, adjusted R^2) right frontal (.048, 0.145; .043, 0.639), right parietal (.005, 0.156; .020, 0.696), and right occipital (.000, 0.157; .007, 0.753) lobes showed a significant association with the presence of JLs or LV. JLV was significant in the right parietal (.018, 0.327) and right occipital (.011, 0.315) lobes. Left frontal cortical thickness was not associated with any of the factors; left temporal lobe thickness was associated with the presence of JLs (P, adjusted R^2) (.009, 0.114) and in left parietal (.002, 0.166; .035, 0.649; .005, 0.368) and left occipital lobules (.004, 0.146; .038, 0.639; .001, 0.417), thickness was associated with the 3 factors (presence JLs, LV, JLV).

Regional Cortical Thickness

Results at a regional level were along the same lines as the ones obtained at a global and lobar level, with the group RRj showing the thinnest cortical thickness, followed by CISj, RRnj, CISnj, and CISn. Significant (post hoc) comparisons indicate that CISn measured cortical thickness was greater compared with RRj in the following regions (by following FreeSurfer nomenclature): right cuneus, right entorhinal, right and left fusiform, right inferior parietal, right lateral occipital, right and left precuneus, and left paracentral. Another (post hoc) comparison that was significant was CISnj over RRj in the right cuneus, right lateral occipital, left isthmus cingulate, left paracentral, and left transverse temporal areas. In addition, RRj showed a significant cortical thinning compared with CISj in the left banks of superior temporal sulcus and left paracentral regions. Finally, cortical thickness for CISnj was significantly thinner compared with CISn at the right frontal pole.

Cortical Thickness and Juxtacortical Lesion Location

Only patients with JLs (CISj and RRj) were included in this subanalysis. The regions analyzed were those in which a JL had been detected in at least 9 patients: banks of superior temporal sulcus, fusiform, inferior temporal, insula, postcentral, rostral middle frontal, superior frontal, superior temporal, and temporal pole. In separate analyses of the CIS and RRMS groups, the mean cortical thickness in each selected region was compared between patients with and without JLs (2-sample t test). In the RRMS group alone, a nonsignificant trend to decreased cortical thickness in the superior frontal region was seen in patients with JLs ($P = .079$). Finally, to visually check whether changes in cortical thickness showed co-localization with JLs, a binary mask of the JL probability map was transferred to the inflated brain representation and overlaid onto the corresponding contrast (CISnj > CISj with the CIS map, and RRnj > RRj with the RRMS map). On visual inspection, cortical thickness changes were not found to co-localize with JL probability maps (Figs 2 and 3).

Subcortical Gray Matter Volume Changes and Presence of Juxtacortical Lesions

The estimated total intracranial volume did not differ between groups: mean (SD) CISn = 1337.73 ± 189.85 mL, CISnj = 1331.71 ± 192.74 mL, CISj = 1381.25 ± 173.46 mL, RRnj = 1363.95 ± 190.06 mL, and RRj = 1392.59 ± 184.77 mL. Subcortical gray matter volumes in all the structures analyzed were lower in patients with RRj (Table 4). Volume loss ranged from 8% (caudate) to almost 20% (accumbens) when compared with CISnj. The largest right-to-left asymmetry was found in the pallidum (ratio, 0.87–0.92), followed by the putamen (0.94–0.98). The caudate was also significantly asymmetrical, though in the opposite direction: right-to-left ratio ranged between 1.03 and 1.06.

On multivariate analysis, the presence of JLs was a significant variable in the right thalamus (P, adjusted R^2) (.000, 0.130), left thalamus (.001, 0.120), right caudate (.000, 0.135), left caudate (.000, 0.152), right putamen (.000, 0.162), left putamen (.000, 0.147), left pallidum (.000, 0.145), right hippocampus (.020, 0.124), left hippocampus (.046, 0.127), right amygdala (.004, 0.081), right accumbens (.000, 0.171) and left accumbens (.000, 0.120); JLV and LV did not reach significance in any region.

DISCUSSION

This study investigated, for the first time, the association between the presence and topography of JLs and cortical thinning, and subcortical gray matter volume measurements in patients with CIS and patients with RRMS.

Patients with RRMS had a larger number of JLs than patients with CIS. In the cohort studied, the JL volume in patients with RRMS was twice the volume seen in patients with CIS, but JL brain distribution was similar in the 2 patient populations. Most JLs were located in the frontal lobe, followed by the parietal, temporal, and occipital lobes, a distribution that is similar to the reported distribution of pure cortical lesions in RRMS.[24,25] When

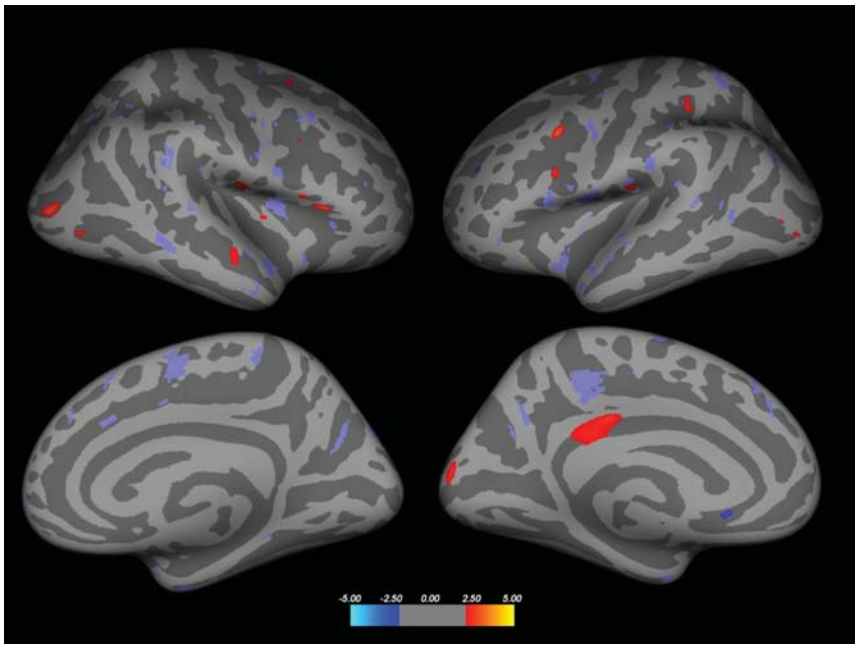

FIG 2. Inflated brain, displaying areas of reduced cortical thickness (red areas) in CISj compared with CISnj (significance level $P < .01$ for display purposes). Blue areas indicate regions where cortical thickness in CISnj is reduced compared with CISj. The CIS JL lesion probability map was overlaid in purple (right column, left hemisphere; left column, right hemisphere; superior row, lateral view; inferior row, medial view). The JL lesion probability map is a binary mask for display purposes. No overlap was seen between the areas, showing significant changes in thickness and the JL lesion probability map.

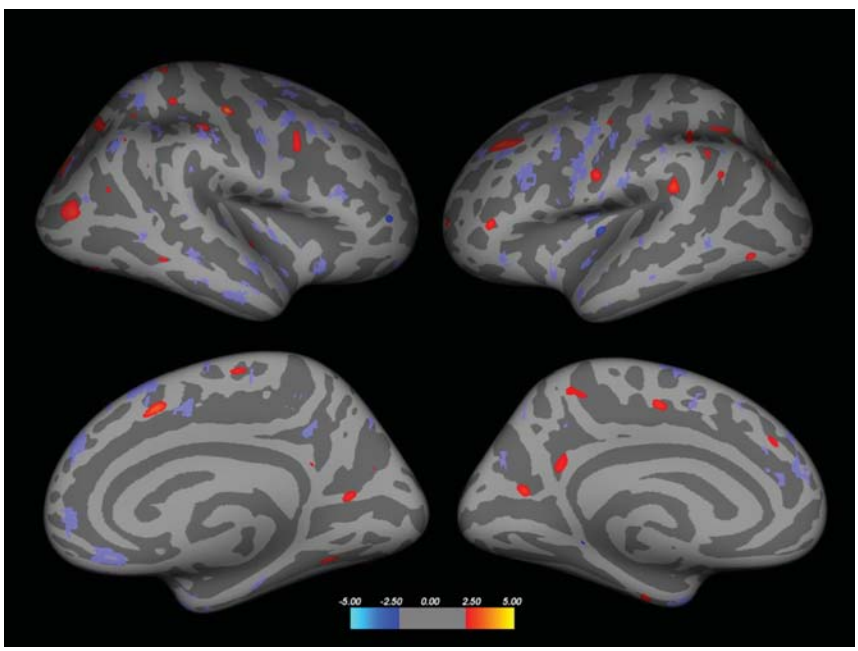

FIG 3. Inflated brain displaying areas of reduced cortical thickness (red areas) in RRj compared with RRnj (significance level $P < .01$, for display purposes). Blue areas indicate regions in which cortical thickness in RRnj is reduced compared with RRj. The RR JL lesion probability map was overlaid in purple (right column, left hemisphere; left column, right hemisphere; superior row, lateral view; inferior row, medial view). The JL lesion probability map was a binary mask, just for display purposes. No overlap was seen between the areas showing significant changes in thickness and the JL lesion probability map.

JLVs were normalized by the lobe volume, the insula appeared to be the region with the highest attenuation of JLs, followed by the temporal, parietal, and frontal lobes. The LV was higher in patients with RRj, but the value in RRnj was even lower than in CISj, though the differences were not significant. These results may indicate that JL accumulation is not disconnected from accumulation of lesions in other areas of the brain and that they both are part of the same disease process regardless of disease stage.

The RRj group was found to have the greatest global and regional cortical thinning in areas of the temporal, parietal, and occipital lobe. The most marked thickness loss (RRj compared with CISn) was in the right entorhinal cortex (8%), in line with the findings of Narayana et al.[26] Entorhinal thinning is considered a predictor of cognitive decline in Alzheimer disease.[27] Our study did not include a neuropsychological evaluation; therefore, we could not analyze the value of entorhinal atrophy for predicting cognitive decline in our patients with MS. When following the entorhinal cortex, we found greater thinning at the right precuneus and cuneus (6%). Decreases in the remaining regions of the right brain hemisphere and all regions of the left brain hemisphere ranged from 3% to 5%. The precuneus and fusiform were the only regions that showed bilateral cortical thinning.

Our results also indicated that cortical thinning was more closely associated with the presence of JLs than with total LV or JL volume, though LV was <10 mL in 90% of patients. Results of studies reported to date, including LV as a variable, are not conclusive because the threshold value used to define high and low LV has not been established univocally.[12,14] In a previous study by Charil et al,[17] the frontal, insula, and temporal regions showed the most marked cortical thinning, and cortical atrophy correlated with lesion load.

Visual inspection of JL probability maps overlaid onto the cortical change maps of the 2 hemispheres showed no overlapping in either patients with CIS or those with RRMS. A more detailed subanalysis of this aspect confirmed that differences in cortical thickness were not directly related to the presence of JLs in any specific region, which indicates that cortical thinning in MS is not closely dependent on the topography of JLs. This discrepancy may arise from the fact that only a percentage of JLs and a minority of intracortical lesions are visible

Table 4: Subcortical gray matter volumes percentage relative to total intracranial volume for the groups studied

Subcortical Gray Matter	*P* Value (Factor Group)[a]	CISn[g]	CISnj[g]	CISj[g]	RRnj[g]	RRj[g]	*P* Value (R vs L)[b]
Thal_R	.000	0.502 (0.041)[f]	0.486 (0.060)[e]	0.473 (0.058)[e]	0.477 (0.092)	0.424 (0.064)	.986
Thal_L	.003	0.492 (0.042)[e]	0.485 (0.053)[e]	0.474 (0.062)	0.476 (0.010)	0.432 (0.066)	
Pallidum_R	.029	0.115 (0.013)[c]	0.114 (0.016)[d]	0.109 (0.015)	0.110 (0.017)	0.103 (0.017)	.000
Pallidum_L	.003	0.132 (0.018)[e]	0.129 (0.017)[d]	0.118 (0.023)	0.124 (0.027)	0.113 (0.021)	
Caudate_R	.069	0.277 (0.037)	0.278 (0.036)	0.257 (0.041)	0.271 (0.052)	0.256 (0.035)	.015
Caudate_L	.025	0.268 (0.036)	0.266 (0.034)	0.247 (0.037)	0.259 (0.043)	0.242 (0.038)	
Putamen_R	.009	0.428 (0.037)[d]	0.427 (0.074)[d]	0.408 (0.072)	0.410 (0.085)	0.369 (0.072)	.020
Putamen_L	.002	0.452 (0.042)[e]	0.452 (0.069)[e]	0.428 (0.081)	0.430 (0.082)	0.384 (0.073)	
Accum_R	.001	0.054 (0.011)[d]	0.056 (0.011)[e]	0.052 (0.009)	0.057 (0.012)[d]	0.045 (0.013)	.745
Accum_L	.002	0.053 (0.007)	0.058 (0.012)[e]	0.052 (0.009)	0.054 (0.010)	0.047 (0.010)	
Hippo_R	.064	0.305 (0.026)	0.315(0.041)[d]	0.306 (0.040)	0.306 (0.053)	0.283 (0.053)	.393
Hippo_L	.121	0.301 (0.026)	0.308 (0.041)	0.303 (0.037)	0.294 (0.056)	0.282 (0.044)	
Amygdala_R	.005	0.129 (0.017)	0.140 (0.023)[e]	0.128 (0.020)	0.131 (0.025)	0.119 (0.024)	.440
Amygdala_L	.158	0.126 (0.020)	0.134 (0.021)	0.129 (0.019)	0.128 (0.021)	0.120 (0.028)	

Note:—Thal indicates thalamus; R, right; L, left; Accum, accumbens; Hippo, hippocampus.
[a] *P* value of the 1-way ANOVA test with group as a factor.
[b] *P* value of the hemisphere effect (R vs L hemispheres values).
[c] $P = .059$.
[d] $P < .05$.
[e] $P < .01$.
[f] $P < .001$ compared with RRj.
[g] Data are expressed as mean (SD).

on conventional MR imaging (mainly because of their size), though those that are seen highly correlate with the overall number of cortical lesions detected on a histopathologic study.[27] A study published by Bakshi et al[28] found the there was a correlation between the number of cortical and juxtacortical lesions for a given region and the cortical atrophy measured in that region. Discrepancy may arise again from the fact that we evaluated the presence and volume (not the number) of juxtacortical lesions, which actually represent a small percentage compared with cortical lesions.

In the present study, the volume of subcortical gray matter structures was systematically smaller in patients with RRj than in patients with CISn. Although the volume of subcortical gray matter structures in RRnj was systematically larger than in CISj, this post hoc comparison was not significant in any of the structures analyzed. A recent study that compared subcortical gray matter volumes between CIS and early RRMS[14] also showed that early RRMS volumes were smaller compared with CIS and that differences were significant in some regions (caudate, putamen, thalamus) but not in others (amygdala, accumbens); this was in contrast with the absence of differences in cortical structures. However, these findings were not stratified by the presence of cortical lesions or JL. In this regard, results from our multivariate analysis indicated that the presence of JL was associated with the volume of a number of subcortical structures, whereas JLV and LV were not.

Taken together, the results reported here would indicate that the presence of JL could be used as a marker of diffuse gray matter damage; it could be speculated that the appearance of JLs is the by-product of the damaging pathologic process ongoing in gray matter of people with MS and not the other way around (JLs and locally related cortical lesions being the main cause of damage to gray matter). This hypothesis should be tested in future studies.

The limitations of our study include the small size of the RRnj group; this is because few patients with RRMS exclusively have lesions other than JLs. Another limitation is that the presence of both JL and JLV were colinear with the LV, and we were not able to add the LV as a covariate in the statistical analysis. The lack of a control group of healthy subjects was also a limitation of the study because comparisons with normative values would be of great interest. Further studies with a larger group and a paired control group would be needed to confirm the main findings of our work. In addition, identification of JLs was based on visual inspection by using conventional T2-FLAIR sequences, which may have underestimated the number of these lesions. The partial volume effect could also play a role, which affected the visualization of the lesions in the axial images. Cortical lesions are abundantly present in MS and are better detected with dedicated pulse sequences, such as double inversion recovery, phase-sensitive inversion recovery, and high-resolution 3D MPRAGE.[3,29-34] Imaging of cortical lesions at standard clinical field strength remains suboptimal even when combinations of these sequences (double inversion recovery, phase-sensitive inversion recovery, and MPRAGE) are used because of limitations in the associated sensitivity and reproducibility.[35,36] Thus, although these sequences have made a major contribution in detecting focal cortical lesions in patients with MS and have provided important insights about cortical abnormalities and their association with clinical disability and cognitive impairment in all MS subtypes, substantial research efforts are needed before they can be used in the diagnostic imaging work-up in clinical practice. Finally, the local and individual effect of brain juxtacortical lesions on cortical thickness measurements should also be closely studied.

CONCLUSIONS

Cortical thinning and subcortical gray matter volume loss in patients with CIS or RRMS was related to the presence of JLs, though the cortical areas with the most marked thinning did not correspond to those with the largest number of JLs, which may indicate that visible focal JLs do not completely explain, but might be used as markers of the diffuse gray matter damage that is already present in the early phases of MS.

ACKNOWLEDGMENTS

We thank the "Red Española de Esclerosis Múltiple)" (RD07/0060; RD12/0032), which is sponsored by the Fondo de Investigación Sanitaria, the Instituto de Salud Carlos III, the Ministry of Economy and Competitiveness in Spain, and the "Ajuts per donar Suport als Grups de Recerca de Catalunya (2009 SGR 0793)," which is sponsored by the "Agència de Gestió d'Ajuts Universitaris i de Recerca" of the Generalitat de Catalunya in Spain.

Disclosures: Jaume Sastre-Garriga—*UNRELATED*: *Consultancy*: Almirall; *Grants/Grants Pending*: Genzyme; *Payment for Lectures (including service on speakers bureaus)*: Genzyme, Merck-Serono, Novartis, Teva, Biogen; *Payment for Development of Educational Presentations*: Novartis; *Travel/Accommodations/Meeting Expenses Unrelated to Activities Listed*: Novartis. Cristina Auger—*UNRELATED*: *Payment for Lectures (including service on speakers bureaus)*: Novartis. Mar Tintoré—*UNRELATED*: *Board Membership*: Biogen, Genzyme, TEVA; *Grants/Grants Pending*: Biogen,* Novartis*; *Payment for Lectures (including service on speakers bureaus)*: Biogen, Genzyme, TEVA, Novartis, Merk, Bayer. Xavier Montalban—*UNRELATED*: *Consultancy*: Actelion, Almirall, Bayer, Biogen Idec, Genzyme, GlaxoSmithKline, Merck, Novartis, Sanofi-Genzyme, Roche, Teva. Alex Rovira—*UNRELATED*: *Board Membership*: Genzyme, Novartis, Biogen, OLEA; *Payment for Lectures (including service on speakers bureaus)*: Novartis, Stendhal, Biogen, Genzyme, Olea, Bracco, Bayer. *Money paid to the institution.

REFERENCES

1. Filippi M, Rocca MA, Barkhof F, et al. **Association between pathological and MRI findings in multiple sclerosis.** *Lancet Neurol* 2012;11:349–60 CrossRef Medline
2. Kutzelnigg A, Lucchinetti CF, Stadelmann C, et al. **Cortical demyelination and diffuse white matter injury in multiple sclerosis.** *Brain* 2005;128:2705–12 CrossRef Medline
3. Geurts JJ, Pouwels PJ, Uitdehaag BM, et al. **Intracortical lesions in multiple sclerosis: improved detection with 3D double inversion-recovery MR imaging.** *Radiology* 2005;236:254–60 CrossRef Medline
4. Geurts JJ, Blezer EL, Vrenken H, et al. **Does high-field MR imaging improve cortical lesion detection in multiple sclerosis?** *J Neurol* 2008;255:183–91 CrossRef Medline
5. Wegner C, Esiri MM, Chance SA, et al. **Neocortical neuronal, synaptic, and glial loss in multiple sclerosis.** *Neurology* 2006:67;960–67 CrossRef
6. Calabrese M, Favaretto A, Martini V, et al. **Grey matter lesions in MS: from histology to clinical implications.** *Prion* 2013;7:20–7 CrossRef Medline
7. Roosendaal SD, Moraal B, Pouwels PJ, et al. **Accumulation of cortical lesions in MS: relation with cognitive impairment.** *Mult Scler* 2009;15:708–14 CrossRef Medline
8. Calabrese M, Rocca MA, Atzori M, et al. **A 3-year magnetic resonance imaging study of cortical lesions in relapse-onset multiple sclerosis.** *Ann Neurol* 2010;67:376–83 CrossRef Medline
9. Calabrese M, Favaretto A, Poretto V, et al. **Low degree of cortical pathology is associated with benign course of multiple sclerosis.** *Mult Scler* 2013;19:904–11 CrossRef Medline
10. Filippi M, Rocca MA, Horsfield MA, et al. **Imaging cortical damage and dysfunction in multiple sclerosis.** *JAMA Neurol* 2013;70:556–64 CrossRef Medline
11. Audoin B, Zaaraoui W, Reuter F, et al. **Atrophy mainly affects the limbic system and the deep grey matter at the first stage of multiple sclerosis.** *J Neurol Neurosurg Psychiatry* 2010;81:690–95 CrossRef Medline
12. Sailer M, Fischl B, Salat D, et al. **Focal thinning of the cerebral cortex in multiple sclerosis.** *Brain* 2003;126:1734–44 CrossRef Medline
13. Calabrese M, Rinaldi F, Mattisi I, et al. **The predictive value of gray matter atrophy in clinically isolated syndromes.** *Neurology* 2011;77:257–63 CrossRef Medline
14. Bergsland N, Horakova D, Dwyer MG, et al. **Subcortical and cortical gray matter atrophy in a large sample of patients with clinically isolated syndrome and early relapsing-remitting multiple sclerosis.** *AJNR Am J Neuroradiol* 2012;33:1573–78 CrossRef Medline
15. Bermel RA, Bakshi R. **The measurement and clinical relevance of brain atrophy in multiple sclerosis.** *Lancet Neurol* 2006;5:158–70 CrossRef Medline
16. Ramasamy DP, Benedict RH, Cox JL, et al. **Extent of cerebellum, subcortical and cortical atrophy in patients with MS: a case-control study.** *J Neurol Sci* 2009;282:47–54 CrossRef Medline
17. Charil A, Dagher A, Lerch JP, et al. **Focal cortical atrophy in multiple sclerosis: relation to lesion load and disability.** *Neuroimage* 2007;34:509–17 CrossRef Medline
18. Miller DH, Chard DT, Ciccarelli O. **Clinically isolated syndromes.** *Lancet Neurol* 2012;11:157–69 CrossRef Medline
19. Tzourio-Mazoyer N, Landeau B, Papathanassiou D, et al. **Automated anatomical labeling of activations in SPM using a macroscopic anatomical parcellation of the MNI MRI single-subject brain.** *Neuroimage* 2002;15:273–89 CrossRef Medline
20. Schmidt P, Gaser C, Arsic M, et al. **An automated tool for detection of FLAIR-hyperintense white-matter lesions in multiple sclerosis.** *Neuroimage* 2012;59:3774–83 CrossRef Medline
21. Pareto D, Sastre-Garriga J, Tintore M, et al. **Grey and white matter segmentation in multiple sclerosis patients: correcting lesion misclassification with the lesion segmentation toolbox (LST).** *Mult Scler* 2013;19:(S1)410
22. Dale AM, Fischl B, Sereno MI. **Cortical surface-based analysis. I. Segmentation and surface reconstruction.** *Neuroimage* 1999;9:179–94 CrossRef Medline
23. Fischl B, Dale AM. **Measuring the thickness of the human cerebral cortex from magnetic resonance images.** *Proc Natl Acad Sci U S A* 2000;97:11050–55 CrossRef Medline
24. Battaglini M, Calabrese M, Stromillo ML, et al. **Similar cortical lesion distribution and cortical atrophy location in patients with relapsing-remitting multiple sclerosis.** *Mult Scler* 2010;16:S197–352
25. Calabrese M, Battaglini M, Giorgio A, et al. **Imaging distribution and frequency of cortical lesions in patients with multiple sclerosis.** *Neurology* 2010;75:1234–40 CrossRef Medline
26. Narayana PA, Govindarajan KA, Goel P, et al. **Regional cortical thickness in relapsing remitting multiple sclerosis: a multi-center study** *Neuroimage Clin* 2012;2:120–31 CrossRef Medline
27. Velayudhan L, Proitsi P, Westman E, et al. **Entorhinal cortex thickness predicts cognitive decline in Alzheimer's disease.** *J Alzheimers Dis* 2013;33:755–66 CrossRef Medline
28. Bakshi R, Ariyaratana S, Benedict RH, et al. **Fluid-attenuated inversion recovery magnetic resonance imaging detects cortical and juxtacortical multiple sclerosis lesions.** *Arch Neurol* 2001;58:742–48 Medline
29. Seewann A, Vrenken H, Kooi EJ, et al. **Imaging the tip of the iceberg: visualization of cortical lesions in multiple sclerosis.** *Mult Scler* 2011;17:1202–10 CrossRef Medline
30. Sethi V, Yousry TA, Muhlert N, et al. **Improved detection of cortical MS lesions with phase-sensitive inversion recovery MRI.** *J Neurol Neurosurg Psychiatry* 2012;83:877–82 CrossRef Medline
31. Calabrese M, De Stefano N, Atzori M, et al. **Detection of cortical inflammatory lesions by double inversion recovery magnetic resonance imaging in patients with multiple sclerosis.** *Arch Neurol* 2007;64:1416–22 CrossRef Medline
32. Wattjes MP, Lutterbey GG, Gieseke J, et al. **Double inversion recovery brain imaging at 3T: diagnostic value in the detection of multiple sclerosis lesions.** *AJNR Am J Neuroradiol* 2007;28:54–59 Medline
33. Simon B, Schmidt S, Lukas C, et al. **Improved in vivo detection of cortical lesions in multiple sclerosis using double inversion recovery MR imaging at 3 Tesla.** *Eur Radiol* 2010;20:1675–83 CrossRef Medline
34. Nelson F, Poonawalla A, Hou P, et al. **3D MPRAGE improves classification of cortical lesions in multiple sclerosis.** *Mult Scler* 2008;14:1214–19 CrossRef Medline
35. Geurts JJ, Roosendaal SD, Calabrese M, et al. **Consensus recommendations for MS cortical lesion scoring using double inversion recovery MRI**. *Neurology* 2011;76:418–24 CrossRef Medline
36. Sethi V, Muhlert N, Ron M, et al. **MS cortical lesions on DIR: not quite what they seem?** *PLoS One* 2013;8:e78879 CrossRef Medline

Responses of the Human Brain to Mild Dehydration and Rehydration Explored In Vivo by ^{1}H-MR Imaging and Spectroscopy

A. Biller, M. Reuter, B. Patenaude, G.A. Homola, F. Breuer, M. Bendszus, and A.J. Bartsch

ABSTRACT

BACKGROUND AND PURPOSE: As yet, there are no in vivo data on tissue water changes and associated morphometric changes involved in the osmo-adaptation of normal brains. Our aim was to evaluate osmoadaptive responses of the healthy human brain to osmotic challenges of de- and rehydration by serial measurements of brain volume, tissue fluid, and metabolites.

MATERIALS AND METHODS: Serial T1-weighted and ^{1}H-MR spectroscopy data were acquired in 15 healthy individuals at normohydration, on 12 hours of dehydration, and during 1 hour of oral rehydration. Osmotic challenges were monitored by serum measures, including osmolality and hematocrit. MR imaging data were analyzed by using FreeSurfer and LCModel.

RESULTS: On dehydration, serum osmolality increased by 0.67% and brain tissue fluid decreased by 1.63%, on average. MR imaging morphometry demonstrated corresponding decreases of cortical thickness and volumes of the whole brain, cortex, white matter, and hypothalamus/thalamus. These changes reversed during rehydration. Continuous fluid ingestion of 1 L of water for 1 hour within the scanner lowered serum osmolality by 0.96% and increased brain tissue fluid by 0.43%, on average. Concomitantly, cortical thickness and volumes of the whole brain, cortex, white matter, and hypothalamus/thalamus increased. Changes in brain tissue fluid were related to volume changes of the whole brain, the white matter, and hypothalamus/thalamus. Only volume changes of the hypothalamus/thalamus significantly correlated with serum osmolality.

CONCLUSIONS: This is the first study simultaneously evaluating changes in brain tissue fluid, metabolites, volume, and cortical thickness. Our results reflect cellular volume regulatory mechanisms at a macroscopic level and emphasize that it is essential to control for hydration levels in studies on brain morphometry and metabolism in order to avoid confounding the findings.

ABBREVIATIONS: HCT = hematocrit; OSM_{serum} = serum osmolality

The regulation of body fluid balance inherently determines serum osmolality. Due to the high permeability of the cell membranes for water, the direction of water movement is determined by the osmotic gradient across the cell membrane between the intra- and extracellular space. Thus, serum hyperosmolality causes cell shrinkage, whereas hypo-osmolality induces cell swelling.

In response, the cell initiates regulatory changes to the opposite direction. Initially, cells quickly re-adjust their volume by transmembranous ion movements. Volume regulation by electrolyte shifts is limited because alterations of ion gradients across the cell membrane interfere with the structure and function of intracellular macromolecules and membrane transporters.[1-3] To avoid the adverse effects of changes in ion composition, the cell uses organic osmolytes, instead of ions, which allow volume adjustment without compromising cell function.[3-6] Organic osmolytes encompass polyalcohols like myo-inositol; methylamines like glycerylphosphocholine; amino acids[7]; and derivatives like glutamine, glutamate, *N*-acetylaspartate and *N*-acetyl aspartylglutamate, and creatine and taurine.[3,8,9]

Metabolic responses to fluid imbalance have primarily been

Received December 18, 2014; accepted after revision May 6, 2015.

From the Department of Neuroradiology (A.B., M.B., A.J.B.), University of Heidelberg, Heidelberg, Germany; Department of Radiology (M.R.), Massachusetts General Hospital/Harvard Medical School, Boston, Massachusetts; Martinos Center for Biomedical Imaging (M.R.), Charlestown, Massachusetts; Massachusetts Institute of Technology Computer Science and AI Lab (M.R.), Cambridge, Massachusetts; Department of Psychiatry and Behavioral Sciences (B.P.), Stanford University, Stanford, California; Department of Clinical Neurology (B.P., A.J.B.), FMRIB Centre, University of Oxford, Oxford, UK; Department of Neuroradiology (G.A.H., A.J.B.), University of Würzburg, Würzburg, Germany; and Research Center for Magnetic-Resonance-Bavaria (F.B.), Würzburg, Germany.

Please address correspondence to Armin Biller, MD, Department of Neuroradiology, University of Heidelberg, Im Neuenheimer Feld 400, 69120 Heidelberg, Germany; e-mail: armin.biller@med.uni-heidelberg.de

Indicates open access to non-subscribers at www.ajnr.org

Indicates article with supplemental on-line appendix and tables.

Indicates article with supplemental on-line photo.

http://dx.doi.org/10.3174/ajnr.A4508

studied in animals and patients with pathologies affecting serum osmolality. Previous brain morphometry findings in healthy subjects undergoing de- and rehydration have remained somewhat inconclusive and inconsistent in terms of the distribution of the changes and the structures affected. Kempton et al,[7,10] Dickson et al,[11] and Watson et al[12] induced dehydration by thermal exercises. They reported no significant effect of dehydration on brain volume. Results on ventricular volume ranged from decrease[12] to increase,[7,10] and Dickson et al found no changes.[11] Duning et al[13] showed a 0.55% brain volume reduction after 16 hours of thirsting and a 0.72% increase after subsequent rehydration. Similarly, Streitbürger et al[14] demonstrated an increase in brain volume on ingestion of 3–4 L of water; however, they failed to show an effect of dehydration on brain volume by 2 days of restricted water intake. In a study on ultramarathon runners, Freund et al[15] described a reversible 6% cortical volume reduction with 2 months of daily running. Currently, there are no in vivo data on tissue water changes and associated morphometric changes involved in the osmoadaptation of normal brains. In this study, we examined healthy individuals during normo-, de-, and rehydration by MR spectroscopy and morphometry and analyzed the resulting changes of global brain volume, gray/white matter volume, cortical thickness, tissue fluid, organic osmolytes, and serum parameters.

MATERIALS AND METHODS

Ethics Statement

The study was approved by the local Medical Ethics Committee (Faculty of Clinical Medicine, University of Würzburg), and all participants gave written informed consent before enrollment. The procedures that followed were in accordance with the Declaration of Helsinki.

Participants

We studied 15 healthy volunteers (6 women, 9 men) who received an allowance for participating in the study. Female and male participants exhibited a narrow age range (mean, 27.67 ± 2.26 years) and body weight (mean, 74.53 ± 12.01 kg), which did not differ across sexes ($P > .05$, Wilcoxon rank sum test). All subjects were nonsmokers and free of medication. Exclusion criteria were current or past substance abuse other than nicotine and any other psychiatric, neurologic, and medical illness.

MR Imaging

All measurements were performed on a 3T Tim Trio MR imaging system (Siemens, Erlangen, Germany) by using a transmit/receive head coil.

T1-Weighted 3D Imaging and Quantitative T1-Mapping. For volumetric and surface-based morphometry, an isotropic ($1.0 \times 1.0 \times 1.0$ mm^3) whole-brain T1-weighted MPRAGE sequence optimized for subsequent image data analysis was acquired (TR = 2300 ms; TE = 2.98 ms; magnetization preparation by nonselective inversion recovery TI = 900 ms; along with fat suppression/fast water excitation to reduce signal from fatty bone marrow, scalp, and dura; excitation flip angle = 9°; 160 sagittal slices; matrix size = 256 × 256).

For quantitative T1-relaxation-time mapping, a partial-brain FLASH (GE Healthcare, Milwaukee, Wisconsin) sequence (TR = 330 ms, TE = 1.8 ms, 22 axial slices, matrix size = 384 × 384, $0.5 \times 0.5 \times 3.0$ mm^3) was recorded at 2 flip angles (8° and 37°).

^{1}H-MR Spectroscopy. Localized ^{1}H-MR spectroscopy data were recorded by single-voxel spectroscopy measurements using a point-resolved spectroscopy sequence (TE = 30 ms, TR = 2000 ms). Automatic dynamic frequency correction was used for MR spectroscopy with least squares optimization across the main peaks of the water-suppressed spectra. For all subjects and each of the longitudinal point-resolved spectroscopy sequence measurements (compare "Protocol of Longitudinal Measurements"), a voxel volume of $20 \times 20 \times 20$ mm^3 placed in the left paracentral lobule was measured. As described earlier,[16-18] placing the voxel with its inferior edge at the callosomarginal sulcus and with its posterior edge at the central sulcus allowed highly reproducible positioning. Because the voxel was placed in white matter mainly (Fig 1) systematic differences between the partial volume contribution of white matter, gray matter, and CSF were excluded (ANOVA, $P > .23$). No partial volume correction was performed. In vivo resonance changes were quantified by ensuring fixed scanner calibration by using in vitro references and by correcting for differences in coil load. Spectra with and without chemical shift selective water suppression were obtained (80 versus 16 acquisitions) to allow eddy current correction and to quantify changes of brain tissue water in the point-resolved spectroscopy sequence voxel by using the spectra without water suppression.[19,20]

Protocol of Longitudinal Measurements

The study consisted of 2 MR imaging examinations measuring healthy volunteers on normo-, de-, and rehydration. The first examination studied the regularly hydrated participants, yielding a baseline ^{1}H-MR spectroscopy and 3D T1-weighted dataset (normohydration). Normohydration at the time of the first examination was confirmed by blood and serum parameters (Table). Then, subjects were asked not to drink, not to eat meals containing more than 0.5 L of fluid, and to refrain from physical activity for 12 hours (dehydration). Subsequently, MR imaging measurements of the second examination included a ^{1}H-MR spectroscopy and 3D T1-weighted dataset with subclinically dehydrated subjects. Participants then remained within the MR imaging scanner without being repositioned, and water was orally ingested via a plastic tube for 60 minutes at a rate of 1 L per hour (by using a MRidium MR imaging Infusion System; IRadimed, Winter Park, Florida) (rehydration). Simultaneously, 19 serial ^{1}H-MR spectroscopy datasets and 1 final 3D T1-weighted structural scan were recorded during 67 minutes 4 seconds ± 6 minutes 45 seconds. To control for circadian hormone effects, we scheduled the first MR image in the evening and the second in the morning of the following day for every participant.

For measuring serum parameters, 3 blood samples were drawn consecutively at normo-, de-, and rehydration via an antecubital IV line. Mean corpuscular hemoglobin concentration and hematocrit (HCT) values were determined by an automated counter using the electrical impedance method (Counter S-Plus IV; Beckmann Coulter, Fullerton, California).

Serum electrolytes were measured by a potentiometric autoanalyzer (Ektachem 700XRC; Eastman Kodak, Rochester, New

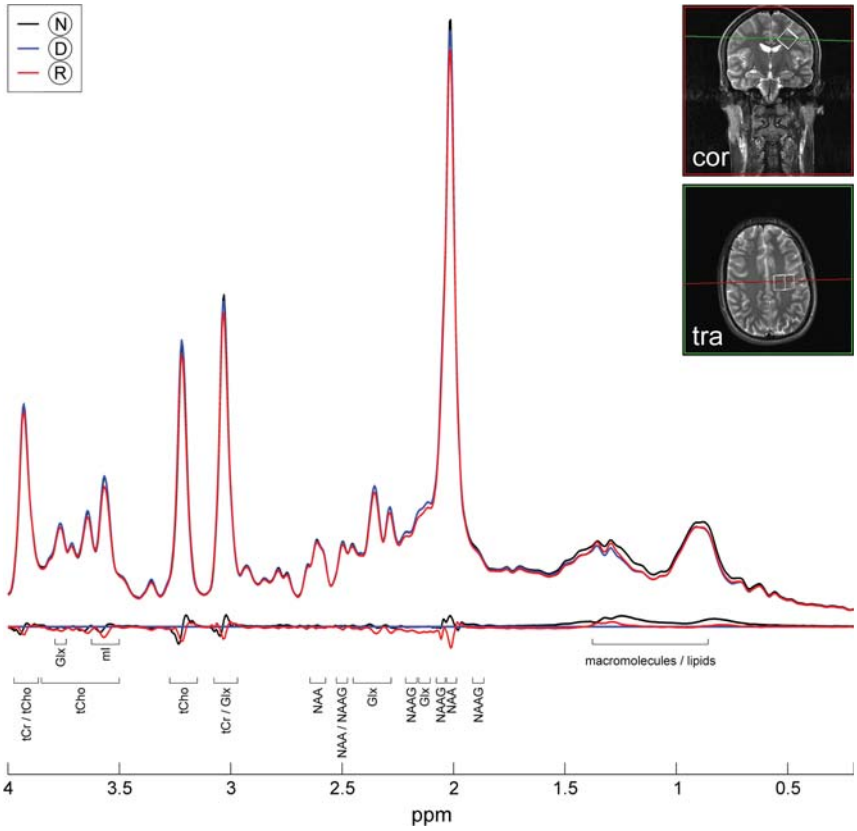

FIG 1. Representative ^{1}H-MR spectroscopy spectral data fits. The voxel was placed in the left paracentral lobule. Spectral data fits (*upper row*) and subtracted spectra (*lower row*) for visualization of metabolite resonances at normo- (*black line*, N), de- (*blue line*, D), and rehydration (*red line*, R). tCr indicates total creatine, mI, myo-inositol; tCho, total choline; NAA+NAAG, *N*-acetylaspartate and *N*-acetyl aspartylglutamate; Glx, glutamine + glutamate.

Blood/serum parameters during normo-, de-, and rehydration

Parameter	Normohyd	Dehyd	Rehyd
Na^+ (mmol/L)	137.1 ± 2.7	138.5 ± 2.2	136.9 ± 2.3
K^+ (mmol/L)	4.6 ± 0.4[a]	5.2 ± 0.6[a]	4.9 ± 0.4[a]
HCT (%)	41.9 ± 2.9	43.8 ± 2.9	42.5 ± 2.9
MCHC (g/dL)	34.3 ± 0.9	34.3 ± 0.8	34.3 ± 0.8
Urea (mg/dL)	27.4 ± 6.2	26.8 ± 5.9	25.5 ± 5.6
OSM_{serum} (mOsm/kg)	312.7 ± 4.8[a]	314.8 ± 4.1[a]	311.8 ± 4.7[a]
Glucose (mg/dL)	92.1 ± 6.8[a]	84.4 ± 6.9[a]	85.5 ± 5.9[a]

Note:—Normohyd indicates normohydration; Dehyd, dehydration; Rehyd, rehydration; MCHC, mean corpuscular hemoglobin concentration.

[a] Significant changes among different levels of hydration (normo-, de-, and rehydration) at type I error probabilities of $P < .05$ (1-sided t tests; $df = 14$).

York). Serum osmolality was assessed by a cryoscopic osmometer (Osmomat 030; Gonotec, Berlin, Germany), and dehydration was confirmed by an increase and rehydration by a decrease in osmolality. Blood glucose levels were determined by photometry (Helios Alpha; Spectronic Unicam, Cambridge, UK).

Data Postprocessing

MR Morphometry. Morphometric analyses were performed to detect changes of whole brain, white matter, subcortical and cortical gray matter volume, and cortical thickness. To extract reliable cortical volume and thickness estimates, we automatically processed images by using the longitudinal stream within FreeSurfer (Version 5.3.0; http://surfer.nmr.mgh.harvard.edu/).[21] For details, please see the On-line Appendix.

^{1}H-MR Spectroscopy. ^{1}H-MR spectroscopy data were analyzed by using the frequency-domain-fitting routine of LCModel (http://www.lcmodel.com/),[22] which computes in vivo spectra as a linear combination of complete model spectra of specific in vitro metabolites predefined in basis sets. These basis sets included spectral data of alanine, aspartate, creatine, glucose, γ-aminobutyric acid, glutamine, glutamate, scyllo-inositol, myo-inositol, *N*-acetylaspartate, *N*-acetyl aspartylglutamate, glycerylphosphocholine, phosphocholine, guanidinoacetate, lipids, and macromolecules. Representative spectral data fits for normo-, de-, and rehydration are shown in Fig 1. For fitting macromolecule resonances, LCModel integrates a priori knowledge on macromolecules on the basis of metabolite-nulled spectra at 3T (ie, macromolecule models are simulated).

On the basis of the principle of reciprocity,[23] differences in coil load were corrected for by dividing the measured metabolite resonances by the required voltage amplitude to obtain maximum signal.

The integral of unsuppressed water was used as a measure of brain tissue water (H_2O_{brain}). Data of each metabolite and of brain tissue fluid were normalized (by subtraction) to the second session (dehydration) by using custom-written Matlab scripts (MathWorks, Natick, Massachusetts). Outliers were defined as values exceeding 2.5 SDs, and data were corrected for outliers. Units were expressed as normalized percentage signal change. Thus, dehydration was chosen as the reference to conveniently plot successive changes (compare "MR Morphometry" above).

Criteria for assessment of spectral quality were the following: 1) the signal-to-noise ratio (defined by the ratio of the maximum in the spectrum-minus-baseline over the analysis window to twice the root-mean-square residuals, 2) the line width (roughly estimated by using the full width at half maximum), 3) the distribution of residuals, and 4) the SD. In the LCModel, SD estimates are Cramer-Rao lower bounds. Cramer-Rao lower bounds of >50% indicate that the metabolite concentration may range from zero to twice the estimated concentration. In this study, we selected for further analysis only spectral data meeting the following: 1) a signal-to-noise ratio of >4; 2) full width at half maximum of ≤0.07 ppm; 3) randomly distributed residuals of ~0; and 4) Cramer-Rao lower bounds of <25%.

Quantitative T1-Mapping. Quantitative T1-relaxation time maps were estimated on a voxelwise basis according to the following formula:

$$T1c_{j,k} = TR/\ln[(\sin(FA_1) \times \cos(FA_2) - Q_{j,k} \times \sin(FA_2) \times \cos(FA_1))/(\sin(FA_1) - Q_{j,k} \times \sin(FA_2))],$$

where $T1c_{j,k}$ is the T1-value, and $Q_{j,k}$ represents the signal intensity ratio for the voxel (j,k). For this purpose, the 2 FLASH acquisitions of the 2 flip angles (FA_1, FA_2) were coregistered by using mri_robust_template (part of FreeSurfer[24]), and the upper and lower slices were discarded. To obtain separate T1-estimates for white and cortical as well as subcortical gray matter, we rigidly coregistered the segmentations/parcellations of FreeSurfer to this individual template space (by using mri_robust_register, also part of FreeSurfer), slightly eroded and applied as masks for extracting corresponding T1-relaxation times.

Statistical Analyses

All statistical analyses were performed in SPSS Statistics (Version 22; IBM Armonk, New York). On the basis of the assumption that organic osmolytes are involved in cerebral fluid regulation, myo-inositol, creatine, glutamine+glutamate, and *N*-acetyl-aspartate and *N*-acetyl-aspartyl-glutamate were analyzed for changes on de- and rehydration. A repeated measures ANOVA was applied to the spectroscopic estimates of these metabolites, brain tissue fluid, and serum parameters to test for experimental changes with time (ie, different levels of hydration) by using a significance level $P \leq .05$, which corresponds to a type I error probability of ≤5%. Thus, in the repeated measures ANOVA, the metabolite signal was the dependent measure, and time (session/level of hydration), the explanatory factor.

Post hoc *t* test comparisons were used to assess changes between the different pairs of longitudinal time points. On the basis of physiologically appropriate assumptions about the directionality of change (ie, that osmolality should increase while brain-water resonances and volume should decrease on dehydration and vice versa on rehydration), corresponding *P* values were estimated 1-sided. All statistical inferences were performed as paired tests.

The Pearson linear correlation coefficient *r* was used to assess 1-sided associations among brain tissue fluid, serum parameters, and morphometry data. *P* values were corrected for multiple comparisons (Bonferroni). Linear regression plots were generated to visualize significant associations among parameters.

Longitudinal morphometric changes of cortical surface boundaries were analyzed by using a Linear Mixed Effects Matlab toolbox (http://www.mathworks.com/help/stats/linear-mixed-effects-models.html).[25] A piece-wise linear model was fitted to the data to detect changes on de- and rehydration.

RESULTS

Blood/Serum Parameters

On dehydration, the hematocrit and osmolality (OSM_{serum}) measures clearly indicated loss of body fluid of all participants (Table). The concentrations of K^+_{serum} ($P = .00$) and serum glucose ($P = .01$), HCT ($P = .00$), and OSM_{serum} ($P = .03$) changed appropriately on de- and rehydration, whereas changes of sodium and urea were insignificant.

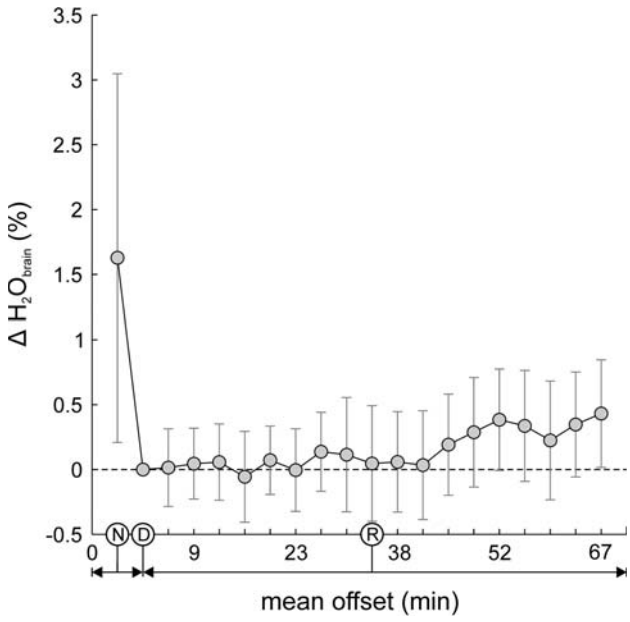

FIG 2. Serial data of brain tissue fluid H_2O_{brain}. Twelve hours of thirsting (dehydration) increased serum osmolality by 0.67% and decreased H_2O_{brain} by 1.63%. Subsequent oral fluid intake (rehydration) during 1 hour lowered serum osmolality by 0.96% and led to an increase of H_2O_{brain} by 0.43%. This finding shows that even subtle changes in H_2O_{brain} on minor osmotic challenges are detectable by ^{1}H-MR spectroscopy.

None of the individuals examined met the criteria for acute hypernatremia (ie, mean sodium levels remained below 145 mmol/L and osmolality remained below 300 mOsm/kg for all participants. Thus, blood/serum parameters indicated subclinical dehydration consistent with 12 hours without drinking overnight. No participant reported symptoms other than fatigue and thirst or exhibited clinical signs of dehydration.

^{1}H-MR Spectroscopy

Brain Tissue Fluid. Normalized resonances of tissue fluid content of H_2O_{brain} decreased on dehydration by 1.63 ± 2.84% and steadily increased by 0.43 ± 0.92% at the end rehydration ($F = 2.49$, $P = .00$) (Fig 2). Post hoc tests demonstrated a significant H_2O_{brain} decrease from normo- to dehydration and significant increases during rehydration (On-line Table 1). Resonance changes of brain tissue fluid were associated with volume changes of the whole brain ($r = 0.22$, $P = .02$), cerebral white matter ($r = 0.34$, $P = .02$), and the hypothalamus/thalamus ($r = 0.18$, $P = .05$) (On-line Table 2).

Brain Osmolytes. Representative ^{1}H-MR spectroscopy spectral data fits for normo-, de-, and rehydration are shown in Fig 1 (upper row); subtracted spectral fits (lower row) represent the respective signal changes. Repeated measurements ANOVA demonstrated no significant changes in myo-inositol, creatine, glutamine+glutamate, and *N*-acetylaspartate and *N*-acetyl-aspartyl-glutamate in subjects on 12 hours of dehydration and during 60 minutes of rehydration.

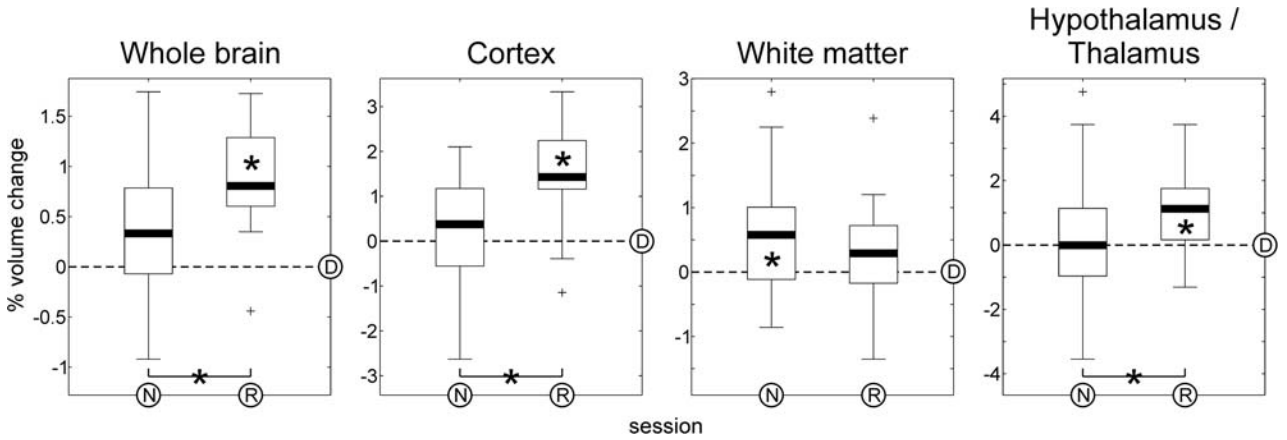

FIG 3. Volumetric morphometry at normo-, de-, and rehydration illustrated as percentage volume change normalized to session 2 (dehydration). Volume changes of the entire brain, cerebral cortex, white matter, and hypothalamus/thalamus were significant in repeated measures ANOVA and compatible with cell shrinking during hyperosmolality and cell swelling during hypo-osmolality. Subject-specific pair-wise differences are plotted with respect to dehydration. Post hoc tests revealed hydration states with significant volume changes between each one (indicated by *asterisks*; for details see On-line Table 3). *Box* indicates upper and lower quartiles; *thick black line*, median; *whiskers*, most extreme values of the interquartile range; *crosses*, outliers; D, dehydration; N, normohydration; R, rehydration; *asterisk*, significant difference.

MR Morphometry

Volumetry. Repeated measures statistical analyses revealed longitudinal changes of the whole brain, cortical gray and white matter volume, and the subcortical hypothalamus/thalamus volume on de- and rehydration ($P = .00$) (Fig 3). Specifically, mean volumes of the whole brain, cerebral cortex, white matter, and hypothalamus/thalamus decreased on dehydration by 0.36 ± 0.68%, 0.19 ± 1.28%, 0.59 ± 0.86%, and 0.30 ± 1.80% and increased on rehydration by 0.87 ± 0.57%, 1.50 ± 1.03%, 0.23 ± 0.82%, and 1.11 ± 1.28%, respectively (Fig 3). Post hoc tests revealed significant volume changes for the whole brain, cerebral cortex, and hypothalamus/thalamus during rehydration (and between normo- and rehydration) and for white matter on dehydration (On-line Table 3). Except for white matter, the magnitude of volume changes detected from normo- to dehydration was lower than that from de- to rehydration, while the associated variance was generally higher.

Correlation analyses revealed associations between the appropriate changes of the whole-brain volume and H_2O_{brain} ($r = 0.22$, $P = .02$) (On-line Fig 1*A*), of the whole-brain volume and hematocrit values ($r = -0.31$, $P = .00$) (On-line Fig 1*B*), of the cortical gray matter volume and HCT ($r = -0.22$, $P = .02$) (On-line Fig 1*C*), of the cerebral white matter volume and H_2O_{brain} ($r = 0.34$, $P = .00$) (On-line Fig 1*D*), of the cerebral white matter volume and HCT ($r = -0.31$, $P = .00$) (On-line Fig 1*E*), of the hypothalamus/thalamus volume and H_2O_{brain} ($r = 0.18$, $P = .05$) (On-line Fig 1*F*), and of the hypothalamus/thalamus volume and OSM_{serum} values ($r = -0.18$, $P = .04$) (On-line Fig 1*G*) (On-line Table 2).

Cortical Thickness and Subcortical Surface Changes. Cortical thinning prevailed on dehydration, and cortical thickening, on rehydration. These changes of cortical thickness, as averaged across subjects, were not uniformly distributed over the cerebral surface (Fig 4*A*). Associated error probabilities (Fig 4*B*) revealed a similar consistent pattern and largely excluded changes to the opposite (ie, thickening on dehydration and thinning on rehydration), which presumably reflect false-positive detections. Error probabilities ensure that the detected cortical thickness changes are not driven by outliers and accompanied by increased variance measures across subjects. Some areas attained high significance levels (ie, low error probabilities) (Fig 4*B*), despite relatively lower mean cortical thickness change (Fig 4*A*), due to low variability of the changes across subjects. The patterns of cortical thinning on dehydration and thickening on rehydration approximately mirrored each other and appeared quite similar (ie, symmetric, for the 2 hemispheres).

Quantitative T1-Relaxation Times

Mean T1-relaxation times during normo-, de-, and rehydration were 1339 ± 86.92 ms, 1314 ± 70.26 ms, and 1321 ± 75.28 ms for the cerebral cortex; 1291 ± 68.07 ms, 1285 ± 66.96 ms, and 1295 ± 68.27 ms for the hypothalamus/thalamus; and 834.52 ± 58.11 ms, 818.15 ± 42.58 ms, and 820.36 ± 46.18 ms for white matter (Fig 5). Statistical analyses revealed no longitudinal differences in T1-relaxation times of the cerebral cortex ($P = .07$), hypothalamus/thalamus ($P = .19$), and white matter ($P = .09$) on de- and rehydration.

DISCUSSION

In this study, for the first time, the effect of hyper- and hypo-osmolality on brain tissue fluid, brain volume, and cortical thickness was monitored in vivo. These findings represent cellular changes of the volume regulatory mechanisms at a macroscopic level.

Hypernatremia is associated with brain-water loss and corresponding volume reduction, whereas hyponatremia is related to brain-water accumulation and associated volume increase. Both conditions have been extensively studied in animal experiments and reflect osmoadaptive responses of the cell to fluid imbalances.[26,27] Acute hypernatremia is defined as a plasma sodium concentration above 150 mmol/L, and acute hyponatremia, as a plasma sodium concentration below 120 mmol/L developing during 24–48 hours.[26] To that end, a mean plasma sodium con-

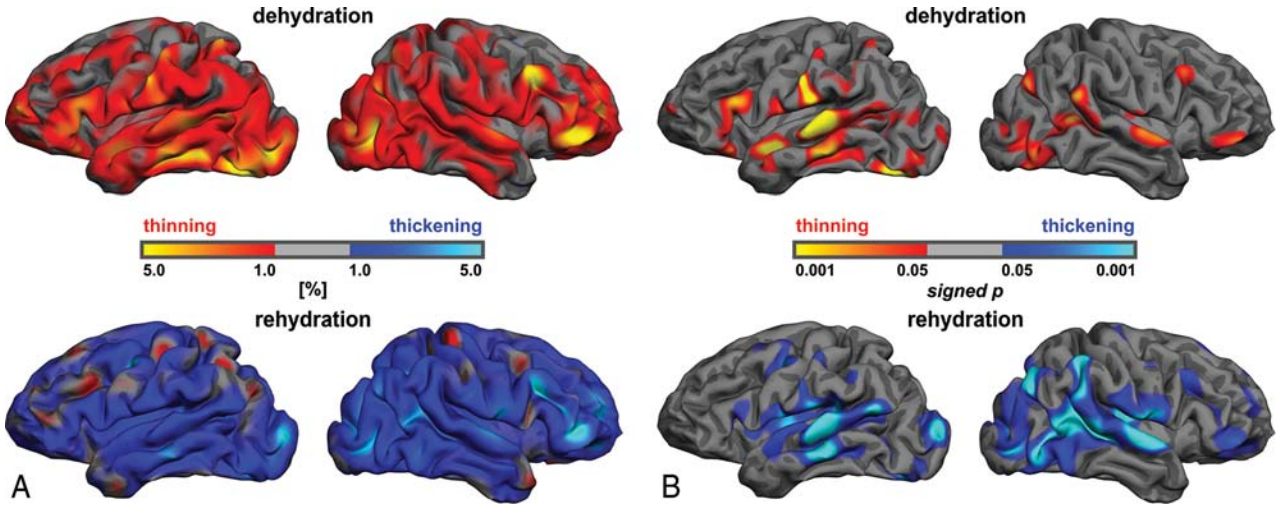

FIG 4. Cortical thickness analysis. Local changes of cortical thickness (*A*, red-to-yellow: for thinning on dehydration; blue-to-light blue: for thickening on rehydration). Dehydration primarily induces cortical thinning (*upper row*), which reverses on rehydration (*bottom row*). Note that these prevailing changes are not uniformly distributed over the cerebral surface. Changes on the mesial surface (not shown) were slightly less pronounced but similar. The corresponding statistical significance (*B*, red-to-yellow: for thinning on dehydration; blue-to-light blue: for thickening upon rehydration) is expressed by increasingly lower false-positive probabilities across subjects.

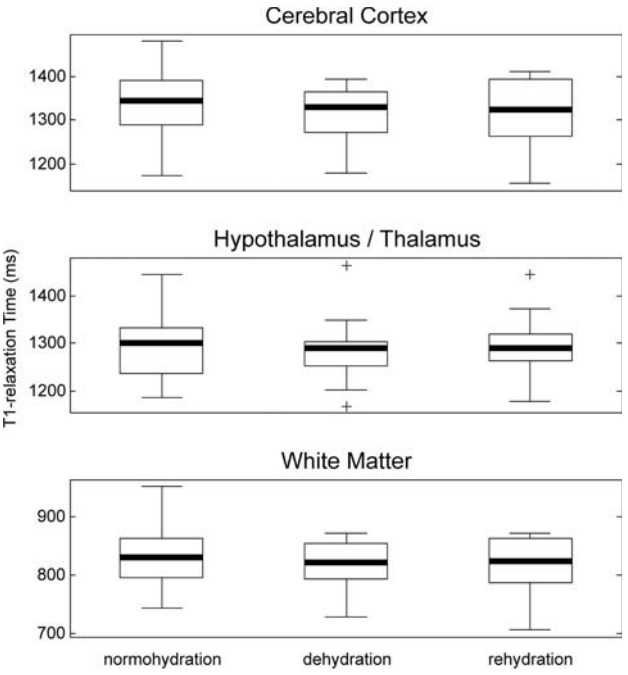

FIG 5. T1-relaxometry. Quantitative T1-relaxation times of the cerebral cortex (*upper row*), the subcortical gray (*middle row*), and white matter (*bottom row*) during normo-, de-, and rehydration. Statistical analyses revealed no longitudinal changes in T1 relaxation times. *Box* indicates upper and lower quartiles; *thick black line*, median; *whiskers*, most extreme values of the interquartile range; *crosses*, outliers.

centration of 138.5 mmol/L on dehydration and 136.9 mmol/L after rehydration as presented in our study is considered subtle. In animal models, induced hypernatremia with 200 mmol/L led to a decrease of brain-water up to 14%, whereas a rapidly evoked (2 hours) hyponatremia with 119 mmol/L resulted in a 16% increase of brain-water. The rate at which osmolar stress develops defines whether the osmoadaptive capacities of the brain are exceeded. Therefore, it is plausible that a slowly induced (48 hours) hyponatremia with 107 mmol/L revealed no changes in brain-water.[28]

In the study here, 12 hours of thirsting elevated serum osmolality by 0.67% and resulted in 1.63% reduction of H_2O_{brain}. One hour of slow continuous oral fluid intake lowered serum osmolality by 0.96% and led to a 0.43% increase in H_2O_{brain}. This finding supports, in principle and within limits, the sensitivity and reliability of the H_2O_{brain} signal, which is, especially with receive-only multichannel phased array coils, commonly used for water scaling in ^{1}H-MR spectroscopy.[19,20,29]

On de- and rehydration, changes of the global brain volume, gray and white matter volume, hypothalamus/thalamus volume, and cortical thickness were observed, which were consistent with the processes of cell shrinkage and swelling, respectively, and are in line with findings in previous studies.[10-13] Global brain volume changes on dehydration (0.36%) and rehydration (0.87%) are in excellent agreement with those in a previous study,[13] which reported volume changes of the same magnitude after 16 hours of thirsting (0.55%) and subsequent rehydration (0.72%). Previous studies of Dickson et al,[11] Kempton et al,[10] and Watson et al,[12] which induced dehydration by thermal exercises, failed to demonstrate brain volume changes.

Freund et al[15] demonstrated a reversible volume reduction of cerebral gray matter (6%) after 2 months of daily running during an ultramarathon, which is in line with the reversible cortical thinning (0.19%) on dehydration reported in our study. On the other hand, a recent study with low sample size[14] failed to reveal thinning of the cerebral cortex and shrinking of the hypothalamus/thalamus, which are reversed on rehydration. Reversible cortical thinning by short-term dehydration is not uniformly distributed over the cerebral surface (Fig 4) (ie, the brain does not seem to simply shrink by global scaling during dehydration). Instead, detected changes of cortical thickness reveal some but no exclusive overlap with the following: 1) known areas of pronounced cortical thickness[30]; and 2) atrophy patterns found in Alzheimer disease,[31] cerebrovascular dementia,[32] and eating disorders,[33] for example. Also, more generally, brain volume changes due to osmotic stress are in/near the magnitude of

changes attributed to annual volume decrease by aging (0.2%),[34,35] Alzheimer disease (2%), Lewy body dementia (1.4%), or vascular dementia (1.9%).[36] These results emphasize that longitudinal changes and cross-sectional differences of cortical thickness in conditions accompanied by altered fluid intake (such as dementias or eating disorders) can be confounded by de- and rehydration, which may then be mistaken for brain atrophy or even regeneration.

Whole-brain, white matter, and hypothalamus/thalamus volumes demonstrated changes related to those in brain tissue fluid. This finding is further supported by the inverse correlation between HCT and volume changes of the whole brain, cerebral cortex, and cerebral white matter. The only brain structure that demonstrated an association between its volume and serum osmolality changes was the hypothalamus/thalamus. This finding is consistent with the fact that the hypothalamus includes magnocellular neurosecretory cells of the paraventricular and supraoptic nucleus, which are able to intrinsically detect and respond to changes in osmolality.[37] The magnocellular neurosecretory cell volume has been shown to be inversely proportional to the osmolality of the extracellular fluid.[38] Moreover, in a magnocellular neurosecretory cell subset of the paraventricular and supraoptic nucleus, vasopressin is synthesized. Axons project into the neurohypophysis, where vasopressin release occurs. Thus, the association between volume changes of the hypothalamus/thalamus as found in our study may reflect the relationship between magnocellular neurosecretory cell volume and osmolality of the extracellular fluid. However, we acknowledge that magnocellular neurosecretory cells are distributed over different subcortical gray matter nuclei and cannot be directly assessed by MR imaging at 3T.

No statistically significant changes of cerebral osmolytes on dehydration or after rehydration were observed. This finding may be due to these changes falling below the between- and within-session reproducibility limits of the spectroscopy measurements. Note that the between-session variance exceeded the within-session variance across subjects for all morphometric and spectroscopic measures studied (Figs 2, 3, and 5), which presumably results from repositioning and reshimming. Alternatively, 12 hours of mild dehydration may not produce changes in organic osmolytes large enough to be detectable by MR spectroscopy—at least not in all individuals—that is, osmolytes may already act as osmotic active substrates in some individuals but not in others. Although the resulting metabolite data might demonstrate plausible kinetics of organic osmolytes in a subset of individuals, there is a high variance in the data across subjects, which emphasizes such interindividual differences. In this study, mild dehydration was associated with a 0.67% increase in serum osmolality, and rehydration resulted in a 0.29% decrease in serum osmolality. For comparison, Videen et al[39] reported cerebral osmolyte changes (reduction of myo-inositol, choline, total creatine, and *N*-acetylaspartate) on hyponatremia in patients with pituitary tumors, congestive heart failure, or syndrome of inappropriate antidiuretic hormone secretion associated with an average 12.98% reduction in serum osmolality. Lien et al[40] examined severe hypernatremia in rats, which led to a mean 33.55% increase in serum osmolality and also demonstrated changes in organic osmolytes (increase of myo-inositol, choline, phosphocreatine, glutamine, and glutamate) in brain tissue.

Limitations of this study are methodologically inherent because assigning resonances of ^{1}H-MR spectroscopy data to metabolites, for example, is itself error-prone. Data quality and selection of an adequate fitting routine are therefore essential.

At least in theory, morphometric changes may also result from purely physical changes in tissue relaxation times and contrast induced by fluid changes influencing tissue segmentation. However, there were no changes in T1-relaxation times of the cerebral cortex and the subcortical gray and the white matter among normo-, de-, and rehydration, while the average T1-values themselves were in excellent agreement with previous data.[41] Also, the correlations between morphometry measures and serum parameters support physiologic effects. Moreover, whether physiologic and/or physical, the key message is that hydration levels constitute an important confound for morphometric studies, and this is the first study demonstrating relevant changes of cortical thickness related to subclinical dehydration and rehydration. Brain tissue fluid resonances, rapidly assessed by unsuppressed ^{1}H-MR spectroscopy, are suitable for water scaling and, along with serum parameters, also correlate with whole-brain, white matter, and hypothalamus/thalamus volume changes.

CONCLUSIONS

This study suggests the following: 1) Morphometric brain changes during de- and rehydration match the concept of osmotically induced cell volume changes, and 2) the cerebral cortex, white matter, and the hypothalamus/thalamus are affected by these changes. Our results emphasize that it is essential to control for hydration levels in any study on cerebral morphometry or metabolism to avoid confounding the findings. This is especially important because hydration levels can systematically differ across population samples and longitudinal follow-up, in particular for patients with dementias, eating disorders, and other conditions accompanied by even slightly altered fluid intake.

ACKNOWLEDGMENTS

We thank Professor Andreas Draguhn (Institute of Physiology and Pathophysiology, Division of Neuro- and Sensory Physiology, University of Heidelberg, Germany) for critical reading of the manuscript and very helpful comments.

Disclosures: Martin Reuter—*RELATED*: *Grant*: National Institutes of Health, Grant K25 CA181632.* Martin Bendszus—*UNRELATED*: *Consultancy*: Codman; *Payment for Lectures (including service on Speakers Bureaus)*: Novartis, Guerbet, Codman, Roche. *Money paid to the institution.

REFERENCES

1. Buche A, Colson P, Houssier C. **Effect of organic effectors on chromatin solubility, DNA-histone H1 interactions, DNA and histone H1 structures.** *J Biomol Struct Dyn* 1993;11:95–119 CrossRef Medline
2. Iyer SS, Pearson DW, Nauseef WM, et al. **Evidence for a readily dissociable complex of p47phox and p67phox in cytosol of unstimulated human neutrophils.** *J Biol Chem* 1994;269:22405–11 Medline
3. Lang F, Busch GL, Ritter M, et al. **Functional significance of cell volume regulatory mechanisms.** *Physiol Rev* 1998;78:247–306 Medline
4. Burg MB. **Molecular basis for osmoregulation of organic osmolytes**

in renal medullary cells. *J Exp Zool* 1994;268:171–75 CrossRef Medline
5. Handler JS, Kwon HM. **Regulation of renal cell organic osmolyte transport by tonicity.** *Am J Physiol* 1993;265(6 pt 1):C1449–55 Medline
6. Kinne RK. **The role of organic osmolytes in osmoregulation: from bacteria to mammals.** *J Exp Zool* 1993;265:346–55 CrossRef Medline
7. Kempton MJ, Ettinger U, Foster R, et al. **Dehydration affects brain structure and function in healthy adolescents.** *Hum Brain Mapp* 2011;32:71–79 CrossRef Medline
8. Law RO. **Amino acids as volume-regulatory osmolytes in mammalian cells.** *Comp Biochem Physiol A Comp Physiol* 1991;99:263–77 CrossRef Medline
9. Garcia-Perez A, Burg MB. **Role of organic osmolytes in adaptation of renal cells to high osmolality.** *J Membr Biol* 1991;119:1–13 CrossRef Medline
10. Kempton MJ, Ettinger U, Schmechtig A, et al. **Effects of acute dehydration on brain morphology in healthy humans.** *Hum Brain Mapp* 2009;30:291–98 CrossRef Medline
11. Dickson JM, Weavers HM, Mitchell N, et al. **The effects of dehydration on brain volume – preliminary results.** *Int J Sports Med* 2005; 26:481–85 CrossRef Medline
12. Watson P, Head K, Pitiot A, et al. **Effect of exercise and heat-induced hypohydration on brain volume.** *Med Sci Sports Exerc* 2010;42:2197–204 CrossRef Medline
13. Duning T, Kloska S, Steinsträter O, et al. **Dehydration confounds the assessment of brain atrophy.** *Neurology* 2005;64:548–50 CrossRef Medline
14. Streitbürger DP, Möller HE, Tittgemeyer M, et al. **Investigating structural brain changes of dehydration using voxel-based morphometry.** *PLoS One* 2012;7:e44195 CrossRef Medline
15. Freund W, Faust S, Birklein F, et al. **Substantial and reversible brain gray matter reduction but no acute brain lesions in ultramarathon runners: experience from the TransEurope-FootRace Project.** *BMC Med* 2012;10:170 CrossRef Medline
16. Biller A, Bartsch AJ, Homola G, et al. **The effect of ethanol on human brain metabolites longitudinally characterized by proton MR spectroscopy.** *J Cereb Blood Flow Metab* 2009;29:891–902 CrossRef Medline
17. Bartsch AJ, Homola G, Biller A, et al. **Manifestations of early brain recovery associated with abstinence from alcoholism.** *Brain* 2007; 130(pt 1):36–47 CrossRef Medline
18. Bendszus M, Weijers HG, Wiesbeck G, et al. **Sequential MR imaging and proton MR spectroscopy in patients who underwent recent detoxification for chronic alcoholism: correlation with clinical and neuropsychological data.** *AJNR Am J Neuroradiol* 2001;22:1926–32 Medline
19. Gasparovic C, Neeb H, Feis DL, et al. **Quantitative spectroscopic imaging with in situ measurements of tissue water T1, T2, and density.** *Magn Reson Med* 2009;62:583–90 CrossRef Medline
20. Soher BJ, Hurd RE, Sailasuta N, et al. **Quantitation of automated single-voxel proton MRS using cerebral water as an internal reference.** *Magn Reson Med* 1996;36:335–39 CrossRef Medline
21. Reuter M, Schmansky NJ, Rosas HD, et al. **Within-subject template estimation for unbiased longitudinal image analysis.** *Neuroimage* 2012;61:1402–18 CrossRef Medline
22. Provencher SW. **Automatic quantitation of localized in vivo 1H spectra with LCModel.** *NMR Biomed* 2001;14:260–64 CrossRef Medline
23. Brooks JC, Roberts N, Kemp GJ, et al. **Magnetic resonance imaging-based compartmentation and its application to measuring metabolite concentrations in the frontal lobe.** *Magn Reson Med* 1999;41: 883–88 CrossRef Medline
24. Reuter M, Rosas HD, Fischl B. **Highly accurate inverse consistent registration: a robust approach.** *Neuroimage* 2010;53:1181–96 CrossRef Medline
25. Bernal-Rusiel JL, Greve DN, Reuter M, et al. **Statistical analysis of longitudinal neuroimage data with linear mixed effects models.** *Neuroimage* 2013;66:249–60 CrossRef Medline
26. Gullans SR, Verbalis JG. **Control of brain volume during hyperosmolar and hypoosmolar conditions.** *Ann Rev Med* 1993;44:289–301 CrossRef Medline
27. Verbalis JG. **Brain volume regulation in response to changes in osmolality.** *Neuroscience* 2010;168:862–70 CrossRef Medline
28. Vajda Z, Berényi E, Bogner P, et al. **Brain adaptation to water loading in rabbits as assessed by NMR relaxometry.** *Pediatr Res* 1999;46: 450–54 CrossRef Medline
29. Gasparovic C, Song T, Devier D, et al. **Use of tissue water as a concentration reference for proton spectroscopic imaging.** *Magn Reson Med* 2006;55:1219–26 CrossRef Medline
30. Fischl B, Dale AM. **Measuring the thickness of the human cerebral cortex from magnetic resonance images.** *Proc Natl Acad Sci U S A* 2000;97:11050–55 CrossRef Medline
31. Becker JA, Hedden T, Carmasin J, et al. **Amyloid-β associated cortical thinning in clinically normal elderly.** *Ann Neurol* 2011;69: 1032–42 CrossRef Medline
32. Kim HJ, Ye BS, Yoon CW, et al. **Cortical thickness and hippocampal shape in pure vascular mild cognitive impairment and dementia of subcortical type.** *Eur J Neurol* 2014;21:744–51 CrossRef Medline
33. Joos A, Klöppel S, Hartmann A, et al. **Voxel-based morphometry in eating disorders: correlation of psychopathology with grey matter volume.** *Psychiatry Res* 2010;182:146–51 CrossRef Medline
34. Good CD, Johnsrude IS, Ashburner J, et al. **A voxel-based morphometric study of ageing in 465 normal adult human brains.** *Neuroimage* 2001;14(1 pt 1):21–36 CrossRef Medline
35. Smith CD, Chebrolu H, Wekstein DR, et al. **Age and gender effects on human brain anatomy: a voxel-based morphometric study in healthy elderly.** *Neurobiol Aging* 2007;28:1075–87 CrossRef Medline
36. O'Brien JT, Paling S, Barber R, et al. **Progressive brain atrophy on serial MRI in dementia with Lewy bodies, AD, and vascular dementia.** *Neurology* 2001;56:1386–88 CrossRef Medline
37. Bourque CW. **Central mechanisms of osmosensation and systemic osmoregulation.** *Nat Rev Neurosci* 2008;9:519–31 CrossRef Medline
38. Zhang Z, Bourque CW. **Osmometry in osmosensory neurons.** *Nat Neurosci* 2003;6:1021–22 CrossRef Medline
39. Videen JS, Michaelis T, Pinto P, et al. **Human cerebral osmolytes during chronic hyponatremia: a proton magnetic resonance spectroscopy study.** *J Clin Invest* 1995;95:788–93 CrossRef Medline
40. Lien YH, Shapiro JI, Chan L. **Effects of hypernatremia on organic brain osmoles.** *J Clin Invest* 1990;85:1427–35 CrossRef Medline
41. Wansapura JP, Holland SK, Dunn RS, et al. **NMR relaxation times in the human brain at 3.0 Tesla.** *J Magn Reson Imaging* 1999;9:531–38 CrossRef Medline

Effect of Collaterals on Clinical Presentation, Baseline Imaging, Complications, and Outcome in Acute Stroke

E.M. Fanou, J. Knight, R.I. Aviv, S.-P. Hojjat, S.P. Symons, L. Zhang, and M. Wintermark

ABSTRACT

BACKGROUND AND PURPOSE: Good CTA collaterals independently predict good outcome in acute ischemic stroke. Our aim was to evaluate the role of collateral circulation and its added benefit over CTP-derived total ischemic volume as a predictor of baseline NIHSS score, total ischemic volume, hemorrhagic transformation, final infarct size, and a modified Rankin Scale score >2.

MATERIALS AND METHODS: This was a retrospective study of 395 patients with stroke dichotomized by recanalization (recanalization positive/recanalization negative) and collateral status. Clot burden score was quantified on baseline CTA. Total ischemic volumes were derived from thresholded CTP maps. Final infarct size was assessed on follow-up CT/MRI. We performed uni-/multivariate analyses for each outcome, adjusting for rtPA status, using general linear (continuous variables) and logistic (binary variables) regression. Model comparison with collateral score and total ischemic volume was performed using the *F* or likelihood ratio test.

RESULTS: Collateral presence independently and inversely predicted all outcomes except hemorrhagic transformation in patients who were recanalization negative and mRS >2 in patients who were recanalization positive. The greatest collateral benefit occurred in patients who were recanalization negative, contributing 16.5% and 19.2% of the variability for final infarct size and mRS >2. The collateral score model is superior to the total ischemic volume for mRS >2 prediction, but a combination of total ischemic volume and collateral score is superior for mRS >2 and final infarct prediction (24% and 28% variability, respectively). In patients who were recanalization positive, a model including collateral score and total ischemic volume was superior to that of total ischemic volume for hemorrhagic transformation and final infarct prediction but was muted compared with patients who were recanalization negative (11.3% and 16.9% variability).

CONCLUSIONS: Collateral circulation is an independent predictor of all outcomes, but the magnitude of significance varies, greater in patients who were recanalization negative versus recanalization positive. Total ischemic volume assessment is complementary to collateral score in many cases.

ABBREVIATIONS: CBS = clot burden score; CS = collateral score; HT = hemorrhagic transformation; R+ = recanalization positive; R− = recanalization negative; TIV = total ischemic volume; bNIHSS, baseline NIHSS score

In the setting of acute ischemic stroke, revascularization therapies are administered with the intent of salvaging ischemic penumbra by restoring antegrade flow.[1] Even though conventional angiography is considered the gold standard for collateral circulation assessment, CT angiography is increasingly used in triaging patients with acute stroke.[2]

Growing evidence underscores the importance of the collateral circulation in maintaining the penumbra and predicting radiological and clinical response to revascularization.[3,4] Good CTA collaterals independently predict good outcome in acute ischemic stroke[1,2] and correlate with smaller admission infarct size.[5] CTA collateral scoring demonstrates good interrater reliability[2,6-8]; is widely available, including after-hours; and has the advantage of not requiring advanced postprocessing, which is subject to a host of technical differences.[9] The best means of accurate collateral assessment is debated[1,10-13]; however, irrespective of the method of assessment, collateral status significantly predicts clinical outcome and risk of infarct.[2,14,15] Limitations of collateral evaluation are that vessel opacification is time- and ac-

Received January 5, 2015; accepted after revision May 14.

From the Division of Neuroradiology (E.M.F., J.K., R.I.A., S.-P.H., S.P.S., L.Z.), Department of Medical Imaging, University of Toronto and Sunnybrook Health Sciences Centre, Toronto, Ontario, Canada; and Division of Neuroradiology (M.W.), Department of Radiology, Stanford University, California.

Please address correspondence to Richard I. Aviv, MD, FRCR, Sunnybrook Health Sciences Centre, 2075 Bayview Ave, Toronto, Ontario, Canada M4N 3M5; e-mail: richard.aviv@sunnybrook.ca

Indicates article with supplemental on-line tables.

http://dx.doi.org/10.3174/ajnr.A4453

quisition speed–dependent, indicating the need for time-invariant CTA imaging.[10,11] Additionally, the tissue perfusion status is not directly imaged in contradistinction to CT perfusion, in which penumbral prediction is well-studied.[16]

A recent study suggested that a good clinical outcome could only be achieved in the presence of recanalization and good-to-intermediate collateral status. No effect was seen in patients without recanalization. Furthermore, the effect of other comorbid clinical (blood pressure, glycemic status, presence of vascular risk factors, and so forth) or radiological features (clot burden score [CBS], clot location, hemorrhagic transformation [HT]) was not considered in outcome determination.[13] The relationship of collateral status and these other imaging and clinical stroke predictors, independent of recanalization status, for major outcomes is also not well-established in large acute stroke populations. Emphasis on collateral status has increased due to its recent inclusion in patient selection for endovascular treatment[17]; however, the added predictive value of collateral score (CS) over perfusion imaging assessment of total ischemia is not well-studied. We hypothesized that for a given recanalization status in the absence of perfusion availability, collateral determination significantly predicts baseline stroke severity (quantified by the baseline National Institutes of Health Stroke Scale score [bNIHSS]) and clinical (hemorrhagic transformation, 90-day modified Rankin Scale score of >2) and radiological outcomes (final infarct volume). In the present study, we also sought to quantify the added value of a CS over CTP-estimated total ischemic volume (TIV). The added contribution was assessed independent of recanalization status and accounted for additional important clinical and imaging covariates in multivariate models.

MATERIALS AND METHODS

Study Design and Patient Cohort

The study and medical chart review were approved by the local research ethics board. Consent was obtained from all patients or legal guardians for participation. We performed a retrospective review of 395 consecutive patients (from a prospectively maintained stroke data base) presenting between 2009 and 2013 with a confirmed anterior circulation stroke diagnosed and treated with IV rtPA by a stroke neurologist within 4.5 hours of onset. Included patients demonstrated a confirmed vessel occlusion on admission stroke work-up, including noncontrast CT, CT angiogram, and CT perfusion. Recanalization was determined on CTA performed at ≤24 hours, while follow-up MR imaging or CT at 5–7 days was used for final infarct assessment. Clinical history, laboratory results, demographics, stroke risk factors, and NIHSS score were collected for all patients by medical chart review. Time to CT was calculated as the time interval between symptom onset (last seen normal for patients with nonwitnessed symptom onset) and the time to arrival in the emergency department CT scanner. A follow-up modified Rankin Scale score was obtained in the stroke prevention clinic at 90 days, with a score of >2 defining a poor outcome.

Imaging Acquisition Protocol and Image Postprocessing

CT stroke protocol was performed on a 64–detector row CT scanner (LightSpeed VCT; GE Healthcare, Milwaukee, Wisconsin). Pre- and postcontrast head CT parameters were as follows: 120 kV(peak); 300 mA; rotation, 1 second; section thickness, 5 mm. Baseline and 24-hour CT angiogram parameters were as follows: 0.7-mL/kg of iodinated contrast agent up to a maximum of 90 mL (iohexol, Omnipaque 300 mg iodine/mL; GE Healthcare, Piscataway, New Jersey); 5- to 10-second delay; 120 kVp; 270 mA; rotation, 1 second; 1.25-mm-thick sections; table speed, 20.62 mm per rotation. Biphasic CT perfusion protocol from the basal ganglia to the lateral ventricles was the following: 80 kVp; 150 mA; collimation, 8×5 mm; rotation, 1 second for 45 seconds followed by 6 further acquisitions 15 seconds apart for a total of 135 seconds. Iodinated contrast agent of 0.5 mL/kg (maximum, 50 mL) at 4 mL/s was administered 5 seconds before start of the sequence. Cerebral blood flow, cerebral blood volume, and mean transit time were calculated as previously described by using a delay-corrected algorithm commercially available on CT Perfusion 4 (GE Healthcare).[18]

Image Analysis

All baseline and follow-up imaging assessments were performed separately by the same neuroradiologist (R.I.A., 10 years of experience) blinded to imaging and clinical outcomes. Baseline imaging features included ASPECTS, clot location, clot burden score, and CS. The occlusion site was considered "proximal" if involving the ICA and proximal M1 MCA segment, whereas clot distal to this was considered "distal." Recanalization status was graded on follow-up CTA by evaluating the restoration of patency of the previously occluded vessel by using the adapted Thrombolysis in Myocardial Infarction score, in which a score of ≥2 was considered recanalization-positive (R+).[19] Collateral flow was graded on a 0–3 scale.[15] Scores of 0 and 1 (<50% of ischemic territory demonstrate collaterals) were considered poor collateral status, whereas scores of ≥2 were assigned a good collateral status. The CBS is a scoring system that defines anterior circulation thrombus extent scored on a scale of 0–10 by using CTA. Two points are subtracted for thrombus in each of the supraclinoid ICAs and the proximal and distal half of the MCA trunk. One point is subtracted for thrombus in each of the infraclinoid ICAs or anterior cerebral artery and each affected M2 MCA branch (to a maximum of 2). A score of 10 connotes clot absence, while zero represents complete multisegment vessel occlusion.[15]

CT perfusion source images were normalized to Montreal Neurological Institute space and segmented into gray and white matter by using SPM8 software (http://www.fil.ion.ucl.ac.uk/spm/software/spm8). Within the ischemic hemisphere, volumes of core, penumbra proceeding to infarction and benign oligemia were calculated by using previously published institution-validated thresholds for GM and WM.[20] Absolute CBF (milliliters/100 g/min) defined the GM/WM core and GM/WM benign oligemia was defined as ≤13.8/9.8 and ≥21.4/14.1, respectively. GM/WM penumbra proceeding to infarction was represented by >13.8 to <21.4/>9.8 to <14.1, respectively, while GM/WM benign oligemia was >21.4/ 14.1, respectively.[20] TIV represents the sum of all thresholded ischemic regions above. Final infarct was traced on follow-up imaging, with either NCCT if clearly delineated or FLAIR MR imaging by using Medical Image Processing,

Analysis, and Visualization (Version 7.0.2; National Institutes of Health, Bethesda, Maryland).

Statistical Analyses

Continuous scaled demographic data were expressed as mean ± SD, whereas discrete data were expressed as median and interquartile range. Frequency data were expressed as proportions. Natural log-transformation was applied if appropriate to some continuous variables to normalize their distribution. Patients were divided into 4 groups according to recanalization and collateral status; groups A and B were recanalization-negative (R−) and collateral-negative and -positive, respectively, whereas groups C and D were R+ and collateral-negative and -positive, respectively. A Bonferroni-adjusted P value $< .0125$ was considered statistically significant after controlling for multiple comparisons and adjusting for rtPA status, by using general linear regression for continuous variables and logistic regression for binary variables. The outcome was each demographic or clinical variable; the independent variable was a categorical variable of "group" with rtPA as a confounding factor. The interaction term "rtPA × group" was also inserted; however, no significant interaction was demonstrated, suggesting that rtPA treatment effects are not additive to the significant group effects, permitting inclusion of patients treated both with and without rtPA within each group. Uni- and multivariate logistic analyses were performed for each group comparison, with the predefined outcomes of bNIHSS, hemorrhagic transformation, final infarct size, and 90-day modified Rankin Scale, after adjusting for rtPA and collateral status as confounding factors. For each independent predictor odds ratio, 95% CI was calculated. Only factors with $P < .10$ in univariate analysis were advanced into a multivariate analysis with backward stepwise selection. TIV/CS collinearity was tested by using a variance inflation factor for all outcomes.

After establishing no collinearity (variance inflation factor of <2), the added benefit of CS over CTP-derived TIV was tested. Each of 2 null-nested models was compared by using an F-test or a likelihood ratio test for continuous or binary outcomes. Null models included either collaterals or TIV, while the alternative model included both collaterals and TIV. The likelihood ratio test statistic was determined by −2 log-likelihood for the null model and +2 log-likelihood for the alternative model, assuming a χ^2 distribution. Degrees of freedom were the difference between the number of parameters of the alternative model and the null model. SAS (Version 9.2; SAS Institute, Cary, North Carolina) was used for all analyses, and a P value $< .05$ was considered significant.

RESULTS

The average patient age was 72 ± 14 years with 198 (50.1%) women. Median (interquartile range) ASPECTS and baseline NIHSS score were 7 (6–9) and 14 (7–19), respectively. A clot burden score of >6 was present in 45.8% (181/395) of patients, and 78.9% (310/395) had good collateral status. Occlusion was proximal in 43% (170/395) and distal in 57% (225/395). Intravenous recombinant tissue plasminogen activator was administered in 273/395 (69.1%) patients, with a median time to treatment of 147 minutes (interquartile range, 125–179 minutes). Recanalization occurred in 220/395 (55.7%) patients diagnosed on CTA at a mean time of 24 ± 6 hours; 26/220 demonstrated poor collaterals (11.8%). Time to scanning was not significantly different between groups and therefore was not considered in multivariate analyses. Poor collaterals were present in 57/175 (32.6%) patients without recanalization. The median 90-day mRS was 3 (interquartile range, 2–5), with a good outcome in 144/395 (37%) patients. Hemorrhagic transformation occurred in 174/395 (44.1%) of patients. Hemorrhagic infarction (HI 1/2) dominated in 133/174 (76.4%) patients overall, but no difference in hemorrhage type (hemorrhagic infarction versus parenchymal hematoma) was seen between collateral-positive and -negative groups for patients who were R+ and R− ($P = .67$ and $P = .31$, respectively). The median final infarct size was 38 cm^3 (interquartile range, 10–124.3 cm^3).

No significant group differences in rtPA use were present on the basis of baseline thresholded ischemic penumbra or core size, though patients receiving rtPA were treated earlier and tended toward higher baseline NIHSS, more proximal clot location, and smaller final infarct size than those receiving supportive medical care. The absence of collaterals was associated with larger total GM/WM ischemic volumes, including infarct core irrespective of recanalization status (On-line Table 1). Significant group interaction with rtPA was present for all outcome measures except hemorrhagic transformation, which just missed significance ($P = .0178$). All outcome measures were significantly worse in the absence of collaterals, irrespective of recanalization status, with the exception of hemorrhage, which did not meet statistical significance (On-line Table 1). In R+, however, there was no significant difference in dichotomized mRS, though the median mRS score was significantly lower in the presence of collaterals.

Outcome Assessment and Added Value of CS Assessment over CTP

Baseline Stroke Severity. Poor collateral circulation, greater clot burden (lower CBS), and TIV were significantly related to bNIHSS, irrespective of recanalization status on uni- and multivariate analyses (On-line Tables 2 and 3). Age remained significant on multivariate analysis for patients who were R+ only ($P < .0051$). If one considered confounders, collateral absence remained significantly related to bNIHSS. There was no significant interaction between CS and other predictive factors. TIV accounted for 33.3% of bNIHSS severity compared with 27.5% by using CS only (27.5%; $P = .0019$). The highest R^2 was achieved when both CS and CTP-derived TIV were included (36.5%) (On-line Table 3).

Hemorrhagic Transformation. HT risk was not related to rtPA or collateral status in patients who were R− (On-line Table 2). In patients who were R+ but not R−, collateral status was a significant predictor of HT (On-line Table 2). In multivariate analysis, collateral presence (OR, 0.36; 95% CI, 0.14–0.88; $P = .0284$) was inversely related to HT risk in patients who were R−, while proximal clot location (OR, 2.22; 95% CI, 1.21–4.12; $P = .0102$) and hyperglycemia (OR, 3.07; 95% CI, 1.45–6.70; $P = .0039$) were positively related to HT in patients who were R+ (On-line Table

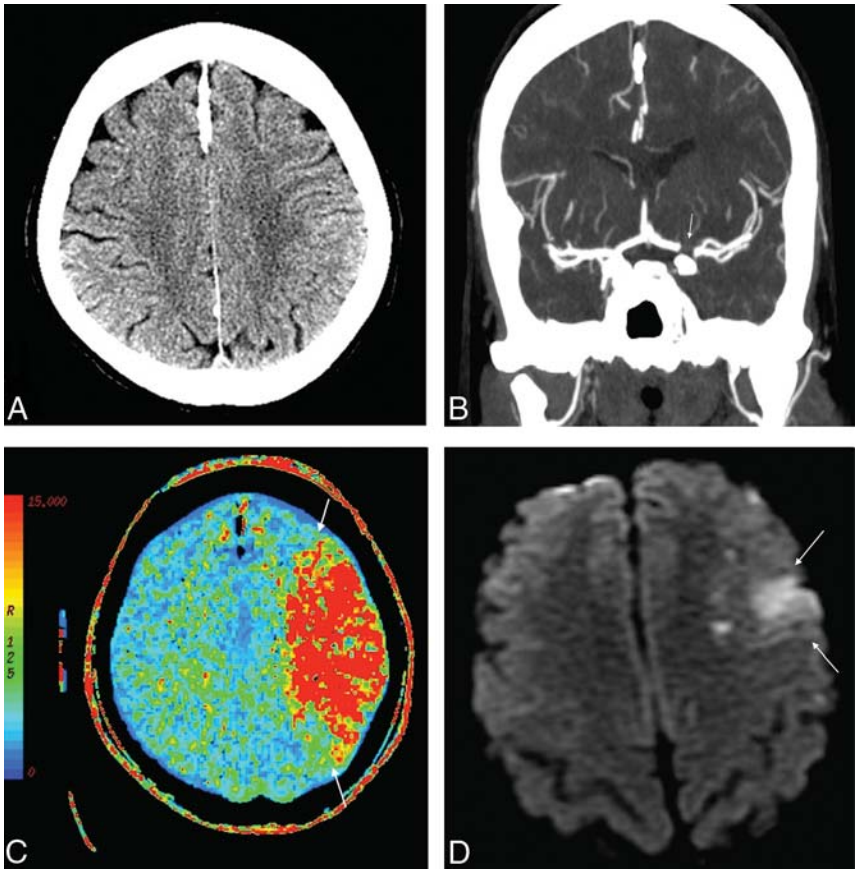

FIG 1. A 57-year-old woman who presented 69 minutes from symptom onset with right-sided acute stroke symptoms. Significant medical history included atrial fibrillation. Her baseline NIHSS score was 11. NCCT shows an ASPECTS of 10 (*A*). CTA shows carotid terminus occlusion involving the proximal M1 segment of the left MCA and proximal A1 segment of the left anterior cerebral artery (CBS = 5) (*arrow*) with a collateral score of 3 (*B*). The CTP MTT map shows perfusion abnormality involving the left MCA territory (*C*, *arrows*). She received rtPA. Follow-up CTA shows nonrecanalization of the occluded vessels (not shown). DWI shows infarct in the left superior frontal region (*D*, *arrows*), significantly smaller than the initial perfusion deficit, highlighting the role of collateral circulation in maintaining the penumbra and its association with smaller infarct size. The follow-up mRS score was 2.

3). In contradistinction to CS, TIV was significantly associated with HT in patients who were R− but not in those who were R+. No significant model differences were seen in patients who were R−, in whom CS and TIV accounted for between 5.7% and 7.3% of HT variability, respectively; however in patients who were R+, CS contributed significantly to a model including TIV, accounting for 11.3% of HT variability (On-line Table 4).

mRS Greater Than 2. The risk of mRS >2 was significantly related to collaterals in patients who were R− but not in those who were R+. Multivariate analysis demonstrated that in patients who were R−, collateral presence was inversely related (OR, 0.15; 95% CI, 0.04–0.48; $P = .0037$) to mRS >2. Older age was associated with poor outcome in both R− and R+ groups (OR, 1.04, 95% CI, 1.01–1.07; $P = .0046$ and OR, 1.05; 95% CI, 1.03–1.08; $P < .0001$, respectively.) In patients who were R−, CS added significantly to a model including only TIV and accounted for 24.1% of mRS >2 variability (On-line Table 3).

Final Infarct Size. The absence of collaterals was strongly associated with larger infarct size irrespective of recanalization status ($P < .0006$ and $P = .0001$). In patients who were R− and R+, collateral absence ($P = .0005$, $P = .0026$) and lower CBS ($P = .0028$, $P = .002$), respectively, were strongly associated with larger infarct size (On-line Table 2). Patients who were R+ receiving rtPA ($P = .0276$) demonstrated smaller infarcts. For patients who were R−, CS contributed little to overall infarct prediction in the presence of TIV assessment, but a model including both CS and TIV accounted for greater variability than CS alone (28% versus 16.5%; $P = .005$, respectively). For patients who were R+, CS significantly improved a model of only TIV and accounted for 16.9% variability for infarct volume (On-line Table 3).

DISCUSSION

Our study demonstrates that collaterals are important for all measured outcomes irrespective of recanalization. However, the magnitude of the added benefit of CS over TIV assessment is dependent on recanalization status, and in many cases, CS and TIV are complementary. The greatest benefit of collaterals occurs in the absence of recanalization, in which collaterals contribute to 16.5% of the variability of final infarct size and 19.2% of the likelihood of mRS >2 but not to the risk of HT. Our results, therefore, extend the findings of a recent study demonstrating effect modification of collaterals in patients who were R+ but not R−.[13] Notably, CS adds benefit over TIV for prediction of mRS >2, but a combination of both TIV and CS is superior to CS alone for both mRS >2 and final infarct prediction, accounting for 24% and 28% of outcome variability, respectively. In patients who were R+, a model including both CS and TIV was superior to that with TIV alone for prediction of HT and final infarct. The variability associated with these outcomes was more muted compared with patients who were R− and accounted for 11.3% and 16.9% of the model's prediction of HT and final infarct size, respectively, in R+ patients. An inverse association between collateral presence and mRS >2 was demonstrated in patients with R+ and R− status but was most significant in the absence of recanalization. Most important, the proportion of patients of mRS >2 in patients who were R− with good collaterals was similar to that of patients who were collateral-negative and R+, reinforcing the importance of both recanalization and collaterals in avoiding futile recanalization.[21,22]

The findings underscore the utility of collateral assessment in predicting outcome irrespective of final recanalization status, consistent with findings of others.[2,4] Preserved collaterals irrespective of recanalization status were associated with reduced

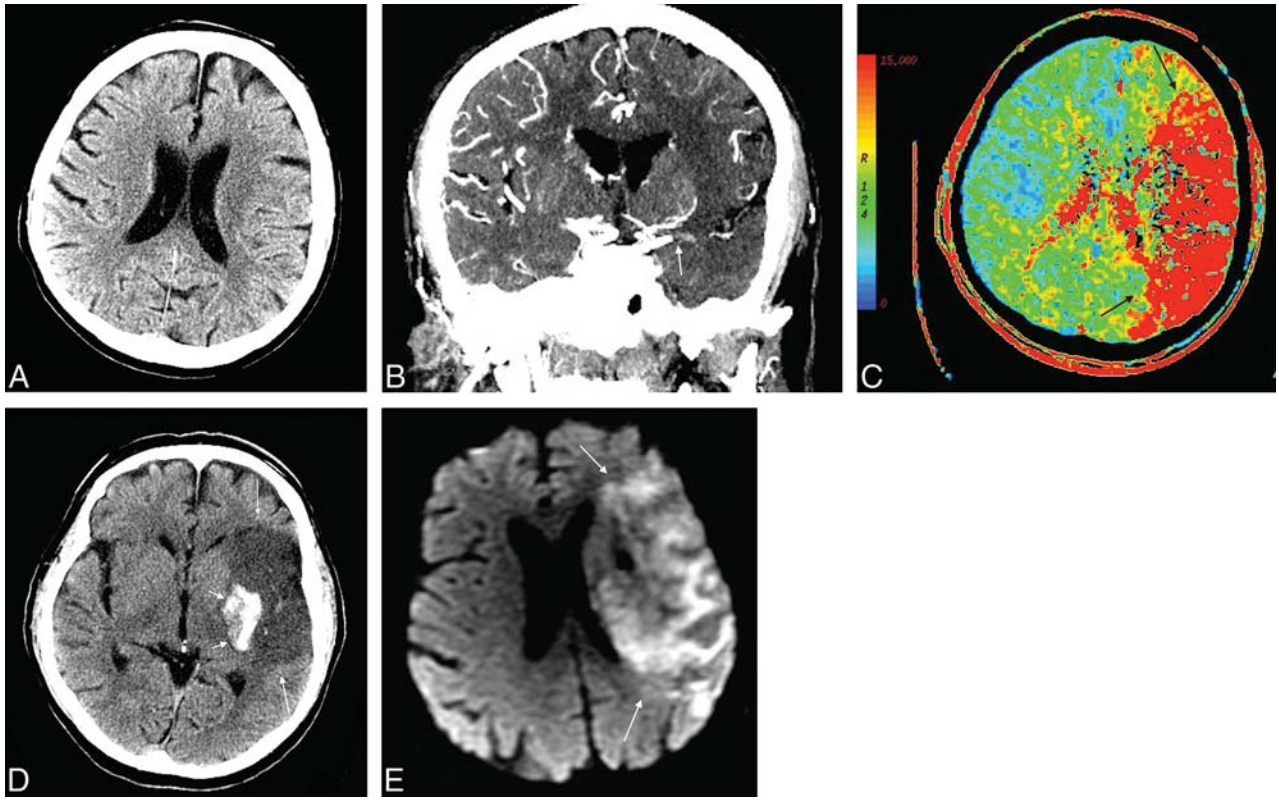

FIG 2. A 69-year-old man who presented 179 minutes from symptom onset with right-sided acute stroke symptoms. Significant medical history included diabetes mellitus, hypertension, high cholesterol, and smoking. His baseline NIHSS score was 25. NCCT shows an ASPECTS of 6 (*A*). CTA shows occlusion of the M1 segment of the left MCA and proximal M2 segment of the left MCA (CBS = 4) (*arrows*) with a CS of 1 (*B*). The CTP MTT map shows perfusion abnormality involving almost the entire left MCA territory (*C*, *arrows*). He received rtPA. Twenty-four-hour CTA shows nonrecanalization of the occluded vessels (not shown), and follow-up DWI on day 5 shows a large infarct in the left MCA territory (*E*, *arrows*), similar in size to the initial perfusion deficit. NCCT shows hemorrhagic transformation in the left basal ganglia region (*D*, *small arrows*). Follow-up mRS was 4.

baseline ischemic tissue (including baseline infarct core) and smaller final infarct volume, contributing to a better outcome (Fig 1). The findings are consistent with prior studies emphasizing the role of collaterals in preserving penumbral viability by minimizing ischemic injury severity and maintaining tissue perfusion.[2,4,23-25]

In the present series, no significant difference in HT frequency was present in the absence of recanalization irrespective of collateral status. Patients who were R+ without collaterals were more likely to undergo HT than those with collaterals. Although recanalization contributes significantly to better outcome in stroke series, our results emphasize that recanalization in the absence of collaterals may have significant adverse outcomes, such as increased HT following restoration of blood flow to nonviable tissue and damaged vasculature.[26] This finding is in agreement with IV rtPA and endovascular therapy studies, in which poor collateral status was associated with higher rates of HT.[7,23] The frequency of poor collaterals in the present series (11% and 30% in patients who were R− and R+, respectively) is similar to that of other series[2,7,24]; this similarity indicates that most patients with acute ischemic stroke manifest collateral preservation at baseline and are eligible for recanalization therapy.

CBS <6 (reflecting larger and usually more proximal clot) was independently associated with greater bNIHSS and infarct volumes, irrespective of recanalization and collateral status.[27] Increased clot burden (low CBS) was also associated with a higher risk of HT (Fig 2). Collateral status is critically dependent on the level and magnitude of clot burden. More proximal clot is associated with larger baseline infarct core and penumbral tissue volumes. These appearances are mediated by a combination of reduced/delayed proximal clot lysis, reduced collateral pathway availability, and cerebral hypoperfusion, provoking profound ischemia inconsistent with viable tissue.[27-29] Indeed Saqqur et al[30] demonstrated that patients with more distal clot were twice as likely to have a favorable clinical outcome as patients with more proximal occlusions. Hence, careful evaluation of collateral status should be made in patients with lower CBS before aggressive recanalization strategies.

We considered the role of collaterals in bNIHSS. Clinical deficit in the hyperacute phase reflects the size of both the infarcted and penumbral zones, whereas early NCCT findings reflect only infarcted tissue. An NIHSS/CT mismatch, therefore, represents salvageable brain[31] and indicates a risk of early neurologic deterioration.[32] We demonstrated that age, clot location, and collaterals were independently associated with stroke severity (On-line Table 2); younger patients with good collateral circulation and distal clot are more likely to have a good outcome. Hyperglycemia was associated with a higher risk of hemorrhagic transformation in patients who were recanalization-positive. Studies evaluating outcome in patients with diabetes and acute stroke have been contradictory. In one study of patients with diabetes and acute ischemic stroke

treated with IV-rtPA, baseline glucose and diabetes were independent predictors of intracranial hemorrhage.[33] However more recent studies have refuted the association between diabetes and intracranial bleed,[34] rather suggesting that hyperglycemia itself accelerates vascular injury in the ischemic area through biochemical changes in the endothelium and by hampering fibrinolysis.[35,36]

A limitation of the present study in view of recent endovascular study results is that none of the patients in the present series underwent mechanical or intra-arterial thrombolysis. Therefore, results are limited to those receiving IV rtPA only. In the present series, a consistent characterization of recanalization was performed at around 24 hours for all patients, thereby attenuating any systematic bias that may have been introduced. However, this approach would not distinguish between early and late recanalizers. Nevertheless the expected findings of reduced infarct size and better outcome in the context of recanalization support our definition as clinically relevant.

CONCLUSIONS

Collateral circulation is an independent predictor of bNIHSS, final infarct volume, hemorrhagic transformation, and mRS >2. The extent of significance varies between patients who are recanalization-negative and -positive, with the greatest impact in those without recanalization. TIV assessment is complementary to CS in many cases.

Disclosures: Sean P. Symons—*UNRELATED: Payment for Lectures (including service on Speakers Bureaus)*: Biogen Idec Canada (for MS talks).

REFERENCES

1. Menon BK, Smith EE, Modi J, et al. **Regional leptomeningeal score on CT angiography predicts clinical and imaging outcomes in patients with acute anterior circulation occlusions.** *AJNR Am J Neuroradiol* 2011;32:1640–45 CrossRef Medline
2. Lima FO, Furie KL, Silva GS, et al. **The pattern of leptomeningeal collaterals on CT angiography is a strong predictor of long-term functional outcome in stroke patients with large vessel intracranial occlusion.** *Stroke* 2010;41:2316–22 CrossRef Medline
3. Zaidat OO, Yoo AJ, Khatri P, et al; Cerebral Angiographic Revascularization Grading (CARG) Collaborators, STIR Revascularization working group, STIR Thrombolysis in Cerebral Infarction (TICI) Task Force. **Recommendations on angiographic revascularization grading standards for acute ischemic stroke: a consensus statement.** *Stroke* 2013;44:2650–63 CrossRef Medline
4. Bang OY, Saver JL, Kim SJ, et al. **Collateral flow predicts response to endovascular therapy for acute ischemic stroke.** *Stroke* 2011;42:693–99 CrossRef Medline
5. Souza LC, Yoo AJ, Chaudhry ZA, et al. **Malignant CTA collateral profile is highly specific for large admission DWI infarct core and poor outcome in acute stroke.** *AJNR Am J Neuroradiol* 2012;33:1331–36 CrossRef Medline
6. Lee M, Saver JL, Alger JR, et al. **Blood-brain barrier permeability derangements in posterior circulation ischemic stroke: frequency and relation to hemorrhagic transformation.** *J Neurol Sci* 2012;313:142–46 CrossRef Medline
7. Brunner F, Tomandl B, Hanken K, et al. **Impact of collateral circulation on early outcome and risk of hemorrhagic complications after systemic thrombolysis.** *Int J Stroke* 2014;9:992–98 CrossRef Medline
8. Shuaib A, Butcher K, Mohammad AA, et al. **Collateral blood vessels in acute ischaemic stroke: a potential therapeutic target.** *Lancet Neurol* 2011;10:909–21 CrossRef Medline
9. González RG. **Current state of acute stroke imaging.** *Stroke* 2013;44:3260–64 CrossRef Medline
10. Frölich AM, Wolff SL, Psychogios MN, et al. **Time-resolved assessment of collateral flow using 4D CT angiography in large-vessel occlusion stroke.** *Eur Radiol* 2014;24:390–96 CrossRef Medline
11. Smit EJ, Vonken EJ, van Seeters T, et al. **Timing-invariant imaging of collateral vessels in acute ischemic stroke.** *Stroke* 2013;44:2194–99 CrossRef Medline
12. Menon BK, O'Brien B, Bivard A, et al. **Assessment of leptomeningeal collaterals using dynamic CT angiography in patients with acute ischemic stroke.** *J Cereb Blood Flow Metab* 2013;33:365–71 CrossRef Medline
13. Nambiar V, Sohn SI, Almekhlafi MA, et al. **CTA collateral status and response to recanalization in patients with acute ischemic stroke.** *AJNR Am J Neuroradiol* 2014;35:884–90 CrossRef Medline
14. Angermaier A, Langner S, Kirsch M, et al. **CT-angiographic collateralization predicts final infarct volume after intra-arterial thrombolysis for acute anterior circulation ischemic stroke.** *Cerebrovasc Dis* 2011;31:177–84 CrossRef Medline
15. Tan IY, Demchuk AM, Hopyan J, et al. **CT angiography clot burden score and collateral score: correlation with clinical and radiologic outcomes in acute middle cerebral artery infarct.** *AJNR Am J Neuroradiol* 2009;30:525–31 CrossRef Medline
16. Bivard A, Levi C, Spratt N, et al. **Perfusion CT in acute stroke: a comprehensive analysis of infarct and penumbra.** *Radiology* 2013;267:543–50 CrossRef Medline
17. Goyal M, Demchuk AM, Menon BK, et al; ESCAPE Trial Investigators. **Randomized assessment of rapid endovascular treatment of ischemic stroke.** *N Engl J Med* 2015;372:1019–30 CrossRef Medline
18. Eilaghi A, Brooks J, d'Esterre C, et al. **Reperfusion is a stronger predictor of good clinical outcome than recanalization in ischemic stroke**. *Radiology* 2013;269:240–48 CrossRef Medline
19. Tomsick T. **TIMI, TIBI, TICI: I came, I saw, I got confused.** *AJNR Am J Neuroradiol* 2007;28:382–84Medline
20. Eilaghi A, d'Esterre CD, Lee TY, et al. **Toward patient-tailored perfusion thresholds for prediction of stroke outcome.** *AJNR Am J Neuroradiol* 2014;35:472–77 CrossRef Medline
21. Murphy A, Symons SP, Hopyan J, et al. **Factors influencing clinically meaningful recanalization after IV-rtPA in acute ischemic stroke.** *AJNR Am J Neuroradiol* 2013;34:146–52 CrossRef Medline
22. Molina CA. **Futile recanalization in mechanical embolectomy trials: a call to improve selection of patients for revascularization.** *Stroke* 2010;41:842–43 CrossRef Medline
23. Bang OY, Saver JL, Kim SJ, et al; UCLA-Samsung Stroke Collaborators. **Collateral flow averts hemorrhagic transformation after endovascular therapy for acute ischemic stroke.** *Stroke* 2011;42:2235–39 CrossRef Medline
24. Miteff F, Levi CR, Bateman GA, et al. **The independent predictive utility of computed tomography angiographic collateral status in acute ischaemic stroke.** *Brain* 2009;132(pt 8):2231–38 CrossRef Medline
25. Jung S, Gilgen M, Slotboom J, et al. **Factors that determine penumbral tissue loss in acute ischaemic stroke.** *Brain* 2012;136(pt 12):3554–60 CrossRef Medline
26. Campbell BC, Christensen S, Tress BM, et al; EPITHET Investigators. **Failure of collateral blood flow is associated with infarct growth in ischemic stroke.** *J Cereb Blood Flow Metab* 2013;33:1168–72 CrossRef Medline
27. Zhu G, Michel P, Aghaebrahim A, et al. **Computed tomography workup of patients suspected of acute ischemic stroke: perfusion computed tomography adds value compared with clinical evaluation, noncontrast computed tomography, and computed tomography angiogram in terms of predicting outcome.** *Stroke* 2013;44:1049–55 CrossRef Medline
28. Gasparotti R, Grassi M, Mardighian D, et al. **Perfusion CT in patients with acute ischemic stroke treated with intra-arterial thrombolysis: predictive value of infarct core size on clinical outcome.** *AJNR Am J Neuroradiol* 2009;30:722–27 CrossRef Medline
29. Yoo AJ, Verduzco LA, Schaefer PW, et al. **MRI-based selection for**

intra-arterial stroke therapy: value of pretreatment diffusion-weighted imaging lesion volume in selecting patients with acute stroke who will benefit from early recanalization. *Stroke* 2009;40: 2046–54 CrossRef Medline

30. Saqqur M, Uchino K, Demchuk AM, et al; CLOTBUST Investigators. **Site of arterial occlusion identified by transcranial Doppler predicts the response to intravenous thrombolysis for stroke.** *Stroke* 2007;38:948–54 CrossRef Medline
31. Kent DM, Hill MD, Ruthazer R, et al. **"Clinical-CT mismatch" and the response to systemic thrombolytic therapy in acute ischemic stroke.** *Stroke* 2005;36:1695–99 CrossRef Medline
32. Tei H, Uchiyama S, Usui T. **Clinical-diffusion mismatch defined by NIHSS and ASPECTS in non-lacunar anterior circulation infarction.** *J Neurol* 2007;254:340–46 CrossRef Medline
33. Demchuk AM, Morgenstern LB, Krieger DW, et al. **Serum glucose level and diabetes predict tissue plasminogen activator-related intracerebral hemorrhage in acute ischemic stroke.** *Stroke* 1999;30: 34–39 CrossRef Medline
34. Reiter M, Teuschl Y, Matz K, et al; Austrian Stroke Unit Registry Collaborators. **Diabetes and thrombolysis for acute stroke: a clear benefit for diabetics.** *Eur J Neurol* 2014;21:5–10 CrossRef Medline
35. Ribo M, Molina C, Montaner J, et al. **Acute hyperglycemia state is associated with lower tPA-induced recanalization rates in stroke patients.** *Stroke* 2005;36:1705–09 CrossRef Medline
36. Martini SR, Kent TA. **Hyperglycemia in acute ischemic stroke: a vascular perspective.** *J Cereb Blood Flow Metab* 2007;27:435–51 CrossRef Medline

Medial Occipital Lobe Hyperperfusion Identified by Arterial Spin-Labeling: A Poor Prognostic Sign in Patients with Hypoxic-Ischemic Encephalopathy

A. de Havenon, A. Sultan-Qurraie, D. Tirschwell, W. Cohen, J. Majersik, and J.B. Andre

ABSTRACT

SUMMARY: Hypoxic-ischemic encephalopathy carries an uncertain prognosis. We sought to retrospectively assess the prognostic value of arterial spin-labeling MR imaging in 22 adult patients diagnosed with hypoxic-ischemic encephalopathy. Quantitative CBF maps were generated from the M0 map, and arterial spin-labeling data on a per-voxel basis were regionally interrogated via visual inspection and ROI placement. Hyperperfusion was defined as regional increases in CBF of >20% (relative to global CBF) and/or >100 mL/100 g/min. Eleven of 22 patients had prominent bilateral medial occipital lobe hyperperfusion, all of whom died before hospital discharge. One patient who had nondistinct arterial spin-labeling hyperperfusion and restricted diffusion survived. Medial occipital lobe hyperperfusion is a distinctive pattern that merits prospective investigation in a cohort of patients with moderate hypoxic-ischemic encephalopathy to determine its predictive ability in patients with a higher likelihood of survival.

ABBREVIATIONS: ASL = arterial spin-labeling; HIE = hypoxic-ischemic encephalopathy; MOLH = medial occipital lobe hyperperfusion

Hypoxic-ischemic encephalopathy (HIE) can result from cardiac arrest, profound hypotension, or respiratory distress secondary to a variety of medical causes, which share the final common pathway of neuronal death from failure of oxidative metabolism.[1] Despite advances in its treatment, patients with HIE have high rates of morbidity and mortality.[2] Given that the severity of HIE varies widely, a wealth of predictive prognostic tools exist, ranging from clinical markers, including level of consciousness and motor response to central noxious stimulation, to neurophysiologic testing, such as electroencephalogram, laboratory markers, and somatosensory-evoked potentials. Although traditionally difficult to perform in this typically clinically unstable population, MR imaging examination is the neuroimaging test of choice, despite the observation that functional recovery following extensive gray matter infarction can occur, suggesting that conventional MR imaging findings lack specificity.[3]

CBF is typically reduced in the first 24–48 hours after HIE, but delayed cerebral hyperperfusion can develop thereafter, a finding first observed with xenon-enhanced CT.[4,5] This hyperperfusion appears to correlate with poor clinical outcome and was theorized to be the result of a loss of vascular resistance. Hyperperfusion after HIE has also been observed with arterial spin-labeling (ASL) MR imaging in both pediatric and adult patients, but in nonspecific patterns that have often corresponded with regions of restricted diffusion.[6,7] ASL is a noninvasive MR imaging technique that produces perfusion maps that are comparable with contrast-based methods such as dynamic susceptibility contrast MR imaging.[8] Because the brain and kidneys are both very sensitive to hypotension and lack of oxygen, HIE is often accompanied by transient acute renal injury, which can be a contraindication to gadolinium-based contrast agent administration in MR imaging.[9,10] In light of this limitation, we sought to further clarify whether the presence of hyperperfusion, as previously reported in patients with HIE[6] and detected with ASL, could be used as a marker of survival prognosis and to examine its relationship to standard prognostic tests.

Case Series

We performed a retrospective data base and patient chart review at an urban tertiary care academic hospital and included adult patients (18 years of age or older) with a discharge diagnosis of HIE. All patients had been admitted to our intensive care unit between September 2012 and January 2014 with a Glasgow Coma Scale score of <8. All patients underwent routine brain MR imaging on a 3T scanner (Tim Trio; Siemens, Erlangen, Germany) as part of standard clinical care. Acquired sequences varied slightly

Received February 10, 2015; accepted after revision April 30.

From the Department of Neurology (A.d.H., J.M.), University of Utah, Salt Lake City, Utah; and Departments of Neurology (A.S.-Q., D.T.) and Radiology (W.C., J.B.A.), University of Washington, Seattle, Washington.

Paper previously presented at: Annual Meeting of the Radiological Society of North America, November 30 to December 5, 2014; Chicago, Illinois.

Please address correspondence to Jalal B. Andre, MD, Department of Radiology, Harborview Medical Center, University of Washington, Box 357115, 1959 NE Pacific St, NW011, Seattle, WA 98195-7115; e-mail: drjalal@uw.edu

http://dx.doi.org/10.3174/ajnr.A4444

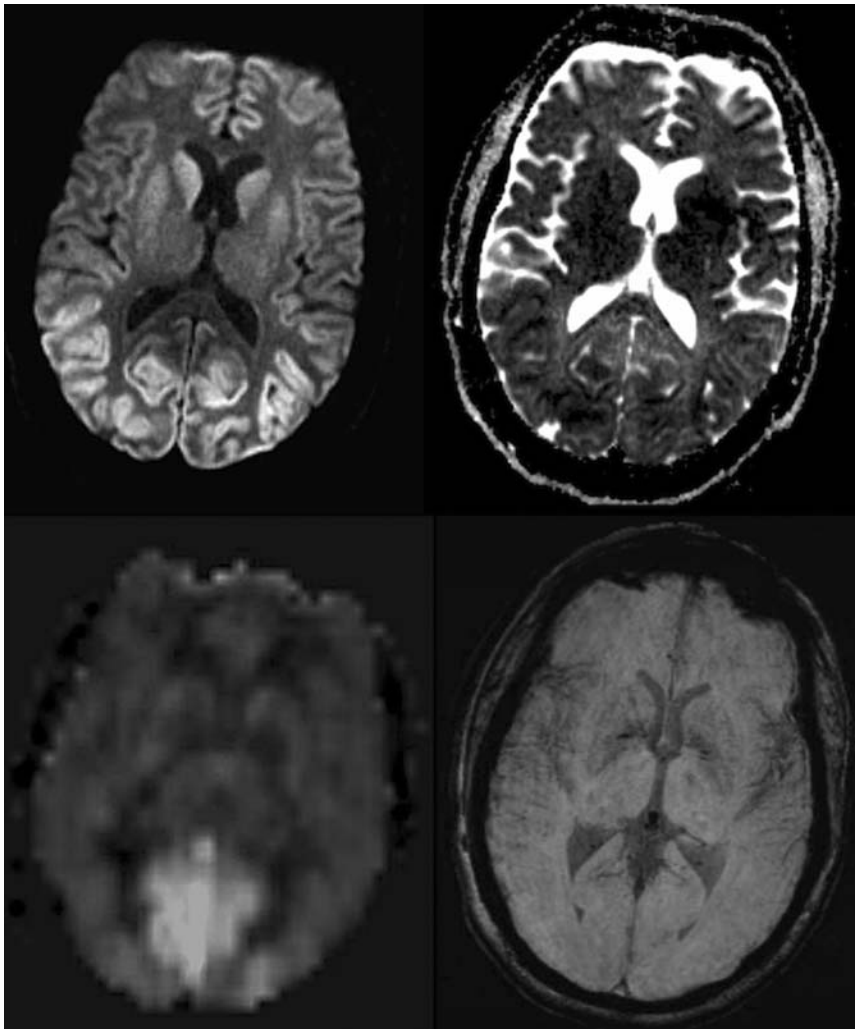

FIG 1. Brain MR imaging from a 44-year-old woman who had a ventricular fibrillation cardiac arrest 5 days prior. *Top left:* axial DWI with extensive parieto-occipital cortical and deep gray matter restricted diffusion. *Top right*: axial ADC map with a lesser amount of corresponding hypointensity from low ADC values, primarily located in the occipital cortex, likely secondary to early pseudonormalization. *Bottom left*: axial ASL CBF with prominent hyperperfusion of the bilateral medial occipital lobes. *Bottom right*: axial SWI MIP with near-absence of venous blood oxygen level–dependent signal in the parieto-occipital cortices.

depending on the specific imaging protocol used but always included axial diffusion, T1- and T2-weighted, fluid-attenuated inversion recovery, and susceptibility-weighted imaging or gradient recalled-echo sequences.

Cerebrovascular perfusion was evaluated by using a commercially available pulsed ASL sequence that incorporates quantitative imaging of perfusion by using a single subtraction (QUIPSS), second version (QUIPSS II), with thin-section TI, periodic saturation (Q2TIPS), and proximal inversion with a control for off-resonance effects (PICORE) with the following parameters: 52 label and control image pairs with section spacing (0-mm section gap); 5 mm for 21 sections or 7.5 mm for 17 sections (dependent on protocol); TE = 12 ms; TI1 = 800 ms; TI2 = 1800 ms; TR = 3400 ms; receiver bandwidth = 2367 Hz/px; flip angle = 90°; FOV = 192; 64 × 64 matrix. Quantitative CBF was calculated from ASL data on a voxelwise basis (in milliliters per 100 g/min).[11] Areas of regional hyperintensity on quantitative CBF maps (suggesting regional hyperperfusion) were visually assessed by 1 reader (J.B.A.) who was blinded to patient clinical history and outcome. Reader assessment was supplemented with ROI placement within the cortical and basal ganglia gray matter. Regional increases in CBF of >20% (relative to global CBF) and/or >100 mL/100 g/min were considered meaningful and defined as hyperperfusion.

After several cases demonstrated hyperperfusion predominantly in the medial occipital lobes, classified as medial occipital lobe hyperperfusion (MOLH), we differentiated MOLH and hyperperfusion in any other vascular distribution, classified as "nondistinct." Additional assessment was performed to determine the extent of diffusion restriction and abnormalities on SWI. Patient chart review was performed (A.d.H) to determine clinical outcome, which was defined as a dichotomous outcome of death or survival before hospital discharge. Descriptive and frequency statistical analyses were obtained by using STATA software, Version 13.1 (StataCorp, College Station, Texas). Statistical significance for intergroup differences was assessed by the Pearson χ^2 or the Fisher exact test for categoric variables and by the Student *t* or Mann-Whitney *U* test for continuous variables.

Twenty-two patients met the inclusion criteria. Mean age was 51.0 ± 19.6 years with a male predominance (77.3%). The mean admission Glasgow Coma Scale score was 3.5 ± 1.1, and the time from hospital admission to MR imaging was 3.2 ± 1.7 days. The etiology of HIE included cardiac arrhythmia and/or arrest (45.5%), respiratory arrest and/or depression (22.7%), drug overdose (18.2%), and hanging (13.6%). Eleven patients (50%) underwent therapeutic hypothermia (32°–34° C for 24–72 hours). Seventeen patients demonstrated nondistinct regional hyperperfusion; 16 died. Eighteen patients had restricted diffusion of the cortical gray matter and/or the basal ganglia, and 17 died. Most patients died secondary to withdrawal of care based on the severity of their injury and poor prognostic indicators. Four of the 5 patients with normal perfusion survived. By visual inspection, the ASL abnormalities comprised smaller volumes than the diffusion abnormalities.

Eleven of 22 patients had MOLH: prominent or isolated hyperperfusion on ASL involving the bilateral medial occipital lobes (Fig 1). The presence of hyperperfusion, either in any vascular territory (nondistinct) or as MOLH, was associated with in-hospital death (nondistinct, $P = .003$; MOLH, $P = .018$). The presence of cortical and/or deep gray matter restricted diffusion was

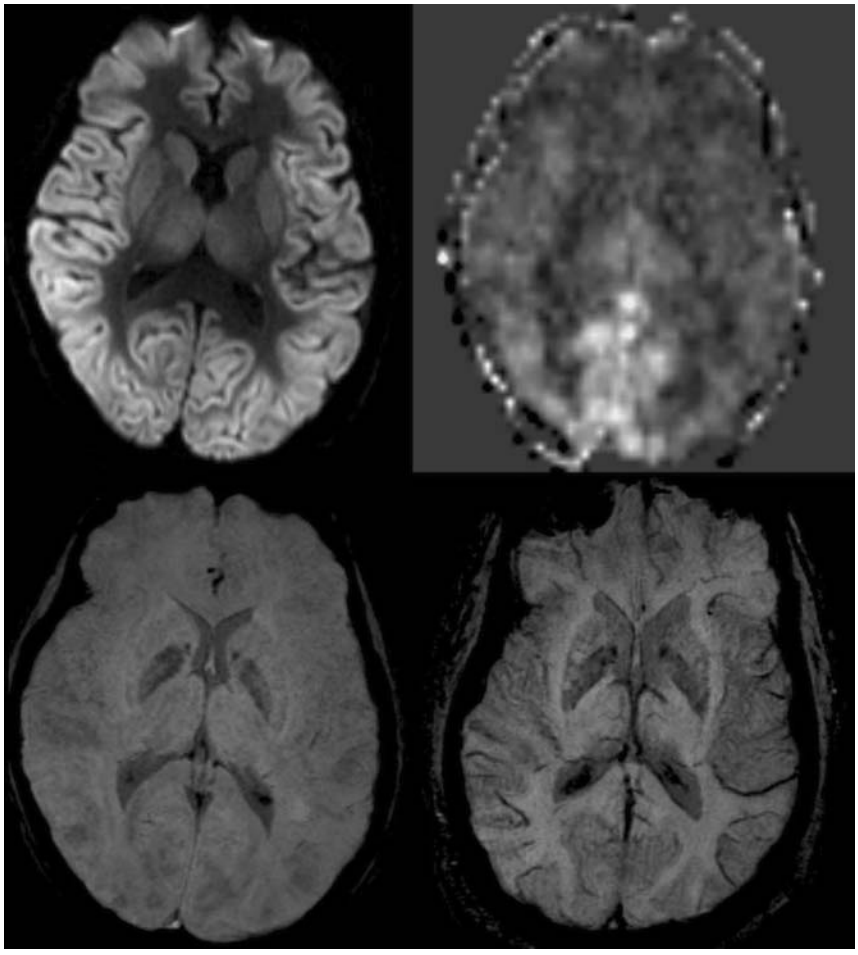

FIG 2. Brain MR imaging of a 36-year-old woman who had respiratory arrest secondary to opiate overdose 2 days prior. *Top left*: axial DWI with global cortical and deep gray matter diffusion restriction. *Top right*: axial ASL CBF with MOLH. *Bottom left*: axial SWI MIP with near-absence of venous blood oxygen level–dependent signal throughout the brain. *Bottom right*: axial SWI MIP from another patient in the cohort, for comparison, who did not have diffusion restriction or hyperperfusion, with ample venous blood oxygen level–dependent signal in both hemispheres.

also associated with in-hospital death ($P = .001$). Seven of the 11 patients with MOLH were treated with therapeutic hypothermia (63.6%), while 4 of the 11 patients without MOLH (36.4%) underwent therapeutic hypothermia ($P = .197$). The patients with MOLH and therapeutic hypothermia were more likely to die (100%, 7/7) than the patients with therapeutic hypothermia without MOLH (25%, 1/4) ($P = .024$). Fifteen patients underwent SWI, of whom 8 demonstrated a relative absence of the typical cortical blood oxygen level–dependent signal from venous structures, which was notable in corresponding areas of hyperperfusion or diffusion restriction (Fig 2) and was associated with inpatient death ($P = .007$). In patients with MOLH, the absent SWI blood oxygen level–dependent venous signal was identified in the occipital lobes in 4/4.

DISCUSSION

Hypoxic-ischemic encephalopathy is often associated with a grim, yet uncertain, prognosis. We evaluated the presence of regional hyperperfusion in a sample of patients with severe HIE, who subsequently underwent MR imaging with ASL, and identified nondistinct regional hyperperfusion in most (77%) patients and a specific pattern of MOLH in half of them (50%). The mechanism of hyperperfusion following HIE is not clearly understood but is theorized to result from a delayed loss of vascular resistance following an initial period of hypoperfusion.[6] The mean time to MR imaging from the hypoxic or anoxic insult was 3.2 days in our cohort, which exceeds the 24- to 48-hour period of hypoperfusion following HIE.[4] The preferential involvement of the medial occipital lobes in HIE is incompletely understood but may be due to the high baseline metabolic demand of this region, rendering it more susceptible to hypoxic or anoxic injury.[12]

ASL hyperperfusion following HIE has been previously described,[6,7] but selective hyperperfusion involving the medial occipital lobes represents a novel finding. Preferential or isolated restricted diffusion involving the occipital lobes has been reported following HIE, though we did not observe such preferential regional cortical involvement in our patient cohort.[13] An interesting finding was the absence of venous deoxyhemoglobin blood oxygen level–dependent signal on SWI in areas of hyperperfusion. Following cardiac arrest, evaluation with PET has demonstrated a reduction of oxygen metabolism and extraction in the occipital lobes, associated with worse outcome.[14] The specific absence of venous deoxyhemoglobin in the medial occipital lobes on minimum-intensity-projection SWI-processed images, observed in the patients with MOLH, would support this observation and suggests the development of possible physiologic shunting of diamagnetic oxygenated blood through dilated vascular channels.

We acknowledge referral bias in this study, because MR imaging examinations were preferentially ordered for patients presumed to have a poor prognosis. As a result, the mortality rate of 77.3% in our sample was notably high for HIE, but it proffered a unique opportunity to identify imaging biomarkers that could be studied in more heterogeneous cohorts of HIE. We did observe survival in 1 patient, who exhibited both deep gray matter restricted diffusion and nondistinct hyperperfusion, which are concerning false-positive findings. Nonetheless, the universal poor prognosis of patients with the highly distinctive imaging pattern of MOLH emerged from our retrospective investigation and can be viewed as hypothesis-generating.

CONCLUSIONS

ASL may have a unique complementary role in the evaluation of patients with HIE, who are often unable to undergo contrast-

based perfusion scans secondary to acute renal insufficiency. In our small cohort, a patient survived despite having poor prognostic indicators, including nondistinct hyperperfusion and restricted diffusion. Multimodal, accurate diagnostic testing is crucial for decision-making in this setting. MOLH is a distinctive imaging pattern with a plausible physiologic basis. Our findings warrant additional study, particularly in light of the potential utility of MOLH in patients undergoing therapeutic hypothermia, which has led to uncertainty in the reliability of traditional prognostic markers validated in the prehypothermia era.[13] A prospective trial would determine if these findings hold true for patients with moderate HIE, both with and without therapeutic hypothermia.

Disclosures: Jalal B. Andre—*UNRELATED: Grants/Grants Pending*: Philips Healthcare,* *Comments*: Grant funding was provided to offset costs of MR imaging scans and related research personnel. *Money paid to the institution.

REFERENCES

1. Howard RS, Holmes PA, Koutroumanidis MA. **Hypoxic-ischaemic brain injury.** *Pract Neurol* 2011;11:4–18 CrossRef Medline
2. Greer DM, Rosenthal ES, Wu O. **Neuroprognostication of hypoxic-ischaemic coma in the therapeutic hypothermia era.** *Nat Rev Neurol* 2014;10:190–203 CrossRef Medline
3. Howard RS, Holmes PA, Siddiqui A, et al. **Hypoxic-ischaemic brain injury: imaging and neurophysiology abnormalities related to outcome.** *QJM* 2012;105:551–61 CrossRef Medline
4. Inoue Y, Shiozaki T, Irisawa T, et al. **Acute cerebral blood flow variations after human cardiac arrest assessed by stable xenon enhanced computed tomography.** *Curr Neurovasc Res* 2007;4:49–54 CrossRef Medline
5. Cohan SL, Mun SK, Petite J, et al. **Cerebral blood flow in humans following resuscitation from cardiac arrest.** *Stroke* 1989;20:761–65 CrossRef Medline
6. Pollock JM, Whitlow CT, Deibler AR, et al. **Anoxic injury-associated cerebral hyperperfusion identified with arterial spin-labeled MR imaging.** *AJNR Am J Neuroradiol* 2008;29:1302–07 CrossRef Medline
7. Wintermark P, Hansen A, Gregas MC, et al. **Brain perfusion in asphyxiated newborns treated with therapeutic hypothermia.** *AJNR Am J Neuroradiol* 2011;32:2023–29 CrossRef Medline
8. Deibler AR, Pollock JM, Kraft RA, et al. **Arterial spin-labeling in routine clinical practice, Part 1: technique and artifacts.** *AJNR Am J Neuroradiol* 2008;29:1228–34 CrossRef Medline
9. Eckardt KU, Bernhardt WM, Weidemann A, et al. **Role of hypoxia in the pathogenesis of renal disease.** *Kidney Int Suppl* 2005:S46–51 CrossRef Medline
10. Devarajan P. **Update on mechanisms of ischemic acute kidney injury.** *J Am Soc Nephrol* 2006;17:1503–20 CrossRef Medline
11. Wang J, Licht DJ, Jahng GH, et al. **Pediatric perfusion imaging using pulsed arterial spin labeling.** *J Magn Reson Imaging* 2003;18:404–13 CrossRef Medline
12. Rabinstein A, Resnick SJ. **Hypoxic-ischemic brain damage**. In: Rabinstein A, Resnick SJ. *Practical Neuroimaging in Stroke: A Case-Based Approach.* Philadelphia: Saunders; 2009:1–17
13. Hahn DK, Geocadin RG, Greer DM. **Quality of evidence in studies evaluating neuroimaging for neurologic prognostication in adult patients resuscitated from cardiac arrest.** *Resuscitation* 2014;85:165–72 CrossRef Medline
14. Edgren E, Enblad P, Grenvik A, et al. **Cerebral blood flow and metabolism after cardiopulmonary resuscitation: a pathophysiologic and prognostic positron emission tomography pilot study.** *Resuscitation* 2003;57:161–70 CrossRef Medline

Brain Magnetic Susceptibility Changes in Patients with Natalizumab-Associated Progressive Multifocal Leukoencephalopathy

J. Hodel, O. Outteryck, S. Verclytte, V. Deramecourt, A. Lacour, J.-P. Pruvo, P. Vermersch, and X. Leclerc

ABSTRACT

SUMMARY: We investigated the brain magnetic susceptibility changes induced by natalizumab-associated progressive multifocal leukoencephalopathy. We retrospectively included 12 patients with natalizumab–progressive multifocal leukoencephalopathy, 5 with progressive multifocal leukoencephalopathy from other causes, and 55 patients with MS without progressive multifocal leukoencephalopathy for comparison. MR imaging examinations included T2* or SWI sequences in patients with progressive multifocal leukoencephalopathy (86 examinations) and SWI in all patients with MS without progressive multifocal leukoencephalopathy. Signal abnormalities on T2* and SWI were defined as low signal intensity within the cortex and/or U-fibers and the basal ganglia. We observed T2* or SWI signal abnormalities at the chronic stage in all patients with progressive multifocal leukoencephalopathy, whereas no area of low SWI signal intensity was detected in patients without progressive multifocal leukoencephalopathy. Among the 8 patients with asymptomatic natalizumab–progressive multifocal leukoencephalopathy, susceptibility changes were observed in 6 (75%). The basal ganglia adjacent to progressive multifocal leukoencephalopathy lesions systematically appeared hypointense by using T2* and/or SWI. Brain magnetic susceptibility changes may be explained by the increased iron deposition and constitute a useful tool for the diagnosis of progressive multifocal leukoencephalopathy.

ABBREVIATIONS: NTZ = natalizumab; PML = progressive multifocal leukoencephalopathy

Natalizumab (NTZ), an effective treatment in patients with relapsing-remitting multiple sclerosis, is associated with a risk of progressive multifocal leukoencephalopathy (PML).[1] Early diagnosis of NTZ-associated PML (NTZ-PML) may improve the functional outcome.[2] However, the diagnosis of asymptomatic NTZ-PML remains difficult due to the coexistence of MS lesions and the different imaging patterns of NTZ-PML lesions.[3-5]

MR imaging is crucial for the recognition of NTZ-PML.[1,4-7] The known imaging findings for asymptomatic NTZ-PML include the following: a subcortical location involving U-fibers, a sharp lesional border toward the gray matter contrasting with an ill-defined border toward the white matter, and increased signal intensity on T2-weighted and diffusion-weighted images.[5] Postcontrast enhancement and T2WI hyperintense punctate lesions have also been reported in patients with NTZ-PML.[4,5,8]

To our knowledge, there are no data available on the susceptibility changes, evaluated by gradient-echo T2* or susceptibility-weighted images, in a cohort of consecutive patients with NTZ-PML. Our purpose was to investigate the brain magnetic susceptibility changes, detected on T2* or SWI, in a cohort of consecutive patients with NTZ-PML.

Case Series

Patients. This retrospective study was approved by our institutional review board. From February 2011 to August 2014, 17 consecutive patients, including 12 patients with relapsing-remitting multiple sclerosis treated with NTZ, 2 with leukemia, 2 treated with immunosuppressive therapies after liver or renal transplant, and 1 with neurosarcoidosis (8 women; mean age, 48.7 years; range, 26–63 years), were diagnosed with PML on the basis of the following:

1) Suggestive clinical and imaging findings associated with positive DNA polymerase chain reaction for the John Cunningham virus in the CSF, in 15 patients ("definite PML" according to the American Academy of Neurology criteria[9])

Received January 23, 2015; accepted after revision April 10.

From the University of Lille, CHU Lille (J.H., O.O., V.D., A.L., J.-P.P., P.V., X.L.), Lille, France; Departments of Neuroradiology (J.H., J.-P.P., X.L.) and Neurology (O.O., A.L., P.V.), Roger Salengro Hospital, Lille, France; Department of Radiology (S.V.), Saint Philibert Hospital, Lille, France; and Department of Pathology (V.D.), Lille University Hospital, Lille, France.

Please address correspondence to Jérôme Hodel, MD, PhD, Department of Neuroradiology, Hôpital Roger Salengro, Rue Emile Laine, 59037 Lille, France; e-mail: Jerome.hodel@gmail.com

Indicates article with supplemental on-line table.

http://dx.doi.org/10.3174/ajnr.A4436

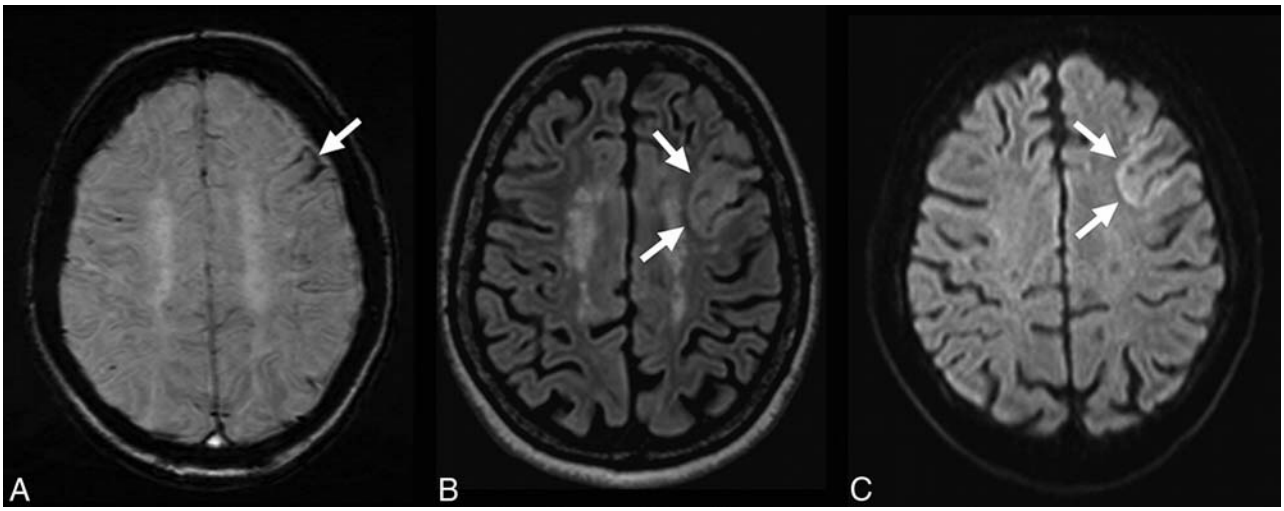

FIG 1. Susceptibility-weighted, FLAIR, and diffusion images in patient 9 with unilobar left frontal NTZ-PML at the asymptomatic stage. A hypointense rim involving the cortex and the U-fibers of the left frontal lobe is visible on SWI (*A*, *arrow*). The NTZ-PML lesion appears hyperintense on FLAIR (*B*, *arrow*) and diffusion (*C*, *arrows*) images.

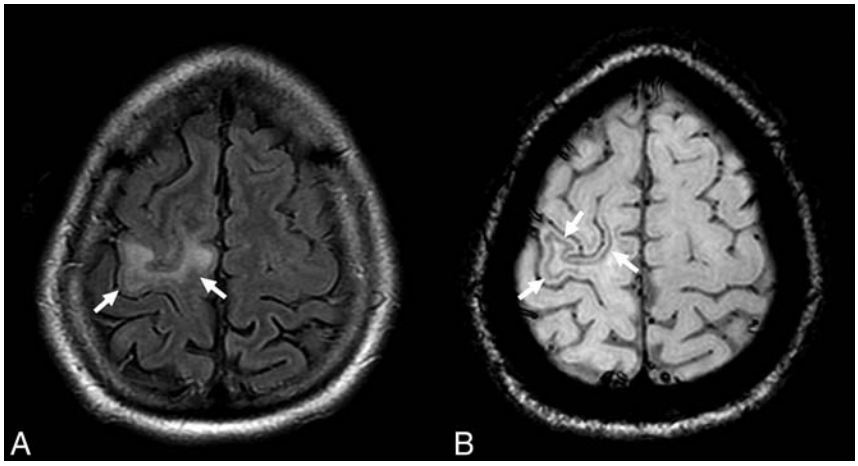

FIG 2. In patient 11 at the symptomatic stage, the NTZ-PML lesion appears hyperintense on the FLAIR image involving the right precentral gyrus (*A*, *arrows*). The SWI sequence reveals a hypointense rim involving the U-fibers adjacent to the PML lesion (*B*, *arrows*).

2) Highly suggestive imaging and clinical follow-up for 2 patients treated with NTZ (patients 10 and 12) for whom iterative CSF examination findings were negative.

Characteristics of patients are summarized in the On-line Table. Patient 2 underwent postmortem brain neuropathologic examination.

Eighty-six brain MR imaging scans (Achieva 1.5T [$n = 32$], 3T [$n = 54$]; Philips Healthcare, Best, the Netherlands) were obtained in these 17 patients with PML (mean MR images per patient, 4.9; range, 1–10). MR imaging was performed at asymptomatic ($n = 8$), symptomatic ($n = 17$), immune reconstitution inflammatory syndrome ($n = 19$), and chronic/follow-up stages ($n = 42$). MR imaging protocol included pre- and postcontrast T1WI, T2WI, fluid-attenuated inversion recovery, and diffusion MR images. The gradient-echo T2* sequence was available in 67 MR imaging examinations; SWI, in 19.

Fifty-five consecutive patients with MS and without NTZ-PML (37 women; mean age, 44.2 years; range, 22–61 years; 23 with clinically isolated syndrome, 32 with relapsing-remitting multiple sclerosis) served as a control group. SWI was performed in all controls at 3T (55 MR imaging examinations, Achieva 3T, Philips Healthcare).

Image Analysis

Three experienced neuroradiologists (J.H., X.L., and J.-P.P.) reviewed the 141 MR imaging examinations available in consensus. For each MR image, they assessed the signal abnormalities on T2* or SWI defined as

1) Areas of low signal intensity within the cortex and/or the U-fibers.

2) Low signal intensity and asymmetry of the signal of the basal ganglia.

In patients with NTZ-PML, consecutive MR images were also reviewed to analyze the longitudinal changes in each patient regarding signal intensity on T2* and SWI.

RESULTS

PML Lesions

Twenty supratentorial and 4 infratentorial PML lesions were visible in the 17 patients with PML involving the frontal ($n = 6$, right; $n = 4$, left), parietal ($n = 6$, left), occipital ($n = 2$, right), and temporal ($n = 1$, right; $n = 1$ left) lobes or the middle cerebellar peduncle ($n = 1$, right; $n = 3$, left). In 2 patients (patients 1 and 13), PML was confined to the middle cerebellar peduncle. Eight patients (11 PML lesions) were explored at the asymptomatic stage, including 6 patients with ≥1 subcortical supratentorial

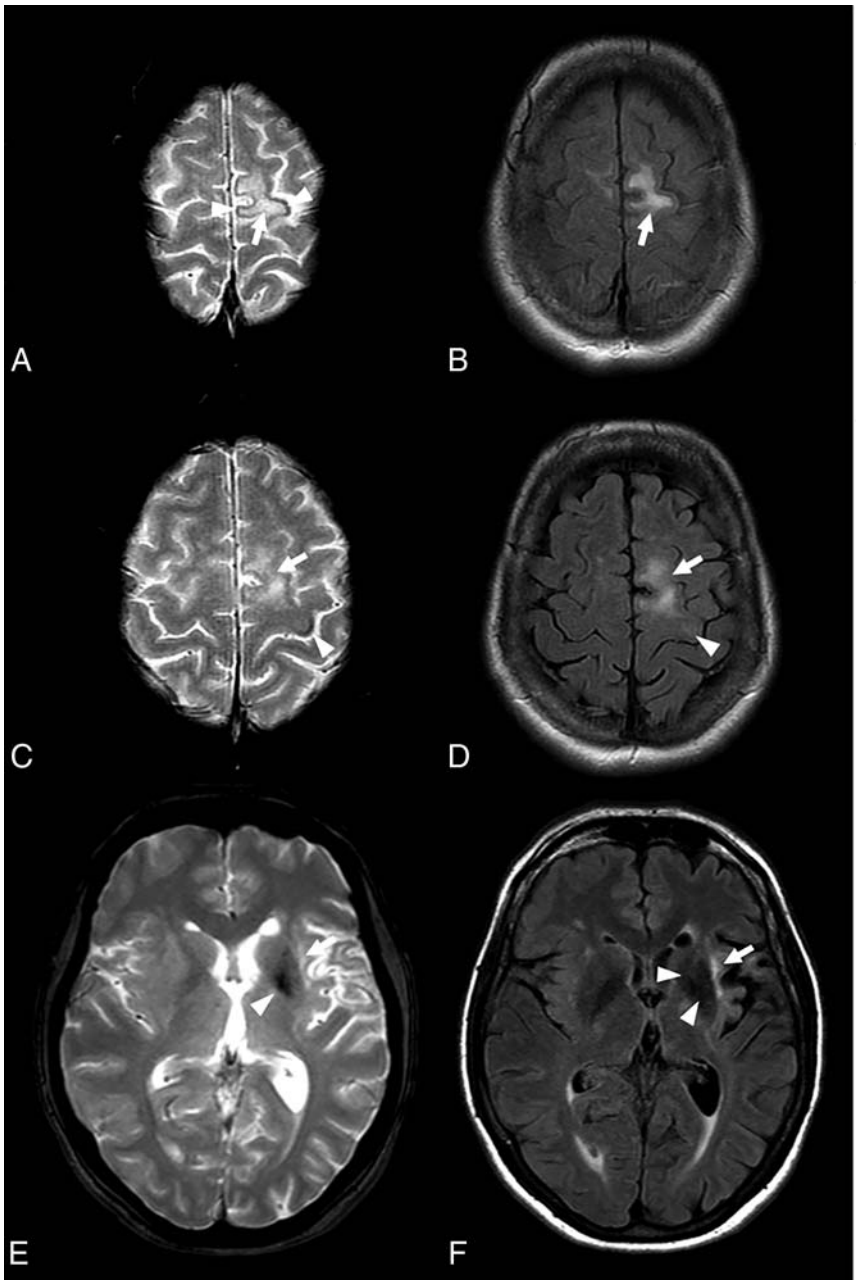

FIG 3. FLAIR and T2* images in patient 7 at the symptomatic stage. Cortical low signal intensity is visible on T2* images (*A*, *arrowheads*) adjacent to the hyperintense PML lesion (*A–C*, *arrows*). Such cortical T2* signal abnormality is also visible (*C*, *arrowhead*) with only subtle adjacent hyperintensity on FLAIR images (*D*, *arrowhead*). Note the low signal intensity of the left basal ganglia on both T2* and FLAIR images (*E* and *F*, *arrowheads*) adjacent to the insular PML lesion (*E* and *F*, *arrows*).

PML lesion, 1 with an infratentorial lesion (patient 1), and 1 with both supra- and infratentorial lesions (patient 11).

Cortex and U-Fibers

Patient imaging findings are summarized in the On-line Table.

When considering the subcortical PML lesions with MR imaging available at the chronic stage (18 lesions), T2* and/or SWI demonstrated areas of cortical low signal intensity in all cases.

For 8 patients (with 11 NTZ-PML lesions), MR imaging, including T2* and/or SWI, was available at the presymptomatic stage. Of the 8 patients scanned at the presymptomatic stage, susceptibility changes were visible in 6 (75%), including 6 PML lesions (55%): 4 small subcortical lesions (2 observed with SWI and 2 with T2*; patients 4, 6, 9, and 12; Fig 1) and 2 lesions involving the middle cerebellar peduncles. For 5 subcortical PML lesions (45%), the cortical low T2* signal intensity was not visible initially at the presymptomatic stage and only appeared at the chronic stage. U-fiber low-signal intensity on SWI is shown in Fig 2.

Longitudinal changes were observed in 8 patients (9 PML lesions), with cortical T2* and/or SWI low signal intensity appearing or becoming more prominent.

Cortical or U-fiber T2* hypointensity was systematically adjacent to a PML lesion, hyperintense on FLAIR images. However, only a faint FLAIR hyperintensity was visible adjacent to the area of

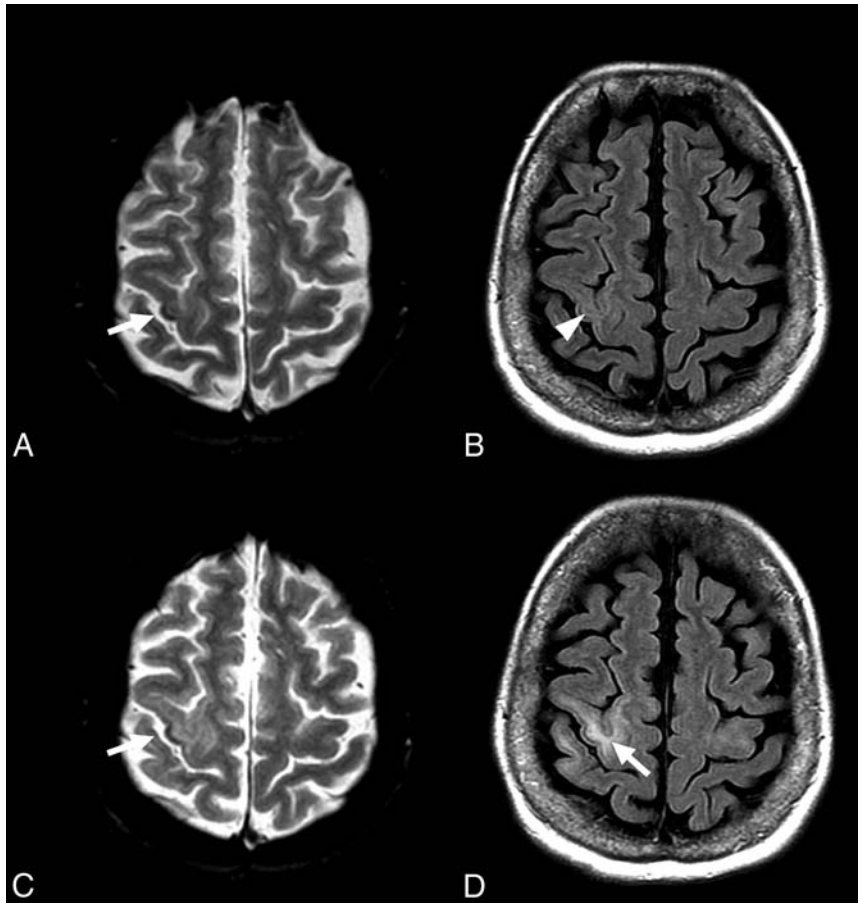

FIG 4. FLAIR and T2* images in patient 12 with NTZ-PML at asymptomatic and symptomatic stages. At the asymptomatic stage, a small area of cortical low signal intensity is visible on T2* image within the right central sulcus (*A*, *arrow*), with faint signal abnormalities on FLAIR image (*B*, *arrowhead*). At the symptomatic stage, the cortical hypointensity on T2* image is more prominent (*C*, *arrow*), while subcortical FLAIR hyperintensity is obvious (*D*, *arrow*).

cortical T2* hypointensity for 3 MR imaging examinations: 2 performed at the symptomatic stage in patient 7 and 1 performed at the asymptomatic stage in patient 12 (Figs 3 and 4, respectively).

Cortical low T2* signal intensity was associated with T1WI hyperintensity in 2 patients (patients 2 and 4) at the chronic stage. For all subjects, the areas of low signal intensity did not match contrast enhancement or diffusion restriction.

A phase map was available in patients scanned with the SWI sequence, showing a paramagnetic dipole matching the low signal intensity observed on magnitude images, suggesting iron deposition.

MR imaging was only available at the chronic stage for patient 2, for whom a postmortem pathologic specimen revealed astrocytic gliosis associated with abundant microglial and macrophage infiltrate within the area of cortical low T2* signal intensity previously visible on T2* images (Fig 5). Macrophages contained degraded myelin-filled vacuoles, and there was no visible calcification or hemorrhage.

Basal Ganglia

Asymmetric T2* hypointensity within the basal ganglia was systematically observed when PML was adjacent to the deep gray matter (7 patients, 8 PML lesions) at any stage (Figs 3 and 6), including the presymptomatic stage for patients 1 and 11.

Consecutive MR images revealed the progressive decrease of signal of the basal ganglia with PML expansion on FLAIR and T2* images for 3 patients once the PML lesion became adjacent to the deep GM.

No low signal intensity was observed within the cortex, U-fibers, or basal ganglia in controls.

DISCUSSION

All the consecutive patients with PML showed at least 1 area of low T2* or SWI signal intensity, involving deep or cortical gray matter, except 1 patient scanned only at the symptomatic stage. Such data may be clinically relevant because we did not observe this finding in consecutive patients with MS without PML. Brain magnetic susceptibility changes may be observed in patients with PML at the presymptomatic stage, while the findings are subtle by using other MR images such as FLAIR; such findings suggest a potential added value for T2* or SWI sequences in patients suspected of having PML. In addition, susceptibility changes induced by PML do not appear specific to NTZ-PML.

The underlying cause of signal hypointensity on T2* and SWI

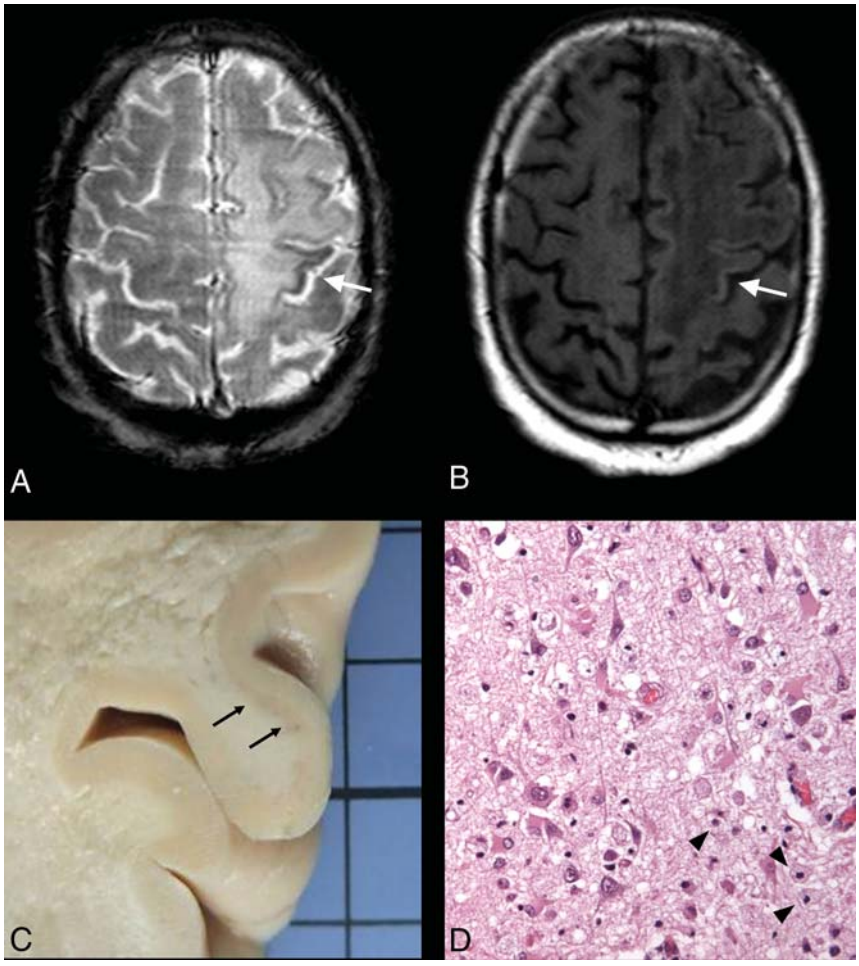

FIG 5. T2* and T1WI at the chronic stage and pathologic specimen (hematoxylin-eosin staining) of patient 2. An extensive PML lesion is visible involving the left frontal and parietal white matter. Low signal intensity of the left precentral cortex is visible on T2* image (*A*, *arrow*), matching the hyperintensity on T1WI (*B*, *arrow*). Pathologic specimen reveals a loss of distinction between GM and WM (*C*, *arrows*) as well as microglial and macrophage infiltrate of the cortical neuropile (*D*, *arrowheads*; hematoxylin-eosin staining, high-power objective).

in patients with NTZ-PML remains unclear. In patients with an asymmetric hypointensity involving the basal ganglia, phase maps revealed a paramagnetic dipole, ruling out asymmetric physiologic calcifications. Moreover, our pathologic case may suggest that an accumulation of iron within the macrophages could potentially explain these findings. Iron accumulation in the deep GM of patients with MS is strongly associated with the duration and severity of the disease. Increases in iron deposition in subcortical regions were recently demonstrated in patients with MS by using quantitative susceptibility and R2* mapping.[10] This effect was strongly correlated with myelin degeneration along the WM skeleton and the Expanded Disability Status Scale.[10] Most interesting, while SWI has been extensively evaluated in patients with MS, such low signal intensity on T2* or susceptibility-weighted MR images had never been previously reported in patients with MS plaques, active or not, to our knowledge. Indeed, we may hypothesize that PML lesions could differ from MS plaques by further increasing myelin degeneration and thus intracellular accumulation of iron within macrophages and microglial cells. Why some PML lesions are associated with T2*/SWI subcortical hypointensity and some are not at the presymptomatic stage remains unclear. We hypothesize that iron deposition may be increased in case of high local iron storage capacity (in the lenticular nucleus, dentate nucleus, and maybe the precentral cortex) or in case of high local myelin content (in the middle cerebral peduncle or pyramidal tract).

Our study had some limitations. We included a relatively small number of patients with NTZ-PML, and the John Cunningham virus DNA polymerase chain reaction was negative in 2. However, the diagnosis of NTZ-PML may be challenging, including negative findings on CSF examinations, as previously reported.[11] Different MR imaging scanners (1.5T and 3T) were used in this retrospective study. However, to assess longitudinal changes with time, we compared MR images obtained at the same MR imaging field strength and with the same MR sequence. In this preliminary clinical report, we did not assess the diagnostic accuracy of low signal intensity on T2* and SWI for the diagnosis of NTZ-PML. Indeed both T2* and SWI sequences were used in patients with NTZ-PML at asymptomatic, symptomatic, and chronic stages. Susceptibility-weighted or T2* MR images are sensitive to nonuniform B1 or B0; however, no area of low signal intensity was observed in the control group, demonstrating that the reported signal anomalies were not related to artifacts. The absence of signal abnormalities observed in patients with MS without PML may

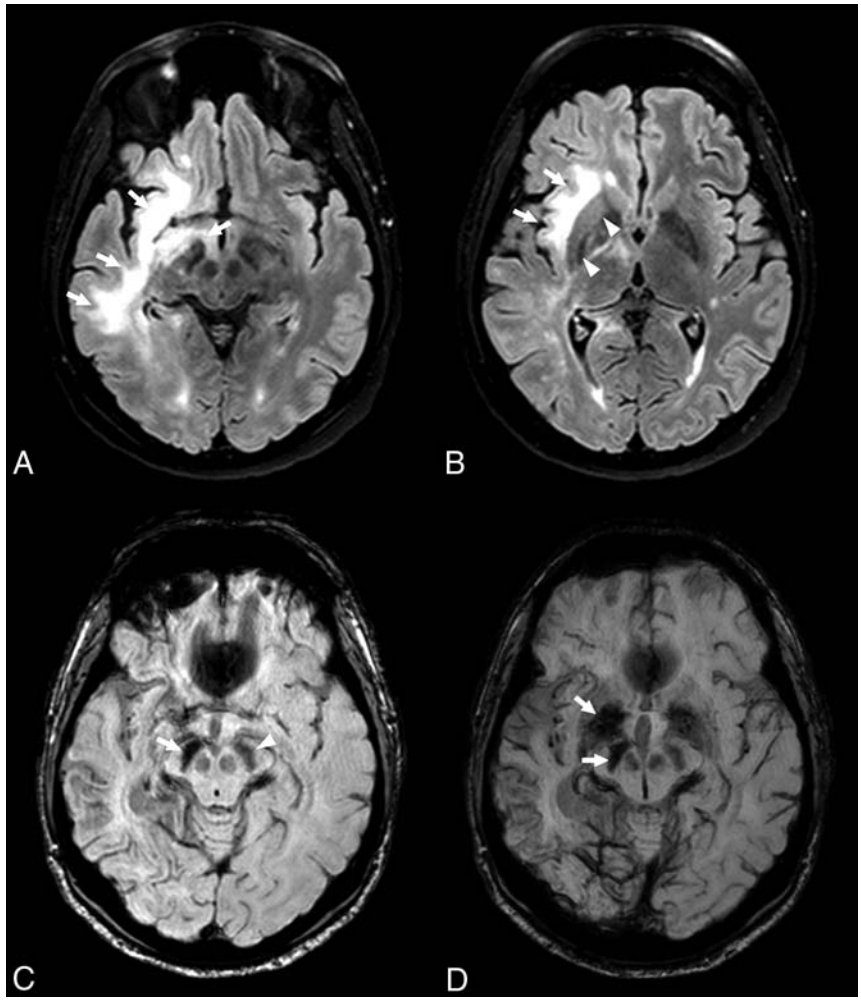

FIG 6. FLAIR and SWI in patient 8 at symptomatic and chronic stages. At the symptomatic stage, an extensive PML lesion is visible on FLAIR images involving the right frontal and temporal white matter and the brain stem (*A* and *B*, *arrows*). Note the low signal intensity of the right lenticular nucleus on FLAIR images (*B*, *arrowheads*). At the chronic stage, the SWI sequence revealed decreased signal-intensity of the right substantia nigra (*C*, *arrow*) compared with the left (*C*, *arrowhead*). SWI minimal-intensity-projection view confirms this pattern of asymmetric hypointensity involving the right lenticular nucleus and substantia nigra, adjacent to the PML lesion (*D*, *arrows*).

also suggest a high specificity of this finding. Further prospective studies are required to assess its real specificity for the diagnosis of asymptomatic NTZ-PML. Finally, the control group used in our study did not match the group of patients with PML in terms of sex, disease severity, and treatment.

CONCLUSIONS

Our study showed that PML, related to NTZ or not, induces brain magnetic susceptibility changes within U-fibers or deep gray matter, visible on T2* or SWI and potentially explained by iron deposition. Such findings were observed at the presymptomatic stage with potential implications for patient care.

Disclosures: Patrick Vermersch—*RELATED*: *Grant*: Biogen Idec*; *Consulting Fee or Honorarium*: Biogen Idec; *Support for Travel to Meetings for the Study or Other Purposes*: Biogen Idec; *UNRELATED*: *Board Membership*: Biogen Idec, Teva, Sanofi, Almirall, Merck-Serono, Novartis; *Consultancy*: Biogen Idec, Novartis, Bayer, Sanofi, Almirall, Merck-Serono, Teva. Olivier Outteryck—*UNRELATED*: *Grants/Grants Pending*: Biogen Idec, Novartis, Bayer-Schering, *Comments*: both direct payment and payment to the institution (grant for research); *Payment for Lectures (including service on Speakers Bureaus)*: Biogen Idec; *Travel/Accommodations/Meeting Expenses Unrelated to Activities Listed*: Novartis,* Biogen Idec,* Merck-Serono,* Sanofi,* Teva.* Arnaud Lacour—*UNRELATED*: *Board Membership*: Octapharma*; *Expert Testimony*: LFB (both direct payment and payment to the institution); *Payment for Lectures (including service on Speakers Bureaus)*: LFB, Pfizer, Octapharma, Merz; *Travel/Accommodations/Meeting Expenses Unrelated to Activities Listed*: Biogen Idec,* Novartis,* Pfizer,* Teva,* LFB.* *Money paid to the institution.

REFERENCES

1. Clifford DB, De Luca A, Simpson DM, et al. **Natalizumab-associated progressive multifocal leukoencephalopathy in patients with multiple sclerosis: lessons from 28 cases.** *Lancet Neurol* 2010;9:438–46 CrossRef Medline
2. Dong-Si T, Richman S, Wattjes MP, et al. **Outcome and survival of asymptomatic PML in natalizumab-treated MS patients.** *Ann Clin Transl Neurol* 2014;1:755–64 CrossRef Medline
3. Wattjes MP, Richert ND, Killestein J, et al. **The chameleon of neuroinflammation: magnetic resonance imaging characteristics of natalizumab-associated progressive multifocal leukoencephalopathy.** *Mult Scler* 2013;19:1826–40 CrossRef Medline
4. Wattjes MP, Vennegoor A, Steenwijk MD, et al. **MRI pattern in asymptomatic natalizumab-associated PML.** *J Neurol Neurosurg Psychiatry* 2015;86:793–98 CrossRef Medline
5. Yousry TA, Pelletier D, Cadavid D, et al. **Magnetic resonance imaging pattern in natalizumab-associated progressive multifocal leukoencephalopathy.** *Ann Neurol* 2012;72:779–87 CrossRef Medline
6. Blair NF, Brew BJ, Halpern JP. **Natalizumab-associated PML iden-**

tified in the presymptomatic phase using MRI surveillance. *Neurology* 2012;78:507–08 CrossRef Medline
7. Bag AK, Curé JK, Chapman PR, et al. **JC virus infection of the brain.** *AJNR Am J Neuroradiol* 2010;31:1564–76 CrossRef Medline
8. Wattjes MP, Verhoeff L, Zentjens W, et al. **Punctate lesion pattern suggestive of perivascular inflammation in acute natalizumab-associated progressive multifocal leukoencephalopathy: productive JC virus infection or preclinical PML-IRIS manifestation?** *J Neurol Neurosurg Psychiatry* 2013;84:1176–77 CrossRef Medline
9. Berger JR, Aksamit AJ, Clifford DB, et al. **PML diagnostic criteria: consensus statement from the AAN Neuroinfectious Disease Section.** *Neurology* 2013;80:1430–38 CrossRef Medline
10. Rudko DA, Solovey I, Gati JS, et al. **Multiple sclerosis: improved identification of disease-relevant changes in gray and white matter by using susceptibility-based MR imaging.** *Radiology* 2014;272:851–64 CrossRef Medline
11. Major EO, Ault GS. **Progressive multifocal leukoencephalopathy: clinical and laboratory observations on a viral induced demyelinating disease in the immunodeficient patient.** *Curr Opin Neurol* 1995;8:184–90 CrossRef Medline

Determinants of Intracranial Hemorrhage Occurrence and Outcome after Neurothrombectomy Therapy: Insights from the Solitaire FR With Intention For Thrombectomy Randomized Trial

R. Raychev, R. Jahan, D. Liebeskind, W. Clark, R.G. Nogueira, and J. Saver; The SWIFT Trial Investigators

ABSTRACT

BACKGROUND AND PURPOSE: Intracranial hemorrhage is the most dreaded complication of neurothrombectomy therapy for acute ischemic stroke. The determinants of intracranial hemorrhage and its impact on clinical course remain incompletely delineated. The purpose of this study is to further investigate the clinical and procedural factors leading to intracranial hemorrhage and to define the clinical impact of different hemorrhagic subtypes.

MATERIALS AND METHODS: We analyzed data prospectively collected in the Solitaire FR With Intention for Thrombectomy randomized clinical trial. A multivariable logistic regression model was used to identify independent clinical, imaging, and procedural predictors of any intracranial hemorrhage and of 7 intracranial hemorrhage subtypes. Univariate analysis was used to determine the impact of each of the intracranial hemorrhage subtypes on clinical outcome.

RESULTS: Among the 144 enrolled patients, any radiologic intracranial hemorrhage (21.3% versus 38.2%, $P = .035$), symptomatic intracranial hemorrhage (1.1% versus 10.9%, $P = .012$), and subarachnoid hemorrhage (2.2% versus 12.7%, $P = .027$) occurred less frequently in the Solitaire FR than in the Merci retriever arms. The most common independent determinant of hemorrhage occurrence was rescue therapy with intra-arterial rtPA, which was associated with any intracranial hemorrhage and 4 subtypes and tended to be used more frequently in the Merci group (10.9% versus 3.4%; $P = .09$). Among the hemorrhage subtypes, basal ganglionic hemorrhage had the strongest impact on good clinical outcome at 90 days (OR, 0.30; $P = .025$) and was associated with higher reperfusion, prolonged time to treatment, and rescue therapy with intra-arterial rtPA.

CONCLUSIONS: Intracranial hemorrhage, especially subarachnoid and symptomatic intracerebral hemorrhage, occurs less frequently with the Solitaire FR than the Merci retriever, in part due to less frequent use of rescue therapy with intra-arterial rtPA. Basal ganglionic hemorrhage strongly affects clinical outcome and is distinctively related to late reperfusion.

ABBREVIATIONS: IA = intra-arterial; ICH = intracranial hemorrhage; IVH = intraventricular hemorrhage; PH = parenchymal hematoma; SICH = symptomatic intracerebral hemorrhage; SWIFT = Solitaire FR With Intention For Thrombectomy

Since the introduction of the recanalization therapy for acute ischemic stroke, both via intravenous fibrinolysis and catheter-based reperfusion, intracranial hemorrhage (ICH) has remained the most feared complication. The potential occurrence of ICH has required that the main risk of acute revascularization be balanced against the benefit of reperfusion.[1] Various pretreatment clinical and imaging factors have been associated with hemorrhagic transformation after reperfusion treatment, including age, severity of pretreatment neurologic deficit, ischemic lesion volume, elevated blood pressure, serum glucose level, history of diabetes, and absence of collateral flow.[2-5] However, most available data on ICH following recanalization therapy in acute ischemic stroke are from studies of intravenous and intra-arterial pharmacologic fibrinolysis and little is known about the clinical and procedural factors contributing to ICH occurrence after mechanical neurothrombectomy.[6,7]

The clinical impact of different ICH subtypes has also been incompletely studied. Initial emphasis in the intravenous lytic literature focused on symptomatic intracerebral hemorrhage (SICH), referring to any intracranial hemorrhage associated with early neurologic deterioration. However, multiple contending criteria have been advanced for defining an intracerebral hemor-

Received January 21, 2015; accepted after revision April 16.

From the Department of Neurology (R.R., D.L., J.S.), Division of Interventional Neuroradiology (R.J.), and Stroke Center (R.R., R.J., D.L., J.S.), University of California, Los Angeles, Los Angeles, California; Oregon Stroke Center (W.C.), Oregon Health and Sciences University, Portland, Oregon; and Department of Neurology (R.G.N.), Emory University, Atlanta, Georgia.

Please address correspondence to Radoslav Raychev, MD, UCLA Stroke Center, 710 Westwood Plaza RNRC, Los Angeles, CA 90095; e-mail: rudoray@gmail.com; rraychev@mednet.ucla.edu

Evidence-Based Medicine Level 2.

http://dx.doi.org/10.3174/ajnr.A4482

Table 1: Factors included in the prediction model

Clinical	Procedural
Age (yr)	Vessel treated (ICA/carotid-T vs M1)
Female sex (vs male)	Vessel treated (M2 vs M1)
BMI (kg/m^2)	Vessel treated (all others vs M1)
Baseline mRS = 0 (vs >0)	Rescue therapy, all
IV-rtPA failed (vs contraindicated)	Rescue therapy, rtPA
Myocardial infarction	Rescue therapy, all mechanical
Hypertension	Rescue therapy, Merci only
Diabetes	Rescue therapy, Penumbra only
Hyperlipidemia	Rescue therapy, angioplasty
Smoker	Rescue therapy, medical and mechanical
Atrial fibrillation	Rescue therapy, only mechanical
Previous ischemic stroke	Any rtPA use (IV or IA, baseline or rescue)
NIHSS at baseline	Time to treatment (min)
ASPECTS at baseline	Time to recanalization (min)
Glucose at baseline	Device passes
Hyperglycemia (>140 mmol/L) at baseline	Anesthesia (sedation vs general)
Systolic BP at baseline	Procedure time (min)
Diastolic BP at baseline	TIMI score (core lab)
Platelet count at baseline	TICI score (core lab)
INR at baseline	TIMI at baseline 1 (vs 0)
aPTT at baseline	

Note:—INR indicates international normalized ratio; BMI, body mass index; aPTT, activated partial thromboplastin time; BP, blood pressure; TIMI, Thrombolysis In Myocardial Infarction.

Table 2: ICH subtype by group

ICH Type	All Solitaire (*n* = 89)	All Merci (*n* = 55)	Difference (*P* Value)
All ICH	21.3% (19/89)	38.2% (21/55)	.035
Symptomatic	1.1% (1/89)	10.9% (6/55)	.012
SAH	2.2% (2/89)	12.7% (7/55)	.027
IVH	1.1% (1/89)	7.3% (4/55)	.070
PH1	4.5% (4/89)	3.6% (2/55)	1.00
PH2	1.1% (1/89)	7.3% (4/55)	.070
Basal ganglia	15.7% (14/89)	14.5% (8/55)	1.00
Cortical	4.5% (4/89)	14.5% (8/55)	.058

rhage as symptomatic.[1,8] In addition, other aspects of ICH, including subarachnoid versus intraparenchymal, extent (petechial hemorrhage versus frank hematoma), and topographic location (deep versus superficial) have been identified in some studies as predictors of poor outcome after interventional treatment of acute ischemic stroke.[9-11] The Solitaire FR With Intention For Thrombectomy (SWIFT; https://clinicaltrials.gov/ct2/show/NCT01054560) trial used a refined definition of SICH: any parenchymal hematoma (PH), subarachnoid hemorrhage, or intraventricular hemorrhage (IVH) associated with a worsening of National Institute of Health Stroke Scale score by ≥4 within 24 hours.[12] Compared with SICH definitions used in earlier intravenous and intra-arterial fibrinolysis trials, this definition incorporated a broader range of hemorrhage types and excluded minor petechial hemorrhages unlikely to be causally related to neurologic worsening.[13-17]

The SWIFT trial demonstrated the superiority of the Solitaire FR stent retriever device (Covidien, Irvine, California) over the Merci coil retriever device (Concentric Medical, Mountain View, California) with respect to revascularization and clinical outcome. Notably, SWIFT also found a substantially lower rate of SICH with stent versus coil retrieval (2.0% versus 11%).

The aims of this study were to define the procedural and clinical factors related to the occurrence of SICH in the SWIFT trial and to determine the ICH features with the greatest impact on clinical outcome.

MATERIALS AND METHODS

The SWIFT trial methods have been previously described.[18] The primary efficacy end point of the study was arterial recanalization of the target vessel measured by a Thrombolysis in Myocardial Infarction score of 2 or 3 without SICH after up to 3 passes of the assigned device, as assessed by an independent core laboratory. In patients for whom adequate recanalization was not achieved, rescue therapy was allowed with a different regulatory agency–cleared neurovascular thrombectomy device, intra-arterial fibrinolysis with rtPA, or both.

In the present study, ICHs were characterized by compartment (intraparenchymal, subarachnoid, intraventricular) and symptomatic status (asymptomatic and SICH). Intraparenchymal hemorrhages were further subdivided by extent (hemorrhagic infarction type 1, hemorrhagic infarction type 2, parenchymal hematoma type 1, parenchymal hematoma type 2) and brain location (cortical versus deep/basal ganglionic). Basal ganglia ICH was determined by vascular distribution and included any hemorrhage within the territory of the lenticulostriate, Heubner, and the anterior choroidal arteries. SAH, IVH, hemorrhagic infarction-1, hemorrhagic infarction-2, PH-1, PH-2, and basal ganglia ICH classifications were defined by an independent blinded core laboratory.

The entire study population was analyzed, including patients enrolled in both the roll-in and randomized phases. All analyzed clinical and imaging data except for ASPECTS were collected prospectively as part of the SWIFT main trial protocol. ASPECTSs were obtained by review of the CT imaging data base by 2 physicians (R.J., D.L.) blinded to the assigned device.

In univariate analysis, candidate predictors of ICH included 21 pretreatment demographic, clinical, and imaging variables and 20 procedural variables (Table 1). The associations of ICH features with clinical outcomes were analyzed for the following end points: NIHSS (at 24 hours, 7 days/discharge, 30 days, 90 days), Barthel Index of Activities of Daily Living (90 days), modified Rankin Scale of global disability (90 days), trial-defined good neurologic outcome (90 days), and mortality at 90 days. The prespecified tripartite definition of good neurologic outcome in the trial was the following: 1) mRS of ≤2, or 2) mRS equal to the prestroke mRS if the prestroke mRS was >2, or 3) NIHSS score improvement of ≥10 points.

Statistical Analysis

The rate of ICH types was compared between groups by using the Fisher exact test. Univariate logistic models with treatment device included as a nuisance parameter were run on each individual predictor, and predictors with a univariate *P* value < .20 were

Table 3: Predictors of ICH subtypes

ICH Subtype	Predictor	Odds Ratio	Lower CI	Upper CI	*P* Value
Any ICH	Rescue therapy, IA rtPA	12.06	1.082	134.457	.043
SICH	NIHSS at baseline	1.24	1.023	1.344	.029
SAH	ASPECTS at baseline	3.113	1.173	8.261	.023
	Rescue therapy, IA rtPA	12.46	1.731	89.708	.012
IVH	Rescue therapy, IA rtPA	8.846	1.184	66.079	.033
PH2	INR at baseline	7.267	1.22	43.288	.029
Basal ganglia	Rescue therapy, IA rtPA	18.29	1.89	176.966	.012
	Time to treatment (min)[a]	1.114	1.029	1.207	.008
	TIMI score (core lab)	1.744	1.009	3.012	.046
Cortical	NIHSS at baseline	1.19	1.015	1.278	.031
	Rescue therapy, IA rtPA	15.406	2.662	89.149	.002

[a] Time to treatment denotes time from symptoms onset to groin puncture.

Table 4: Difference in ICH predictors between the 2 treatment groups

ICH Predictors	All Solitaire (*n* = 89)	All Merci (*n* = 55)	*P* Value
NIHSS (baseline) (mean)	17.4 ± 4.5 (89)	17.5 ± 5.1 (55)	.88
INR (baseline) (mean)	1.2 ± 0.3 (88)	1.2 ± 0.3 (54)	.97
ASPECTS (baseline) (median)	8.4 ± 1.6 (86)	8.4 ± 1.4 (53)	.98
TIMI 2–3 (final)	66.7% (54/81)	30.2% (16/53)	<.001
Rescue therapy with IA rtPA	3.4% (3/89)	10.9% (6/55)	.085

entered into a multivariable logistic regression model. The backward selection method by using a criterion of $P < .10$ was used to identify the predictors of each ICH type. The difference in the identified independent predictors between groups was tested by using a *t* test for continuous measures and a Fisher exact test for discrete measures. The effect of ICH type on outcomes was tested by using univariate logistic models with the treatment device included as a nuisance parameter.

RESULTS

Hemorrhage Frequency by Treatment Group

As shown in Table 2, among the 144 enrolled patients, any radiologic intracranial hemorrhage (21.3% versus 38.2%) and symptomatic intracranial hemorrhage (1.1% versus 10.9%) occurred less frequently in the Solitaire FR than Merci retriever arms. Among the hemorrhage compartment and anatomic subtypes, subarachnoid hemorrhage (2.2% versus 12.7%) occurred less frequently with the Solitaire FR than the Merci retriever, with trends also toward less frequent intraventricular hemorrhage, parenchymal hematoma type 2, and cortical intracerebral hemorrhage.

Predictors of Hemorrhagic Subtypes

Table 3 shows the independent predictors for all intracranial hemorrhage and 6 hemorrhage subtypes. Among all analyzed clinical, imaging, and procedural parameters for each individual hemorrhage subtype included in the multivariate model, the most consistent predictor was rescue therapy with intra-arterial (IA)-rtPA, which was an independent predictor for any intracranial hemorrhage, SICH, SAH, IVH, PH2, and cortical hemorrhage. Other predictors included the following: baseline NIHSS score (for SICH and cortical ICH), baseline ASPECTS (for SAH), baseline international normalized ratio (for PH2), and time to treatment and recanalization (Thrombolysis In Myocardial Infarction 2–3 for basal ganglionic ICH). Among the identified independent predictors of hemorrhage, achievement of recanalization differed strongly between the 2 treatment arms, and the use of rescue IA-rtPA showed a trend toward a difference (Table 4).

Effect on Outcome

Among all hemorrhagic types analyzed, basal ganglia ICH and SICH had the greatest effect on outcomes, each statistically associated with 4 of 8 outcomes and trending toward association with 3 additional outcomes (Table 5). The basal ganglia ICH was inversely associated with good neurologic outcome at 90 days (OR, 0.300; 95% CI, 0.105–0.860; $P = .025$), nondisabled outcome (mRS, 0–2) at 90 days (OR, 0.248; 95% CI, 0.068–0.897; $P = .034$), higher NIHSS scores at 24 hours (OR, 5.772; 95% CI, 2.209–9.337; $P = .002$), and NIHSS score at 7 days/discharge (OR, 8.008; 95% CI, 2.247–13.545; $P = .005$). SICH was associated with mortality at 90 days (OR, 5.734; 95% CI, 1.012–32.489; $P = .048$), NIHSS score at 7 days/discharge, (OR, 17.998; 95% CI, 8.006–27.990; $P = .001$), NIHSS score at 90 days (OR, 22.354; 95% CI, 7.285–37.424; $P = .004$), and level of disability (mRS shift) at 90 days (OR, 2.414; 95% CI, 0.582–4.247; $P = .011$). Any intracranial hemorrhage was associated with NIHSS score at 24 hours (OR, 4.856; 95% CI, 1.964–7.749; $P = .001$) and NIHSS score at 7 days/discharge (OR, 6.130; 95% CI, 1.538–10.722; $P = .002$). PH1, PH2, SAH, IVH, and cortical ICH were not associated with any of the clinical outcomes.

DISCUSSION

This study provides important insight into the pathophysiologic mechanisms of different ICH subtypes after mechanical revascularization and their respective impacts on clinical outcome.

Among all clinical and baseline predictors, NIHSS score was the strongest predictor of SICH in this study. However, this association does not explain the lower incidence of hemorrhage in the patients treated with the Solitaire because the baseline NIHSS score did not differ between the 2 groups. It is likely that other procedural factors causing specific hemorrhagic subtypes were contributing to the overall higher rate of SICH in the Merci group.

The higher incidence of SAH in the Merci group compared with the Solitaire group (12.7% versus 2.2%; $P = .027$) is similar to that in previously reported data. The higher frequency of SAH with coil retrievers has several potential sources, including greater device injury to the vessel wall; greater required traction of the device on clot resulting in displacement of the vascular tree; the need for multiple retriever passes, increasing the likelihood of dissection; and the more frequent need for rescue therapy with IA-rtPA with attendant increased bleeding risk.[19]

As opposed to the Merci device, which is initially delivered distal to the target thrombus, the Solitaire FR expands radially within the thrombus when unsheathed from the microcatheter. This outward expansion through the thrombus allows stable positioning within the vessel wall, which likely minimizes the risk of vessel perforation and/or microdissection during delivery.[20] In addition, the mechanical properties of the Solitaire allow optimal

Table 5: Effects on outcome (*P* values)[a]

Outcome	Hemorrhage Type							
	All ICH	BG	SICH	PH1	PH2	SAH	IVH	Cortical
NIHSS at 24 hours	.001 (OR, 4.85)	.002 (OR, 5.77)	.067	.329	.087	.659	.988	.798
NIHSS at 7 days/discharge	.002 (OR, 6.13)	.005 (OR, 8.01)	.001 (OR, 17.99)	.747	.089	.386	.160	.508
NIHSS at 30 days	.141	.055	.068	.609	.453	.795	.070	.611
NIHSS at 90 days	.195	.067	.004 (OR, 22.35)	.821	.362	.725	.152	.464
mRS shift at 90 days	.088	.061	.011 (OR, 2.41)	.675	.431	.949	.771	.453
mRS 0–2 at 90 days	.057	.034 (OR, 0.24)	.122	.899	.770	.671	.770	.626
Good neuro-outcome at 90 days[b]	.079	.025 (OR, 0.30)	.062	.960	.528	.531	.528	.271
Mortality at 90 days	.731	.382	.048 (OR, 5.73)	.575	.763	.994	.763	.250

Note:—BG indicates basal ganglia.

[a] ORs are provided for *P* values ≤ .05, which are significant.

[b] An mRS of ≤2 or equal to the prestroke mRS if the prestroke mRS was >2 or an NIHSS score improvement of ≥10 points.

wall conformance and flexibility and a minimal vessel-straightening effect, likely reducing the risk of endothelial damage during the pull. Finally, the efficient clot engagement and rapid revascularization decrease the need for multiple passes and additional rescue therapy. Although our data did not reveal any association between the number of passes and hemorrhage occurrence, rescue therapy with IA-rtPA strongly correlated with multiple hemorrhagic subtypes, including any intracranial hemorrhage, SICH, SAH, IVH, PH2, and cortical hemorrhage. Any use of rtPA (IV or IA, baseline, or rescue) did not impact hemorrhage occurrence; this outcome suggests that the deleterious effect of the thrombolytic therapy is only present when used intra-arterially as a rescue therapy, after initial mechanical thrombectomy. As such, preinterventional use of IV-rtPA is not discouraged. The relationship between IA-rtPA rescue therapy and subarachnoid hemorrhage was particularly strong, increasing the odds of SAH more than 12-fold. These findings indicate that the fibrinolytic effect of the medication used as a rescue therapy likely potentiates device-induced vascular injury, eventually resulting in intracranial hemorrhage, particularly SAH.

Of all hemorrhagic subtypes, basal ganglia was the only hemorrhage associated with successful reperfusion. Parenchymal ischemic injury may progress particularly rapidly in subcortical, basal ganglia regions, due to rapidly evolving infarction within the deep subcortical tissue in the presence of occluded ostia of lenticulostriate arteries that lack collateral flow. This more advanced ischemic tissue destruction may render subcortical tissues more vulnerable to reperfusion-mediated hemorrhage. Basal ganglionic hemorrhage has been previously associated with poor outcome after mechanical thrombectomy.[10] The association of time to treatment with basal ganglia ICH (OR, 1.14; 95% CI, 1.029–1.207; $P = .008$) in our study demonstrates that for every 10-minute delay, there is an approximate 11% higher risk of hemorrhage within the basal ganglia (Fig 1). This significant impact on time to treatment confirms the vulnerability of the deep subcortical structures to prolonged ischemia. The distinctive determinants and clinical impact of basal ganglionic-versus-cortical hemorrhage demonstrate the importance of identifying these subtypes, in addition to clinical type (symptomatic versus asymptomatic) and extent (hematoma versus hemorrhagic infarction). Given the strong impact of basal ganglionic hemorrhages on the outcome in our study, it is reasonable to consider this hemorrhagic subtype as an important predictor of outcome in clinical practice and in future studies of endovascular revascularization for acute ischemic stroke.

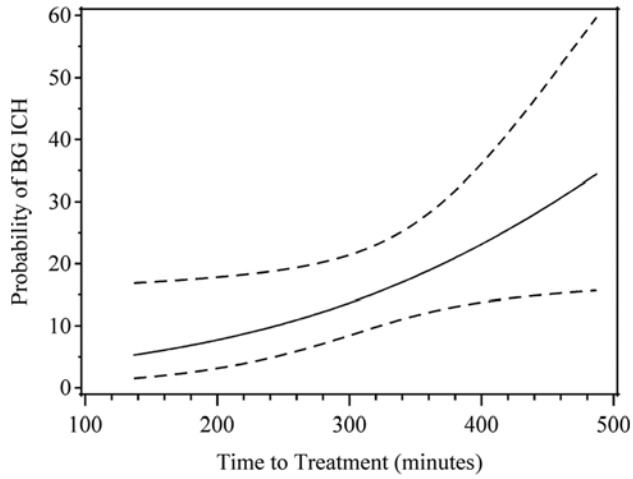

FIG 1. Plot of predicted probability (%) of basal ganglia ICH based on time to treatment. The dotted lines represent the upper and lower confidence bounds of the predicted probability.

Limitations

The main limitation of our study was the relatively small number of hemorrhages in the SWIFT trial, potentially confounding the results of the regression model as demonstrated by the wide confidence intervals in Table 3. This limitation explains the lack of definitive association between PH2 and clinical outcome (Table 5). In addition, our outcome data were derived on the basis of univariate analysis instead of multivariate regression, focusing only on the hemorrhage effect and excluding other clinical and procedural variables. However, the goal of the outcome analysis was to analyze the clinical effect of each ICH subtype compared with all other hemorrhages, rather than identifying overall predictors of clinical outcome.

CONCLUSIONS

The higher rate of intracranial hemorrhage observed in the SWIFT trial with the Merci retriever versus the Solitaire FR was mostly related to increased occurrence of SAH and to a lesser degree of IVH, PH2, and cortical ICH. Each one of these ICH subtypes was strongly associated with IA-rtPA rescue therapy. In comparison with the Merci device, the Solitaire likely offsets SICH due to a lower incidence of vascular injury and a decreased need for additional IA rtPA administration.

Basal ganglia ICH has a substantial deleterious effect on clinical outcome and is related in part to reperfusion of subcortical tissues that have already sustained advanced ischemic injury, independent of the type of device used.

These findings warrant cautious use of additional rescue IA-rtPA after mechanical thrombectomy, particularly in patients with established basal ganglia infarcts and prolonged time from symptom onset.

Disclosures: Reza Jahan—*RELATED*: Covidien*; *Consulting Fee or Honorarium*: Covidien; *Support for Travel to Meetings for the Study or Other Purposes*: Covidien; *UNRELATED*: *Consultancy*: Covidien; *Payment for Lectures (including service on speakers bureaus)*: Covidien; *OTHER*: Covidien (consultant; member of executive steering committee for SWIFT PRIME; International Neurointerventional Advisor SWIFT PRIME; member of steering committee for the Systemic Evaluation of Patients Treated with Neurothrombectomy Devices for Acute Ischemic Stroke [STARTIS] registry), Medina Medical (Chief Scientific Advisor), Stryker Neurovascular (Speakers Bureau). David Liebeskind—*UNRELATED*: *Consultancy*: Stryker Neurovascular,* Covidien*; *Payment for Lectures (including service on Speakers Bureaus)*: Stryker Neurovascular,* Covidien.* Wayne Clark—*UNRELATED*: *Grants/Grants Pending*: Oregon Health and Science University.* Raul G. Nogueira—*UNRELATED*: *Fees for Participation in Review Activities such as Data Monitoring Boards, Statistical Analysis, End Point Committees, and the Like*: Stryker Neurovascular, Covidien, Penumbra, *Comments*: Stryker Neurovascular (Thrombectomy Revascularization of Large Vessel Occlusions in Acute Ischemic Stroke–2 and Trevo and Medical Management Versus Medical Management Alone in Wake up and Late Presenting Strokes [DAWN] Trials Principal Investigator; both modest); Covidien (SWIFT and SWIFT PRIME trials steering committee; both modest; Study of Tamoxifen and Raloxifene Trial Angiographic Core Lab; significant); Penumbra (3D Separator Trial Executive Committee; no payment); Editor-In-Chief of *Interventional Neurology Journal* (no payment); *OTHER*: CoAxia (clinical trials steering committee). Jeffrey Saver—*RELATED*: *Grant*: ev3/Covidien*; *Consulting Fee or Honorarium*: ev3/Covidien*; *UNRELATED*: *Consultancy*: Covidien,* Stryker Neurovascular*; *OTHER*: St. Jude Medical Clinical Trial Steering Committee, ev3 Clinical Trial Steering Committee, CoAxia Clinical Trial Steering Committee, Grifols Clinical Trial Steering Committee, Genervon Clinical Trial Steering Committee, BrainsGate Clinical Trial Steering Committee, Stryker Neurovascular Clinical Trial Steering Committee. *Money paid to the institution.

REFERENCES

1. National Institute of Neurological Disorders and Stroke rt-PA Stroke Study Group. **Tissue plasminogen activator for acute ischemic stroke.** *N Engl J Med* 1995;333:1581–87 CrossRef Medline
2. Hallevi H, Barreto AD, Liebeskind DS, et al. **The HIAT score: identifying patients at high risk for poor outcome after intra arterial therapy for acute ischemic stroke.** *Stroke* 2009;40:E164 CrossRef
3. Flint AC, Faigeles BS, Cullen SP, et al; VISTA Collaboration. **THRIVE score predicts ischemic stroke outcomes and thrombolytic hemorrhage risk in VISTA.** *Stroke* 2013;44:3365–69 CrossRef Medline
4. Christoforidis GA, Karakasis C, Mohammad Y, et al. **Predictors of hemorrhage following intra-arterial thrombolysis for acute ischemic stroke: the role of pial collateral formation.** *AJNR Am J Neuroradiol* 2009;30:165–70 CrossRef Medline
5. Bang OY, Buck BH, Saver JL, et al. **Prediction of hemorrhagic transformation after recanalization therapy using T2*-permeability magnetic resonance imaging.** *Ann Neurol* 2007;62:170–76 CrossRef Medline
6. Khatri P, Broderick JP, Khoury JC, et al; IMS I and II Investigators. **Microcatheter contrast injections during intra-arterial thrombolysis may increase intracranial hemorrhage risk.** *Stroke* 2008;39:3283–87 CrossRef Medline
7. Brekenfeld C, Remonda L, Nedeltchev K, et al. **Symptomatic intracranial haemorrhage after intra-arterial thrombolysis in acute ischaemic stroke: assessment of 294 patients treated with urokinase.** *J Neurol Neurosurg Psychiatry* 2007;78:280–85 Medline
8. Saver JL. **Hemorrhage after thrombolytic therapy for stroke: the clinically relevant number needed to harm.** *Stroke* 2007;38:2279–83 CrossRef Medline
9. Larrue V, von Kummer RR, Müller A, et al. **Risk factors for severe hemorrhagic transformation in ischemic stroke patients treated with recombinant tissue plasminogen activator: a secondary analysis of the European-Australasian Acute Stroke Study (ECASS II).** *Stroke* 2001;32:438–41 CrossRef Medline
10. Loh Y, Towfighi A, Liebeskind DS, et al. **Basal ganglionic infarction before mechanical thrombectomy predicts poor outcome.** *Stroke* 2009;40:3315–20 CrossRef Medline
11. Wahlgren N, Ahmed N, Dávalos A, et al; SITS-MOST investigators. **Thrombolysis with alteplase for acute ischaemic stroke in the Safe Implementation of Thrombolysis in Stroke-Monitoring Study (SITS-MOST): an observational study.** *Lancet* 2007;369:275–82 CrossRef Medline
12. Saver JL, Jahan R, Levy EI, et al; SWIFT Trialists. **Solitaire flow restoration device versus the Merci retriever in patients with acute ischaemic stroke (SWIFT): a randomised, parallel-group, non-inferiority trial.** *Lancet* 2012;380:1241–49 CrossRef Medline
13. Gobin YP, Starkman S, Duckwiler GR, et al. **MERCI 1: a phase 1 study of mechanical embolus removal in cerebral ischemia.** *Stroke* 2004;35:2848–54 CrossRef Medline
14. Smith WS, Sung G, Starkman S, et al; MERCI Trial Investigators. **Safety and efficacy of mechanical embolectomy in acute ischemic stroke: results of the MERCI trial.** *Stroke* 2005;36:1432–38 CrossRef Medline
15. Smith WS, Sung G, Saver J, et al; Multi MERCI Investigators. **Mechanical thrombectomy for acute ischemic stroke: final results of the Multi MERCI trial.** *Stroke* 2008;39:1205–12 CrossRef Medline
16. Penumbra Pivotal Stroke Trial Investigators. **The Penumbra pivotal stroke trial: safety and effectiveness of a new generation of mechanical devices for clot removal in intracranial large vessel occlusive disease.** *Stroke* 2009;40:2761–68 CrossRef Medline
17. Furlan A, Higashida R, Wechsler L, et al; PROACT Investigators. **Intra-arterial prourokinase for acute ischemic stroke: the PROACT II study—a randomized controlled trial.** *JAMA* 1999;282:2003–11 CrossRef Medline
18. Saver JL, Jahan R, Levy EI, et al; SWIFT Trialists. **SOLITAIRE™ with the intention for thrombectomy (SWIFT) trial: design of a randomized, controlled, multicenter study comparing the SOLITAIRE™ Flow Restoration device and the MERCI Retriever in acute ischaemic stroke.** *Int J Stroke* 2014;9:658–68 CrossRef Medline
19. Shi ZS, Liebeskind DS, Loh Y, et al; UCLA Endovascular Stroke Therapy Investigators. **Predictors of subarachnoid hemorrhage in acute ischemic stroke with endovascular therapy.** *Stroke* 2010;41:2775–81 CrossRef Medline
20. Akins PT, Amar AP, Pakbaz RS, et al; SWIFT Investigators. **Complications of endovascular treatment for acute stroke in the SWIFT trial with Solitaire and Merci devices.** *AJNR Am J Neuroradiol* 2014;35:524–28 CrossRef Medline

Risk Factors for Hemorrhagic Complications following Pipeline Embolization Device Treatment of Intracranial Aneurysms: Results from the International Retrospective Study of the Pipeline Embolization Device

W. Brinjikji, G. Lanzino, H.J. Cloft, A.H. Siddiqui, and D.F. Kallmes

ABSTRACT

BACKGROUND AND PURPOSE: Spontaneous intraparenchymal hemorrhage is a dreaded complication of unknown etiology following flow-diversion treatment. Using the International Retrospective Study of the Pipeline Embolization Device registry, we studied demographic, aneurysm, and procedural characteristics associated with intraparenchymal hemorrhage following Pipeline Embolization Device treatment.

MATERIALS AND METHODS: We identified patients in the International Retrospective Study of the Pipeline Embolization Device registry with intraparenchymal hemorrhage unrelated to index aneurysm rupture post-Pipeline Embolization Device treatment. The rate of intraparenchymal hemorrhage was determined by baseline demographics, comorbidities, aneurysm characteristics, and procedural characteristics (including anticoagulation use, platelet testing, number of devices used, sheaths, catheters, and guidewires). Categoric variables were compared with χ^2 testing, and continuous variables were compared with the Student *t* test.

RESULTS: Of 793 patients with 906 aneurysms, 20 (2.5%) had intraparenchymal hemorrhage. Fifteen intraparenchymal hemorrhages (75.0%) occurred within 30 days of treatment (median, 5 days; range, 0–150 days). Nine patients with intraparenchymal hemorrhage (45.0%) died, 10 (50.0%) had major neurologic morbidity, and 1 had minor neurologic morbidity (5.0%). Intraparenchymal hemorrhage was ipsilateral to the Pipeline Embolization Device in 16 patients (80%) and contralateral in 3 patients (15.0%). Variables associated with higher odds of intraparenchymal hemorrhage included treatment of ruptured aneurysms (OR, 4.44; 95% CI, 1.65–11.94; $P = .005$) and the use of ≥3 Pipeline Embolization Devices (OR, 4.10; 95% CI, 1.34–12.58; $P = .04$). The Shuttle sheath was not associated with intraparenchymal hemorrhage (OR, 0.97; 95% CI, 0.38–2.45; $P = .95$).

CONCLUSIONS: Spontaneous intraparenchymal hemorrhage following Pipeline Embolization Device treatment is a rare-but-devastating complication, with nearly all patients having morbidity or mortality. Variables associated with intraparenchymal hemorrhage included the use of multiple Pipeline Embolization Devices and treatment of ruptured aneurysms. The Shuttle, a device that was previously thought to be associated with intraparenchymal hemorrhage, was not associated with it.

ABBREVIATIONS: IntrePED = International Retrospective Study of the Pipeline Embolization Device; IPH = intraparenchymal hemorrhage; PED = Pipeline Embolization Device

The Pipeline Embolization Device (PED; Covidien, Irvine, California) is increasingly used in the treatment of intracranial aneurysms.[1-4] The bare metal construct of the PED serves as a scaffold for neointimal proliferation, thereby excluding the aneurysm sac from the parent artery.[5,6] A number of previous studies have demonstrated that the PED is associated with high rates of aneurysm occlusion with relatively low complication rates.[1,3]

Spontaneous intraparenchymal hemorrhage (IPH) is one of the most dreaded complications of aneurysm treatment with flow diverters.[7-13] Although rarely reported after stent-assisted coiling of aneurysms, systematic reviews of flow-diverter treatment suggest that this complication occurs in 2%–4% of patients. Little is known regarding the exact etiology or risk factors of post-flow-diverter IPH.[7-13] A number of theories have been proposed, including the use of dual antiplatelet therapy, activation of platelets despite antiplatelet therapy by shearing over the metal surface area and subsequent hemorrhagic transformation of embolic platelet plug–mediated ischemic stroke, hemodynamic perturbations (hypo- or hyperperfusion states) during and immediately

Received February 9, 2015; accepted after revision May 10.

From the Departments of Radiology (W.B., G.L., H.J.C., D.F.K.) and Neurosurgery (G.L., H.J.C., D.F.K.), Mayo Clinic, Rochester, Minnesota; and Department of Neurosurgery (A.H.S.), State University of New York, Buffalo, New York.

Please address correspondence to Waleed Brinjikji, MD, Mayo Clinic, 200 First St SW, OL1-112 SMH, Rochester, MN 55905; e-mail: brinjikji.waleed@mayo.edu; @Wbrinjikji

http://dx.doi.org/10.3174/ajnr.A4443

after flow-diverter treatment, and embolization of polyvinylpyrrolidone, a compound found in a number of catheters including the Shuttle guide sheath (Cook, Bloomington, Indiana).[10] Using the International Retrospective Study of the Pipeline Embolization Device (IntrePED) registry, we compared the clinical and procedural characteristics of patients who had postoperative IPH and those who did not, to determine which clinical and procedural characteristics were associated with IPH.

MATERIALS AND METHODS

Study Design and Participants

This study is a subanalysis of the IntrePED study, which has been previously published.[14] Details regarding ethics committee and institutional review board approval and inclusion and exclusion criteria are provided in the original article.[14] Several additional subgroup analyses separate from this study are currently underway by using data from the IntrePED registry. This study will be the only subgroup analysis performed examining variables associated with IPH in the IntrePED registry. We retrospectively evaluated all patients with intracranial aneurysms treated with the Pipeline Embolization Device in the IntrePED registry. Seven hundred ninety-three patients treated for 906 aneurysms were enrolled.

Procedures

Because this was a retrospective registry, procedural details and patient management varied across centers. All centers reported baseline characteristics of patients and aneurysms, procedural information, and follow-up information from clinic visits or telephone calls by using a common study protocol form. Site investigators identified patients who had IPH by using the study protocol form. All complications including IPH were reviewed in detail by an Adverse Events Review Committee, comprising 3 members of the Steering Committee, including the overall study Principal Investigator. The committee determined whether the IPH was major or minor. A "major" adverse event was defined as an ongoing clinical deficit at 7 days following the event. All major adverse events were included in the neurologic morbidity and mortality rates. Timing of all adverse events was in relation to the time of the PED placement.

Baseline Characteristics and Outcomes

For each patient, the following characteristics were collected as part of this study: age, sex, hypertension, control of hypertension, smoking status, aneurysm location, aneurysm rupture status, aneurysm type, aneurysm size, use of antiplatelet medications before the procedure, use of platelet aggregation studies, heparin administration and reversal, number of PEDs used, type of sheath used, type of guide catheter used, type of microcatheter used, type of guidewire used, balloons used, and type of closure device used. The incidence of IPH was calculated for each of the above-mentioned variables.

In addition, for patients with any cerebrovascular hemorrhagic complication, we obtained the following information: whether the hemorrhage was ipsilateral or contralateral to the device; timing after surgery; final clinical outcome (minor morbidity, major morbidity, death); and a clinical report of a preceding embolic event and other procedural complications, including but not limited to vessel perforation. "Minor morbidity" was defined as a clinical deficit that persisted <7 days, and "major morbidity" was defined as a clinical deficit that persisted ≥ 7 days.

Statistical Analysis

Statistical analyses were performed by using SAS, Version 9.2 or higher (SAS Institute, Cary, North Carolina). Descriptive statistics will be used to present the data and to summarize the results. Discrete variables will be presented by using frequency distributions and cross-tabulations. Continuous variables will be summarized by presenting the number of observations and mean, SD, median, minimum, and maximum values. For categoric variables, differences between the randomized arms were tested by using appropriate contingency table analyses (Exact or χ^2 approximations). For continuous variables, the differences were tested by using an unpaired Student t test or a nonparametric test, depending on variable distribution. Odds ratios and 95% confidence intervals were obtained by using the univariate logistic regression. All statistical analyses were performed on a per-patient basis.

Role of the Funding Source

An academic Principal Investigator and an academic Steering Committee supervised the trial design and operations. The Principal Investigator and Steering Committee were independent of the funding source. The Steering Committee interpreted the results, and the Principal Investigator wrote the report. The study sponsor was responsible for site management, data management, statistical analysis, and safety reporting. The corresponding author had full access to all study data and had final responsibility for the decision to submit for publication.

RESULTS

Patient and Aneurysm Characteristics and IPH

A summary of the baseline characteristics of all patients included in the IntrePED registry is provided elsewhere.[14] Twenty (2.5%) patients with 21 treated aneurysms had IPH, while 773 patients (97.5%) did not. There was no difference in the mean age of patients with and without IPH (61.4 $\pm$ 13.4 years versus 56.8 $\pm$ 14.2 years, $P = .16$). Smoking rates (OR, 1.41; 95% CI, 0.40–4.92; $P = .59$) were not associated with IPH. There was a trend toward higher odds of IPH in the hypertension group (OR, 2.45; 95% CI, 0.96–6.23; $P = .06$). These data are summarized in Table 1.

No aneurysm locations were associated with higher or lower odds of IPH. There was a similar rate of IPH in anterior circulation versus posterior circulation aneurysms (OR, 1.14; 95% CI, 0.26–5.00; $P = .86$). Treatment of ruptured aneurysms was associated with higher odds of IPH (OR, 4.44; 95% CI, 1.65–11.95; $P = .005$). There was no difference in IPH rates by aneurysm type or aneurysm size. These data are summarized in Table 1.

Procedure Characteristics

Use of ≥ 3 PEDs (OR, 4.10; 95% CI, 1.34–12.58; $P = .04$) was associated with higher odds of IPH. Use of the Shuttle was not associated with higher odds of IPH (OR, 0.95; 95% CI, 0.38–2.45; $P = .95$). Pretreatment antiplatelet therapy (OR, 0.93; 95% CI,

Table 1: Demographic and aneurysm characteristics

Characteristics	IPH/Subtotal	OR	*P* Value
Sex			
Male	2.5% (4/161)	Ref	
Female	2.5% (16/632)	1.02 (0.34–3.09)	.97
Hypertension			
Yes	5.2% (13/249)	2.45 (0.96–6.23)	.06
No	2.2% (7/318)	Ref	
Controlled hypertension			
Yes	5.8% (12/206)	0.58 (0.02–15.92)	.75
No	0.0% (0/4)	Ref	
Current smoker			
Yes	3.2% (3/94)	1.32 (0.38–4.60)	.66
No	2.4% (17/699)	Ref	
Aneurysm location			
Posterior circulation	2.2% (2/89)	Ref	
Anterior circulation	2.6% (18/704)	1.14 (0.26–5.00)	.86
Aneurysm location by vessel			
Internal carotid artery	2.4% (14/590)	Ref	
PcomA	3.8% (2/53)	1.61 (0.36–7.30)	.78
ACA	25.0% (2/8)	13.71 (2.54–74.02)	.01
Basilar artery	2.3% (1/43)	0.98 (0.13–7.63)	.43
Vertebral artery	3.0% (1/33)	1.29 (0.16–10.09)	.63
Rupture status			
Unruptured	1.9% (14/719)	Ref	
Ruptured	8.1% (6/74)	4.44 (1.65–11.94)	.00
Aneurysm type			
Saccular	2.0% (12/600)	Ref	
Fusiform	3.9% (4/102)	1.92 (0.42–8.82)	.91
Dissecting	3.8% (2/53)	2.00 (0.63–6.33)	.82
Other	5.3% (2/38)	2.72 (0.59–12.63)	.48
Aneurysm size			
<10 mm	1.6% (6/387)	Ref	
10–24.9 mm	3.3% (11/338)	2.14 (0.78–5.84)	.70
≥25 mm	4.8% (3/63)	3.18 (0.77–13.04)	.23

Note:—PcomA indicates posterior communicating artery; ACA, anterior cerebral artery; Ref, reference.

0.27–3.23), preprocedual platelet aggregation studies (OR, 0.95; 95% CI, 0.36–2.49; $P = .91$), and heparin administration (OR, 1.14; 95% CI, 0.26–5.00; $P = .92$) were not associated with IPH. No microcatheters, sheaths, or guidewires were associated with IPH. The use of closure devices was not associated with IPH. These data are summarized in Table 2.

Timing and Clinical Outcomes of IPH

Of the 20 patients who had IPH, 11 (55.0%) had it within 1 week of the procedure. Four patients (20.0%) had IPH between 1 week and 1 month of the procedure, 1 patient had IPH between 1 and 3 months of the procedure (5.0%), and 3 patients had IPH between 3 and 6 months of the procedure (15.0%). No patients had IPH after 6 months following treatment. The median time of onset for IPH was 5 days, the mode was 1 day as 6 patients had IPH 1 day following treatment. In 1 patient, the timing of the IPH was uncertain. Among patients with IPH, 9 (45.0%) died, 10 (50.0%) had major neurologic morbidity, and 1 patient (5.0%) had minor neurologic morbidity. The location of the IPH was ipsilateral to the device in 16 patients (80.0%) and contralateral to the device in 3 patients (15.0%). In 1 patient, the location of the hemorrhage was unknown. Four patients with IPH (20.0%) had a clinical ischemic event (transient ischemic attack or stroke) before the IPH. One patient had IPH the day after the procedure following perforation of a vessel with a guidewire, and 1 patient had IPH with associated SAH resulting from spontaneous rupture of a treated giant cavernous carotid aneurysm.

DISCUSSION

Our current large, multicenter study of flow-diversion therapy confirms that approximately 2% of patients will have ipsilateral IPH. All patients who experienced IPH in our study had either major morbidity or mortality. Most IPH cases occurred within the first week of the procedure, and all cases occurred within 6 months of the procedure. In our series, treatment variables associated with IPH included treatment of ruptured aneurysms and the use of ≥3 PEDs. The Shuttle, a device that was previously postulated to be associated with IPH, was not associated with IPH in our study.[10,12] These findings suggest that the etiology of IPH following PED treatment is multifactorial, due to a constellation of risk factors, including aneurysm rupture status and the use of multiple PEDs.

The exact mechanism of IPH following PED treatment is uncertain, but a number of different theories have been proposed. One histopathologic study of 3 patients who died after PED-associated intracranial hemorrhage demonstrated that in each case, there was evidence of a foreign material (polyvinylpyrrolidone) in the distal vasculature of the hemorrhagic lesion.[10] Polyvinylpyrrolidone is a substance that is commonly used as a coating material for a number of interventional devices, including the Shuttle guide sheath. In that study, the authors demonstrated that macroscopic bits of polyvinylpyrrolidone could be released from this device with minimal manipulation.[10] In addition, other studies from the interventional cardiology literature have demonstrated that friction during placement and manipulation of the Shuttle sheath results in deposition of hydrophilic embolic materials causing substantial foreign-body reactions.[15-17] Polyvinylpyrrolidone emboli have been shown to result in angiothrombosis and granulomatous angiitis, with resultant vascular injuries.[18] However, Hu et al[10] did not find any evidence of such granulomatous reaction in association with these polyvinylpyrrolidone emboli following PED treatment. In our current study, we found no association between the Shuttle and IPH following flow-diversion therapy. Given the large size of our study compared with prior studies implicating the Shuttle as causing IPH, our data call into question the association.

The use of dual antiplatelet agents has also been proposed as a potential etiology of IPH. In general, patients treated with flow diverters such as the PED are treated with at least 3 months of dual antiplatelet therapy. A number of studies have demonstrated that most IPHs following PED placement occur within 1 month and

Table 2: Procedure and device characteristics

Characteristics	IPH/Subtotal[a]	OR	*P* Value
Preprocedural antiplatelet use			
Yes	2.5% (17/681)	0.93 (0.27–3.23)	.91
No	2.7% (3/112)	Ref	
Preprocedural platelet aggregation studies			
Yes	2.5% (14/564)	0.95 (0.36–2.49)	.91
No	2.6% (6/229)	Ref	
Heparin administration			
Yes	2.6% (18/704)	1.14 (0.26–5.00)	.86
No	2.2% (2/89)	Ref	
Reversal of heparin			
Yes	5.6% (1/18)	2.33 (0.29–18.49)	.43
No	2.5% (17/689)	Ref	
No. of PEDs used			
1	1.7% (9/533)	Ref	
2	3.3% (6/183)	1.97 (0.69–5.62)	.96
3+	6.6% (5/76)	4.10 (1.34–12.58)	.04
How multiple PEDs were used			
Overlapping	1.4% (2/140)	Ref	
Multiple layers	7.5% (3/40)	5.59 (0.90–34.72)	.96
Additional length	7.9% (6/76)	5.91 (1.16–30.06)	.96
Multiple layers and overlapping	0.0% (0/2)	NA	
Sheaths used			
Medical Arrow-Flex[b]			
Yes	0.0% (0/35)	NA	
No	3.5% (19/546)		
Medical Shuttle Select			
Yes	3.2% (8/249)	0.97 (0.38–2.45)	.95
No	3.3% (11/332)	Ref	
Pinnacle Destination[c]			
Yes	5.9% (2/34)	1.95 (0.43–8.80)	.39
No	3.1% (17/547)	Ref	
Microcatheter used			
Marksman[d]			
Yes	3.2% (18/557)	0.77 (0.10–6.00)	.80
No	4.2% (1/24)	Ref	

[a] The number of IPHs does not add up to 20 in all subanalyses because these data were missing in some patients.
[b] Teleflex, Limerick, Pennsylvania.
[c] Terumo, Tokyo, Japan.
[d] Covidien, Irvine, California.

events occurring beyond 6 months are exceedingly rare.[8,10,11] The fact that the timing of these events and the duration of dual antiplatelet therapy coincide cannot be dismissed. In our study, it would be impossible to find a statistical correlation between the use of antiplatelet agents and hemorrhage as by design, all patients were to be maintained on dual antiplatelet regimens. Studies examining the association between preprocedural P2Y12 reaction units and the risk of hemorrhagic complications have demonstrated that P2Y12 reaction unit values of <60 portend a higher risk of hemorrhage.[11,19] We did not study the association between P2Y12 reaction unit values and hemorrhagic complications. However, we found no association between the use of platelet testing and the risk of hemorrhagic complications. To date, no studies have demonstrated a decreased risk of hemorrhagic complications among patients receiving a titration of dual antiplatelet therapy in response to results of platelet testing, to our knowledge.

Intraparenchymal hemorrhages have been previously reported following standard stent-assisted coiling of intracranial aneurysms; however, these events tend to be exceedingly rare.[20-22] Typically, intracranial stent placement requires dual antiplatelet therapy for at least 3 months, similar to PED use, so the increased number of reported IPHs among PED patients relative to stent-coil patients suggests an innate increase in the incidence with PEDs. One may speculate that the increased metal surface area to which the platelets are exposed may result in activation through increased shear, despite antiplatelet therapy. This may cause activated platelet plugs embolizing distally with secondary hemorrhagic transformation of resulting ischemic infarcts. This hypothesis is given credence through our findings of a 4-fold increase in IPH following multiple PEDs, which would nominally reflect a much greater metal surface shear area exposed to platelets. To date, no studies have conclusively linked silent infarcts to IPH, to our knowledge. In fact, 1 small study of 4 patients with post-flow-diverter-therapy IPH and imaging in the immediate postoperative period before the IPH found no cases of ischemic lesions preceding the development of IPH.[23]

The exact cause behind the significantly increased incidence following treatment of ruptured aneurysms as noted in our study is not clear. It is possible that the increased acute-phase reactant environment could facilitate platelet activation and result in subsequent embolic and thereby hemorrhagic events. While most of the ruptured aneurysms treated in this study were not treated in the acute phase of subarachnoid hemorrhage, studies suggest that acute-phase proteins can remain elevated for several months following subarachnoid hemorrhage.[24]

Another hypothesis that has been suggested regarding the etiology of IPH is one of hyperperfusion following PED placement. This is thought to be due to a sudden loss of a large capacitance chamber in the form of a giant aneurysm. Chiu and Wenderoth[25] postulated that cerebral hyperperfusion syndrome can occur following the placement of a flow-diverting device across an aneurysm neck. In their case report, the authors suggested that by diverting blood flow from the aneurysm sac into the parent vessel and reducing aneurysm expansion during systole, flow-diverting stents effectively increase the degree of perfusion to the distal arterial territory and can result in cerebral hyperperfusion syndrome due to the Windkessel effect.[7,25] Similar hemodynamic perturbations have been seen following surgical clipping.[26] However, our data found no correlation with aneurysm size, which would argue against this concept.

Our study demonstrated a strong association between the use of multiple PEDs and hemorrhagic events. The use of multiple PEDs has been shown to be associated with poor neurologic outcome related to thromboembolic and hemorrhagic complications in 1 previous series of 74 patients.[27] However, to our knowledge,

no previous study has to date demonstrated a strong statistical correlation between the use of multiple PEDs and IPH. The association between the use of multiple PEDs and hemorrhagic complications is likely due to multiple factors including prolonged procedural time, increased platelet activation, and possible hemodynamic alterations from the placement of multiple stents.[19,25]

Limitations

Our study has limitations. First, because the number of IPH events was low, we are limited in our power to detect associations between IPH and the above-mentioned variables. Our study protocol did not require regular postoperative imaging with CT or MR imaging. Thus, we cannot determine whether these areas of hemorrhage are due to hemorrhagic transformation of silent infarctions. Another limitation is that for patients receiving platelet testing, we do not have information regarding platelet responsiveness before the hemorrhagic event or whether and how antiplatelet prescriptions changed in response to these tests.

Last, we do not have any consistent data regarding how these hemorrhages were managed. A recent study by Tomas et al[23] demonstrated that surgical evacuation of IPHs following flow-diverter treatment resulted in favorable clinical outcome on follow-up. These procedures were safe and effective in all 4 cases in the Tomas et al study, despite the use of dual antiplatelet therapy as all patients had platelet transfusion immediately before the surgical procedure. Single antiplatelet therapy with aspirin in the immediate postoperative period was safe and effective in all 4 cases as no patients had rehemorrhage or in-stent thrombosis or stroke.

CONCLUSIONS

Spontaneous IPH following endovascular treatment of intracranial aneurysms with the PED is a rare-but-devastating complication with 100% of patients having major morbidity or mortality. The exact cause of this complication is not well-established and is likely multifactorial. Variables associated with IPH include use of multiple PEDs and treatment of ruptured aneurysms. All IPHs occurred within 6 months of the procedures, suggesting that the use of antiplatelet therapy is a potential risk factor. The Shuttle, a device that was previously thought to be associated with IPH, was not associated with it in this study. Future efforts for reducing the risk of hemorrhagic complications following PED placement should focus on limiting the number of PEDs used, when possible.

Disclosures: Giuseppe Lanzino—*UNRELATED*: *Consultancy*: Covidien.* Adnan Siddiqui—*UNRELATED*: *Board Membership*: Codman & Shurtleff, Covidien, Intersocietal Commission for the Accreditation of Vascular Laboratories, Medina Medical; *Consultancy*: Codman & Shurtleff, Covidien, GuidePoint Global, Penumbra, Stryker, Pulsar Vascular, MicroVention, Lazarus Effect, Blockade Medical, Reverse Medical; *Grants/Grants Pending*: National Institutes of Health,* University at Buffalo,* *Comments*: The National Institutes of Health (coinvestigator: National Institute of Neurological Disorders and Stroke, 1R01NS064592–01A1, Hemodynamic Induction of Pathologic Remodeling Leading to Intracranial Aneurysms); University at Buffalo (Research Development Award); the National Institutes of Health (coinvestigator: National Institute of Biomedical Imaging and Bioengineering, 5 R01 EB002873–07, Micro-Radiographic Image for Neurovascular Interventions); *Payment for Lectures (including service on Speakers Bureaus)*: Codman & Shurtleff; *Stock/Stock Options*: Hotspur, Intratech Medical, STIMSOX, Valor Medical, Blockade Medical, Lazarus Effect, Pulsar Vascular, Medina Medical; *Other*: national steering committees for various trials; honoraria from Abbott Vascular and Penumbra, *Comments*: Penumbra, 3D Separator Trial; Covidien, Solitaire With the Intention For Thrombectomy as PRIMary Endovascular Treatment Trial; MicroVention, Flow Re-Direction Endoluminal Device Trial. David F. Kallmes—*RELATED*: *Grant*: ev3/Covidien,* *Comments*: funding for a clinical trial; *Consulting Fee or Honorarium*: ev3/Covidien,* *Comments*: funding for the Steering Committee; *Fees for Participation in Review Activities such as Data Monitoring Boards, Statistical Analysis, Endpoint Committees, and the Like*: ev3/Covidien,* *Comments*: funding for Adverse Event Review Committee; *UNRELATED*: *Board Membership*: GE Healthcare (Cost-Effectiveness Board); *Grants/Grants Pending*: MicroVention,* Codman,* SurModics,* NeuroSigma,* Sequent Medical,* ev3/Covidien, *Comments*: support for preclinical and clinical trials; *Royalties*: University of Virginia Patent Foundation (Spine Fusion). *Money paid to the institution.

REFERENCES

1. Arrese I, Sarabia R, Pintado R, et al. **Flow-diverter devices for intracranial aneurysms: systematic review and meta-analysis.** *Neurosurgery* 2013;73:193–99; discussion 199–200 CrossRef Medline
2. Briganti F, Napoli M, Tortora F, et al. **Italian multicenter experience with flow-diverter devices for intracranial unruptured aneurysm treatment with periprocedural complications: a retrospective data analysis.** *Neuroradiology* 2012;54:1145–52 CrossRef Medline
3. Brinjikji W, Murad MH, Lanzino G, et al. **Endovascular treatment of intracranial aneurysms with flow diverters: a meta-analysis.** *Stroke* 2013;44:442–47 CrossRef Medline
4. Yu SC, Kwok CK, Cheng PW, et al. **Intracranial aneurysms: mid-term outcome of Pipeline embolization device—a prospective study in 143 patients with 178 aneurysms.** *Radiology* 2012;265:893–901 CrossRef Medline
5. Kallmes DF, Ding YH, Dai D, et al. **A new endoluminal, flow-disrupting device for treatment of saccular aneurysms.** *Stroke* 2007;38:2346–52 CrossRef Medline
6. Kallmes DF, Ding YH, Dai D, et al. **A second-generation, endoluminal, flow-disrupting device for treatment of saccular aneurysms.** *AJNR Am J Neuroradiol* 2009;30:1153–58 CrossRef Medline
7. Velat GJ, Fargen KM, Lawson MF, et al. **Delayed intraparenchymal hemorrhage following Pipeline embolization device treatment for a giant recanalized ophthalmic aneurysm.** *J Neurointerv Surg* 2012;4:e24 CrossRef Medline
8. Cruz JP, Chow M, O'Kelly C, et al. **Delayed ipsilateral parenchymal hemorrhage following flow diversion for the treatment of anterior circulation aneurysms.** *AJNR Am J Neuroradiol* 2012;33:603–08 CrossRef Medline
9. Turowski B, Macht S, Kulcsár Z, et al. **Early fatal hemorrhage after endovascular cerebral aneurysm treatment with a flow diverter (SILK-stent): do we need to rethink our concepts?** *Neuroradiology* 2011;53:37–41 CrossRef Medline
10. Hu YC, Deshmukh VR, Albuquerque FC, et al. **Histopathological assessment of fatal ipsilateral intraparenchymal hemorrhages after the treatment of supraclinoid aneurysms with the Pipeline embolization device.** *J Neurosurg* 2014;120:365–74 CrossRef Medline
11. Chalouhi N, Zanaty M, Jabbour PM, et al. **Intracerebral hemorrhage after Pipeline embolization: management of antiplatelet agents and the case for point-of-care testing—case reports and review of literature.** *Clin Neurol Neurosurg* 2014;124:21–24 CrossRef Medline
12. Fargen KM, Hoh BL. **Ipsilateral cerebral hemorrhage following deployment of the Pipeline embolization device.** *J Neurosurg* 2014;120:363–64 CrossRef Medline
13. Delgado Almandoz JE, Crandall BM, Scholz JM, et al. **Last-recorded P2Y12 reaction units value is strongly associated with thromboembolic and hemorrhagic complications occurring up to 6 months after treatment in patients with cerebral aneurysms treated with the Pipeline embolization device.** *AJNR Am J Neuroradiol* 2014;35:128–35 CrossRef Medline
14. Kallmes DF, Hanel R, Lopes D, et al. **International retrospective study of the Pipeline embolization device: a multicenter aneurysm treatment study.** *AJNR Am J Neuroradiol* 2015;36:108–15 CrossRef Medline
15. De Leon D, Swank G, Mirza MA. **Radial artery sterile granulomatous reaction secondary to hydrophilic-coated sheath used for tran-**

sradial cardiac catheterization: a case series. *Angiology* 2012;63:560–62 CrossRef Medline
16. Zellner C, Ports TA, Yeghiazarians Y, et al. **Sterile radial artery granuloma after transradial procedures: a unique and avoidable complication.** *Catheter Cardiovasc Interv* 2010;76:673–76 CrossRef Medline
17. Zellner C, Yeghiazarians Y, Ports TA, et al. **Sterile radial artery granuloma after transradial cardiac catheterization.** *Cardiovasc Revasc Med* 2011;12:187–89 CrossRef Medline
18. Ganesan S, Felo J, Saldana M, et al. **Embolized crospovidone (poly[N-vinyl-2-pyrrolidone]) in the lungs of intravenous drug users.** *Mod Pathol* 2003;16:286–92 CrossRef Medline
19. Delgado Almandoz JE, Crandall BM, Scholz JM, et al. **Pre-procedure P2Y12 reaction units value predicts perioperative thromboembolic and hemorrhagic complications in patients with cerebral aneurysms treated with the Pipeline embolization device.** *J Neurointerv Surg* 2013;5(suppl 3):iii3–10 CrossRef Medline
20. Takigawa T, Suzuki K, Sugiura Y, et al. **Thromboembolic events associated with single balloon-, double balloon-, and stent-assisted coil embolization of asymptomatic unruptured cerebral aneurysms: evaluation with diffusion-weighted MR imaging.** *Neuroradiology* 2014;56:1079–86 CrossRef Medline
21. Hong Y, Wang YJ, Deng Z, et al. **Stent-assisted coiling versus coiling in treatment of intracranial aneurysm: a systematic review and meta-analysis.** *PLoS One* 2014;9:e82311 CrossRef Medline
22. McLaughlin N, McArthur DL, Martin NA. **Use of stent-assisted coil embolization for the treatment of wide-necked aneurysms: a systematic review.** *Surg Neurol Int* 2013;4:43 CrossRef Medline
23. Tomas C, Benaissa A, Herbreteau D, et al. **Delayed ipsilateral parenchymal hemorrhage following treatment of intracranial aneurysms with flow diverter.** *Neuroradiology* 2014;56:155–61 CrossRef Medline
24. Rodling-Wahlstrom M, Olivecrona M, Koskinen LO, et al. **Subarachnoid haemorrhage induces an inflammatory response followed by a delayed persisting increase in asymmetric dimethylarginine.** *Scand J Clin Lab Invest* 2012;72:484–89 CrossRef Medline
25. Chiu AH, Wenderoth J. **Cerebral hyperperfusion after flow diversion of large intracranial aneurysms.** *J Neurointerv Surg* 2013;5:e48 CrossRef Medline
26. Murakami H, Inaba M, Nakamura A, et al. **Ipsilateral hyperperfusion after neck clipping of a giant internal carotid artery aneurysm: case report.** *J Neurosurg* 2002;97:1233–36 CrossRef Medline
27. Tan LA, Keigher KM, Munich SA, et al. **Thromboembolic complications with Pipeline embolization device placement: impact of procedure time, number of stents and pre-procedure P2Y12 reaction unit (PRU) value.** *J Neurointerv Surg* 2015;7:217–21 CrossRef Medline

WEB-DL Endovascular Treatment of Wide-Neck Bifurcation Aneurysms: Long-Term Results in a European Series

L. Pierot, J. Klisch, T. Liebig, J.-Y. Gauvrit, M. Leonardi, N.P. Nuzzi, F. Di Paola, V. Sychra, B. Mine, and B. Lubicz

ABSTRACT

BACKGROUND AND PURPOSE: Flow disruption with the WEB-DL device has been used safely for the treatment of wide-neck bifurcation aneurysms. The stability of aneurysm occlusion after this treatment was evaluated in the short and midterm, but not in the long term. This retrospective multicenter European study is the continuation of an already published series dealing with short- and midterm anatomic results and analyzes long-term data in patients treated with the WEB-DL.

MATERIALS AND METHODS: Twelve European neurointerventional centers initially participated in the study. In addition to data collected for the initial publication, images obtained at long-term follow-up were collected and independently analyzed by the same experienced interventional neuroradiologist.

RESULTS: Of the initial 45 patients, 26 (20 women and 6 men; 35–73 years of age; mean, 55.2 ± 10.6 years; median, 55.5 years) with 26 aneurysms treated with the WEB-DL device had long-term follow-up (median, 27.4 months). Three of 26 patients (11.5%) were retreated between short- and midterm follow-up, and none, between mid- and long-term follow-up. Long-term aneurysm occlusion in the 19 patients treated with the WEB only and not retreated during follow-up was complete occlusion in 13/19 patients (68.4%), including aneurysms with opacification of the proximal recess in 9/19 patients (47.4%), neck remnant in 3/19 patients (15.8%), and aneurysm remnant in 3/19 patients (15.8%). In all patients (100.0%), aneurysm occlusion was stable between midterm and long-term follow-up.

CONCLUSIONS: The results suggest that WEB treatment of wide-neck bifurcation aneurysms offers long-term stable occlusion.

ABBREVIATIONS: DL = Dual Layer; WEBCAST = WEB Clinical Assessment of IntraSaccular Aneurysm Therapy

Endovascular treatment is now the first-line treatment for both ruptured and unruptured intracranial aneurysms.[1-4] However, the limitations of standard coiling have contributed to the development of new endovascular approaches, including balloon-assisted coiling, stent-assisted coiling, flow diversion, and flow disruption.[5]

The WEB aneurysm embolization system (Sequent Medical, Aliso Viejo, California) is an intrasaccular device designed to disrupt the intra-aneurysmal flow at the level of the neck.[6-9] Several devices are now available in the WEB family: WEB–Dual Layer (DL) and the more recently introduced WEB–Single Layer (SL) and WEB–Single Layer Sphere (SLS).[10] Initial clinical experience and recent multicenter series have shown the clinical utility of this device in wide-neck bifurcation aneurysms with high technical success and low acute morbidity and mortality.[7-11] Also, the initial WEB-DL literature suggested good efficacy with a high percentage of complete and adequate occlusion (complete occlusion or neck remnant) in the postoperative period and in the short-term follow-up. In the WEB Clinical Assessment of IntraSaccular Aneurysm Therapy (WEBCAST) trial, complete and adequate occlusion was observed in, respectively, 56.1% and 85.4% of aneurysms.[11] A retrospective series evaluating both short- (median, 6 months) and midterm (median, 13 months) follow-up showed adequate occlusion in, respectively, 81.1% and 89.7% of aneu-

Received February 20, 2015; accepted after revision April 15.

From the Department of Neuroradiology (L.P.), Hôpital Maison-Blanche, Université Reims-Champagne-Ardenne, Reims, France; Department of Diagnostic and Interventional Radiology and Neuroradiology (J.K., V.S.), Helios General Hospital, Erfurt, Germany; Department of Neuroradiology (T.L.), Universitätsklinikum Köln, Cologne, Germany; Department of Neuroradiology (J.-Y.G.), CHU Rennes, Rennes, France; Department of Neuroradiology (M.L.), Ospedale Bellaria, Bologna University, Bologna, Italy; Department of Neuroradiology (N.P.N.), Ospedale Galliera, Genova, Italy; Department of Neuroradiology (F.D.P.), Ospedale Santa Maria, Treviso, Italy; and Department of Neuroradiology (B.M., B.L.), Erasme University Hospital, Brussels, Belgium.

Please address correspondence to Laurent Pierot, MD, PhD, Service de Radiologie, Hôpital Maison-Blanche, 45, rue Cognacq-Jay, 51092 Reims cedex; e-mail: lpierot@gmail.com

Indicates open access to non-subscribers at www.ajnr.org

http://dx.doi.org/10.3174/ajnr.A4445

rysms.[12] Between short- and midterm follow-up, aneurysm occlusion was stable in 92.9% of aneurysms.

Aneurysm recanalization is an important issue in endovascular therapy, and wide-neck aneurysms (typical indications for the WEB) are highly prone to recanalization.[13,14] Because the WEB is dedicated to the treatment of wide-neck bifurcation aneurysms, it is important to assess the long-term stability of aneurysm occlusion after WEB treatment. As a multicenter trial, the European study was already conducted in the first patients treated with the WEB; therefore, the decision was made to collect and analyze long-term follow-up in this series of patients when available.[12] In this initial series, it was shown that opacification of the proximal recess was always stable at midterm and that it was equivalent to complete occlusion.[12]

MATERIALS AND METHODS

Population

The study received institutional review board approval, and according to the design of the trial, informed consent was waived. European neurointerventional centers selected for the previous series were contacted to inquire whether long-term anatomic follow-up was performed for their patients and whether they agreed to participate in this new analysis. Of the 12 European centers participating in the initial study, 10 had follow-up for some or all of their patients and agreed to participate.

WEB-DL Device and Procedural Modalities

The WEB-DL device and procedural modalities were previously presented in the initial article describing short- and midterm follow-up.[12]

Data Collection

As previously described, each center completed a patient file with the following data: patient age and sex, aneurysm status (ruptured/unruptured), aneurysm characteristics including location classified into 4 groups (ICA, MCA, posterior circulation, anterior communicating artery), size and neck size, date of the procedure, occurrence of complications during or after the procedure, use of additional devices during the procedure (coils, remodeling balloons, stents, or flow diverters), and the modified Rankin Scale score at discharge and at last follow-up.[12]

In complement to images already collected (pre- and postoperative, short-term, and midterm), long-term images were collected. Short-term follow-up was defined as the first follow-up performed <8 months after initial treatment. The second follow-up was defined as midterm follow-up, and the third follow-up, as long-term follow-up.

For digital subtraction angiography, frontal, lateral, and working views were collected as well as 3D angiography when available. For MR angiography and CT angiography, frontal, lateral, and working view reconstructions were collected. MRA or CTA examinations were used exclusively when DSA was not performed.

Data Analysis

To evaluate the anatomic results in a homogeneous population with typical indications for WEB-DL, we included patients if their aneurysms met precise criteria:

- Located at a bifurcation: ICA, MCA, anterior communicating artery, basilar artery, and PICA
- Nonthrombosed
- With a wide neck (≥4 mm)
- With a maximum diameter of ≤12 mm.

The independent reader, who already analyzed the images (pre- and postoperative, short-term and midterm follow-up) for the initial series (J.-Y.G.), reviewed the long-term follow-up images. They were evaluated by using a 3-grade scale: complete occlusion (including complete occlusion with opacification of the proximal recess of the device), neck remnant, and aneurysm remnant. The reader also analyzed the evolution of aneurysm occlusion between mid- and long-term follow-up and classified it as improved, stable, or worsened.

Clinical data were already reviewed and analyzed by the 2 principal investigators of the study (B.L. and L.P.) for the initial series.

RESULTS

Patient and Aneurysm Population

The population of the initial series (midterm follow-up) was 45 patients.[12] Among these 45 patients, 26 (20 women and 6 men; 35–73 years of age; mean, 55.2 ± 10.6 years; median, 55.5 years) with 26 aneurysms treated with the WEB-DL device had long-term follow-up.

Aneurysm locations were the following: the MCA in 13 patients, posterior circulation in 9 patients (including 8 patients with basilar artery aneurysms and 1 with PICA aneurysm), anterior communicating artery in 3 patients, and ICA terminus in 1 patient. Two aneurysms were ruptured, and 24 were unruptured. Aneurysm size was 5.0–11.5 mm (mean, 7.8 ± 1.6 mm; median, 8.0 mm). Neck size was 4.0–9.0 mm (mean, 5.7 ± 1.4 mm; median, 5.6 mm).

Treatment Modalities

Treatment was conducted in a standard manner in 21 patients with 1 device deployed in the aneurysm. In 1 patient, 2 WEB-DL devices were deployed in the aneurysm due to the aneurysm shape. In 3 patients, stent placement was used as an additional treatment due to WEB-DL protrusion (2 patients) and to thromboembolic complication treated with abciximab and stent (1 patient). One patient had additional treatment with coils.

Technical Issues, Complications, and Clinical Outcome

Three thromboembolic complications were observed during the treatment. At last clinical follow-up, the mRS score was zero in 2 patients and 1 in 1 patient.

No intraoperative rupture was observed in this series.

Overall clinical outcome results at last clinical follow-up (6–28 months; mean, 13.8 ± 5.6 months; median, 13.0 months) were as follows: 24 patients with mRS 0 and 2 patients with mRS 1 (1 related to initial bleeding; 1, to a thromboembolic event).

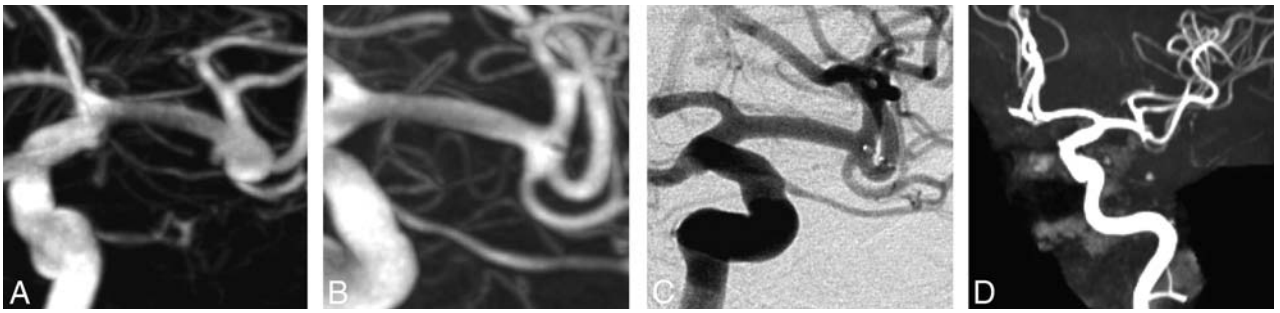

FIG 1. *A*, Preoperative DSA shows a wide-neck middle cerebral artery aneurysm with a daughter sac. *B* and *C*, Three- and 12-month DSA show complete aneurysm occlusion. *D*, Twenty-seven-month MRA shows complete aneurysm occlusion.

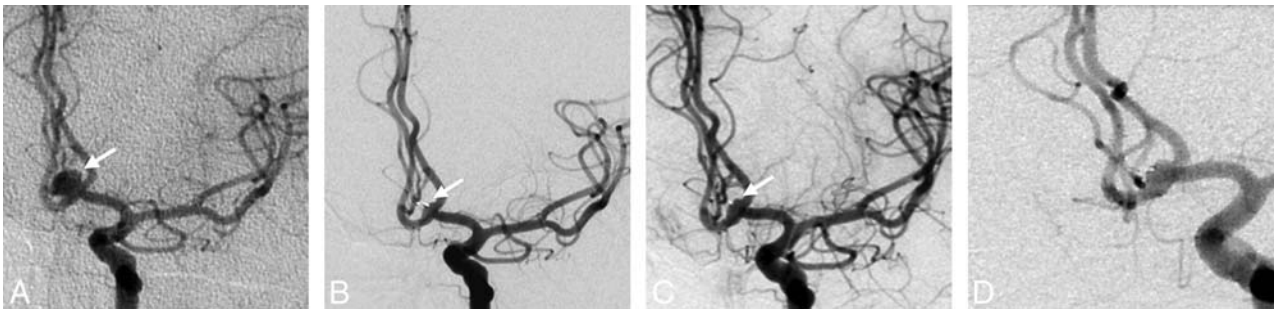

FIG 2. *A*, Preoperative DSA shows a wide-neck anterior communicating artery aneurysm. *B–D*, Six-, 12-, and 26-month DSA show stable complete aneurysm occlusion with opacification of the proximal recess.

Retreatment

Three of 26 patients (11.5%) were retreated between short- and midterm follow-up. Two of these retreatments were planned according to aneurysm morphology and were part of the treatment strategy. Retreatment was performed with coils in 1 patient and coils + stent in 1 patient. One retreatment was unplanned, due to initial undersizing of the WEB, and was performed with coils.

No retreatment was performed between mid- and long-term follow-up.

Short-Term Anatomic Outcome

Because the goal of the study was to evaluate the quality and stability of aneurysm occlusion after WEB-DL treatment, the 4 patients with additional coiling and/or stent placement were not included in the evaluation. Finally 22/26 patients (84.6%) were evaluated in the short-term. Short-term follow-up was obtained from 2 to 8 months after the initial treatment (mean, 4.8 ± 2.5 months; median, 5 months). Modalities of short-term follow-up were DSA in 19 patients, MRA in 2 patients, and CTA in 1 patient.

Complete aneurysm occlusion was obtained in 13/22 patients (59.1%) (Fig 1), including opacification of the proximal recess with complete occlusion of the aneurysm in 9/22 patients (40.9%) (Fig 2). Neck remnant was observed in 5/22 patients (22.7%), and aneurysm remnant in 4/22 patients (18.2%). Adequate occlusion (complete occlusion or neck remnant) was observed in 18/22 patients (81.8%).

Midterm Anatomic Outcome

Because the goal of the study was to evaluate the quality and stability of aneurysm occlusion after WEB-DL treatment, 7 patients with additional coiling and/or stent placement during the initial procedure or retreatment were not included in the evaluation. One patient refused midterm follow-up examination. Finally 18/26 patients (69.2%) were evaluated in the midterm. Midterm follow-up was obtained from 8 to 28 months after the initial treatment (mean, 14.9 ± 8.3 months; median, 13.0 months). Modalities of midterm follow-up were DSA in 14 patients and MRA in 4 patients.

Complete aneurysm occlusion was obtained in 13/18 patients (72.2%) (Fig 1), including opacification of the proximal recess with complete occlusion of the aneurysm in 9/18 patients (50.0%) (Fig 2). Neck remnant was observed in 3/18 patients (16.7%), and aneurysm remnant in 2/18 patients (11.1%). Adequate occlusion (complete occlusion, opacification of the proximal recess, or neck remnant) was observed in 16/18 patients (88.9%).

Evolution between Short-Term and Midterm Follow-Up

In 16/18 patients (88.9%), aneurysm occlusion was stable (Fig 1). In 2/18 patients (11.1%) with a neck remnant at 3 months, a worsening of the aneurysm occlusion was observed in midterm follow-up with aneurysm remnants in both cases. These 2 patients were not retreated and had no further worsening of aneurysm occlusion at long-term follow-up.

All patients with opacification of the proximal recess at short-term follow-up had a stable aneurysm occlusion at midterm follow-up (Fig 2).

Long-Term Anatomic Outcome

Long-term follow-up was analyzed in 19 patients. The patient who refused the second (midterm) follow-up finally accepted the third follow-up. Seven patients with additional coiling and/or

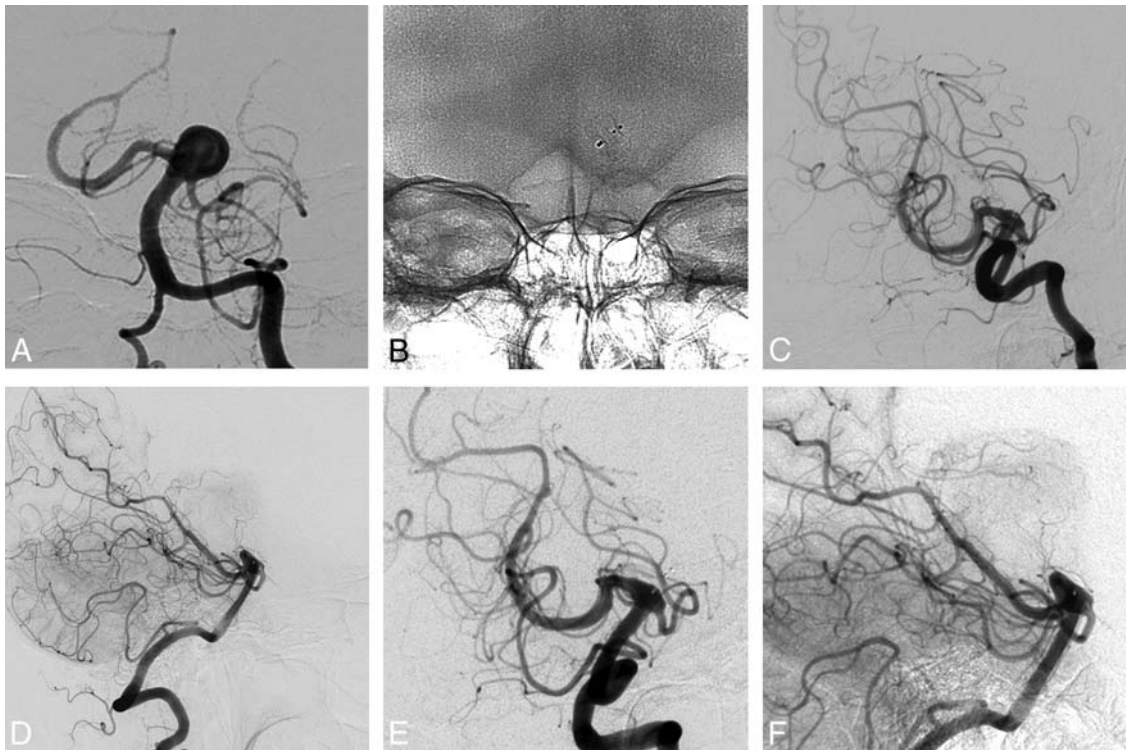

FIG 3. *A*, Preoperative DSA shows a wide-neck basilar artery aneurysm. *B*, The WEB device is deployed in the aneurysm. *C* and *D*, Six-month DSA (oblique and lateral views) shows a small aneurysm remnant. *E* and *F*, Twenty-one-month DSA (oblique and lateral views) shows that the aneurysm remnant has not grown.

stent placement during the initial procedure or retreatment were not included in the evaluation.

Long-term follow-up was obtained from 18 to 41 months after the initial treatment (mean, 27.9 ± 13.7 months; median, 26.0 months). Modalities of midterm follow-up were DSA in 6 patients, MRA in 9 patients, and CTA in 4 patients.

Complete aneurysm occlusion was obtained in 13/19 patients (68.4%) (Fig 1), including opacification of the proximal recess with complete occlusion of the aneurysm in 9/19 patients (47.4%) (Fig 2). Neck remnant was observed in 3/19 patients (15.8%), and aneurysm remnant in 3/19 patients (15.8%). Adequate occlusion (complete occlusion, opacification of the proximal recess, or neck remnant) was observed in 16/19 patients (84.2%).

Evolution between Midterm and Long-Term Follow-Up

In all patients (100.0%), aneurysm occlusion was stable between midterm and long-term follow-up (Figs 1 and 2).

All patients with opacification of the proximal recess at midterm follow-up had a stable aneurysm occlusion at long-term follow-up; this result was equivalent to complete occlusion.

DISCUSSION

Precise evaluation of new endovascular techniques for intracranial aneurysm treatment is mandatory to determine their safety and efficacy compared with already established techniques. Efficacy has to be analyzed not only with short- and midterm anatomic results but also in longer follow-up.

The prospective good clinical practice studies (WEBCAST, French Observatory) conducted with the WEB have shown good safety of flow disruption in the treatment of wide-neck bifurcation aneurysms with no mortality and low morbidity.[10,11] Short-term (6 months) anatomic results were already reported in the WEBCAST study, showing complete occlusion in 56.1% of patients, neck remnant in 29.3%, and aneurysm remnant in only 14.6%. In the WEBCAST and French Observatory studies, evaluation of anatomic results will be performed at 1 year and then at 3 and 5 years.

Due to the issue of recanalization after endovascular treatment of aneurysms, WEB efficacy must be evaluated not only at short term but also at midterm and long term. It is singularly true for WEB treatment because its major indication is wide-neck bifurcation aneurysms, which are prone to recurrence.[14] After the beginning of clinical experience with the WEB in 2010, it was important to have early and ongoing evaluation of aneurysm occlusion after WEB treatment. A retrospective analysis was conducted in 12 European centers in the first 45 patients treated with the WEB-DL.[12] In this series, 4/45 patients (8.9%) were retreated within months following the initial WEB-DL treatment, 2 of these retreatments being planned according to aneurysm morphology and part of the treatment strategy. Short-term anatomic follow-up showed complete aneurysm occlusion in 21/37 patients (56.8%) that includes aneurysms with opacification of the proximal recess in 12/37 patients (32.4%), neck remnant in 9/37 patients (24.3%), and aneurysm remnant in 7/37 patients (18.9%). Midterm anatomic follow-up (median, 13 months) showed complete aneurysm occlusion in 20/29 patients (69.0%) that includes aneurysms with opacification of the proximal recess in 12/29 patients (41.4%), neck remnant in 6/29 patients (20.7%), and aneurysm remnant in 3/29 patients (10.3%). Aneurysm occlusion

was stable between short- and midterm follow-up in 26/28 patients (92.9%). In 2/28 patients (7.1%) with neck remnants, a worsening of the aneurysm occlusion was observed in midterm follow-up, leading to aneurysm remnant in both cases. All patients with opacification of the proximal recess at short-term follow-up had a stable aneurysm occlusion at midterm follow-up, and this result was equivalent to complete occlusion.

Recently, a single center reported different results in a relatively small number of aneurysms.[15] In this series that included 15 patients with 15 aneurysms consecutively treated with the WEB, aneurysm occlusion evaluated in 7 patients at midterm follow-up (median, 18.6 months) was complete occlusion in 0/7 aneurysms (0.0%), neck remnant in 4/7 (52.7%), and aneurysm remnant in 3/7 (47.3%). The reasons for the discrepancy between the study of Cognard and Januel[15] and the present series are multiple. One is probably related to the selection of aneurysms treated with the WEB. As indicated by Cognard and Januel, only very complicated wide-neck bifurcation aneurysms untreatable with other techniques were included in their series. Another factor is the treatment technique. As outlined during the initial experience with the WEB, sizing of the device is critical and undersizing of the device may be associated with poor anatomic results. It is difficult to know whether appropriate sizing was used in this series. However, the postoperative results were mostly neck and aneurysm remnants (respectively, 8/15 and 1/15), suggesting that WEB undersizing was accepted in some cases. All 15 patients were asymptomatic and were not retreated at follow-up; instead, they were controlled by ongoing angiography.

The present series evaluates the long-term follow-up (median, 27.4 months) of the patients of the previous series. Unfortunately, not all patients had long-term follow-up, and the same expert independently analyzed only 26 of them. The results are focused on patients treated exclusively with the WEB because the goal of the study was to analyze the anatomic stability after such treatment. At long-term follow-up, complete aneurysm occlusion was obtained in 13/19 patients (68.4%) that includes aneurysms with opacification of the proximal recess in 9/19 patients (47.4%), neck remnant in 3/19 patients (15.8%), and aneurysm remnant in 3/19 patients (15.8%). Adequate occlusion (complete occlusion, opacification of the proximal recess, or neck remnant) was observed in 16/19 patients (84.2%). Aneurysm occlusion was stable in all patients between mid- and long-term follow-ups.

This series has several limitations. First, it is retrospective and has a limited number of patients, and long-term follow-up after treatment with the WEB only was evaluated in only 19 patients. Larger series are mandatory to precisely analyze long-term stability of aneurysm occlusion after WEB treatment. However, it is important to have a preliminary evaluation showing that there is no major instability of aneurysm occlusion in the long term. Some recent techniques were very little evaluated in the long term, for example, stent placement or flow diversion. A second limitation is that short- and midterm anatomic evaluations were conducted by using heterogeneous modalities (mostly DSA and MRA). However, recent publications confirm the value of MRA in the follow-up of intracranial aneurysms.[16,17] A third limitation is that only WEB-DL (and not WEB-Single Layer and WEB-Single Layer Sphere) treatment was evaluated.

CONCLUSIONS

The present series shows that in this group of complex wide-neck bifurcation aneurysms, appropriate occlusion was obtained in a high percentage of cases in the short- (81.8%), mid- (88.9%), and long-term (84.2%) follow-up. The results were overall quite stable. Only 2 patients (11.1%) had progressed from neck remnant to aneurysm remnant at midterm follow-up, and there was no case of late recanalization. Most important, all aneurysms with opacification of the proximal recess at short-term follow-up had stable aneurysm occlusion at mid- and long-term follow-up.

Disclosures: Laurent Pierot—*RELATED*: *Consulting Fee or Honorarium*: Sequent; *UNRELATED*: *Consultancy*: Codman, Covidien/ev3, MicroVention, Neuravi. Joachim Klisch—*RELATED*: *Consulting Fee or Honorarium*: Sequent Medical*; *UNRELATED*: *Consultancy*: proctoring and consultancy for Sequent Medical.* Thomas Liebig—*RELATED*: *Consulting Fee or Honorarium*: Sequent Medical, Germany (consulting and proctoring). Nunzio Paolo Nuzzi—*UNRELATED*: *Consultancy*: Sequent Medical, Covidien, *Comments*: fees received as a proctor. Boris Lubicz—*UNRELATED*: *Consultancy*: Codman, MicroVention. *Money paid to the institution.

REFERENCES

1. Molyneux A, Kerr R, Stratton I, et al; International Subarachnoid Aneurysm Trial (ISAT) Collaborative Group. **International Subarachnoid Aneurysm Trial (ISAT) of neurosurgical clipping versus endovascular coiling in 2143 patients with ruptured intracranial aneurysms: a randomised trial.** *Lancet* 2002;360:1267–74 CrossRef Medline
2. McDougall CG, Spetzler RF, Zabramski JM, et al. **The Barrow Ruptured Aneurysm Trial.** *J Neurosurg* 2012;116:135–44 CrossRef Medline
3. Cognard C, Pierot L, Anxionnat R, et al; Clarity Study Group. **Results of embolization used as the first treatment choice in a consecutive nonselected population of ruptured aneurysms: clinical results of the Clarity GDC study.** *Neurosurgery* 2011;69:837–41; discussion 842 CrossRef Medline
4. Pierot L, Spelle L, Vitry F; ATENA Investigators. **Immediate clinical outcome of patients harboring unruptured intracranial aneurysms treated by endovascular approach: results of the ATENA study.** *Stroke* 2008;39:2497–504 CrossRef Medline
5. Pierot L, Wakhloo A. **Endovascular treatment of intracranial aneurysms: current status.** *Stroke* 2013;44:2046–54 CrossRef Medline
6. Ding YH, Lewis DA, Kadirvel R, et al. **The Woven EndoBridge: a new aneurysm occlusion device.** *AJNR Am J Neuroradiol* 2011;32:607–11 CrossRef Medline
7. Pierot L, Liebig T, Sychra V, et al. **Intrasaccular flow-disruption treatment of intracranial aneurysms: preliminary results of a multicenter clinical study.** *AJNR Am J Neuroradiol* 2012;33:1232–38 CrossRef Medline
8. Lubicz B, Mine B, Collignon L, et al. **WEB device for endovascular treatment of wide-necked bifurcation aneurysms.** *AJNR Am J Neuroradiol* 2013;34:1209–14 CrossRef Medline
9. Pierot L, Klisch J, Cognard C, et al. **Endovascular WEB flow disruption in middle cerebral artery aneurysms: preliminary feasibility, clinical, and anatomical results in a multicenter study.** *Neurosurgery* 2013;73:27–34; discussion 34–35 CrossRef Medline
10. Pierot L, Moret J, Turjman F, et al. **WEB treatment of intracranial aneurysms: feasibility, complications, and 1-month safety results with WEB DL and WEB SL/SLS in the French Observatory.** *AJNR Am J Neuroradiol* 2015;36:922–27 CrossRef Medline
11. Pierot L, Costalat V, Moret J, et al. **Safety and efficacy of aneurysm treatment with WEB: results of WEBCAST study.** *J Neurosurg.* In press
12. Lubicz B, Klisch J, Gauvrit JY, at al. **WEB-DL endovascular treatment of wide-neck bifurcation aneurysms: short- and midterm re-**

sults in a European study. *AJNR Am J Neuroradiol* 2014;35:432–38 CrossRef Medline

13. Benaissa A, Barbe C, Pierot L. **Analysis of recanalization after endovascular treatment of intracranial aneurysm (ARETA trial): presentation of a prospective multicenter study.** *J Neuroradiol* 2015;42: 80–85 CrossRef Medline
14. Pierot L, Cognard C, Anxionnat R, et al; CLARITY Investigators. **Endovascular treatment of ruptured intracranial aneurysms: factors affecting midterm quality anatomic results—analysis in a prospective multicenter series of patients (CLARITY).** *AJNR Am J Neuroradiol* 2012;33:1475–80 CrossRef Medline
15. Cognard C, Januel AC. **Remnants and recurrences after the use of the WEB intrasaccular device in large-neck bifurcation aneurysms.** *Neurosurgery* 2015;76:522–30; discussion 530 CrossRef Medline
16. Pierot L, Portefaix C, Gauvrit JY, et al. **Follow-up of coiled intracranial aneurysms: comparison of 3D time-of-flight MR angiography at 3T and 1.5T in a large prospective series.** *AJNR Am J Neuroradiol* 2012;33:2162–66 CrossRef Medline
17. Pierot L, Portefaix C, Boulin A, et al. **Follow-up of coiled intracranial aneurysms: comparison of 3D time-of-flight and contrast-enhanced magnetic resonance angiography at 3T in a large, prospective series.** *Eur Radiol* 2012;22:2255–63 CrossRef Medline

One-Year Angiographic Follow-Up after WEB-SL Endovascular Treatment of Wide-Neck Bifurcation Intracranial Aneurysms

R. Sivan-Hoffmann, B. Gory, R. Riva, P.-E. Labeyrie, F. Signorelli, I. Eldesouky, U. Gonike-Sadeh, X. Armoiry, and F. Turjman

ABSTRACT

BACKGROUND AND PURPOSE: Endovascular coiling of wide-neck intracranial aneurysms is associated with low rates of initial angiographic occlusion and high rates of recurrence. The WEB intrasaccular device has been developed specifically for this indication. To date, there has been no report of the long-term follow-up of a series of patients with aneurysms treated with this type of device, to our knowledge. Our aim was to evaluate a 1-year follow-up of angiographic results in a prospective single-center series of patients treated with the WEB-Single-Layer (SL) device.

MATERIALS AND METHODS: All patients treated with the WEB-SL device in our center between August 2013 and May 2014 were prospectively included. One-year angiographic outcomes were assessed. Results at follow-up were graded as complete occlusion, neck remnant, or residual aneurysm.

RESULTS: Eight patients with 8 unruptured wide-neck aneurysms were enrolled in this study. Average dome width was 7.5 mm (range, 5.4–10.7 mm), and average neck size was 4.9 mm (range, 2.6–6.5 mm). One-year angiographic follow-up obtained in all aneurysms included 1 complete aneurysm occlusion (12.5%), 6 neck remnants (75%), and 1 aneurysm remnant (12.5%). Of 8 aneurysms, worsening of aneurysm occlusion was observed in 2 (25%) by compression of the WEB device. There was no angiographic recurrence of initially totally occluded aneurysms. No bleeding was observed during the follow-up period.

CONCLUSIONS: Endovascular therapy of intracranial aneurysms with the WEB-SL device allows treatment of wide-neck aneurysms with a high rate of neck remnant at 1 year, at least partially explained by WEB compression. Initial size selection and technologic improvements could be an option for optimization of aneurysm occlusion in WEB-SL treatment.

ABBREVIATIONS: AcomA = anterior communicating artery; DL = Dual-Layer; SL = Single-Layer

The WEB aneurysm embolization system (Sequent Medical, Aliso Viejo, California) is an intrasaccular braided device specifically developed for endovascular treatment of wide-neck intracranial aneurysms with the goal of disrupting flow at the aneurysm neck and promoting aneurysmal thrombosis without the need for reconstruction of the entire parent artery segment with a stent. Several types of WEB devices are currently available[1]: the WEB-Dual-Layer (DL), which is made of 2 layers held together and creating 2 compartments, and the WEB-Single-Layer (SL), which is a single-layer device creating only 1 compartment. Only a few studies on the treatment of intracranial aneurysms by using the WEB-DL have been published,[2-5] and to date, only a single published article on aneurysms treated with WEB-SL reported a series including any anatomic follow-up.[6] We recently published the 6-month clinical and anatomic outcomes of WEB-SL endovascular treatment.[7]

The purpose of this study was to evaluate the 1-year angiographic results of patients managed with the WEB-SL device in a prospective single-center series.

MATERIALS AND METHODS

Population

All patients treated in the Neurologic Pierre Wertheimer Hospital in Lyon (France) with the WEB-SL device for intracranial unruptured aneurysms between August 2013 and May 2014 were prospectively included. The indication for treatment and the technique chosen (surgery or endovascular) were decided by a

Received December 20, 2014; accepted after revision March 2, 2015.

From the DHU IRIS, Departments of Interventional Neuroradiology (R.S.-H., B.G., R.R., P.-E.L., I.E., U.G.-S., F.T.) and Neurosurgery (F.S.), Hôpital Neurologique Pierre Wertheimer, Hospices Civils de Lyon, Lyon, France; and Hospices Civils de Lyon (X.A.), Délégation à la Recherche Clinique et à l'Innovation, Cellule Innovation/UMR-CNRS 5510/MATEIS, Lyon, France.

R.S.-H. and B.G. contributed equally to this work.

Please address correspondence to Benjamin Gory, MD, MSc, DHU IRIS, Department of Interventional Neuroradiology, Hôpital Neurologique Pierre Wertheimer, Hospices Civils de Lyon, 59 Boulevard Pinel, 69677 Bron, France; e-mail: benjamin.gory@chu-lyon.fr

http://dx.doi.org/10.3174/ajnr.A4457

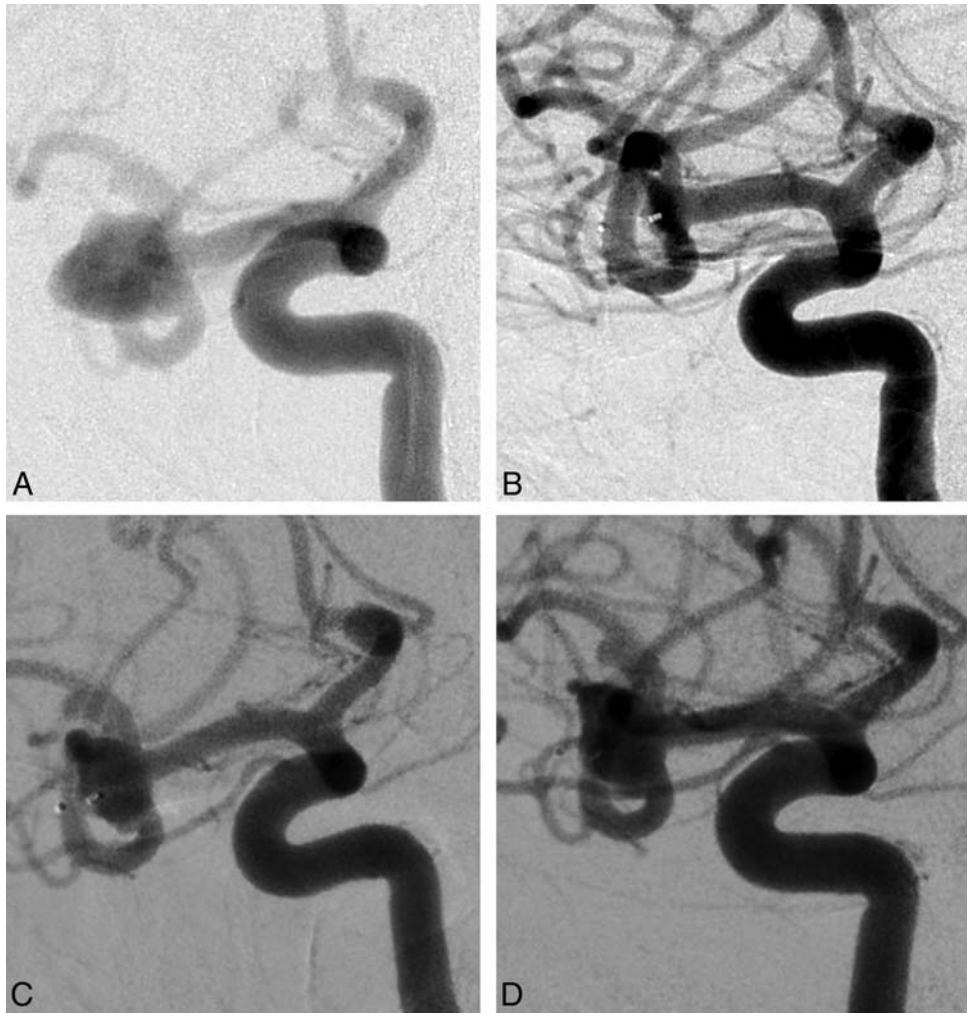

FIG 1. Case 1 (patient 5) involves a right unruptured MCA aneurysm in a 44-year-old woman. *A*, Subtracted angiography of the internal carotid artery shows a wide-neck MCA aneurysm. The inferior branch is emerging from the neck of the aneurysm. *B*, Subtracted angiography of the internal carotid artery at the end of the procedure shows a small neck remnant. *C*, Subtracted angiography of the internal carotid artery at 6 months shows a growing neck remnant by WEB compression. *D*, Subtracted angiography of the internal carotid artery at 12 months shows a worsening of the neck remnant compared with the one at 6 months.

multidisciplinary team according to the aneurysm characteristics (size, neck, and width). In the case of an endovascular approach, wide-neck aneurysms were treated with an intrasaccular device. The protocol was approved by the local ethics committee. Written informed consent was obtained from each patient or legal representative before entry into the study.

Endovascular Procedure

No preinterventional medication was administered. The procedure was performed with the patient under general anesthesia and full heparinization (bolus of 80 IU/kg). Cerebral angiograms were obtained via a femoral approach. 3D angiography was performed to determine the size of the dome and length and neck of the aneurysm.

A VIA Microcatheter (Sequent Medical) was then inserted coaxially over a 0.014-inch microguidewire to reach within the aneurysm. The VIA 27 was used for the WEB-SL with a width of $\leq$9 mm, and a VIA 33, for a width of $\geq$10 mm. After adequate positioning of the WEB device inside the aneurysmal sac, we performed a control angiogram to evaluate the position of the device and the flow stagnation inside. If the position was not satisfactory, the device was resheathed and repositioned. When the size was found to be incorrect, the device was resheathed and replaced by a different-sized WEB. At the end of the procedure, 500 mg of aspirin was administrated intravenously. Oral aspirin (75 mg) was continued for another month to prevent delayed thromboembolic events due to the contact between the blood and the device covering a wide neck.

Clinical Follow-Up

Bleeding or rebleeding occurrence during the period of follow-up was evaluated.

Outcome Evaluation

Angiograms were obtained in anteroposterior, lateral, and working projections before the treatment, immediately after, at 6 months, and at 1-year follow-up. A simplified 3-point Raymond scale (complete occlusion, neck remnant, aneurysm remnant) was used to assess the results of the procedure.[8] Adequate aneurysm occlusion was defined as total aneurysm occlusion or neck remnant.

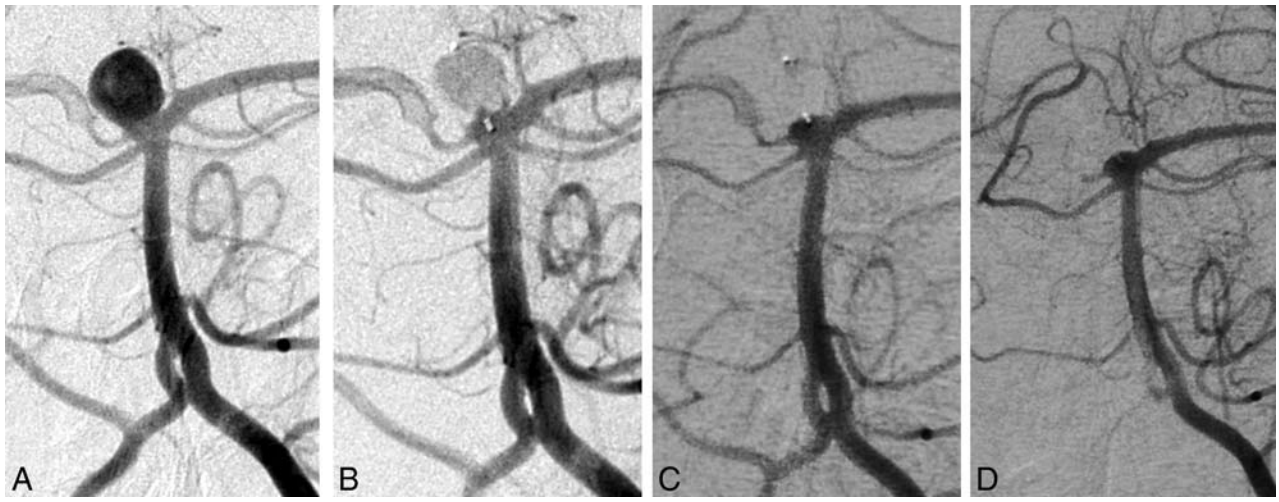

FIG 2. Case 2 (patient 6) involves a right unruptured basilar tip aneurysm in a 59-year-old man. *A*, Subtracted angiography of the left vertebral artery shows a basilar tip aneurysm. *B*, Subtracted angiography of the left vertebral artery at the end of the procedure shows complete aneurysm occlusion. Subtracted angiographies of the left vertebral artery at 6 months (*C*) and 12 months (*D*) show near-complete aneurysm occlusion with a small compression of the proximal WEB portion.

Aneurysm characteristics and angiographic outcome at 6 and 12 months

									Angiographic Outcomes	
Patient No.	Age (yr), Sex	Location	WEB Type	D (mm)	T (mm)	N (mm)	D/N (Ratio)	WEB Size (mm)	6 Months	1 Year
1	45, M	AcomA	SL	8.9	5.8	5.3	1.7	7 × 5	NR	NR
2	59, M	MCA	SL	6.2	7.5	5.1	1.2	9 × 5	AR	AR
3	56, M	AcomA	SL	7.9	6.9	2.6	3.0	7 × 5	NR	NR (w)
4	53, F	MCA	SL	5.7	4.6	4.7	1.2	6 × 4	NR	NR
5	44, F	MCA	SL	8.9	8.2	6.5	1.4	8 × 4	NR	NR (w)
6	59, M	Basilar tip	SLS	6.1	5.9	4	1.5	7 × 4	NR	NR
7	65, M	AcomA	SL	10.7	6.4	5.6	1.9	6 × 3	C	C
8	68, F	AcomA	SL	5.4	5.1	5.1	1.1	7 × 6	NR	NR

Note:—D indicates dome; T, transverse diameter; N, neck; C, complete aneurysm occlusion; NR, neck remnant; AR, aneurysm remnant; w, worsening; SLS, Single-Layer Spheric.

RESULTS

Eight patients (5 men and 3 women) with 8 wide-neck intracranial aneurysms were prospectively included during the study period. The mean age of these patients was 58 years (range, 44–70 years). Three aneurysms were located at the middle cerebral artery bifurcation; 4, at the anterior communicating artery (AcomA); and 1, at the basilar tip artery. On the working projections, the mean width of the aneurysm sac (dome) was 7.5 mm (range, 5.4–10.7 mm), the mean transversal diameter was 6.3 mm (range, 4.6–8.2 mm), and the mean diameter of the aneurysm neck was 4.9 mm (range, 2.6–6.5 mm). All procedures required only 1 WEB-SL implant with no additional devices.

Clinical Outcomes

All patients initially included were followed up. No death or bleeding was reported during the follow-up period. No patient experienced even slight worsening at 1 year. The permanent 1-year morbidity rate was 0%, and the mortality rate was 0%.

Angiographic Outcomes

Angiograms at 1-year follow-up are detailed in the Table. Angiographic follow-up at 1 year was obtained in all patients, including 1 complete aneurysm occlusion (12.5%), 6 neck remnants (75%), and 1 incomplete aneurysm occlusion (12.5%). Adequate aneurysm occlusion (total occlusion or neck remnant) was observed in 87.5%. Among the 6 neck remnants at 6- and 12-month follow-up, 3 were ≤2 mm.

In 2 cases (25%), the aneurysm remnants increased at 1-year follow-up with WEB compression. No retreatment was performed.

DISCUSSION

In this preliminary study, we assessed the 1-year angiographic results of patients managed only with the WEB-SL intrasaccular device.

Although adequate aneurysm occlusion was achieved in most cases (87.5%), the anatomic results are in some ways disappointing, owing to the high rate of neck remnant and recanalization in this small series of 8 patients. In fact, we observed a neck remnant in 75% of cases with half of them a size of superior 3 mm; however, a majority of cases were challenging aneurysms with wide necks. The average dome width was 7.5 mm, and average neck size was 4.9 mm in our series. Other authors have observed this high rate of neck remnant at short-term follow-up with the WEB-DL device. In Pierot et al,[4] adequate occlusion (total occlusion or neck remnant) was observed in 83.3% of 33 treated aneurysms. In Lubicz et al,[3] in a series of 18 treated wide-neck bifurcations aneurysms, 2 complete occlusions, 15 near-complete occlusions (89.5% adequate occlusion), and 2 incomplete occlusions were

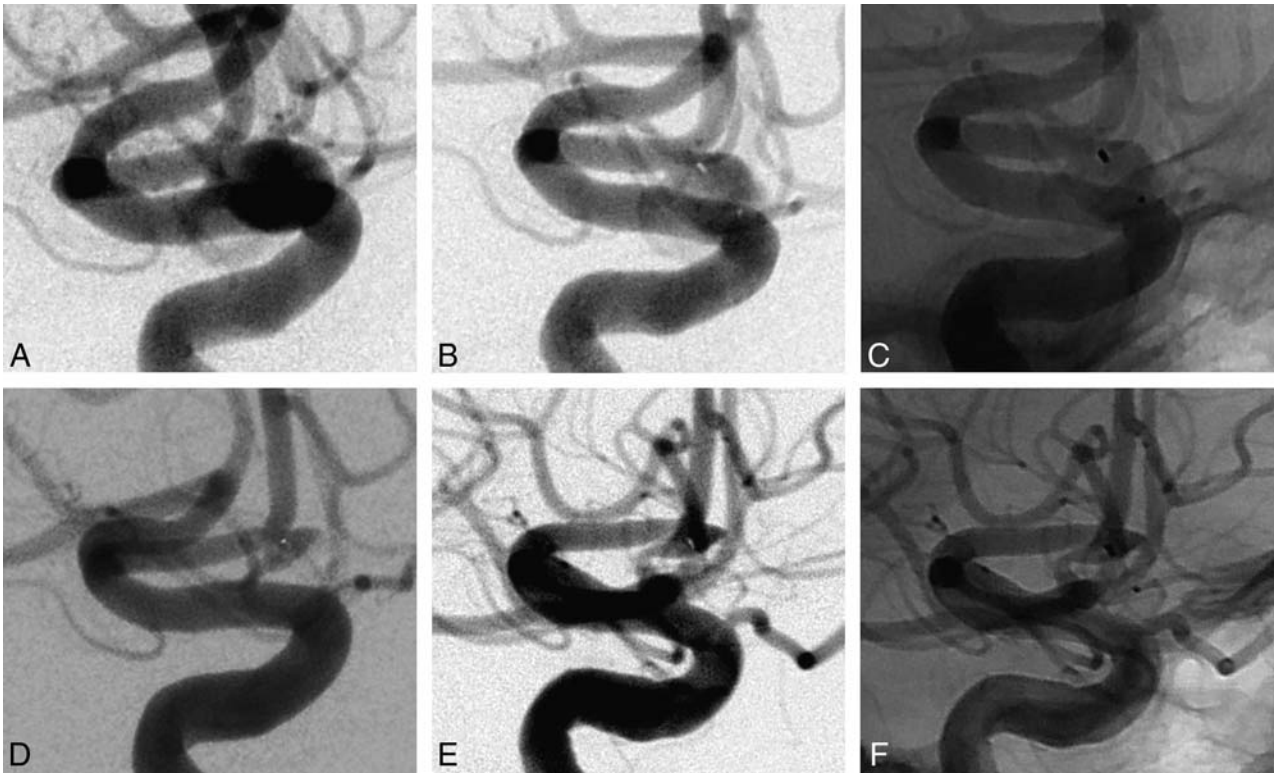

FIG 3. Case 3 (patient 1) involves an AcomA aneurysm in a 45-year-old man. *A*, Subtracted angiography of the internal carotid artery shows an AcomA aneurysm. The inferior branch is emerging from the neck of the aneurysm. *B* and *C*, Subtracted and unsubtracted angiography of the internal carotid artery at the end of the procedure shows a small neck remnant. *D*, Subtracted angiography of the internal carotid artery at 6 months shows near-complete aneurysm occlusion with a neck remnant size of <2 mm. *E* and *F*, Subtracted angiography of the internal carotid artery at 12 months shows a near-complete occlusion with a neck remnant that is stable in size. No compression of the device was observed by digital subtraction angiography.

reported at 6-month angiographic follow-up. Similar findings were also reported in a large prospective French series of 85 patients (92.3%).[2] To date, few results of the treatment with the WEB-SL device have been published, to our knowledge. Pierot et al[6] reported immediate and 1-month safety results after endovascular treatment of intracranial aneurysms by using the WEB-DL and WEB-SL/Single-Layer Spheric device. We recently reported the 6-month efficacy of a WEB-DL and WEB-SL for the treatment of 10 wide-neck anterior communicating artery aneurysms.[1] Five aneurysms were treated with the WEB-SL; we observed 2 complete aneurysm occlusions and 3 neck remnants at 3- to 6-month follow-up.

At 1-year angiographic follow-up, we reported a 75% rate of neck remnants and found the remnants to increase in size in 2 neck remnant cases. Our high rate of neck remnants seems to be at least partially explained by the compression and deformation of the WEB-SL device. This frequency of neck remnant is also probably due to the shape of the WEB. The proximal surface of the WEB is not flat but has a recess, which is concave from the direction of the parent artery. It was designed to minimize protrusion of the proximal marker in the parent vessel, but it contributes to the appearance of a neck remnant so that in the 1-year follow-up, we noticed advanced neck size, along with further compaction of the device. In some cases, the device was found at a different angle than on deployment, and in others, the neck was bulging toward the device. Cognard and Januel[9] recently reported similar findings in a series of 15 consecutive patients. Compression of the WEB cage (12 WEB-DLs and 3 WEB-SLs) was observed at first follow-up (3–6 months) in 8 of 14 (57.2%) patients and in an additional 3 of 7 patients (42.8%) at second follow-up (18 ± 3 months). The last angiography showed complete occlusion in 1 of 14 (7.2%), neck remnant in 8 of 14 (57.2%), and residual aneurysm in 5 of 14 (35.7%) patients.

In this specific situation of challenging aneurysms with a wide neck at the middle cerebral artery or anterior communicating artery locations, stent- and balloon-assisted coiling are 2 well-established techniques.[10–12] Compared with balloon-assisted coiling, stent-assisted coiling was found to yield higher rates of aneurysm obliteration and progression of occlusion at follow-up.[13] However, compared with the WEB device, the major disadvantage of using a stent is the need for dual antiplatelet therapy, which seems to be associated with a high incidence of adverse events and outcomes.[11,14,15] A novel device (pCONus aneurysm implant; phenox, Bochum, Germany) has recently been developed to improve the safety of endovascular treatment of wide-neck aneurysms. To date, few results of aneurysms treated with the pCONus have been reported in the literature.[16,17] In a series of 40 consecutive MCA aneurysms (mean dome size, 7.7 mm; mean neck size, 5.6 mm), Gory et al[17] reported stable or improved results in all cases except 3 patients with a mean follow-up of 6.8 months, including 48.5% complete occlusions (16/33), 30.3% neck remnants (10/33), and 21.2% aneurysm remnants (7/33).

CONCLUSIONS

Endovascular therapy of intracranial aneurysms with the WEB-SL device allows the treatment of wide-neck aneurysms with a high rate of neck remnant at 1 year, at least partially explained by WEB compression. Initial size selection and technologic improvements could be an option to optimize the aneurysm occlusion in WEB-SL treatment.

Disclosures: Francis Turjman—*UNRELATED*: *Consultancy*: Covidien,* Codman,* Stryker*; *Grants/Grants Pending*: Covidien*; *Payment for Development of Educational Presentations*: Codman,* Stryker*; *Travel/Accommodations/Meeting Expenses Unrelated to Activities Listed*: Covidien,* Stryker.* *Money paid to the institution.

REFERENCES

1. Gherasim DN, Gory B, Sivan-Hoffmann R, et al. **Endovascular treatment of wide-neck anterior communicating artery aneurysms using WEB-DL and WEB-SL: short-term results in a multicenter study.** *AJNR Am J Neuroradiol* 2015;36:1150–54 CrossRef Medline
2. Papagiannaki C, Spelle L, Januel AC, et al. **WEB intrasaccular flow disruptor-prospective, multicenter experience in 83 patients with 85 aneurysms.** *AJNR Am J Neuroradiol* 2014;35:2106–11 CrossRef Medline
3. Lubicz B, Mine B, Collignon L, et al. **WEB device for endovascular treatment of wide-neck bifurcation aneurysms.** *AJNR Am J Neuroradiol* 2013;34:1209–14 CrossRef Medline
4. Pierot L, Klisch J, Cognard C, et al. **Endovascular WEB flow disruption in middle cerebral artery aneurysms: preliminary feasibility, clinical, and anatomical results in a multicenter study.** *Neurosurgery* 2013;73:27–34; discussion 34–45 CrossRef Medline
5. Pierot L, Liebig T, Sychra V, et al. **Intrasaccular flow-disruption treatment of intracranial aneurysms: preliminary results of a multicenter clinical study.** *AJNR Am J Neuroradiol* 2012;33:1232–38 CrossRef Medline
6. Pierot L, Moret J, Turjman F, et al. **WEB treatment of intracranial aneurysms: feasibility, complications, and 1-month safety results with the WEB DL and WEB SL/SLS in the French Observatory.** *AJNR Am J Neuroradiol* 2015;36:922–27 CrossRef Medline
7. Bozzetto Ambrosi P, Gory B, Sivan-Hoffmann R, et al. **Endovascular treatment of bifurcation intracranial aneurysms with the WEB SL/SLS: 6-month clinical and angiographic results.** *Interv Neuroradiol* 2015;21:462–69. CrossRef Medline
8. Raymond J, Guilbert F, Weill A, et al. **Long-term angiographic recurrences after selective endovascular treatment of aneurysms with detachable coils.** *Stroke* 2003;34:1398–403 CrossRef Medline
9. Cognard C, Januel AC. **Remnants and recurrences after the use of the WEB intrasaccular device in large-neck bifurcation aneurysms.** *Neurosurgery* 2015;76:522–30; discussion 530 CrossRef Medline
10. Gory B, Kessler I, Seizem Nekiri G, et al. **Initial experience of intracranial aneurysm embolization using the balloon remodeling technique with Scepter C, a new double-lumen balloon.** *Interv Neuroradiol* 2012;18:284–87 CrossRef Medline
11. Gory B, Rouchaud A, Saleme S, et al. **Endovascular treatment of middle cerebral artery aneurysms for 120 nonselected patients: a prospective cohort study.** *AJNR Am J Neuroradiol* 2014;35:715–20 CrossRef Medline
12. Gory B, Klisch J, Bonafé A, et al. **Solitaire AB stent-assisted coiling of wide-necked intracranial aneurysms: mid-term results from the SOLARE Study.** *Neurosurgery* 2014;75:215–19; discussion 219 CrossRef Medline
13. Chalouhi N, Starke RM, Koltz MT, et al. **Stent-assisted coiling versus balloon remodeling of wide-neck aneurysms: comparison of angiographic outcomes.** *AJNR Am J Neuroradiol* 2013;34:1987–92 CrossRef Medline
14. Piotin M, Blanc R, Spelle L, et al. **Stent-assisted coiling of intracranial aneurysms: clinical and angiographic results in 216 consecutive aneurysms.** *Stroke* 2010;41:110–15 CrossRef Medline
15. Bartolini B, Blanc R, Pistocchi S, et al. **"Y" and "X" stent-assisted coiling of complex and wide-neck intracranial bifurcation aneurysms.** *AJNR Am J Neuroradiol* 2014;35:2153–58 CrossRef Medline
16. Aguilar-Pérez M, Kurre W, Fischer S, et al. **Coil occlusion of wide-neck bifurcation aneurysms assisted by a novel intra- to extra-aneurysmatic neck-bridging device (pCONus): initial experience.** *AJNR Am J Neuroradiol* 2014;35:965–71 CrossRef Medline
17. Gory B, Aguilar-Pérez M, Pomero E, et al. **pCONus device for the treatment of wide-neck middle cerebral artery aneurysms.** *AJNR Am J Neuroradiol* 2015 Jul 23. [Epub ahead of print] CrossRef Medline

Flow Diversion versus Standard Endovascular Techniques for the Treatment of Unruptured Carotid-Ophthalmic Aneurysms

F. Di Maria, S. Pistocchi, F. Clarençon, B. Bartolini, R. Blanc, A. Biondi, H. Redjem, J. Chiras, N. Sourour, and M. Piotin

ABSTRACT

BACKGROUND AND PURPOSE: Over the past few years, flow diversion has been increasingly adopted for the treatment of intracranial aneurysms, especially in the paraclinoid and paraophthalmic carotid segment. We compared clinical and angiographic outcomes and complication rates in 2 groups of patients with unruptured carotid-ophthalmic aneurysms treated for 7 years by either standard coil-based techniques or flow diversion.

MATERIALS AND METHODS: From February 2006 to December 2013, 162 unruptured carotid-ophthalmic aneurysms were treated endovascularly in 138 patients. Sixty-seven aneurysms were treated by coil-based techniques in 61 patients. Flow diverters were deployed in 95 unruptured aneurysms (77 patients), with additional coiling in 27 patients. Complication rates, clinical outcome, and immediate and long-term angiographic results were retrospectively analyzed.

RESULTS: No procedure-related deaths occurred. Four procedure-related thromboembolic events (6.6%) leading to permanent morbidity in 1 case (1.6%) occurred in the coiling group. Neurologic complications were observed in 6 patients (7.8%) in the flow-diversion group, resulting in 3.9% permanent morbidity. No statistically significant difference was found between complication ($P = .9$) and morbidity rates ($P = .6$). In the coiling group (median follow-up, 31.5 ± 24.5 months), recanalization occurred at 1 year in 23/50 (54%) aneurysms and 27/55 aneurysms (50.9%) at the latest follow-up, leading to retreatment in 6 patients (9%). In the flow-diversion group (mean follow-up, 13.5 ± 10.8 months), 85.3% (35/41) of all aneurysms were occluded after 12 months, and 74.6% (50/67) on latest follow-up. The retreatment rate was 2.1%. Occlusion rates between the 2 groups differed significantly at 12 months ($P < .001$) and at the latest follow-up ($P < .005$).

CONCLUSIONS: Our retrospective analysis shows better long-term occlusion of carotid-ophthalmic aneurysms after use of flow diverters compared with standard coil-based techniques, without significant differences in permanent morbidity.

ABBREVIATION: PED = Pipeline Embolization Device

Carotid-ophthalmic aneurysms are defined as aneurysmal dilation of the supraclinoid internal carotid artery whose neck is attached to the origin of the ophthalmic artery. These intracranial aneurysms are challenging to treat because they are often prone to recanalization after endovascular treatment by conventional coil embolization.[1]

In recent years, flow-diverter stents have become an important tool in the management of intracranial aneurysms; they are now helpful in the endovascular treatment of intracranial aneurysms previously considered untreatable. These new devices are currently mainly indicated for the treatment of complex aneurysms such as large and giant ICA aneurysms and fusiform, dissecting, or blood blister-like aneurysms.[2-5]

Carotid-ophthalmic aneurysms represent an important subset of ICA aneurysms for which flow diversion may be a promising option in the quest for a safe and more effective treatment aiming for stable aneurysmal exclusion.

In this study, we sought to compare clinical and angiographic outcomes between the 2 groups of patients with carotid-ophthalmic aneurysms treated by either standard coil-based techniques (ie, regular coiling, balloon-assisted coiling, or stent-assisted coiling) or with flow diversion, during a 7-year period.

MATERIALS AND METHODS

Ethical Statement

Neither approval of the institutional review board nor patient informed consent is required by the ethics committee of our

Received January 27, 2015; accepted after revision April 17.

From the Department of Neuroradiology (F.D.M., F.C., H.R., J.C., N.S.), Groupe Hospitalier Pitié-Salpêtrière, Paris, France; Department of Neuroradiology (S.P., B.B., R.B., H.R., M.P.), Fondation Ophtalmologique Adolphe de Rothschild, Paris, France; and Department of Neuroradiology (A.B.), Centre Hospitalier J. Minjoz, Besançon, France.

Please address correspondence to Federico Di Maria, MD, Department of Neuroradiology, Groupe Hospitalier Pitié-Salpêtrière, 47-83 Boulevard de l'Hôpital, 75651 Paris, France; e-mail: federico.dimaria@gmail.com

http://dx.doi.org/10.3174/ajnr.A4437

institutions for retrospective analyses of patient records and imaging data.

Patient Population and Treatment

From prospectively maintained data bases of 2 institutions (Pitié-Salpêtrière Hospital and Fondation Ophtalmologique Adolphe de Rothschild), we identified 138 consecutive patients with 161 unruptured, previously untreated, carotid-ophthalmic aneurysms treated by endovascular means between April 2006 and December 2013. Therapeutic alternatives were discussed between neurosurgical and neurointerventional teams in a multidisciplinary decision-making process; patient selection for treatment with standard techniques versus flow diversion was left to the operator's discretion. Eight operators with at least 5 years' experience were involved in the endovascular treatments.

Sixty-seven aneurysms were treated by coil-based techniques in 61 patients. Within this group, 7 patients presented with a history of subarachnoid hemorrhage due to rupture of another intracranial aneurysm. Another 5 patients were treated in the setting of a subarachnoid hemorrhage due to the rupture of a second aneurysm that was treated in the same session. A balloon-remodeling technique was adopted in 32 procedures, elective stent-assisted technique in 23, and both techniques in 12. The Neuroform EZ stent (Stryker Neurovascular, Fremont, California) and the Enterprise self-expanding stent (Codman & Shurtleff, Raynham, Massachusetts) were used in 16 and 7 patients, respectively. The Solitaire AB stent (Covidien, Irvine, California) and the LVIS stent (MicroVention, Tustin, California) were used in 3 and 2 aneurysms respectively. Stent-assisted coiling was performed by using the microcatheter jailing technique in 9 patients.

Ninety-five aneurysms were treated by flow diversion in 77 subjects. Patients undergoing either flow-diversion treatment or stent placement received 75 mg/day of clopidogrel and 160 mg/day of aspirin for 5 days before the intervention. In the first institution (Fondation Ophtalmologique Adolphe de Rothschild), platelet function tests were routinely performed by using the VerifyNow P2Y12 assay (Accumetrics, San Diego, California) with a target of platelet inhibition between 30% and 90%. Patients with inhibition of <30% were reloaded with a double dose of clopidogrel, and the assay was rechecked. In the second institution (Pitié Salpêtrière Hospital), platelet aggregation was tested by aspirin assay and the P2Y12 assay (Multiplate 5.0 analyzer; Roche, Basel, Switzerland). In case of a poor response, patients were switched to ticagrelor. An initial 50 IU/kg heparin bolus was administered, and activated clotting time was maintained between 2- and 3-fold of the baseline intraoperatively. Heparin was discontinued but not reversed at the end of the procedure. Patients were subsequently left on dual antiplatelet therapy for 3 months, then on aspirin-only for 9 months. Procedures were performed with the patient under general anesthesia.

The Pipeline Embolization Device (PED; Covidien) was deployed through a Marksman microcatheter (Covidien) by using a triaxial guide-catheter system. The Silk flow diverter (Balt Extrusion, Montmorency, France), the Surpass stent (Stryker), and the FRED flow diverter (MicroVention) were used in a minority of cases at the operator's discretion. The number of stents deployed was left to the operator's discretion, but in general, only a single device was used for most aneurysms. The correct apposition of the flow diverter was documented under fluoroscopy and with additional flat panel CT angiography at the operator's discretion. Any stent misopening was remedied with either the Gateway PTA balloon catheter (Stryker) or the HyperGlide balloon (Covidien) angioplasty when needed. When bilateral aneurysms were treated, the contralateral aneurysm was treated usually 3 months after the first one.

Table 1: Baseline characteristics for the 2 study groups

	Coil-Based Technique (n = 61)	FD (n = 77)	P Value
Mean age (yr)	49.2 ± 13.9	49.7 ± 11.8	.79
Male patients	10 (16.4%)	17 (22.1%)	.52
Female patients	51 (83.6%)	60 (77.9%)	
An. size (mm) (mean)	6.7 ± 3.6	8.7 ± 6.3	.03
D/N ratio	1.8 ± 0.63	1.9 ± 1.05	.46

Note:—An. indicates aneurysm; FD, flow diverter; D/N, dome/neck.

Medical charts were reviewed to determine patient demographics, aneurysm characteristics, procedural techniques, and complications. The outcomes of 77 patients treated by flow diversion and 61 patients treated by coiling techniques were compared. Clinical follow-up was performed by the referring interventionalist through physical examination in most cases. Patients unable or unwilling to reach the treatment center for logistic reasons were assessed by telephone interview by the referring interventionalist. An independent neurologist was consulted in case of clinical signs of procedural complications. Angiographic follow-up by either digital subtraction angiography or MR angiography was scheduled at 3–6 months. A further control DSA was performed at 6 months to 1 year. In case of complete aneurysm thrombosis, follow-up was then continued by MRA scans on a yearly basis. Deployment of additional flow diverters was considered at follow-up if the aneurysm remained unchanged or did not thrombose completely.

For statistical analysis, angiographic outcome was dichotomized into complete (100%) and incomplete obliteration (<100%). Regardless of the need for further intervention, any filling at the neck or the dome of the aneurysm was considered incomplete obliteration. Clinical outcomes at the last available follow-up were classified according to the modified Rankin Scale.

Statistical Analysis

The Student t test was used to compare continuous variables, whereas the χ^2 test or the Fisher exact test was used for categoric variables. Univariate conditional analysis was used to test covariates predictive of treatment complications, follow-up obliteration, and clinical outcome (mRS, 0–2 versus 3–6). Factors predictive in univariate analysis ($P < .20$) were entered into a multivariate conditional logistic regression. P values ≤ .05 were statistically significant. Calculations were made by using MedCalc for Windows software, Version .7.4 (MedCalc Software, Mariakerke, Belgium).

RESULTS

Demographics and Aneurysm Characteristics

Main baseline characteristics are summarized in Table 1.

The percentage of aneurysms of >6 mm was similar in patients with flow diverters (60%) and those with coils (46.2%, $P = .4$). Bilateral aneurysms were treated in 4 patients in the coiling group and in 12 patients in the flow-diversion group.

Postprocedure Angiographic Results

In the coiling group ($n = 67$), initial self-adjudicated Roy Raymond scores were 1 (complete occlusion) in 39 (58.2%) cases, 2 (residual neck) in 14 (20.9%), and 3 (residual sac) in 14 (20.9%).

In the flow-diversion group ($n = 95$), a single device was deployed in 82 (86.3%) aneurysms. The PED was used in most of the procedures ($n = 55$, 57.9%). Two or more devices were used in 13 (13.7%) patients. Adjunctive coils were deployed within the aneurysmal sac in 27 patients, in a loose fashion, notably in large and giant aneurysms. Device deployment was successful in 94/95 (99%) aneurysms. In 1 patient, the deployment of the stent was too proximal and the distal end fell into the aneurysmal sac. The delivery of a second stent was attempted unsuccessfully; therefore, a carotid occlusion test and parent vessel occlusion were performed. Balloon angioplasty was performed successfully for better flow-diverter expansion in 3 patients. In another 3 patients, a second laser-cut stent (Enterprise; Codman & Shurtleff) was deployed inside the flow diverter (Silk; Balt Extrusion) to ensure better wall apposition.

The initial occlusion rate after the procedure was 6.4% (6/94; 1 patient was excluded because he or she was treated by parent vessel occlusion).

Procedural Complications

Neither procedure-related deaths nor aneurysmal bleeding was reported during the procedure or follow-up in either group.

In the coiling group, 4 procedure-related thromboembolic events (6.6%) occurred, causing neurologic symptoms in 3 patients (NIHSS scores of 3, 5, and 4, respectively) and leading to permanent morbidity in 1 case of monocular blindness due to occlusion of the central artery of the retina (1.6%).

All procedures in the 28 patients treated by stent-assisted coiling were uneventful.

In the flow-diversion group, 2 delayed homolateral intraparenchymal hemorrhages (2.6%) were reported at days 10 and 15, respectively; 2 optic nerve compressions and 2 thromboembolic events, with NIHSS scores of 4 and 5 respectively, were observed (7.8% complication rate) and resulted in 3.9% permanent morbidity, consisting of 1 case of monocular blindness, 1 case of secondary epilepsy, and 1 visual field reduction due to hypoperfusion of the ophthalmic artery after parent vessel occlusion. In the latter case, the choice of parent vessel occlusion was motivated by a technical complication (ie, device foreshortening due to downsizing and/or stretching, which subsequently caused the distal end to fall into the aneurysmal sac, with failure to retrieve the device or to deploy a second one). No statistically significant difference was found between complication ($P = .9$) and morbidity ($P = .63$) rates.

The following factors were tested as predictors of complications: age, sex, aneurysm size, dome/neck ratio, and type of treatment. In univariate analysis, only aneurysm size (OR, 1.78; 95% CI, 0.14–3.23; $P < .01$) predicted procedural complications in the flow-diversion group. This finding was confirmed in multivariate analysis (OR, 1.43; 95% CI, 0.41–4.96; $P < .001$). The type of treatment was not a predictor of complications after adjusting for age.

Table 2: Comparison of rates of aneurysmal occlusion according to follow-up intervals for coil-based techniques and flow-diversion groups

	≤6 Months	7–12 Months	>12 Months	Latest Follow-Up
Coiling group	17/26 (65.4%)	16/28 (57.1%)	23/50 (46%)	27/55 (49,1%)
Flow diverter	21/39 (53.8%)	16/22 (72.2%)	35/41 (85.3%)	50/67 (74.6%)
P value	.44	.37	.00015[a]	.0047[a]

[a] Significant.

Table 3: Comparison of rates of aneurysmal occlusion according to follow-up intervals for the stent-assisted coiling subgroup and flow-diversion group

	≤6 Months	7–12 Months	>12 Months	Latest Follow-Up
Stent-coil	9/11 (81.8%)	11/17 (64.7%)	14/24 (58.3%)	16/24 (66.7%)
Flow diverter	21/39 (53.8%)	16/22 (72.2%)	35/41 (85.3%)	50/67 (74.6%)
P value	.16	.73	.019[a]	.59

[a] Significant.

Angiographic Outcome

Angiographic follow-up was available for 66/95 (69.4%) aneurysms treated by flow diverters and 55/67 (82.1%) patients treated with coil-based techniques. Median angiographic follow-up time was 13.5 months in the PED group and 31.5 months in the coiling group ($P < .001$). At the latest follow-up, a higher proportion of aneurysms treated by flow diverters (85.3%; $n = 35/41$) showed complete obliteration (100%) compared with 46% ($n = 23/50$) in the coiling group ($P = .0047$, Table 2). A comparison between patients with flow diverters and those with stent-coils showed a significant difference in favor of flow diversion after only 12 months from treatment (Table 3). In the flow-diversion group, no aneurysmal recanalization was observed after thrombosis had occurred. In the coiling group ($n = 67$), self-adjudicated Roy Raymond scores at the latest follow-up were 1 (complete occlusion) in 27 (49%) patients, 2 (residual neck) in 13 (23.6%) patients, and 3 (dome filling) in 15 (27.3%).

We tested the following factors as predictors of angiographic outcome: age, sex, aneurysm size, dome/neck ratio, and type of treatment. In univariable analysis, dome/neck ratio (OR, 1.54; 95% CI, 0.76–2.87; $P < .033$) and type of treatment (OR, 2.67; 95% CI, 0.56–1.83; $P < .02$) were predictive of angiographic exclusion. In multivariable analysis, flow-diversion treatment was found to be a predictor of complete angiographic exclusion (OR, 4.3; 95% CI, 1.98–9.35; $P < .005$).

Retreatment

Retreatment was necessary for 2/95 (2.1%) aneurysms that showed only partial thrombosis in the flow-diversion group, the procedure consisting of the positioning of a second device within the previous one. One patient was retreated a second time 1 year after retreatment due to a persisting residual sac. In the coiling group, retreatment was performed in 6/68 aneurysms (9%, $P =$

.068). Two patients were retreated once by laser-cut stents and coils. Two patients were retreated twice: the first time by simple coiling, then by stent-assisted coiling; the second time by stent-coils and then by flow diversion.

Clinical Outcome

Clinical follow-up was available for 75 (97.5%) patients in the PED group and 59 (96.7%) patients in the stent-coil group. The median follow-up time was 18.5 months in the PED group and 37.4 months in the stent-coil group ($P < .001$). The proportion of patients with mRS 0–2 was 97.3% (73/75) in the PED group and 96.6% in the coiling group (57/59, $P = 1$). The proportion of patients with mRS 0–1 was 96% (72/75) in the flow-diversion group and 95% in the stent-coil group (56/59, $P = 1$). The 5 patients who had presented with a contemporary history of subarachnoid hemorrhage in the coiling group all had a favorable outcome (mRS 1) at latest follow-up.

None of the following factors proved as predictors of clinical outcome after testing: age, sex, aneurysm size, type of treatment, and complications.

DISCUSSION

The adoption of flow diverters has begun a new concept in the endovascular treatment of intracranial aneurysms. Since their introduction into clinical practice, however, a debate has ensued concerning both the long-term stability of treatment and complication rates. Many interventionalists still prefer traditional endovascular approaches.

The complications of coiling and stent-assisted coiling are essentially limited to thromboembolic events and intraprocedural aneurysmal rupture.[3,6] Even in flow diversion, cases of thromboembolism due to in-stent thrombosis or delayed migration of the device, distal parenchymal hemorrhage, or aneurysm rupture due to degradation of the aneurysmal wall or endoleak have been reported.[4,7-12]A meta-analysis by Brinjikji et al,[13] including 1451 patients with 1654 aneurysms, found procedure-related morbidity and mortality rates for flow diversion of 5% and 4%, respectively. The authors concluded that the procedure-related risk with flow diverters is not negligible and should be taken into account when considering the best therapeutic option. Conversely, several studies have presented convincing evidence that the PED carries a high safety and efficacy profile. A first multicenter international trial reported a success rate of 99%, an occlusion rate of 74%, and a major ipsilateral stroke or neurologic death rate of only 5.6%.[2] A more recent retrospective international study on 906 aneurysms showed a morbimortality rate of 4.8% in the anterior circulation.[14] Burrows et al[15] reported a mortality and permanent morbidity rate of 1%, with an occlusion rate of 69% at 1 year. These studies, however, analyzed a heterogeneous population and did not compare directly the results of flow diversion with those of conventional endovascular techniques, especially stent-assisted coiling, for which excellent safety and efficacy in several studies have been proved.[3,6,16,17]

In our study, the technical success rate was high (99%) and consistent with that in the published literature. Most interesting, there was no significant difference in terms of complication rates between flow diversion and conventional endovascular techniques. We did not report any procedure-related deaths, and the permanent morbidity rate in the flow-diversion group was 3.9% (ie, nonsignificantly higher than that in the coiling group) despite an evident numeric trend toward a higher morbidity rate in the flow-diversion group. Thus, a possible lack of statistical power cannot be excluded. However, our results are still in line with the results from the other studies,[4,5,18] including smaller series on carotid-ophthalmic aneurysms that reported an occlusion rate at latest follow-up between 73% and 92.1%, an overall permanent morbidity between 0% and 2.3%, and a mortality between 0% and 4.4%.[19-21]

Moreover, our results are similar to those reported in a recent study comparing flow diversion and stent-coiling for aneurysms of <10 mm by Chalouhi et al,[22] who reported complication rates of 5% and 3%, respectively. Procedure-related mortality was 0% in both groups. Concerning aneurysm occlusion on long-term follow-up, the authors did not find any statistical difference between the 2 groups, though a trend in favor of flow diversion (80% versus 70%) was reported. The authors concluded that the study was likely underpowered to detect small differences between the 2 techniques, both leading to high occlusion rates. In a previous report, the authors had compared the procedural, angiographic, and clinical outcomes of flow diversion and coiling in unruptured, large (>10), and giant (>25 mm) aneurysms,[3] thereby finding a similar complication rate (7.5%) along with a higher aneurysm occlusion rate (86% versus 41%) and a lower retreatment rate with flow diversion (2.8% versus 37%). These results led to the conclusion that flow diverters were a preferred option for large and giant aneurysms because they resulted in similar clinical outcomes compared with stent-assisted coiling.

In the present study, we observed a stable progression with time toward complete aneurysm occlusion in the flow-diversion group, as opposed to a gradual increase in the number of recanalized aneurysms in the coiling group. The difference between the long-term aneurysm occlusion rates was strong and statistically significant. In a multivariate analysis, treatment by flow diversion was an independent predictor of long-term aneurysmal occlusion. Nonetheless, retreatment rates did not differ significantly between the 2 groups, despite a lower rate for patients with flow diverters.

Lanzino et al[23] compared 22 paraclinoid aneurysms treated by flow diversion with conventional coiling. The authors reported a significantly higher rate of complete occlusion in patients with flow diverters (76%) than in those with coils (21%), with a similar rate of morbidity, and concluded that long-term follow-up was important to validate flow diversion as a superior therapeutic strategy for proximal internal carotid artery aneurysms.

The present study is thus not the first to compare flow diverters with coiling, but to our knowledge, it is the first to specifically compare these 2 techniques in a homogeneous subset of carotid-ophthalmic aneurysms divided into 2 well-matched groups in terms of demographics and aneurysm features.

Randomized controlled trials comparing flow diversion and conventional endovascular techniques are currently underway[24-26] and may provide high-level evidence on the safety and efficacy of flow diversion.

Limitations

This study is retrospective and reflects the experience of only 2 centers. Patients were not randomized to either one technique or the other. In the flow-diversion group, imaging follow-up was available in <70% of patients only, because several patients were foreigners and returned to their home country after treatment. As in the study by Chalouhi et al,[22] we could not provide occlusion rates at standard time points, which would have allowed a better comprehension of the history of aneurysm thrombosis. Instead, we compared aneurysm occlusion rates at the latest follow-up. Moreover, we were bound to include different techniques (simple coiling, balloon remodeling, stent placement), all within the same coiling group, to reach an acceptable statistical power. For the same reason, we did not distinguish between those aneurysms treated by flow diverter only and those treated by flow diverter + coils. This omission, in our opinion, does not impair the significance of our findings in terms of treatment results at follow-up. All estimates of aneurysm occlusion and complications were adjudicated by the team of interventionalists, and these do often differ from estimates of blinded core laboratories.

A separate comparison between patients with flow diverters and the subset treated by stent-assisted coiling led to less conclusive results, showing a slightly statistically significant difference in favor of flow diversion-only after 12 months of follow-up. As in the study by Chalouhi et al,[22] this analysis may have a lack of statistical power, given the small sample of patients with stent-coils ($n = 28$).

Despite the good match between the 2 groups in terms of demographics, aneurysm location, and size, the clinical and angiographic follow-up time differed significantly. We hypothesize, therefore, that the occlusion rate with flow diverters may have been even higher if patients had been followed up for longer periods; this potential outcome adds further support to the efficacy of flow diverters.[5,27]

Even if one considers these limitations, this study provides a comparative analysis of clinical and angiographic outcomes in a homogeneous cohort of carotid-ophthalmic aneurysms treated with either flow diversion or coiling.

CONCLUSIONS

In our retrospective study, flow diversion for elective treatment of carotid-ophthalmic aneurysms was feasible and effective, with complication and morbidity rates comparable with those of standard endovascular approaches. At long-term follow-up, flow diversion achieved a more stable sac thrombosis compared with other techniques. Further larger prospective studies may help confirm these findings and better assess complication rates of aneurysms treatment with flow diverters.

Disclosures: Silvia Pistocchi—*UNRELATED*: *Payment for Development of Educational Presentations*: Covidien and Stryker,* MicroVention and Balt.* Bruno Bartolini—*UNRELATED*: Covidien,* Stryker,* Balt,* MicroVention. Raphaël Blanc—*UNRELATED*: *Consultancy*: Balt,* Covidien,* MicroVention,* Stryker,* Penumbra.* Nader Sourour—*UNRELATED*: *Consultancy*: Covidien (consultant, proctor); *Payment for Development of Educational Presentations*: Covidien (workshops). Michael Piotin—*UNRELATED*: *Consultancy*: Covidien,* Stryker,* Balt,* MicroVention*; *Payment for Development of Educational Presentations*: Covidien; *Stock/Stock Options*: Lazarus. *Money paid to the institution.

REFERENCES

1. D'Urso PI, Karadeli HH, Kallmes DF, et al. **Coiling for paraclinoid aneurysms: time to make way for flow diverters?** *AJNR Am J Neuroradiol* 2012;33:1470–74 CrossRef Medline
2. Becske T, Kallmes DF, Saatci I, et al. **Pipeline for uncoilable or failed aneurysms: results from a multicenter clinical trial.** *Radiology* 2013; 267:858–68 CrossRef Medline
3. Chalouhi N, Jabbour P, Singhal S, et al. **Stent-assisted coiling of intracranial aneurysms: predictors of complications, recanalization, and outcome in 508 cases.** *Stroke* 2013;44:1348–53 CrossRef Medline
4. Kan P, Siddiqui AH, Veznedaroglu E, et al. **Early postmarket results after treatment of intracranial aneurysms with the Pipeline embolization device: a U.S. multicenter experience.** *Neurosurgery* 2012; 71:1080–87; discussion 1087–88 CrossRef Medline
5. Yu SC, Kwok CK, Cheng PW, et al. **Intracranial aneurysms: mid-term outcome of Pipeline embolization device–a prospective study in 143 patients with 178 aneurysms.** *Radiology* 2012;265:893–901 CrossRef Medline
6. Chalouhi N, Starke RM, Koltz MT, et al. **Stent-assisted coiling versus balloon remodeling of wide-neck aneurysms: comparison of angiographic outcomes.** *AJNR Am J Neuroradiol* 2013;34:1987–92 CrossRef Medline
7. Chalouhi N, Tjoumakaris SI, Gonzalez LF, et al. **Spontaneous delayed migration/shortening of the Pipeline embolization device: report of 5 cases.** *AJNR Am J Neuroradiol* 2013;34:2326–30 CrossRef Medline
8. Jabbour P, Chalouhi N, Tjoumakaris S, et al. **The Pipeline embolization device: learning curve and predictors of complications and aneurysm obliteration.** *Neurosurgery* 2013;73:113–20; discussion 120 CrossRef Medline
9. Chalouhi N, Satti SR, Tjoumakaris S, et al. **Delayed migration of a Pipeline embolization device.** *Neurosurgery* 2013;72:ons229–234; discussion ons234 CrossRef Medline
10. Chitale R, Gonzalez LF, Randazzo C, et al. **Single center experience with Pipeline stent: feasibility, technique, and complications.** *Neurosurgery* 2012;71:679–91; discussion 691 CrossRef Medline
11. O'Kelly CJ, Spears J, Chow M, et al. **Canadian experience with the Pipeline embolization device for repair of unruptured intracranial aneurysms.** *AJNR Am J Neuroradiol* 2013;34:381–87 CrossRef Medline
12. Hu YC, Deshmukh VR, Albuquerque FC, et al. **Histopathological assessment of fatal ipsilateral intraparenchymal hemorrhages after the treatment of supraclinoid aneurysms with the Pipeline embolization device.** *J Neurosurg* 2014;120:365–74 CrossRef Medline
13. Brinjikji W, Murad MH, Lanzino G, et al. **Endovascular treatment of intracranial aneurysms with flow diverters: a meta-analysis.** *Stroke* 2013;44:442–47 CrossRef Medline
14. Kallmes DF, Hanel R, Lopes D, et al. **International retrospective study of the Pipeline embolization device: a multicenter aneurysm treatment study.** *AJNR Am J Neuroradiol* 2015;36:108–15 CrossRef Medline
15. Burrows AM, Cloft H, Kallmes DF, et al. **Periprocedural and mid-term technical and clinical events after flow diversion for intracranial aneurysms.** *J Neurointerv Surg* 2014 Jul 31. [Epub ahead of print] CrossRef
16. Jahshan S, Abla AA, Natarajan SK, et al. **Results of stent-assisted vs non-stent-assisted endovascular therapies in 489 cerebral aneurysms: single-center experience.** *Neurosurgery* 2013;72:232–39 CrossRef Medline
17. Geyik S, Yavuz K, Yurttutan N, et al. **Stent-assisted coiling in endovascular treatment of 500 consecutive cerebral aneurysms with long-term follow-up.** *AJNR Am J Neuroradiol* 2013;34:2157–62 CrossRef Medline
18. Saatci I, Yavuz K, Ozer C, et al. **Treatment of intracranial aneurysms using the Pipeline flow-diverter embolization device: a single-center experience with long-term follow-up results.** *AJNR Am J Neuroradiol* 2012;33:1436–46 CrossRef Medline
19. Zanaty M, Chalouhi N, Barros G, et al. **Flow-diversion for ophthalmic segment aneurysms.** *Neurosurgery* 2015;76:286–89; discussion 289–90 CrossRef Medline
20. Grossberg J, Tong F, Cawley C, et al. **E-039 safety and efficacy of flow**

diverter treatment for carotid-ophthalmic aneurysms. *J Neurointerv Surg* 2914;6(suppl 1):A55–56 CrossRef Medline
21. Moon K, Albuquerque FC, Ducruet AF, et al. **Treatment of ophthalmic segment carotid aneurysms using the Pipeline embolization device: clinical and angiographic follow-up.** *Neurol Res* 2014;36:344–50 CrossRef Medline
22. Chalouhi N, Starke RM, Yang S, et al. **Extending the indications of flow diversion to small, unruptured, saccular aneurysms of the anterior circulation.** *Stroke* 2014;45:54–58 CrossRef Medline
23. Lanzino G, Crobeddu E, Cloft HJ, et al. **Efficacy and safety of flow diversion for paraclinoid aneurysms: a matched-pair analysis compared with standard endovascular approaches.** *AJNR Am J Neuroradiol* 2012;33:2158–61 CrossRef Medline
24. Turk AS 3rd, Martin RH, Fiorella D, et al. **Flow diversion versus traditional endovascular coiling therapy: design of the prospective LARGE aneurysm randomized trial.** *AJNR Am J Neuroradiol* 2014;35:1341–45 CrossRef Medline
25. Raymond J, Darsaut TE, Guilbert F, et al. **Flow diversion in aneurysms trial: the design of the FIAT study.** *Interv Neuroradiol* 2011;17:147–53 Medline
26. Turjman F, Levrier O, Combaz X, et al. **EVIDENCE trial: design of a phase 2, randomized, controlled, multicenter study comparing flow diversion and traditional endovascular strategy in unruptured saccular wide-necked intracranial aneurysms.** *Neuroradiology* 2015;57:49–54 CrossRef Medline
27. Lylyk P, Miranda C, Ceratto R, et al. **Curative endovascular reconstruction of cerebral aneurysms with the Pipeline embolization device: the Buenos Aires experience.** *Neurosurgery* 2009;64:632–42; discussion 642–43; quiz N6 CrossRef Medline

Endovascular Treatment of Ruptured Blister-Like Aneurysms: A Systematic Review and Meta-Analysis with Focus on Deconstructive versus Reconstructive and Flow-Diverter Treatments

A. Rouchaud, W. Brinjikji, H.J. Cloft, and D.F. Kallmes

ABSTRACT

BACKGROUND AND PURPOSE: Various endovascular techniques have been applied to treat blister-like aneurysms. We performed a systematic review to evaluate endovascular treatment for ruptured blister-like aneurysms.

MATERIALS AND METHODS: We performed a comprehensive literature search and subgroup analyses to compare deconstructive versus reconstructive techniques and flow diversion versus other reconstructive options.

RESULTS: Thirty-one studies with 265 procedures for ruptured blister-like aneurysms were included. Endovascular treatment was associated with a 72.8% (95% CI, 64.2%–81.5%) mid- to long-term occlusion rate and a 19.3% (95% CI, 13.6%–25.1%) retreatment rate. Mid- to long-term neurologic outcome was good in 76.2% (95% CI, 68.9%–8.4%) of patients. Two hundred forty procedures (90.6%) were reconstructive techniques (coiling, stent-assisted coiling, overlapped stent placement, flow diversion) and 25 treatments (9.4%) were deconstructive. Deconstructive techniques had higher rates of initial complete occlusion than reconstructive techniques (77.3% versus 33.0%, $P = .0003$) but a higher risk for perioperative stroke (29.1% versus 5.0%, $P = .04$). There was no difference in good mid- to long-term neurologic outcome between groups, with 76.2% for the reconstructive group versus 79.9% for the deconstructive group ($P = .30$). Of 240 reconstructive procedures, 62 (25.8%) involved flow-diverter stents, with higher rates of mid- to long-term complete occlusion than other reconstructive techniques (90.8% versus 67.9%, $P = .03$) and a lower rate of retreatment (6.6% versus 30.7%, $P < .0001$).

CONCLUSIONS: Endovascular treatment of ruptured blister-like aneurysms is associated with high rates of complete occlusion and good mid- to long-term neurologic outcomes in most patients. Deconstructive techniques are associated with higher occlusion rates but a higher risk of perioperative ischemic stroke. In the reconstructive group, flow diversion carries a higher level of complete occlusion and similar clinical outcomes.

ABBREVIATION: BLA = blister-like aneurysm

Blister-like aneurysms (BLAs) are intracranial arterial lesions originating at nonbranching sites of the dorsal supraclinoid internal carotid artery and basilar artery. BLAs account for 0.3%–1% of intracranial aneurysms and 0.9%–6.5% of ruptured aneurysms.[1-6] They are attributed to subadventitial dissections resulting in a focal wall defect with absence of internal elastic lamina and media, leading, in most cases, to acute subarachnoid hemorrhage. The arterial gap is only covered with adventitia and thin fibrinous tissue.[4,7-10]

Ruptured BLAs have a high mortality rate. Furthermore, treatment of these lesions is technically difficult because they often lack a defined neck and the aneurysm sac has a very thin wall.[4,11-13] Thus, ruptured BLAs are associated with high rates of spontaneous or treatment-induced rebleed and death, regardless of treatment type.[2,4,13,14]

Many surgical techniques such as wrapping or trapping with bypass have been described for the treatment of these lesions. However, such techniques are often associated with high perioperative morbidity and mortality rates.[8,10,11,13,15-20] Because of these results, endovascular techniques, both reconstructive and deconstructive, have emerged as the treatment of choice due to perceived lower rates of treatment-related morbidity and higher efficacy.[2-4,12,21-25] However, because of the rarity of these lesions,

Received February 2, 2015; accepted after revision April 9.

From the Department of Radiology, Mayo Clinic, Rochester, Minnesota.

Aymeric Rouchaud received financial support by a research grant from the French Society of Radiology and the Fondation Therese Planiol.

Please address correspondence to Aymeric Rouchaud, MD, Department of Radiology, Mayo Clinic, 200 First St SW, Rochester, MN 55905; e-mail: Rouchaud.Aymeric@mayo.edu; aymeric.rouchaud@gmail.com

Indicates article with supplemental on-line table.

http://dx.doi.org/10.3174/ajnr.A4438

most series on endovascular treatment of BLAs are small retrospective single-center case series. Thus, the efficacy and safety of endovascular treatment of these lesions have not been well-established.[4] In addition, little is known regarding whether reconstructive techniques with parent artery preservation are associated with similar rates of angiographic occlusion and improved clinical outcomes compared with deconstructive parent artery sacrifice.[13] Therefore, we performed a systematic review of the literature examining the overall efficacy of endovascular treatments for ruptured BLAs and comparing outcomes of reconstructive techniques such as stent placement, flow diversion, and stent-assisted coiling with deconstructive techniques such as parent artery occlusion and trapping. We also performed a subgroup analysis comparing the safety and efficacy of flow-diverter treatment with other reconstructive techniques.

MATERIALS AND METHODS

Literature Search

We identified all studies published between 1980 and November 2014 that reported patients treated with endovascular therapy for ruptured BLAs. A comprehensive literature search of the databases PubMed, Ovid MEDLINE, and Ovid EMBASE was designed and conducted by an experienced librarian with input from the authors. The key words "blister," "aneurysm," "endovascular," "coil," "clip," "stent," "intravascular," and "flow diverter" were used in both "AND" and "OR" combinations. Studies were selected by using the following criteria: 1) ruptured BLAs treated by an endovascular approach; 2) involving subjects 18 years of age or older; 3) with available data on clinical and/or angiographic outcomes; 4) retrospective or prospective with at least 3 patients; and 5) published in English.

Two authors jointly searched the data base and selected potentially relevant articles on the basis of the title and abstract and obtained the full text for detailed review. We also searched the reference lists of retrieved articles and published review articles for additional studies. We also screened duplicate publications that drew on the same datasets (ie, data overlapped that in other included studies); only the publication with the most complete data was included. The included studies reported their own definition of blister aneurysms with homogeneity in the classification as small lesions without a defined neck located at nonbranching sites. The included series are homogeneous according to the definition of blister aneurysms as small lesions without definite neck located at nonbranching sites and with a dome/neck ratio of <1. Some included cohorts reported larger aneurysms, which are mainly a recurrence after a first treatment. All of the included series stated that the aneurysms were all blister aneurysms according to their "Materials and Methods" section.

Data were extracted independently by 2 authors by using a standardized form, and any disagreement was resolved by consensus. We did not contact the authors of the studies to request incomplete or unpublished data. For each study, we extracted the following data: patient demographics, initial clinical status (Hunt and Hess scale grade), treatment technique (coiling, stent-assisted coiling, stent placement alone, flow-diverter stent, endovascular parent artery occlusion), immediate angiographic occlusion, mid- to long-term angiographic occlusion, perioperative morbidity (resulting from procedural complications), perioperative mortality (all causes), rebleeding (for ruptured only), recurrence, retreatment, and mid- to long-term good neurologic outcome (>3 months of follow-up). Good neurologic outcome was defined as a modified Rankin Scale score of ≤ 2. In cases in which a modified Rankin Scale score was not available, good neurologic outcome was determined if the study used terms such as "no morbidity" or "good recovery."

Outcomes were obtained for the overall population of patients receiving endovascular treatment of ruptured BLAs. Separate analyses were also performed comparing outcomes between patients receiving reconstructive techniques with preservation of the parent artery, including coiling, stent placement, stent-assisted coiling, or flow-diverter stent versus those undergoing deconstructive techniques such as endovascular trapping or parent artery occlusion. Patients undergoing parent artery occlusion with surgical bypass were excluded. In addition, we compared outcomes between patients treated with a flow-diverter stent versus other reconstructive endovascular treatments.

Statistical Analysis

All included studies were noncomparative. From each cohort, we estimated the cumulative incidence (event rate) and 95% confidence interval for each outcome. Event rates for each intervention were pooled in a meta-analysis across studies by using the random effects model.[26] Anticipating heterogeneity among studies, we chose this model a priori because it incorporates within-study variance and between-study variance. For all outcomes, we quantified between-study heterogeneity by using a homogeneity test based on the Cochran Q statistics and by calculating the I^2 statistics.[27]

RESULTS

Literature Review

The initial literature search yielded 157 articles. On initial abstract and title review, we excluded 72 studies: 20 studies because they dealt with surgical treatment, 20 because they did not report detailed outcomes for blister aneurysms, and 32, because they were either case reports or had fewer than 3 patients. Eighty-five studies were reviewed in additional detail. Of them, 20 were excluded because they reported only surgical treatments; 24, because they did not report detailed clinical outcomes; and 10, because they were review articles. The identified non-English publications excluded from the analysis were all case reports with fewer than 3 patients.

In total, 31 studies with 258 patients with ruptured BLAs were included. Seventy-three percent of patients were women, their mean age was 47.6 years (range, 19–84 years), 19.3% (44/228) of patients had a grade 4 or 5 Hunt and Hess scale hemorrhage, and the mean dome size of the blister aneurysms was 2.4 mm (range, 1–12 mm). This wide range in the aneurysm sizes, up to 12 mm, is because blister aneurysms are characterized by early frequent recurrence and some of the studies from our analysis included regrowth of blister aneurysms. Overall, 265 procedures were included; of them, 25 treatments (9.4%) were deconstructive techniques and 240 procedures (90.6%) were reconstructive techniques. Of the 240 reconstructive procedures, 62 (25.8%) in-

volved flow-diverter stents and 178 were non-flow-diverter reconstructive techniques with stent-assisted coiling in 106, coiling with or without balloon remodeling in 15, stent placement (1 or several overlapped stents) in 45, Onyx (Covidien, Irvine, California) with stent in 3, and merged reconstructive techniques in 9. Mean follow-up was 14.2 months (range, 1–54) with at least 6 months for 23 of the 31 studies. A summary of the included studies is provided in the On-line Table.

Overall Outcomes of Endovascular Treatment of Ruptured BLAs

When we considered all patients treated with either reconstructive or deconstructive techniques, immediate occlusion rate was 40.6% (62/172; 95% CI, 28.5%–52.7%) and mid- to long-term occlusion rate was 72.8% (197/266; 95% CI, 64.2%–81.5%). The retreatment rate was 19.3% (52/265; 95% CI, 13.6%–25.1%). Perioperative intracranial hemorrhage occurred in 7.0% (18/245; 95% CI, 4.1%–9.9%) of procedures and rebleeding of the BLA occurred in 8.3% (17/242; 95% CI, 5.0%–11.5%) of cases. The overall perioperative complication incidence rate was 12.6% (37/251; 95% CI, 8.3%–16.8%). The perioperative morbidity rate was 13.4% (34/225; 95% CI, 8.9%–17.9%), and the perioperative stroke rate was 8.1% (18/230; 95% CI, 4.7%–11.5%). All-cause perioperative mortality was 7.3% (16/265; 95% CI, 4.4%–10.1%). Mid- to long-term neurologic outcome was good in 76.2% (207/265; 95% CI, 68.9%–8.4%) of patients. These data are summarized in Table 1.

Table 1: Outcomes of the overall population

Outcome	No. Events/Patients	% (95%CI)	I^2
Procedural complications	37/251	12.6 (8.3–16.8)	21
Perioperative stroke	18/230	8.1 (4.7–11.5)	10
Initial occlusion	62/172	40.6 (28.5–52.7)	81
Perioperative mortality	16/265	7.3 (4.4–10.1)	0
Perioperative morbidity	34/225	13.4 (8.9–17.9)	15
Perioperative ICH	18/245	7.0 (4.1–9.9)	0
Early rebleeding	17/242	8.3 (5.0–11.5)	0
Retreatment	49/259	17.1 (111.9–22.3)	38
Mid- to long-term occlusion	196/263	74.0 (65.5–82.5)	72
Mid- to long-term good neurologic outcome	200/259	76.1 (68.5–83.7)	68

Note:—ICH indicates intracranial hemorrhage.

Deconstructive versus Reconstructive Techniques

Patients treated with deconstructive techniques had higher rates of complete occlusion on immediate posttreatment angiography than those treated with reconstructive techniques (77.3% versus 33.0%, $P = .0003$, Fig 1) but had a higher risk for perioperative stroke (29.1% versus 5.0%, $P = .04$, Fig 2). No other statistically significant difference was noted between deconstructive and reconstructive techniques for the treatment of ruptured BLAs. Specifically, mid- to long-term good clinical outcome rates were similar between the reconstructive (76.2%; 95% CI, 67.5%–84.8%) and deconstructive

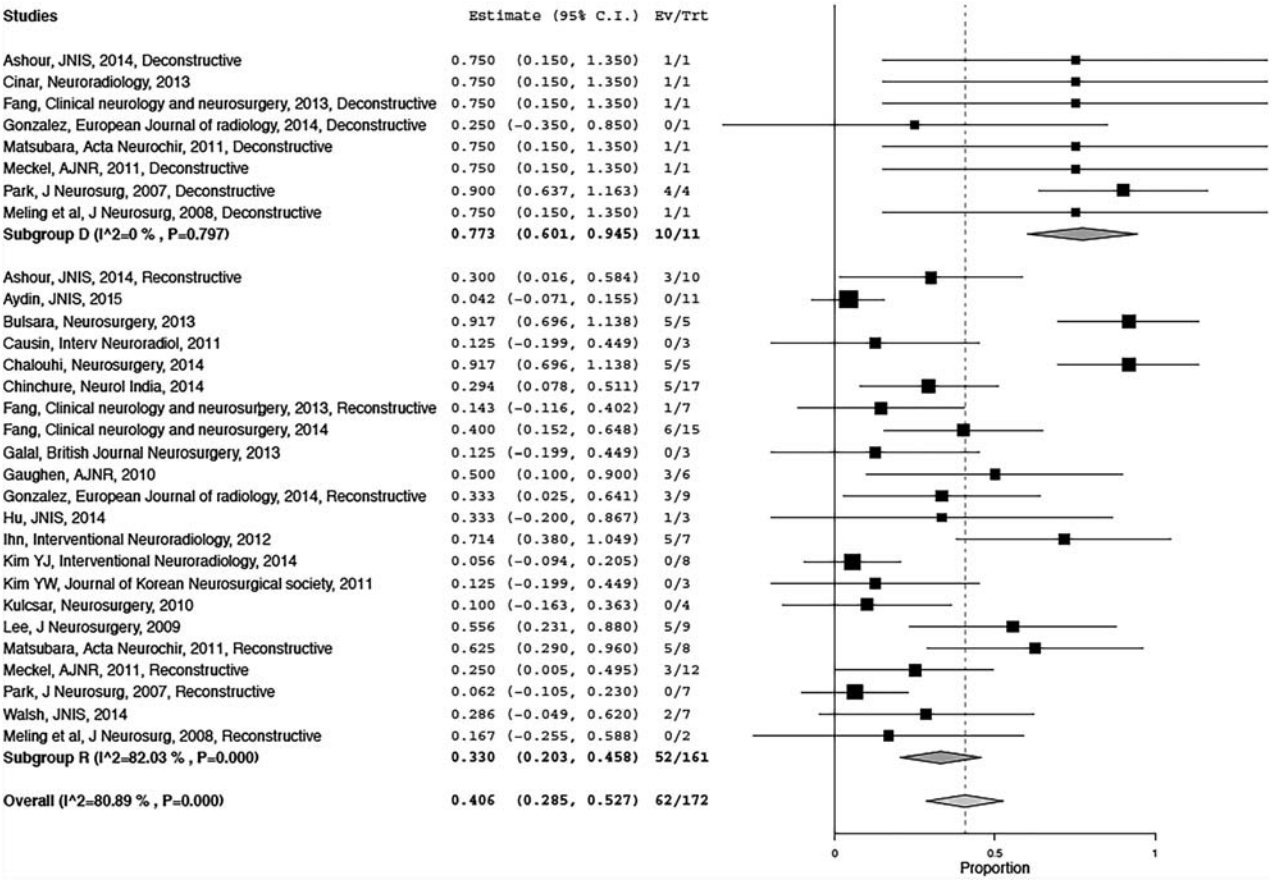

FIG 1. Meta-analysis. Comparison of initial occlusion rates between deconstructive and reconstructive techniques.

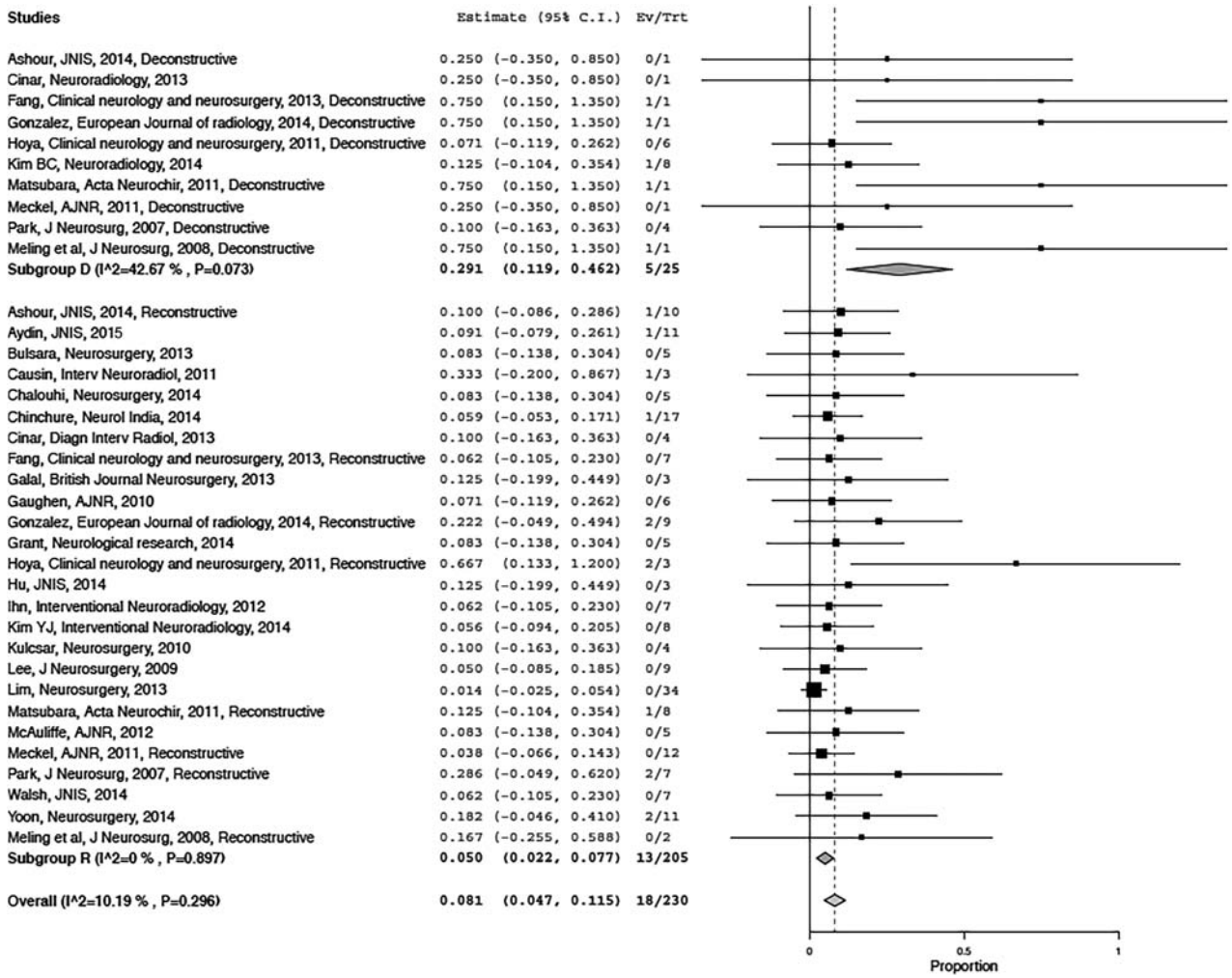

FIG 2. Meta-analysis. Comparison of the perioperative stroke rate between deconstructive and reconstructive techniques.

Table 2: Meta-analysis—comparison of outcomes with deconstructive versus reconstructive techniques

Outcome	Deconstructive (%) (95% CI)	Deconstructive (I^2)	Reconstructive (%) (95% CI)	Reconstructive (I^2)	*P* Value
Procedural complications	26.1 (10.6–41.7)	25	10.1 (6.1–14.1)	13	.63
Perioperative stroke	29.1 (11.9–46.1)	43	5.0 (2.2–7.7)	0	.04[a]
Initial occlusion	77.3 (60.1–94.5)	0	33.0 (20.3–45.8)	82	.0003[a]
Perioperative mortality	15.1 (3.5–26.7)	13	6.7 (3.8–9.7)	0	.98
Perioperative morbidity	23.4 (8.5–38.2)	28	10.5 (6.4–14.7)	5	.89
Perioperative ICH	12.4 (2.3–22.6)	0	6.5 (3.4–9.6)	0	.89
Early rebleeding	11.0 (0.9–21.2)	0	8.0 (4.6–11.4)	0	.83
Retreatment	19.0 (5.3–32.8)	0	17.2(11.3–23.0)	49	.51
Mid- to long-term occlusion	81.0 (67.2–94.7)	0	73.6 (63.8–83.3)	78	.20
Mid- to long-term good neurologic outcome	79.9 (64.7–95.0)	19	76.2 (67.5–84.8)	74	.30

Note:—ICH indicates intracranial hemorrhage.
[a] Significant.

groups (79.9%; 95% CI, 64.7%–95.0%) ($P = .30$). These data are summarized in Table 2.

Flow-Diverter Arterial Reconstruction versus Other Non-Flow-Diverter Reconstructive Techniques

Patients treated with flow-diverter stents had higher rates of mid- to long-term complete occlusion than those treated with other reconstructive techniques (90.8% versus 69.7%, $P = .005$, Fig 3) and a lower rate of retreatment (6.6% versus 27.1%, $P = .0002$, Fig 4). Perioperative morbidity rates were similar in the flow-diverter group compared with the non-flow-diverter reconstructive group (12.6% versus 13.2%, $P = .64$). Perioperative mortality was 8.7% (95% CI, 2.1%–15.2%) in the flow-diverter group versus 7.2% (95% CI, 3.5%–15.9%) in the non-flow-diverter reconstructive group ($P = .46$). Mid- to long-term good clinical outcome rates were statistically similar between the flow-diverter group (86.0%; 95% CI, 77.8%–94.2%) and non-flow-diverter reconstructive group (75.0%;

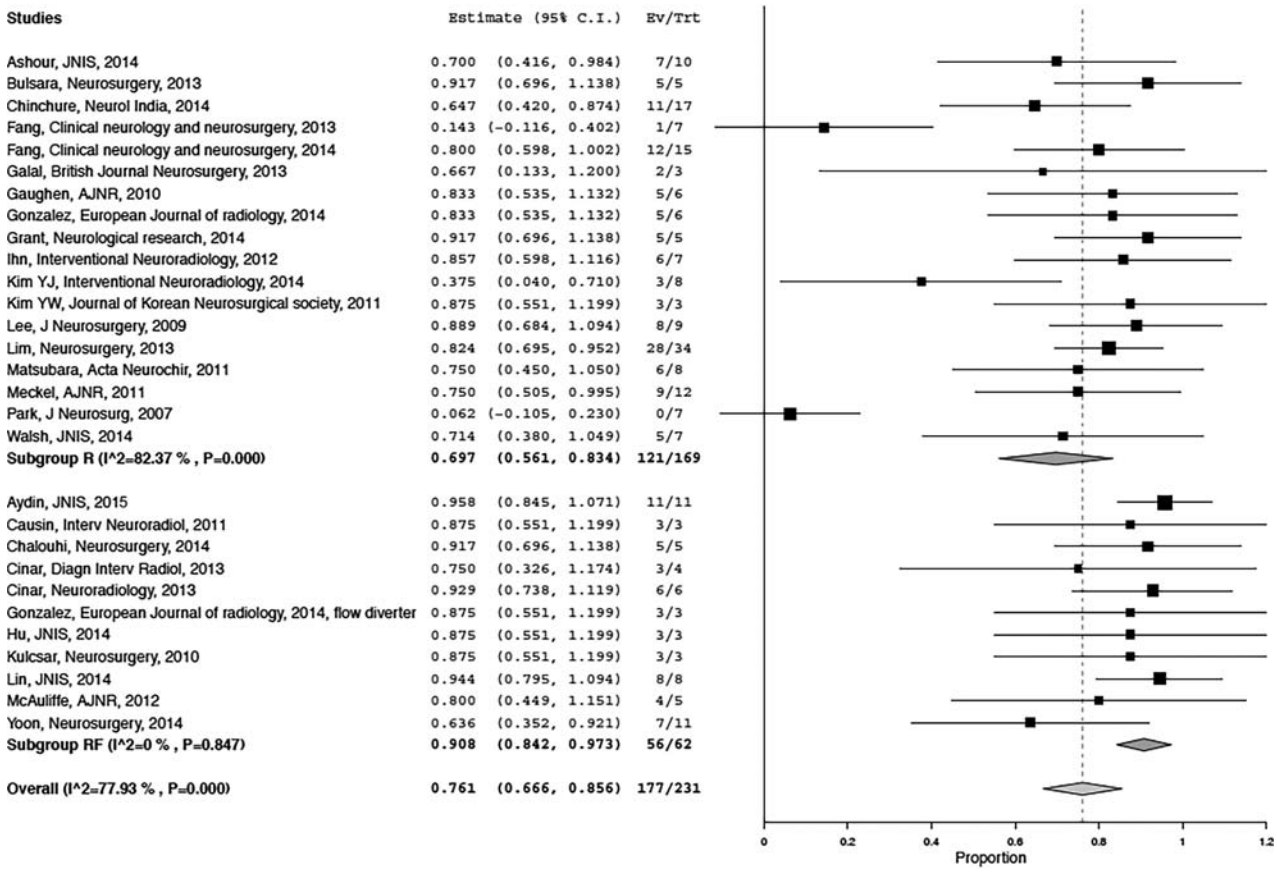

FIG 3. Meta-analysis. Comparison of mid- to long-term occlusion rates between non-flow-diverter reconstructive techniques and flow-diverter techniques.

95% CI, 63.7%–86.2%) ($P = .23$). Perioperative intracranial hemorrhage rates were similar between the flow-diverter (7.6%; 95% CI, 0.8%–14.9%) and non-flow-diverter reconstructive group (6.3%; 95% CI, 2.6%–9.7%) techniques ($P = .21$). These data are summarized in Table 3.

DISCUSSION

Our meta-analysis demonstrated that both deconstructive (endovascular parent artery occlusion) and reconstructive (stenting/stent-assisted coiling/flow-diversion) techniques are effective in the treatment of ruptured BLAs. Deconstructive techniques achieved higher rates of initial complete angiographic occlusion compared with reconstructive techniques, albeit with higher rates of periprocedural stroke. However, there were no statistically significant differences between deconstructive and reconstructive techniques on mid- to long-term occlusion rates, retreatment, rebleeding, or clinical outcomes. Stroke severity was not reported in most of the studies; but it is possible that perioperative strokes were minor and did not result in substantial morbidity. Overall, these findings suggest that reconstructive techniques are as effective and potentially safer than endovascular parent artery occlusion, considering the ischemic risk. These findings are important, especially in deciding treatment options for patients who cannot tolerate parent artery occlusion.

When considering differences between different reconstructive techniques, our meta-analysis demonstrated that flow-diverter stents result in better occlusion rates and lower retreatment rates than non-flow-diverter reconstructive techniques (simple coiling, stent-assisted coiling, or overlapped stents). We found a trend toward better clinical outcomes with flow-diverter techniques, but our results were not statistically significant. These findings are particularly important given the increased use of flow-diverter stent placement in the treatment of complex intracranial aneurysms.

Most interesting is the higher rate of the overall mid- to long-term occlusion (72.8%; range, 64.2%–81.5%) compared with initial occlusion (40.6%; range, 28.5%–52.7%). We suppose that this improvement is mainly due to the remodeling after flow diversion because the patients treated with flow-diverter stents experienced an occlusion rate increase from 35.9% to 90.8%, while patients treated with non-flow-diverter reconstructive techniques experienced an increase from 32.8% initial occlusion to 67.9% at mid- to long-term follow-up and occlusion rates were quite stable for deconstructive techniques, varying only from 77.3% to 81% between initial and mid- to long-term evaluations. This increase in occlusion rates is potentially also driven by the interruption of antiplatelet treatment for flow-diversion and non-flow-diversion reconstructive techniques.

Comparing the safety and efficacy of various surgical and endovascular techniques in the treatment of BLAs is difficult because most studies were small single-center case series and did not compare the efficacy of various treatments. One recent systematic review published by Gonzalez et al[4] evaluated the overall out-

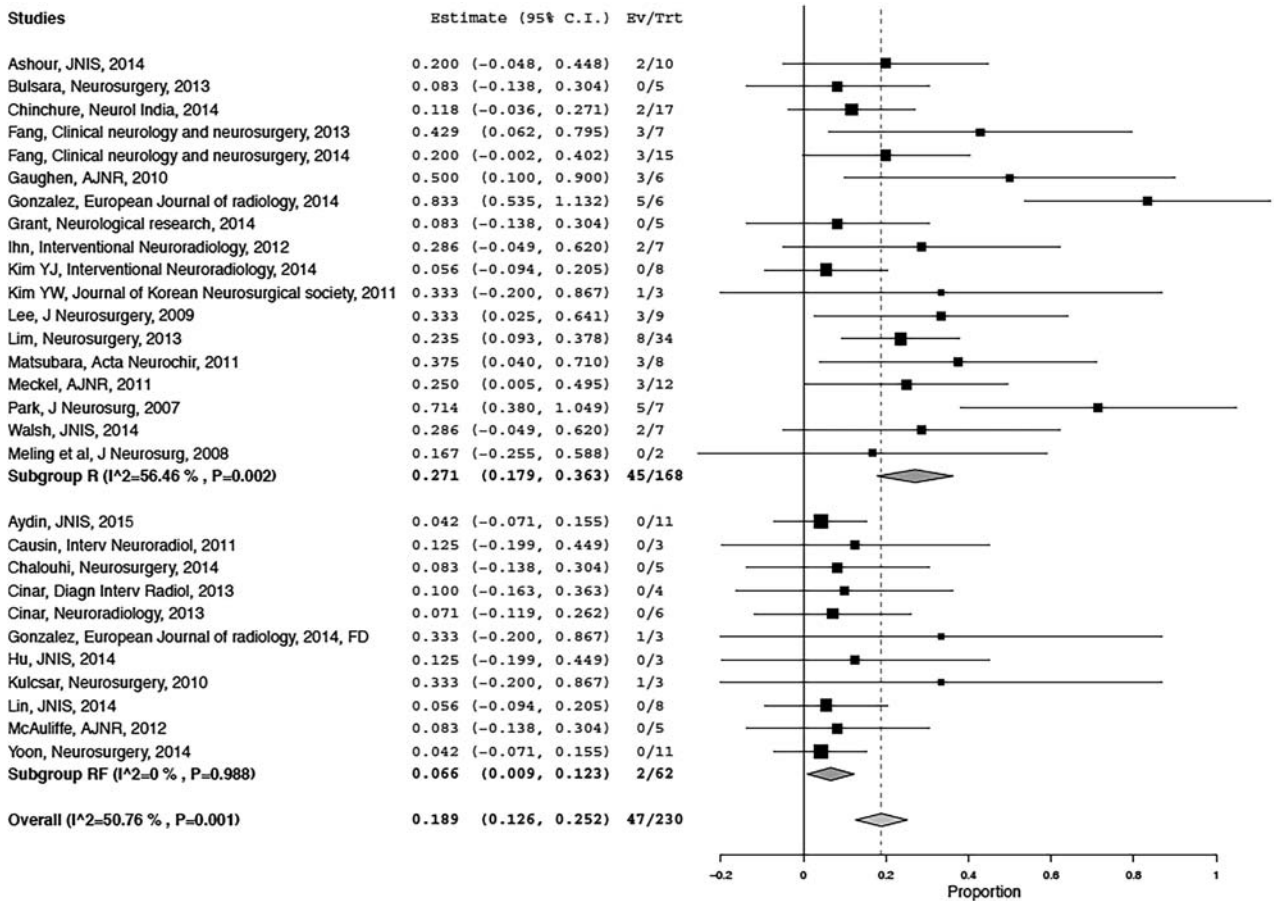

FIG 4. Meta-analysis. Comparison of retreatment rates between non-flow-diverter reconstructive techniques and flow-diverter techniques.

Table 3: Meta-analysis—comparison of outcomes with flow-diverter versus non-flow-diverter reconstructive techniques

Outcome	Flow-Diverter Reconstructive (%) (95% CI)	Flow-Diverter Reconstructive (I^2)	Non-Flow-Diverter Reconstructive (%) (95% CI)	Non-Flow-Diverter Reconstructive (I^2)	*P* Value
Retreatment	6.6 (0.9–12.3)	0	27.1 (17.9–36.3)	56	.0002[a]
Procedural complications	17.0 (6.3–27.7)	28	7.8 (3.9–11.7)	4	.21
Perioperative stroke	11.5 (3.1–19.9)	0	4.2 (1.3–7.1)	0	.77
Perioperative mortality	8.7 (2.1–15.2)	0	7.2 (3.5–10.9)	0	.46
Perioperative morbidity	12.6 (3.3–22.0)	0	13.2 (7.1–19.2)	26	.64
Perioperative ICH	7.6 (0.8–14.7)	0	6.3 (2.6–9.7)	0	.21
Mid to long-term occlusion	90.8 (84.2–97.3)	0	69.7 (56.1–83.4)	83	.005[a]
Initial occlusion	35.9 (0.0–72.0)	76	32.8 (19.7–45.9)	90	.79
Mid- to long-term good neurologic outcome	86.0 (77.8–94.2)	80	75.0 (63.7–86.2)	0	.23
Early rebleeding	6.5 (0.0–12.8)	0	8.7 (4.6–12.8)	0	.06

Note:—ICH indicates intracranial hemorrhage.

[a] Significant.

comes of patients with BLAs but pooled patients with and without rupture and surgical with endovascular treatments. This previous review included 87 patients treated with a primary endovascular approach, with rates of morbidity and mortality for endovascular techniques slightly higher than the numbers presented here. In the Gonzalez et al[4] study, surgical morbidity for BLAs was estimated to be 21%, with a mortality rate of 17%, which is much higher than that observed in our systematic review, suggesting a favorable efficacy and safety profile for endovascular treatment in the management of ruptured BLAs. The higher morbidity and mortality rates among surgically treated aneurysms may be partly because these aneurysms lack a definitive saccular component and the parent vessel wall is often friable and involves a long vessel segment. These qualities tend to result in high rates of intraoperative rupture.[2,28]

To date, no large studies have compared the safety and efficacy of deconstructive and reconstructive endovascular techniques in the treatment of BLAs, to our knowledge. Reconstructive techniques should be strongly considered over deconstructive techniques in the treatment of BLAs for the following reasons: First, many patients are unable to tolerate balloon test occlusion of the parent vessel, and in these situations, reconstructive techniques

may be the only available treatment option. Vasospasm is a commonly reported complication of subarachnoid hemorrhage resulting from BLA rupture. Deconstructive techniques may interfere with endovascular access for the treatment of potential delayed vasospasm, whereas reconstructive techniques with preservation of parent artery flow would allow access and treatment of vasospasm, when needed.[22] In addition, the preservation of the parent artery flow can also result in the preservation of normal intracranial vascular hemodynamics.[4]

A number of reconstructive techniques have been used in the treatment of BLAs. Previous studies have reported the use of a stent-in-stent technique to promote flow diversion and decrease the hemodynamic stress on the BLAs without an intrasaccular device. However, the results of such treatments are complicated by high recurrence rates and a risk for stent misdeployment.[21,25,28-30] Endovascular treatment by using a traditional approach of coil embolization (with or without adjunctive stent placement) is difficult because of the very small size of BLAs without a defined saccular component to allow the introduction of coils safely.[3,13,31-33] In fact, the placement of coils into the saccular component of BLAs is a potentially dangerous maneuver and may cause perforation and rehemorrhage.[28] Furthermore, the effectiveness of coil embolization for the management of dorsal wall ICA aneurysms remains controversial.[34] One major disadvantage of flow diverters is the need for dual antiplatelet therapy in the acute phase of ruptured aneurysms. However, despite the uniform use of these medications in the perioperative period among flow-diverter placements, this meta-analysis demonstrated similar rebleeding, hemorrhage, and clinical outcomes between flow-diverter and other reconstructive therapies and higher rates of angiographic occlusion with flow diverters. These results suggest that in the correct clinical setting, flow diverters may be superior to other reconstructive methods in the treatment of BLAs.

Strengths and Limitations

The strengths of this study include following: an a priori established protocol, a comprehensive literature search that involved multiple databases, and the process of study selection by independent reviewers. The main limitation of this analysis is the noncomparative nature of the studies. Our study undoubtedly has publication bias. Moreover, treatment modalities have varied during the time course of the published series; these differences make standardization of treatment paradigms difficult. Furthermore, given the small size of some of the treatment groups included in this analysis, our ability to detect differences among groups is limited. Last, uniform assessment and reporting of complications in a standardized fashion were lacking. When we used the Grading of Recommendations, Assessment, Development and Evaluation framework, the quality of evidence (confidence in estimates) was very low because of imprecision, heterogeneity, and methodologic limitations of the included studies; most important, they were noncomparative.[35,36] Nevertheless, to the best of our knowledge, this systematic review is the first one focusing on endovascular treatment for ruptured BLAs. The last systematic review of BLAs published in 2014 by Gonzalez et al[4] reported only 87 patients treated with a primary endovascular approach. Given the low number of reported BLAs and the difficulty of collecting prospective data, this meta-analysis provides useful information to share with patients and families when assessing the risks of treatment of BLAs and represents a benchmark against which future studies can be compared.

CONCLUSIONS

Endovascular treatment of ruptured BLAs is associated with high rates of complete occlusion and good mid- to long-term neurologic outcomes. Deconstructive techniques result in higher rates of immediate complete angiographic occlusion but carry a higher risk of ischemic complications compared with reconstructive techniques. Among reconstructive techniques, flow diversion appears to have a higher rate of complete occlusion and lower rate of retreatment. Use of either deconstructive or reconstructive endovascular treatment seems to be safe and effective in the right clinical setting. When one opts for the reconstructive treatment, flow diversion appears to be a reasonable choice despite the need for antiplatelet treatment.

Disclosures: David F. Kallmes—*UNRELATED*: *Board Membership*: GE Healthcare, *Comments*: Cost-Effectiveness Board; *Consultancy*: ev3,* *Comments*: planning and implementing clinical trials; *Grants/Grants Pending*: MicroVention,* Codman,* SurModics,* NeuroSigma,* Sequent,* *Comments*: preclinical and clinical research; *Royalties:* University of Virginia Patent Foundation, *Comments*: spine fusion. *Money paid to the institution.

REFERENCES

1. Nakagawa F, Kobayashi S, Takemae T, et al. **Aneurysms protruding from the dorsal wall of the internal carotid artery.** *J Neurosurg* 1986; 65:303–08 CrossRef Medline
2. McLaughlin N, Laroche M, Bojanowski MW. **Blister-like aneurysms of the internal carotid artery: management considerations.** *Neurochirurgie* 2012;58:170–86 CrossRef Medline
3. Ahn JY, Cho JH, Jung JY, et al. **Blister-like aneurysms of the supraclinoid internal carotid artery: challenging endovascular treatment with stent-assisted coiling.** *J Clin Neurosci* 2008;15:1058–61 CrossRef Medline
4. Gonzalez AM, Narata AP, Yilmaz H, et al. **Blood blister-like aneurysms: single center experience and systematic literature review.** *Eur J Radiol* 2014;83:197–205 CrossRef Medline
5. Abe M, Tabuchi K, Yokoyama H, et al. **Blood blisterlike aneurysms of the internal carotid artery.** *J Neurosurg* 1998;89:419–24 CrossRef Medline
6. Jha AN, Gupta V. **Blister aneurysms.** *Neurol India* 2009;57:2–3 CrossRef Medline
7. Ishikawa T, Nakamura N, Houkin K, et al. **Pathological consideration of a "blister-like" aneurysm at the superior wall of the internal carotid artery: case report.** *Neurosurgery* 1997;40:403–05; discussion 405–06 CrossRef Medline
8. Lee JW, Choi HG, Jung JY, et al. **Surgical strategies for ruptured blister-like aneurysms arising from the internal carotid artery: a clinical analysis of 18 consecutive patients.** *Acta Neurochir (Wien)* 2009;151:125–30 CrossRef Medline
9. Tanoue S, Kiyosue H, Matsumoto S, et al. **Ruptured "blisterlike" aneurysm with a pseudoaneurysm formation requiring delayed intervention with endovascular coil embolization: case report.** *J Neurosurg* 2004;101:159–62 CrossRef Medline
10. Ogawa A, Suzuki M, Ogasawara K. **Aneurysms at nonbranching sites in the surpaclinoid portion of the internal carotid artery: internal carotid artery trunk aneurysms.** *Neurosurgery* 2000;47:578–83; discussion 583–86 CrossRef Medline
11. McLaughlin N, Laroche M, Bojanowski MW. **Surgical management**

of blood blister-like aneurysms of the internal carotid artery. *World Neurosurg* 2010;74:483–93 CrossRef Medline
12. Chinchure SD, Gupta V, Goel G, et al. **Subarachnoid hemorrhage with blister aneurysms: endovascular management.** *Neurol India* 2014;62:393–99 CrossRef Medline
13. Meling TR, Sorteberg A, Bakke SJ, et al. **Blood blister-like aneurysms of the internal carotid artery trunk causing subarachnoid hemorrhage: treatment and outcome.** *J Neurosurg* 2008;108:662–71 CrossRef Medline
14. Le Feuvre DE, Taylor AG. **The management of very small/blister internal carotid artery aneurysms.** *Interv Neuroradiol* 2011;17: 431–34 Medline
15. Sim SY, Shin YS, Cho KG, et al. **Blood blister-like aneurysms at nonbranching sites of the internal carotid artery.** *J Neurosurg* 2006; 105:400–05 CrossRef Medline
16. Wrobel CJ, Taubman K. **Blood-blister-like aneurysms.** *J Neurosurg* 2000;92:1076–77 Medline
17. Kurokawa Y, Wanibuchi M, Ishiguro M, et al. **New method for obliterative treatment of an anterior wall aneurysm in the internal carotid artery: encircling silicone sheet clip procedure—technical case report.** *Neurosurgery* 2001;49:469–72 CrossRef Medline
18. Kubo Y, Ogasawara K, Tomitsuka N, et al. **Wrap-clipping with polytetrafluoroethylene for ruptured blisterlike aneurysms of the internal carotid artery: technical note.** *J Neurosurg* 2006;105:785–87 CrossRef Medline
19. Sekula RF Jr. Cohen DB, Quigley MR, et al. **Primary treatment of a blister-like aneurysm with an encircling clip graft: technical case report.** *Neurosurgery* 2006;59:ONSE168; discussion ONSE168 Medline
20. Shigeta H, Kyoshima K, Nakagawa F, et al. **Dorsal internal carotid artery aneurysms with special reference to angiographic presentation and surgical management.** *Acta Neurochir (Wien)* 1992;119: 42–48 CrossRef Medline
21. Gaughen JR Jr, Hasan D, Dumont AS, et al. **The efficacy of endovascular stenting in the treatment of supraclinoid internal carotid artery blister aneurysms using a stent-in-stent technique.** *AJNR Am J Neuroradiol* 2010;31:1132–38 CrossRef Medline
22. Meckel S, Singh TP, Undrén P, et al. **Endovascular treatment using predominantly stent-assisted coil embolization and antiplatelet and anticoagulation management of ruptured blood blister-like aneurysms.** *AJNR Am J Neuroradiol* 2011;32:764–71 CrossRef Medline
23. Ashour R, Dodson S, Aziz-Sultan MA. **Endovascular management of intracranial blister aneurysms: spectrum and limitations of contemporary techniques.** *J Neurointerv Surg* 2014 Nov 6. [Epub ahead of print] CrossRef Medline
24. Grant RA, Quon JL, Bulsara KR. **Oversized self-expanding stents as an alternative to flow-diverters for blister-like aneurysms.** *Neurol Res* 2014;36:351–55 CrossRef Medline
25. Fang YB, Li Q, Wu YN, et al. **Overlapping stents for blood blister-like aneurysms of the internal carotid artery.** *Clin Neurol Neurosurg* 2014;123:34–39 CrossRef Medline
26. DerSimonian R, Laird N. **Meta-analysis in clinical trials.** *Control Clin Trials* 1986;7:177–88 CrossRef Medline
27. Higgins JP, Thompson SG, Deeks JJ, et al. **Measuring inconsistency in meta-analyses.** *BMJ* 2003;327:557–60 CrossRef Medline
28. Walsh KM, Moskowitz SI, Hui FK, et al. **Multiple overlapping stents as monotherapy in the treatment of 'blister' pseudoaneurysms arising from the supraclinoid internal carotid artery: a single institution series and review of the literature.** *J Neurointerv Surg* 2014;6: 184–94 CrossRef Medline
29. Cantón G, Levy DI, Lasheras JC, et al. **Flow changes caused by the sequential placement of stents across the neck of sidewall cerebral aneurysms.** *J Neurosurg* 2005;103:891–902 CrossRef Medline
30. Chung J, Kim BM, Lim YC. **Five overlapping Enterprise stents in the internal carotid artery-to-middle cerebral artery to treat a ruptured blood blister-like aneurysm.** *Neurol Sci* 2013;34:1485–87 CrossRef Medline
31. Matsubara N, Miyachi S, Tsukamoto N, et al. **Endovascular coil embolization for saccular-shaped blood blister-like aneurysms of the internal carotid artery.** *Acta Neurochir (Wien)* 2011;153:287–94 CrossRef Medline
32. Doorenbosch X, Harding M. **Primary treatment of a blood-blister-like aneurysm of the internal carotid artery with Guglielmi detachable coil embolisation.** *J Clin Neurosci* 2008;15:1276–79 CrossRef Medline
33. Lim YC, Kim BM, Suh SH, et al. **Reconstructive treatment of ruptured blood blister-like aneurysms with stent and coil.** *Neurosurgery* 2013;73:480–88 CrossRef Medline
34. Peschillo S, Missori P, Piano M, et al. **Blister-like aneurysms of middle cerebral artery: a multicenter retrospective review of diagnosis and treatment in three patients.** *Neurosurg Rev* 2015;38:197–202; discussion 202–193 CrossRef Medline
35. Balshem H, Helfand M, Schünemann HJ, et al. **GRADE guidelines, 3: rating the quality of evidence.** *J Clin Epidemiol* 2011;64:401–06 CrossRef Medline
36. Guyatt GH, Oxman AD, Kunz R, et al. **GRADE guidelines, 6: rating the quality of evidence—imprecision.** *J Clin Epidemiol* 2011;64: 1283–93 CrossRef Medline
37. Aydin K, Arat A, Sencer S, et al. **Treatment of ruptured blood blister-like aneurysms with flow diverter SILK stents.** *J Neurointerv Surg* 2015;7:202–09 CrossRef Medline
38. Bulsara KR, Kuzmik GA, Hebert R, et al. **Stenting as monotherapy for uncoilable intracranial aneurysms.** *Neurosurgery* 2013;73(1 suppl operative):ons80–85; discussion ons85 CrossRef Medline
39. Causin F, Pascarella R, Pavesi G, et al. **Acute endovascular treatment (<48 hours) of uncoilable ruptured aneurysms at non-branching sites using Silk flow-diverting devices.** *Interv Neuroradiol* 2011;17: 357–64 Medline
40. Chalouhi N, Zanaty M, Tjoumakaris S, et al. **Treatment of blister-like aneurysms with the Pipeline embolization device.** *Neurosurgery* 2014;74:527–32; discussion 532 CrossRef Medline
41. Çinar C, Bozkaya H, Oran I. **Endovascular treatment of cranial aneurysms with the Pipeline flow-diverting stent: preliminary mid-term results.** *Diagn Interv Radiol (Ank)* 2013;19:154–64 CrossRef Medline
42. Çinar C, Oran İ, Bozkaya H, et al. **Endovascular treatment of ruptured blister-like aneurysms with special reference to the flow-diverting strategy.** *Neuroradiology* 2013;55:441–47 CrossRef Medline
43. Fang YB, Li Q, Yang PF, et al. **Treatment of blood blister-like aneurysms of the internal carotid artery with stent-assisted coil embolization.** *Clin Neurol Neurosurg* 2013;115:920–25 CrossRef Medline
44. Galal A, Bahrassa F, Dalfino JC, et al. **Stent-assisted treatment of unruptured and ruptured intracranial aneurysms: clinical and angiographic outcome.** *Br J Neurosurg* 2013;27:607–16 CrossRef Medline
45. Hoya K, Tanaka Y, Uchida T, et al. **Treatment of ruptured internal carotid artery trunk aneurysms: feasibility of endovascular trapping or proximal obliteration of the ICA.** *Clin Neurol Neurosurg* 2011;113:285–88 CrossRef Medline
46. Hu YC, Chugh C, Mehta H, et al. **Early angiographic occlusion of ruptured blister aneurysms of the internal carotid artery using the Pipeline embolization device as a primary treatment option.** *J Neurointerv Surg* 2014;6:740–43 CrossRef Medline
47. Ihn YK, Kim SH, Sung JH, et al. **The efficacy of endovascular treatment of ruptured blood blister-like aneurysms using stent-assisted coil embolization.** *Interv Neuroradiol* 2012;18:432–41 Medline
48. Kim BC, Kwon OK, Oh CW, et al. **Endovascular internal carotid artery trapping for ruptured blood blister-like aneurysms: long-term results from a single centre.** *Neuroradiology* 2014;56:211–17 CrossRef Medline
49. Kim YJ, Ko JH. **Sole stenting with large cell stents for very small ruptured intracranial aneurysms.** *Interv Neuroradiol* 2014;20:45–53 CrossRef Medline
50. Kim YW, Park IS, Baik MW, et al. **Endovascular treatment of**

blood blister-like aneurysms using multiple self-expanding stents. *J Korean Neurosurg Soc* 2011;49:116–19 CrossRef Medline
51. Kulcsár Z, Wetzel SG, Augsburger L, et al. **Effect of flow diversion treatment on very small ruptured aneurysms.** *Neurosurgery* 2010;67: 789–93 CrossRef Medline
52. Lee BH, Kim BM, Park MS, et al. **Reconstructive endovascular treatment of ruptured blood blister-like aneurysms of the internal carotid artery.** *J Neurosurg* 2009;110:431–36 CrossRef Medline
53. Lin N, Brouillard AM, Keigher KM, et al. **Utilization of Pipeline embolization device for treatment of ruptured intracranial aneurysms: US multicenter experience.** *J Neurointerv Surg* 2014 Sep 17. [Epub ahead of print] CrossRef Medline
54. McAuliffe W, Wenderoth JD. **Immediate and midterm results following treatment of recently ruptured intracranial aneurysms with the Pipeline embolization device.** *AJNR Am J Neuroradiol* 2012;33: 487–93 CrossRef Medline
55. Park JH, Park IS, Han DH, et al. **Endovascular treatment of blood blister-like aneurysms of the internal carotid artery.** *J Neurosurg* 2007;106:812–19 CrossRef Medline
56. Yoon JW, Siddiqui AH, Dumont TM, et al; Endovascular Neurosurgery Research Group. **Feasibility and safety of Pipeline embolization device in patients with ruptured carotid blister aneurysms.** *Neurosurgery* 2014;75:419–29; discussion 429 CrossRef Medline

Emergency Stenting of the Extracranial Internal Carotid Artery in Combination with Anterior Circulation Thrombectomy in Acute Ischemic Stroke: A Retrospective Multicenter Study

D. Behme, A. Mpotsaris, P. Zeyen, M.N. Psychogios, A. Kowoll, C.J. Maurer, F. Joachimski, J. Liman, K. Wasser, C. Kabbasch, A. Berlis, M. Knauth, T. Liebig, and W. Weber

ABSTRACT

BACKGROUND AND PURPOSE: Several small case series reported a favorable clinical outcome for emergency stent placement in the extracranial internal carotid artery combined with mechanical thrombectomy in acute stroke. The rate of postinterventional symptomatic intracranial hemorrhages was reported to be as high as 20%. Therefore, we investigated the safety and efficacy of this technique in a large multicentric cohort.

MATERIALS AND METHODS: The data bases of 4 German stroke centers were screened for all patients who received emergency stent placement of the extracranial internal carotid artery in combination with mechanical thrombectomy of the anterior circulation between 2007 and 2014. The primary outcome measure was the rate of symptomatic intracranial hemorrhage according to the European Cooperative Acute Stroke Study III criteria; secondary outcome measures included the angiographic revascularization results and clinical outcome.

RESULTS: One hundred seventy patients with a median age of 64 years (range, 25–88 years) were treated. They presented after a median of 98 minutes (range, 52–160 minutes) with a median NIHSS score of 15 (range, 12–19). Symptomatic intracranial hemorrhages occurred in 15/170 (9%) patients; there was no statistically significant difference among groups pertaining to age, sex, intravenous rtPA, procedural timings, and the rate of successful recanalization. In 130/170 (77%) patients, a TICI score of ≥2b could be achieved. The in-hospital mortality rate was 19%, and 36% of patients had a favorable outcome at follow-up.

CONCLUSIONS: Emergency stent placement in the extracranial internal carotid artery in combination with anterior circulation thrombectomy is effective and safe. It is not associated with a significantly higher risk of symptomatic intracranial hemorrhage compared with published series for mechanical thrombectomy alone.

ABBREVIATIONS: PH = parenchymal hematoma; sICH = symptomatic intracranial hemorrhage

Ten-to-twenty percent of patients with acute ischemic stroke have a high-grade ipsilateral extracranial ICA stenosis, which usually causes major stroke if an additional intracranial large-artery occlusion of the anterior circulation is present.[1,2] In such a cohort, IV thrombolysis alone has a very limited rate of successful recanalization.[3] Endovascular therapy is an option in these cases, consisting of a stent implantation at the level of the ICA stenosis/occlusion in conjunction with mechanical thrombectomy before or after the stent placement. Several small case series reported promising results when this combined approach was performed.[4-9] One of the major concerns in these patients is the risk of postinterventional symptomatic intracranial hemorrhage (sICH), which may be influenced by the mandatory antiplatelet medication of the stent-placement procedure. The reported rate of sICH varies considerably in the literature, ranging from 0% to 20%.[5-10] Unfortunately, the small number of patients included in these series limits the validity of these findings. Some important randomized trials excluded patients with high-grade ipsilateral ICA stenosis (eg, the Solitaire Flow Restoration Device versus the Merci Retriever in Patients with Acute Ischemic Stroke and the Trevo versus Merci Retrievers

Received February 26, 2015; accepted after revision May 13.

From the Departments of Neuroradiology (D.B., M.N.P., M.K.) and Neurology (J.L., K.W.), Georg-August-University Göttingen, University Medical Center, Göttingen, Germany; Department of Radiology and Neuroradiology (A.M., P.Z., C.K., T.L.), University Cologne, University Hospital Cologne, Cologne, Germany; Department of Radiology and Neuroradiology (A.K., W.W.), Ruhr-University-Bochum, University Medical Center Langendreer, Bochum, Germany; and Departments of Radiology and Neuroradiology (C.J.M., A.B.), and Neurology (F.J.), Klinikum Augsburg, Augsburg, Germany.

Paper previously presented at: Annual Meeting of the Anatomy-Biology-Clinical Correlations–Working Group in Interventional Radiology, January 18–23, 2015; Val d Isere, France; and European Stroke Organization Conference, April 17–19, 2015; Glasgow, UK.

This work received no private or public funding and no specific financial support.

Please address correspondence to Daniel Behme, MD, Department of Neuroradiology, University Medical Center Göttingen, Georg-August-University Göttingen, Robert-Koch-Str 40 37075 Göttingen; e-mail: daniel.behme@med.uni-goettingen.de

Indicates article with supplemental on-line table.

http://dx.doi.org/10.3174/ajnr.A4459

for Thrombectomy Revascularisation of Large Vessel Occlusions in Acute Ischemic Stroke),[11,12] while other recently published studies like a Randomized Trial of Intra-Arterial Treatment for Acute Ischemic Stroke or the Randomized Assessment of Rapid Endovascular Treatment of Ischemic Stroke trial included relatively small numbers of patients with tandem occlusions (30 [13%] and 21 [13%], respectively).[13,14]

The aim of this retrospective study was to determine the risk of sICH and the angiographic results and the clinical outcome after emergency ICA stent placement in combination with anterior circulation thrombectomy in a large multicentric cohort.

MATERIALS AND METHODS

We conducted a retrospective multicenter study of all patients who received combined extracranial ICA stent placement and anterior circulation thrombectomy between 2007 and 2014. According to the institutional guidelines, no ethics committee approval was required for this retrospective observational study. The clinical results of some of these cases have been published in case series before.[4,5,7,15,16] All 4 centers screened their prospectively kept neurointerventional data bases for eligible patients according to the following inclusion and exclusion criteria.

Inclusion Criteria

The centers were free to include either all patients since 2007 (before the introduction of stent retrievers for mechanical thrombectomy) or only patients who received a stent retriever and/or direct aspiration treatment.

Eligibility for mechanical thrombectomy was decided at the local institution according to the guidelines of each center. Patients were eligible for concomitant IV thrombolysis according to the guidelines of the German Society of Neurologists. There were no general limitations on procedural timings, age, or baseline NIHSS score. Patients had to present with an angiographically (CTA or DSA) proved high-grade stenosis or occlusion of the ipsilateral ICA and additional large-artery occlusion of the anterior circulation. A high-grade ipsilateral stenosis was thereby defined as a stenosis of ≥70% according to the NASCET criteria. Anterior large-artery occlusions were subdivided into terminal ICA, carotid-T, and MCA occlusions.

Patients were included only if the ipsilateral ICA was stented and the occlusion of the anterior circulation was treated either in an antegrade (stent before thrombectomy) or retrograde (stent after thrombectomy) fashion. There was no limitation on the stent used or on the technique for the intracranial thrombectomy.

All patients were included independent of the administered antiplatelet medication, which was different in all 4 centers.

The antiplatelet regimens were as follows:

Center A: If the patient had no prior medication with dual antiplatelets before the intervention, eptifibatide was continuously infused for 24 hours (after an initial bolus [180 mcg/kg for 2 minutes]) to prevent secondary stent occlusion. Patients were monitored in the intensive care unit postinterventionally. A control CT scan was obtained within 24 hours. After exclusion of a relevant intracranial hemorrhage, the regimen was switched to a secondary prophylaxis of stent occlusion based on a dual antiplatelet therapy: Under continuous IV eptifibatide, patients received a loading dose of 300 mg clopidogrel and 500 mg aspirin. Patients with daily aspirin medication before the intervention did not receive an aspirin loading dose. The administration of eptifibatide was stopped 4 hours after loading with clopidogrel (and aspirin whenever applicable). Patients continued with life-long aspirin (100 mg/day) and additional clopidogrel (75 mg/day) for 8 weeks.

Center B: Patients received an IV bolus of 500 mg aspirin directly before stent placement and, additionally, 375 mg clopidogrel over a nasogastric tube. After exclusion of a relevant intracranial hemorrhage (control CT scan within 24 hours), the dual antiplatelet medication with aspirin (100 mg/day) and clopidogrel (75 mg/day) was continued for 3 months and then switched to a life-long aspirin (100 mg/day) monotherapy.

Center C: All patients who were not on an antiplatelet medication before the treatment received a weight-adapted bolus of tirofiban followed by a continuous IV infusion for 24 hours. After exclusion of a cerebral hemorrhage (CT scan), 500 mg aspirin and 300 mg clopidogrel were given orally or through a nasogastric tube. Aspirin (100 mg/day) and clopidogrel (75 mg/day) were continued for 3 months followed by a life-long antiplatelet monotherapy with either aspirin or clopidogrel.

Center D: Immediately before stent placement, patients received an IV bolus of aspirin (500 mg) and an IV bolus of heparin (5000 IU). Alternatively, tirofiban was used. At the end of the intervention, a flat panel CT scan was performed to rule out intracranial hemorrhage; if so, the patients received a loading dose of clopidogrel (600 mg) orally. Aspirin (100 mg/day) and clopidogrel (75 mg/day) were continued for 3 months and then switched to a life-long aspirin (100 mg/day) monotherapy.

Exclusion Criteria

Any infarction of equal to or more than one-third of the MCA territory or evidence of an intracranial hemorrhage on the initial CT scan led to exclusion. Additionally, all patients without persistent intracranial occlusion after extracranial stent placement were excluded.

Endovascular Procedures

The endovascular procedures have been described in detail previously.[4,5,7,15] None of the centers used a balloon-guide occlusion catheter. In brief, the procedures were the following:

Antegrade approach: A large guide catheter (Neuron MAX 088; Penumbra, Alameda, California; Mach1; Boston Scientific, Natick, Massachusetts; VISTA BRITE TIP; Cordis, Fremont, California) was placed into the distal common carotid artery. A 0.014-inch wire was then carefully navigated through the ICA occlusion up to the petrous portion in conjunction with a microcatheter. A slow and careful contrast injection was then performed to verify passage into the true lumen. Pre-stenting balloon angioplasty was performed whenever necessary with a 3.0- or 3.5-mm monorail balloon. The subsequent MT in the intracranial portions was performed in a usual manner. In case of a biaxial approach with a stent retriever (Trevo variants, Stryker, Kalamazoo, Michigan; Separator 3D, Penumbra; Solitaire AB/FR; Covidien, Irvine, California), the stent was passed with the guiding catheter before retraction of the stent retriever; in a triaxial set-

Table 1: Baseline characteristics

	All (*n* = 170)	Center A (*n* = 57)	Center B (*n* = 42)	Center C (*n* = 44)	Center D (*n* = 27)
Treatment period/characteristics		October 2009 to July 2014	March 2007 to July 2014	January 2011 to February 2014	December 2009 to February 2013
Age (yr) (median) (range)	64 (25–88)	64 (40–86)	60 (25–88)	64 (37–87)	70 (48–82)
Male sex (*n*/*N*) (%)	119/170 (70%)	39/57 (68%)	30/42 (71%)	32/44 (76%)	18/27 (67%)
IV thrombolysis (*n*/*N*) (%)	122/170 (72%)	49/57 (85%)	31/42 (74%)	19/44 (43%)	23/27 (85%)
Baseline NIHSS (median) (range)	15 (12–19)	16 (13–19)	16 (9–21)	16 (14–20)	15 (10–17)
Symptom onset to admission (min) (median) (range)	98 (52–160)	102 (49–153)	83 (50–180)	108 (60–183)	86 (63–183)
Distal occlusion site					
Carotid-T (*n*/*N*) (%)	51/170 (30%)	28/57 (49%)	17/42 (40%)	3/44 (7%)	3/27 (11%)
Terminal ICA (*n*/*N*) (%)	3/170 (2%)	2/57 (4%)	1/42 (2%)	–	–
MCA M1 (*n*/*N*) (%)	99/170 (58%)	19/57 (33%)	19/42 (45%)	37/84 (%)	24/27 (89%)
MCA M2 (*n*/*N*) (%)	17/170 (10%)	8/57 (14%)	5/42 (12%)	4/44 (9%)	–

Note:— – indicates none.

ting, the stent was passed with the intermediate catheter and the stent retriever was retracted into it to not interfere with the stent. No such precautions were necessary in cases of direct-aspiration-treatment technique without the use of a retriever.

Retrograde approach: Analogously, a large guide catheter was placed in the distal common carotid artery; the proximal ICA stenosis was then passed with a 0.014-inch micro-guidewire followed by an intermediate catheter (054 or 5MAX, Penumbra; DAC, Stryker; Navien, Covidien). The intermediate catheter was positioned as close to the clot as possible, allowing lesional aspiration. We then performed MT using a stent retriever in the usual fashion. After successful revascularization of the occluded intracranial vessel, an exchange microwire was introduced over the intermediate catheter and then exchanged for the stent at the proximal occlusion/stenosis site.

Imaging Evaluation

All imaging data were analyzed at the level of the participating centers by an interventional neuroradiologist; the angiographic results were locally graded according to the TICI score. A successful recanalization was defined as a TICI result of ≥2b.

All postinterventional control CT scans of the patients were screened for intracranial hemorrhages, and all centers reported all parenchymal type 1 (parenchymal hematoma [PH]1: bleeding <30% of the infarcted area with a mild space-occupying effect and parenchymal hematoma) and type 2 (PH2: bleeding of >30% of the infarcted area with a relevant space-occupying effect) hematomas and all sICHs, according to the European Cooperative Acute Stroke Study criteria (any apparently extravascular blood in the brain or within the cranium that was associated with clinical deterioration, as defined by an increase of ≥4 points in the NIHSS score, or that led to death and that was identified as the predominant cause of the neurologic deterioration).[17]

Clinical Evaluation

A stroke neurologist assessed all patients clinically on admission (NIHSS) and discharge (NIHSS and mRS) from the stroke center and the rehabilitation unit (follow-up mRS at ~90 days; range, 70–100 days). In cases with missing follow-up data, the discharge mRS was used instead.[18]

Data Analysis and Statistics

The data were collected at each center according the above-mentioned criteria, pooled, and then analyzed at 1 of the 4 centers. Continuous study parameters were compared among patients by either the Welch *t* test in case of a normal distribution or by the Mann-Whitney *U* test in case of a non normal distribution. The Fisher exact test was used for categoric variables. All statistical analyses were performed by using GraphPad Prism software, Version 6.1 (GraphPad Software, San Diego, California); the significance level was set at $\alpha = .05$.

RESULTS

One hundred seventy patients were treated between July 2007 and July 2014. The median age was 64 years (range, 25–88 years); 119/170 (70%) were male. The patients presented after a median of 98 minutes (range, 52–160 minutes) with a median NIHSS score of 15 (range, 12–19). Distal occlusion sites were the following: MCA M1 in 99/170 (58%), MCA M2 in 17/170 (10%), terminal ICA in 3/170 (2%), and carotid-T in 51/170 (31%). IV thrombolysis was applied in 122/170 (72%) patients (Table 1).

Technical and Angiographic Results

All patients received ICA stent placement with at least 1 stent, in most cases (153/170, 90%) with the Carotid Wallstent (Boston Scientific). One hundred thirty-three of 170 patients (78%) underwent treatment with new-generation devices (stent retriever and/or direct aspiration catheter); the remainder were treated by aspiration with a first-generation aspiration catheter (Penumbra System, Penumbra). One hundred fifty-one of 170 cases (89%) were performed with an antegrade approach. The median groin puncture to recanalization time was 88 minutes (range, 59–121 minutes); overall, the median symptom onset to recanalization time was 296 minutes (range, 236–367 minutes). A favorable angiographic result (TICI ≥ 2b) was achieved in 130/170 cases (77%); in another 21/170 (12%), a TICI2a result could be reached. In the subgroup that underwent treatment with a modern stent retriever or direct aspiration, a favorable angiographic result was reached in 113/133 (85%). The control CT scans revealed a PH1 in 13/170 (8%) and a PH2 in 11/170 patients (9%). Of these 24 hematomas, only 15 were classified as sICH, whereby 11/15 (73%) led to death in the acute phase. The overall all-cause in-hospital mortality was 19% (32/170). The median NIHSS score at discharge was 6, and at the time of the follow-up examination, 62/170 patients (36%) had a favorable outcome (Table 2).

To identify factors contributing to the risk of sICH, we analyzed several cofactors in respect to the subgroups of patients with

Table 2: Clinical and angiographic outcome

	All (*n* = 170)	Center A (*n* = 57)	Center B (*n* = 42)	Center C (*n* = 44)	Center D (*n* = 27)
Clinical outcome					
NIHSS at discharge (median) (range)	6 (3–12)	6 (3–11)	8 (4–15)	8 (3–15)	5 (2–10)
FU mRS ≤ 2	62/170 (36%)	22/57 (39%)	16/42 (38%)	15/44 (34%)	9/27 (33%)
In-hospital mortality (all cause)	32/170 (19%)	11/57 (19%)	5/42 (12%)	9/44 (20%)	7/27 (26%)
PH1 (*n/N*) (%)	13/170 (8%)	4/57 (7%)	2/42 (5%)	5/44 (11%)	2/27 (7%)
PH2 (*n/N*) (%)	11/170 (6%)	5/57 (7%)	2/42 (5%)	1/44 (2%)	3/27 (11%)
sICH (*n/N*) (%)	15/170 (9%)	5/57 (9%)	3/42 (7%)	3/44 (7%)	4/27 (15%)
Angiographic outcome					
Groin puncture to recanalization (min) (median) (range)	88 (59–121)	75 (56–95)	81 (41–118)	111 (70–148)	119 (84–147)
Symptom onset to recanalization (min) (median) (range)	296 (236–367)	263 (217–317)	332 (259–401)	317 (252–420)	306 (227–365)
TICI ≥ 2b (*n/N*) (%)	130/170 (77%), 113/133 (85%)[b]	48/57 (84%)	22/42 (53%)[a]	36/44 (82%)	24/27 (89%)
TICI 2a (*n/N*) (%)	21/170 (12%)	3/57 (5%)	13/42 (31%)	4/44 (9%)	1/27 (4%)

Note:—FU indicates follow-up.

[a] Includes results from 2007/2008, treatment without a stent retriever.

[b] Only cases with stent retriever or direct aspiration treatment.

Table 3: Potential risk factors for sICH after stenting and MT

	sICH	No sICH	*P* Value
Characteristics			
Age (yr) (median) (range)	71 (46–86)	64 (25–88)	.1
Age above median (*n/N*) (%)	10/15 (66%)	74/155 (48%)	.2
Male sex (*n/N*) (%)	12/15 (80%)	107/155 (70%)	.6
IV thrombolysis (*n/N*) (%)	8/15 (53%)	114/155 (74%)	.1
Initial ASPECTS (median) (IQR)	7 (6–9)	7 (5–8)	1.0
Symptom onset to recanalization (min) (median) (range)	300 (264–419)	294 (233–363)	.3
Groin puncture to recanalization (min) (median) (range)	95 (68–140)	83 (58–120)	.2
TICI ≥ 2b (*n/N*) (%)	13/15 (87%)	117/155 (75%)	.5
Occlusion site			
Carotid-T (*n/N*) (%)	4/15 (27%)	47/155 (30%)	1.0
MCA (*n/N*) (%)	11/15 (73%)	88/155 (57%)	.3
Antiplatelet medication (*n/N*) (%)			
Eptifibatide, tirofiban	5/57 (9%), 7/71 (11%)	52/57 (91%), 64/71 (89%)	1.0
Eptifibatide, aspirin + clopidogrel	5/57 (9%), 3/42 (7%)	52/57 (91%), 39/42 (93%)	1.0
Tirofiban, aspirin + clopidogrel	7/71 (11), 3/42 (7%)	66/71 (89%), 39/42 (93%)	.7

Note:—MT indicates mechanical thrombectomy; IQR, interquartile range.

and without sICH (Table 3). We could not find statistically significant differences among the median age (71 versus 64 years, $P = .1$), the percentage of male patients (80% versus 70%, $P = .6$), the number of patients who received iv thrombolysis (53% versus 74%), the initial ASPECTS (7 versus 7, $P = 1.0$), the median time from symptom onset to recanalization (300 versus 294 minutes, $P = .3$), the groin puncture to recanalization timings (95 versus 83 minutes), the rate of favorable angiographic results (87% versus 75%), or the occlusion sites. Additionally, there was no significant difference between the rates of sICH in respect to the administered antiplatelet medication (eptifibatide versus tirofiban, $P = 1.0$; tirofiban versus aspirin and clopidogrel, $P = .7$; eptifibatide versus aspirin and clopidogrel, $P = 1.0$).

DISCUSSION

Endovascular therapies for acute ischemic stroke caused by underlying large-artery occlusion have emerged significantly with time, and very recently randomized trials have shown a significant benefit regarding the rate of functional independence after endovascular treatment.[13,14,19] However, 10%–20% of these patients with acute ischemic stroke present with an additional proximal high-grade stenosis or occlusion of the ipsilateral ICA.[1] These patients have been excluded from several studies investigating the efficacy of mechanical thrombectomy, though it has been shown that IV thrombolysis alone is less effective in these cases.[3,11] Endovascular therapy consisting of ICA stent placement and anterior circulation thrombectomy has yielded promising results in small case series so far.[4,8] Alas, bleeding complications, especially in the setting of a mandatory dual antiplatelet medication—sometimes even in addition to IV thrombolysis—might impose a higher risk for added morbidity and mortality in the postinterventional phase.

The endovascular treatment of acute tandem occlusions using ICA stent placement has been investigated for more than a decade.[20,21] At the same time, there was a fundamental development of catheters and clot-extraction devices; stent retrievers have been shown to be technically and clinically superior to older devices.[11,12] Recently, several case series investigated the efficacy and safety of endovascular therapy when ICA stent placement was performed in combination with anterior circulation thrombectomy (On-line Table). Most interesting, these series report relevant differences of the revascularization efficacy, with TICI ≥ 2b results ranging from 63% to 79% of cases and the rate of favorable clinical outcome spanning a range of 29%–76%.[5-10,22] Moreover, the reported rates of sICH range from 0% to almost 22%, most probably due to low numbers of included patients in single-center designs (On-line Table).

The present retrospective, multicenter trial represents a large number of patients with acute ischemic stroke with underlying extracranial ICA stenosis/occlusion and an additional anterior circulation occlusion treated by ICA stent placement and anterior circulation MT. Compared with data published by Malik et al,[9] (77 patients with such tandem occlusions) who did not use stent retrievers for the intracranial recanalization, our rates of favorable angiographic results (75% [Malik et al] versus 77%), clinical outcome (42% versus 36%), and sICH (10% versus 9%) are in the same range. When comparing our data with a recently published meta-analysis, we found the rate of sICH and favorable clinical outcome to be similar (9% sICH in our cohort versus 7% in the group that was treated by stent retrievers and ICA stent placement and 36% versus 35% favorable outcome).[23]

In contrast to more recent publications, we found the rate of sICH to be lower in our series compared with data that were published by Heck and Brown[6] (21% sICH) or Stampfl et al[8] (17% sICH), though they used similar antiplatelet medication strategies.[6,8] Notably, the very high rate of sICH in the Heck and Brown cohort was associated with the use of abciximab (4/13 [31%] sICH in the group of patients who received abciximab) and a high mean age of their patients.

Regarding the clinical outcome, our results (36% favorable outcome) lay between the results of the above-mentioned studies (52% and 29% respectively).

Antiplatelet medication is a prerequisite for ICA stent placement to prevent in-stent thrombosis, and it might go along with a higher risk of sICH, especially if IV thrombolysis is administered additionally. Our retrospective multicenter study could not find significant differences between the various antithrombotic approaches that were used in the participating centers (Table 3). The administration of neither tirofiban nor eptifibatide seems to be associated with an increased risk of sICH. Most interesting, we could not determine any specific cofactor that increased the risk of intracranial hemorrhage peri-interventionally because the variables of age, sex, procedural timings, revascularization results, initial ASPECTS, and rate of IV thrombolysis were not significantly different among the groups (Table 3).

Most important, our study did not show significant differences regarding the rate of sICH compared with recently published, randomized trials like the Randomized Trial of Intra-Arterial Treatment for Acute Ischemic Stroke, which reported an sICH rate of 8% ($P = .7$) in the endovascular arm or the Intra-Arterial Versus Systemic Thrombolysis for Acute Ischemic Stroke expansion trial, which also found the sICH rate to be 6% in both arms ($P = .3$).[13,24]

Several limitations have to be considered when interpreting the current data, most important the retrospective study design, the missing control groups, and the lack of core lab control for imaging evaluation, which might have biased the angiographic results toward higher scores of successful recanalizations. The participating centers used different antiplatelet regimens, which might still have an influence on the rate of sICH but could not be elucidated in the present study because it might still be statistically underpowered to detect such an effect.

CONCLUSIONS

Emergency stent placement in the extracranial ICA combined with anterior circulation thrombectomy is safe and effective. The rate of good outcome is in the range of MT alone. The endovascular treatment of these complex cases is not associated with a significantly higher risk of postinterventional sICH compared with MT without concomitant extracranial stent placement.

Disclosures: Daniel Behme—*UNRELATED*: *Travel/Accommodations/Meeting Expenses Unrelated to Activities Listed*: Penumbra. Anastasios Mpotsaris—*UNRELATED*: *Consultancy*: Penumbra (minor honoraria); *Travel/Accommodations/Meeting Expenses Unrelated to Activities Listed*: Neuravi, Penumbra, *Comments*: travel grants. Christoph Johannes Maurer—*UNRELATED*: *Grants/Grants Pending*: Boston Scientific, Stryker, *Comments*: I received educational grants from Boston Scientific and Stryker; *Travel/Accommodations/Meeting Expenses Unrelated to Activities Listed*: MicroVention, *Comments*: I received a travel grant for the meeting of the German Society of Neuroradiology from MicroVention. Ansgar Berlis—*UNRELATED*: *Consultancy*: consultancy agreements with Covidien, Stryker, and MicroVention for proctoring; *Payment for Lectures (including service on Speakers Bureaus)*: honorarium for invited lectures from Penumbra and Stryker. Michael Knauth—*UNRELATED*: *Payment for Lectures (including service on Speakers Bureaus)*: Siemens (paid lecture on intracranial thrombectomy). Thomas Liebig—*UNRELATED*: *Consultancy*: consulting and proctoring for MicroVention; Acandis; Sequent Medical, Germany. Werner Weber—*UNRELATED*: *Payment for Lectures (including service on Speakers Bureaus)*: Penumbra, *Comments*: Most of the patients from our group were treated with devices from Penumbra.

REFERENCES

1. Grau AJ, Weimar C, Buggle F, et al. **Risk factors, outcome, and treatment in subtypes of ischemic stroke: the German stroke data bank.** *Stroke* 2001;32:2559–66 CrossRef Medline
2. Rubiera M, Ribo M, Delgado-Mederos R, et al. **Tandem internal carotid artery/middle cerebral artery occlusion: an independent predictor of poor outcome after systemic thrombolysis.** *Stroke* 2006;37:2301–05 CrossRef Medline
3. Kim YS, Garami Z, Mikulik R, et al; CLOTBUST Collaborators. **Early recanalization rates and clinical outcomes in patients with tandem internal carotid artery/middle cerebral artery occlusion and isolated middle cerebral artery occlusion.** *Stroke* 2005;36:869–71 CrossRef Medline
4. Mpotsaris A, Bussmeyer M, Buchner H, et al. **Clinical outcome of neurointerventional emergency treatment of extra- or intracranial tandem occlusions in acute major stroke: antegrade approach with Wallstent and Solitaire stent retriever.** *Clin Neuroradiol* 2013;23:207–15 CrossRef Medline
5. Lockau H, Liebig T, Henning T, et al. **Mechanical thrombectomy in tandem occlusion: procedural considerations and clinical results.** *Neuroradiology* 2015;57:589–98 CrossRef Medline
6. Heck DV, Brown MD. **Carotid stenting and intracranial thrombectomy for treatment of acute stroke due to tandem occlusions with aggressive antiplatelet therapy may be associated with a high incidence of intracranial hemorrhage.** *J Neurointerv Surg* 2015;7:170–75 CrossRef Medline
7. Maurer CJ, Joachimski F, Berlis A. **Two in one: endovascular treatment of acute tandem occlusions in the anterior circulation.** *Clin Neuroradiol* 2014 Jul 3. [Epub ahead of print] Medline
8. Stampfl S, Ringleb PA, Möhlenbruch M, et al. **Emergency cervical internal carotid artery stenting in combination with intracranial thrombectomy in acute stroke.** *AJNR Am J Neuroradiol* 2014;35:741–46 CrossRef Medline
9. Malik AM, Vora NA, Lin R, et al. **Endovascular treatment of tandem extracranial/intracranial anterior circulation occlusions: preliminary single-center experience.** *Stroke* 2011;42:1653–57 CrossRef Medline
10. Cohen JE, Gomori JM, Rajz G, et al. **Extracranial carotid artery stenting followed by intracranial stent-based thrombectomy for acute tandem occlusive disease.** *J Neurointerv Surg* 2015;7:412–17 CrossRef Medline

11. Saver JL, Jahan R, Levy EI, et al. **Solitaire flow restoration device versus the Merci retriever in patients with acute ischaemic stroke (SWIFT): a randomised, parallel-group, non-inferiority trial.** *Lancet* 2012;380:1241–49 CrossRef Medline
12. Nogueira RG, Lutsep HL, Gupta R, et al; TREVO 2 Trialists. **Trevo versus Merci retrievers for thrombectomy revascularisation of large vessel occlusions in acute ischaemic stroke (TREVO 2): a randomised trial.** *Lancet* 2012;380:1231–40 CrossRef Medline
13. Berkhemer OA, Fransen PS, Beumer D, et al. **A randomized trial of intraarterial treatment for acute ischemic stroke.** *N Engl J Med* 2015; 372:11–20 CrossRef Medline
14. Goyal M, Demchuk AM, Menon BK, et al; ESCAPE Trial Investigators. **Randomized assessment of rapid endovascular treatment of ischemic stroke.** *New Engl J Med* 2015;372:1019–30 CrossRef Medline
15. Behme D, Kowoll A, Mpotsaris A, et al. **Multicenter clinical experience in over 125 patients with the Penumbra Separator 3D for mechanical thrombectomy in acute ischemic stroke.** *J Neurointerv Surg* 2014 Nov 3. [Epub ahead of print] CrossRef Medline
16. Psychogios MN, Kreusch A, Wasser K, et al. **Recanalization of large intracranial vessels using the Penumbra system: a single-center experience.** *AJNR Am J Neuroradiol* 2012;33:1488–93 CrossRef Medline
17. Hacke W, Kaste M, Bluhmki E, et al; ECASS Investigators. **Thrombolysis with alteplase 3 to 4.5 hours after acute ischemic stroke.** *N Engl J Med* 2008;359:1317–29 CrossRef Medline
18. Ovbiagele B, Saver JL. **Day-90 acute ischemic stroke outcomes can be derived from early functional activity level.** *Cerebrovasc Dis* 2010; 29:50–56 CrossRef Medline
19. Campbell BC, Mitchell PJ, Kleinig TJ, et al; EXTEND-IA Investigators. **Endovascular therapy for ischemic stroke with perfusion-imaging selection.** *N Engl J Med* 2015;372:1009–18 CrossRef Medline
20. Nedeltchev K, Brekenfeld C, Remonda L, et al. **Internal carotid artery stent implantation in 25 patients with acute stroke: preliminary results.** *Radiology* 2005;237:1029–37 CrossRef Medline
21. Fischer U, Mono ML, Schroth G, et al. **Endovascular therapy in 201 patients with acute symptomatic occlusion of the internal carotid artery.** *Eur J Neurol* 2013;20:1017–24, e87
22. Puri AS, Kühn AL, Kwon HJ, et al. **Endovascular treatment of tandem vascular occlusions in acute ischemic stroke.** *J Neurointerv Surg* 2015;7:158–63 CrossRef Medline
23. Kappelhof M, Marquering HA, Berkhemer OA, et al. **Intra-arterial treatment of patients with acute ischemic stroke and internal carotid artery occlusion: a literature review.** *J Neurointerv Surg* 2015; 7:8–15 CrossRef Medline
24. Ciccone A, Valvassori L. **Endovascular treatment for acute ischemic stroke.** *N Engl J Med* 2013;368:2433–34Medline

Susceptibility Vessel Sign on MRI Predicts Favorable Clinical Outcome in Patients with Anterior Circulation Acute Stroke Treated with Mechanical Thrombectomy

R. Bourcier, S. Volpi, B. Guyomarch, B. Daumas-Duport, A. Lintia-Gaultier, C. Papagiannaki, J.M. Serfaty, and H. Desal

ABSTRACT

BACKGROUND AND PURPOSE: The susceptibility vessel sign on MR imaging has been reported to indicate acute occlusion from erythrocyte-rich thrombus. The purpose of this study was to evaluate the influence of the susceptibility vessel sign seen on MR imaging before treatment on the clinical outcome after mechanical thrombectomy for anterior circulation acute stroke.

MATERIALS AND METHODS: We retrospectively included 73 consecutive patients who were treated for anterior circulation acute stroke by mechanical thrombectomy from December 2009 to September 2013. Each patient underwent MR imaging before mechanical thrombectomy. The presence (susceptibility vessel sign+) or absence of the susceptibility vessel sign (susceptibility vessel sign−) was recorded. Mechanical thrombectomy was performed either alone or in association with IV tPA according to the site and time after occlusion. Good functional outcome was defined by an mRS ≤2 at 3 months in susceptibility vessel sign+ and susceptibility vessel sign− groups. Patient clinical characteristics, initial NIHSS score and ASPECTS, site of occlusion, time between onset to groin puncture, TICI after mechanical thrombectomy, NIHSS score at day 1, and spontaneous hyperattenuation on CT at day 1 were also analyzed.

RESULTS: Fifty-three patients with susceptibility vessel sign+ and 20 with susceptibility vessel sign− were included in our study. mRS ≤2 at 3 months occurred in 65% patients in the susceptibility vessel sign+ group and 26% in the susceptibility vessel sign− group ($P = .004$). On multivariate analysis, the susceptibility vessel sign was the only parameter before treatment that could predict mRS ≤2 at 3 months (OR, 8.7; 95% CI, 1.1–69.4; $P = .04$).

CONCLUSIONS: Our study strongly suggests that the susceptibility vessel sign on MR imaging before treatment is predictive of favorable clinical outcome for patients presenting with anterior circulation acute stroke and treated with mechanical thrombectomy.

ABBREVIATIONS: ACAS = anterior circulation acute stroke; GRE = gradient recalled-echo; MT = mechanical thrombectomy; SVS = susceptibility vessel sign

Stroke is a leading cause of adult disability. Approximately two-thirds of stroke survivors have long-term functional deficits that affect their quality of life.[1,2] Very recently, large prospective randomized trials have proved the clinical benefit of endovascular recanalization and, in particular, mechanical thrombectomy (MT) in patients with proximal anterior circulation acute stroke (ACAS).[3,4] In these studies, patients were included on the basis of the presence of a proximal artery occlusion without any characterization of thrombus subtypes (ie, fibrin-rich or erythrocyte-rich thrombus). A gradient recalled-echo (GRE) MR imaging sequence is commonly used to identify brain hemorrhage, and it may also differentiate fibrin-rich from erythrocyte-rich thrombus on the basis of the presence of a susceptibility vessel sign (SVS).[5,6]

There has been no study addressing the prognostic value of SVS in predicting good clinical recovery after MT, to our knowledge. The goal of our study was, therefore, to investigate whether the presence of the SVS is related to better clinical outcomes after MT with stent retrievers in patients presenting with ACAS.

MATERIALS AND METHODS

This was a retrospective descriptive study according to the protocol of stroke treatment at our center. Observational retrospective studies according to the French legislation (articles L.1121–1

Received January 22, 2015; accepted after revision April 18.

From the Departments of Diagnostic and Interventional Neuroradiology (R.B., S.V., B.D.-D., A.L.-G., H.D.) and Diagnostic Cardiac and Vascular Imaging (J.M.S.), Centre Hospitalier Universitaire Nantes Hôpital G et R Laënnec, Nantes, France; Centre d'investigation clinique Thorax (B.G.), l'institut du thorax, Centre Hospitalier Universitaire Nantes, Nantes, France; Institut National de la Santé et de la Recherche Médicale, UMR1087 (B.G., J.M.S., H.D.), l'institut du thorax, Nantes, France; Centre national de la recherche scientifique (B.G.), UMR 6291, Nantes, France; and Department of Diagnostic and Interventional Neuroradiology (C.P.), Centre Hospitalier Régional Universitaire de Tours, Bretonneau Hospital, Tours, France.

J.M.S. and H.D. have participated equally in the supervision of this study.

Please address correspondence to Romain Bourcier, MD, CHU NANTES HGRL, Department of Diagnostic and Interventional Neuroradiology, Nantes, F-44000 France; e-mail: romain.bourcier2@gmail.com

http://dx.doi.org/10.3174/ajnr.A4483

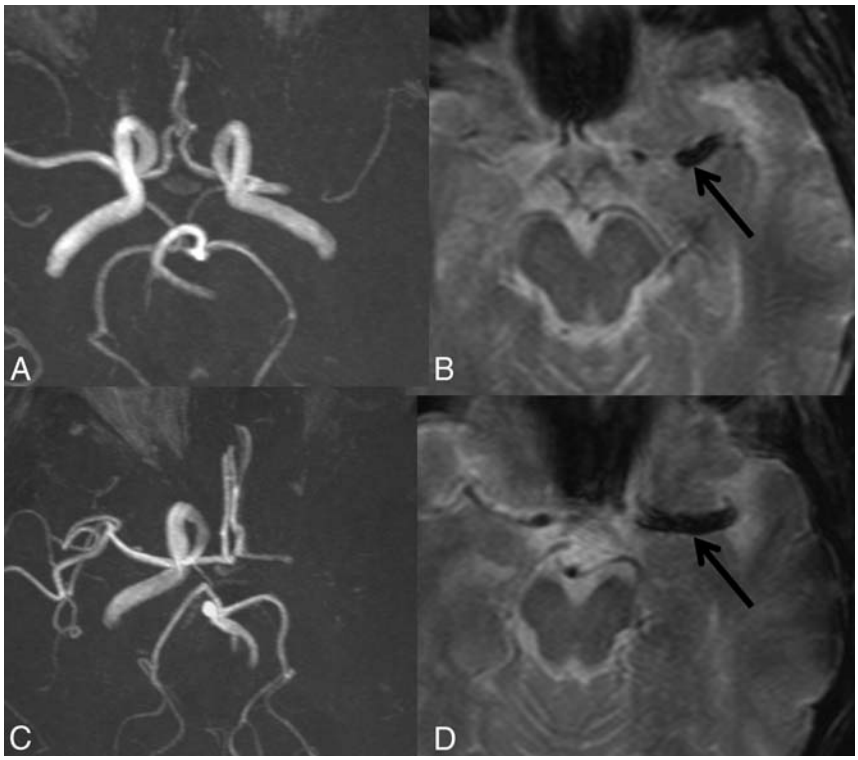

FIG 1. MR imaging showing MCA and ICA-MCA occlusions with SVS (*black arrow*). *A* and *B*, TOF and T2* sequences show occlusion of the left MCA. *C* and *D*, TOF and T2* sequences show occlusion of the left ICA-MCA.

paragraph 1 and R1121–2, Public Health Code) do not require an ethics committee approval to use data for an epidemiologic study.

Patients

We retrospectively included 73 consecutive patients who were treated by MT between September 2009 and December 2013 for ACAS in our center.

All these patients underwent MR imaging before treatment with a GRE T2* sequence and were classified in 2 groups: "SVS +" if they presented an SVS in the occluded artery or "SVS−" if they did not.

Vascular risk factors were registered for each patient and defined as follows: 1) hypertension, when there was a history of antihypertensive medication use, a systolic blood pressure of ≥140 mm Hg, or a diastolic blood pressure of ≥90 mm Hg at hospital discharge; 2) diabetes mellitus, when the use of hypoglycemic drugs or a random glucose level ≥200 mg/dL or glycosylated hemoglobin level of >6.4% on admission were observed; 3) hyperlipidemia, when a history of the use of antihyperlipidemic agents was mentioned or a serum cholesterol level of >220 mg/dL was present; 4) smoking, whatever the level of consumption; and 5) obesity defined as a body mass index of >30.

Initial NIHSS score, site of occlusion, IV tPA before MT, and time between onset and groin puncture were also recorded. Patients with ASPECTS <5 on DWI, estimated by the method of Barber et al,[7] were excluded.

MR Imaging Protocol

MR imaging was performed on a 1.5T magnet (Sonata; Siemens, Erlangen, Germany) with a phased array head coil. First, a GRE T2* imaging was performed to screen for intracranial hemorrhage and SVS. Acquisition parameters for GRE T2* were the following: TR, 800 ms; TE, 30 ms; section thickness, 5 mm; intersection gap, 1 mm; FOV, 250 × 250 mm; flip angle, 20°. Second, DWI sequences $b=0$, $b=500$, and $b=1000$ were acquired, as was an apparent diffusion coefficient map to identify the necrotic core. Acquisition parameters for DWI sequences were set as follows: TR, 6900 ms; TE, 89 ms; section thickness, 5 mm; intersection gap, 0 mm; FOV, 230 × 230 mm. Then, a FLAIR sequence was performed with the following acquisition parameters: TR, 9000 ms; TE, 95 ms; section thickness, 5 mm; intersection gap, 0 mm; FOV, 240 × 210 mm; flip angle, 150°. Finally, a TOF sequence focused on the circle of Willis was obtained to screen large-vessel occlusion. Acquisition parameters for the TOF sequence were the following: TR, 24 ms; TE, 7 ms; section thickness, 0.7 mm; intersection gap, −3.5 mm; FOV, 180 × 180 mm; flip angle, 20°.

Occlusion of the MCA (either M1 and/or M2) was classified as MCA occlusion. Occlusion involving the ICA ending, extending or not to M1, was classified as ICA occlusion. "SVS" was defined as a hypointense signal on T2* within a vessel, exceeding the size of the homologous contralateral artery diameter (Fig 1).[5,6]

All MR imaging and CT on day 1 were analyzed by a junior radiologist (S.V.) and an experienced neuroradiologist (R.B.), and in case of discrepancy, a third experienced neuroradiologist (J.M.S.) analyzed images in consensus.

Endovascular Treatment

When an MCA or ICA occlusion was observed, MT was performed with or without preliminary IV tPA according to the Rescue, Combined, and Stand-Alone Thrombectomy study and neurologic expertise.[8]

All endovascular procedures were performed on a biplane system (Integris Allura 20/20; Philips Healthcare, Best, the Netherlands) by experienced interventional neuroradiologists (H.D., A.L.-G., B.D.-D.).

An 8F Envoy (Codman & Shurtleff, Raynham, Massachusetts) guiding catheter was introduced through a femoral sheath into the concerned carotid artery. Navigation into the target vessel was made with a 0.014-inch microguidewire (Traxcess; MicroVention, Tustin, California) and a 0.021-inch microcatheter (Rebar; Covidien, Irvine, California). The microguidewire was exchanged with the MT device. Once the device was deployed, angiography was performed to evaluate its correct placement and expansion. The device was left in place for 2–7 minutes. Then, the fully deployed device together with the delivery microcatheter was

gently pulled back as a single unit and recovered. Before and during this retrieval, manual aspiration was performed with a 50-mL syringe through the hemostatic valve of the guiding catheter.

Results were assessed according to the TICI grading scale: 0–2a for failure of recanalization on angiography and 2b–3 for successful recanalization.[9] The procedure was repeated 5 times maximum until a TICI score of 2b or 3 was obtained. After the fifth attempt, if a TICI score of 2b or 3 was not achieved, MT was considered a failure.

Immediate Post-MT Imaging and Follow-Up

The TICI scores at the end of the procedure were reviewed by a neuroradiologist who did not perform the MT (R.B.).

NIHSS score at day 1, mRS, and death at 3 months were retrospectively recorded from patient files. NIHSS and mRS scores (mRS ≤2 was considered a good outcome, and >2, a bad outcome) after MT were assessed by independent vascular neurologists working in our institution. The presence of spontaneous hyperattenuation on CT on day 1 after MT was also recorded. In the early follow-up period, any other CT control was performed only in case of clinical worsening.

Symptomatic intracranial hemorrhage was defined according to the European Cooperative Acute Stroke Study definition.[10]

Statistical Analysis

Results were expressed as mean, SD, median, minimum, and maximum for quantitative variables and as count and percentage for categoric variables. Usual bivariate parametric (χ^2 test or Fisher exact test) statistical tests were used for group comparisons. Logistic regression analysis was used to assess the association of the SVS and the favorable functional outcome 90 days after MT. We used the following clinical characteristics: age, sex, initial and day 1 NIHSS score, ASPECTS, dissection, site of occlusion, SVS, IV tPA, onset-to-groin puncture time, TICI, and spontaneous hyperattenuation on CT on day 1. First, a univariate analysis was performed, and only factors with a P value ≤ .25 were selected for the multivariate analysis. All statistical tests were 2-sided, and the significance level was set at .05. Statistical analysis was performed by using SAS, Version 9.4 (SAS Institute, Cary, North Carolina).

RESULTS

Baseline Characteristics

Among 73 patients (36 men and 37 women; median age, 59 years; range, 25–85 years) treated for ACAS with MT, 53 patients (73%) were SVS+ and 20 patients (27%) were SVS−. Intra- and interobserver agreement (κ) for the SVS on MR imaging was 0.86 and 0.86, respectively. The baseline characteristics are summarized in Table 1. The median NIHSS score (2–27) at admission was 18.

Occlusion involved the MCA in 47% of the cases, and the ICA (extending or not to the MCA), in 53% of cases with 11 ICA cervical dissections included in this group. Ten patients with cervical dissection presented with an SVS+. One was SVS−, but this difference was not statistically significant (P = .27). MT alone was used in 45% of cases, and IV tPA + MT, in 55% of cases. Age, cardiovascular risk factors, initial NIHSS score, ASPECTS, and side of occlusion were similar between the 2 groups (Table 1).

Table 1: Patient characteristics and MRI findings before MT and complications and clinical outcome after MT in patients with and without SVS

	SVS− (*n* = 20)	SVS+ (*n* = 53)	*P* Value
Before thrombectomy			
Age (yr) (mean)	59 ± 12	59 ± 14	.93
Sex ratio			
Female	10 (50%)	27 (51%)	.94
Male	10 (50%)	26 (49%)	
Cardiovascular risk factors			
Hypertension	9 (45%)	18 (35%)	.42
Diabetes	2 (10%)	4 (8%)	.67
Hyperlipidemia	8 (40%)	14 (27%)	.28
Smoking	7 (35%)	9 (17%)	.12
Obesity	1 (5%)	7 (13%)	.43
Initial NIHSS			.66
≤10	1 (5%)	6 (11%)	
10–20	11 (55%)	27 (51%)	
>20	8 (40%)	20 (38%)	
ASPECTS			.68
≤7	8 (40%)	24 (45%)	
>7	12 (60%)	29 (55%)	
Side of occlusion			.45
Left	14 (70%)	32 (60%)	
Right	6 (30%)	21 (40%)	
Site of occlusion			.37
ICA	9 (45%)	30 (57%)	
MCA	11 (55%)	23 (43%)	
Dissection	1 (5%)	10 (19%)	.27
IV tPA	11 (55%)	29 (55%)	.98
Onset-to-groin puncture			
≤270 min	5 (25%)	13 (25%)	.98
270 min to 360 min	8 (40%)	20 (38%)	
>360 min	7 (35%)	20 (38%)	
After thrombectomy			
TICI ≥2b–3	14 (70%)	43 (81%)	.34
Lack of spontaneous hyperattenuation on CT	11 (55%)	31 (58%)	.79
NIHSS at day 1			.03
≤10	6 (30%)	29 (55%)	
10–20	9 (45%)	21 (40%)	
>20	5 (25%)	3 (6%)	
mRS ≤2	5 (26%)	33 (65%)	.004

Mechanical Thrombectomy

Mean time from the stroke onset to groin puncture was 255 minutes in patients with SVS and 228 minutes in patients without SVS (P = .98). Successful recanalization (TICI 2b-3) was observed in 78% of patients, in 81% in the SVS+ group and in 70% in the SVS− group (P = .34) (Table 1).

Short-Term Complications and Mortality after MT

A spontaneous hyperattenuation on CT at day 1 after MT was observed in 30 (42%) patients.

Because we performed another CT in the early follow-up only when a clinical worsening occurred, we were not able to distinguish intracranial hemorrhage from contrast extravasation. From these patients, 5 (7%) developed a symptomatic intracranial hemorrhage, 3 of them belonging in the SVS+ group.

The overall short-term mortality was 4% (3 of 73 patients).

Table 2: Patient characteristics, MRI findings before MT, complications, and clinical outcome after MT in patients with good (mRS ≤2) and bad (mRS ≥2) outcomes

	mRS ≤2 (*n* = 38)	mRS >2 (*n* = 32)	*P* Value
Before thrombectomy			
Age (mean)	58 ± 13	61 ± 13	.25
Sex ratio			
Female	21 (55%)	15 (47%)	.43
Male	17 (45%)	17 (53%)	
Cardiovascular risk factors			
Hypertension	12 (32%)	15 (48%)	.16
Diabetes	2 (5%)	4 (13%)	.40
Hyperlipidemia	13 (34%)	8 (26%)	.45
Smoking	6 (16%)	8 (26%)	.37
Obesity	4 (11%)	3 (10%)	.61
Initial NIHSS			
≤10	7 (18%)	0 (0%)	.01
10–20	21 (55%)	16 (50%)	
>20	10 (26%)	16 (50%)	
ASPECTS			.54
≤7	16 (42%)	14 (44%)	
>7	22 (58%)	18 (56%)	
Side of occlusion			
Left	24 (63%)	19 (59%)	.75
Right	14 (37%)	13 (41%)	
Site of occlusion			.24
ICA	17 (45%)	19 (59%)	
MCA	21 (55%)	13 (41%)	
Dissection	5 (13%)	5 (16%)	.52
SVS+	33 (87%)	18 (56%)	.004
IV tPA	22 (58%)	17 (53%)	.81
Onset-to-groin puncture			.59
≤270 min	10 (26%)	7 (22%)	
270 min to 360 min	16 (42%)	11 (34%)	
>360 min	12 (32%)	14 (44%)	
After thrombectomy			
TICI ≥2b–3	34 (89%)	20 (63%)	.01
Lack of spontaneous hyperattenuation on CT	27 (71%)	13 (41%)	.03
NIHSS at day 1			<.001
≤10	31 (82%)	3 (9%)	
10–20	7 (18%)	22 (69%)	
>20	0 (0%)	7 (22%)	

The first patient, a man 85 years of age, had an initial NIHSS score of 24 and SVS−. MT failed with a TICI score of 0. NIHSS score at day 1 was 24; the patient died at day 4. The second patient, an 83-year-old woman with an initial NIHSS score of 10, presented with a SVS + and a dissection. Recanalization failed (TICI = 0), and an early intracranial hemorrhage occurred with an NIHSS score at day 1 of 24. Death occurred at day 6. The third patient was a 75-year-old woman, with an initial NIHSS score of 11, SVS −. She had a TICI 2a, and an NIHSS score at day 1 of 20. Death occurred at day 10.

Clinical Outcome after MT

Three patients were lost for follow-up. For the remaining patients (n = 70), the median NIHSS score (2–27) at day 1 was 12. The functional clinical outcome 3 months after MT was favorable (mRS 0–2) in 38 patients (54%) and poor (mRS 3–6) in 32 (46%) (Table 2). The NIHSS score at day 1 was lower in the SVS+ group than in the SVS− group (P = .03), and the mRS at 3 months was

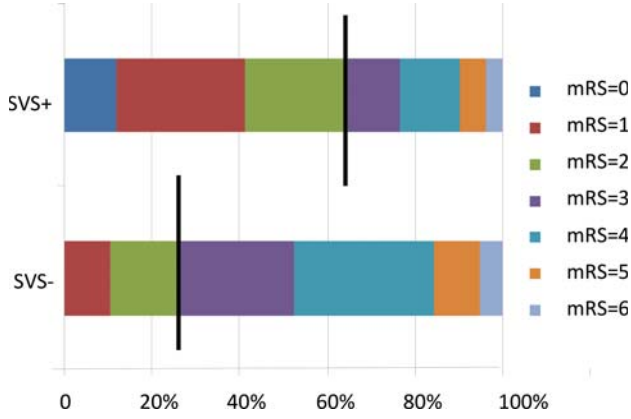

FIG 2. Three-month mRS after MT in patients with SVS (n = 53) and in patients without SVS (n = 20). *Brackets* indicate the percentage of patients achieving a good mRS score of 0–2; mRS scores of 3, 4–5, and 6 represent intermediate neurologic outcome, poor neurologic outcome, and death, respectively.

≤2 in 5 cases (26%) in the SVS− group and in 33 cases (65%) in the SVS+ group (P = .004) (Table 1 and Fig 2).

Predictive Factors of Clinical Outcome at 3 Months

Before MT, only the initial NIHSS score (P = .01) and the presence of SVS+ (P = .004) were significantly associated with a good functional outcome (Table 2). On univariate and multivariate logistic regression analysis, good functional outcome was associated only with the presence of a SVS+ (univariate: OR, 5; 95% CI, 1.6–16.6; P = .01; multivariate: OR, 8.7; 95% CI, 1.1–69.4; P = .04) (Table 3).

After MT, a TICI ≥2b–3 (P = .01), the lack of spontaneous hyperattenuation on CT (P = .03), and a lower NIHSS score at day 1 (≤ 10) (P < .001) were significantly associated with a good functional outcome (Table 2). On univariate analysis, a TICI ≥2b–3 (OR, 5.1; 95% CI, 1.4–17.9; P = .01), the lack of spontaneous hyperattenuation on CT (OR, 3.6; 95% CI, 1.3–9.7; P = .01), and a lower NIHSS score at day 1 (OR, 51.5; 95% CI, 11.8–225.1, P < .001) were significantly associated with a good functional outcome. On multivariate analysis, a lower NIHSS score at day 1 (≤ 10) (OR, 51.9; 95% CI, 8.4–320.5; P < .001) was significantly associated with a good functional outcome (Table 3 and Figs 3 and 4).

DISCUSSION

Our study shows that in patients with ACAS selected for MT by using stent retrievers, SVS is a strong predictor of favorable clinical outcome before treatment. There is no other study focusing on the ability of SVS to predict mRS, to our knowledge

The GRE T2* MR imaging sequence is widely used in clinical routine to rule out brain hemorrhage and detect arterial thrombus.[11] Identification of SVS on these GRE T2* sequences is considered reliable and reproducible because studies have shown excellent inter- and intraobserver agreement.[12] Similarly, our study, excellent intra- and interreader variabilities were observed confirming these results.

Overall, we found that among 73 patients treated for ACAS with MT, SVS was present in 53 patients (73%). This rate of SVS on GRE T2* imaging was in accordance with previous re-

Table 3: Univariate and multivariate logistic regression analyses for factors associated with mRS ≤2

	Univariate			Multivariate		
	OR	95% CI	*P* Value	OR	95% CI	*P* Value
Age	0.9	0.9–1.01	.25	0.9	0.9–1.01	.13
Sex	1.4	0.5–3.6	.48			
Initial NIHSS (≤20 vs >20)	0.8	0.3–2.1	.66			
ASPECTS (≤7 vs >7)	0.9	0.4–2.4	.89			
Dissection	1.2	0.3–4.7	.77			
ICA occlusion	1.8	0.7–4.7	.22			
IV tPA	0.8	0.3–2.1	.69			
Onset-to-groin puncture			.58			
270 min to 6 hr vs >360 min	1.7	0.6–5.0				
≤270 min vs >360 min	1.7	0.5–5.7				
SVS+	5	1.6–16.6	.01[a]	8.7	1.1–69.4	.04[a]
Lack of spontaneous hyperattenuation on CT	3.6	1.3–9.7	.01[a]	3.6	0.7–18.9	013
Day 1 NIHSS (≤10 vs >10)	51.5	11.8–225.1	<.001[a]	51.9	8.4–320.5	<.001[a]
TICI (≥2b vs <2b)	5.1	1.4–17.9	.01[a]	7.1	0.4–112.8	.16

[a] Significant.

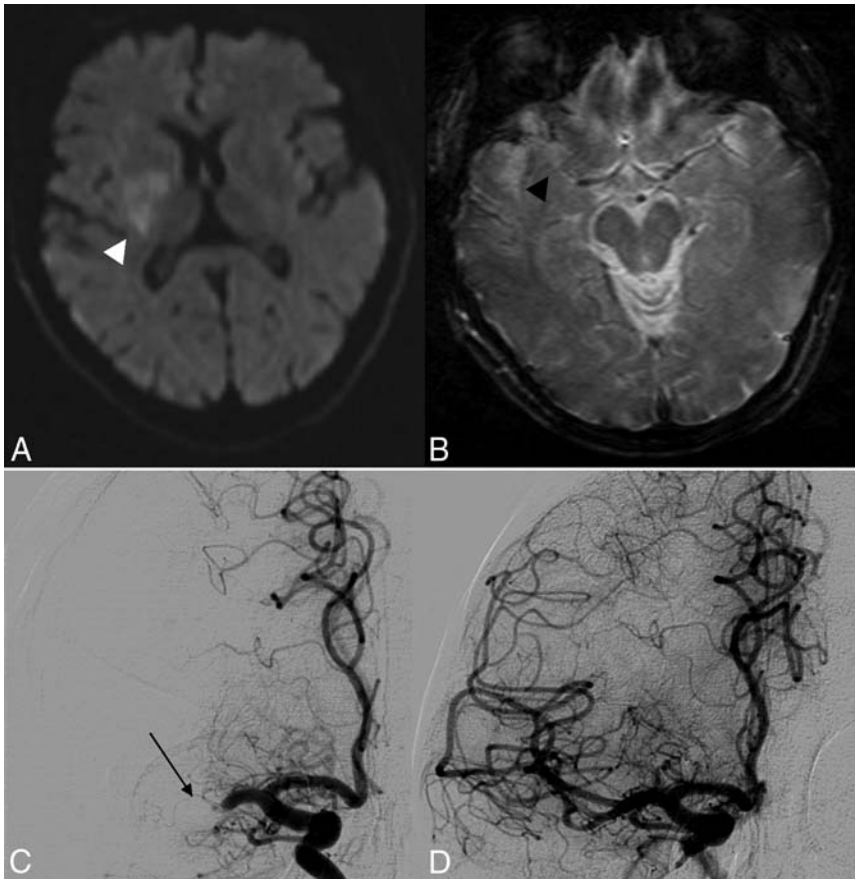

FIG 3. A 52-year-old patient with an initial NIHSS score of 19. At day 1, the NIHSS score was 17 without recovery on the following days. There was no spontaneous hyperattenuation on CT at day 1. At 3 months, mRS was 4. *A*, DWI shows restriction of diffusion with an initial ASPECTS of 7 (*white arrowhead*). *B*, GRE T2* shows a right SVS− occlusion (*black arrowhead*). *C*, Pretreatment DSA shows right MCA occlusion (*thin black arrow*); the time between onset and groin puncture was 270 minutes. *D*, Post-MT DSA shows successful recanalization (TICI 3).

ports.[13,14] The SVS+ is related to the presence of either deoxyhemoglobin, intracellular methemoglobin, or hemosiderin in the red blood cell count of the clot.[15,16] Moreover, red blood cell–rich clots originate from the cardiac system, whereas white thrombi (fibrin-rich) develop on ruptured atherosclerotic plaques.[16] Kimura et al[15] suggested that thrombi that integrate less deoxyhemoglobin, intracellular methemoglobin, or hemosiderin are SVS− and therefore younger. Our hypothesis is that younger thrombi (SVS−) are immediately symptomatic when developed in situ in cerebral atherosclerotic vessels. However, lack of histologic examination in our series does not allow any correlation between imaging findings and thrombus characteristics.

The SVS sign has been studied in the literature on ischemic stroke treated by IV tPA, with an end point defined either on TICI recanalization or mRS. Kimura et al[15,17] focused on the potential of SVS to predict the success of IV tPA in 132 patients with MCA and ICA occlusions. In this retrospective study, they found that the SVS sign was the only independent factor predictive of early recanalization failure after IV tPA. No data were reported regarding the potential of SVS to predict mRS in this study. Similarly, Aoki et al[14] found, in a retrospective study of 158 patients, that SVS+ was a predictor of both recanalization failure and worse mRS at 3 months and that patients with SVS− are better candidates for IV tPA. Regarding endovascular treatment, only 1 study investigated the impact of SVS in patients treated by MT, but it was limited to patients with SVS−.[13] In this study, the authors suggested that patients with SVS− could benefit from MT. However, it was performed on a small population of 11 patients, in which a combination of MT and intra-arterial thrombolysis was used in only 6 of the 11 patients. Our study compared the potential of SVS− and SVS+ to predict recanalization and mRS after MT, combining the use of a stent retriever with simultaneous continuous aspiration from the guiding catheter. We found a trend toward a better rate of recanalization in case of SVS+ compared with SVS− ($P = .34$) and better clinical outcome ($P = .004$), suggesting that as opposed to IV tPA studies, patients with SVS+ are better candidates for MT.

In the emergency context of an ACAS, one needs simple and reproducible biomarkers to decide whether to treat and whether to select either IV tPA or endovascular therapy. The Totaled Health Risks in Vascular Events score, MR imaging–DRAGON score, and ASPECTS help to decide whether to treat with IV tPA on the basis of a prognostic

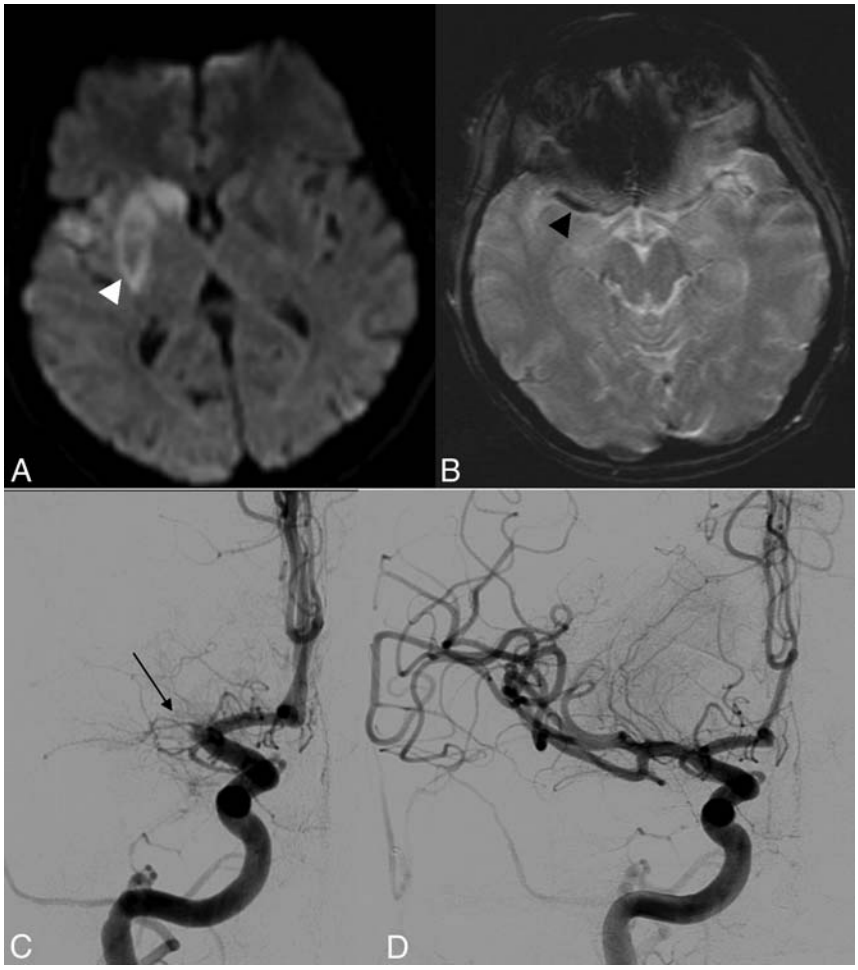

FIG 4. A 48-year-old patient with an initial NIHSS score of 21 and a 3-month mRS of 1. *A*, DWI shows restriction of diffusion with an initial ASPECTS of 6 (*white arrowhead*). *B*, GRE T2* shows a right SVS+ occlusion (*black arrowhead*). *C*, Pretreatment DSA shows a right MCA occlusion (*thin black arrow*); the time between onset and groin puncture was 240 minutes. *D*, Post-MT DSA shows successful recanalization (TICI 3).

algorithm.[18-21] The Diffusion and Perfusion Imaging Evaluation for Understanding Stroke Evolution Study 2 study helps select patients who can benefit from additional endovascular therapy on the basis of diffusion-perfusion mismatch.[22] However, the interpretation of perfusion images is not easily reproducible among centers.[23] Our study demonstrates that a simple and reproducible sign (SVS) on pretreatment MR imaging may help to select patients for MT and could be integrated in future prospective comparative trials.

It may be argued that GRE T2* and MR imaging are time-consuming compared with CT. In the Multicenter Randomized Clinical Trial of Endovascular Treatment for Acute Ischemic Stroke in the Netherlands (MR CLEAN) and the Endovascular Treatment for Small Core and Proximal Occlusion Ischemic Stroke (ESCAPE) trial,[3,4] patients were randomized on the basis of CT. As in other centers, we believe that MR imaging before treatment is, when available, the best imaging technique.[24-26] Although we did not specifically measure the length of each MR imaging in our study, our MR imaging protocol is performed without injection and includes 4 short sequences, with an 11-minute acquisition time. This acquisition time is no longer than a CT scan, with and without contrast agent injection. Our results showing a potential predictive role of SVS support our strategy to recommend the use of MR imaging if available rather than CT in stroke evaluation.

Several limitations might apply to our study. IV tPA performed before MT, age, time between onset and groin puncture, initial stroke severity, stroke territory and subtype, imaging findings, and medical comorbidities might have influenced our recanalization and outcome results.[27-29] However, these were similar between the 2 groups; this similarity made MT the major contributor to the TICI score and underlined the clinical outcome differences between the 2 groups. Even though better mRS scores were observed in the SVS+ group ($P = .004$), TICI scores did not present statistically significant differences between the 2 groups ($P = .34$). This might be related to our small sample size and because patients with SVS− who presented initially with a good post-MT TICI score had delayed rethrombosis. Pre-existent underlying vessel disease, with atherosclerotic plaque or injured intima after numerous thrombectomy attempts, increases the risk of rethrombosis.[30,31] However, because we did not perform a control DSA, we cannot demonstrate the validity of this hypothesis. Moreover, regarding the primary objective of our study, mRS was the most important parameter because it represented the clinical outcome (Figs 3 and 4). The presence of 11 cervical ICA dissections in our cohort might bias the recanalization rate and clinical outcome.[32] In these patients, no significant difference between the SVS+ and SVS− groups was found. Last, a good collateral circulation has been associated with better recanalization, reperfusion, and subsequent better clinical outcomes.[33] We did not assess these collaterals in our study because we only performed a DSA in the concerned occluded vessel and not in the contralateral carotid artery. Although we performed a FLAIR sequence in all patients, it was not possible to assess collaterals because the FLAIR sequence has been well-validated for MCA occlusion only and not for ICA occlusion.[34-36]

CONCLUSIONS

Decision-making regarding patient eligibility for endovascular treatment is complex. There is a need for better selection of patients who might benefit most from endovascular stroke treatment. Our study focused on patients with ACAS treated with MT and showed that in this population, the presence of an SVS on MR imaging is a reliable, reproducible, and simple radiologic bio-

marker that may predict favorable clinical outcome at 3 months after MT. Future prospective studies by using MR imaging and assessing the efficacy of endovascular treatment in ACAS should integrate SVS in their design.

REFERENCES

1. Nichols-Larsen DS, Clark PC, Zeringue A, et al. **Factors influencing stroke survivors' quality of life during subacute recovery.** *Stroke* 2005;36:1480–84 CrossRef Medline
2. Langhorne P, Coupar F, Pollock A. **Motor recovery after stroke: a systematic review.** *Lancet Neurol* 2009;8:741–54 CrossRef Medline
3. Berkhemer OA, Fransen PS, Beumer D, et al. **A randomized trial of intraarterial treatment for acute ischemic stroke.** *N Engl J Med* 2015; 372:11–20 CrossRef Medline
4. Goyal M, Demchuk AM, Menon BK, et al; ESCAPE Trial Investigators. **Randomized assessment of rapid endovascular treatment of ischemic stroke.** *N Engl J Med* 2015;372:1019–30 CrossRef Medline
5. Rovira A, Orellana P, Alvarez-Sabín J, et al. **Hyperacute ischemic stroke: middle cerebral artery susceptibility sign at echo-planar gradient-echo MR imaging.** *Radiology* 2004;232:466–73 CrossRef Medline
6. Flacke S, Urbach H, Keller E, et al. **Middle cerebral artery (MCA) susceptibility sign at susceptibility-based perfusion MR imaging: clinical importance and comparison with hyperdense MCA sign at CT.** *Radiology* 2000;215:476–82 CrossRef Medline
7. Barber PA, Hill MD, Eliasziw M, et al; ASPECTS Study Group. **Imaging of the brain in acute ischaemic stroke: comparison of computed tomography and magnetic resonance diffusion-weighted imaging.** *J Neurol Neurosurg Psychiatry* 2005;76: 1528–33 CrossRef Medline
8. Costalat V, Machi P, Lobotesis K, et al. **Rescue, combined, and stand-alone thrombectomy in the management of large vessel occlusion stroke using the Solitaire device: a prospective 50-patient single-center study: timing, safety, and efficacy.** *Stroke* 2011;42:1929–35 CrossRef Medline
9. Tomsick T. **TIMI, TIBI, TICI: I came, I saw, I got confused.** *AJNR Am J Neuroradiol* 2007;28:382–84 Medline
10. Hacke W, Kaste M, Fieschi C, et al. **Randomised double-blind placebo-controlled trial of thrombolytic therapy with intravenous alteplase in acute ischaemic stroke (ECASS II): Second European-Australasian Acute Stroke Study Investigators.** *Lancet* 1998;352: 1245–51 CrossRef Medline
11. Hodel J, Leclerc X, Khaled W, et al. **Comparison of 3D multi-echo gradient-echo and 2D T2* MR sequences for the detection of arterial thrombus in patients with acute stroke.** *Eur Radiol* 2014;24: 762–69 CrossRef Medline
12. Naggara O, Raymond J, Domingo Ayllon M, et al. **T2* "susceptibility vessel sign" demonstrates clot location and length in acute ischemic stroke.** *PLoS One* 2013;8:e76727 CrossRef Medline
13. Bae YJ, Jung C, Kim JH, et al. **Potential for the use of the Solitaire stent for recanalization of middle cerebral artery occlusion without a susceptibility vessel sign.** *AJNR Am J Neuroradiol* 2014;35:149–55 CrossRef Medline
14. Aoki J, Kimura K, Shibazaki K, et al. **Location of the susceptibility vessel sign on T2*-weighted MRI and early recanalization within 1 hour after tissue plasminogen activator administration.** *Cerebrovasc Dis Extra* 2013;3:111–20 CrossRef Medline
15. Kimura K, Sakamoto Y, Aoki J, et al. **Clinical and MRI predictors of no early recanalization within 1 hour after tissue-type plasminogen activator administration.** *Stroke* 2011;42:3150–55 CrossRef Medline
16. Cho KH, Kim JS, Kwon SU, et al. **Significance of susceptibility vessel sign on T2*-weighted gradient echo imaging for identification of stroke subtypes.** *Stroke* 2005;36:2379–83 CrossRef Medline
17. Kimura K, Sakamoto Y, Iguchi Y, et al. **Clinical and MRI scale to predict very poor outcome in tissue plasminogen activator patients.** *Eur Neurol* 2011;65:291–95 CrossRef Medline
18. Flint AC, Cullen SP, Rao VA, et al; SWIFT and STAR trialists. **The THRIVE score strongly predicts outcomes in patients treated with the Solitaire device in the SWIFT and STAR trials.** *Int J Stroke* 2014; 9:698–704 CrossRef Medline
19. del Zoppo GJ, Higashida RT, Furlan AJ, et al; PROACT Investigators. **PROACT: a phase II randomized trial of recombinant pro-urokinase by direct arterial delivery in acute middle cerebral artery stroke.** *Stroke* 1998;29:4–11 CrossRef Medline
20. Turc G, Apoil M, Naggara O, et al. **Magnetic resonance imaging-DRAGON score: 3-month outcome prediction after intravenous thrombolysis for anterior circulation stroke.** *Stroke* 2013;44: 1323–28 CrossRef Medline
21. Turc G, Aguettaz P, Ponchelle-Dequatre N, et al. **External validation of the MRI-DRAGON score: early prediction of stroke outcome after intravenous thrombolysis.** *PLoS One* 2014;9:e99164 CrossRef Medline
22. Inoue M, Mlynash M, Straka M, et al; DEFUSE 1 and 2 Investigators. **Clinical outcomes strongly associated with the degree of reperfusion achieved in target mismatch patients: pooled data from the Diffusion and Perfusion Imaging Evaluation for Understanding Stroke Evolution studies.** *Stroke* 2013;44:1885–90 CrossRef Medline
23. Dani KA, Thomas RG, Chappell FM, et al. **Systematic review of perfusion imaging with computed tomography and magnetic resonance in acute ischemic stroke: heterogeneity of acquisition and postprocessing parameters—a translational medicine research collaboration multicentre acute stroke imaging study.** *Stroke* 2012;43: 563–66 CrossRef Medline
24. Adams H, Adams R, Del Zoppo G, et al; Stroke Council of the American Heart Association; American Stroke Association. **Guidelines for the early management of patients with ischemic stroke: 2005 guidelines update a scientific statement from the Stroke Council of the American Heart Association/American Stroke Association.** *Stroke* 2005;36:916–23 CrossRef Medline
25. Chalela JA, Kidwell CS, Nentwich LM, et al. **Magnetic resonance imaging and computed tomography in emergency assessment of patients with suspected acute stroke: a prospective comparison.** *Lancet* 2007;369:293–98 CrossRef Medline
26. Wisco D, Uchino K, Saqqur M, et al. **Addition of hyperacute MRI AIDS in patient selection, decreasing the use of endovascular stroke therapy.** *Stroke* 2014;45:467–72 CrossRef Medline
27. Khatri P, Yeatts SD, Mazighi M, et al; IMS III Trialists. **Time to angiographic reperfusion and clinical outcome after acute ischaemic stroke: an analysis of data from the Interventional Management of Stroke (IMS III) phase 3 trial.** *Lancet Neurol* 2014;13:567–74 CrossRef Medline
28. Natarajan SK, Karmon Y, Snyder KV, et al. **Prospective acute ischemic stroke outcomes after endovascular therapy: a real-world experience.** *World Neurosurg* 2010;74:455–64 CrossRef Medline
29. Baker WL, Colby JA, Tongbram V, et al. **Neurothrombectomy devices for the treatment of acute ischemic stroke: state of the evidence.** *Ann Intern Med* 2011;154:243–52 CrossRef Medline
30. Marder VJ, Chute DJ, Starkman S, et al. **Analysis of thrombi retrieved from cerebral arteries of patients with acute ischemic stroke.** *Stroke* 2006;37:2086–93 CrossRef Medline
31. Kalinowski M, Wagner HJ. **Adjunctive techniques in percutaneous mechanical thrombectomy.** *Tech Vasc Interv Radiol* 2003;6:6–13 CrossRef Medline
32. Machi P, Lobotesis K, Maldonado IL, et al. **Endovascular treatment of tandem occlusions of the anterior cerebral circulation with Solitaire FR thrombectomy system: initial experience.** *Eur J Radiol* 2012;81:3479–84 CrossRef Medline

33. Bang OY, Saver JL, Kim SJ, et al. **Collateral flow predicts response to endovascular therapy for acute ischemic stroke.** *Stroke* 2011;42: 693–99 CrossRef Medline
34. Liu W, Xu G, Yue X, et al. **Hyperintense vessels on FLAIR: a useful non-invasive method for assessing intracerebral collaterals.** *Eur J Radiol* 2011;80:786–91 CrossRef Medline
35. Azizyan A, Sanossian N, Mogensen MA, et al. **Fluid-attenuated inversion recovery vascular hyperintensities: an important imaging marker for cerebrovascular disease.** *AJNR Am J Neuroradiol* 2011; 32:1771–75 CrossRef Medline
36. Sanossian N, Saver JL, Alger JR, et al. **Angiography reveals that fluid-attenuated inversion recovery vascular hyperintensities are due to slow flow, not thrombus.** *AJNR Am J Neuroradiol* 2009;30:564–68 CrossRef Medline

An Enhanced Model of Middle Cerebral Artery Occlusion in Nonhuman Primates Using an Endovascular Trapping Technique

F.C. Tong, X. Zhang, D.J. Kempf, M.S. Yepes, F.R. Connor-Stroud, S. Zola, and L. Howell

ABSTRACT

BACKGROUND AND PURPOSE: Current nonhuman primate stroke models are limited by either stroke variability or survivability. A new nonhuman primate stroke model was developed by using endovascular trapping techniques to limit collateral vessels with serial MR imaging and neurologic assessments.

MATERIALS AND METHODS: Eight adult rhesus monkeys (female, 7–13 years of age) underwent MR imaging and Spetzler neurologic assessment followed by endovascular stroke induction consisting of superselective endovascular placement of surgical silk sutures into the right MCA by using a trapping technique. Two initial subjects were euthanized immediately following postocclusion MR imaging. The subsequent 6 subjects recovered and underwent follow-up MR imaging and Spetzler neurologic assessments at 48 hours, with 4 being followed to 96 hours. Stroke infarct volumes were measured, and the longitudinal Spetzler clinical neurologic scores were assessed. The brain tissues were harvested and prepared with hematoxylin-eosin staining.

RESULTS: Focal permanent cerebral ischemia was induced in the targeted right MCA territory in all subjects. The volumes of the ischemic lesions at 6, 48, and 96 hours were 3.18 $\pm$ 1.007 mL (standard error of the mean) ($n = 8$), 6.70 $\pm$ 1.666 mL (standard error of the mean) ($n = 6$), and 7.23 $\pm$ 1.371 mL (standard error of the mean) ($n = 4$). For the survival animals, the immediate postsurgical Spetzler grading score improved from 60.7 at 24 hours to 68.7 at 48 hours.

CONCLUSIONS: We report a trapping modification to an established endovascular suture stroke model that yielded reproducible ischemia and clinically quantifiable neurologic deficits with no strokes in nontarget areas. This technique may be useful in evaluating translational stroke and penumbral imaging research in addition to preclinical testing of neuroprotective therapies.

Rodent stroke research models often fail to translate to human stroke. The use of nonhuman primates has advantages in preclinical translational stroke studies.[1] Gyrencephalic primate species with larger brains demonstrate similar cortical and subcortical organization, with collateral flow that more accurately simulates that in humans.[2] Early nonhuman primate stroke models used baboons with transorbital neurosurgical clipping of the middle cerebral artery to address collateral vessels. The resultant strokes involved both the cortex and deep nuclei, requiring prolonged intensive care limiting the opportunity to perform behavioral assessments.[3]

Recent surgical and endovascular stroke models have used nonhuman primates with less robust collaterals and greater similarity to humans, resulting in more consistent stroke results and allowing postoperative neurologic assessments. Approaches include the surgical introduction of an intraluminal thread from the external carotid artery to the origin of the MCA,[4] injection of autologous clot into the ICA,[5] injection of silk suture into the MCA,[6] transient microcatheter occlusion of the MCA,[7] permanent MCA occlusion with cyanoacrylate,[8] and combined neurosurgical and endovascular thrombin-injection techniques.[9] Ideally, a preclinical cortical stroke model would be reproducible, minimally invasive, minimize pain and distress, spare the deep nuclei, and allow serial behavioral assessments. Neurosurgical approaches typically offer more reliable stroke-induction volumes while giving up at least some ability to track neurologic assessments. Endovascular approaches minimize postoperative impair-

Received December 12, 2014; accepted after revision May 20, 2015.

From the Departments of Radiology and Neurosurgery (F.C.T.), Neurology (M.S.Y.), Psychiatry and Behavioral Sciences (S.Z.. L.H.), School of Medicine, and Yerkes National Primate Research Center (X.Z., D.J.K., F.R.C.-S, S.Z., L.H.), Emory University, Atlanta, Georgia; and Atlanta Veterans Affairs Medical Center (S.Z.), Decatur, Georgia.

This project was supported in part by the National Center for Research Resources and currently by the Office of Research Infrastructure Programs, OD P51OD011132, P51RR000165, DA 031246; and the National Center for Advancing Translational Sciences of the National Institutes of Health under Award Number UL1TR000454.

Please address correspondence to Frank C. Tong, MD, Department of Radiology, Emory University Hospital, 1364 Clifton Rd, NE, Atlanta, GA 30322; e-mail: ftong@emory.edu

http://dx.doi.org/10.3174/ajnr.A4448

ment but have more stroke volume and distribution variability. We describe a new survivable endovascular trapping technique of ischemic stroke induction in the rhesus monkey (*Macaca mulatta*), allowing serial behavioral assessment and relative sparing of the deep nuclei.

MATERIALS AND METHODS

Eight rhesus monkeys were sourced from the Yerkes National Primate Research Center with procedures designed to minimize pain and suffering and approval by the Institutional Animal Care and Use Committee. The subjects were female and ranging from 7 years 9 months to 13 years 7 months and from 6.93 to 9.90 kg. The animals were housed indoors on a standard light-dark cycle individually with routine laboratory diet supplemented by fruits and vegetables with water available at liberty. Two weeks before planned surgery, each subject underwent a routine health and neurologic assessment by using the Spetzler grading scale,[10] followed by general anesthesia and baseline brain MR imaging.

Two initial animals underwent endovascular stroke induction and serial MR imaging examination with immediate sacrifice. Six subsequent subjects underwent stroke induction, MR imaging scanning, and survival with daily follow-up neurologic assessments and MR imaging at 48 hours (6 of 6 subjects) and 96 hours (4 of 6 subjects). Immediately following the final MR imaging, the animals were sacrificed and the brain tissue was preserved in formalin.

Prescan

MR imaging prescanning of the brain was performed at least 7 days before stroke induction. Each subject was anesthetized with 3–5 mg/kg of tiletamine/zolazepam (Telazol) or 10 mg/kg of ketamine followed by induction of general anesthesia by using ~1.0% isoflurane mixed with 100% O_2. The pulse rate, respiratory rate, pulse oximetry, end-tidal gas, blood pressure, and end-tidal CO_2 were monitored and maintained in the normal range.[11] Body temperature was maintained at 37.5°C by a circulating warm-water blanket, and each subject was supine and immobilized with a head holder during scanning. The MR imaging consisted of T1 (magnetization-prepared rapid acquisition of gradient echo sequence with TR = 2500 ms, TE = 3.33 ms, FOV = 96 × 96 mm, flip angle = 8°, TI = 950 ms, matrix = 192 × 192, section thickness = 1 mm, 112 sections, 1 average), T2 (fast spin-echo with TR = 5000 ms, TE = 115 ms, FOV = 96 × 96 mm, 256 × 256 matrix, section thickness = 2 mm, 2 averages), DWI (single-shot EPI sequence with generalized autocalibrating partially parallel acquisition acceleration factor = 3, TR = 5000 ms, TE = 80 ms, FOV = 96 × 96 mm, data matrix = 64 × 64, section thickness = 1.5 mm, 30 directions with b-value = 0, 1000 s/cm^2), FLAIR (TR = 10,000 ms, TI = 2800 ms, TE = 115 ms, FOV = 96 × 96 mm, data matrix = 256 × 256, turbo factor = 17, section thickness = 2 mm, 2 averages), and MRA TOF (FOV = 96 × 96 mm, section thickness = 1 mm, TR = 39 ms, TE = 5.74 ms, single slab = 40 sections, 448 × 448 matrix, single average) on a Magnetom Trio MR imaging scanner (Siemens, Erlangen, German) with an 8-channel phased array knee coil (Invivo Inc. Gainesville, Florida).

Stroke Induction

The subject was brought to the operating suite, where general anesthesia was administered, and placed in a radiolucent head holder. The bilateral groin regions were shaved, prepped, and draped. Sonographic guidance was used to visualize the right common femoral artery. A small skin nick was placed by using a No. 11 scalpel blade, and a 22-ga access needle (French Silhouette Transitionless Micropunture Introducer Set, Cook Incorporated, Bloomington, Indiana) was placed into the right common femoral artery. This was exchanged over a 0.018-inch Cope Mandrel (Cook Medical) by using a 4F microdilator (Cook Medical). A 4F 65-cm Glide catheter (Terumo, Tokyo, Japan) was placed over a 0.035-inch Bentson guidewire (Olympus, Shinjuku, Japan) by using the Seldinger technique, and 500 U of IV heparin was administered. The 4 French non-taper angle Glide catheter (Terumo; Medical Corporation, Somerset, New Jersey) was placed into the right ICA by using C-arm fluoroscopic guidance (Siremobil Compact, Siemens), and positioning was checked with manual injection of iohexol (Omnipaque 300 contrast; GE Healthcare, Piscataway, New Jersey). Anteroposterior and lateral cerebral angiograms were obtained.

An Echelon 10 (Covidien, Irvine, California) microcather was inserted into the targeted M2/M3 branches of the right MCA under roadmap through the 4F diagnostic catheter over a 0.010-inch SilverSpeed microguidewire (Covidien). Superselective angiography was performed by hand injection to verify suitable placement and stroke targeting. Multiple 5-mm segments of 4–0 silk suture (Ethicon, Johnson & Johnson, Cincinnati, Ohio) were injected through the microcatheter until slowing of flow within the desired M3 branch was seen. The microcatheter was partially withdrawn into the M1 segment of the right MCA. A final 10-mm segment of suture was injected, and the microcatheter was removed. Anteroposterior and lateral postangiograms were repeated before catheter removal and administration of 2 mg of protamine sulfate IV. Hemostasis was obtained with manual compression for 15 minutes and a single 4–0 polydioxanone suture (PDS Plus Sutures; Ethicon).

Poststroke Imaging, Neurologic Assessment, and Recovery

Poststroke images were repeated up to 7 hours after stroke induction. The 2 initial subjects were then euthanized, while the subsequent 6 subjects recovered from anesthesia and were monitored. The survival subjects were maintained in an individual cage with veterinary staff supervision and 24-hour continuous video monitoring. Softened routine veterinary chow, fruit, and water were offered. Assessment of overall well-being and Spetzler neurologic deficit scoring were performed daily, with MR imaging scans repeated at 48 hours (6 of 6 subjects) and 96 hours (4 of 6 subjects) poststroke. Two of the 6 survival subjects were sacrificed following the 48-hour scanning at the recommendation of the veterinary staff. MR images were reviewed, and stroke volumes were calculated from DWI by using a threshold of the mean ± 2 SDs with the contralateral side as a reference. Lesion volumes from DWI were derived from the threshold (mean ± 2 SDs) of the DWI intensity on the contralateral side by using custom Matlab scripts (MathWorks, Natick, Massachusetts). Statistical analysis of the

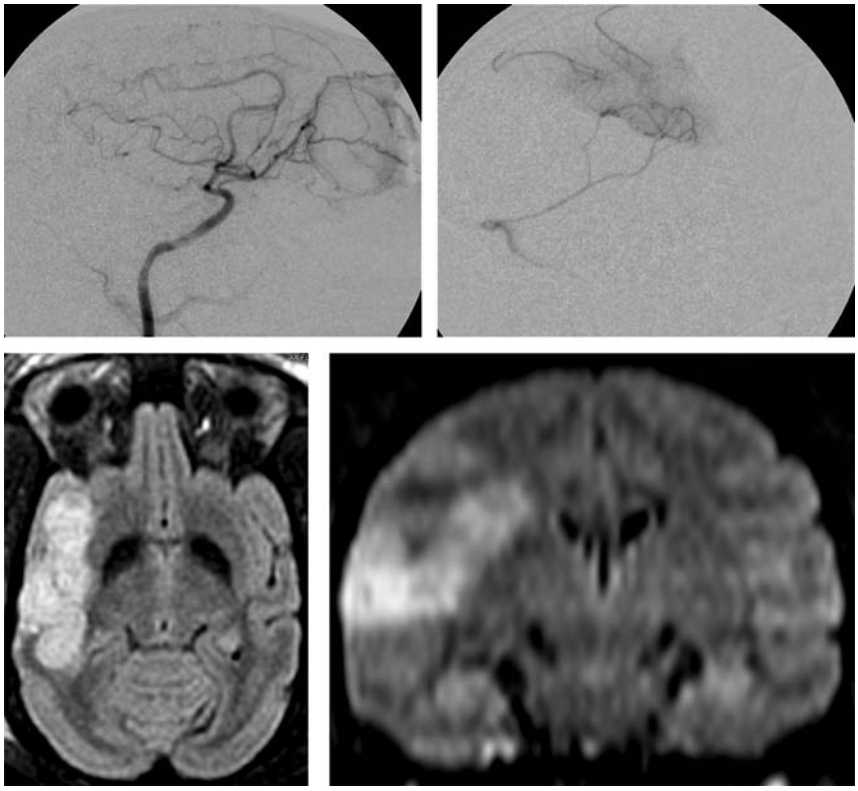

FIG 1. Upper left: lateral angiogram from right internal carotid artery injection. Upper Right: superselective microcatheter angiogram in the right M3 branch. Lower Left: 96-hour FLAIR image showing cortical infarct. Lower Right: 96-hour reconstructed coronal FLAIR image showing cortical infarct with sparing of the basal ganglia.

lesion volumes was performed for the 3 time points by using unpaired 2-tailed *t* tests.

Sacrifice and Histology

After the 96-hour scan, the subjects were euthanized immediately while still under general anesthesia by using IV pentobarbital, 100 mg, and transcardial perfusion with saline solution and 10% buffered formalin following the approved protocols of the Emory Institutional Animal Care and Use Committee. The brains were harvested, immersed in 10% buffered formalin, sectioned onto 50-μm sections, and stained with the hematoxylin-eosin technique.

RESULTS

Stroke Induction

Angiograms demonstrating microcatheter placement during the stroke-induction procedure and resultant MR imaging are shown in Fig 1. All 8 subjects had new strokes in the targeted right MCA territories on the postoperative MR images. Each of the 6 designated survival animals recovered from anesthesia successfully. Immediate and delayed MR imaging showed no stroke or emboli in unintended territories or hemorrhage in any of the subjects.

MR Imaging, Stroke Volumes, and Histology

Stroke volumes were calculated from the 6-, 48-, and 96-hour DWI scans and are summarized in Table 1. The average stroke volume at 6 hours was 3.18 mL ($n = 8$; range, 0.5–8.8 mL) for all 8 subjects. For the 6 survival subjects, the average stroke volume was 6.70 mL at 48 hours ($n = 6$; range, 3.0–12.9 mL) and 7.23 mL at 96 hours ($n = 4$; range, 3.3–9.5 mL). For the 4 subjects that survived to 96 hours, the 48-hour average infarct volume was 6.0 mL ($n = 4$; range, 3.0–10.0 mL). Infarct volume difference reached statistical significance from 6 to 96 hours ($P = .041$; 95% CI, 0.193–7.882) but not from 6 to 48 hours or from 48 to 96 hours. Representative coronal FLAIR images and the corresponding anatomic sections are shown in Fig 2.

Complications

Technical Complications. There were no procedural complications encountered in this series. Specifically, there were no vessel perforations, no unintended embolic stroke, no intracranial hemorrhage, no vessel dissection, and no groin complications.

Clinical Complications/Early Clinical Sacrifice. Two subjects were sacrificed immediately following the 48-hour scan at the recommendation of the veterinary staff in accordance with the end points approved by Institutional Animal Care and Use Committee. RPF6 had a relatively small right basal ganglia and insular stroke and started to manifest seizure activity before the 48-hour scan and was subsequently euthanized immediately after the 48-hour scan. RJJ3 was also euthanized after the 48-hour scan with symptoms of hemineglect, left hemiparesis, and gaze deviation while lying recumbent on the right side unable to maintain upright posture without assistance.

Cognitive Evaluation/Neurologic Assessment

Formal daily neurologic assessments were performed by using the Spetzler neurologic deficit scoring scale shown in Table 2, ranging from 1 to 100 with 70 points for motor function, 20 points for behavior (awareness and aggression), 5 points for visual fields, and 5 points for cranial nerve function. The average scores of the 6 survival subjects are shown in Table 3 and were 60.7 at 6 hours and 68.7 at 48 hours, with the most common score deductions for contralateral motor weakness. With euthanasia of 2 subjects at 48 hours, the remaining 4 subjects that survived to 96 hours had an average neurologic score of 85 at 48 hours (range, 85–85) and 84 at 96 hours (range, 81–84).

DISCUSSION

Collateral Flow and Stroke Models

One of the challenges in using nonhuman primates for modeling human stroke is that the degree of collateral circulation is often more robust compared with human circulation.[2,12] This difference makes the nonhuman primate brain more resistant to stroke

induction, requiring temporary or permanent elimination of collateral vessels. Published series of stroke and temporary ischemia models have used open surgical, endovascular, or mixed techniques,[4,9,13-16] many targeting collateral vessels as a means of decreasing cerebral flow. Management of collateral vessels is critical in achieving cerebral blood flow below the infarct threshold of approximately 0.12 mL/g per minute. While values above this threshold may result in cessation of function, flow rates below this level are required to achieve cell death within the targeted region.[17] With this requirement in mind, our study used older subjects that could potentially have fewer collateral vessels; fewer collateral vessels have been shown in both aging mice[18] and humans with proximal MCA occlusion.[19]

Hudgins and Garcia[20] published an approach in 1970 consisting of orbital enucleation followed by MCA microclip placement to regulate the degree of cerebral ischemia. This method is still used, with the primary drawback being its invasive nature and disallowance of thrombolytics used in current stroke therapy. Another approach used temporary clipping of the bilateral anterior cerebral arteries and MCA for reducing collateral flow,[12] and this approach yielded relatively consistent cortical stroke volumes of approximately 25% of the entire cortical volume. Comparatively, our method is less invasive and avoids the MR imaging artifacts due to surgical clip placement.

A purely endovascular reversible stroke model was published by Jungreis et al[21] by using permanent coiling of the right posterior cerebral artery and temporary balloon occlusion at the junction of the ICA terminus, anterior cerebral artery, and MCA. The reversible nature of this MCA-occlusion model used permanent coil occlusion of the posterior cerebral artery, and the authors did not comment on the actual stroke volumes or survivability. A subsequent study using this model resulted in relatively large infarct volumes with involvement of the basal ganglia in a small nonsurvival study.[22] Our approach offers the advantage of basal ganglia sparing in 7 of 8 subjects and stroke volumes better suited to survivability studies.

Other endovascular models used temporary mechanical catheter occlusion, injection of *n*-butyl-cyanoacrylate or other permanent agents.[8] One disadvantage of these approaches is again inconsistent lesion sizes, though it may reflect similar variation in human stroke. Our endovascular approach resulted in stroke in the targeted territory in 100% of subjects with 100% 48-hour survivability without procedural complications or unintended strokes. However, 2 of the intended survival subjects were euthanized for compassionate rather than medical reasons at the recommendation of the supervising veterinarian.

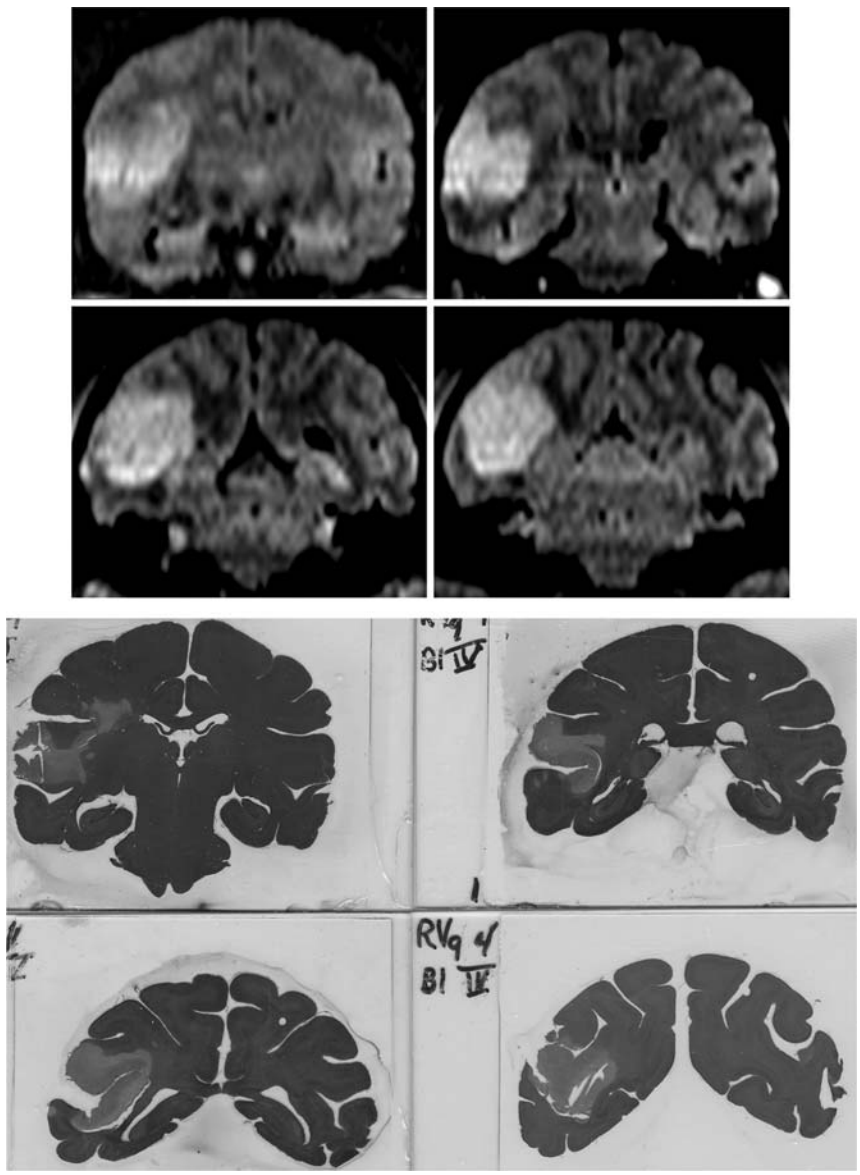

FIG 2. Upper: coronal FLAIR images showing cortical infarction at 96 hours. Lower: corresponding hematoxylin-eosin-stained anatomic sections following sacrifice.

Table 1: Experimental infarct volumes (cc) estimated from the diffusion-weighted images at various time intervals postocclusion

Stroke Timing	RVI3	RCE3	RFP6	RJJ3	RFA5	RRI3	PH1019	RVG4	Average (±SEM)
6 Hours	3.3	8.8	0.6	4.6	4.9	1.6	0.5	1.2	3.18 ± 1.007
48 Hours			3.3	12.9	10.0	3.0	7.2	3.8	6.70 ± 1.666
96 Hours					9.5	3.3	8.6	7.5	7.23 ± 1.371

Note:—SEM indicates standard error of the mean; RV13, RCE3, RFP6, RJJ3, RFA5, RR13, PH1019, RVG4, rhesus monkey subjects.

Stroke Induction and Survivability

RPF6 was the first subject in the survival cohort and developed a small stroke in the right basal ganglia. Postrecovery, the subject developed clinical seizure activity just before the 48-hour MR imaging scan and was euthanized immediately after the scan. The imaging would suggest that the basal ganglia stroke location was the most likely source of the seizure activity. While this type of stroke is not uncommonly seen and routinely supported in human patients, the ability to care for the nonhuman primate in the absence of an intensive care unit–type environment necessitated early sacrifice. Clinically, this was not unexpected because the overall rate of poststroke seizure in human patients ranges from 4.4% to 11.1%,[23,24] with approximately 3.1%[25] developing poststroke seizure within the first 24 hours. Subsequently, the endovascular technique was modified slightly to spare the basal ganglia in the remaining 5 survival subjects, and no additional basal ganglia strokes were observed.

The other 5 survival subjects had purely cortical strokes without basal ganglia involvement and manifested seizure activity with progression of stroke volumes. One survival subject was euthanized for compassionate reasons for symptoms of generalized lethargy and diminished oral intake (an end point approved by Institutional Animal Care and Use Committee). Clinically, the relatively large stroke in this subject is commonly seen and treated in human patients; 15%–20% of patients require hospital care in the intensive care unit.[26] The remaining 4 survival subjects tolerated their strokes well and demonstrated consistent clinical grades on the Spetzler grading scale. There was a trend toward increasing infarct size between the 6- to 48-hour scans and the 48- to 96-hour scans, with only the 6- to 96-hour infarct volume reaching statistical significance. Overall, there was no symptomatic worsening in clinical examination findings from 24 to 48 hours for the survival arm of the study. At the 96-hour mark, the remaining subjects were in no clinical distress, which suggests that they could likely have potentially survived for a longer period. Given our experimental and clinical results, longer survival periods would be facilitated by avoidance of basal ganglia strokes in addition to very large stroke volumes.

Table 2: Spetzler neurologic deficit scoring

Scoring	
Motor function	
Severe hemiparesis	10
Mild hemiparesis	25
Normal strength: favors opposite extremity	55
Normal strength: normal function	70
Behavior	
Death	0
Coma	1
Aware of surroundings: not active	5
Aware of surroundings: moves in response to examiner	15
Normal aggression	20
Ocular and cranial nerve function	
Facial movement: paretic	1
Facial movement: normal	5
Visual field: hemianopic	1
Visual field: normal	5

Table 3: Survival subject neurologic score

Subject	Baseline	24 Hours	48 Hours	96 Hours	Basal Ganglia Involvement	Sxs
RFP6	100	46	51		Yes	Seizures
RJJ3	100	21	21		No	Severe hemiparesis, hemianopsia
RFA5	100	46	85	85	No	
RRI3	100	81	85	85	No	
PH1019	100	85	85	85	No	
RVG4	100	85	85	81	No	
Mean	100	60.7	68.7	84		

Note:—Sxs indicates major symptoms.

Endovascular Trapping and Stroke Accuracy

Embolic silk suture has been described in the treatment of brain AVMs and does not cause significant inflammatory change, making it suitable for use in a permanent stroke model.[27,28] It is deliverable through a microcatheter, is MR imaging–compatible, and has been previously used in the nonhuman primate model, with the injection of very short segments of silk from the proximal MCA with variable clinical and imaging results.[6] Comparatively, our superselective trapping method results in better survivability and more controlled stroke volumes and localization.

Each of the 8 experimental strokes had positive DWI changes located precisely between the selected distal M3 branch and the pullback proximal M1 position of the endovascularly placed microcatheter. Although more technically demanding, placement of the smaller 5-mm suture segments into the distal M3 segment of the MCA effectively eliminates retrograde collateral flow in the MCA branch. Similarly, placement of the proximal 10-mm suture effectively traps the desired MCA segment more precisely than if the suture were injected from the proximal MCA segment.

The need to spare the lenticulostriate arteries was shown by the basal ganglia stroke/seizure in the first survival subject. The endovascular trapping technique was subsequently enhanced with no additional basal ganglia strokes in the remaining 5 survival subjects. First-time seizures occur at a rate of up to 15% in patients with clinical stroke,[29] so it is not unexpected for seizures to occur in our series. However, it is not practical to care for these types of seizures in the animal care environment, and the subject was euthanized to preserve its comfort in compliance with the Institutional Animal Care and Use Committee guidelines. Similarly, the second subject showed symptoms of generalized lethargy and diminished oral uptake that would be within the expected scope of human stroke intermediate level care. Our results suggest enhanced accuracy and stroke yield with better basal ganglia sparing.

CONCLUSIONS

Our endovascular trapping modification of an existing suture-injection stroke model allows rapid poststroke recovery. Accurate neurologic assessments can be performed immediately in a noncritical care setting. This assessment results in improved survivability, basal ganglia sparing, and consistency compared with previously published endovascular methods. Furthermore,

translational thrombolytic or neuroprotective therapies can be evaluated; these evaluations are not possible with open neurosurgery and the resulting confounding postoperative factors. Endovascular trapping offers a greater degree of precision for stroke location and size. Although 1 limitation of our model is that it uses a permanent agent, it could be easily adapted to a temporary occlusion model if a suitable injectable agent were identified.

ACKNOWLEDGMENTS

The authors recognize the contributions of Sudeep Patel, Chunxia Li, Govind Nair, Yumei Yan, Ruth Connelly, Wendy Williamson Coyne, Juliet Brown, Anapatricia Garcia, E. Chris Muly, and Marcelia Maddox.

REFERENCES

1. Stroke Therapy Academic Industry Roundtable (STAIR). **Recommendations for standards regarding preclinical neuroprotective and restorative drug development.** *Stroke* 1999;30:2752–58 CrossRef Medline
2. Cook DJ, Tymianski M. **Nonhuman primate models of stroke for translational neuroprotection research.** *Neurotherapeutics* 2012;9:371–79 CrossRef Medline
3. Nehls DG, Cartwright M, Spetzler RF. **Experimental primate stroke model.** *Neurosurgery* 1986;18:388–89 CrossRef Medline
4. Freret T, Bouet V, Toutain J, et al. **Intraluminal thread model of focal stroke in the non-human primate.** *J Cereb Blood Flow Metab* 2008;28:786–96 CrossRef Medline
5. Yoshikawa T, Akiyoshi Y, Susumu T, et al. **Ginsenoside Rb1 reduces neurodegeneration in the peri-infarct area of a thromboembolic stroke model in non-human primates.** *J Pharmacol Sci* 2008;107:32–40 CrossRef Medline
6. Rodriguez-Mercado R, Ford GD, Xu Z, et al. **Acute neuronal injury and blood genomic profiles in a nonhuman primate model for ischemic stroke.** *Comp Med* 2012;62:427–38 Medline
7. de Crespigny AJ, D'Arceuil HE, Maynard KI, et al. **Acute studies of a new primate model of reversible middle cerebral artery occlusion.** *J Stroke Cerebrovasc Dis* 2005;14:80–87 CrossRef Medline
8. Liu Y, D'Arceuil HE, Westmoreland S, et al. **Serial diffusion tensor MRI after transient and permanent cerebral ischemia in nonhuman primates.** *Stroke* 2007;38:138–45 CrossRef Medline
9. Gauberti M, Obiang P, Guedin P, et al. **Thrombotic stroke in the anesthetized monkey (*Macaca mulatta*): characterization by MRI—a pilot study.** *Cerebrovasc Dis* 2012;33:329–39 CrossRef Medline
10. Spetzler RF, Selman WR, Weinstein P, et al. **Chronic reversible cerebral ischemia: evaluation of a new baboon model.** *Neurosurgery* 1980;7:257–61 CrossRef Medline
11. Li CX, Patel S, Auerbach EJ, et al. **Dose-dependent effect of isoflurane on regional cerebral blood flow in anesthetized macaque monkeys.** *Neurosci Lett* 2013;541:58–62 CrossRef Medline
12. West GA, Golshani KJ, Doyle KP, et al. **A new model of cortical stroke in the rhesus macaque.** *J Cereb Blood Flow Metab* 2009;29:1175–86 CrossRef Medline
13. Cui Y, Takamatsu H, Kakiuchi T, et al. **Neuroprotection by a central nervous system-type prostacyclin receptor ligand demonstrated in monkeys subjected to middle cerebral artery occlusion and reperfusion: a positron emission tomography study.** *Stroke* 2006;37:2830–36 CrossRef Medline
14. Nudo RJ, Larson D, Plautz EJ, et al. **A squirrel monkey model of post-stroke motor recovery.** *ILAR J* 2003;44:161–74 CrossRef Medline
15. Chin Y, Sato Y, Mase M, et al. **Transient decrease in cerebral motor pathway fractional anisotropy after focal ischemic stroke in monkey.** *Neurosci Res* 2010;66:406–11 CrossRef Medline
16. Del Zoppo GJ, Copeland BR, Harker LA, et al. **Experimental acute thrombotic stroke in baboons.** *Stroke* 1986;17:1254–65 CrossRef Medline
17. Sakoh M, Ostergaard L, Rohl L, et al. **Relationship between residual cerebral blood flow and oxygen metabolism as predictive of ischemic tissue viability: sequential multitracer positron emission tomography scanning of middle cerebral artery occlusion during the critical first 6 hours after stroke in pigs.** *J Neurosurg* 2000;93:647–57 CrossRef Medline
18. Faber JE, Zhang H, Lassance-Soares RM, et al. **Aging causes collateral rarefaction and increased severity of ischemic injury in multiple tissues.** *Arterioscler Thromb Vasc Biol* 2011;31:1748–56 CrossRef Medline
19. Arsava EM, Vural A, Akpinar E, et al. **The detrimental effect of aging on leptomeningeal collaterals in ischemic stroke.** *J Stroke Cerebrovasc Dis* 2014;23:421–26 CrossRef Medline
20. Hudgins WR, Garcia JH. **Transorbital approach to the middle cerebral artery of the squirrel monkey: a technique for experimental cerebral infarction applicable to ultrastructural studies.** *Stroke* 1970;1:107–11 CrossRef Medline
21. Jungreis CA, Nemoto E, Boada F, et al. **Model of reversible cerebral ischemia in a monkey model.** *AJNR Am J Neuroradiol* 2003;24:1834–36 Medline
22. Kharlamov A, LaVerde GC, Nemoto EM, et al. **Map2 immunostaining in thick sections for early ischemic stroke infarct volume in non-human primate brain.** *J Neurosci Methods* 2009;182:205–10 CrossRef Medline
23. Graham NS, Crichton S, Koutroumanidis M, et al. **Incidence and associations of poststroke epilepsy: the prospective South London Stroke Register.** *Stroke* 2013;44:605–11 CrossRef Medline
24. Wang G, Jia H, Chen C, et al. **Analysis of risk factors for first seizure after stroke in Chinese patients.** *Biomed Res Int* 2013;2013:702871 CrossRef Medline
25. Szaflarski JP, Rackley AY, Kleindorfer DO, et al. **Incidence of seizures in the acute phase of stroke: a population-based study.** *Epilepsia.* 2008;49:974–81 CrossRef Medline
26. Zazulia AR. **Critical care management of acute ischemic stroke.** *Continuum Lifelong Learning in Neurology* 2009;15:68–82 CrossRef
27. Schmutz F, McAuliffe W, Anderson DM, et al. **Embolization of cerebral arteriovenous malformations with silk: histopathologic changes and hemorrhagic complications.** *AJNR Am J Neuroradiol* 1997;18:1233–37 Medline
28. Dehdashti AR, Muster M, Reverdin A, et al. **Preoperative silk suture embolization of cerebral and dural arteriovenous malformations.** *Neurosurg Focus* 2001;11:e6 Medline
29. Velioğlu SK, Ozmenoğlu M, Boz C, et al. **Status epilepticus after stroke.** *Stroke* 2001;32:1169–72 CrossRef Medline

Optimal Prediction of Carotid Intraplaque Hemorrhage Using Clinical and Lumen Imaging Markers

M.S. McLaughlin, P.J. Hinckley, S.M. Treiman, S.-E. Kim, G.J. Stoddard, D.L. Parker, G.S. Treiman, and J.S. McNally

ABSTRACT

BACKGROUND AND PURPOSE: MR imaging detects intraplaque hemorrhage with high accuracy by using the magnetization-prepared rapid acquisition of gradient echo sequence. Still, MR imaging is not readily available for all patients, and many undergo CTA instead. Our goal was to determine essential clinical and lumen imaging predictors of intraplaque hemorrhage, as indicators of its presence and clues to its pathogenesis.

MATERIALS AND METHODS: In this retrospective cross-sectional study, patients undergoing stroke work-up with MR imaging/MRA underwent carotid intraplaque hemorrhage imaging. We analyzed 726 carotid plaques, excluding vessels with non-carotid stroke sources ($n = 420$), occlusions ($n = 7$), or near-occlusions ($n = 3$). Potential carotid imaging predictors of intraplaque hemorrhage included percentage diameter and millimeter stenosis, plaque thickness, ulceration, and intraluminal thrombus. Clinical predictors were recorded, and a multivariable logistic regression model was fitted. Backward elimination was used to determine essential intraplaque hemorrhage predictors with a thresholded 2-sided $P < .10$. Receiver operating characteristic analysis was also performed.

RESULTS: Predictors of carotid intraplaque hemorrhage included plaque thickness (OR = 2.20, $P < .001$), millimeter stenosis (OR = 0.46, $P < .001$), ulceration (OR = 4.25, $P = .020$), age (OR = 1.11, $P = .001$), and male sex (OR = 3.23, $P = .077$). The final model discriminatory value was excellent (area under the curve = 0.932). This was significantly higher than models using only plaque thickness (area under the curve = 0.881), millimeter stenosis (area under the curve = 0.830), or ulceration (area under the curve= 0.715, $P < .001$).

CONCLUSIONS: Optimal discrimination of carotid intraplaque hemorrhage requires information on plaque thickness, millimeter stenosis, ulceration, age, and male sex. These factors predict intraplaque hemorrhage with high discriminatory power and may provide clues to the pathogenesis of intraplaque hemorrhage. This model could be used to predict the presence of intraplaque hemorrhage when MR imaging is contraindicated.

ABBREVIATIONS: IPH = intraplaque hemorrhage; AUC = area under the curve

For >20 years, stenosis has been the primary predictor of stroke risk from carotid disease based on landmark studies including the North American Symptomatic Carotid Endarterectomy Trial, Asymptomatic Carotid Atherosclerosis Study, and European Carotid Surgery Trial.[1-3] During the past 10 years, advances have been made in MR imaging detection of plaque components, most notably with carotid intraplaque hemorrhage (IPH). Moody et al[4] first reported that high MR imaging signal within the carotid wall was shown to detect complex atheromas. Since that time, carotid IPH has been detectable with high accuracy by using heavily T1-weighted sequences such as magnetization-prepared rapid acquisition of gradient echo.[5] MR imaging–detected carotid IPH is an essential indicator of stroke risk and is independent of stenosis.[6-9] However, MR imaging in general and the MPRAGE sequence specifically may not be available in all clinical settings.

While most reports have correlated IPH with other markers of plaque vulnerability, none have generated a predictive model of IPH based on all available clinical and imaging markers. Many researchers have demonstrated that the likelihood of IPH increases with increasing carotid stenosis.[10] Others have shown that IPH positively correlates with not only stenosis but also plaque volume or

Received January 25, 2015; accepted after revision May 3.

From the Department of Radiology (M.S.M., P.J.H., S.M.T., S.-E.K., D.L.P., G.S.T., J.S.M.), Utah Center for Advanced Imaging Research; Department of Orthopedics (G.J.S.), Study Design and Biostatistics Center, and Department of Surgery (G.S.T.), University of Utah, Salt Lake City, Utah; and Department of Surgery (G.S.T.), VA Salt Lake City Health Care System, Salt Lake City, Utah.

This work was supported by the University of Utah Study Design and Biostatistics Center, with funding in part from the National Center for Research Resources and the National Center for Advancing Translational Sciences, National Institutes of Health, through grant 8UL1TR000105 (formerly UL1RR025764).

Please address correspondence to J. Scott McNally, MD, PhD, University of Utah, Department of Radiology, 30 N 1900 East, Salt Lake City, UT 84132; e-mail: scott.mcnally@hsc.utah.edu

http://dx.doi.org/10.3174/ajnr.A4454

thickness.[11] Recently, CTA-detected ulceration was found to act as a surrogate marker for IPH.[12] These data suggest that IPH can be predicted, with some degree of accuracy, on the basis of lumen imaging findings. In addition, IPH has been found at a higher prevalence in males and in higher age groups.[13] With these findings in mind, the goal of this study was to determine a predictive model of IPH by using available imaging and clinical markers.

We began with the hypothesis that lumen imaging and clinical factors could be used to predict the presence of IPH. Doing so may provide clues to the pathogenesis of IPH. Another potential benefit would be to patients in whom MR imaging is contraindicated. To detect IPH, we used an MPRAGE sequence included as part of a clinical protocol beginning in November 2009. Data were gathered prospectively and analyzed in a retrospective cross-sectional study. We included all patients imaged with carotid MRA by using the MPRAGE sequence for 4.5 years. A multivariable logistic regression model was fitted to determine essential imaging and clinical markers of IPH. This cohort of patients was used previously to determine predictors of carotid-source stroke, which were found to include intraluminal thrombus, intraplaque hemorrhage, plaque thickness, and current smoking.[8]

MATERIALS AND METHODS

Clinical Study Design

Institutional review board approval was obtained for this cross-sectional study on patients undergoing stroke evaluation with brain MR imaging/carotid MRA from November 2009 to January 2014. The carotid MPRAGE sequence was added to the clinical MRA imaging protocol in November 2009. Patients presenting for stroke work-up were scanned within 1 week of symptom onset. From November 2009 to January 2014, 578 patients underwent brain MR imaging/carotid MRA for acute stroke evaluation with the additional MPRAGE sequence. This resulted in 1156 carotid artery–ipsilateral brain image pairs.

Exclusions were determined after reviewing electronic medical records for non-carotid plaque stroke sources: those outside 2 cm above and below the carotid bifurcation. We excluded 430 carotid-brain pairs. These included craniocervical dissections ($n = 118$), atrial fibrillation ($n = 94$), intracardiac/extracardiac shunt ($n = 86$), cardiac thrombus ($n = 26$), recent aortic or mitral valve replacement ($n = 16$), vasculitis ($n = 14$), global hypoxic/ischemic injury ($n = 10$), recent cardiac or neurovascular catheterization ($n = 10$), recent cardiovascular surgery ($n = 8$), dural venous sinus thrombosis ($n = 8$), fibromuscular dysplasia or lupus vasculopathy ($n = 8$), proximal common carotid stenosis >50% ($n = 6$), rheumatic heart disease ($n = 4$), brain neoplasm ($n = 4$), endocarditis ($n = 2$), idiopathic hypertrophic subaortic stenosis ($n = 2$), aortic graft complication ($n = 2$), and distal vessel atherosclerosis ($n = 2$). We also excluded occluded carotid arteries ($n = 7$), and extremely high-grade lesions ($n = 3$). We used 726 carotid plaques in the final analysis. Although a few scans showed mild motion artifacts primarily from swallowing, these artifacts were not sufficient to exclude any carotid arteries from interpretation.

MR Imaging/MRA Clinical Protocol

Images were obtained on 3T and 1.5T MR imaging scanners (Verio and Avanto, Siemens, Erlangen, Germany) with standard head/neck coils. The standard clinical MR imaging/MRA protocol for these patients included brain MR imaging (axial DWI, axial T2-weighted, axial FLAIR, and sagittal T1-weighted images), brain MRA (3D axial TOF), and neck MRA (2D axial TOF, coronal precontrast T1-weighted, and coronal postcontrast arterial and venous phase images). Coronal postcontrast MRA neck images were obtained from the aortic arch through the circle of Willis. Total scan time was approximately 45 minutes, of which the MPRAGE sequence required approximately 5 minutes. In cases in which renal insufficiency precluded intravenous contrast (glomerular filtration rate, < 30 mL/min/1.73 m^2), postcontrast MRA images were replaced with 3D noncontrast TOF with 1-mm section thickness combined with duplex sonography.

Carotid MPRAGE Sequence

MPRAGE parameters were first optimized at 3T and were as follows: 3D, TR/TE/TI = 6.39/2.37/370 ms, flip angle = 15°, FOV = $130 \times 130 \times 48$ mm^3, matrix = $256 \times 256 \times 48$, voxel = $0.5 \times 0.5 \times 1.0$ mm^3, fat saturation, time ~ 5 minutes. The TI was initially optimized for 3T and transferred to 1.5T. An initial TI of approximately 500 ms was chosen on the basis of prior computer simulations at 3T and was adjusted down to a TI of 370 ms to maximize contrast between hemorrhage and inflowing blood in human volunteers as described previously.[14,15] Images were obtained from 20 mm below to 20 mm above the carotid bifurcation at 1.0-mm section thickness. To produce 3D images, we used a secondary phase-encoding gradient in the section-select direction, and measurements for all section-selection phase-encodings were performed with rapid acquisition in each segment.

Carotid Lumen Imaging Markers

All carotid imaging markers were determined by consensus review of 2 reviewers (M.S.M. and J.S.M.), both blinded to findings on brain MR imaging and clinical covariates. In addition, IPH was determined independently of other carotid imaging markers of stroke risk. Lumen markers included percentage diameter stenosis, millimeter stenosis, maximum plaque thickness, ulceration, and intraluminal thrombus.

Percentage diameter stenosis was determined by using the NASCET criteria on contrast MRA. Briefly, the diameter (b) at the level of maximal stenosis and the diameter (a) of the internal carotid artery distal to the stenosis were used to calculate the percentage diameter stenosis by using the formula $[(a - b)/a] \times 100\%$. Carotid stenosis was measured at the narrowest segment of the carotid plaque (b) on the axial images, perpendicular to the long axis of the vessel on multiplanar reformats by using a submillimeter measurement tool (Fig 1*A*). The distal ICA diameter (a) was measured beyond the bulb where the walls are parallel and no longer tapering per NASCET criteria.[16-18] We performed the multivariable regression analysis by using both the NASCET measurement of percentage diameter stenosis $[(a - b)/a] \times 100\%$ and a millimeter stenosis (b) measurement adapted from the millimeter stenosis method first described on CTA.[19] To identify near-occlusions, we excluded an ICA from the percentage stenosis calculation if it met the following criteria: visible bulb stenosis, distal ICA diameter of ≤3 mm, and distal ICA/distal ECA ratio of ≤1.25. These criteria were further adapted from those used by Bartlett et al[18] to recognize

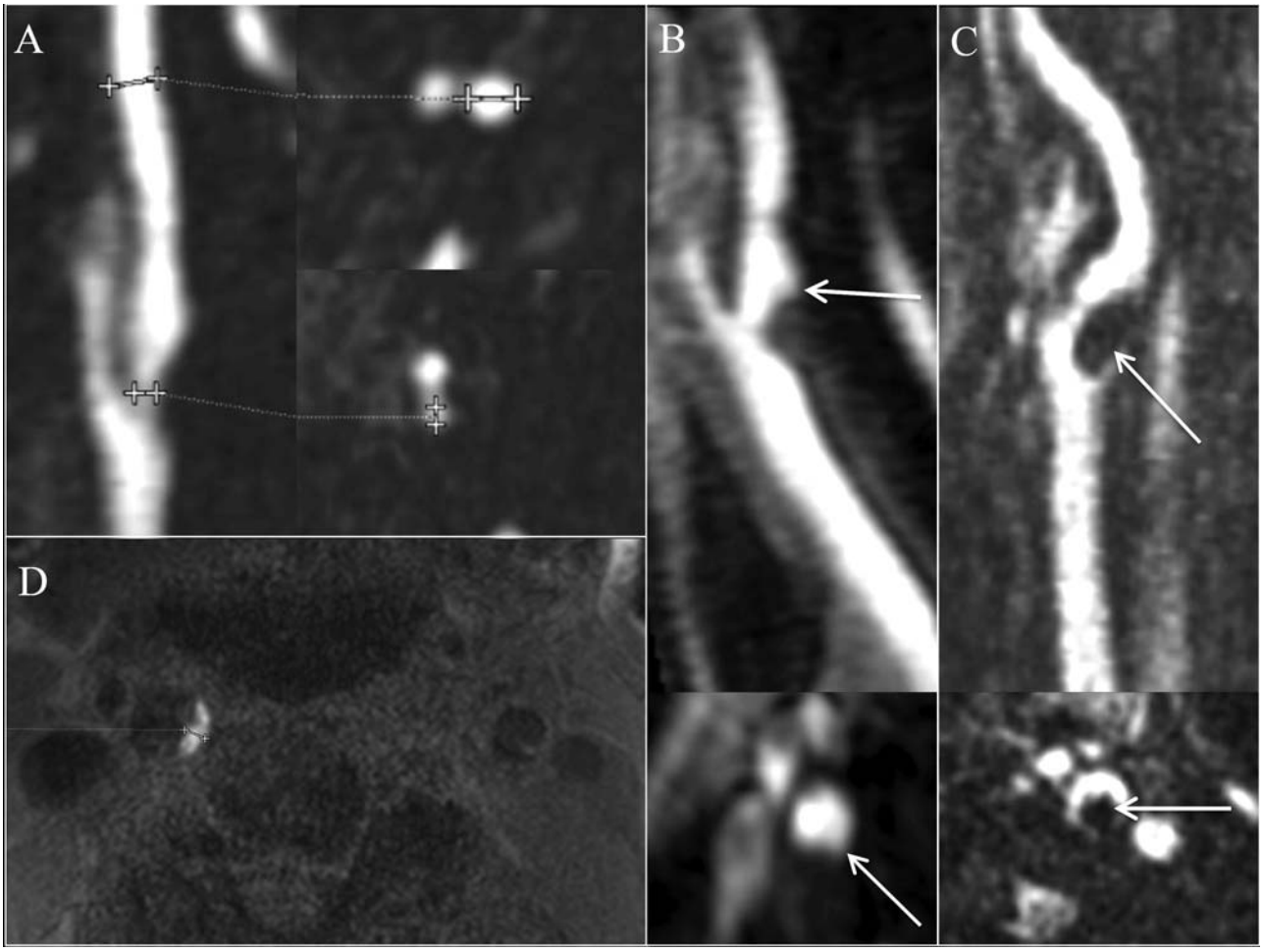

FIG 1. Carotid plaque imaging markers. Stenosis is measured by using percentage diameter stenosis [(*a* − *b*) / *a*] and millimeter stenosis (*b*) (*A, cursors*). The presence of ulceration is determined on contrast MRA images by using a 2-mm measurement threshold (*B, arrow*). Intraluminal thrombus is defined as a filling defect on contrast MRA images (*C, arrow*). IPH is defined by MPRAGE-positive plaque, by using a signal threshold of 2-fold signal intensity over the adjacent sternocleidomastoid muscle (*D*, right carotid artery is MPRAGE-positive; left side of image). Maximum plaque thickness is measured in the transverse plane on 3D MPRAGE image (*D, cursors*).

subtle near-occlusions on CTA and originally adapted from standard conventional angiography.[18,19]

The presence of ulceration was determined on contrast MRA images by using a size threshold of 2 mm as previously described with CTA (Fig 1*B*).[12] Intraluminal thrombus was defined by an intraluminal filling defect on MRA axial reformats, previously described on CTA (Fig 1*C*).[20] In arteries from patients with renal failure (glomerular filtration rate, < 30 mL/min/1.73 m^2; 68/726; or 9.4% of carotid-brain image pairs), the above imaging markers were determined from 3D noncontrast TOF with 1-mm section thickness combined with duplex sonography. Maximum plaque thickness was measured in the transverse plane on MPRAGE images (Fig 1*D*). IPH was defined quantitatively as MPRAGE-positive plaque, with at least 1 voxel demonstrating at least a 2-fold higher signal intensity relative to the adjacent sternocleidomastoid muscle as previously described (Fig 1*D*; right carotid is MPRAGE-positive; left side of image).[6]

Statistical Analysis

A mixed-effects multivariable logistic regression model was used. This model accounted for 2 vessels per patient. The multivariable logistic regression model was fitted for the outcome of carotid IPH, with carotid imaging predictors including percentage diameter stenosis, millimeter stenosis, maximum plaque thickness, ulceration, and intraluminal thrombus. Clinical covariates included age, male sex, diabetes, hypertension, hyperlipidemia, and body mass index. Cardiovascular medication confounders included antihypertension, antiplatelet, anticoagulation, and statin medication classes. In addition, magnet strength (3T or 1.5T) was included as a potential confounder in the logistic regression model. A backward-elimination method was used to determine the final model, in which all remaining predictors had a $P < .10$. Odds ratios and *P* values were reported for each factor alone and for the factors found to be significant from the backward elimination. Receiver operating characteristic comparison analysis was performed to determine the discriminatory value of the final model compared with the following: 1) a model using only plaque thickness, 2) a model using only percentage stenosis as a continuous variable, and 3) a model by using only plaque ulceration. All statistical analyses were performed with STATA, Version 13.1 (StataCorp, College Station, Texas).

RESULTS

Patient Demographics

Patient demographics are listed by vessel and depicted in Table 1.

Carotid Plaque Markers and Stroke Imaging

The carotid imaging features used in this study included the outcome, IPH, and predictors, including percentage diameter stenosis, millimeter stenosis, maximum plaque thickness, ulceration, and intraluminal thrombus as described in the "Materials and Methods" section (Fig 1).

Multivariable Logistic Regression

Intraplaque hemorrhage predictors are depicted in Table 2, with odds ratios adjusted by using multivariable logistic regression.

Final Multivariable Logistic Regression Model

The final model for predictors of carotid IPH is depicted in Table 3. After backward elimination with a threshold of $P < .10$, the remaining significant factors predicting carotid IPH included maximum plaque thickness (OR = 2.20; $P < .001$; 95% confidence interval, 1.50–3.22), millimeter stenosis (OR = 0.46; $P < .001$; 95% CI, 0.30–0.71), ulceration (OR = 4.25; $P = .020$; 95% CI, 1.25–14.4), age (OR = 1.11; $P = .001$; 95% CI, 1.05, 1.18), and male sex (OR = 3.23; $P = .077$; 95% CI, 0.88, 11.9). Note that millimeter stenosis is a measure of the lumen diameter (b) at the level of stenosis described in the "Materials and Methods" section. Thus, carotid plaque with severe stenosis (small b) is associated with IPH, and carotid plaque without stenosis (large b) is not associated with IPH. This difference accounts for the seemingly counterintuitive OR of 0.46 in the final model. In addition, percentage diameter stenosis measured by NASCET is not in the final model due to the nonsignificant $P > .10$ during backward elimination. If, alternatively, millimeter stenosis was not measured, then percentage stenosis would meet the $P < .10$ criteria (full model: OR = 23.7; $P = .003$; 95% CI, 3.00–187.2; final model: OR = 31.0; $P = .001$; 95% CI, 3.89–246.2). However, because we measured both percentage and millimeter

Table 1: Patient demographics

Carotid Stroke Predictor	Demographics by Vessel
Male sex (No./total No.) (%)	387/726 (53.3)
Age (yr) (mean) (SD)	64.2 (15.6)
BMI (mean) (SD) (kg/m^2)	28.4 (6.4)
Smoking (No./total No.) (%)	
Current smoker	138/726 (19.0)
Prior smoker	158/726 (21.8)
Never smoked	430/726 (59.2)
Hypertension (No./total No.) (%)	499/726 (68.7)
Hyperlipidemia (No./total No.) (%)	358/726 (49.3)
Diabetes (No./total No.) (%)	227/726 (31.3)
Cardiovascular medications	
Antihypertension (No./total No.) (%)	412/726 (56.8)
Statins (No./total No.) (%)	316/726 (43.5)
Antiplatelet (No./total No.) (%)	294/726 (40.5)
Anticoagulation (No./total No.) (%)	74/726 (10.2)
Carotid plaque imaging markers	
Stenosis (mean) (SD) (%)	12.2 (23.1)
Mild stenosis (0%–49%) (No./total No.) (%)	647/726 (89.1)
Moderate stenosis (50%–69%) (No./total No.) (%)	45/726 (6.2)
Severe stenosis (70%–99%) (No./total No.) (%)	34/726 (4.7)
Stenosis (mean) (SD) (mm)	4.1 (1.2)
Maximum plaque thickness (mean) (SD) (mm)	3.0 (1.6)
Ulceration (No./total No.) (%)	96/726 (13.2)
Intraluminal thrombus (No./total No.) (%)	19/726 (2.6)
Intraplaque hemorrhage (No./total No.) (%)	65/726 (9.0)
Magnet strength = 3T (No./total No.) (%)	58/726 (8.0)

Note:—BMI indicates body mass index.

Table 2: Multivariable logistic regression

Carotid-IPH Predictor	IPH+ (n = 65)	IPH- (n = 661)	OR	P Value	95% CI	
Cardiovascular risk factors						
Male sex (No./total No.) (%)	55/65 (70.0)	332/661 (50.2)	3.05	.104	0.79	11.7
Age (yr) (mean) (SD)	76.0 (9.7)	63.1 (15.6)	1.11	.003	1.04	1.19
BMI (yr) (mean) (kg/m^2)	26.8 (4.0)	28.5 (6.6)	0.94	.325	0.84	1.06
Smoking (No./total No.) (%)						
Current smoker	12/65 (18.5)	126/661 (19.1)	1.52	.620	0.29	7.88
Prior smoker	24/65 (36.9)	134/661 (20.3)	1.74	.399	0.48	6.36
Hypertension (No./total No.) (%)	46/65 (70.8)	453/661 (68.5)	0.30	.126	0.06	1.41
Hyperlipidemia (No./total No.) (%)	46/65 (70.8)	312/661 (47.2)	1.08	.895	0.33	3.62
Diabetes (No./total No.) (%)	23/65 (35.4)	204/661 (30.9)	1.04	.948	0.33	3.30
Cardiovascular medications (No./total No.) (%)						
Antihypertension	43/65 (66.2)	369/661 (55.8)	2.70	.170	0.65	11.1
Statin	42/65 (64.6)	274/661 (41.5)	1.24	.749	0.33	4.70
Antiplatelet	38/65 (58.5)	256/661 (38.7)	1.07	.922	0.29	3.88
Anticoagulation	7/65 (10.8)	67/661 (10.1)	0.63	.628	0.10	4.00
Carotid plaque imaging markers						
Stenosis (mean) (SD) (%)	46.5 (30.1)	8.9 (19.3)	.09	.409	0.0003	25.7
Stenosis (mean) (SD) (mm)	2.5 (1.5)	4.3 (1.0)	0.31	.052	0.09	1.01
Maximum plaque thickness (mean) (SD) (mm)	5.4 (1.9)	2.8 (1.4)	2.26	<.001	0.09	1.01
Ulceration (No./total No.) (%)	34/65 (52.3)	62/661 (9.4)	4.36	.017	1.30	14.7
Intraluminal thrombus (No./total No.) (%)	5/65 (7.7)	14/661 (2.1)	0.49	.496	0.06	3.85
Magnet strength = 3T (No./total No.) (%)	16/65 (24.6)	42/661 (6.4)	1.63	.544	0.34	7.82

Note:—BMI indicates body mass index.

Table 3: Final model

Carotid IPH predictor	OR	*P* Value	95% CI	
Ulceration	4.25	.020	1.25	14.4
Male sex	3.23	.077	0.88	11.9
Maximum plaque thickness	2.20	<.001	1.50	3.22
Age	1.11	.001	1.05	1.18
Stenosis (mm)	0.46	<.001	0.30	0.71

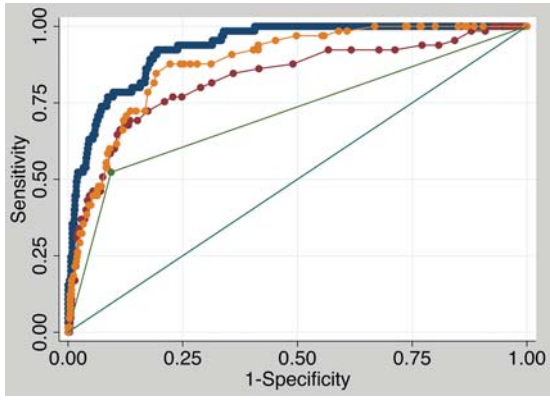

FIG 2. Receiver operating characteristic comparison analysis. The final model IPH discriminatory value is excellent (blue, AUC = 0.932). The final model discriminatory value (blue) is significantly higher than a model with maximum plaque thickness only (yellow, AUC = 0.881, $P < .001$), a model with millimeter stenosis only (red, AUC = 0.830, $P < .001$), and a model with ulceration only (green, AUC = 0.715, $P < .001$).

stenosis and millimeter stenosis was a better predictor of IPH, we have kept it in the final model.

Receiver Operating Characteristic Comparison Analysis

Receiver operating characteristic comparison analysis is shown in Fig 2. The final model discriminatory value was excellent (area under the curve [AUC] = 0.932) and was significantly higher than models using only plaque thickness (AUC = 0.881), only millimeter stenosis (AUC = 0.830), or only ulceration (AUC = 0.715, $P < .001$.

DISCUSSION

Along with other clinical and imaging factors, carotid IPH allows optimal prediction of carotid sources of stroke.[8] Currently, optimal medical treatment for carotid IPH is unknown. It is, therefore, essential to determine predictors of IPH. These predictors could be used as surrogate markers to calculate the likelihood for IPH when MR imaging is not available or is contraindicated. In addition, these predisposing factors may serve as clues to the pathogenesis of IPH.

Lumen imaging is far more often used in the work-up of carotid-source stroke. CTA is also used more frequently than MRA, by as much as 4 times at our institutions. Lumen imaging of stenosis alone provides poor prediction of IPH.[21] This study demonstrates that the presence of lumen markers, such as maximum plaque thickness, millimeter stenosis, and ulceration combined with the patient's age and whether the patient is male, predict carotid IPH with high discriminatory power.

These results indicate that plaque ulceration is strongly predictive of IPH. This finding may be because both ulceration and IPH are markers of unstable plaque and frequently coexist. Alternatively, IPH may predispose to endothelial dysfunction, erosion, and eventual ulceration through proinflammatory effects of iron on reactive oxygen species formation.[22] Plaque ulceration has been previously suggested as a surrogate marker of carotid IPH.[12] Our research argues that while ulceration is an essential predictor of IPH, it cannot fully act as a surrogate for IPH without determining the other clinical and imaging factors in the regression analysis. In the assessment of carotid stroke risk, the presence of ulceration alone could prompt further evaluation with MR imaging to assess IPH.

Our study also shows that maximum plaque thickness is an essential predictor of IPH. This suggests that larger plaques are inherently more unstable and prone to hemorrhage, potentially due to a larger lipid-rich core and/or a higher number or more permeable plaque neovessels. Delayed contrast imaging may allow better detection of lipid-rich cores, and dynamic contrast-enhanced MR imaging may better characterize microvascularity predisposing to IPH.[23,24]

In addition to plaque thickness, millimeter stenosis was a significant indicator of IPH. Most interesting, millimeter stenosis was a better predictor than percentage diameter stenosis, and when both were used, percentage stenosis was eliminated from the final model due to its failure to achieve significance. In support of this, millimeter stenosis has been shown to be a reliable measurement with low interobserver variability.[19] The single measurement of millimeter stenosis is without the inherent variability of NASCET ratios with 2 measurements and variable distal ICA caliber within and between patients.

It is unclear why millimeter stenosis adds further value to plaque thickness in the prediction of IPH. One possibility is that higher degrees of stenosis are associated with further impaired flow dynamics and oscillatory shear stress. In *apolipoprotein E* mice on a Western diet and treated with angiotensin II and carotid ligation, IPH develops in areas of stenosis and low wall shear stress.[25] This is likely related to altered endothelial cell mechanotransduction, because low mean shear stress and oscillatory shear stress lead to endothelial reactive oxygen species formation in cell culture models.[26-29] The shear stress environment at branch points and stenotic vessels could act to sustain IPH through oxidative stress, chronic plaque inflammation, and sustained neovessel permeability.

Of the clinical factors assessed in this study, only patient age and male sex were found to significantly increase the risk of IPH. Both of these factors have been associated with IPH in recent research.[13] Atherosclerosis has long been known to be an age-related phenomenon. Arterial plaques form preferentially at branch points and may be fundamental to the process of aging, having been found in ancient mummies from at least 4 different cultures.[30] Aging may lead to atherosclerosis via increased levels of oxidative stress, DNA damage, mitochondrial dysfunction, and altered balance of cell proliferation and apoptosis.[31]

While the correlation with age is not surprising, what specific role male sex plays in the development of IPH remains to be seen. It has long been known that atherosclerosis incidence is lower in women compared with men, but this increases after menopause, suggesting an atheroprotective effect of estrogen.[32] However, randomized controlled clinical trials have found no benefit to estrogen therapy in cardiovascular disease.[33] Androgens may also benefit male patients through direct action on the vasculature or

through a more favorable lipid profile, though the effect of androgen therapy after andropause is unknown.[34] There may also be sex differences accounting for platelet activation, coagulation, and endothelial cell function that may contribute to plaque inflammation and IPH.[35]

In conclusion, this study identifies lumen markers and clinical factors that can predict IPH with a high discriminatory power. These predictors provide clues to the pathogenesis of IPH. In addition, when MR imaging is not available or contraindicated, these markers may allow clinicians to estimate the likelihood of IPH being present. Identifying patients who are likely to be negative for IPH can prevent unneeded surgeries or interventions. Furthermore, prescreening patients before they undergo MRA can significantly improve the positive or negative predictive value of T1-weighted sequences in identifying IPH. This will be important in recruiting patients for future studies aimed at determining optimal IPH treatment.

CONCLUSIONS

Optimal prediction of carotid IPH is achieved by using information on maximum plaque thickness, millimeter stenosis, ulceration, patient age, and male sex. These factors can be used to determine IPH with a high discriminatory power and may provide clues to the pathogenesis of IPH. Together, they may also be used to determine whether IPH is present in patients in whom MR imaging is contraindicated.

Disclosures: Michael S. McLaughlin—*RELATED*: *Grant*: National Center for Research Resources and the National Center for Advancing Translational Sciences, National Institutes of Health,* *Comments*: grant 8UL1TR000105 (formerly UL1RR025764). J. Scott McNally—*RELATED*: *Grant*: Radiological Society of North America Research Scholar Grant 2014–2016.* *Money paid to the institution.

REFERENCES

1. North American Symptomatic Carotid Endarterectomy Trial Collaborators. **Beneficial effect of carotid endarterectomy in symptomatic patients with high-grade carotid stenosis.** *N Engl J Med* 1991;325:445–53 CrossRef Medline
2. **Endarterectomy for asymptomatic carotid artery stenosis: Executive Committee for the Asymptomatic Carotid Atherosclerosis Study.** *JAMA* 1995;273:1421–28 CrossRef Medline
3. **Randomised trial of endarterectomy for recently symptomatic carotid stenosis: final results of the MRC European Carotid Surgery Trial (ECST).** *Lancet* 1998;351:1379–87 CrossRef Medline
4. Moody AR, Murphy RE, Morgan PS, et al. **Characterization of complicated carotid plaque with magnetic resonance direct thrombus imaging in patients with cerebral ischemia.** *Circulation* 2003;107:3047–52 CrossRef Medline
5. Ota H, Yarnykh VL, Ferguson MS, et al. **Carotid intraplaque hemorrhage imaging at 3.0-T MR imaging: comparison of the diagnostic performance of three T1-weighted sequences.** *Radiology* 2010;254:551–63 CrossRef Medline
6. Yamada N, Higashi M, Otsubo R, et al. **Association between signal hyperintensity on T1-weighted MR imaging of carotid plaques and ipsilateral ischemic events.** *AJNR Am J Neuroradiol* 2007;28:287–92 Medline
7. Takaya N, Yuan C, Chu B, et al. **Association between carotid plaque characteristics and subsequent ischemic cerebrovascular events: a prospective assessment with MRI—initial results.** *Stroke* 2006;37:818–23 CrossRef Medline
8. McNally JS, McLaughlin MS, Hinckley PJ, et al. **Intraluminal thrombus, intraplaque hemorrhage, plaque thickness, and current smoking optimally predict carotid stroke.** *Stroke* 2015;46:84–90 CrossRef Medline
9. McNally JS, Kim SE, Yoon HC, et al. **Carotid magnetization-prepared rapid acquisition with gradient-echo signal is associated with acute territorial cerebral ischemic events detected by diffusion-weighted MRI.** *Circ Cardiovasc Imaging* 2012;5:376–82 CrossRef Medline
10. Sun J, Song Y, Chen H, et al. **Adventitial perfusion and intraplaque hemorrhage: a dynamic contrast-enhanced MRI study in the carotid artery.** *Stroke* 2013;44:1031–36 CrossRef Medline
11. Zhao X, Underhill HR, Zhao Q, et al. **Discriminating carotid atherosclerotic lesion severity by luminal stenosis and plaque burden: a comparison utilizing high-resolution magnetic resonance imaging at 3.0 Tesla.** *Stroke* 2011;42:347–53 CrossRef Medline
12. U-King-Im JM, Fox AJ, Aviv RI, et al. **Characterization of carotid plaque hemorrhage: a CT angiography and MR intraplaque hemorrhage study.** *Stroke* 2010;41:1623–29 CrossRef Medline
13. Zhao XQ, Hatsukami TS, Hippe DS, et al; AIM-HIGH Carotid MRI Sub-study Investigators. **Clinical factors associated with high-risk carotid plaque features as assessed by magnetic resonance imaging in patients with established vascular disease (from the AIM-HIGH Study).** *Am J Cardiol* 2014;114:1412–19 CrossRef Medline
14. Zhu DC, Ferguson MS, DeMarco JK. **An optimized 3D inversion recovery prepared fast spoiled gradient recalled sequence for carotid plaque hemorrhage imaging at 3.0 T.** *Magn Reson Imaging* 2008;26:1360–66 CrossRef Medline
15. Hadley JR, Roberts JA, Goodrich KC, et al. **Relative RF coil performance in carotid imaging.** *Magn Reson Imaging* 2005;23:629–39 CrossRef Medline
16. **North American Symptomatic Carotid Endarterectomy Trial: methods, patient characteristics, and progress.** *Stroke* 1991;22:711–20 CrossRef Medline
17. Fox AJ. **How to measure carotid stenosis.** *Radiology* 1993;186:316–18 CrossRef Medline
18. Bartlett ES, Walters TD, Symons SP, et al. **Quantification of carotid stenosis on CT angiography.** *AJNR Am J Neuroradiol* 2006;27:13–19 Medline
19. Fox AJ, Eliasziw M, Rothwell PM, et al. **Identification, prognosis, and management of patients with carotid artery near occlusion.** *AJNR Am J Neuroradiol* 2005;26:2086–94 Medline
20. Menon BK, Singh J, Al-Khataami A, et al; Calgary CTA Study Group. **The donut sign on CT angiography: an indicator of reversible intraluminal carotid thrombus?** *Neuroradiology* 2010;52:1055–56 CrossRef Medline
21. Anzidei M, Napoli A, Zaccagna F, et al. **Diagnostic accuracy of colour Doppler ultrasonography, CT angiography and blood-pool-enhanced MR angiography in assessing carotid stenosis: a comparative study with DSA in 170 patients.** *Radiol Med* 2012;117:54–71 CrossRef Medline
22. Buttari B, Profumo E, Businaro R, et al. **Oxidized haemoglobin-driven endothelial dysfunction and immune cell activation: novel therapeutic targets for atherosclerosis.** *Curr Med Chem* 2013;20:4806–14 CrossRef Medline
23. Kerwin WS, O'Brien KD, Ferguson MS, et al. **Inflammation in carotid atherosclerotic plaque: a dynamic contrast-enhanced MR imaging study.** *Radiology* 2006;241:459–68 CrossRef Medline
24. Mendes J, Parker DL, McNally S, et al. **Three-dimensional dynamic contrast enhanced imaging of the carotid artery with direct arterial input function measurement.** *Magn Reson Med* 2014;72:816–22 CrossRef Medline
25. Cheng C, Tempel D, van Haperen R, et al. **Atherosclerotic lesion size and vulnerability are determined by patterns of fluid shear stress.** *Circulation* 2006;113:2744–53 CrossRef Medline
26. McNally JS, Davis ME, Giddens DP, et al. **Role of xanthine oxidoreductase and NAD(P)H oxidase in endothelial superoxide production in response to oscillatory shear stress.** *Am J Physiol Heart Circ Physiol* 2003;285:H2290–97 CrossRef Medline

27. Davies PF, Polacek DC, Shi C, et al. **The convergence of haemodynamics, genomics, and endothelial structure in studies of the focal origin of atherosclerosis.** *Biorheology* 2002;39:299–306 Medline
28. Pedersen EM, Oyre S, Agerbaek M, et al. **Distribution of early atherosclerotic lesions in the human abdominal aorta correlates with wall shear stresses measured in vivo.** *Eur J Vasc Endovasc Surg* 1999; 18:328–33 CrossRef Medline
29. Wentzel JJ, Kloet J, Andhyiswara I, et al. **Shear-stress and wall-stress regulation of vascular remodeling after balloon angioplasty: effect of matrix metalloproteinase inhibition.** *Circulation* 2001;104:91–96 CrossRef Medline
30. Clarke EM, Thompson RC, Allam AH, et al. **Is atherosclerosis fundamental to human aging? Lessons from ancient mummies.** *J Cardiol* 2014;63:329–34 CrossRef Medline
31. Sobenin IA, Zhelankin AV, Sinyov VV, et al. **Mitochondrial aging: focus on mitochondrial DNA damage in atherosclerosis—a mini-review.** *Gerontology* 2015;61:343–49 CrossRef Medline
32. Akishita M, Yu J. **Hormonal effects on blood vessels.** *Hypertens Res* 2012;35:363–69 CrossRef Medline
33. Howard BV, Rossouw JE. **Estrogens and cardiovascular disease risk revisited: the Women's Health Initiative.** *Curr Opin Lipidol* 2013;24: 493–99 CrossRef Medline
34. Traish AM, Kypreos KE. **Testosterone and cardiovascular disease: an old idea with modern clinical implications.** *Atherosclerosis* 2011; 214:244–48 CrossRef Medline
35. Roy-O'Reilly M, McCullough LD. **Sex differences in stroke: the contribution of coagulation.** *Exp Neurol* 2014;259:16–27 CrossRef Medline

Comparison of Inner Ear Contrast Enhancement among Patients with Unilateral Inner Ear Symptoms in MR Images Obtained 10 Minutes and 4 Hours after Gadolinium Injection

T.Y. Kim, D.W. Park, Y.J. Lee, J.Y. Lee, S.H. Lee, J.H. Chung, and S. Lee

ABSTRACT

BACKGROUND AND PURPOSE: Recently 4-hour delayed-enhanced 3D-FLAIR MR imaging has been used in pathophysiologic analysis of the inner ear in many auditory diseases, including sudden sensorineural hearing loss, but comparison among different time points is not clear in patients with unilateral inner ear symptoms. We compared the signal-intensity ratios of the inner ears in patients with unilateral inner ear symptoms on 10-minute delayed-enhanced and 4-hour delayed-enhanced 3D-FLAIR MR images after IV gadolinium injection.

MATERIALS AND METHODS: The 10-minute delayed-enhanced and 4-hour delayed-enhanced 3D-FLAIR MR images were retrospectively analyzed. Signal-intensity ratios between the cerebellum and inner ear structures, such as the cochleae, vestibules, and vestibulocochlear nerve were assessed. Multiple comparisons were performed.

RESULTS: Signal-intensity ratios of the affected cochleae, vestibules, and vestibulocochlear nerve were higher than those of unaffected sides in both 10-minute delayed-enhanced and 4-hour delayed-enhanced images. At the affected side, signal-intensity ratios of the vestibulocochlear nerve were higher in patients with nonsudden sensorineural hearing loss than in those with sudden sensorineural hearing loss on both 10-minute delayed-enhanced and 4-hour delayed-enhanced images. The signal-intensity ratios of some affected inner ear structures were higher than those of the unaffected sides in a group of 30 patients with sudden sensorineural hearing loss and 20 patients with nonsudden sensorineural hearing loss on 10-minute delayed-enhanced and 4-hour delayed-enhanced images.

CONCLUSIONS: Signal-intensity ratios of the inner ear show statistically significant increases in many diseases, especially neuritis, in 10-minute delayed-enhanced and 4-hour delayed-enhanced images. The 4-hour delayed-enhanced images may be superior in neural inflammatory–dominant conditions, while 10-minute delayed-enhanced images may be superior in neural noninflammatory–dominant conditions.

ABBREVIATIONS: sSNHL = sudden sensorineural hearing loss; nsSNHL = nonsudden sensorineural hearing loss

3D fluid-attenuated inversion recovery MR imaging has recently been applied to the inner ear to investigate inner ear pathology. The increased signal intensity of diseased inner ears can also be observed on 3D-FLAIR imaging after intravenous gadolinium injection. This technique is useful for the pathophysiologic analysis of the inner ear in many auditory diseases, such as sudden sensorineural hearing loss (sSNHL), cholesteatoma, cochlear otosclerosis, and vestibular schwannoma.[1-4] Compared with intratympanic gadolinium injection, 3D-FLAIR MR imaging after IV gadolinium injection is less invasive and enables observation of the bilateral cochleae and other inner ear structures.[5]

The signal-intensity ratio of the inner ear to other parts of the brain allows semiquantitative expression of the signal intensity and may be useful for comparing results among patients or among ears. Recent articles have reported that the signal-intensity ratio of the inner ear and other parts of the brain is useful in patients with sudden deafness, Ménière disease, and vestibular schwannoma.[4,6-8]

The signal-intensity ratio of the inner ear and brain stem may indicate disruption of the blood-labyrinthine barrier in patients with inner ear disease with 4-hour enhancement after gadolinium injection.[7] To our knowledge, the difference in inner ear signal intensity between 10-minute and 4-hour delayed MRI has not

Received February 22, 2015; accepted after revision May 2.

From the Departments of Radiology (T.Y.K., D.W.P., S.L.) and Otolaryngology-Head and Neck Surgery (S.H.L., J.H.C.), Hanyang University Guri Hospital, Guri, Republic of Korea; and Department of Radiology (Y.J.L., J.Y.L.), Hanyang University Hospital, Seoul, Republic of Korea.

Paper previously presented in part as a scientific poster at: Annual Meeting of the Radiological Society of North America, November 30 to December 5, 2014; Chicago, Illinois; and as a scientific exhibition at: Annual Meeting of the Korean Congress of Radiology, October 8–11, 2014; Seoul, Republic of Korea.

Please address correspondence to Dong Woo Park, MD, Department of Radiology, College of Medicine, Hanyang University, Guri Hospital, 153 Gyeongchun-ro, Guri 471-701, Republic of Korea; e-mail: dwpark@hanyang.ac.kr

http://dx.doi.org/10.3174/ajnr.A4439

been evaluated in most patients with unilateral symptoms, however, including those with sSNHL.

The purpose of this study was to compare signal intensities of the inner ear among patients with unilateral symptomatic ear diseases. Comparisons were made between the affected and unaffected sides, between patients with sSNHL and nonsudden sensorineural hearing loss (nsSNHL), and between 10-minute and 4-hour delayed intravenous gadolinium-enhanced 3D-FLAIR MR imaging.

MATERIALS AND METHODS

Patients

From May 2012 to October 2013, 60 patients who presented with inner ear symptoms and underwent contrast-enhanced 3T temporal MRI were enrolled in our study. The MR imaging data and the electronic medical records of the 60 patients (120 ears) were then retrospectively analyzed. Our institutional review board approved this study, and informed consent was waived due to the retrospective nature of the study.

Ten patients were excluded from the study because they did not have lateralized symptoms, including 4 patients with nonspecific dizziness, 3 patients with benign paroxysmal positional vertigo, and 3 patients with other bilateral symptoms.

The study therefore included 50 subjects with lateralizing inner ear symptoms, including hearing loss, tinnitus, ear fullness, nystagmus, and vertigo. Patients underwent 3D-FLAIR MR imaging with 10-minute and 4-hour delayed intravenous gadolinium enhancement (Fig 1).

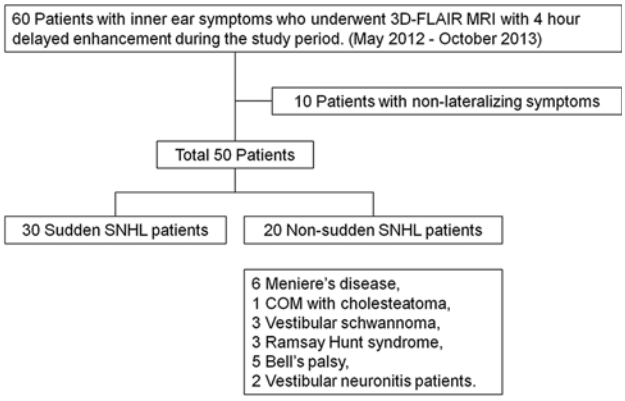

FIG 1. Flowchart shows inclusion and exclusion criteria applied for the collection and composition of the study group. COM indicates chronic otitis media.

Table 1: Patient characteristics

	No. (%) of patients
Sex	
Male	17 (34)
Female	33 (66)
Age (yr) (mean ± SD)	45.6 ± 15.4
Laterality of symptoms	
Right	22 (44)
Left	28 (56)

The patient group consisted of 17 men and 33 women, with ages ranging from 8 years to 72 years (mean age, 45.6 years). There were 22 right symptomatic ears and 28 left symptomatic ears (Table 1).

sSNHL is defined as a >30-dB hearing loss occurring in at least 3 contiguous frequencies in <72 hours without obvious cause.

The patient population consisted of 30 patients with sSNHL and 20 with nsSNHL. Patients with nsSNHL included the following: 6 (12% of 50 total patients) with Ménière disease, 1 (2%) with chronic otitis media with cholesteatoma, 3 (6%) with vestibular schwannoma, 3 (6%) with Ramsay Hunt syndrome, 5 (10%) with Bell palsy, and 2 (4%) with vestibular neuronitis. The patients clinically diagnosed with Bell palsy or Ramsay Hunt syndrome were included because they had combined hearing loss.

MR Imaging Protocol

All scans were obtained on a 3T MR imaging scanner (Achieva 3T; Philips Healthcare, Best, the Netherlands) by using a receive-only 32-channel phased array coil. Double-dose (0.2-mmol/kg) gadolinium-DTPA (Bono-I; CMS, Korea) was used to evaluate the pathophysiology analysis of the inner ear.

The images obtained included the following: pre- and postenhanced T1WI; 3D thin-section proton attenuation images (0.3- to 0.6-mm thickness); whole-brain FLAIR images; and pre-, 10-minute, and 4-hour delayed-enhanced FLAIR volume isotropic turbo spin-echo acquisition images.

The parameters for 3D-FLAIR are summarized in Table 2.

MR Imaging Evaluation and Statistical Analysis

Circular 0.6-mm^2 ROIs were determined within the basal turn of the cochlea, vestibule, cochlear and vestibular nerves in the labyrinth, and the cisternal segment of the trigeminal nerve. ROIs were examined with 10-minute and 4-hour delayed 3D FLAIR MR imaging after an IV gadolinium injection. Circular 10-mm^2 ROIs of the Meckel cave were also measured (Fig 2). Circular 50-mm^2 ROIs of the medulla oblongata and cerebellar white matter were obtained at the level of the internal acoustic meatus. Inner ear signal-intensity ratios were then bilaterally estimated as follows: cochlea/medulla, vestibule/medulla, vestibulocochlear nerve/medulla, cisternal segment of trigeminal nerve/medulla, and the Meckel cave of the trigeminal nerve/medulla.

Two radiologists who were blinded to patient information measured the ROIs. Every ROI was examined twice for each patient on different days to ensure the reliability of the signal intensity and diminish measurement error. The signal intensities of the 4 measurements were averaged for analysis. Differences between radiologists were then resolved by consensus.

Circular 50-mm^2 ROIs for the cerebellar white matter of both cerebellar hemispheres at identical sections of the medulla oblongata were obtained on each image. The signal-intensity ratio of the cerebellar white matter to the medulla oblongata was calculated for each image. Cerebellar white matter/medulla ratios were then bilaterally estimated to evaluate the uniformity of the magnetic field.

Table 2: The parameters for 3D-FLAIR MRI

TR (ms)	TE (ms)	Flip Angle (degree)	Section Orientation	Section Thickness (mm)	FOV (mm)	Voxel Size (mm)	NEX	Acquisition Time (min:sec)
8000	261	90	Axial	1.2	180 × 180	0.8 × 0.8 × 0.6	2	4:48

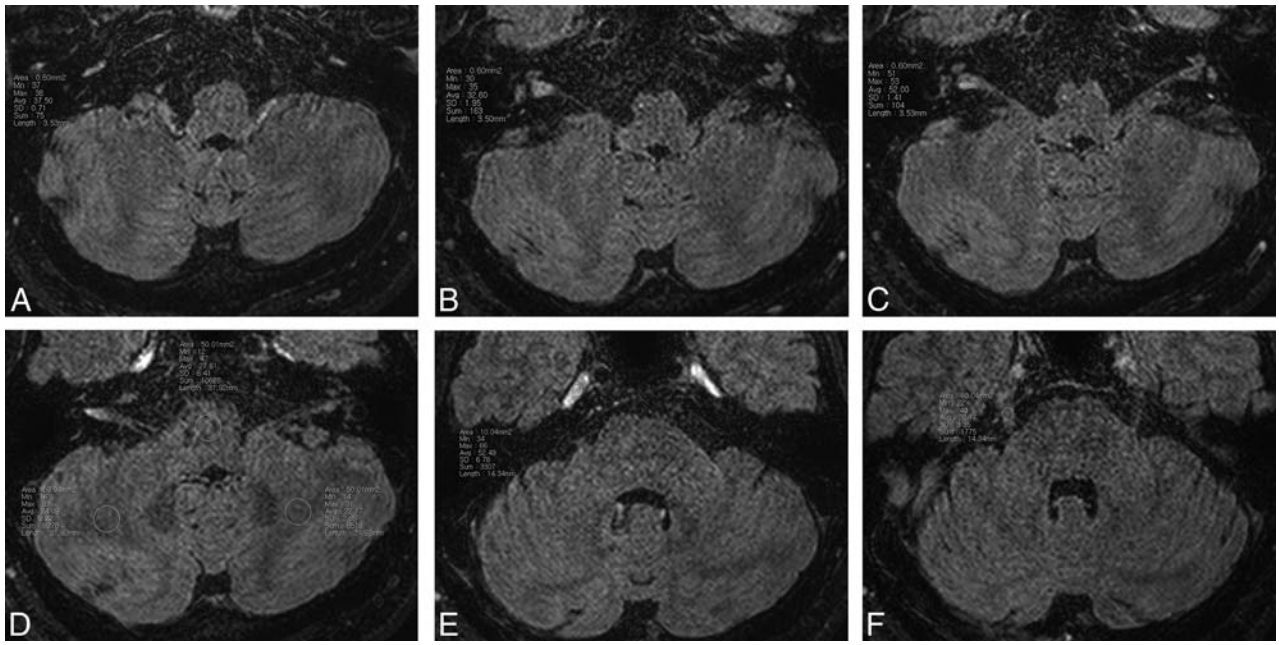

FIG 2. Example of the ROIs on 4-hour delayed contrast-enhanced 3D-FLAIR images: cochlear (*A*), vestibule (*B*), vestibulocochlear nerve (*C*), medulla and cerebellar white matter (*D*), the Meckel cave of the trigeminal nerve (*E*), and the cisternal segment of the trigeminal nerve (*F*).

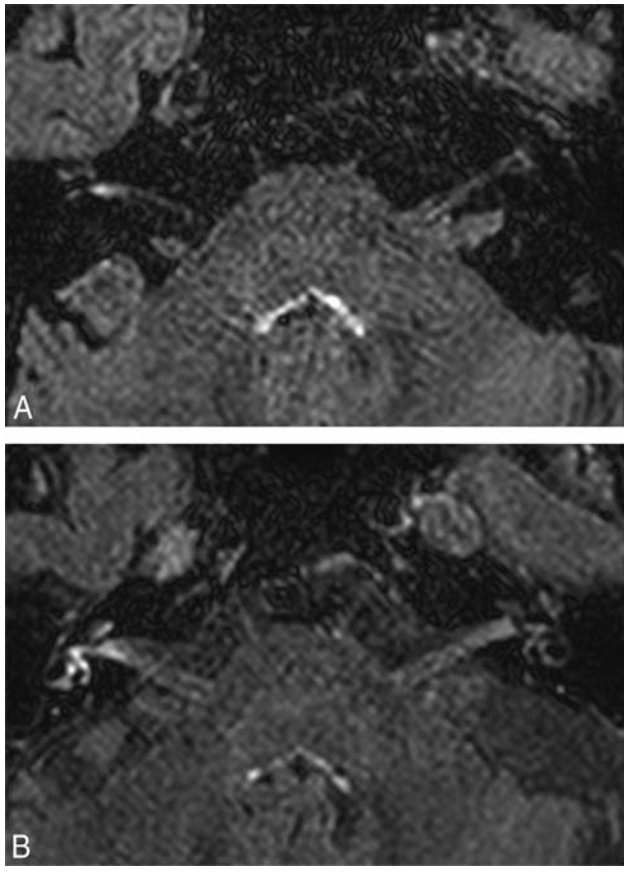

FIG 3. Ten-minute versus 4-hour delayed-enhanced 3D-FLAIR MR imaging in 72-year-old woman diagnosed with vestibular neuronitis (right). Four-hour delayed-enhanced 3D-FLAIR MR imaging (*B*) shows more definite anatomy of inner ear structures compared with 10-minute delayed-enhanced 3D-FLAIR MR imaging (*A*).

Table 3: Comparisons of mean signal-intensity ratios of inner ear structures between affected and unaffected sides at different times

	Affected Side (mean)	Unaffected Side (mean)	*P* Value
10 Minutes: CM ratio	0.78	0.53	.003
4 Hours: CM ratio	1.70	1.24	.000
10 Minutes: VM ratio	0.62	0.46	.010
4 Hours: VM ratio	1.40	1.10	.004
10 Minutes: VIIInM ratio	1.31	1.13	.004
4 Hours: VIIInM ratio	1.63	1.46	.015
10 Minutes: mVnM ratio	0.57	0.53	.356
4 Hours: mVnM ratio	1.44	1.50	.495
10 Minutes: cVnM ratio	1.09	1.07	.564
4 Hours: cVnM ratio	1.09	1.10	.684

Note:—CM indicates cochlea/medulla; VM, vestibule/medulla; VIIInM, vestibulocochlear nerve/medulla; cVnM, cisternal segment of the trigeminal nerve/medulla; mVnM, the Meckel cave of the trigeminal nerve/medulla ratio.

The Student *t* test was used to compare the differences in each inner ear signal-intensity ratio, both between 10 minutes and 4 hours and between affected and unaffected sides. A paired *t* test and Wilcoxon signed rank test were used to compare the differences in the affected ear signal-intensity ratio between patients with unilateral sSNHL and those with nsSNHL and to compare the WM ratio between the right and left sides. Pearson correlation analysis was used to compare the Meckel cave of the trigeminal nerve/medulla and the unaffected inner ear signal-intensity ratios.

Motion artifacts, visible signal abnormalities of the medulla, and mastoid air cells were visually assessed simultaneously.

RESULTS

There were no visible motion artifacts, visible signal abnormalities of the medulla, or abnormalities of the mastoid air cells. The WM ratio between the right and left sides did not

differ significantly for either method. The mean age and sex ratio did not differ significantly between patients with sSNHL and those with nsSNHL ($P = .84$ for mean age, $P = .06$ for sex ratio).

In this study, IV double-dose gadolinium administration provided anatomic discrimination in the 10-minute delayed images, but the 4-hour delayed images showed more accurate anatomic discrimination (Fig 3).

The signal-intensity ratios of the affected cochleae, vestibules, and vestibulocochlear nerves were higher than those of the unaffected side in both 10-minute and 4-hour delayed images (Table 3). However, there was no significant difference between sides for the trigeminal nerve.

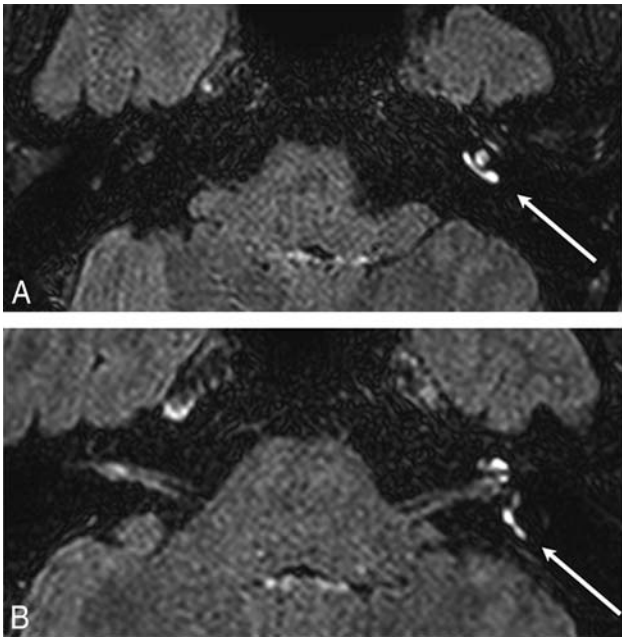

FIG 4. Images of the inner ears obtained at 10 minutes after intravenous gadolinium administration in a 43-year-old female patient who was diagnosed sudden sensorineural hearing loss (left). Enhancement in the left cochlea (*A*, *arrow*) in the posterior semicircular canal (*B*, *arrow*).

On affected sides, the signal-intensity ratio of the vestibulocochlear nerve was higher in patients with nsSNHL than in those with sSNHL on both 10-minute and 4-hour delayed images ($P = .01$, $P = .01$, Mann-Whitney test). However, there was no significant difference in the cochlea or vestibule.

Among 30 patients with sSNHL, the signal-intensity ratio of the affected cochleae was significantly higher than that of the unaffected side in 10-minute delayed images ($P = .01$, paired *t* test). There was no statistically significant signal-intensity ratio difference in the cochleae with 4 hours of delayed enhancement. There was also no significant signal-intensity ratio difference in the vestibule and vestibulocochlear nerve with 10 minutes and 4 hours of delayed enhancement (Fig 4).

Among 20 patients with nsSNHL, the signal-intensity ratios of affected cochleae and vestibulocochlear nerves were significantly higher than those of unaffected sides in 10-minute delayed images ($P = .004$, $P = .021$, Wilcoxon signed rank test). On 4-hour delayed images, the signal-intensity ratios of the affected cochleae, vestibules, and vestibulocochlear nerves were also significantly higher than those of unaffected sides.

Table 4: *P* values of signal-intensity ratio difference between affected and unaffected ears in each subgroup at different times (paired *t* test or Wilcoxon signed rank test)

	30 Patients with sSNHL		20 Patients with nsSNHL	
Organ	10 Minutes	4 Hours	10 Minutes	4 Hours
Vestibule	.069	.086	.093	.033
Vestibulocochlear nerve	.089	.328	.021	.016

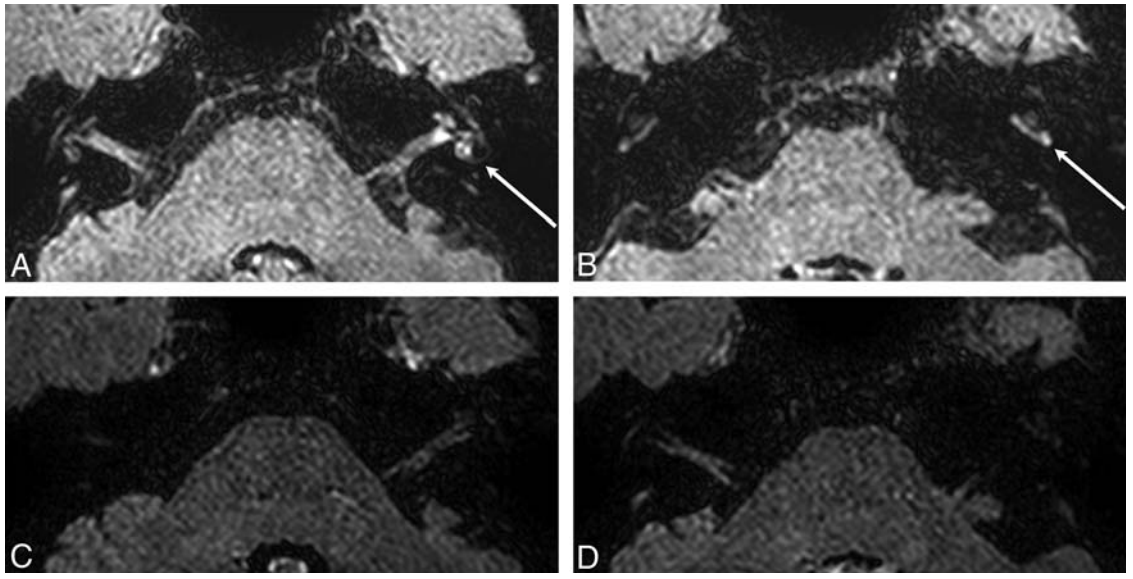

FIG 5. Images of inner ears after intravenous gadolinium administration in a 35-year-old female patient diagnosed with Herpes zoster oticus (left). *A* and *B*, Four-hour delayed images. *A*, Enhancement in the left cochlea, vestibule, labyrinthine segment of the facial nerve, and cochlear and vestibular nerves. *B*, Enhanced basal turn of the left cochlea (*arrow*). *C* and *D*, Ten-minute delayed images. No definite distinguishable enhancement was seen.

($P = .001$, paired t test; $P = .033$, Wilcoxon signed rank test; $P = .016$, paired t test; Fig 5 and Table 4).

DISCUSSION

We found that the signal-intensity ratios of the affected cochleae, vestibules, and vestibulocochlear nerves were higher than those of the unaffected side in both 10-minute and 4-hour delayed images in patients with SNHL. There are increasing reports that 4-hour enhancement shows more pronounced and increased signal intensity than 10-minute enhancement, especially in symptomatic ears of dizzy patients.[9]

Recent articles report that IV gadolinium administration is useful in evaluating the blood-labyrinth barrier in patients with inner ear diseases.[7,10] In patients with unilateral Ménière disease who underwent IV gadolinium injection, the affected side was significantly more enhanced than the unaffected side.[7] The ratio between the signal intensity of the inner ear and that of the cerebellar hemisphere has been reported as higher in patients with sudden sensorineural hearing loss compared with healthy volunteers.[9,11] Signal-intensity ratios may be useful for semiquantitative evaluation of disrupted blood-labyrinthine barriers.[6]

The results of the present study and previous reports suggest increased permeability of the blood-labyrinth (perilymph) barrier on the affected side for patients with unilateral inner ear symptoms. This increased permeability may have common underlying pathology for diverse otologic disorders, and further investigation is required to clarify this matter.

Among patients with sSNHL, the signal-intensity ratios of the affected cochleae are significantly higher than those of the unaffected side only in 10-minute delayed images. Many recent studies have explored the cause and pathogenesis of sSNHL, but most cases of sSNHL remain idiopathic.[12,13] This feature indicates a low possibility of definitive neuritis in patients with sSNHL. In a study of 46 patients with sSNHL, 3D-FLAIR MRI obtained precontrast and at 10 minutes after intravenous gadolinium injection showed significant signal-intensity ratio differences.[8] These results may indicate that 10-minute delayed images are superior to 4-hour delayed images in conditions without definitive neuritis, such as sSNHL. In 4-hour delayed images, the contrast enhancement of most structures is washed out except for mild enhancement of the perilymphatic space. Consequently, a mild signal-intensity ratio difference may be less conspicuous in 4-hour delayed images compared with 10-minute delayed images.

Significantly higher signal-intensity ratios of the affected cochleae, vestibules, and vestibulocochlear nerves were identified in patients with nsSNHL with 4-hour delayed images. The signal-intensity ratios of the affected cochleae and vestibulocochlear nerves were higher than those of the unaffected side on 10-minute delayed images. One-quarter of patients with nsSNHL in our group had Ramsay Hunt syndrome and vestibular neuronitis, which are definitely associated with viral origins. This finding may indicate increased nerve sheath permeability due to neuritis. Furthermore, data may indicate that 4-hour delayed images are superior to 10-minute delayed images in conditions with neuritis.

There are some limitations of the present study. First, a degree of selection bias occurred due to the retrospective nature of the study, and the study included only patients with unilateral symptoms. Second, the signal-intensity measurement method was semiquantitative, without the use of an external phantom for reference. Third, the small number of enrolled patients in this study requires validation of our findings in further studies. Fourth, ROIs were small, though we believe that the small size of the ROI of the inner ear structure was accurate. To ensure the reliability of the signal intensity measured in the small ROIs of the inner ear structure and to diminish the measurement error, we determined every ROI twice for each patient on different days and averaged the signal intensities of the 2 measurements, for each of the 2 radiologists. In addition, the differences between the radiologists were then resolved with consensus.

CONCLUSIONS

Inner ear signal-intensity ratios with 10-minute and 4-hour delayed intravenous gadolinium enhancement show statistically significant increases in many diseases, especially those associated with neuritis. Anatomic discrimination of inner ear structures is superior with 4-hour delayed enhancement compared with 10-minute delayed enhancement. The images with 4-hour delayed enhancement may be superior in neural inflammatory–dominant conditions, while 10-minute delayed-enhancement images may be superior in neural noninflammatory–dominant conditions.

REFERENCES

1. Sugiura M, Naganawa S, Teranishi M, et al. **Three-dimensional fluid-attenuated inversion recovery magnetic resonance imaging findings in patients with sudden sensorineural hearing loss.** *Laryngoscope* 2006;116:1451–54 CrossRef Medline
2. Sone M, Mizuno T, Sugiura M, et al. **Three-dimensional fluid-attenuated inversion recovery magnetic resonance imaging investigation of inner ear disturbances in cases of middle ear cholesteatoma with labyrinthine fistula.** *Otol Neurotol* 2007;28:1029–33 CrossRef Medline
3. Sugiura M, Naganawa S, Sone M, et al. **Three-dimensional fluid-attenuated inversion recovery magnetic resonance imaging findings in a patient with cochlear otosclerosis.** *Auris Nasus Larynx* 2008; 35:269–72 CrossRef Medline
4. Yamazaki M, Naganawa S, Kawai H, et al. **Increased signal intensity of the cochlea on pre- and post-contrast enhanced 3D-FLAIR in patients with vestibular schwannoma.** *Neuroradiology* 2009;51: 855–63 CrossRef Medline
5. Yamazaki M, Naganawa S, Tagaya M, et al. **Comparison of contrast effect on the cochlear perilymph after intratympanic and intravenous gadolinium injection.** *AJNR Am J Neuroradiol* 2012;33:773–78 CrossRef Medline
6. Tagaya M, Teranishi M, Naganawa S, et al. **3 Tesla magnetic resonance imaging obtained 4 hours after intravenous gadolinium injection in patients with sudden deafness.** *Acta Otolaryngol* 2010;130: 665–69 CrossRef Medline
7. Tagaya M, Yamazaki M, Teranishi M, et al. **Endolymphatic hydrops and blood-labyrinth barrier in Ménière's disease.** *Acta Otolaryngol* 2011;131:474–79 CrossRef Medline
8. Zhu H, Ou Y, Fu J, et al. **A comparison of inner ear imaging features at different time points of sudden sensorineural hearing loss with three-dimensional fluid-attenuated inversion recovery magnetic resonance imaging.** *Eur Arch Otorhinolaryngol* 2014 Aug 6. [Epub ahead of print] CrossRef Medline

9. Sano R, Teranishi M, Yamazaki M, et al. **Contrast enhancement of the inner ear in magnetic resonance images taken at 10 minutes or 4 hours after intravenous gadolinium injection.** *Acta Otolaryngol* 2012;132:241–46 CrossRef Medline
10. Nakashima T, Naganawa S, Teranishi M, et al. **Endolymphatic hydrops revealed by intravenous gadolinium injection in patients with Ménière's disease.** *Acta Otolaryngol* 2010;130:338–43 CrossRef Medline
11. Naganawa S, Komada T, Fukatsu H, et al. **Observation of contrast enhancement in the cochlear fluid space of healthy subjects using a 3D-FLAIR sequence at 3 Tesla.** *Eur Radiol* 2006;16:733–37 CrossRef Medline
12. Chau JK, Lin JR, Atashband S, et al. **Systematic review of the evidence for the etiology of adult sudden sensorineural hearing loss.** *Laryngoscope* 2010;120:1011–21 CrossRef Medline
13. Fusconi M, Chistolini A, Angelosanto N, et al. **Role of genetic and acquired prothrombotic risk factors in genesis of sudden sensorineural hearing loss.** *Audiol Neurootol* 2011;16:185–90 CrossRef Medline

Accuracy of 2-Phase Parathyroid CT for the Preoperative Localization of Parathyroid Adenomas in Primary Hyperparathyroidism

B. Griffith, H. Chaudhary, G. Mahmood, A.M. Carlin, E. Peterson, M. Singer, and S.C. Patel

ABSTRACT

BACKGROUND AND PURPOSE: Minimally invasive parathyroidectomy requires accurate preoperative localization of suspected adenomas, and multiphase CT allows adenoma characterization while providing detailed anatomic information. The purpose of this study was to assess the feasibility of a protocol using only arterial and venous phases to localize pathologic glands in patients with primary hyperparathyroidism.

MATERIALS AND METHODS: We identified 278 patients with primary hyperparathyroidism who had undergone 2-phase CT with surgical cure. All scans were read prospectively by board-certified neuroradiologists. A neuroradiology fellow retrospectively reviewed images and reports and classified suspected adenomas on the basis of anatomic location. Accuracy was determined by comparing imaging results with surgical findings. The ability of 2-phase CT to localize adenomas to 1 of 4 neck quadrants and lateralize them to the correct side was assessed. Accuracy of identifying multigland disease was also evaluated.

RESULTS: In patients with single-gland disease, the sensitivity and specificity of 2-phase CT to correctly localize the quadrant were 55.4% and 85.9%, respectively. The sensitivity and specificity of correct lateralization were 78.8% and 67.8%, respectively. The sensitivity and specificity to identify multigland disease were 22.9% and 79.5%, respectively.

CONCLUSIONS: While the 2-phase CT protocol in this study demonstrates lower accuracy compared with reports of other techniques, its lower radiation compared with 3- and 4-phase techniques may make it a feasible alternative for preoperative parathyroid localization. Further prospective studies are needed to identify patients for whom this technique is most suitable.

Primary hyperparathyroidism, a disorder caused by the presence of ≥1 hyperfunctioning parathyroid gland, is characterized by the overproduction of parathyroid hormone and is the most common cause of hypercalcemia in nonhospitalized patients.[1-3] Primary hyperparathyroidism is most commonly due to a single adenoma (85%) but can also be caused by multiple adenomas, 4-gland hyperplasia, and parathyroid carcinoma.[2]

The treatment of choice for primary hyperparathyroidism is surgical removal of the hyperfunctional tissue.[1] In the past, surgical management required bilateral cervical exploration. Improvements in preoperative localization of abnormal glands, however, and the use of intraoperative parathyroid hormone assays have led to increased use of minimally invasive, or focused, parathyroidectomy techniques.[3,4] Compared with bilateral exploration, minimally invasive parathyroidectomy achieves the same outcomes while offering a lower risk profile, causing less pain, and providing superior cosmetic outcomes.

The success of minimally invasive parathyroidectomy depends on the accurate preoperative localization of a potentially hyperfunctioning gland. A number of imaging modalities are currently used, both alone and in combination, for preoperative localization, including radionuclide scintigraphy and radionuclide single-photon emission CT, sonography, and contrast-enhanced CT. Radionuclide scintigraphy and sonography have both demonstrated success in preoperative localization, but each has limitations as well. In particular, both modalities lack detail regarding surrounding anatomy, and sonography is highly operator-dependent.[5-7]

In the past decade, multiphase CT has emerged as an additional technique for adenoma localization.[1,2,8-14] In addition to lesion identification, CT allows precise localization based on well-defined anatomic landmarks. Following its introduction, multiphase CT was referred to as 4D-CT.[9] The term "4D" referred to the 3 dimensions provided by the CT scan with the added dimen-

Received February 23, 2015; accepted after revision May 15.

From the Departments of Radiology (B.G., S.C.P.), Otolaryngology (H.C., M.S.), Surgery (A.M.C.), and Health Sciences (E.P.), Henry Ford Health System, Detroit, Michigan; and Department of Surgery (G.M.), University of Toledo, Toledo, Ohio.

Please address correspondence to Brent Griffith, MD, Department of Radiology, K3, Henry Ford Hospital, 2799 West Grand Blvd, Detroit, MI 48202; e-mail: brentg@rad.hfh.edu

http://dx.doi.org/10.3174/ajnr.A4473

sion of time due to the functional information offered by the multiple phases of imaging.[9] Since the initial description of 4D-CT by Rodgers et al[9] in 2006, many studies have attempted to define the optimal number of phases needed for parathyroid adenoma detection.

Two-phase parathyroid CT uses only 2 phases of imaging for characterization and localization purposes, which, in this study, included an arterial and a venous phase. Identification of parathyroid adenomas is based on the principle that parathyroid lesions show rapid enhancement followed by washout, which is demonstrated on the arterial and venous phases, respectively. The obvious major benefit of 2-phase CT over 3- or 4-phase CT is the decreased radiation dose. This is of particular importance given the increasing attention paid to radiation exposure from medical imaging.[15] In addition, studies have suggested that multiple phases do not improve localization, with a recent study finding that the arterial phase alone was comparable with the combination of other phases in correctly localizing and lateralizing adenomas.[16] Our institution began using this 2-phase parathyroid CT exclusively in 2009 for the preoperative work-up of parathyroid adenomas when cross-sectional imaging localization was requested by the referring surgeon.

The purpose of this study was to retrospectively assess the accuracy of 2-phase parathyroid CT for localizing surgically proved parathyroid adenomas in patients with primary hyperparathyroidism. We hypothesized that 2-phase CT would be a feasible technique for preoperative localization compared with techniques using 3 or 4 phases, while offering a reduction in radiation dose.

MATERIALS AND METHODS

This retrospective study was conducted in accordance with Health Insurance Portability and Accountability Act regulations. The study was approved by our institutional review board, and a waiver of informed consent was obtained.

Patients

Between May 2009 and August 2013, 444 two-phase parathyroid CT scans were obtained on 428 patients at our institution. Of these, 278 patients met the following inclusion criteria:

- Laboratory data consistent with primary hyperparathyroidism
- First-time parathyroidectomy surgery with subsequent cure (defined as normal calcium levels at 6 months or a 50% drop in intraoperative parathyroid hormone levels and into the normal range).

One hundred sixty-six CT scans were excluded for the following reasons: Seventy patients underwent 1 or multiple 2-phase CT scans without surgery performed, 14 patients had operative or pathology reports that were indeterminate, 18 patients did not have a cure following surgery, 25 patients had inadequate preoperative documentation, 27 patients were either lost to follow-up or had no postoperative laboratory data, and 12 patients were undergoing repeat surgeries.

Of the 278 included patients, 250 had either radionuclide scintigraphy or radionuclide single-photon emission CT performed. Of those, 140 patients had a suspected adenoma identified on the scan.

The decision to obtain a CT scan at our institution is variable and is determined by the individual surgeons on a patient-by-patient basis. There is no differentiation of patients who had previously undergone successful or unsuccessful localization by other modalities, whether sestamibi or sonography.

CT Technique

All examinations were performed with a 16– or 64–detector row CT scanner. Patients were positioned supine, head first on the CT gantry. Examinations included a scout scanogram and 2 phases of imaging following the intravenous administration of contrast material. One hundred milliliters of iopamidol (Isovue-350; Bracco, Princeton, New Jersey) or ioversol (Optiray-300; Mallinckrodt, St. Louis, Missouri) was administered at an injection rate of 5 mL/s via an 18-ga catheter followed by 40 mL of saline at 2 mL/s.

Timing of the 2 phases of imaging (arterial and venous) was dependent on patient age. In patients older than 55 years, the first-phase scanning started following a 22-second delay. The delay was 18 seconds in patients younger than 55 years of age. The second (venous) phase was obtained immediately following the first phase.

The multiphase CT was acquired at 2.5-mm section thickness with a 2.5-mm interval. Automatic exposure control was used (range, 200–400 mA) at 120 kV with a noise index of 13.81. Craniocaudal coverage was from the base of the orbit to the aortic arch. The mean CT dose index per imaging phase was 24.49 mGy. Coronal and sagittal reformats were obtained for both phases at 2.5-mm section thickness with a 2.5-mm interval.

Image Analysis

All 2-phase parathyroid CT reports and images were retrospectively reviewed by a neuroradiology fellow, and suspected adenomas were classified on the basis of their anatomic location: right upper quadrant, right lower quadrant, left upper quadrant, and left lower quadrant. Localization was based on a combination of image annotations (eg, measurements, arrows) placed at the time of the initial interpretation and the anatomic description on the report. All initial image interpretations were performed prospectively by board-certified neuroradiologists. No images were reinterpreted by the fellow at review. Quadrants were based on lesion location with respect to the vertical midline (right and left) and a transverse plane through the middle of the thyroid gland (Fig 1). Potential adenomas were also assigned a lateralization (right or left) based on their position relative to the midline. Suspected adenomas crossing a quadrant line were localized to the quadrant where the greatest proportion of the gland was located. Nontraditional locations, including ectopic and intrathyroidal glands, were also identified.

Surgical Localization

The surgery and pathology records were reviewed by a third-year medical student and a fourth-year otolaryngology resident with all final determinations of gland location confirmed with an otolaryngology staff member specializing in parathyroid surgery. Because surgeries were performed by multiple surgeons, if surgical localization could not be confidently determined on the basis of operative and pathology reports, the patient was excluded from analysis.

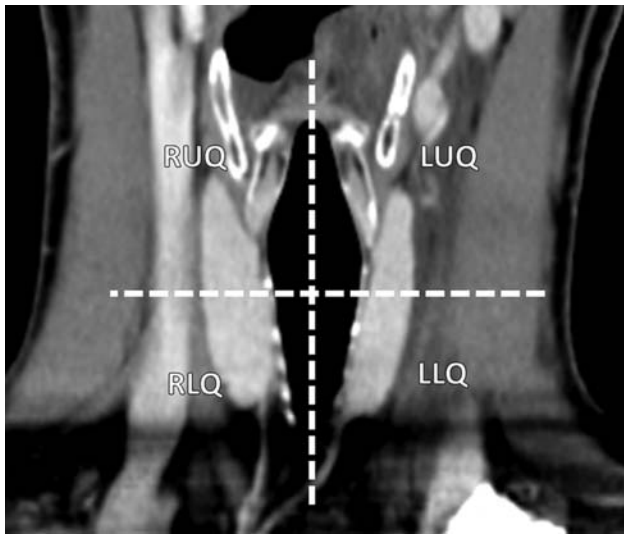

FIG 1. Coronal reformat image demonstrates the 4 quadrants used for imaging localization purposes. Quadrants were based on lesion location with respect to the vertical midline (right and left) and a transverse plane through the middle of the thyroid gland.

Gland location was classified by the same method as imaging localization. Medical records were reviewed to obtain patient demographic data, including age, sex, weight, body mass index, and preoperative and postoperative parathyroid hormone and calcium levels.

For diagnostic accuracy, surgical and pathologic findings were treated as the criterion standard.

Statistical Analysis

Suspected adenomas localized to the correct quadrant on the basis of surgical and pathologic findings were scored as true-positive. Suspected adenomas localized to the incorrect quadrant were scored as false-positive. The remaining quadrants not identified with possible adenomas were evaluated as a "no adenoma" guess—if correct on the basis of surgery, they were classified as a true-negative, and if misclassified, they were considered a false-negative. Each individual had 4 determinations, 1 for each quadrant. Screening parameters of sensitivity, specificity, positive predictive value, and negative predictive value were estimated by using a ratio estimator commonly used in sampling theory. Standard errors were also estimated. This estimation was performed for both single-gland quadrant localization and single-gland lateralization, considering only 2 areas on the 2-phase CT scan instead of 4.

For purposes of determining the accuracy of multigland identification, true-positives were those patients with multigland disease found at surgery and suspected adenomas identified at multiple locations on CT. False-negatives were those patients found to have multigland disease at surgery but without suspected multiple glands identified on CT. True-negatives and false-positives were those patients with only a single gland found at the time of surgery and with a single suspected gland or multiple suspected glands identified on CT, respectively.

Sensitivity, specificity, positive predictive value, and negative predictive value were compared for both localization and lateralization for those patients with single-gland disease within 1 of the 4 quadrants at the time of surgery. The following variables were assessed when information was available: body mass index of ≥30, history of diabetes, prior neck surgery other than parathyroid surgery, presence of hypothyroidism, presence of thyroid goiter or nodules, history of prior radioiodine treatment for thyroid disease, gland weight (>1 g), preoperative parathyroid hormone level (≥150), and calcium level (≥11). A test from sampling theory was used for the independent estimates of sensitivity in the 2 groups. This test was performed separately for localization and lateralization.

Table 1: Patient demographics

Demographics	
Age (yr) (n = 278)	60.5 ± 12.7
Weight (kg) (n = 241)	85.23 ± 21
Body mass index (n = 209)	31.4 ± 7.0
Preoperative PTH level (n = 278)[a]	128.5 (26.7–1900)
Intraoperative PTH level (n = 278)[a]	23.6 (0–151.7)
Preoperative calcium level[a]	10.6 (8.7–14.6)
Multigland disease at surgery (No. of patients)	48
Nontraditional-location disease at surgery (No. of patients)	8
Single-gland weight[a,b] (g) (n = 222)	0.481 (0.007–13.5)

Note:—PTH indicates parathyroid hormone.
[a] Denotes median value with range (mean and SD for all other values unless specified).
[b] Includes patients with single glands in a traditional location (4 quadrants) removed at surgery.

Table 2: Single-gland detection accuracy

	Single-Gland Localization	Single-Gland Lateralization
Sensitivity, %	55.4 ± 3.5	78.8 ± 2.8
Specificity, %	85.9 ± 1.4	67.8 ± 3.2
Positive predictive value, %	56.8 ± 3.4	71.0 ± 2.7
Negative predictive value, %	85.3 ± 1.1	76.2 ± 3.1

RESULTS

Patients

Between 2009 and 2013, 278 patients met the inclusion criteria. Table 1 shows the descriptive data regarding our patient population.

Localization and Lateralization

Of the 278 patients, 48 (17.3%) had multigland disease found at surgery and 8 had single glands located outside the 4 quadrants. These patients were excluded from localization and lateralization analysis, leaving 222 patients with single-gland disease in 1 of the 4 quadrants.

The sensitivity and specificity of 2-phase parathyroid CT to correctly localize a single gland to 1 of the 4 quadrants were 55.4% ± 3.5% and 85.9% ± 1.4%, respectively (Table 2). The positive and negative predictive values for single-gland localization were 56.8% ± 3.4% and 85.3% ± 1.1%, respectively.

The sensitivity and specificity of 2-phase parathyroid CT to correctly lateralize a single gland were 78.8% ± 2.8% and 67.8% ± 3.2%, respectively. The positive and negative predictive values for single-gland localization were 71.0% ± 2.7% and 76.2% ± 3.1%, respectively.

We further evaluated the sensitivities and specificities for localization and lateralization for single adenomas on the basis of specific quadrants. These data are provided in Table 3.

Multigland Disease and Nontraditional Location Glands

The ability of 2-phase parathyroid CT to correctly identify the presence of multiple glands was also assessed. For the 48 patients with multiglandular disease, the sensitivity and specificity of the 2-phase parathyroid CT to correctly identify their disease was 22.9% ± 6.1% and 79.5% ± 2.7%, respectively. The positive and negative predictive values were 19.0% ± 5.1% and 83.1% ± 2.5%.

Eight patients were identified as having nontraditionally located glands at the time of surgery, including 4 patients with glands identified within the superior mediastinum, 1 patient with an inferiorly descended superior parathyroid gland in a right paratracheal location, 1 patient with a gland located within the left piriform sinus, and 2 patients with intrathyroidal parathyroid adenomas. Mediastinal or ectopic glands in all 6 patients were correctly identified, though the piriform sinus lesion was not prospectively inferred to be an adenoma. The 2 intrathyroidal adenomas were not identified.

Clinical Factors Affecting Accuracy

A variety of clinical factors in patients with single adenomas was evaluated for their effects on sensitivity and specificity for localization and lateralization (Table 4). For localization, only the gland weight of ≥1 g led to a higher sensitivity (69.8% versus 50.0%, $P = .014$). The group with a calcium level ≥11 had a higher sensitivity, 62.7%–49.7%, which demonstrated a trend toward statistical significance ($P = .070$). There were no other statistically significant results.

Similarly, patients with a gland weight of ≥1 g or a body mass index of <30 demonstrated higher sensitivity for lateralization (90.7% versus 71.9%, $P = .001$, and 84.0% versus 69.2%, $P = .022$, respectively). In addition, patients with a history of hypothyroidism had a lower sensitivity than those without (59.4% versus 77.8%, $P = .049$) and lower specificity (46.9% versus 66.1%, $P = .046$).

DISCUSSION

Between 0.2% and 0.5% of the population are affected by primary hyperparathyroidism, with approximately 100,000 new cases diagnosed annually in the United States.[17] In the past, treatment of primary hyperparathyroidism required subjecting a patient to bilateral cervical exploration. In recent years, however, treatment has shifted toward the use of minimally invasive, or focused, parathyroidectomy. A 2011 study by Udelsman et al[3] evaluating 1650 patients undergoing surgery for primary hyperparathyroidism found that patients undergoing minimally invasive parathyroidectomy demonstrated improved cure and complication rates and a decreased length of hospital stay and lower total hospital charges.

Table 3: Quadrant-specific single-gland detection accuracy

	Right Upper	Right Lower	Left Upper	Left Lower
Sensitivity, %	26.2 ± 6.9	73.6 ± 6.1	51.0 ± 7.1	63.8 ± 6.4
Specificity, %	70.6 ± 3.4	95.6 ± 2.0	83.0 ± 2.9	90.8 ± 2.3
Positive predictive value, %	79.2 ± 2.2	89.8 ± 6.1	50.0 ± 6.4	69.8 ± 6.2
Negative predictive value, %	76.2 ± 3.1	91.6 ± 1.8	83.6 ± 2.2	88.3 ± 1.9

Table 4: Effect of clinical variables on sensitivity and specificity of localization and lateralization in patients with single adenomas

	Localization			Lateralization		
	Variable: Yes	Variable: No	*P* Value	Variable: Yes	Variable: No	*P* Value
BMI ≥ 30 (n[a] = 166)						
Sensitivity, %	48.4	56.0	.328	69.2	84.0	.022
Specificity, %	87.9	82.2	.081	59.3	69.3	.180
Diabetes (n = 213)						
Sensitivity, %	45.2	53.3	.407	71.0	75.3	.628
Specificity, %	88.2	85.7	.456	61.3	63.7	.799
Prior neck surgery (n = 201)						
Sensitivity, %	55.0	53.0	.870	75.0	75.7	.947
Specificity, %	91.7	85.6	.99	75.0	63.5	.278
Hypothyroidism (n = 212)						
Sensitivity, %	43.8	54.4	.268	59.4	77.8	.049
Specificity, %	86.5	85.7	.872	46.9	66.1	.046
Thyroid goiter or nodules (n = 218)						
Sensitivity, %	46.4	57.0	.143	69.6	78.5	.170
Specificity, %	87.4	85.7	.540	58.0	67.1	.199
Radioactive iodine therapy (n = 218)						
Sensitivity, %	42.9	53.6	.602	57.1	75.8	.360
Specificity, %	81.0	86.3	.596	42.9	64.5	.291
Gland weight ≥1 g (n = 221)						
Sensitivity, %	69.8	50.0	.014	90.7	71.9	.001
Specificity, %	85.3	86.5	.736	72.1	62.4	.213
Preoperative PTH level ≥ 150 (n = 221)						
Sensitivity, %	53.8	53.1	.911	81.3	71.5	.087
Specificity, %	84.6	87.7	0.274	64.8	64.6	0.973
Preoperative calcium level ≥11 (n = 222)						
Sensitivity, %	62.7	49.7	0.070	80.6	73.5	0.242
Specificity, %	86.1	86.2	0.957	67.2	63.2	0.572

Note:—BMI indicates body mass index; PTH, parathyroid hormone.

[a] Total number of patients in whom this variable could be confirmed on retrospective chart review.

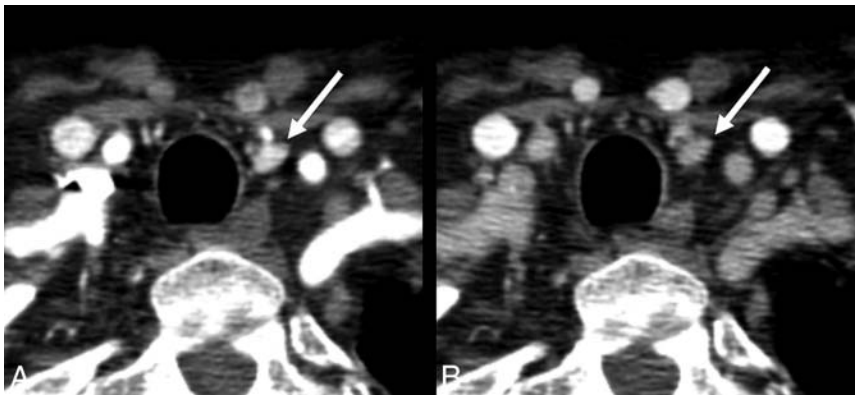

FIG 2. Axial arterial phase (*A*) and axial venous phase (*B*) images show a left inferior parathyroid adenoma, which demonstrates avid early contrast enhancement on the arterial phase and washout on the venous phase.

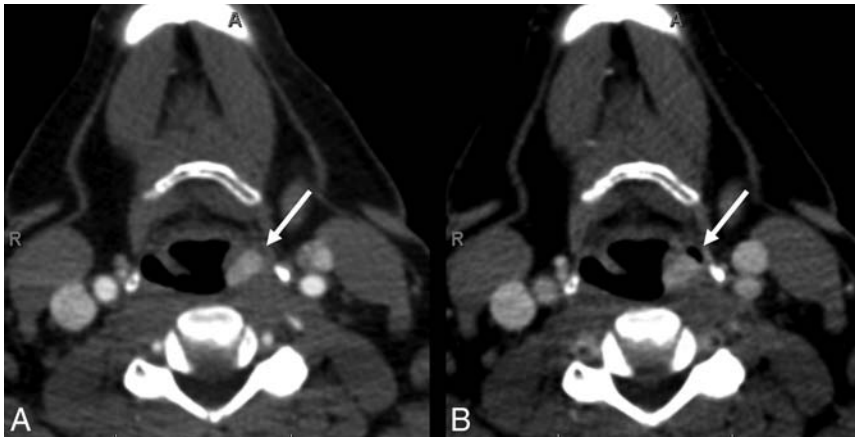

FIG 3. Axial arterial phase (*A*) and axial venous phase (*B*) images show an ectopic superior left parathyroid adenoma, which was surgically found to be within the submucosa of the left piriform sinus.

The success of minimally invasive parathyroidectomy depends on the appropriate selection of candidates—namely, those with localizable adenomas on preoperative imaging.[18] A number of imaging modalities, including radionuclide scintigraphy, sonography, and CT, are currently used, both alone and in combination, for localization purposes, with varying levels of success.

A prior meta-analysis of 20,225 cases of primary hyperparathyroidism demonstrated radionuclide scintigraphy having a sensitivity of 88% for detecting solitary adenomas,[19] though the sensitivity decreased to between 51% and 69% for adenomas of ≤500 mg.[20,21] Similarly, sonography is reported to have sensitivities for lateralization ranging from 61% to 88%. Many consider sonography to be the first-line imaging study, due to its ability to localize enlarged parathyroid glands while concurrently determining the presence of relevant thyroid disease. Both of these modalities are plagued by poor spatial resolution, however, and sonography is limited in its ability to adequately visualize the mediastinum.[13] In addition, sonography is user-dependent and, as such, is limited by the skill and experience of the ultrasonographer.[22]

Regardless of the preferred technique, in select patients, neither sonography nor radionuclide scintigraphy provides adequate localizing information. These patients may benefit from further attempts at preoperative localization. In addition, because of individual patient characteristics, such as high body mass index, a surgeon may want additional imaging studies.

In recent years, multiphase CT has been increasingly used at our institution as a means of localizing adenomas before surgery in select patients. The ability of multiphase CT to identify parathyroid adenomas is dependent on differences in enhancement characteristics between parathyroid lesions and other soft-tissue structures in the neck, with parathyroid lesions demonstrating rapid uptake and washout of contrast (Figs 2 and 3) versus the progressive enhancement pattern seen in normal lymph nodes.[12] In addition, CT has the added benefit of providing the surgeon with exquisite anatomic detail that can be used for surgical planning.

In 2006, 4D-CT was first reported in the literature as a means of identifying parathyroid adenomas. In that study, patients underwent sestamibi imaging, sonography, and 4D-CT, which consisted of precontrast, postcontrast, and delayed images.[9] Investigators demonstrated the improved sensitivity (88%) of 4D-CT compared with sestamibi imaging (65%) and sonography (57%) for lateralizing hyperfunctioning parathyroid glands to 1 side of the neck.[9] In addition, the sensitivity of 4D-CT in localizing parathyroid tumors to the correct quadrant of the neck was 70% compared with only 33% and 29% for sestamibi and sonography, respectively.[9]

Since that initial report by Rodgers et al in 2006,[9] many studies have attempted to determine the number of imaging phases needed to optimize parathyroid adenoma detection. A 2011 study by Starker et al[10] found that a 4D-CT consisting of 4 phases (precontrast followed by imaging at 30, 60, and 120 seconds following intravenous contrast injection) had improved sensitivity (85.7%) compared with sestamibi with SPECT (40.4%) and ultrasound (48.0%) for localizing parathyroid adenomas to the correct quadrant of the neck. That study showed similar superiority of 4D-CT for lateralizing parathyroid lesions as well (93.9% for 4D-CT, 71.2% for ultrasound, 61.5% for sestamibi with SPECT).[10] Similarly, a study by Eichhorn-Wharry et al[14] found 4-phase CT to be significantly more sensitive than sestamibi in correctly lateralizing parathyroid adenomas (73% versus 62%), with an even greater difference seen in patients with serum calcium levels of <10.8 mg/dL (45% versus 29%). Additional studies by Beland et al[12] and Hunter et al[13] also evaluated 4D-CT with 4 imaging phases. In the former, investigators found a sensitivity of 82% and a specificity of 92%. In the latter, Hunter et al found 4D-CT to have a 93.7% accuracy for correct lateralization and an 86.6% accuracy for quadrant localization.

Investigators have also evaluated the use of 3-phase 4D-CT. Chazen et al,[23] by using 3 phases consisting of precontrast, postcontrast, and delayed, found a sensitivity for correct lateralization of 93% and correct localization of 92% in 32 pathologically proved cases of single parathyroid adenomas. Similarly, Sepahdari et al[24] reported 97% accuracy for single-gland disease in a 3-phase protocol with precontrast, arterial, and venous phase imaging.

Finally, Kutler et al[11] used a modified technique of 4D-CT/sonography to identify parathyroid adenomas and found that it had a sensitivity and specificity of 94% and 96%, respectively, for lateralizing hyperfunctioning parathyroid glands and 82% and 93%, respectively, for localizing abnormal parathyroid glands to 1 quadrant of the neck. A similar study found that this technique demonstrated a good sensitivity for localization even in adenomas weighing <150 mg.[1]

Despite high reported localization success rates, 4D-CT remains burdened by the substantial radiation dose associated with scanning the patient multiple times. In addition, the optimal number of phases and the timing of contrast are still under investigation. In fact, a recent study by Raghavan et al[16] evaluated the accuracy of different combinations of CT phases to accurately localize parathyroid adenomas in 29 patients with primary hyperparathyroidism and found that the lateralization and localization accuracy of the arterial phase alone were comparable with that in other combinations of phases.

Our study, which includes 278 patients with surgically cured primary hyperparathyroidism, is the largest to date evaluating the accuracy of multiphase CT in preoperatively localizing pathologic parathyroid glands. Compared with the literature, our findings demonstrate a more modest success rate of our 2-phase CT protocol, with an overall sensitivity of 55.4% and specificity of 85.9% for localizing disease to a specific quadrant, which are less than those reported by others in the literature.[1,9,10,12,13,23] Similarly, the success of 2-phase CT to correctly lateralize adenomas, with a sensitivity and specificity of 78.8% and 67.8%, respectively, is also less than that reported for 4-phase CT in the literature.

A number of factors could account for the decreased accuracy of 2-phase CT in this study. The most important is related to study design, because this was a retrospective analysis designed specifically to reflect the performance of 2-phase-CT in a true clinical setting. As such, the study is prone to the same limitations that affect radiologists' interpretations on a routine clinical basis. These include issues related to the following: 1) patient factors, such as streak artifacts from the shoulders and clavicles, and artifacts related to breathing and swallowing; 2) gland-specific factors that may hinder accurate characterization by dynamic CT, such as in the case of cystic adenomas; 3) technical factors related to the CT scan itself, such as poor contrast bolus timing and streak artifacts due to venous contrast pooling; and 4) finally, interpretation-related factors, such as differences in reader experience and skill in interpreting 2-phase studies. Although these factors influence the sensitivity and specificity of parathyroid CT studies regardless of the number of phases performed, these may be less apparent in more controlled settings with smaller sample sizes of patients and smaller numbers of more experienced readers.

An additional factor that could potentially affect the accuracy of this 2-phase protocol in identifying parathyroid adenomas is problems with differentiating juxtathyroidal adenomas from thyroid tissue because both can have similar contrast-enhancement characteristics. As such, the lack of a precontrast phase may limit the ability to accurately identify juxtathyroidal adenomas, particularly in the setting of multinodular goiter, but our analysis of clinical factors affecting the accuracy of detection did not find a difference between patients with multinodular goiter and those without.

Additional factors in this study must also be taken into account as well. First, the 4-quadrant classification system used in this study is unable to differentiate an inferior parathyroid adenoma from a superior parathyroid adenoma that has overly descended along the tracheoesophageal groove. At imaging, this gland would be classified in the inferior quadrant due to its relationship with the thyroid, while at surgery it would be classified as a superior gland. This study did not attempt to differentiate these glands on imaging. This limitation is reflected in the quadrant-specific analysis of sensitivity, with the upper quadrants demonstrating lower sensitivities compared with the lower quadrants (26.2% and 51.0% versus 73.6% and 63.8%). An additional limitation relates to the study-selection criteria—in particular, exclusion of 18 patients who were not cured following surgery. Unfortunately, this limitation is due to the retrospective design of the study and was necessary because surgical localization was treated as the criterion standard, without which the accuracy of the technique could not be determined. However, this failed cure rate of 6.1% (18 of 296 patients) is not much different from the failure rate of up to 5% often reported in the literature, and the small difference may reflect a slightly more surgically challenging patient population requiring 2-phase CT.[25-27] Similarly, patients undergoing repeat surgery (12 of 296 patients) were excluded because the purpose of this study was to evaluate the accuracy of 2-phase CT in patients at initial presentation.

CONCLUSIONS

Two-phase parathyroid CT offers an additional potential method for the preoperative localization of parathyroid adenomas with sensitivities for lateralization and quadrant-specific localization of 78.8% and 55.4%, respectively. Despite lower accuracy rates than those of 4D-CT techniques in the literature, the lower accuracy rates must be balanced with the potential reduction in radiation dose. In addition, the clinical environment in which this study was performed, which subjects radiologists to the same limitations routinely encountered during study interpretation, may more fairly represent the accuracy of this technique when implemented in everyday clinical practice. Further large cohort prospective studies are needed to definitively determine the optimal number of phases required and the appropriate population for each technique.

REFERENCES

1. Stucken EZ, Kutler DI, Moquete R, et al. **Localization of small parathyroid adenomas using modified 4-dimensional computed to-**

mography/ultrasound. *Otolaryngol Head Neck Surg* 2012;146:33–39 CrossRef Medline
2. Ellika S, Patel S, Aho T, et al. **Preoperative localization of parathyroid adenomas using 4-dimensional computed tomography: a pictorial essay.** *Can Assoc Radiol J* 2013;64:258–68 CrossRef Medline
3. Udelsman R, Lin Z, Donovan P. **The superiority of minimally invasive parathyroidectomy based on 1650 consecutive patients with primary hyperparathyroidism.** *Ann Surg* 2011;253:585–91 CrossRef Medline
4. Udelsman R. **Six hundred fifty-six consecutive explorations for primary hyperparathyroidism.** *Ann Surg* 2002;235:665–70; discussion 670–72 CrossRef Medline
5. Vitetta GM, Neri P, Chiecchio A, et al. **Role of ultrasonography in the management of patients with primary hyperparathyroidism: retrospective comparison with technetium-99m sestamibi scintigraphy.** *J Ultrasound* 2014;17:1–12 CrossRef Medline
6. Grosso I, Sargiotto A, D'Amelio P, et al. **Preoperative localization of parathyroid adenoma with sonography and 99mTc-sestamibi scintigraphy in primary hyperparathyroidism.** *J Clin Ultrasound* 2007; 35:186–90 CrossRef Medline
7. Reeder SB, Desser TS, Weigel RJ, et al. **Sonography in primary hyperparathyroidism: review with emphasis on scanning technique.** *J Ultrasound Med* 2002;21:539–52; quiz 553–54 Medline
8. Hoang JK, Sung WK, Bahl M, et al. **How to perform parathyroid 4D CT: tips and traps for technique and interpretation.** *Radiology* 2014; 270:15–24 CrossRef Medline
9. Rodgers SE, Hunter GJ, Hamberg LM, et al. **Improved preoperative planning for directed parathyroidectomy with 4-dimensional computed tomography.** *Surgery* 2006;140:932–40; discussion 940–41 CrossRef Medline
10. Starker LF, Mahajan A, Björklund P, et al. **4D parathyroid CT as the initial localization study for patients with de novo primary hyperparathyroidism.** *Ann Surg Oncol* 2011;18:1723–28 CrossRef Medline
11. Kutler DI, Moquete R, Kazam E, et al. **Parathyroid localization with modified 4D-computed tomography and ultrasonography for patients with primary hyperparathyroidism.** *Laryngoscope* 2011;121: 1219–24 CrossRef Medline
12. Beland MD, Mayo-Smith WW, Grand DJ, et al. **Dynamic MDCT for localization of occult parathyroid adenomas in 26 patients with primary hyperparathyroidism.** *AJR Am J Roentgenol* 2011;196:61–65 CrossRef Medline
13. Hunter GJ, Schellingerhout D, Vu TH, et al. **Accuracy of four-dimensional CT for the localization of abnormal parathyroid glands in patients with primary hyperparathyroidism.** *Radiology* 2012;264: 789–95 CrossRef Medline
14. Eichhorn-Wharry LI, Carlin AM, Talpos GB. **Mild hypercalcemia: an indication to select 4-dimensional computed tomography scan for preoperative localization of parathyroid adenomas.** *Am J Surg* 2011; 201:334–38; discussion 338 CrossRef Medline
15. US Food and Drug Administration. Initiative to Reduce Unnecessary Radiation Exposure from Medical Imaging. Updated March 24, 2015. http://www.fda.gov/Radiation-emittingProducts/RadiationSafety/RadiationDoseReduction/default.htm. Accessed March 24, 2015
16. Raghavan P, Durst CR, Ornan DA, et al. **Dynamic CT for parathyroid disease: are multiple phases necessary?** *AJNR Am J Neuroradiol* 2014;35:1959–64 CrossRef Medline
17. Pruhs ZM, Starling JR, Mack E, et al. **Changing trends for surgery in elderly patients with hyperparathyroidism at a single institution.** *J Surg Res* 2005;127:58–62 CrossRef Medline
18. van Dalen A, Smit CP, van Vroonhoven TJ, et al. **Minimally invasive surgery for solitary parathyroid adenomas in patients with primary hyperparathyroidism: role of US with supplemental CT.** *Radiology* 2001;220:631–39 CrossRef Medline
19. Ruda JM, Hollenbeak CS, Stack BC Jr. **A systematic review of the diagnosis and treatment of primary hyperparathyroidism from 1995 to 2003.** *Otolaryngol Head Neck Surg* 2005;132:359–72 CrossRef Medline
20. Bergenfelz A, Tennvall J, Valdermarsson S, et al. **Sestamibi versus thallium subtraction scintigraphy in parathyroid localization: a prospective comparative study in patients with predominantly mild primary hyperparathyroidism.** *Surgery* 1997;121:601–05 CrossRef Medline
21. Jones JM, Russell CF, Ferguson WR, et al. **Pre-operative sestamibi-technetium subtraction scintigraphy in primary hyperparathyroidism: experience with 156 consecutive patients.** *Clin Radiol* 2001;56:556–59 CrossRef Medline
22. Steward DL, Danielson GP, Afman CE, et al. **Parathyroid adenoma localization: surgeon-performed ultrasound versus sestamibi.** *Laryngoscope* 2006;116:1380–84 CrossRef Medline
23. Chazen JL, Gupta A, Dunning A, et al. **Diagnostic accuracy of 4D-CT for parathyroid adenomas and hyperplasia.** *AJNR Am J Neuroradiol* 2012;33:429–33 CrossRef Medline
24. Sepahdari AR, Yeh MW, Rodrigues D, et al. **Three-phase parathyroid 4-dimensional computed tomography initial experience: inexperienced readers have high accuracy and high interobserver agreement.** *J Comput Assist Tomogr* 2013;37:511–17 CrossRef Medline
25. Boggs JE, Irvin III GL, Carneiro DM, et al. **The evolution of parathyroidectomy failures.** *Surgery* 1999;126:998–1002; discussion 1002–3 Medline
26. Carneiro DM, Solorzano CC, Irvin III GL. **Recurrent disease after limited parathyroidectomy for sporadic primary hyperparathyroidism.** *J Am Coll Surg* 2004;199:849–53; discussion 853–55 CrossRef Medline
27. Lew JI, Rivera M, Irvin III GL, et al. **Operative failure in the era of focused parathyroidectomy.** *Arch Surg* 2010;145:628–33 CrossRef Medline

Detection of Nasopharyngeal Carcinoma by MR Imaging: Diagnostic Accuracy of MRI Compared with Endoscopy and Endoscopic Biopsy Based on Long-Term Follow-Up

A.D. King, A.C. Vlantis, T.W.C. Yuen, B.K.H. Law, K.S. Bhatia, B.C.Y. Zee, J.K.S. Woo, A.T.C. Chan, K.C.A. Chan, and A.T. Ahuja

ABSTRACT

BACKGROUND AND PURPOSE: Our previous nasopharyngeal carcinoma detection study, comparing MR imaging, endoscopy, and endoscopic biopsy, showed that MR imaging is a highly sensitive test that identifies nasopharyngeal carcinomas missed by endoscopy. However, at the close of that study, patients without biopsy-proved nasopharyngeal carcinoma nevertheless had shown suspicious abnormalities on endoscopy and/or MR imaging. The aim of this study was to determine whether there were any patients with undiagnosed nasopharyngeal carcinoma by obtaining long-term follow-up and to use these data to re-evaluate the diagnostic performance of MR imaging.

MATERIALS AND METHODS: In the previous study, 246 patients referred to a hospital ear, nose, and throat clinic with suspected nasopharyngeal carcinoma, based on a wide range of clinical indications, had undergone MR imaging, endoscopy, and endoscopic biopsy, and 77 had biopsy-proved nasopharyngeal carcinoma. One hundred twenty-six of 169 patients without biopsy-proved nasopharyngeal carcinoma underwent re-examination of the nasopharynx after a minimum of 3 years, including 17 patients in whom a previous examination (MR imaging = 11; endoscopy = 7) had been positive for nasopharyngeal carcinoma, but the biopsy had been negative for it. Patients with nasopharyngeal carcinoma were identified by biopsy obtained in the previous and this follow-up study; patients without nasopharyngeal carcinoma were identified by the absence of a tumor on re-examination of the nasopharynx. The sensitivity and specificity of the previous investigations were updated and compared by using the Fisher exact test.

RESULTS: One patient with a previous positive MR imaging finding was subsequently proved to have nasopharyngeal carcinoma. Nasopharyngeal carcinomas were not found in the remaining 125 patients at follow-up, and the previous positive findings for nasopharyngeal carcinoma on MR imaging and endoscopy were attributed to benign lymphoid hyperplasia. The diagnostic performances for the previous MR imaging, endoscopy, and endoscopic biopsy were 100%, 88%, and 94%, respectively, for sensitivity, and 92%, 94%, and 100%, respectively, for specificity; the differences between MR imaging and endoscopy were significant for sensitivity ($P = .003$) but not specificity ($P = .617$).

CONCLUSIONS: MR imaging detected the 12% of nasopharyngeal carcinomas that were endoscopically invisible, including 1 cancer that remained endoscopically occult for several years. Lymphoid hyperplasia reduced the specificity of MR imaging.

ABBREVIATION: NPC = nasopharyngeal carcinoma

Nasopharyngeal carcinoma (NPC) is a radiosensitive tumor that can often be cured when detected early, but the nasopharynx is a clinically silent region and patients often present in the later stages of the disease.[1] Currently, the investigations for confirmation of NPC entail a nasopharyngeal endoscopy followed by an endoscopically directed biopsy at the site of an abnormality or sampling biopsies from an endoscopically normal nasopharynx. These methods may miss small nasopharyngeal carcinomas, however, because they are typically submucosal tumors or tumors located at the lateral aspect of the pharyngeal

Received February 9, 2015; accepted after revision May 2.

From the Department of Imaging and Interventional Radiology (A.D.K., T.W.C.Y., B.K.H.L., K.S.B., A.T.A.); Department of Otorhinolaryngology, Head and Neck Surgery (A.C.V., J.K.S.W.); Jockey Club School of Public Health and Primary Care (B.C.Y.Z.); and Departments of Clinical Oncology (A.T.C.C.) and Chemical Pathology (K.C.A.C.), The Chinese University of Hong Kong, Prince of Wales Hospital, Hong Kong S.A.R., China.

This work was supported by a grant from the Research Grants Council of the Hong Kong Special Administrative Region, China (Project No. CUHK4656/12 and SEG_CUHK02).

Please address correspondence to A.D. King, MD, FRCR, Department of Imaging and Interventional Radiology, Faculty of Medicine, The Chinese University of Hong Kong, Prince of Wales Hospital, 30-32 Ngan Shing St, Shatin, New Territories, Hong Kong S.A.R., China; e-mail king2015@cuhk.edu.hk

http://dx.doi.org/10.3174/ajnr.A4456

Table 1: Imaging criteria for grading the nasopharynx by MRI[a]

MRI Grade	MRI Appearance
Grade 1 = normal	Symmetric mucosa <3 mm thick with or without small retention cysts
Grade 2 = low index of suspicion of NPC	1) Symmetric mucosal thickening >3 mm thick (marked contrast enhancement > NPC) with or without small retention cysts or a Thornwaldt cyst, or 2) symmetric enlargement of the adenoid in the central roof/upper posterior wall with a striped appearance ± a smooth band (mild contrast enhancement < NPC) extending from the roof down the posterior and lateral nasopharyngeal walls
Grade 3 = high index of suspicion of NPC	Asymmetric: asymmetry between the right and left sides of the nasopharynx in grade 1 or 2 appearance
Grade 4 = NPC	Asymmetric mucosal thickening of homogeneous intermediate signal intensity on T2-weighted images and moderate contrast enhancement on T1-weighted images (performed without fat saturation), with or without infiltration outside the nasopharynx, or a focal homogeneous enhancing mass with or without infiltration outside the nasopharynx

[a] Grades 1 and 2 were negative for NPC; grades 3 and 4 were positive for NPC.

recess. These small nasopharyngeal carcinomas are becoming an even greater diagnostic challenge in the era of NPC screening[2] by using the Epstein-Barr virus as a surrogate, whether by serology, DNA, or nasopharyngeal brushings.

New methods for the early detection of NPC, such as narrow band imaging[3,4] and sonography, are currently undergoing evaluation,[5] but one of the most promising modalities in this regard is MR imaging. MR imaging has been used to stage biopsy-proved NPC for nearly 20 years,[6-8] but it is also ideally suited for the initial detection of the primary tumor.[9] In a previous prospective NPC-detection study,[10] we compared the diagnostic accuracy of nasopharyngeal MR imaging with that of nasopharyngeal endoscopy and endoscopic biopsy. The results of that study showed that MR imaging is a highly sensitive technique for NPC detection and one that has a significantly higher sensitivity for NPC detection than endoscopy. At the close of that study, however, there were subjects who nevertheless had shown MR imaging or endoscopic abnormalities that were suspicious for NPC, but the biopsy had been negative for NPC. Therefore, we planned to determine whether there were any patients with undiagnosed NPC, by obtaining long-term follow-up of all those patients without biopsy-proved NPC, on the basis of re-examination of the nasopharynx after a minimum of 3 years. Our goal was to determine whether the previous MR imaging examinations had been able to identify any further nasopharyngeal carcinomas or indeed whether the previous MR imaging examinations had missed any nasopharyngeal carcinomas. In addition, we planned to evaluate the MR imaging examinations with false-positive findings to determine whether the specificity of MR imaging could be improved.

MATERIALS AND METHODS

Previous Study

Patients with suspected NPC had been entered into the previous prospective study[10] comparing MR imaging, endoscopy, and endoscopic biopsy (biopsy from the site of an endoscopic abnormality or sampling biopsies from the endoscopically normal nasopharynx). Full details have been published previously,[10] but to summarize, patients with suspected NPC were recruited from the ear, nose, and throat out patient clinic at a referral hospital in a region where NPC is endemic. To avoid bias, we based a clinical suspicion of NPC on a wide range of indications, such as positive serology for Epstein-Barr; metastatic cervical lymph nodes; ^{18}F fluorodeoxyglucose positron-emission tomography scan with abnormal findings; and nonspecific symptoms (such as epistaxis, blood-stained saliva, nasal obstruction, or hearing loss) in the presence of a nasopharyngeal abnormality on flexible nasopharyngeal endoscopy.

MR imaging targeted to the nasopharynx had been obtained in all patients by using the following 4 sequences: 1) axial fat-suppressed T2-weighted images; 2) axial T1-weighted spin-echo images; 3 and 4) T1-weighted spin-echo images after a bolus injection of contrast in the axial (3) and coronal (4) planes. MR imaging had been graded independently by 2 radiologists (A.D.K and K.S.B with 15 and 4 years' experience, respectively, in head and neck radiology), and in cases of discordance, the grade had been obtained by consensus. MR imaging had been assessed without knowledge of the endoscopic findings and vice versa. MR imaging findings had been designated as NPC-negative (grades 1 and 2) or NPC-positive (grades 3 and 4), and details of the MR imaging grading system are shown in Table 1. A diagnosis of NPC had been made by histology from a nasopharyngeal biopsy, which had been obtained from either the initial endoscopic biopsy (directed by the endoscopic examination or sampling biopsies from an endoscopically normal nasopharynx) or a repeat biopsy directed by the MR imaging examination. The previous study had performed MR imaging, endoscopy, and endoscopic biopsy in 246 patients; at the close of that study, 77 patients had biopsy-proved NPC and 169 patients did not.[10]

Long-Term Follow-Up Study

The current study aimed to follow up those 169 patients without biopsy-proved NPC in the previous study at a minimum of 3 years by using MR imaging and endoscopy to re-examine the nasopharynx. The presumption was that any small undiagnosed NPCs from the previous study should have grown and would now be more apparent and amenable to biopsy; therefore, biopsy was performed only in those patients with a suspected tumor on re-examination.

The previous study and follow-up study were approved by the institutional review board with written informed consent obtained.

Statistical Analysis

Patients with NPC were identified on the basis of a biopsy-proved NPC obtained in the previous and this follow-up study. Patients without NPC were identified by the absence of a biopsy-proved NPC after re-examination of the nasopharynx in this follow-up study. The sensitivity, specificity, negative predictive value, posi-

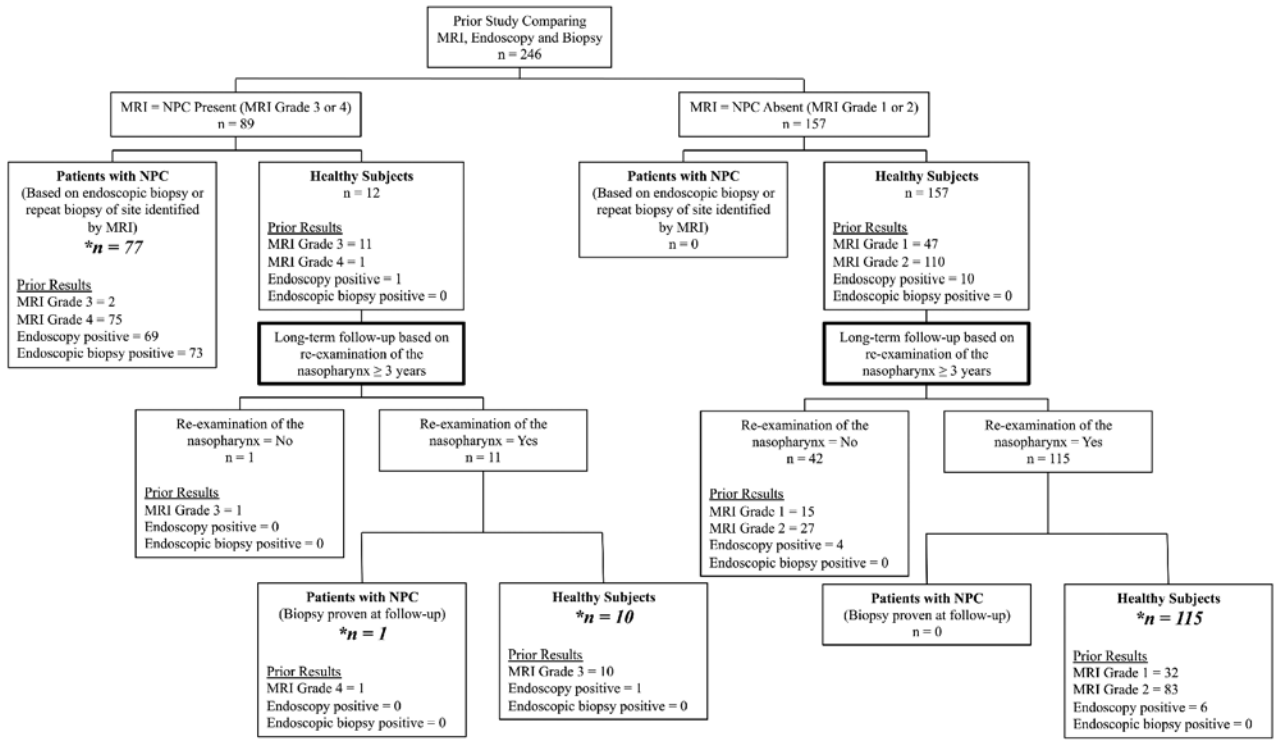

FIG 1. Flow chart of the study design.

tive predictive value, and the accuracy of the previous nasopharyngeal MR imaging, endoscopy, and endoscopic biopsy were updated by using the long-term follow-up data. The sensitivity and specificity were compared by using the Fisher exact test. A P value $< .05$ was considered statistically significant.

RESULTS

Long-Term Outcome

Forty-three of 169 (25.4%) patients without any clinical history of NPC were excluded from analysis because they did not undergo re-examination of the nasopharynx (Fig 1). They comprised 35 patients with follow-up of >3 years (mean, 62.3 months; range, 39–86 months), of whom 31 declined further nasopharyngeal examination, 3 died from causes unrelated to NPC, and 1 could not be contacted; and 8 patients with follow-up of <3 years (mean, 11.2 months; range, 0.5–32 months), of whom 7 died from causes unrelated to NPC and 1 could not be contacted. Of the 43 patients excluded from analysis, 5 had previous positive examination findings (MR imaging, $n = 1$; endoscopy, $n = 4$); 1 with a previous positive endoscopy examination finding had follow-up for 19 months, while the other 4 patients had follow-up ranging from 39 to 73 months (mean, 56 months).

One hundred twenty-six of 169 patients (74.6%) had re-examination of the nasopharynx and were included in the analysis (Fig 1). Re-examination was performed after 3 years (mean, 58.5 months; range, 36–84 months) comprising MR imaging and endoscopy ($n = 113$), MR imaging only ($n = 4$), and endoscopy only ($n = 9$). NPC was identified in 1/126 patients, a patient with a previous positive grade 4 MR imaging finding but without a diagnosis of NPC at the close of the previous study. MR imaging had identified a tumor in the pharyngeal recess, but endoscopy had been negative for tumor and endoscopic biopsies had not revealed a tumor even after the repeat biopsy at the site of the abnormal MR imaging findings. This small tumor grew very slowly until the NPC was confirmed by endoscopy and histology 43 months later (Fig 2). NPC was not found in the 10 patients whose previous MR imaging findings had been positive on the basis of asymmetry in a generalized lymphoid hyperplasia pattern (grade 3) or in the 115 patients whose previous MR imaging findings had been negative (grade 1 = 32; grade 2 = 83). NPC was not found in the 7 patients whose previous endoscopic findings had been positive.

Updated Results of the Previous NPC Detection Study Based on Long-Term Outcome

The updated diagnostic performances of MR imaging, endoscopy, and endoscopic biopsy are shown in Table 2 and are based on data from 203 patients, comprising 78 patients with biopsy-proved NPC (77 detected during the previous study and 1 during follow-up) and 125 patients without NPC based on re-examination of the nasopharynx after a minimum of 3 years (Fig 1).

NPC was present in 76/76 patients with a positive MR imaging finding showing a tumor (grade 4); 9 of these NPCs could not be visualized by endoscopic examination and 7 of these 9 NPCs had involved the pharyngeal recess on MR imaging. NPC was present in 2/12 patients with a positive MR imaging finding based on asymmetry in a generalized lymphoid hyperplasia pattern (grade 3); tumors in the nasopharyngeal wall of both patients were identified by endoscopy and biopsy. None of the remaining 10 patients with a positive grade 3 MR imaging finding had NPC: 9 with a negative endoscopy examination finding and 1 with a positive endoscopy examination finding in the nasopharyngeal wall (whose abnormal findings on MR imaging and endoscopy had regressed at 61 months). Analysis of these 10 grade 3 (Fig 3) false-

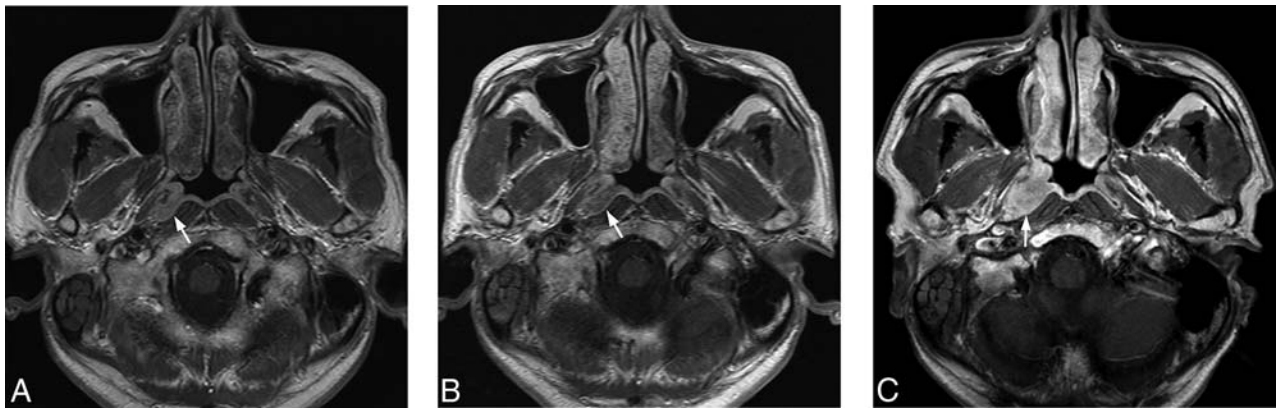

FIG 2. Axial T1-weighted postcontrast MR imaging of a 48-year-old man with NPC (*arrow*). *A*, Note a small moderately contrast-enhancing NPC in the right pharyngeal recess on MR imaging at presentation (grade 4), which was not detected by endoscopy or endoscopic biopsy or at repeat biopsy targeted to the site of the MR imaging abnormality. *B*, Persistent NPC on MR imaging is seen at 31 months, but without a tumor on endoscopic examination. A further biopsy was declined. *C*, An increase in the size of the NPC on MR imaging at 43 months when the tumor was confirmed by endoscopy and biopsy.

Table 2: NPC detection—grading of the previous MRI and updated diagnostic performances of the previous MRI, endoscopy, and endoscopic biopsy based on long-term outcome at 3 years in 203 patients (78 with NPC and 125 without NPC)

	MRI	Endoscopy	Endoscopic Biopsy[a]
True-Positive	78 Grade 3 ($n = 2$); grade 4 ($n = 76$)	69	73
True-Negative	115 Grade 1 ($n = 32$); grade 2 ($n = 83$)	118	125
False-Positive	10 Grade 3 ($n = 10$); grade 4 ($n = 0$)	7	0
False-Negative	0 Grade 1 ($n = 0$); grade 2 ($n = 0$)	9	5
Sensitivity (%)	100	88	94
Specificity (%)	92	94	100
PPV (%)	89	91	100
NPV (%)	100	93	96
Accuracy (%)	95	92	98

Note:—PPV indicates positive predictive value; NPV, negative predictive value.

[a] Endoscopic biopsy is endoscopically directed biopsy obtained at the site of the abnormality seen at endoscopy or sampling biopsies obtained from the endoscopically normal nasopharynx.

positive MR imaging examination findings had shown a benign pattern at the adenoid, which extended into the adjacent nasopharyngeal walls but with minor asymmetry between the left and right sides of the nasopharynx, which involved the adenoid ($n = 2$), nasopharyngeal walls ($n = 5$), or both the adenoid and the walls ($n = 3$). These false-positive MR imaging examination findings have been attributed to asymmetric benign lymphoid hyperplasia. Six of 7 false-positive endoscopic examination findings occurred at the adenoid; in these 6 patients, the MR imaging finding was negative for NPC on the basis of the symmetric striped appearance of the enlarged adenoid (grade 2), indicating benign lymphoid hyperplasia (Fig 4).

Nasopharyngeal MR imaging had a higher sensitivity than endoscopy or endoscopic biopsy for the detection of NPC (100% versus 88% and 94%, respectively), the difference being statistically significant between MR imaging and endoscopy ($P = .003$), and of borderline significance between MR imaging and endoscopic biopsy ($P = .059$). Nasopharyngeal MR imaging had a lower specificity for the detection of NPC than endoscopy or endoscopic biopsy (92% versus 94% and 100%, respectively); the difference was statistically significant between MR imaging and endoscopic biopsy ($P = .002$), but not between MR imaging and endoscopy ($P = .617$).

DISCUSSION

The results from this long-term follow-up study show that MR imaging is a highly sensitive tool for NPC detection because all biopsy-proven NPCs in the initial and 3-year follow-up study had been detected on the initial evaluation by MR imaging. By comparison, tumors in 12% and 6% of patients with NPC confirmed at histology were missed by initial endoscopy and by endoscopic biopsy, respectively. In our opinion, these findings demonstrate the necessity of greater use of MR imaging for the diagnostic work-up of patients with suspected NPC because neither endoscopy nor endoscopy plus biopsy can exclude NPC.

A particular strength of MR imaging is that it can assess the nasopharyngeal recess, which is where most NPCs originate. This site is often difficult to inspect endoscopically due to its lateral projection and apposition of its anterior and posterior walls. In 1 patient in the study, both initial and repeat MR imaging examinations detected an NPC within the pharyngeal recess that was missed on initial endoscopy and biopsy and on a repeat biopsy

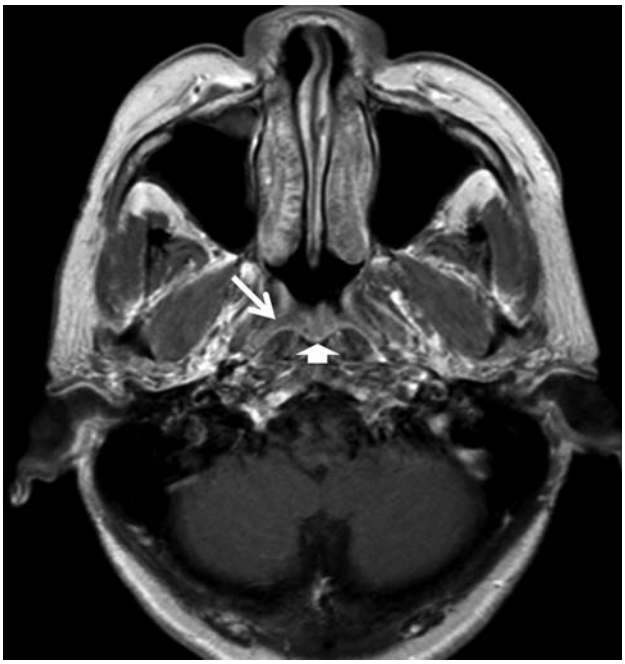

FIG 3. Axial T1-weighted postcontrast MR imaging of a 54-year-old man with lymphoid hyperplasia. MR imaging shows a smooth band with mild enhancement in the right side of the walls of the nasopharynx (*arrows*), extending from the adenoid (*arrowhead*), which is asymmetric in thickness compared with the left side and had been misdiagnosed as positive for NPC by MR imaging (grade 3).

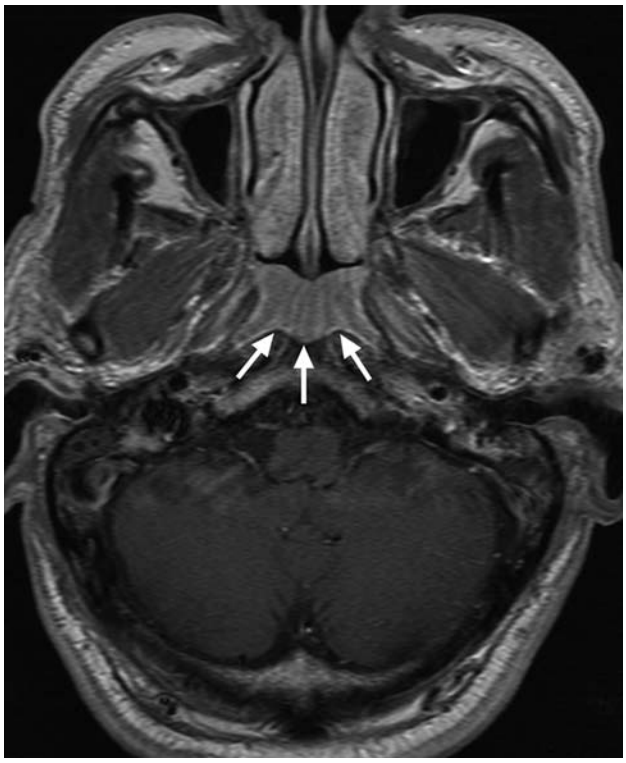

FIG 4. Axial T1-weighted postcontrast MR imaging of a 69-year-old man with benign lymphoid hyperplasia in the adenoid (*arrows*), which had been positive for NPC by endoscopy but was correctly diagnosed as benign by endoscopic biopsy and MR imaging on the basis of the symmetric alternating bands of marked and mild contrast enhancement causing a striped appearance to the enlarged adenoid (grade 2).

that was targeted to the MR imaging–detected abnormality, and it was only finally confirmed after a repeat biopsy several years later. In this regard, blind biopsies of this site can be hazardous due to the close proximity of the internal carotid artery to the lateral aspect of the recess; and as in our case, deeply sited small tumors may be missed even with targeted biopsies. These findings highlight the importance of maintaining a high index of suspicion for NPC even if initial biopsies are negative for it.

The optimal management of patients with a suspected but unproved small deeply sited tumor on MR imaging is unclear, though it probably should entail a combination of close imaging surveillance with MR imaging to document whether abnormalities persist or regress, serology, and endoscopy with repeat biopsies as appropriate. In this respect, the optimum timing, frequency, and duration of follow-up MR imaging examinations are unknown. Our example demonstrated only a small increase in tumor size during >3 years, suggesting that early NPCs may have slow growth initially. In fact, there is a paucity of data on growth rates of early NPCs, though published reports[11] of long latency periods between finding an abnormal serology test result and the eventual proof of NPC could be explained by small tumors that remain endoscopically occult for several years. The role of FDG-PET in early NPC detection is unclear because although NPCs are typically metabolically active, small tumors may have insufficient metabolic load to be detectable and may be obscured by metabolic activity due to normal lymphatic tissue and/or concomitant inflammatory changes in the nasopharynx. In those regions of the world where NPC is endemic, there are major resource implications for further imaging of these patients; therefore, follow-up is usually based on endoscopy plus or minus serology testing. However, the results of this long-term study suggest that further imaging, by FDG-PET/CT or serial MR imaging, would be best used for those patients with a grade 4 tumor on MR imaging because all of these patients had proved NPC.

The present study confirmed that MR imaging had a 100% negative predictive value for NPC, which supports the previous conclusion that invasive biopsies are not required when MR imaging findings are negative, especially when the endoscopic examination findings are also negative.[10] These findings also suggest that a negative MR imaging finding could potentially override a positive endoscopy result, in which a suspicious midline nasopharyngeal mass is seen on endoscopy that is characteristic of adenoidal hyperplasia on MR imaging, based on the presence of a mass with a symmetric striped or striated appearance.[12]

All patients with a tumor identified by MR imaging (grade 4) had NPC, but MR imaging had an imperfect specificity (92%), which was attributable to false-positive cases in patients with asymmetry in an otherwise generalized lymphoid hyperplasia MR imaging pattern (grade 3). Clearly, it would be beneficial to improve the positive predictive value of MR imaging to avoid unnecessary biopsies in healthy subjects, especially if MR imaging is to be used more widely to support NPC serology screening programs in areas with endemic NPC. In this respect, of those patients with a grade 3 positive MR imaging finding, only those who also had an accompanying positive endoscopy examination finding had NPC. Therefore, we speculate that a grade 3 pattern should undergo biopsy only if the endoscopic examination also

shows a suspected tumor, though caution would still be advised for those patients with asymmetry in a striped pattern of the adenoid because the internal structure of the adenoid cannot be visualized endoscopically.

The only method that currently can reliably exclude NPC in this patient population is follow-up to ensure that patients did not have a subclinical tumor at initial presentation. Follow-up was performed by re-examination of the nasopharynx at a minimum of 3 years, with a mean of almost 5 years, but 1 remaining limitation of the study is that patients with small slow-growing cancers may not have been identified.

CONCLUSIONS

MR imaging should be used more widely as a complementary tool to endoscopy and endoscopic biopsy for the detection of nasopharyngeal carcinoma. MR imaging identifies small tumors that cannot be identified through the endoscope, especially those in the pharyngeal recess, where MR imaging may identify a tumor several years before it becomes endoscopically visible. The results of this long-term follow-up study confirm that a normal or symmetric lymphoid hyperplasia pattern in the nasopharyngeal walls or adenoid (grade 1 or 2) by MR imaging has a high negative predictive value for NPC. This result supports the assertion that following a normal endoscopy examination finding or one that shows an adenoidal mass, invasive biopsies are not required when MR imaging shows these patterns. Finally, asymmetry in the generalized lymphoid hyperplasia pattern (grade 3) on MR imaging had a low positive predictive value for NPC, and in this study, only those who also had an accompanying positive endoscopy examination finding had NPC.

Disclosures: Ann D. King, Alexander C. Vlantis, Tom Wing Cheung Yuen, Benjamin King Hong Law, Kunwar S. Bhatia, Benny C.Y. Zee, John Woo, Anil T. Ahuja—*RELATED*: *Grant*: Research Grants Council of the Hong Kong,* *Comments*: Project No. CUHK4656/12 and SEG_CUHK02. Anthony T.C. Chan—*UNRELATED*: theme-based research from the Research Grants Council of Hong Kong*; *Other*: research funding from Pfizer,* Boehringer Ingelheim,* Merck Serono,* Bristol-Myers Squibb,* Eli Lilly.* K.C. Allen Chan—*UNRELATED*: *Consultancy:* I am a consultant to Xcelom Limited; *Patents (planned, pending or issued)*: I have filed patents/patent applications on technologies related to noninvasive diagnostics based on nucleic acid analysis; *Royalties*: The Chinese University of Hong Kong receives royalties on technologies related to noninvasive diagnostic tests based on nucleic acid analysis*; *Stock/Stock Options*: The Chinese University of Hong Kong holds equities in Sequenom.* *Money paid to the institution.

REFERENCES

1. Lee AW, Ng WT, Chan LL, et al. **Evolution of treatment for nasopharyngeal cancer: success and setback in the intensity-modulated radiotherapy era.** *Radiother Oncol* 2014;110:377–84 CrossRef Medline
2. Chan KC, Hung EC, Woo JK, et al. **Early detection of nasopharyngeal carcinoma by plasma Epstein-Barr virus DNA analysis in a surveillance program.** *Cancer* 2013;119:1838–44 CrossRef Medline
3. Wen YH, Zhu XL, Lei WB, et al. **Narrow-band imaging: a novel screening tool for early nasopharyngeal carcinoma.** *Arch Otolaryngol Head Neck Surg* 2012;138:183–88 CrossRef Medline
4. Wang WH, Lin YC, Lee KF, et al. **Nasopharyngeal carcinoma detected by narrow-band imaging endoscopy.** *Oral Oncol* 2011;47:736–41 CrossRef Medline
5. Gao Y, Zhu SY, Dai Y, et al. **Diagnostic accuracy of sonography versus magnetic resonance imaging for primary nasopharyngeal carcinoma.** *J Ultrasound Med* 2014;33:827–34 CrossRef Medline
6. Olmi P, Fallai C, Colagrande S, et al. **Staging and follow-up of nasopharyngeal carcinoma: magnetic resonance imaging versus computerized tomography.** *Int J Radiat Oncol Biol Phys* 1995;32:795–800 CrossRef Medline
7. Chong VF, Fan YF, Khoo JB. **Nasopharyngeal carcinoma with intracranial spread: CT and MR characteristics.** *J Comput Assist Tomogr* 1996;20:563–69 CrossRef Medline
8. King AD, Lam WW, Leung SF, et al. **MR imaging of local disease in nasopharyngeal carcinoma: tumour extent vs tumour stage.** *Br J Radiol* 1999;72:734–41 CrossRef Medline
9. King AD, Vlantis AC, Tsang RK, et al. **Magnetic resonance imaging for the detection of nasopharyngeal carcinoma.** *AJNR Am J Neuroradiol* 2006;27:1288–91 Medline
10. King AD, Vlantis AC, Bhatia KS, et al. **Primary nasopharyngeal carcinoma: diagnostic accuracy of MR imaging versus that of endoscopy and endoscopic biopsy.** *Radiology* 2011;258:531–37 CrossRef Medline
11. Ji MF, Wang DK, Yu YL, et al. **Sustained elevation of Epstein-Barr virus antibody levels preceding clinical onset of nasopharyngeal carcinoma.** *Br J Cancer* 2007;96:623–30 CrossRef Medline
12. Bhatia SS, King AD, Vlantis AC, et al. **Nasopharyngeal mucosa and adenoids: appearance at MR imaging.** *Radiology* 2012;263:437–43 CrossRef Medline

MR Imaging Characteristics of Wingless-Type–Subgroup Pediatric Medulloblastoma

Z. Patay, L.A. DeSain, S.N. Hwang, A. Coan, Y. Li, and D.W. Ellison

ABSTRACT

BACKGROUND AND PURPOSE: "Transcriptionally different" medulloblastoma groups are associated with specific signaling pathway abnormalities; hence, they may present with distinct imaging manifestations. In this study, we sought to describe the MR imaging features of wingless-type–subgroup medulloblastomas with embryologic correlations.

MATERIALS AND METHODS: Pre- and postoperative imaging studies of 16 patients with wingless-type–subgroup medulloblastoma were evaluated for tumor location, involvement of surrounding CSF spaces or parenchymal structures, conventional and DWI signal properties, and postsurgical damage patterns. Laterality scores were assigned to tumors at each step in the evaluation process. Continuous variables were summarized by using descriptive statistics. The Wilcoxon signed rank test was performed to compare laterality scores. To determine the interobserver variability, we computed the intraclass correlation and Cohen κ coefficients.

RESULTS: Wingless-type–subgroup medulloblastomas in our series were histopathologically "classic." Wingless-type–subgroup medulloblastomas occur in specific sites, with involvement of the foramen of Luschka (75%), the fourth ventricle (68.75%), the cisterna magna (31.25%), and the cerebellopontine angle cistern (18.75%). Laterality scores were low (<2) when preoperative primary and secondary anatomic features were evaluated separately, but they increased (>2) when all pre- and postoperative anatomic features were considered. Results were statistically shown to be reproducible (interclass correlation coefficient, 0.71–0.94; Cohen κ, 0.63–1.00). On the basis of anatomic lesion patterns, 4 location-based subtypes may be distinguished: 1) midline-intraventricular, 2) midline-extraventricular, 3) off-midline–intraventricular, and 4) off-midline–extraventricular, which represent a continuum.

CONCLUSIONS: Wingless-type–subgroup medulloblastomas are lateralized tumors arising from the brain stem and cerebellum around the foramen of Luschka. Our current understanding of their embryologic origins is in concordance with the spatial distribution of these tumors.

ABBREVIATIONS: CP = cerebellopontine; L = left; LS = laterality score; R = right; SHH = sonic hedgehog; WNT = wingless-type mouse mammary tumor virus integration site family

Medulloblastoma is a World Health Organization grade IV embryonal tumor occurring mainly, but not exclusively, in the pediatric population and is the most common malignant CNS tumor in children. Beyond the traditional histopathologic classification, molecular subgroups based on gene-expression profiling have recently been recognized in these tumors.[1-4] The subgroups, sonic hedgehog (SHH), wingless (WNT), group 3, and group 4, are biologically and clinically distinct disease entities, and distinguishing these groups in the clinical environment has become feasible.[5-8]

Studies suggest a distinct histogenesis for WNT, SHH, and group 3 medulloblastomas.[9] WNT tumors arise from the lower rhombic lip in the dorsolateral primitive brain stem, whereas SHH tumors arise from cerebellar granule neuron precursors in the upper rhombic lip. The different progenitor cell populations follow distinctly different migration tracts. These observations prompted us to hypothesize that WNT-subgroup medulloblastomas might present with distinct imaging characteristics, particularly in relation to spatial distribution in the posterior fossa. In this study, we report how the conventional MR imaging evalua-

Received November 24, 2014; accepted after revision April 13, 2015.

From the Departments of Diagnostic Imaging (Z.P., L.A.D., S.N.H.), Biostatistics (A.C., Y.L.), and Pathology (D.W.E.), St. Jude Children's Research Hospital, Memphis, Tennessee.

This work was supported in part by grant no. CA21765 from the National Cancer Institute and by the American Lebanese Syrian Associated Charities.

Please address correspondence to Zoltan Patay, MD, PhD, Department of Diagnostic Imaging, MS220, St. Jude Children's Research Hospital, 262 Danny Thomas Place, Memphis, TN 38105; e-mail: zoltan.patay@stjude.org

Indicates open access to non-subscribers at www.ajnr.org
Indicates article with supplemental on-line appendix and tables.
Indicates article with supplemental on-line photos.

http://dx.doi.org/10.3174/ajnr.A4495

tion of WNT-subgroup medulloblastomas addresses this hypothesis.

MATERIALS AND METHODS

A retrospective institutional data base search was conducted with institutional review board approval and waiver of consent. Of the 238 patients (male/female ratio = 1.74:1; age range = 0.23–22.4 years) who were treated for medulloblastoma at our institution during a 10-year period (2000–2010), molecular subgrouping data were available for 143 (male/female ratio = 1.92:1; age range = 0.23–22.24 years). Data obtained by immunohistochemistry, fluorescent in situ hybridization, and direct sequencing of formalin-fixed paraffin-embedded tissue showed that 16 (11.18%) of these 143 patients had WNT-subgroup medulloblastomas (male/female ratio = 1:1; age range = 6.47–14.53 years; mean age = 9.82 ± 2.18 years). The initial diagnostic and first postoperative follow-up brain imaging studies of these patients were reviewed by using a standardized set of evaluation criteria. Fifteen patients had MR imaging studies available preoperatively; 1 had a CT only. All 16 patients had MR imaging studies postoperatively. Because many of the imaging studies were performed at referring institutions, imaging protocols were inconsistent. Preoperative, precontrast T1WI was available for 14 patients; T2WI, for 15 patients; FLAIR images, for 14 patients; and postcontrast T1WI, for 15 patients (as mentioned before, the only available preoperative imaging in 1 of the patients was precontrast CT). DWI data were available for 14 patients, but ADC map images were available for only 9. Review and evaluation of the imaging data were completed by 2 experienced pediatric neuroradiologists (reviewer 1 and reviewer 2). The second reviewer was requested to evaluate the preoperative and postoperative anatomic tumor features only to allow assessment of interobserver variability in the determination of the putative points of origin of the tumors. Including the second reviewer was to show that results related to tumor location features are reproducible.

Evaluation of Conventional MR Imaging Features of WNT-Subgroup Medulloblastomas

Evaluation was completed by 1 reviewer and included the description of the tumor signal properties and other tumor features (cyst, necrosis, hemorrhage) by conventional MR imaging and DWI techniques. We estimated the volume of each tumor by using the sum of 3D, orthogonal tumor diameters. Additional detailed explanation of the methods used for the evaluation is provided in the On-line Appendix ("Methods 1").

Preoperative Evaluation of Anatomic Tumor Features

To evaluate the key anatomic tumor features (including the epicenter, hence the putative point of origin of the tumor), we adopted a stepwise, iterative evaluation process to create laterality scores (LS-1, LS-2, and LS-3), described in the On-line Appendix ("Methods 2").

Postoperative Imaging Evaluation of Anatomic Tumor Features

The next step of the evaluation process was focused on the abnormalities in the first available postoperative MR imaging study, which was typically performed shortly after near-total or gross-total tumor resection (mean = 5.3 days, range = 1–18 days). The rationale for this step was the assumption that visible (ie, T2 and/or FLAIR hyperintense) postsurgical lesions within cerebellar and/or brain stem parenchyma (ie, the postoperative damage pattern) reflect invasion of specific anatomic structures by the original tumor and provide clues to the epicenter (point-of-origin) of the tumor. Laterality scores (LS-4) were generated for the postoperative cerebellar and brain stem lesions (On-line Appendix "Methods 3"). We also recorded postoperative imaging evidence of any infarction in a PICA territory.

Combined Pre- and Postoperative Evaluation of Location Features

By using all available imaging data and the previously assigned laterality scores, a final LS (LS-5) was created for each tumor and was used to assign a consolidated score (LS-5c) for each patient (On-line Appendix "Methods 4").

The combined pre- and postoperative evaluation process is illustrated in Figs 1–4.

Statistical Analyses

Statistical analyses were performed by using SAS 9.3 statistical software (SAS Institute, Cary, North Carolina). Significance was assumed with $P < .05$. Continuous variables were summarized by using descriptive statistics, including number, mean, SD, and range; categoric variables were summarized by using number and percentage. The Wilcoxon signed rank test was performed to compare the laterality scores at different steps and stages of the imaging evaluation (eg, preoperative, postoperative). To determine the interobserver variability of laterality scores, intraclass correlation coefficients were estimated from a mixed-effects linear model analysis. The interobserver agreement of posterior fossa CSF-space involvement and tumor group assignment was examined by computing the Cohen κ coefficient. Published guidelines were used to interpret intraclass correlation coefficients (<0.40 = poor; 0.40–0.59 = fair; 0.60–0.74 = good; and 0.75–1.0 = excellent)[10] and Cohen κ coefficients (0–0.2 = slight; 0.21–0.40 = fair; 0.41–0.60 = moderate; 0.61–0.80 = substantial; 0.81–1.0 = almost perfect or perfect).[11]

RESULTS

All WNT-subgroup medulloblastomas in our series were histopathologically classic tumors.[5]

Conventional MR Imaging Features

All tumors for which precontrast T1WI was available exhibited hypointense signal. In T2WI, 6 (40%) of 15 tumors were isointense compared with the cerebellar cortex, and the remaining 9 (60%) were hyperintense. In FLAIR images, the signal properties of the solid tumor components were similar to the T2WI findings for all patients who had both T2-weighted and FLAIR images available. All tumors exhibited obvious hyperintense signal in diffusion-weighted images. In ADC images, 2 (22%) of 9 tumors were hypointense, 6 (67%) were hypointense+, and 1 (11%) was hypointense++. In postcontrast T1WI, all

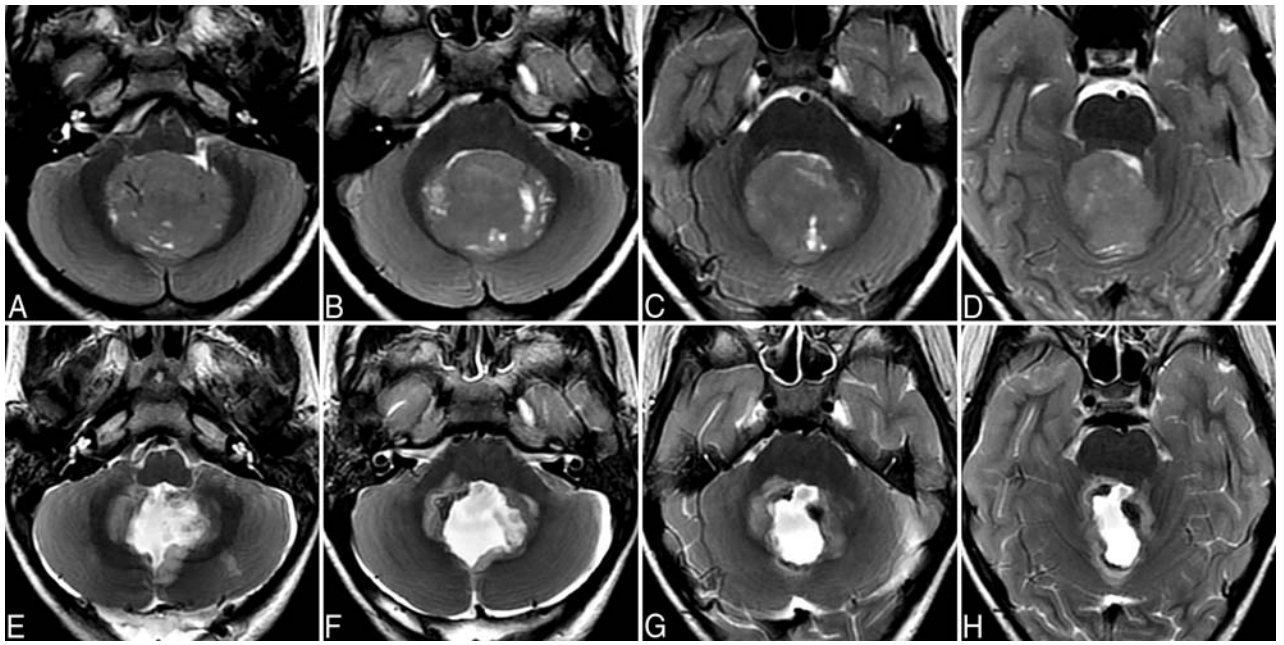

FIG 1. Pre- and postoperative transverse T2WI of a midline-intraventricular (subtype A) WNT-subgroup medulloblastoma. In the preoperative images (*A–D*), fullness at the level of the right foramen of Luschka (LS-1c: R1) and right superior cerebellar peduncle (LS-2c: R1) suggests some laterality, yielding an LS-3c of R2. In the postoperative images (*E–H*), the damage pattern is essentially bilateral, with bilateral involvement of the superior cerebellar peduncles (R1, L1), the dentate nuclei (R1, L1), inferomedial cerebellum (R1, L1), and tonsils (R1, L1). However the pattern shows some right-sided dominance, with unilateral involvement of the right pontine tegmentum (R1) and bilateral but dominantly right-sided involvement of the middle cerebellar peduncles (R2, L1). Although the tumor appears to be midline-intraventricular in the preoperative images, overall right-sidedness is suggested when all pre- and postoperative lesions and laterality scores are considered (LS-4c = R2, LS-5c = R4).

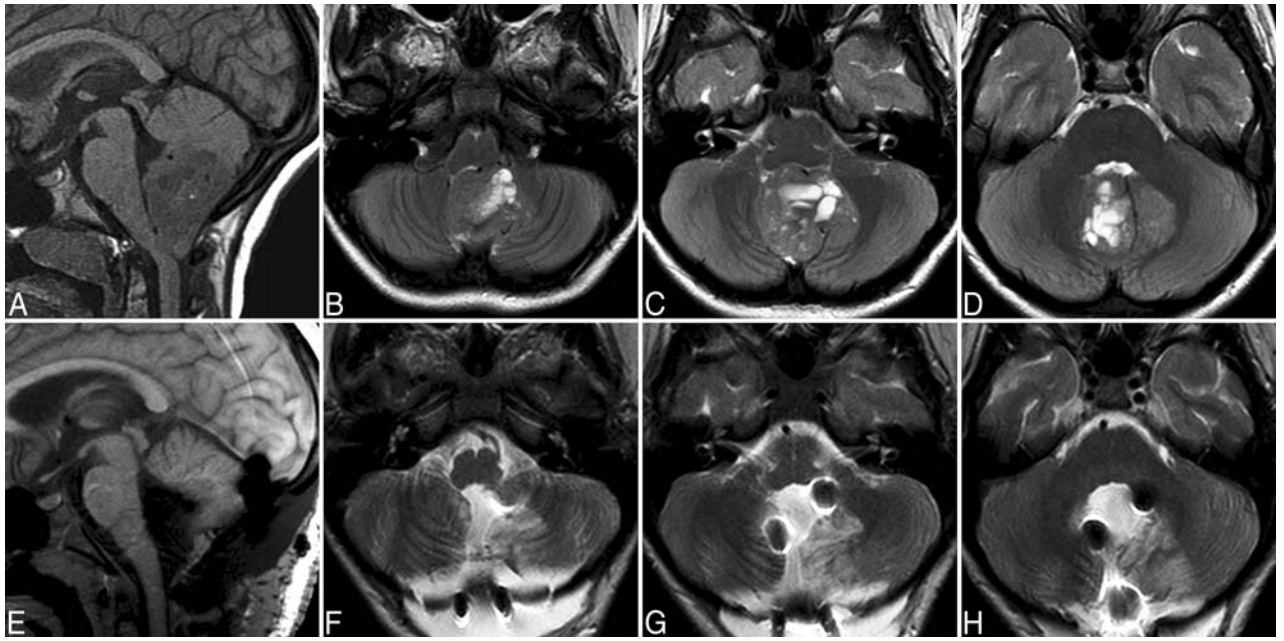

FIG 2. Pre- and postoperative sagittal T1-weighted and transverse T2-weighted images of a midline-extraventricular (subtype B) WNT-subgroup medulloblastoma. The preoperative sagittal T1-weighted image (*A*) shows a low-lying tumor in the posterior fossa, which is centered on the cisterna magna and pushing the vermis cranially, with extension to the foramen of Magendie but only minimal extension into the fourth ventricle. In transverse T2WI (*B–D*), no definite laterality is seen; hence, the tumor appears to be gross midline, but there is some involvement of the left foramen of Luschka (LS-1c = L1) and left inferomedial cerebellum (LS-2c = L1). The combined preoperative laterality score is ambiguous (LS-3c = L2). One of the PICAs (probably the left) is running over the upper aspect of the tumor, indicating displacement from below (*D*). Postoperative images (*E–H*) show a relatively spared vermis and more pronounced abnormalities on the left side, which include damage to the left dentate nucleus and the left inferomedial cerebellum (LS-4c = L2) and a left PICA territory infarction. The combined pre- and postoperative laterality score suggests a left-sided tumor origin (LS-5c = L4).

tumors showed some signal enhancement; in 1 patient, it was faint; in 9 patients, it was moderate; and in the remaining 5 patients, it was avid. In 13 (87%) of 15 patients, enhancement was seen within the entire tumor; in 2 (13%) of 15 patients, smaller or larger areas of the solid tumor lacked perceptible enhancement and were labeled as inhomogenous. In another 6

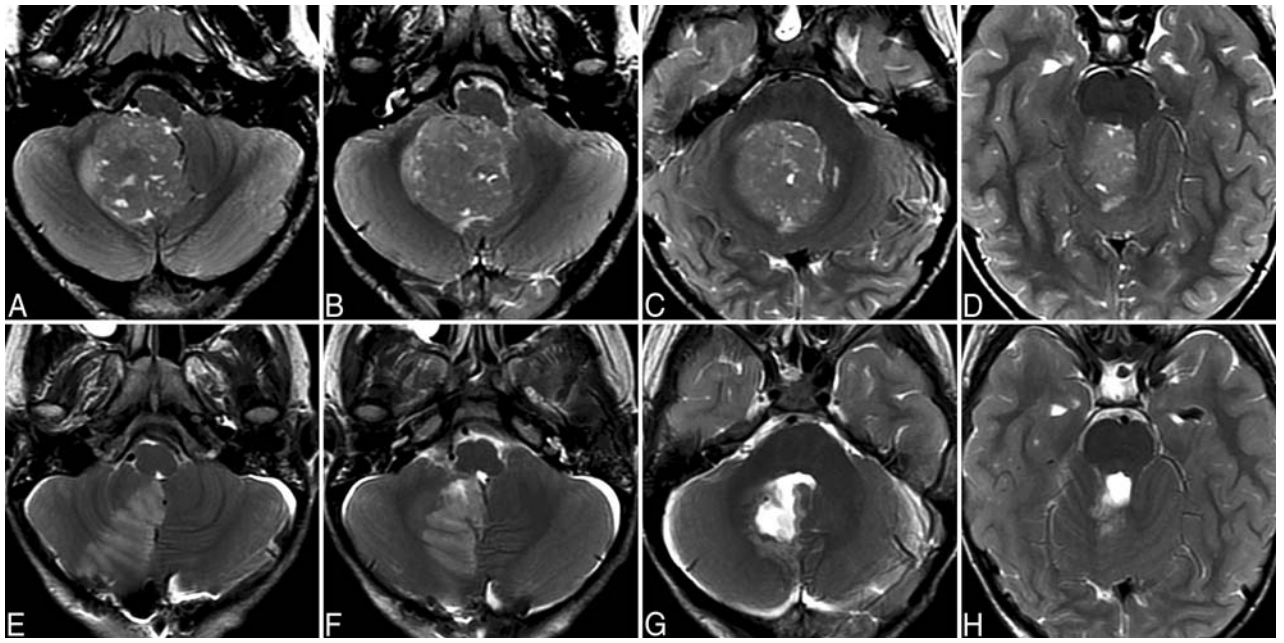

FIG 3. Pre- and postoperative transverse T2WI of an off-midline–intraventricular (subtype C) WNT-subgroup medulloblastoma. A right-sided predominance is evident in the preoperative images, but the tumor has a substantial intraventricular component (*A–D*). This pattern is highlighted by the involvement of the right foramen of Luschka (LS-1c = R1) and by invasion of the right dentate nucleus and right superior cerebellar peduncle (LS-2c = R2). Preoperative imaging data suggest that overall, this tumor is off-midline, with a right-sided predominance (LS-3c = R3). The postoperative damage pattern is identical, with lesions in the right dentate nucleus and superior cerebellar peduncle (LS-4c = R2) and a right PICA territory infarction (*E–H*). The aggregate laterality score indicates a clear right-sided laterality (LS-5c = R5).

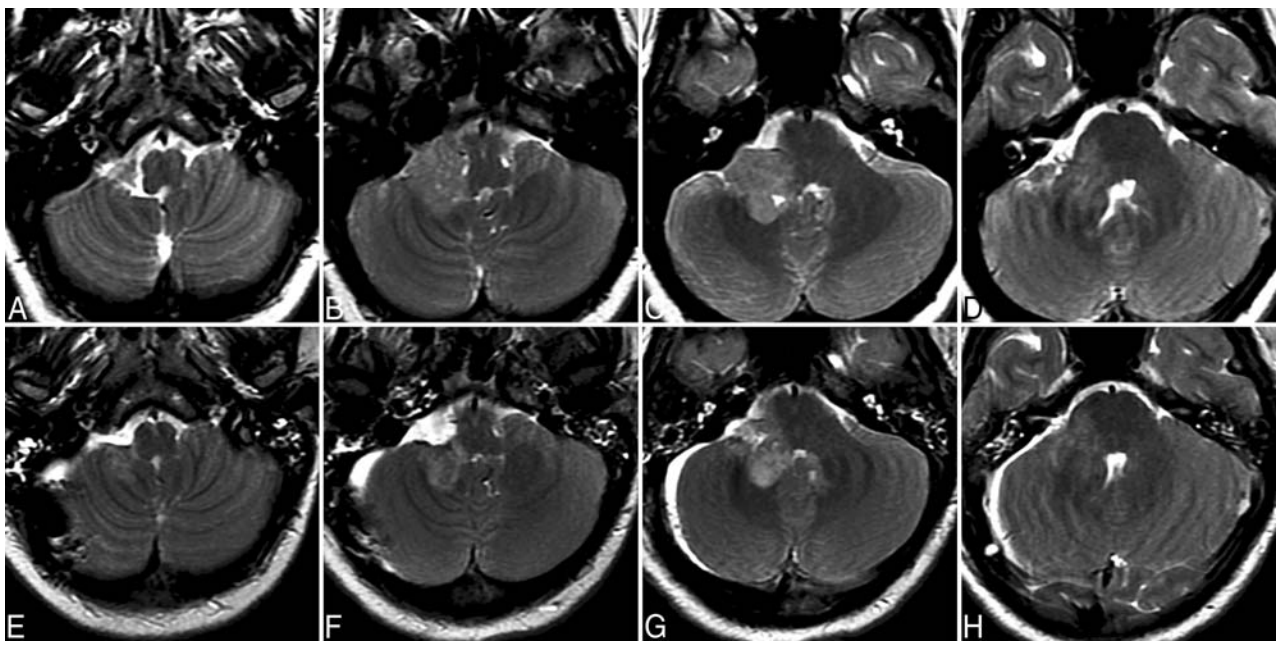

FIG 4. Pre- and postoperative transverse T2WI of an off-midline–extraventricular (subtype D) WNT-subgroup medulloblastoma. This tumor is centered on the right cerebellopontine angle cistern and involves the right foramen of Luschka (*B–C*), with no extension to the fourth ventricle (LS-1c = R2). Invasion of the right lateral brain stem and right inferomedial cerebellum is also suggested (LS-2c = R2). Accordingly, preoperative anatomic imaging data indicate a definite laterality (LS-3c = R4). In postoperative images, damage is seen within the right lower brain stem (*F*), right inferomedial cerebellum (*F–G*), and right middle cerebellar peduncle (*H*) (LS-4c = R3), with no damage to juxtaventricular structures (dentate nucleus, superior cerebellar peduncle). The aggregate laterality score indicates right-sided laterality (LS-5c = R7).

(40%) of 15 patients, considerable signal inhomogeneities were found within the tumor field. In 7 (47%) of 15 patients, the enhancement was homogeneous and involved the entire tumor. At least 1 tumor cyst was found in 7 (47%) of 15 patients. Some degree of intratumoral necrosis was noted in all except 2 patients. Evidence of intratumoral hemorrhage existed in 5 (31.25%) of 16 patients; final diagnosis was MR imaging–based in 4 cases and CT-based in 1 case.

Pre- and Postoperative Anatomic Tumor Features

These results reflect the findings of reviewer 1. Observations by reviewer 2 were used to validate overall reproducibility (see results of the statistical analysis later in this section) and are not detailed here (but some are shown in On-line Tables 3–9).

All 16 WNT tumors appeared to be dominantly extraparenchymal and attached to the surface of the brain stem and/or the cerebellum. The posterior fossa CSF-space involvement is summarized in On-line Table 1.

Altogether, 36 distinct, secondary anatomic structures/sites were preoperatively found to be involved by tumor (range = 1–5/patient, mean = 2.2/patient). The most commonly observed site of invasion was the dentate nucleus (11 [68.75%] of 16 patients). In 9 patients, the invasion was unilateral (6 left, 3 right); in 2 patients, it appeared to be bilateral. The superior cerebellar peduncle was invaded in 5 patients, and the middle cerebellar peduncle, in 3. One side of the inferomedial portion of the cerebellar hemisphere was apparently invaded by the tumor in 6 (37.5%) of 16 cases: the lateral brain stem, in 4 cases (25% overall, 3 on the right and 1 on the left); and the floor of the fourth ventricle, in the other 2 cases (12.5% overall, both on the left).

Altogether, 63 secondary anatomic structures showed postoperative imaging evidence of structural damage (range = 1–8/patient, mean = 3.9/patient). Of the 36 parenchymal invasion sites suggested preoperatively, 30 were confirmed in the postoperative images. Postoperative images showed 33 new lesions that were not recognized preoperatively (these did not include PICA territory infarctions); therefore, those 33 lesions were thought to represent collateral surgical damage.

Laterality Scores

The first consolidated laterality score (LS-1c), which was based on preoperative primary anatomic features, suggested some laterality (LS-1c: range = 1–2) in the tumors of 11 patients (68.75%) and showed no laterality (both LS-1 and LS-1c: 0) or uncertain laterality (LS-1: R1, L1, hence LS-1c: 0) in those of the remaining 5 patients (31.25%). The mean of LS-1c was 0.94 ± 0.77. The second consolidated laterality score (LS-2c), which was based on preoperative secondary anatomic features, suggested laterality in the tumors of all patients (LS-2c range = 1–5, mean = 2.00 ± 1.15). The third consolidated laterality score (LS-3c), which was based on combined preoperative primary and secondary anatomic features, showed even stronger laterality in the tumors of all patients (LS-3c range = 1–6, mean = 2.94 ± 1.53).

Considering the specific CSF-space involvement pattern in conjunction with LS-3c, we established a group assignment for each tumor based on gross location categories (intra- versus extraventricular, midline versus off-midline). This categorization was based on 2 assumptions: 1) for individual tumors, any LS of 0–2 was weak and would not indicate definite laterality, but any LS of 3 or higher was strong and indicative of laterality; and 2) involvement of the fourth ventricle (with or without involvement of other CSF spaces) would indicate an intraventricular tumor. According to this scheme, 6 tumors were midline-intraventricular (subtype A), 2 were midline-extraventricular (subtype B), 5 were off-midline–intraventricular (subtype C), and 3 were off-midline–extraventricular (subtype D) by reviewer 1. There was perfect agreement between reviewer 1 and reviewer 2 in subgroups B and D and some disagreement in subgroups A and C; reviewer 2 actually saw stronger laterality than reviewer 1 (On-line Tables 3–8). The ratio between apparent midline tumors (subtypes A and B) and off-midline tumors (subtypes C and D) was 1:1 (and was 1:1.7 for reviewer 2). For examples, see Figs 1–4.

LS-4c, which was based on the postoperative damage pattern, suggested laterality (LS-4c: range = 1–6) in the tumors of 15 patients (93.75%) and was ambiguous (eg, LS-4 of R3, L3) in the 1 remaining patient (6.25%). The mean of LS-4c was 3.06 ± 1.48. LS-5c, which was based on all (pre- and postoperative) anatomic lesion data, showed tumor laterality in all patients (LS-5c: range = 1–8; mean = 4.69 ± 2.09).

Overall, LS-2c was significantly greater than LS-1c; LS-3c was significantly greater than LS-2c, and LS-5c was significantly greater than LS-4c. However, LS-4c was not significantly different from LS-3c (On-line Table 2).

The mean of the sum of the 3D tumor measures was 11.68 ± 1.83 cm, (range = 7.4–15.1 cm) for the entire cohort. The largest tumors were found in the midline-extraventricular group (mean sum of orthogonal diameters = 12.7 ± 1.27 cm); but on average, off-midline–intraventricular tumors were only slightly smaller (mean = 12.48 ± 1.75 cm). The size of midline-intraventricular tumors was close to the mean size of the tumors of the entire cohort (mean = 11.53 ± 1.43 cm), and off-midline–extraventricular tumors were the smallest (mean = 9.97 ± 2.42 cm) (On-line Tables 3–7).

PICA territory infarction was found in 4 patients (25%). Three of these instances corresponded to an ipsilaterally positive LS (LS-4c values of 1, 2, or 3; LS-5c values of 3, 4, or 5); the other occurred without definite laterality in the postoperative damage pattern (LS-4c: 0) or the overall lesion involvement pattern (LS-5c: 1). Two of those cases involved tumors of subtype B; 1, of subtype A; and 1, of subtype C.

Interobserver Variability and Agreement

There was "substantial" to "perfect" agreement among the 2 neuroradiologists in determining posterior fossa CSF-space involvement (Cohen κ range = 0.63–1.00; On-line Tables 3–7). There was "substantial" agreement among the 2 neuroradiologists for the location-based "group assignments" (subtypes A–D) of each tumor (Cohen κ = 0.65, On-line Table 8). All laterality scores showed "good" to "excellent" consistency between 2 neuroradiologists (intraclass correlation coefficient range = 0.69–0.94; On-line Table 9). Overall, the results were shown to be reproducible, with acceptable interobserver agreement.

DISCUSSION

In this article, we describe the conventional MR imaging features and common locations of WNT-subgroup medulloblastomas by using an MR imaging–based descriptive approach to analyze pre- and postoperative images. Our results suggest that WNT-subgroup medulloblastomas are close to the midline yet are lateralized tumors originating from structures around the foramen of Luschka (superficial layers of the dorsolateral brain stem under the middle cerebellar peduncle and paramedian structures of the inferomedial cerebellar hemispheres). These findings advance

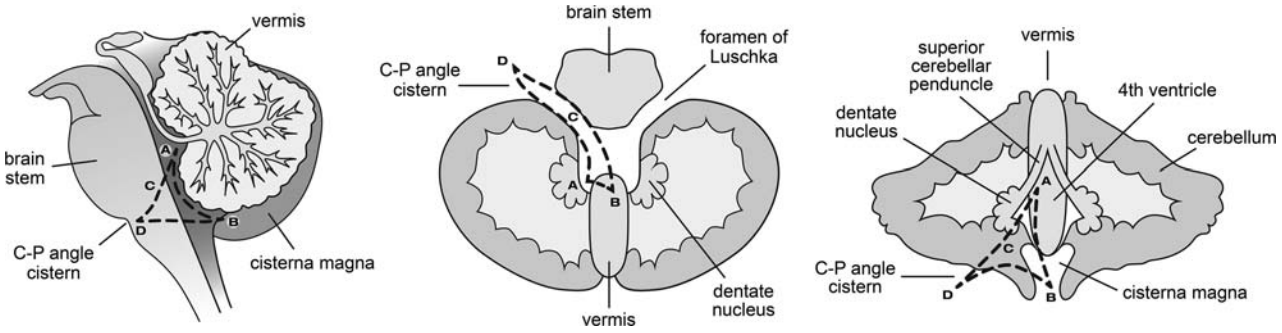

FIG 5. Putative points of origins of WNT-subgroup medulloblastoma in sagittal, transverse, and coronal planes. Letters (*A*–*D*) indicate the theoretic epicenter of tumors in the different subtypes; however, the points of origin represent a continuum, and actual tumors may be centered anywhere along the *dotted lines*.

our current understanding of the implications of tumor location in molecular medulloblastoma subgroups and correlate well with recent discoveries about the developmental origins of WNT-subgroup medulloblastoma and pertinent aspects of the WNT molecular signaling mechanism.[9,12]

In the human embryo, the cerebellum, pons, and medulla oblongata develop from the primitive rhombencephalon. The rhombencephalon is initially formed by 8 rhombomeres, which are present by the end of the fourth fetal week of life, but the development of the cerebellum, in particular, continues even after birth. Each rhombomere has specific sets of transcription factors and receptors, and specific progenitor cell populations have been identified within each rhombomere, which give rise to various cell populations that form the future cerebellum or brain stem. SHH tumors originate from glutamatergic granule cell neuron precursor cells, which are derived from the upper rhombic lip. Conversely, WNT tumors originate from cells arising from the lower rhombic lip.[9] The latter normally migrate along the anterior precerebellar extramural migratory stream (AES) to form nuclei within the posterior portion of the brain stem, but mutant cell populations may give rise to tumors such as WNT-subgroup medulloblastomas in childhood. WNT pathway derangements (somatic mutations of the β-catenin gene, *CTNNB1*) have been found in up to 10% of sporadic medulloblastomas, and WNT tumors represented approximately 11% of our cohort with available molecular data.[4,13]

Conventional and DWI features of WNT-subgroup medulloblastomas are quite similar to those described in the literature.[14,15] Consistent with the high cell attenuation in embryonal tumors of the CNS, WNT-subgroup medulloblastomas have lower T2 signal than do other common pediatric posterior fossa tumors, such as juvenile pilocytic astrocytomas, ependymomas, and choroid plexus tumors. Our data suggest that the diagnostic value of precontrast T2WI and FLAIR imaging is not substantially different. The only potential diagnostic benefit of precontrast FLAIR imaging may be its ability to distinguish a tumor cyst and a sequestrated fourth ventricle space (both may appear quite similar in T2- and T1WI); but in clinical settings, this advantage may not affect disease management enough to justify the additional examination time. DWI remains the most valuable technique in the differentiation of medulloblastomas and all other nonembryonal tumors in the posterior fossa. It invariably shows more-or-less restricted diffusivity within solid tumor areas with corresponding low signal in ADC map images. Although quantitative analysis of ADC data could not be performed in our cohort, variations in ADC signal were recognized, but their significance is still unclear. Because all of our patients had histopathologically classic medulloblastoma, specific correlations between radiologic and histopathologic data were not sought in this cohort. Previous attempts at making such correlations have led to limited or controversial results.[16,17]

Regarding the spatial distribution of WNT-subgroup medulloblastomas in the posterior fossa, our study provides new insights into the most common sites of predilection more precisely than is described in a recent report,[18] which found that 75% of WNT-subgroup tumors occurred along the cerebellar peduncle and the cerebellopontine (CP) angle cistern. Our findings are concordant in that CP angle and foramen of Luschka locations (subtypes C and D in our spatial classification scheme) are highly characteristic of WNT tumors, but we found that the "off-midline" subtypes account for only 50% of the cases. In our experience, WNT tumors seem to develop along an oblique-curved triangle centered on the foramen of Luschka, with 1 peak extending ventrolaterally to the CP-angle cistern, another posteroinferomedially to the cisterna magna, and the third posterosuperomedially to the fourth ventricle (Fig 5).

Consequently, MR imaging shows many of these tumors as clearly off-midline (subtypes C and D) and others as apparently midline (subtypes A and B). To investigate putative points of origin of the latter 2 subtypes, we developed an iterative evaluation process that takes into account pre- and postoperative imaging features indicating tumor invasion of specific anatomic regions and structures. The resultant LSs suggest laterality even in the apparent midline cases; therefore, we speculate that midline-intraventricular WNT-subgroup medulloblastomas may originate near the ventricular orifice of the foramen of Luschka (eg, lateral recess of the fourth ventricle) and spread upward along the lateral wall of the fourth ventricle, which would explain the high incidence of dentate nucleus invasion.

Most interesting, the LS, if based solely on the postoperative damage pattern, is relatively low and, by itself, does not much affect determinations of the laterality of the tumor. The most likely explanation for this phenomenon may be that the postoperative damage pattern may include a few inadvertent lesions ("collateral damage"); therefore, the resultant LS is somewhat reduced by those. Nonetheless, we found the meticulous evaluation

of the postoperative damage pattern to be helpful in understanding typical tumor locations.

On the basis of the observed involvement patterns, we propose that 4 apparent topographic phenotypes may be distinguished in WNT-subgroup medulloblastomas: 1) midline-intraventricular; 2) midline-extraventricular (centered on the cisterna magna with possible extensions toward the foramen magnum and/or the foramen of Magendie); 3) off-midline–intraventricular (centered on the foramen of Luschka with systematic extension to the fourth ventricle and optional extension into the CP angle cistern); and 4) off-midline–extraventricular (centered on the CP angle cistern, with more-or-less involvement of the foramen of Luschka). The extreme forms in each subtype are fairly straightforward, but overall, these phenotypic subtypes exhibit spatial overlaps, representing a continuum rather than 4 distinct categories. We have reason to believe that "midline" tumors (subtypes A and B) in the WNT-subgroup are actually paramedian (ie, close to the midline but not originating from the vermis) as opposed to the usually more lateralized SHH-subgroup tumors. Given that SHH-subgroup medulloblastomas are usually hemispheric (with few originating from the vermis) and typically extraventricular, and if WNT-subgroup medulloblastomas are indeed paramedian, then the only true midline-intraventricular tumors may be group 3 and 4 medulloblastomas. Further studies are needed to examine this hypothesis.

The incidence of PICA territory infarction in our patient cohort was high. The infarctions did not include the retro-olivary area; therefore, we speculate that the increased surgical risk to these patients may have to do with the often-suggested possible engulfment of the artery in its retromedullary course. We speculate that WNT-subgroup medulloblastomas may be associated with an increased risk for PICA infarction at surgery.

The laterality in conjunction with the dominantly extraparenchymal location of WNT-subgroup medulloblastomas would suggest that these tumors originate from mutant precursor cells on one side of the lower rhombic lip that fail to migrate along the anterior precerebellar extramural migratory stream. As a function of other modulating factors, these precursors may subsequently undergo neoplastic transformation and spread from the foramen of Luschka toward adjacent CSF spaces along the surface of the cerebellum and brain stem. This scenario implies that WNT-subgroup medulloblastomas are not cerebellar tumors.

We found that in midline-intraventricular (subtype A) WNT medulloblastomas, an obvious laterality is usually difficult to recognize at preoperative diagnostic imaging evaluation, complicating the differential diagnosis between these and other midline-intraventricular tumors, including group 3 and 4 medulloblastomas, some ependymomas, and choroid plexus tumors. Conversely, a tumor with DWI evidence of hypercellularity in any of the other 3 locations (subtypes B–D) may be more suggestive of WNT-subgroup medulloblastoma, but overlaps may occur. The infravermian (subtype B) tumors are rare but fairly characteristic, as are tumors with a clearly unilateral foramen of Luschka epicenter (subtype C). These location subtypes, however, may overlap with the typically hemispheric SHH-subgroup medulloblastomas (if those are inferomedial) and with some of the posterior fossa ependymomas. The CP angle cistern is also a well-known location for atypical teratoid rhabdoid tumors, complicating the initial imaging differential diagnosis of subtype D WNT-subgroup medulloblastomas; however, the biologic behavior and prognosis of the 2 are different. Bilateral involvement of the foramina of Luschka and of the CP angle cisterns is common in ependymoma and is rare in WNT-subgroup medulloblastoma. Choroid plexus tumors arising from the fourth ventricle are often midline-intraventricular but may be lateralized to involve the foramen of Luschka; however, their DWI appearance usually differs from that of embryonal tumors.

CONCLUSIONS

The spatial distribution of WNT-subgroup medulloblastomas in the posterior fossa appears to be in concordance with our current understanding of the embryologic origins of this tumor subtype. Our results contribute to the growing body of data showing the potential of "imaging genomics" for use in research and in the diagnostic imaging of certain genetically determined pathologies of the central nervous system.

Disclosures: Zoltan Patay—*RELATED*: *Grant*: National Institutes of Health,* American Lebanese Syrian Associated Charities,* *Comments*: St. Jude Children's Research Hospital is a Comprehensive Cancer Center receiving grant support from the National Cancer Institute. The American Lebanese Syrian Associated Charities is the fundraising arm of St. Jude Children's Research Hospital. St. Jude Children's Research Hospital received support from the United States National Institutes of Health Cancer Center Support grant P30 CA21765 and the American Lebanese Syrian Associated Charities while the author participated in this research; *UNRELATED*: *Consultancy*: Guerbet, *Comments*: one-time consultancy in 2013; *Grants/Grants Pending*: Pediatric Brain Tumor Consortium, *Comments*: salary support from the Pediatric Brain Tumor Consortium; *Travel/Accommodations/Meeting Expenses Unrelated to Activities Listed*: Italian Society of Pediatric Neuroradiology (2014), European Course of MRI (2012–14), Kuwait Radiology Society (2013), Sao Paolo Radiology Society (2013), Hungarian Neuroradiology Society (2013), Indian Neuroradiology Society (2013), Arab Radiology Congress (2014), International Radiology Congress (2014), Symposium Neuroradiologicum (2014), *Comments*: travel and hotel reimbursement for giving invited educational lectures. David W. Ellison—*UNRELATED*: *Patents (planned, pending, or issued)*: The patent is held for the immunophenotyping of medulloblastomas, but no payments are received. *Money paid to the institution.

REFERENCES

1. Northcott PA, Korshunov A, Witt H, et al. **Medulloblastoma comprises four distinct molecular variants.** *J Clin Oncol* 2011;29:1408–14 CrossRef Medline
2. Northcott PA, Dubuc AM, Pfister S, et al. **Molecular subgroups of medulloblastoma.** *Expert Rev Neurother* 2012;12:871–84 CrossRef Medline
3. Northcott PA, Jones DT, Kool M, et al. **Medulloblastomics: the end of the beginning.** *Nat Rev Cancer* 2012;12:818–34 CrossRef Medline
4. Kool M, Korshunov A, Remke M, et al. **Molecular subgroups of medulloblastoma: an international meta-analysis of transcriptome, genetic aberrations, and clinical data of WNT, SHH, group 3, and group 4 medulloblastomas.** *Acta Neuropathol* 2012;123:473–84 CrossRef Medline
5. Ellison DW, Dalton J, Kocak M, et al. **Medulloblastoma: clinicopathological correlates of SHH, WNT, and non-SHH/WNT molecular subgroups.** *Acta Neuropathol* 2011;121:381–96 CrossRef Medline
6. Ellison DW, Kocak M, Dalton J, et al. **Definition of disease-risk stratification groups in childhood medulloblastoma using combined clinical, pathologic, and molecular variables.** *J Clin Oncol* 2011;29:1400–07 CrossRef Medline
7. Ellison DW. **Childhood medulloblastoma: novel approaches to the classification of a heterogeneous disease.** *Acta Neuropathol* 2010;120:305–16 CrossRef Medline
8. Ramaswamy V, Remke M, Bouffet E, et al. **Recurrence patterns**

across medulloblastoma subgroups: an integrated clinical and molecular analysis. *Lancet Oncol* 2013;14:1200–07 CrossRef Medline
9. Gibson P, Tong Y, Robinson G, et al. **Subtypes of medulloblastoma have distinct developmental origins.** *Nature* 2010;468:1095–99 CrossRef Medline
10. Cicchetti DV. **Guidelines, criteria, and rules of thumb for evaluating normed and standardized assessment instruments in psychology.** *Psychol Assess* 1994;6:284–90 CrossRef
11. Landis JR, Koch GG. **The measurement of observer agreement for categorical data.** *Biometrics* 1977;33:159–74 CrossRef Medline
12. Teo WY, Shen J, Su JM, et al. **Implications of tumor location on subtypes of medulloblastoma.** *Pediatr Blood Cancer* 2013;60:1408–10 CrossRef Medline
13. Ellison DW, Onilude OE, Lindsey JC, et al; United Kingdom Children's Cancer Study Group Brain Tumour Committee. **β-Catenin status predicts a favorable outcome in childhood medulloblastoma: the United Kingdom Children's Cancer Study Group Brain Tumour Committee.** *J Clin Oncol* 2005;23:7951–57 CrossRef Medline
14. Mueller DP, Moore SA, Sato Y, et al. **MRI spectrum of medulloblastoma.** *Clin Imaging* 1992;16:250–55 CrossRef Medline
15. Eran A, Ozturk A, Aygun N, et al. **Medulloblastoma: atypical CT and MRI findings in children.** *Pediatr Radiol* 2010;40:1254–62 CrossRef Medline
16. Fruehwald-Pallamar J, Puchner SB, Rossi A, et al. **Magnetic resonance imaging spectrum of medulloblastoma.** *Neuroradiology* 2011;53:387–96 CrossRef Medline
17. Yeom KW, Mobley BC, Lober RM, et al. **Distinctive MRI features of pediatric medulloblastoma subtypes.** *AJR Am J Roentgenol* 2013;200:895–903 CrossRef Medline
18. Perreault S, Ramaswamy V, Achrol AS, et al. **MRI surrogates for molecular subgroups of medulloblastoma.** *AJNR Am J Neuroradiol* 2014;35:1263–69 CrossRef Medline

MRI Findings of Disc Degeneration are More Prevalent in Adults with Low Back Pain than in Asymptomatic Controls: A Systematic Review and Meta-Analysis

W. Brinjikji, F.E. Diehn, J.G. Jarvik, C.M. Carr, D.F. Kallmes, M.H. Murad, and P.H. Luetmer

ABSTRACT

BACKGROUND AND PURPOSE: Imaging features of spine degeneration are common in symptomatic and asymptomatic individuals. We compared the prevalence of MR imaging features of lumbar spine degeneration in adults 50 years of age and younger with and without self-reported low back pain.

MATERIALS AND METHODS: We performed a meta-analysis of studies reporting the prevalence of degenerative lumbar spine MR imaging findings in asymptomatic and symptomatic adults 50 years of age or younger. Symptomatic individuals had axial low back pain with or without radicular symptoms. Two reviewers evaluated each article for the following outcomes: disc bulge, disc degeneration, disc extrusion, disc protrusion, annular fissures, Modic 1 changes, any Modic changes, central canal stenosis, spondylolisthesis, and spondylolysis. The meta-analysis was performed by using a random-effects model.

RESULTS: An initial search yielded 280 unique studies. Fourteen (5.0%) met the inclusion criteria (3097 individuals; 1193, 38.6%, asymptomatic; 1904, 61.4%, symptomatic). Imaging findings with a higher prevalence in symptomatic individuals 50 years of age or younger included disc bulge (OR, 7.54; 95% CI, 1.28–44.56; $P = .03$), spondylolysis (OR, 5.06; 95% CI, 1.65–15.53; $P < .01$), disc extrusion (OR, 4.38; 95% CI, 1.98–9.68; $P < .01$), Modic 1 changes (OR, 4.01; 95% CI, 1.10–14.55; $P = .04$), disc protrusion (OR, 2.65; 95% CI, 1.52–4.62; $P < .01$), and disc degeneration (OR, 2.24; 95% CI, 1.21–4.15, $P = .01$). Imaging findings not associated with low back pain included any Modic change (OR, 1.62; 95% CI, 0.48–5.41, $P = .43$), central canal stenosis (OR, 20.58; 95% CI, 0.05–798.77; $P = .32$), high-intensity zone (OR = 2.10; 95% CI, 0.73–6.02; $P = .17$), annular fissures (OR = 1.79; 95% CI, 0.97–3.31; $P = .06$), and spondylolisthesis (OR = 1.59; 95% CI, 0.78–3.24; $P = .20$).

CONCLUSIONS: Meta-analysis demonstrates that MR imaging evidence of disc bulge, degeneration, extrusion, protrusion, Modic 1 changes, and spondylolysis are more prevalent in adults 50 years of age or younger with back pain compared with asymptomatic individuals.

Low back pain affects up to two-thirds of adults at some point in their lives.[1] Back pain–related disability has significant economic consequences due to consumption of health care resources and loss of economic productivity.[2] Increased use of MR imaging and CT in the evaluation of patients with back pain consumes a large amount of health care resources.[3] Imaging findings such as disc bulge and disc protrusion/extrusion are often interpreted as causes of back pain, triggering both medical and surgical interventions.[4] Furthermore, prior studies have demonstrated that imaging findings of spinal degeneration associated with back pain are present in a large proportion of both symptomatic and asymptomatic individuals, thus limiting the diagnostic value of these findings.[5-7]

Numerous studies have examined and compared the prevalence of degenerative spine findings in symptomatic and asymptomatic populations. Given the large number of adults who undergo advanced imaging to help determine the etiology of their back pain, it is important to know whether these findings are indeed more prevalent in symptomatic-versus-asymptomatic patients. Such information will help radiologists, referring clinicians, and patients interpret the importance of degenerative findings noted in radiology reports. The purpose of this meta-analysis of case-control studies was to compare the prevalence of MR imaging features of lumbar spine degeneration in adult individuals

Received February 25, 2015; accepted after revision April 7.

From the Department of Radiology (W.B., F.E.D., C.M.C., D.F.K., P.H.L.) and Center for Science of Healthcare Delivery (M.H.M.), Mayo Clinic, Rochester, Minnesota; and Department of Neurological Surgery and Health Services, Comparative Effectiveness Cost and Outcomes Research Center (J.G.J.) and Department of Radiology (J.G.J.), University of Washington, Seattle, Washington.

Please address correspondence to Waleed Brinjikji, MD, Mayo Clinic, Department of Radiology, Mayo Clinic, 200 1st St SW, Rochester, MN 55905; brinjikji.waleed@mayo.edu; @WBrinjikji

Indicates article with supplemental online tables.

Evidence-Based Medicine Level 1.

http://dx.doi.org/10.3174/ajnr.A4498

50 years of age or younger with and without self-reported low back pain.

MATERIALS AND METHODS

Data Sources and Searches

We performed a comprehensive search for studies describing relevant imaging findings as described below by using MEDLINE and EMBASE. To identify studies on imaging of symptomatic and asymptomatic spinal disorders, a medical librarian searched Ovid MEDLINE, Ovid EMBASE, and the Web of Science through April 24, 2014 (week 16). EMBASE was searched beginning in 1988 to April 24, 2014, and MEDLINE was searched beginning in 1946 through April 24, 2014. The Web of Science is text-word-based, but it tends to be more current and multidisciplinary, so studies may be discovered that are not included in the other data bases. The search strategy is further detailed in the On-line Tables 1 and 2. The initial search terms included spinal diseases or disorders affecting the spine: intervertebral disc degeneration or displacement, spondylolysis, low back pain, or specific vertebrae and joints (eg, lumbar vertebrae). This search term was combined with diagnostic imaging techniques (MR imaging) and the terms "symptomatic," "pain," "undetected," "asymptomatic," and "asymptomatic disease" (subject heading available in EMBASE, but not MEDLINE). Studies identified from the literature search underwent further evaluation for inclusion in the meta-analysis. We also searched references from the studies included in this meta-analysis to find any additional case-control studies that reported lumbar spine MR imaging findings. This systematic review was not registered with the Cochrane Collaborative.

Study Selection and Data Extraction

To be included in our review, a study needed to be published in English and report the prevalence of degenerative findings on spine MR imaging in both asymptomatic and symptomatic individuals. Case-control and cross-sectional studies were included in this analysis. Patient symptomatology was generally determined at the time of the MR imaging findings. We defined asymptomatic individuals as those with no history of back pain and symptomatic individuals as those with any history of back pain, which included axial back pain and/or sciatica or radiculopathies. The age range for included individuals was 15–50 years. Any studies reporting the prevalence of degenerative findings in patients older than 50 years of age were reviewed to determine whether they stratified outcomes by age so that findings in individuals 50 years of age or younger could be abstracted. Inclusion criteria, including age cutoffs, were agreed on by the authors by consensus. One reviewer examined abstracts of studies identified from the literature search to determine whether the studies met the inclusion criteria and to exclude any studies that were not relevant to the topic being studied (ie, neck pain, studies correlating CT or radiographs and low back pain, review articles, and so forth).

For each study that met inclusion criteria, we used a standard form to abstract imaging technique, sample sizes, and the prevalence rates for the following imaging findings: central spinal canal stenosis, disc degeneration, annular fissure (including high-intensity zones), high-intensity zones (a subgroup of annular fissures defined as "annular fissures with a focal area of increased T2 signal"), disc bulge, disc protrusion, disc extrusion, Modic changes (type 1 Modic changes and all Modic changes), spondylolisthesis, and spondylolysis. These entities are defined in detail by the combined task forces of the American Society of Neuroradiology, American Society of Spine Radiology, and North American Spine Society.[8] Each study that met the initial inclusion criteria was abstracted by 2 reviewers. Any differences in data abstraction were resolved by having a third, independent reviewer arbitrate the findings. There were 6 studies that, when further reviewed during data abstraction, were not thought to meet the inclusion criteria. These studies were sent to an independent reviewer to verify that they did not meet the inclusion criteria.

Quality Assessment

We performed quality assessment of the studies by using the Newcastle-Ottawa Scale. This tool is used for assessing the quality of nonrandomized studies included in systematic reviews and/or meta-analyses. Each study is judged on 8 items categorized into 3 groups: 1) selection of the study groups, 2) comparability of the study groups, and 3) ascertainment of the outcome of interest.[9]

Statistical Analysis

From each study, we extracted a 2×2 table for binary outcomes. Random-effects meta-analysis was used for pooling across studies.[10] The I^2 statistic was used to express the proportion of inconsistency that was not attributable to chance.[11] I^2 values of $>50\%$ indicated substantial heterogeneity of the observed odds ratios. Meta-analysis results were expressed as odds ratios for binary outcomes with respective 95% confidence intervals. $P < .05$ was statistically significant. To further explore heterogeneity and the effect of confounding by age, in addition to conducting subgroup analysis based on age, we conducted meta-regression. In the regression model, the dependent variable is the log of the odds ratio and the independent variable is age as a continuous outcome. We conducted the meta-analysis by using Comprehensive Meta-Analysis, Version 2.2 (Biostat Inc, Englewood, New Jersey). We also reported the mean prevalence and 95% CI for each imaging finding. The mean prevalence was determined by using a pooled analysis. We provide these data for reference but did not use them for statistical comparison.

RESULTS

Literature Search

On-line Table 3 summarizes the included studies, and Fig 1 summarizes the search and selection process. Our initial search yielded 280 unique studies. On the basis of the abstracts of these studies, we excluded 243 studies (86.8%) that did not meet our review inclusion criteria. Of the remaining 37, we excluded 17 (45.9%) because they either did not separate the prevalence of findings by symptomatic status, did not include a truly asymptomatic cohort, or had ambiguous symptomatic status of the patients. We excluded an additional 6 case-control studies because they either did not include patients 50 years of age or younger or findings of patients 50 years of age or younger could not be differentiated from those of the rest of the cohort. In total, 14 (5.0%) studies comprising 3097 patients met the inclusion criteria. Asymptomatic individuals composed 38.6% of the overall cohort

(1193 individuals), and symptomatic individuals composed 61.4% of the overall cohort (1904 individuals).

Study Quality

All included studies had a high-quality as assessed by the New Castle–Ottawa Scale. All included studies demonstrated a high degree of comparability based on variables such as race/ethnicity, demographic groups, and age. Outcomes were clearly reported in all included studies. Three included studies were at risk for selection bias because they studied the prevalence of degenerative findings in elite athletes.

Degenerative Spine Findings by Symptomatic Status in Individuals 50 Years of Age and Younger

In order of decreasing OR, imaging findings with a higher prevalence in individuals with low back pain 50 years of age or younger compared with asymptomatic individuals 50 years of age or younger included disc bulge (OR, 7.54; 95% CI, 1.28–44.56; $P = .01$), spondylolysis (OR, 5.06; 95% CI, 1.65–15.53; $P < .01$), disc extrusion (OR, 4.38; 95% CI, 1.98–9.68; $P < .01$), Modic 1 changes (OR, 4.01; 95% CI, 1.10–14.55; $P = .04$), disc protrusion (OR, 2.65; 95% CI, 1.52–4.62; $P = .03$), and disc degeneration (OR, 2.24; 95% CI, 1.21–4.15; $P = .01$).

Imaging findings not associated with low back pain included any Modic change (OR, 1.62; 95% CI, 0.48–5.41; $P = .43$), central canal stenosis (OR, 20.58; 95% CI, 0.05–798.77; $P = .32$), high-intensity zone (OR, 2.10; 95% CI, 0.73–6.02, $P = .17$), annular fissures (including patients with and without high-intensity zones) (OR, 1.79; 95% CI, 0.97–3.31; $P = .06$), and spondylolisthesis (OR, 1.59; 95% CI, 0.78–3.24; $P = .20$). These data, including the prevalences and 95% CIs of each of these findings, are summarized in the Table.

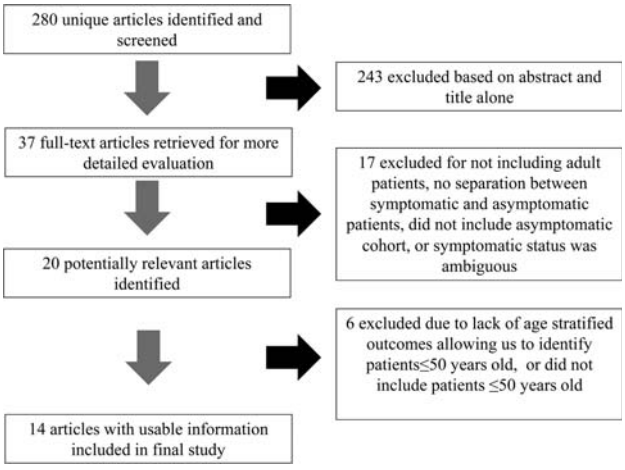

FIG 1. Search strategy.

Meta-Regression Results

Meta-regression based on age was possible only in 2 outcomes (disc degeneration and protrusion, with 12 and 9 studies, respectively). The number of studies evaluating the remaining outcomes was too small to do a meaningful meta-regression. We were unable to demonstrate a statistically significant association between age and these 2 outcomes (P values for the model of .22 and .49; respectively). This is likely due to low power and the small number of available studies and should not be interpreted as lack of effect of age on these 2 outcomes.

Study Heterogeneity

Meta-analysis of the following findings demonstrated I^2 values of <50%, indicating a lack of substantial heterogeneity in reported ORs: Modic 1 changes (0%), disc extrusion (0%), spondylolisthesis (0%), and spondylolysis (0%). Meta-analysis of the following findings demonstrated I^2 values of >50%, indicating substantial heterogeneity of reported ORs: central spinal canal stenosis (94%), disc bulge (90%), disc degeneration (89%), high-intensity zones (72%), disc protrusion (62%), annular fissure (59%), and any Modic changes (65%).

DISCUSSION

This meta-analysis of 14 high-quality case-control studies including >3000 individuals demonstrates that many degenerative spine findings have a higher prevalence in individuals 50 years of age or younger with self-reported low back pain compared with asymptomatic individuals. Disc findings, including disc bulge, disc degeneration, and disc extrusion and protrusions, had significant associations with low back pain. Type 1 Modic changes and spondylolysis also demonstrated a significant association with low back pain. While these findings do not prove that disc- and endplate-related imaging and spondylolysis are pain generators, they do suggest that evidence of these findings could be explored as candidates for biomarkers of low back pain.

Our findings corroborate those of other studies examining the association between disc imaging findings and low back pain. Multiple previous studies have demonstrated a higher prevalence

Outcomes

Outcome	No. of Studies	OR (95% CI)	Prevalence Asymptomatic	Prevalence Symptomatic	*P* Value[a]	I^2 (%)
Annular fissure	6	1.79 (0.97–3.31)	11.3% (9.0%–14.2%)	20.1% (17.7%–22.8%)	.06	59
High-intensity zone	4	2.10 (0.73–6.02)	9.5% (6.7%–13.4%)	10.4% (8.0%–13.4%)	.17	72
Central spinal canal stenosis	2	20.58 (0.05–798.77)	14.0% (10.4%–18.6%)	59.5% (54.9%–63.9%)	.32	94
Disc bulge	3	7.54 (1.28–44.56)	5.9% (3.8%–8.9%)	43.2% (38.2%–48.2%)	.03	90
Disc degeneration	12	2.24 (1.21–4.15)	34.4% (31.5%–37.5%)	57.4% (54.8%–59.8%)	.01	89
Disc extrusion	4	4.38 (1.98–9.68)	1.8% (0.1%–3.7%)	7.1% (5.4%–9.4%)	<.01	0
Disc protrusion	9	2.65 (1.52–4.62)	19.1% (16.5%–22.3%)	42.2% (39.3%–45.1%)	.00	62
Modic changes	5	1.62 (0.48–5.41)	12.1% (9.6%–15.2%)	23.2% (21.7%–27.3%)	.43	65
Modic 1 changes	2	4.01 (1.10–14.55)	3.2% (0.7%–9.4%)	6.7% (4.2%–10.4%)	.04	0
Spondylolisthesis	4	1.59 (0.78–3.24)	3.2% (1.8%–5.8%)	6.2% (4.4%–8.7%)	.20	0
Spondylolysis	2	5.06 (1.65–15.53)	1.8% (0.0%–5.3%)	9.4% (6.6%–12.4%)	<.01	0

[a] *P* values are computed from the meta-analysis of ORs. Prevalence data are provided for reference but are not meant for statistical comparison.

of disc findings in symptomatic-versus-asymptomatic individuals. Disc protrusions are not uncommon in asymptomatic adult populations, with prevalences ranging from 10% to 30%, depending on the studied age group.[12-20] In general, epidemiologic studies demonstrate that the prevalence of disc protrusions in asymptomatic populations increases with age.[12-20] Our study found that nearly 20% of asymptomatic patients 50 years of age or younger had disc protrusion compared with nearly 40% in the symptomatic group. Disc extrusions are rare in asymptomatic populations. The prevalence of disc extrusions ranged from 0% to 4% in asymptomatic patients, with most studies reporting prevalence rates of <2%.[21-24] On the contrary, prevalence of disc extrusions ranged from 5% to 10% in symptomatic populations.[21-24]

One surprising finding from our study was that disc bulge had a strong association with low back pain. Because of the high prevalence in the asymptomatic population, disc bulges are often considered incidental findings and not associated with low back pain. The prevalence of disc bulges in asymptomatic populations ranges from 20% in young adults to >75% in patients older than 70 years of age.[25-30] Our meta-analysis found a prevalence of disc bulges of 6% in asymptomatic populations and 43% of symptomatic populations. All 3 studies included in our meta-analysis assessing the association between disc bulges and pain demonstrated a very strong association between disc bulge with low back pain.[19,21,31] Two of these studies only included patients younger than 30 years of age.[21,31] These findings suggest that the association between disc bulge and low back pain may be more significant in younger adults, in whom the prevalence in the general asymptomatic population is much lower. It is possible that the association between disc bulges and low back pain disappears in older populations, in whom the prevalence of this imaging finding is >90% in the asymptomatic population.[32]

Similar to disc bulge, disc degeneration also has a very high prevalence in asymptomatic individuals, ranging from 30% to 95%, depending on the age group.[5,13,15,18,19,23,27,29,32-36] Some studies have demonstrated no association between disc degeneration and low back pain, especially in older individuals.[37,38] Our meta-analysis on 12 studies found a strong association of disc degeneration and low back pain in individuals 50 years of age or younger, with >30% of asymptomatic individuals and >50% of symptomatic individuals found to have disc degeneration on MR imaging.

Our study also found that in the adult population of 50 years of age or younger, annular fissures and high-intensity zones had no association with low back pain. The association between annular fissures and low back pain is controversial. A majority of studies in our analysis demonstrated a higher prevalence of annular fissures in symptomatic-versus-asymptomatic patients. However, the largest study in our analysis, which included >500 patients 18–21 years of age, demonstrated no association between annular fissures and low back pain.[25]

Modic 1 changes had a significant association with low back pain in our analysis. However, Modic changes as a whole (Modic 1–3) did not have an association with low back pain. In a systematic review of Modic change prevalence in asymptomatic and symptomatic populations, Jensen et al[39] found that the median prevalence of any type of Modic changes in symptomatic individuals in the literature was 36% compared with 14% in non-back pain populations. However, when considering case-control studies, this analysis demonstrated no association between Modic changes and low back pain. Large cohort studies have demonstrated that type 1 Modic changes are, in fact, strongly associated with low back pain.[40] Spondylolysis was strongly associated with low back pain in patients 50 years of age or younger. These findings are supported in studies from the surgical literature that demonstrate that direct screw repair of pars interarticularis defects provides long-term pain relief and improves the biomechanical function of the lower lumbar spine.[41]

Findings not directly related to the disc such as spondylolisthesis and central canal stenosis demonstrated no association with low back pain in our study. These findings are consistent with what has been previously reported in the literature. Spondylolisthesis is also consistently not associated with low back pain in case-control studies.[6] However, in general, the grade or average grade of spondylolisthesis found in these population-based studies was low, and none of the studies included in our meta-analysis evaluated the presence of dynamic instability. Our finding that central canal stenosis was not associated with low back pain is likely because this entity typically presents with lower extremity rather than back pain (ie, neurogenic claudication). In addition, only the presence rather than the severity of central canal stenosis was evaluated.

Limitations

Our study has limitations. It was limited to individuals 50 years of age or younger; thus, our findings pertain only to this specific population. With the increasing prevalence of some degenerative findings such as degenerative disc and disc bulge with increasing age, it is possible that the association between these entities and low back pain is less significant in older age groups. There was substantial geographic, ethnic, and occupational heterogeneity in the populations included our analysis. Another major limitation is that the studies included in our analysis were published during a broad time period, and not all of the studies used the original or more recent Fardon et al[8] and Fardon and Milette[42] combined task force nomenclature recommendations. Thus, differences in nomenclature and definitions of some entities could affect our results.

Another limitation is that our study defined back pain broadly, including axial, sciatica and radicular pain. Most of the studies did not explicitly define whether patients had axial or radicular symptoms or both. In general, the studies in our analysis included patients with self-reported low back pain, which was confirmed on physical examination at or around the time of the MR imaging examination. Another important limitation is that only the presence of these degenerative findings was considered, not the extent or severity. This is especially important because increased severity and extent of Modic changes, spinal stenosis, and disc degeneration are associated with increased pain.[43] Modic changes could only be analyzed as type 1 changes and combined type 2 and 3 changes because the included studies generally did not differentiate between type 2 and 3 changes. As such, we did not have the opportunity to study whether type 2 or 3 changes were associated with low back pain.

Regarding the study design, our study included primarily case-control and cross-sectional studies but did not include cohort studies. As such, we did not study the association between MR imaging findings and future back pain. Symptomatology was determined at the time of imaging. In addition, we could not perform separate subgroup analyses by decade of life due to a paucity of studies that stratified findings by decade of life. It is possible that the association of pain and degenerative findings is different for patients 30 years of age and younger and those 30–50 years of age. Many of the I^2 values were >50%, suggesting substantial heterogeneity in reported results. The imaging features examined in this study are correlated (ie, a patient with one finding is more likely to have another). Hence, the observed associations are affected by confounding and cannot be used for diagnostic purposes. Last, some of the specific MR imaging finding meta-analyses included as few as 2 studies. All these limitations highlight the need for further studies on the association between MR imaging findings and low back pain. One disadvantage of evaluating only case-control studies is that we excluded the populations included in cohort studies reporting the prevalence of degenerative findings in asymptomatic subjects only.

CONCLUSIONS

This meta-analysis of epidemiologic studies demonstrates that MR imaging evidence of disc bulge, disc degeneration, disc extrusions and protrusions, Modic 1 changes, and spondylolysis had significant associations with low back pain in adult patients 50 years of age or younger. The association between these degenerative findings and pain should not be interpreted as causation. These imaging findings may be considered as candidate biomarkers for low back pain in younger patients (younger than 50 years of age). The role of these findings in determining treatment strategies or prognosis of low back pain has not been established.

Disclosures: Jeffrey G. Jarvik—*UNRELATED*: *Board Membership*: AUR GE Radiology Research Academic Fellowship, *Comments*: Faculty Advisory Board; *Consultancy*: HealthHelp; *Royalties*: PhysioSonics, *Comments*: a high-intensity focused ultrasound company; *Stock/Stock Options*: PhysioSonics, *Comments*: a high-intensity focused ultrasound company. David F. Kallmes—*UNRELATED*: *Board Membership*: GE Healthcare, *Comments*: Cost-Effectiveness Board; *Royalties*: University of Virginia Patent Foundation, *Comments*: spine fusion. Patrick H. Luetmer—*UNRELATED*: *Grants/Grants Pending*: National Institutes of Health,* *Comments*: Lumbar Image Reporting with Epidemiology. Funded by the National Institutes of Health. (UH3 AR 66795) 01/01/2014-12/31/2017. *Money paid to the institution.

REFERENCES

1. Jarvik JG, Deyo RA. **Diagnostic evaluation of low back pain with emphasis on imaging.** *Ann Intern Med* 2002;137:586–97 CrossRef Medline
2. Deyo RA, Cherkin D, Conrad D, et al. **Cost, controversy, crisis: low back pain and the health of the public.** *Annu Rev Public Health* 1991;12:141–56 CrossRef Medline
3. Li AL, Yen D. **Effect of increased MRI and CT scan utilization on clinical decision-making in patients referred to a surgical clinic for back pain.** *Can J Surg* 2011;54:128–32 CrossRef Medline
4. Carragee E, Alamin T, Cheng I, et al. **Are first-time episodes of serious LBP associated with new MRI findings?** *Spine J* 2006;6:624–35 CrossRef Medline
5. Boden SD, Davis DO, Dina TS, et al. **Abnormal magnetic-resonance scans of the lumbar spine in asymptomatic subjects: a prospective investigation.** *J Bone Joint Surg Am* 1990;72:403–08 Medline
6. Kalichman L, Kim DH, Li L, et al. **Computed tomography-evaluated features of spinal degeneration: prevalence, intercorrelation, and association with self-reported low back pain.** *Spine J* 2010;10:200–08 CrossRef Medline
7. Wiesel SW, Tsourmas N, Feffer HL, et al. **A study of computer-assisted tomography, I: the incidence of positive CAT scans in an asymptomatic group of patients.** *Spine (Phila Pa 1976)* 1984;9:549–51 CrossRef Medline
8. Fardon DF, Williams AL, Dohring EJ, et al. **Lumbar disc nomenclature: version 2.0—recommendations of the combined task forces of the North American Spine Society, the American Society of Spine Radiology and the American Society of Neuroradiology.** *Spine J* 2014;14:2525–45 CrossRef Medline
9. Deeks JJ, Dinnes J, D'Amico R, et al; International Stroke Trial Collaborative Group; European Carotid Surgery Trial Collaborative Group. **Evaluating non-randomised intervention studies.** *Health Technol Assess* 2003;7:iii–x, 1–173 CrossRef Medline
10. DerSimonian R, Laird N. **Meta-analysis in clinical trials.** *Control Clin Trials* 1986;7:177–88 CrossRef Medline
11. Higgins JP, Thompson SG, Deeks JJ, et al. **Measuring inconsistency in meta-analyses.** *BMJ* 2003;327:557–60 CrossRef Medline
12. Boos N, Dreier D, Hilfiker E, et al. **Tissue characterization of symptomatic and asymptomatic disc herniations by quantitative magnetic resonance imaging.** *J Orthop Res* 1997;15:141–49 CrossRef Medline
13. Capel A, Medina FS, Medina D, et al. **Magnetic resonance study of lumbar disks in female dancers.** *Am J Sports Med* 2009;37:1208–13 CrossRef Medline
14. Danielson B, Willén J. **Axially loaded magnetic resonance image of the lumbar spine in asymptomatic individuals.** *Spine (Phila Pa 1976)* 2001;26:2601–06 CrossRef Medline
15. Dora C, Wälchli B, Elfering A, et al. **The significance of spinal canal dimensions in discriminating symptomatic from asymptomatic disc herniations.** *Eur Spine J* 2002;11:575–81 CrossRef Medline
16. Edmondston SJ, Song S, Bricknell RV, et al. **MRI evaluation of lumbar spine flexion and extension in asymptomatic individuals.** *Man Ther* 2000;5:158–64 CrossRef Medline
17. Feng T, Zhao P, Liang G. **Clinical significance on protruded nucleus pulposus: a comparative study of 44 patients with lumbar intervertebral disc protrusion and 73 asymptomatic control in tridimensional computed tomography** [in Chinese]. *Zhongguo Zhong Xi Yi Jie He Za Zhi* 2000;20:347–49 Medline
18. Gibson MJ, Szypryt EP, Buckley JH, et al. **Magnetic resonance imaging of adolescent disc herniation.** *J Bone Joint Surg Br* 1987;69:699–703 Medline
19. Jensen MC, Brant-Zawadzki MN, Obuchowski N, et al. **Magnetic resonance imaging of the lumbar spine in people without back pain.** *N Engl J Med* 1994;331:69–73 CrossRef Medline
20. Matsumoto M, Okada E, Toyama Y, et al. **Tandem age-related lumbar and cervical intervertebral disc changes in asymptomatic subjects.** *Eur Spine J* 2013;22:708–13 CrossRef Medline
21. Al-Saeed O, Al-Jarallah K, Raeess M, et al. **Magnetic resonance imaging of the lumbar spine in young Arabs with low back pain.** *Asian Spine J* 2012;6:249–56 CrossRef Medline
22. Bennett DL, Nassar L, DeLano MC. **Lumbar spine MRI in the elite-level female gymnast with low back pain.** *Skeletal Radiol* 2006;35:503–09 CrossRef Medline
23. Boos N, Rieder R, Schade V, et al. **1995 Volvo Award in clinical sciences: the diagnostic accuracy of magnetic resonance imaging, work perception, and psychosocial factors in identifying symptomatic disc herniations.** *Spine (Phila Pa 1976)* 1995;20:2613–25 CrossRef Medline
24. Takatalo J, Karppinen J, Niinimäki J, et al. **Association of Modic changes, Schmorl's nodes, spondylolytic defects, high-intensity zone lesions, disc herniations, and radial tears with low back symptom severity among young Finnish adults.** *Spine (Phila Pa 1976)* 2012;37:1231–39 CrossRef Medline
25. Boden SD, McCowin PR, Davis DO, et al. **Abnormal magnetic-resonance scans of the cervical spine in asymptomatic subjects: a pro-**

spective investigation. *J Bone Joint Surg Am* 1990;72:1178–84 Medline
26. Greenberg JO, Schnell RG. **Magnetic resonance imaging of the lumbar spine in asymptomatic adults: cooperative study—American Society of Neuroimaging.** *J Neuroimaging* 1991;1:2–7 Medline
27. Healy JF, Healy BB, Wong WH, et al. **Cervical and lumbar MRI in asymptomatic older male lifelong athletes: frequency of degenerative findings.** *J Comput Assist Tomogr* 1996;20:107–12 CrossRef Medline
28. Savage RA, Whitehouse GH, Roberts N. **The relationship between the magnetic resonance imaging appearance of the lumbar spine and low back pain, age and occupation in males.** *Eur Spine J* 1997;6: 106–14 CrossRef Medline
29. Silcox DH 3rd, Horton WC, Silverstein AM. **MRI of lumbar intervertebral discs: diurnal variations in signal intensities.** *Spine (Phila Pa 1976)* 1995;20:807–11; discussion 811–12 CrossRef Medline
30. Weinreb JC, Wolbarsht LB, Cohen JM, et al. **Prevalence of lumbosacral intervertebral disc abnormalities on MR images in pregnant and asymptomatic nonpregnant women.** *Radiology* 1989;170: 125–28 CrossRef Medline
31. Visuri T, Ulaska J, Eskelin M, et al. **Narrowing of lumbar spinal canal predicts chronic low back pain more accurately than intervertebral disc degeneration: a magnetic resonance imaging study in young Finnish male conscripts.** *Mil Med* 2005;170:926–30 CrossRef Medline
32. Brinjikji W, Luetmer PH, Comstock B, et al. **Systematic literature review of imaging features of spinal degeneration in asymptomatic populations.** *AJNR Am J Neuroradiol* 2015;36:811–16 CrossRef Medline
33. Karakida O, Ueda H, Ueda M, et al. **Diurnal T2 value changes in the lumbar intervertebral discs.** *Clin Radiol* 2003;58:389–92 CrossRef Medline
34. Kjaer P, Leboeuf-Yde C, Korsholm L, et al. **Magnetic resonance imaging and low back pain in adults: a diagnostic imaging study of 40-year-old men and women.** *Spine (Phila Pa 1976)* 2005;30: 1173–80 CrossRef Medline
35. Ranson CA, Kerslake RW, Burnett AF, et al. **Magnetic resonance imaging of the lumbar spine in asymptomatic professional fast bowlers in cricket.** *J Bone Joint Surg Br* 2005;87:1111–16 CrossRef Medline
36. Zobel BB, Vadalà G, Del Vescovo R, et al. **T1ρ magnetic resonance imaging quantification of early lumbar intervertebral disc degeneration in healthy young adults.** *Spine (Phila Pa 1976)* 2012;37: 1224–30 CrossRef Medline
37. Jarvik JG, Hollingworth W, Heagerty PJ, et al. **Three-year incidence of low back pain in an initially asymptomatic cohort: clinical and imaging risk factors.** *Spine (Phila Pa 1976)* 2005;30:1541–48; discussion 1549 CrossRef Medline
38. Jarvik JJ, Hollingworth W, Heagerty P, et al. **The Longitudinal Assessment of Imaging and Disability of the Back (LAIDBack) study: baseline data.** *Spine (Phila Pa 1976)* 2001;26:1158–66 CrossRef Medline
39. Jensen TS, Karppinen J, Sorensen JS, et al. **Vertebral endplate signal changes (Modic change): a systematic literature review of prevalence and association with non-specific low back pain.** *Eur Spine J* 2008;17:1407–22 CrossRef Medline
40. Jensen RK, Leboeuf-Yde C, Wedderkopp N, et al. **Is the development of Modic changes associated with clinical symptoms? A 14-month cohort study with MRI.** *Eur Spine J* 2012;21:2271–79 CrossRef Medline
41. Snyder LA, Shufflebarger H, O'Brien MF, et al. **Spondylolysis outcomes in adolescents after direct screw repair of the pars interarticularis.** *J Neurosurg Spine* 2014;21:329–33 CrossRef Medline
42. Fardon DF, Milette PC. **Nomenclature and classification of lumbar disc pathology: recommendations of the combined task forces of the North American Spine Society, American Society of Spine Radiology, and American Society of Neuroradiology.** *Spine (Phila Pa 1976)* 2001;26:E93–E113 CrossRef Medline
43. Kuisma M, Karppinen J, Niinimäki J J, et al. **Modic changes in endplates of lumbar vertebral bodies: prevalence and association with low back and sciatic pain among middle-aged male workers.** *Spine (Phila Pa 1976)* 2007;32:1116–22 CrossRef Medline
44. Carragee EJ, Paragioudakis SJ, Khurana S. **2000 Volvo Award winner in clinical studies: lumbar high-intensity zone and discography in subjects without low back problems.** *Spine (Phila Pa 1976)* 2000;25: 2987–92 CrossRef Medline
45. Kovacs FM, Arana E, Royuela A, et al. **Disc degeneration and chronic low back pain: an association which becomes nonsignificant when endplate changes and disc contour are taken into account.** *Neuroradiology* 2014;56:25–33 CrossRef Medline
46. Paajanen H, Erkintalo M, Parkkola R, et al. **Age-dependent correlation of low-back pain and lumbar disc regeneration.** *Arch Orthop Trauma Surg* 1997;116:106–07 CrossRef Medline
47. Koyama K, Nakazato K, Min S, et al. **Radiological abnormalities and low back pain in gymnasts.** *Int J Sports Med* 2013;34:218–22 CrossRef Medline
48. Hancock M, Maher C, Macaskill P, et al. **MRI findings are more common in selected patients with acute low back pain than controls?** *Eur Spine J* 2012;21:240–46 CrossRef Medline
49. Kaneoka K, Shimizu K, Hangai M, et al. **Lumbar intervertebral disk degeneration in elite competitive swimmers: a case control study.** *Am J Sports Med* 2007;35:1341–45 CrossRef Medline
50. Tertti MO, Salminen JJ, Paajanen HE, et al. **Low-back pain and disk degeneration in children: a case-control MR imaging study.** *Radiology* 1991;180:503–07 CrossRef Medline
51. Takatalo J, Karppinen J, Niinimäki J, et al. **Does lumbar disc degeneration on magnetic resonance imaging associate with low back symptom severity in young Finnish adults?** *Spine (Phila Pa 1976)* 2011;36:2180–89 CrossRef Medline
52. Paajanen H, Erkintalo M, Kuusela T, et al. **Magnetic resonance study of disc degeneration in young low-back pain patients.** *Spine (Phila Pa 1976)* 1989;14:982–85. Medline

Bone-Subtracted Spinal CT Angiography Using Nonrigid Registration for Better Visualization of Arterial Feeders in Spinal Arteriovenous Fistulas

T. Nishii, A.K. Kono, M. Nishio, N. Negi, A. Fujita, E. Kohmura, and K. Sugimura

ABSTRACT

BACKGROUND AND PURPOSE: Pretreatment diagnosis for the location of shunts and arterial feeders of spinal arteriovenous fistulas is crucial. This study aimed to evaluate the utility of subtracted CT angiography imaging by using nonrigid registration (R-CTA) in patients with spinal arteriovenous fistulas compared with conventional CTA imaging.

MATERIALS AND METHODS: The records of 15 consecutive subjects (mean age, 65 years; 2 women) who had undergone CTA and digital subtraction angiography for clinically suspected spinal arteriovenous fistula were reviewed. From CTA images obtained at the arterial and late arterial phases, warped images of the late arterial phase were obtained by using nonrigid registration that was adjusted to the arterial phase images. R-CTA images were then obtained by subtracting the warped images from the arterial phase images. The accuracies of using nonrigid registration and conventional spinal CTA and the time required for detecting arterial feeders in spinal arteriovenous fistulas were analyzed for each patient with DSA results as a standard reference. The difference between R-CTA and conventional spinal CTA was assessed by the Welch test and the McNemar χ^2 test.

RESULTS: R-CTA had a higher accuracy compared with conventional spinal CTA (80% versus 47%, $P = .025$). The time for interpretation was reduced in R-CTA compared with conventional spinal CTA (45.1 versus 97.1 seconds, $P = .002$).

CONCLUSIONS: Our subtracted CTA imaging by using nonrigid registration detects feeders of spinal arteriovenous fistulas more accurately and quickly than conventional CTA.

ABBREVIATIONS: ANTs = Advanced Normalization Tools software; C-CTA = conventional spinal CTA; R-CTA = bone-subtracted spinal CTA using novel nonrigid registration; SAVF = spinal arteriovenous fistula; SyN = symmetric diffeomorphic image normalization algorithm

Spinal arteriovenous fistulas (SAVFs) are the most common spinal vascular malformation.[1] Early and accurate diagnosis with proper treatment is required for avoiding progressive spinal cord symptoms.[2] Treatment in SAVFs is achieved by shunt occlusion with an endovascular or surgical approach. Pretreatment diagnosis for the location of shunts and arterial feeders of SAVFs is crucial.[1] Selective spinal digital subtraction angiography is a definitive examination in the diagnosis and planning of the treatment of SAVFs. However, selective catheterization for each segmental artery is relatively invasive and time-consuming and requires expertise.[3]

Therefore, spinal CT angiography has been introduced to detect the location of shunts and feeders as a noninvasive imaging method.[3-6] Whether spinal CTA can be substituted for the invasive method of spinal DSA is still controversial. However, preangiographic detection of the location of feeders makes it possible to avoid the invasive method of DSA due to reduction in fluoroscopy time.[7] Spinal CTA has been widely used because of its simplicity in the clinical setting, after introduction for visualization of the artery of Adamkiewicz.[8,9] However, CTA has several issues that need to be considered as follows: 1) The detectability of arterial feeders is insufficient,[5,6] 2) the reproducibility is relatively lower than that of magnetic resonance angiography,[6] and 3) identifying these feeders is sometimes time-consuming. These problems are because the feeders are small and run close to the osseous structures, which show high attenuation in CT images and cause artifacts, such as blooming and streak artifacts, to the neighboring area.

Subtracted CTA is one of the solutions for distinguishing the osseous structures and enhanced vessels.[10] If the bones can be removed from spinal CTA, the diagnosis of feeders to the SAVF

Received January 6, 2015; accepted after revision March 29.

From the Departments of Radiology (T.N., A.K.K., M.N., K.S.) and Neurosurgery (A.F., E.K.), Kobe University Graduate School of Medicine, Kobe, Japan; and Division of Radiology (N.N.), Center for Radiology and Radiation Oncology, Kobe University Hospital, Kobe, Japan.

Please address correspondence to Tatsuya Nishii, MD, Department of Radiology, Kobe University Graduate School of Medicine, 7–5-1 Kusunoki-cho, Chuo-ku, Kobe, Hyogo 650-0017 Japan; e-mail: ttsynishii@gmail.com

http://dx.doi.org/10.3174/ajnr.A4435

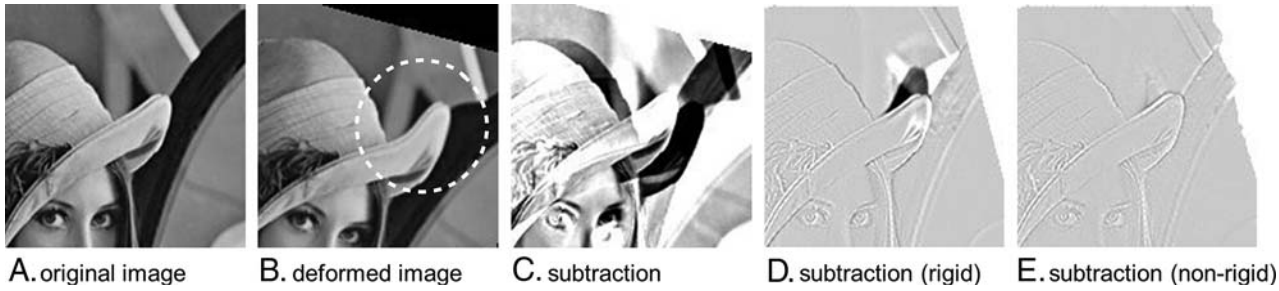

FIG 1. *A*, An original image. *B*, Image generated by rotating *A* and deforming the tip of the hat (*dashed circle*). *C*, An ordinary subtracted image that was obtained by subtracting image *B* from *A*. This step causes misregistration in which a large amount of the white or black area is seen. *D* and *E*, Subtracted images that were obtained by subtracting image *A* from the warped image of image *B* created by rigid and nonrigid registration, respectively. *D*, Deformation of the hat remains and leads to misregistration around the tip of the hat. *E*, Perfect subtraction by restoring the rotation and deformation.

will be improved. Recently, bone-subtraction CTA has been widely used in intracranial lesions.[11-13] However, the application of the subtraction technique to spinal lesions is still challenging. To the best of our knowledge, this application has not been reported because the patient's breathing and involuntary motions cause the body position to easily change between the 2 datasets. In most parts of the body, except for cranial lesions, deformation and distortion between 2 datasets will occur.[14] Misregistration is inevitable when the conventional subtraction method is used. To overcome this misregistration, we introduced rigid or nonrigid registration (Fig 1). Rigid registration is a technique in which 1 image is subtracted with parallel shift or rotation. An example of the application of this method is brain perfusion imaging. Moreover, compared with rigid registration, nonrigid registration is a better processing method, compensating for organ motion or transformation between 2 datasets,[14] and this can minimize misregistration, even if the target organ moves between the acquisition of images. Recently, several novel nonrigid registration algorithms were introduced, and the performance of these methods is improving.[15,16]

We hypothesized that subtracted spinal CTA imaging by using nonrigid registration (R-CTA) provides precise subtraction and facilitates the diagnosis of arterial feeders to SAVFs. This study aimed to evaluate the utility of R-CTA in patients with SAVFs compared with conventional CTA imaging (C-CTA).

MATERIALS AND METHODS

Our institutional review board approved this retrospective study. Written informed consent from all subjects was waived by the institutional review board because of the retrospective nature of the study. The patient records and information were anonymized and de-identified before analysis.

Subjects

The records of 15 consecutive subjects (mean age, 65 years; range, 39–87 years; 2 females) who had undergone CTA and DSA for clinically suspected SAVFs between June 2009 and December 2013 were retrospectively reviewed.

DSA Technique

Selective spinal DSA was performed by a trained board-certified neurosurgeon (A.F., with 20 years' experience) in a biplane angiography suite (Artis zee BA twin; Siemens, Erlangen, Germany) by injecting 3 mL (1 mL/s) of 300-mg/mL iodinated contrast agent (iopamidol, Oypalomin 300; Fuji Pharma, Tokyo, Japan; or iopromide, Proscope 300; Alfresa Pharma, Osaka, Japan) into the segmental arteries. The images were obtained with the following parameters: 4 frames/s, 720 × 720 matrix, and 32-cm FOV. When prior CTA findings suggested the location of the feeders, the predicted level was first selected. After the main feeder was recognized, the bilateral segmental arteries ranging from 3 levels above to 3 levels below the identified feeders were assessed to identify the collateral feeders for complete evaluation. If the feeders were not identified, all the bilateral segmental arteries from the cranial level to the median sacral arteries, the bilateral subclavian arteries, and the bilateral iliac arteries were assessed. The DSA diagnosis was performed by the same neurosurgeon.

Acquisition and Reconstruction of CTA

All the CTA examinations were performed with a 64–detector row CT scanner (Aquilion 64; Toshiba Medical Systems, Tokyo, Japan) by using the method for visualization of the artery of Adamkiewicz (as previously described).[17] The parameters were set as follows: 0.5-mm collimated section width, 0.60 seconds per rotation, 0.641 pitch, 120 kV, and 400 mAs. Iopamidol at 370 mg I/mL (Iopamiron 370; Bayer Yakuhin, Osaka, Japan) was injected via a 20-ga catheter in the right antecubital vein (100 mL, 5 mL/s), followed by a 30-mL saline flush. Bolus tracking was used with an ROI at the descending aorta. The scan was automatically started 7 seconds after contrast enhancement of the ROIs reached a threshold of 150 HU. The scan covered the entire spinal canal from the foramen magnum to the coccygeal bone. To avoid misreading between the radiculomedullary arteries and veins, we consecutively repeated dual-phase dynamic scanning to obtain images in the arterial and late arterial phases. The interval between the phases was approximately 40 seconds, which was needed to perform the arterial phase scanning and to move the table into the starting position for the late arterial phase scan. This interval differed slightly on the basis of the patient's body size. The CT dose index of the arterial and late arterial phases was set as 47.1 mGy for each phase.

The data were reconstructed in the axial plane with a 0.5-mm section thickness, 0.5-mm reconstruction interval, 200-mm FOV, and a medium soft-tissue convolution kernel.

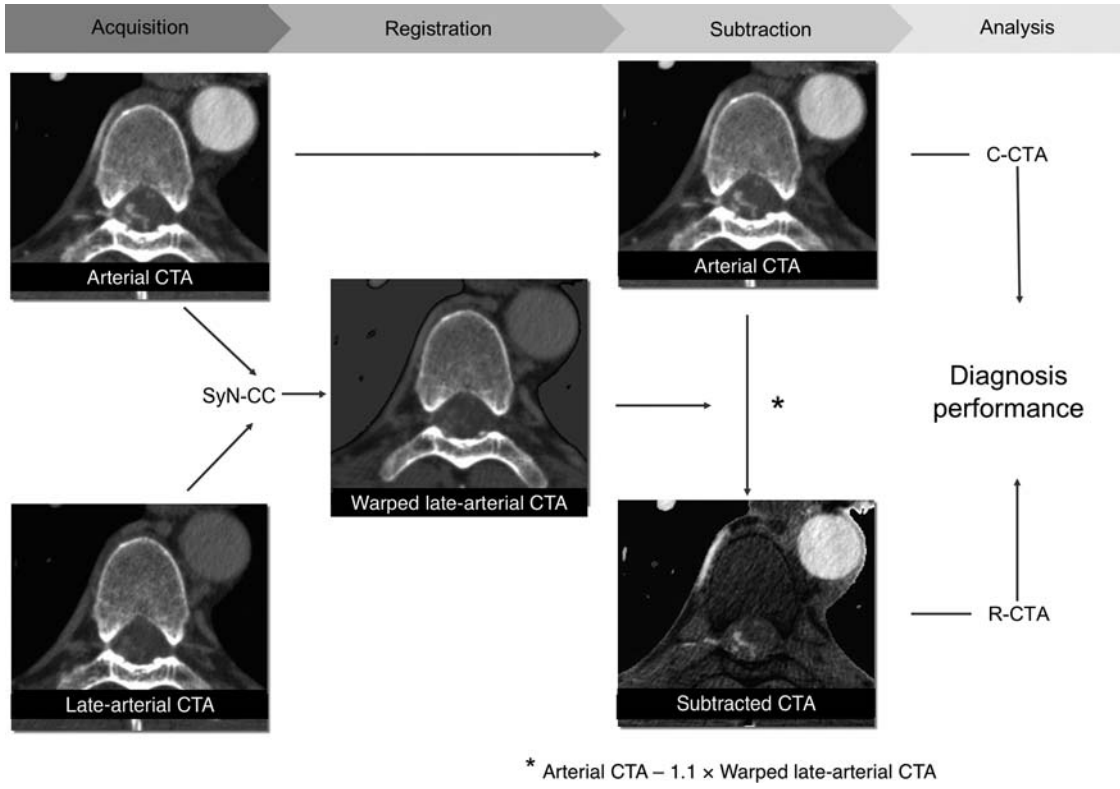

FIG 2. First, warped images of the late arterial phase were obtained by using nonrigid registration (SyN–cross-correlation) adjusted to the arterial phase images. The subtracted spinal CTA by using nonrigid registration was then obtained by subtracting warped images that were multiplied by 1.1 from the arterial phase images. R-CTA and conventional spinal CTA were analyzed with digital subtraction angiography results as a reference standard, and the difference in diagnostic performance was assessed.

Postprocessing Method

One author (T.N., board-certified diagnostic radiologist with 6 years' experience) who was blinded to the subjects' identities performed further image postprocessing. The schema of the postprocessing methods is shown in Fig 2.

Each dataset was cropped at the center of the image with 256 × 256 pixels, and the Otsu segmentation method was used to remove the lungs with ImageJ software (National Institutes of Health, Bethesda, Maryland). Warped images of the late arterial phase were obtained by using nonrigid registration adjusted to the arterial phase images. Nonrigid registration was performed by using open-source Advanced Normalization Tools software (ANTs; http://stnava.github.io/ANTs/). Details of this process are explained in the next paragraph. R-CTA images were then obtained by subtracting the warped images from the arterial phase images. Weighted subtraction images were used to invert bone attenuation and to easily recognize the level of the intervertebral foramen. Weighted subtraction images were obtained by subtracting warped images that were multiplied by 1.1 from the arterial phase images.

Symmetric Diffeomorphic Image Normalization Algorithm

The symmetric diffeomorphic image normalization algorithm (SyN),[15] which is provided through ANTs, is a nonrigid registration algorithm that performs well.[16] SyN uses an optimization strategy based on minimizing the shape and appearance distances between the input data and reference data. Furthermore, cross-correlation, a similarity metric that is commonly used for intramodality registration, was specified and included when performing the SyN.

Analyses of Images

Two board-certified diagnostic radiologists (T.N., 6 years' experience; A.K.K., 11 years' experience) who were blinded to the identity of subjects independently performed the following analyses by using OsiriX Imaging Software (http://www.osirix-viewer.com). They were allowed to change the window level or width and the image size as common practice. In addition to the axial images, multiplanar reformation images and thin-slab maximum-intensity-projection images were used.

For the preliminary analysis, the initial 5 cases of R-CTA were compared with the bone-subtracted image with rigid registration by the 5-point scoring system for subtraction performance (5 = excellent, 4 = acceptable, 3 = intermediate, 2 = partial, and 1 = inadequate). The rigid registration was performed by using ANTs with the same datasets used for R-CTA.

Subject-based and intervertebral foramen-based analyses were performed separately in at least 2-week intervals. First, for subject-based analysis, the levels of feeders to the SAVF were recorded, and these were identified from the feeders' continuity between the aorta and abnormal spinal vessels. Furthermore, the required time to interpret the images was concurrently recorded. The 2 examiners performed this analysis independently.

Second, for the intervertebral foramen-based analysis, the in-

Table 1: Subject characteristics and the level of feeders as shown by spinal digital subtraction angiography results

Case	Age (yr)	Sex	Clinical Manifestation	Feeder		Type
				Side and Level	Origin	
1	60	F	Paraplegia	–	–	No AVF
2	83	M	Claudication	Lt. L1	LA	D
3	71	M	Paraplegia	Rt. L2	LA	D
4	78	M	Paraplegia	Rt. T7, Lt. T11	ICA	D
5	53	M	Paraplegia	Rt. T9	ICA	D
6	74	M	Paraparesis	–	–	No AVF
7	49	M	Paraplegia	Lt. T6	ICA	PM
8	66	M	Paraplegia	Lt. T6, Lt. T7	ICA	D
9	39	M	Paraplegia	Lt.T5, Lt. T6	ICA	D
10	57	M	Paraplegia	Rt. L2	LA	D
11	67	F	Paraplegia	Lt. L3	LA	PM
12	80	M	Paraplegia	Rt. T4, Rt. T5	ICA	D
13	45	M	Paraplegia	Rt. T4	ICA	D
14	71	M	Paraplegia	Lt. T3, Rt. T5	ICA	PM
15	87	M	Paraplegia	Lt. T4	ICA	D

Note:—D indicates dural AVF; LA, lumber artery; PM, perimedullary AVF; –, data not available; ICA, intercostal artery; T, thoracic spine; L, lumbar spine; Rt., right; Lt, left.

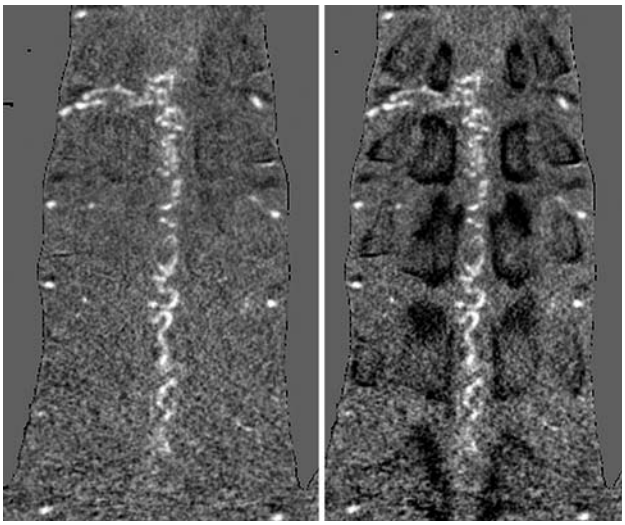

FIG 3. In an ordinary subtraction image (*left*), determining the level of the vertebra is difficult because the background is totally equaled. However, in a weighted subtraction image (*right*), the bone is displayed as a darker structure than background attenuation.

tervertebral foramen was assessed from the level of the third thoracic vertebra to the level of the third lumbar vertebra (390 foramens). The diagnostic likelihood of the presence of a feeder was scored on a 5-point scale (1 = definitely negative, 5 = definitely positive) with a consensus reading of the 2 radiologists.

For quantitative image-quality analysis, the SDs of C-CTA and R-CTA were obtained by setting the circular ROI in the descending aorta at the center level of the 10th thoracic vertebra. The image noise was determined as the SD of the CT value in the descending aorta.

Statistical Analyses

For assessment of diagnostic performance, the result of DSA was used as the reference standard.

For the preliminary analysis, the scores of subtraction performance of C-CTA and R-CTA were compared using the Cochran-Armitage test.

For subject-based analysis, only when the results of each CTA and DSA were perfectly matched did we judge the diagnosis accurate. The differences in the accuracy and time to interpretation between C-CTA and R-CTA were assessed by the McNemar χ^2 test and the Welch test, respectively.

For intervertebral foramen–based analysis, if the score was ≥4, we first determined that a feeder was present at the vertebral foramen. Second, the generalized estimation equation was used to generate a model to marginalize the intersubject effect. The sensitivity, specificity, and accuracy for C-CTA and R-CTA were then calculated, and the differences between C-CTA and R-CTA were assessed by each odds ratio estimated by using the generalized estimation equation. The link function was set as a logit link, and an independent working correlation matrix was used for the generalized estimation equation.

For quantitative image analysis, the image noises of C-CTA and R-CTA were compared using the Welch test.

For statistical analysis, JMP 9.0 (SAS Institute, Cary, North Carolina) and R statistical computing software (http://www.r-project.org) were used. The significance level was set at $P = .05$.

RESULTS

CTA and selected spinal DSA were successfully performed in all 15 subjects. A summary of the characteristics of the subjects and the level of feeders from the results of DSA are shown in Table 1. From the preliminary analysis, R-CTA showed significantly higher subtraction performance than subtraction with the rigid registration (median score, 5 versus 2, respectively; $P = .001$). Thus, for bone subtraction in spinal CTA, the use of nonrigid registration was considered more suitable than the use of rigid registration.

Illustrative cases of a 53-year-old man (case 5) and 57-year-old man (case 10) are shown in Figs 4 and 5, respectively. In case 5, although the feeder from the right ninth intercostal artery (Fig 4*A*) was detected by using C-CTA (Fig 4*B*) and R-CTA (Fig 4*C*), the continuity of the feeder and the aorta was clear when R-CTA was used. In case 10, by using C-CTA (Fig 5*B*), a false feeder from the right 12th intercostal artery was only observed instead of the true feeder from the right second lumbar artery (Fig 5*A*), while this true feeder was clearly visualized by using R-CTA (Fig 5*C*).

In subject-based analysis, the accuracies of C-CTA compared with R-CTA were 47% (7/15) versus 80% (12/15) by observer 1 and 40% (6/15) versus 73% (11/15) by observer 2, respectively. The required time for detecting feeders of C-CTA compared with R-CTA was 97.1 seconds versus 45.1 seconds by observer 1 and 89.5 seconds versus 45.6 seconds by observer 2, respectively. R-CTA was significantly more accurate ($P = .025$ in both observers) and reduced the time for interpretation ($P = .002$ and $P = .020$, respectively) compared with C-CTA (Table 2).

In intervertebral foramen–based analysis, the diagnostic performance of C-CTA compared with R-CTA was as follows: sensi-

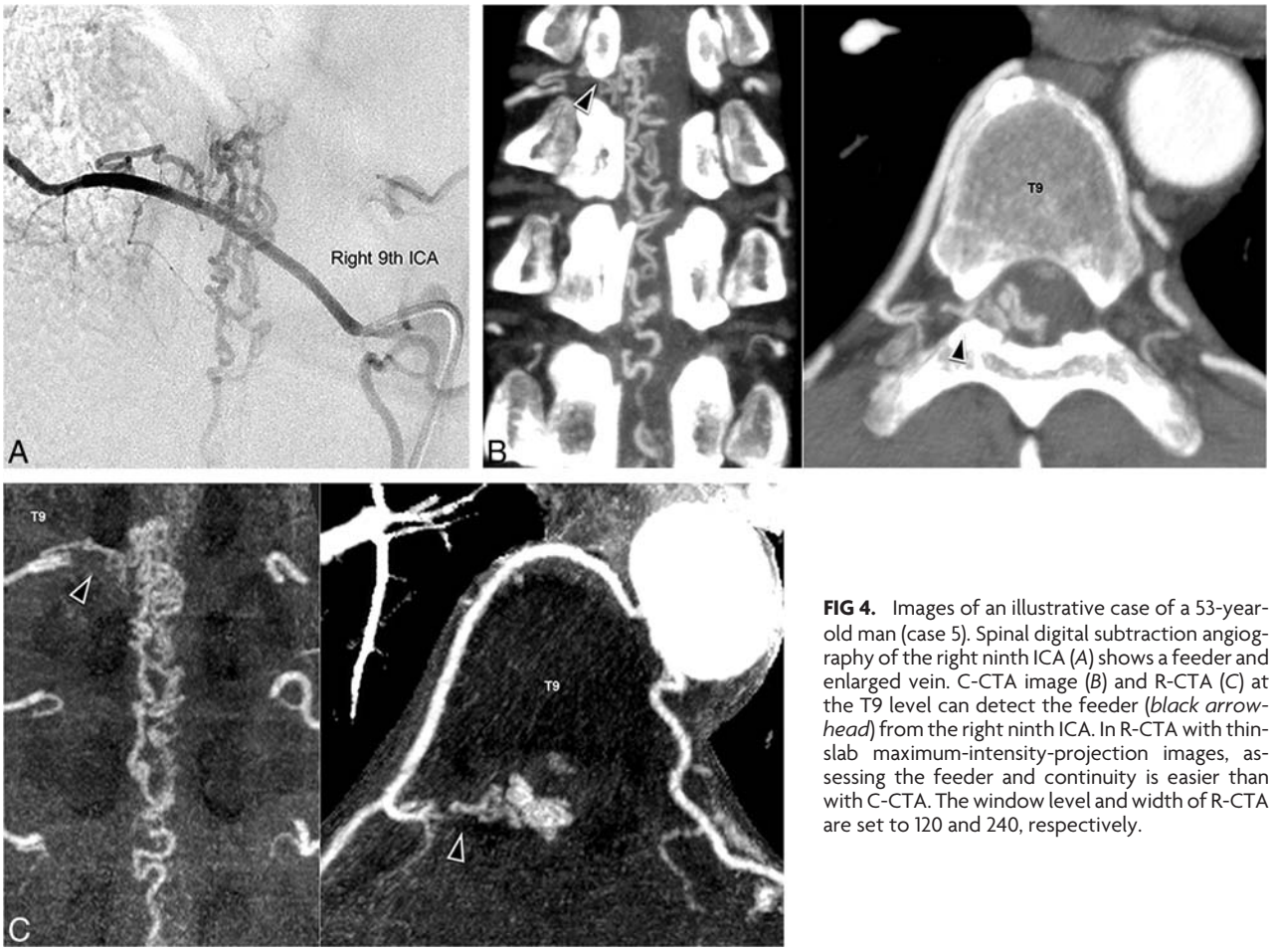

FIG 4. Images of an illustrative case of a 53-year-old man (case 5). Spinal digital subtraction angiography of the right ninth ICA (*A*) shows a feeder and enlarged vein. C-CTA image (*B*) and R-CTA (*C*) at the T9 level can detect the feeder (*black arrowhead*) from the right ninth ICA. In R-CTA with thin-slab maximum-intensity-projection images, assessing the feeder and continuity is easier than with C-CTA. The window level and width of R-CTA are set to 120 and 240, respectively.

tivity, 44.4% versus 72.2%; specificity, 98.1% versus 99.5%; and accuracy, 95.6% versus 98.2%, respectively (Table 2). R-CTA showed a significantly higher accuracy (odds ratio = 2.494; 95% confidence interval, 1.037–5.996; $P = .041$) compared with C-CTA.

The quantitative image-quality analysis showed that the image noise was higher in R-CTA than C-CTA (27.9 ± 15.5 versus 18.6 ± 7.0 HU, respectively; $P = .047$).

The radiation exposure by using the dose-length product for dual-phase CTA was 5238.1 ± 1220.8 mGy × cm.

DISCUSSION

Our study showed that R-CTA had a significantly better accuracy than C-CTA, and R-CTA reduced the time required for detection of arterial feeders to the SAVF. Furthermore, in intervertebral foramen–based analysis, R-CTA was significantly more accurate than C-CTA.

The diagnostic accuracy of feeders of SAVFs by using nonsubtracted CTA was previously reported as 58%–90%.[3,5,6] The diagnostic accuracy of C-CTA (40%–47%) in our study was relatively low compared with that in previous studies.[3,5,6] The reason for this difference between studies might be because of a difference in study populations. Thirty-eight percent (5/13) of patients had 2 feeders in this study, while the previous studies mentioned only 1 vessel as the main feeder in their populations. Because smaller feeders are easy to miss, the accuracy of C-CTA was not high in this study. Dynamic contrast-enhanced MR angiography is another noninvasive imaging method, which has a detectability of feeders of 40%–93%.[3,6,7] Dynamic contrast-enhanced MR angiography has several advantages, including separating the signal between bone and vessels; and it also performs multiphase scanning without any radiation exposure. The advantages of CTA compared with MR imaging are that it has simple and rapid acquisition, wide coverage, and high versatility.[3,6] In particular, for surgical planning, 3D visualization of both vessels and bones on CTA images is advantageous. Despite the above-mentioned advantages, radiation exposure is a disadvantage in CTA. However, as the CT machine and reconstruction methods improve, they will be able to reduce radiation exposure.

With R-CTA, separation from bony structures and reduction of blooming artifacts[18] and extensibility by using thin-slab MIP for easier analysis of continuity[19] from the aorta to feeders could explain the improving diagnostic performance. Several disadvantages of R-CTA should be considered. First, the subtracted image is theoretically noisier than the original images.[19] The quantitative image-quality analysis showed that the image noise was higher in R-CTA than in C-CTA. However, the diagnostic performance of R-CTA was not obscured. Thus, the effect of increasing noise was low enough to diagnose the level of feeders in this study because of good visibility of vessels in R-CTA. Second, preparation of 2 CT datasets for obtaining R-CTA could be an issue be-

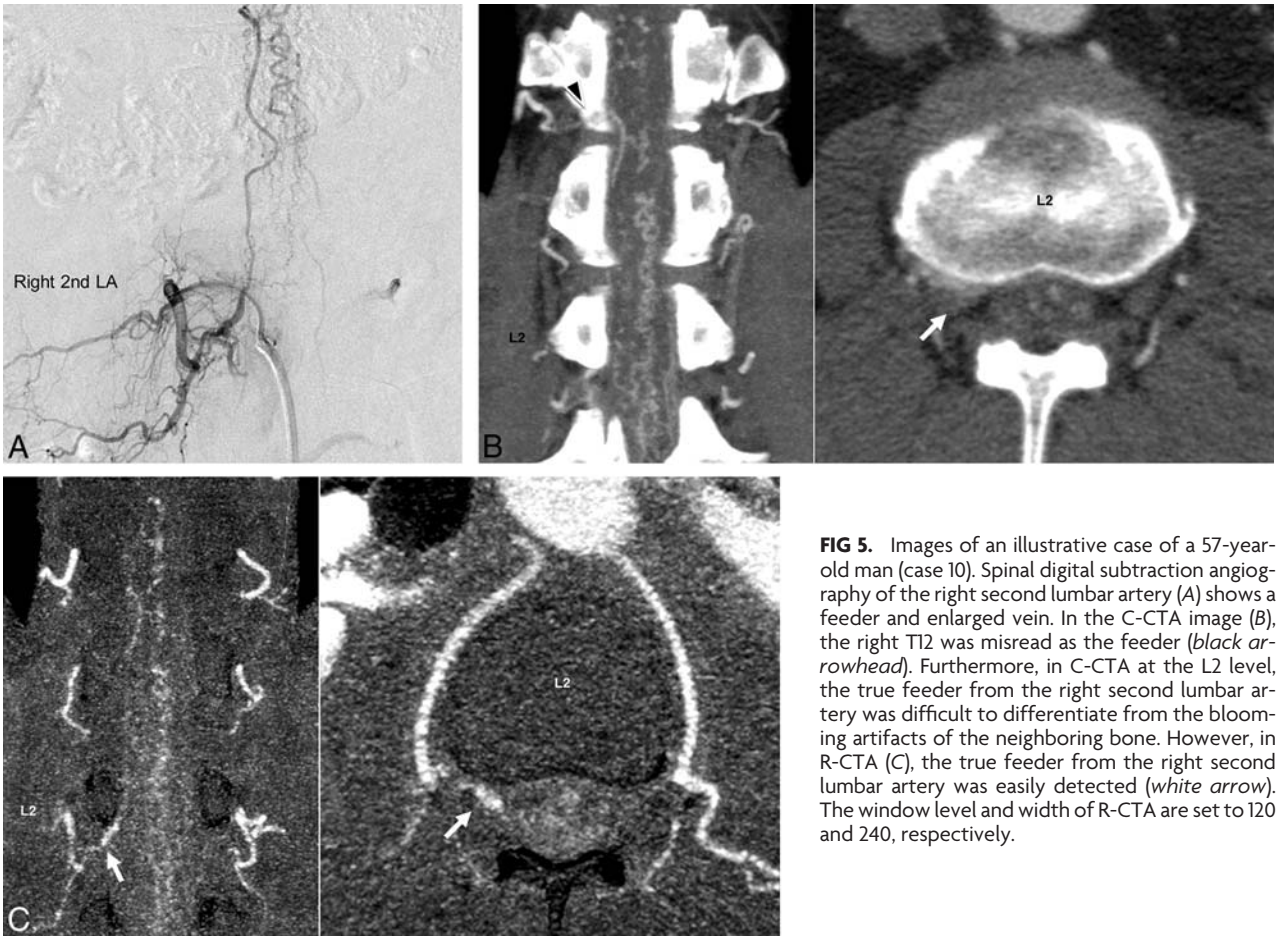

FIG 5. Images of an illustrative case of a 57-year-old man (case 10). Spinal digital subtraction angiography of the right second lumbar artery (*A*) shows a feeder and enlarged vein. In the C-CTA image (*B*), the right T12 was misread as the feeder (*black arrowhead*). Furthermore, in C-CTA at the L2 level, the true feeder from the right second lumbar artery was difficult to differentiate from the blooming artifacts of the neighboring bone. However, in R-CTA (*C*), the true feeder from the right second lumbar artery was easily detected (*white arrow*). The window level and width of R-CTA are set to 120 and 240, respectively.

Table 2: Differences in diagnostic performance of C-CTA and R-CTA

Variables	C-CTA	R-CTA	OR[a]	*P* Values
Subject-based analysis				
Feeder detection accuracy (%)				
Observer 1	47 (7/15)	80 (12/15)		.025[b]
Observer 2	40 (6/15)	73 (11/15)		.025[b]
Time required for diagnosis (sec)				
Observer 1	97.1 ± 37.4	45.1 ± 23.6		.002[b]
Observer 2	89.5 ± 60.0	45.6 ± 24.1		.020[b]
Intervertebral foramen–based analysis				
Sensitivity (%)[c]	44.4 (22.2–66.7)	72.2 (50.0–94.4)	3.26 (0.82–13.0)	.095
Specificity (%)[c]	98.1 (97.8–99.5)	99.5 (98.7–100)	3.55 (0.87–14.5)	.077
Accuracy (%)[c]	95.6 (93.8–97.2)	98.2 (96.9–99.2)	2.49 (1.04–6.00)	.041[b]

[a] ORs of R-CTA against C-CTA are shown.
[b] Significant.
[c] 95% Confidence intervals are shown.

cause of the radiation dose. High-radiation-dose imaging is usually needed for the detection of feeders of SAVFs. Although dual-phase spinal CTA had been reported beneficial for avoiding contamination between the radiculomedullary arteries and veins,[9,17,20] its contribution to detecting the feeders of SAVFs is not fully understood. However, accurate preangiographic detection of the location of the feeders is associated with a reduction of approximately half of the following fluoroscopy time.[7] Therefore, R-CTA is also expected to reduce the radiation dose of the following DSA. Because accurate detection of feeders of SAVFs is also possible, use of R-CTA should be considered. Further clinical studies are required to confirm this recommendation. Third, a relatively long postprocessing time is required. More than 4 hours were needed in each case for registration of the 2 large image datasets (>1000 images per 1 dataset), even if we used a powerful workstation. For clinical use, the current level of postprocessing time is unacceptable. However, further technical innovations of algorithms and workstations would solve this issue. For instance, the reduction of computation time by 93% compared with ANTs has been reported by using the deformable registration method in a hybrid framework.[21] While there are some issues, notably, nonrigid registration was successfully applied to spinal CTA and it could accurately subtract bones. As a result, accurate diagnosis of feeders of SAVFs was achieved, despite the shorter interpretation time than conventional CTA.

In our study, we proposed weighted subtraction to invert bone attenuation to easily diagnose the level of the intervertebral foramen (Fig 3). In the usual bone-subtraction method, the background is totally equaled. Therefore, once optimal subtraction is performed, the landmark has disappeared. This feature makes it difficult to determine the level of the vertebra, which is the landmark for determination of the level of the segmental artery by using subtraction images alone. However, our proposed weighted subtraction provided an inverted shadow of the bones on the subtracted CTA images. The bone is displayed as a darker struc-

ture than the background attenuation (Fig 3). As a result, the time for detecting feeders was reduced because the vertebral body or the rib bone could be recognized on the subtracted CTA images. Moreover, because the inverted bone shadow did not affect the visibility of vessels in MIP images, R-CTA provided clear, thin-slab MIP images. Despite these advantages, this method slightly lowers the contrast of enhanced vessels compared with the usual bone-subtraction method. In addition, the optimization of the weighted value should be further investigated.

Our study has several limitations. First, the DSA results might not be independent from prior CTA results. However, routine DSA for the entire segmental artery in every patient is unacceptable because of its invasiveness. Second, R-CTA was generated by subtracting late arterial phase CTA. Noncontrast CT is theoretically suitable for subtraction because of the high difference in attenuation of vessels between contrast and noncontrast CT. However, we did not perform noncontrast CT with the same settings as spinal CTA. Finally, the population was small, and the study design was retrospective. Further larger and multicenter studies are required to clarify the feasibility of our proposed subtraction method in the clinical setting.

CONCLUSIONS

Bone-subtracted spinal CT angiography imaging by using novel nonrigid registration helps radiologists assess feeders of SAVFs more accurately and quickly than the conventional method.

ACKNOWLEDGMENTS

We are grateful to Dr Kensuke Uotani for his contribution of establishing the spinal CTA acquisition sequence. We also thank Mr Hajime Yamakage for assistance with statistical analysis in this study.

Disclosures: Mizuho Nishio—*UNRELATED*: *Grants/Grants Pending*: Toshiba,* *Comments*: The grant was for CT research; *Patents (planned, pending or issued)*: submission of patents with Toshiba,* *Comments*: The patent is related to computer-aided diagnosis. Eiji Kohmura—*UNRELATED*: *Grants/Grants Pending*: Ministry of Education, Culture and Science,* *Comments*: mainly on basic research on malignant brain tumor; *Payment for Lectures (including service on Speakers Bureaus)*: Medtronic Japan; *Royalties:* microsurgical dissector development (Muranaka Medical Instruments Co., Ltd.). *Money paid to the institution.

REFERENCES

1. Krings T, Geibprasert S. **Spinal dural arteriovenous fistulas.** *AJNR Am J Neuroradiol* 2009;30:639–48 CrossRef Medline
2. Ofran Y, Yovchev I, Hiller N, et al. **Correlation between time to diagnosis and rehabilitation outcomes in patients with spinal dural arteriovenous fistula.** *J Spinal Cord Med* 2013;36:200–06 CrossRef Medline
3. Zampakis P, Santosh C, Taylor W, et al. **The role of non-invasive computed tomography in patients with suspected dural fistulas with spinal drainage.** *Neurosurgery* 2006;58:686–94; discussion 686–94 Medline
4. Lai PH, Weng MJ, Lee KW, et al. **Multidetector CT angiography in diagnosing type I and type IVA spinal vascular malformations.** *AJNR Am J Neuroradiol* 2006;27:813–17 Medline
5. Yamaguchi S, Nagayama T, Eguchi K, et al. **Accuracy and pitfalls of multidetector-row computed tomography in detecting spinal dural arteriovenous fistulas.** *J Neurosurg Spine* 2010;12:243–48 CrossRef Medline
6. Oda S, Utsunomiya D, Hirai T, et al. **Comparison of dynamic contrast-enhanced 3T MR and 64-row multidetector CT angiography for the localization of spinal dural arteriovenous fistulas.** *AJNR Am J Neuroradiol* 2014;35:407–12 CrossRef Medline
7. Luetmer PH, Lane JI, Gilbertson JR, et al. **Preangiographic evaluation of spinal dural arteriovenous fistulas with elliptic centric contrast-enhanced MR angiography and effect on radiation dose and volume of iodinated contrast material.** *AJNR Am J Neuroradiol* 2005;26:711–18 Medline
8. Takase K, Akasaka J, Sawamura Y, et al. **Preoperative MDCT evaluation of the artery of Adamkiewicz and its origin.** *J Comput Assist Tomogr* 2006;30:716–22 CrossRef Medline
9. Yoshioka K, Niinuma H, Ehara S, et al. **MR angiography and CT angiography of the artery of Adamkiewicz: state of the art.** *Radiographics* 2006;26(suppl 1):S63-73 CrossRef Medline
10. Jayakrishnan VK, White PM, Aitken D, et al. **Subtraction helical CT angiography of intra- and extracranial vessels: technical considerations and preliminary experience.** *AJNR Am J Neuroradiol* 2003;24:451–55 Medline
11. Tomandl BF, Hammen T, Klotz E, et al. **Bone-subtraction CT angiography for the evaluation of intracranial aneurysms.** *AJNR Am J Neuroradiol* 2006;27:55–59 Medline
12. Lell MM, Ditt H, Panknin C, et al. **Bone-subtraction CT angiography: evaluation of two different fully automated image-registration procedures for interscan motion compensation.** *AJNR Am J Neuroradiol* 2007;28:1362–68 CrossRef Medline
13. Fujiwara H, Momoshima S, Akiyama T, et al. **Whole-brain CT digital subtraction angiography of cerebral dural arteriovenous fistula using 320-detector row CT.** *Neuroradiology* 2013;55:837–43 CrossRef Medline
14. Crum WR, Hartkens T, Hill DL. **Non-rigid image registration: theory and practice.** *Br J Radiol* 2004;77(Spec No 2):S140-53 CrossRef Medline
15. Avants BB, Epstein CL, Grossman M, et al. **Symmetric diffeomorphic image registration with cross-correlation: evaluating automated labeling of elderly and neurodegenerative brain.** *Med Image Anal* 2008;12:26–41 CrossRef Medline
16. Klein A, Andersson J, Ardekani BA, et al. **Evaluation of 14 nonlinear deformation algorithms applied to human brain MRI registration.** *Neuroimage* 2009;46:786–802 CrossRef Medline
17. Nishii T, Kono AK, Negi N, et al. **The feasibility of a 64-slice MDCT for detection of the Adamkiewicz artery: comparison of the detection rate of intravenous injection CT angiography using a 64-slice MDCT versus intra-arterial and intravenous injection CT angiography using a 16-slice MDCT.** *Int J Cardiovasc Imaging* 2013;29(suppl 2):127–33 CrossRef Medline
18. Tanaka R, Yoshioka K, Muranaka K, et al. **Improved evaluation of calcified segments on coronary CT angiography: a feasibility study of coronary calcium subtraction.** *Int J Cardiovasc Imaging* 2013;29(suppl 2):75–81 CrossRef Medline
19. Venema HW, Hulsmans FJ, den Heeten GJ. **CT angiography of the circle of Willis and intracranial internal carotid arteries: maximum intensity projection with matched mask bone elimination-feasibility study.** *Radiology* 2001;218:893–98 CrossRef Medline
20. Uotani K, Yamada N, Kono AK, et al. **Preoperative visualization of the artery of Adamkiewicz by intra-arterial CT angiography.** *AJNR Am J Neuroradiol* 2008;29:314–18 CrossRef Medline
21. Xia W, Gao X. **A fast deformable registration method for 4D lung CT in hybrid framework.** *Int J Comput Assist Radiol Surg* 2014;9:523–33 CrossRef Medline

Ipilimumab Therapy for Melanoma: A Mimic of Leptomeningeal Metastases

We have recently observed that patients with malignant melanoma on treatment with ipilimumab can demonstrate leptomeningeal enhancement on brain MR imaging mimicking metastatic disease. In Fig 1 is shown one such case of a 40-year-old man presenting with subacute onset of headaches, right-sided facial hemiparesis, and facial paresthesias. He also showed evidence of tongue deviation on neurologic examination suggestive of cranial neuropathy. The patient had a history of stage IIIC melanoma from an unknown primary site with metastasis to the axilla and was undergoing therapy with ipilimumab. MR imaging demonstrated multifocal leptomeningeal and cranial nerve enhancement. Lumbar puncture revealed CSF lymphocytosis and mildly elevated proteins (findings that can be seen with inflammatory processes) and cultures and cytology negative for infection and malignancy, despite repeat examinations. Following drug discontinuation and high-dose steroid therapy, the patient gradually recovered. Lymphocytosis in the CSF also resolved.

To our knowledge, these brain imaging findings have not been shown in the literature. Ipilimumab, also known as MDX-010, is a human monoclonal antibody that augments T-cell-mediated immunity by blocking inhibitory signals that suppress T-cell function (more specifically, it blocks cytotoxic T lymphocyte antigen-4).[1] It is approved for the treatment of late-stage melanoma and is currently undergoing clinical trials for other cancers. Manousakis et al[2] reported a case of an inflammatory multifocal radiculoneuropathy during ipilimumab therapy with a lumbar spine MR image in their article showing leptomeningeal enhancement along the cauda equina nerve roots. Their patient also had clinical evidence of cranial neuropathies with facial nerve enhancement, though the brain MR images were not included in the article. Carpenter et al[3] showed 3 cases of hypophysitis associated with ipilimumab, which was also thought to represent an immune-mediated response. Our case shows leptomeningeal enhancement and perivascular enhancement in the cerebral hemispheres and pons, findings perhaps analogous to an inflammatory process such as neurosarcoidosis or chronic lymphocytic inflammation with pontine perivascular enhancement responsive to steroids (CLIPPERS). Prominent perivascular enhancement may therefore be a subtle clue to an inflammatory process rather than metastatic disease, though supportive clinical and laboratory findings are needed to make a confident diagnosis.

As immunotherapeutics are increasingly used as antineoplastic agents, neuroradiologists must be aware of their unusual adverse effects and imaging findings. Brain MR imaging to evaluate for metastatic melanoma is not an uncommon study, and oncologists may plan chemotherapy or radiation treatment without histologic or CSF cytologic proof of intracranial metastasis. We should therefore be aware of this potential pitfall and are reminded to be cognizant of the specific chemotherapeutic agents our patients are receiving when providing interpretations.

http://dx.doi.org/10.3174/ajnr.A4581

REFERENCES

1. Keilholz U. **CTLA-4: negative regulator of the immune response and a target for cancer therapy.** *J Immunother* 2008;31:431–39 CrossRef Medline
2. Manousakis G, Koch J, Sommerville RB, et al. **Multifocal radiculoneuropathy during ipilimumab treatment of melanoma.** *Muscle Nerve* 2013;48:440–44 CrossRef Medline
3. Carpenter KJ, Murtagh RD, Lilienfeld H, et al. **Ipilimumab-induced hypophysitis: MR imaging findings.** *AJNR Am J Neuroradiol* 2009; 30:1751–53 CrossRef Medline

S. Ali
S.-K. Lee
Department of Radiology, Section of Neuroradiology
University of Chicago Medical Center
Chicago, Illinois

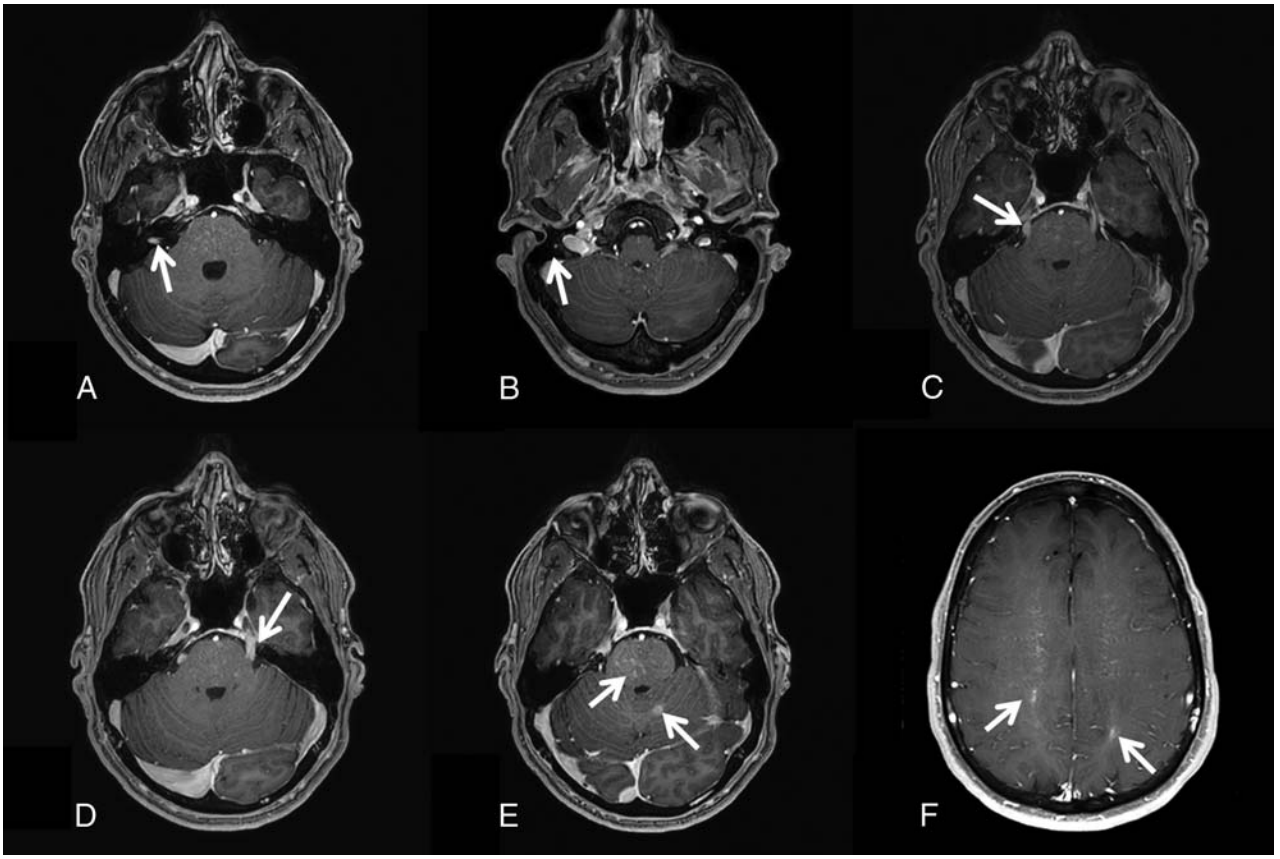

FIG 1. Postcontrast T1-weighted images demonstrate nodular enhancement involving the right facial nerve in the meatal (*A*) and mastoid (*B*) segments and the bilateral trigeminal nerves (*C* and *D*). Leptomeningeal enhancement along the cerebellar surface (*E*) and abnormal enhancement along the perivascular spaces in the pons and cerebral hemispheres (*E* and *F*) are also seen.

The authors regret that in the October 2015 article "We Are Not Alone" (*AJNR Am J Neuroradiol* 2015;36:1794–95, originally published on-line on September 3, 2015, doi:10.3174/ajnr.A4531), the Table shows the average radiologist salary in Israel incorrectly. The correct average radiologist salary in Israel is $72,000. The Table is reproduced below with the corrected segment shown in bold.

http://dx.doi.org/10.3174/ajnr.A4619

Survey research data collected

Country	Average Radiologist Salary	Radiologist/ Practice Pays for Insurance	Average Insurance Premium	Radiology Malpractice Rate	Representative Radiologist Sued for Malpractice	Fear of Being Sued[a]	Practices Defensive Medicine[a]	Malpractice Affects Practice[a]
Africa								
Egypt	$50,000	No	Null	5%	No	3	4	2
Americas								
Argentina	$37,000	Yes	$1200	5%	Yes	1	2	2
Brazil	$130,000	Yes	$560	1%	No	1	1	2
Canada	$300,000	No	$3000	5%	Yes	2	2	2
Chile	$120,000	Yes	$1000	10%	Yes	3	3	4
Guatemala	$35,000	No	Null	1%	No	1	1	1
United States	$340,000	Yes	$21,000	46%	No	4	4	Null
Asia								
Indonesia	$60,000	Yes	$300	0%	Yes	5	5	4
Japan	$100,000	Yes	$70	1%	Yes	2	4	4
Malaysia	$190,000	Yes	$8400	0%	No	2	2	2
Philippines	$21,000	No	Null	2%	No	2	1	2
Singapore	$200,000	Yes	$1750	5%	Yes	3	3	3
South Korea	$200,000	Yes	$5000	3%	Yes	2	1	2
Sri Lanka	$12,000	No	Null	0%	No	2	3	2
Taiwan	$120,000	Yes	$600	3%	Yes	4	4	4
Australia/Oceania								
Australia	$450,000	Yes	$5000	5%	No	2	2	2
New Zealand	$240,000	Yes	$1300	0.1%	No	2	2	2
Europe								
Belgium	$300,000	No	Null	1%	No	3	3	3
Bosnia/Herzegovina	$17,000	No	Null	2%	No	3	2	2
Croatia	$25,000	No	Null	2%	Null	2	3	2
Cyprus	$84,000	Yes	Null	5%	Yes	2	2	3
Denmark	$100,000	No	Null	10%	Yes	2	2	1
Finland	$100,000	No	Null	1%	No	1	2	2
France	$180,000	Yes	$1360	5%	Yes	3	5	4
Germany	$300,000	Yes	$1670	30%	Yes	2	3	2
Greece	$30,000	No	$750	1%	No	2	3	2
Ireland	$235,000	Yes	$8000	35%	No	4	3	4
Italy	$300,000	Yes	$3000	50%	Yes	3	3	4
Lithuania	$14,000	No	Null	3%	No	3	4	4
The Netherlands	$165,000	No	Null	1%	No	2	1	2
Norway	$200,000	Yes	$70	1%	Yes	1	1	1
Portugal	$150,000	Yes	$2000	1%	Yes	2	3	3
Spain	$65,000	Yes	$550	10%	Yes	2	2	3
Sweden	$130,000	No	$550	10%	Yes	2	2	1
Turkey	$40,000	Yes	$300	3%	No	3	3.2	3.4
United Kingdom	$175,000	Yes	$1700	2%	No	2	2	2
Middle East								
Iran	$36,000	Yes	$400	4%	Yes	4	4	3
Iraq	$19,200	No	Null	0%	Yes	3	4	5
Israel	**$72,000**	Yes	$330	2%	No	2	2	2
Lebanon	$120,000	Yes	$200	1%	Yes	4	4	3
Saudi Arabia	$300,000	Yes	$8500	10%	Yes	5	4	3

Note:—Null indicates no response/not applicable.

[a] 1 = never, 2 = rarely, 3 = sometimes, 4 = often, 5 = always.